

CRANFIELD UNIVERSITY

DANAE MARINA PROKOPIOU

DEVELOPMENT OF FOCAL CONSTRUCT GEOMETRY
WITH NON-IDEAL SAMPLES

CRANFIELD DEFENCE AND SECURITY

PhD Thesis
Academic Year: 2013 - 2014

Supervisors: Professor Keith Rogers & Professor Paul Evans
September 2014

CRANFIELD UNIVERSITY

CRANFIELD DEFENCE AND SECURITY

PhD Thesis

Academic Year 2013 - 2014

DANAE MARINA PROKOPIOU

DEVELOPMENT OF FOCAL CONSTRUCT GEOMETRY
WITH NON-IDEAL SAMPLES

Supervisors: Professor Keith Rogers & Professor Paul Evans
September 2014

This thesis is submitted in partial fulfilment of the requirements for the degree of
PhD

© Cranfield University 2014. All rights reserved. No part of this publication may be
reproduced without the written permission of the copyright owner.

ABSTRACT

A novel geometry for powder X-ray diffraction (XRD), termed 'focal construct geometry' (FCG) is introduced and developed with both non-ideal samples and non-ideal sample conditions. FCG utilises an annular beam that has the unique feature of 'focusing' scattering maxima at single loci along a primary axis, hence offering diffraction data of enhanced intensity. This main advantage of FCG can be used within fields in need of rapid material identification, such as security screening in airports.

A theoretical comparison between FCG and conventional transmission mode XRD showed that even though FCG suffers from broader diffraction peaks, an alternative approach to FCG data interpretation has the potential to provide narrower scattering maxima than conventional XRD. However, in order to employ this approach, discrimination between converging and diverging FCG scattering maxima is essential. Peak broadening was investigated by altering various aspects of FCG instrumentation components by either pencil beam XRD or FCG, indicating broad diffraction peaks independent of the beam geometry employed.

Development of FCG resulted in the successful analysis of non-ideal samples, such as non-crystalline liquid samples, samples exhibiting preferred orientation and samples with large grain size, demonstrating advantages over conventional XRD. Furthermore, ideal samples (in terms of crystallinity, preferred orientation and grain size) were analysed by FCG under non-ideal conditions. This involved randomly orientating a single planar sample with respect to the primary axis, contrary to previous research that present FCG with a single planar sample normal to the primary axis. Sample rotation resulted in FCG scattering maxima with different xyz coordinates depending on the degree, axis and direction of rotation. Moreover, FCG analysis of multiple samples (normal to the primary axis) showed that as with all XRD arrangements, *a priori* knowledge of the samples' position along the primary axis is required for effective data analysis.

Investigation into the ability of FCG's annular beam to act as a pre-sample coded aperture demonstrated an alternative method to interpret FCG images by recovering conventional XRD data. Additionally, two novel post-sample encoders (linear wire and Archimedean spiral) were considered. This enabled spatial

ABSTRACT

discrimination of unknown samples along a primary axis and material identification for conventional XRD techniques. Combination of FCG with an absorbing edge post-sample encoder indicated discrimination between converging and diverging FCG scattering maxima. This ability can enable interpretation of single FCG images, as well as depth information of unknown samples within an inspection volume (e.g. airport luggage), hence enabling material identification.

Keywords:

X-ray diffraction, beam geometry, aviation security, coded apertures, encoders, peak broadening, threat liquids, preferred orientation, large grain size, rotated samples, multiple scatterers.

ACKNOWLEDGEMENTS

First and foremost, I would like to express my sincere gratitude to my supervisors Professor Keith Rogers and Professor Paul Evans for their constant guidance and support throughout this study. I am truly grateful for Professor Keith Rogers's endless help, and for sharing his knowledge and experience with me. You have been a great mentor to me and I thank you for that. Professor Paul Evans's advice and encouragement throughout this research have been invaluable, and for that, I am truly grateful.

I would also like to thank my thesis committee, Dr David Lane and Dr Sophie Beckett, for their guidance and recommendations throughout this project.

I thank Dr Anthony Dicken for all his help and guidance, and for always being on the other end of the phone, whenever I had a question. I am also grateful to Dr Simon Godber for his support and technical assistance throughout this study. A huge thank you goes to Adrian Mustey for all his help, whenever I needed technical support or advice.

I would also like to acknowledge the financial support provided. This project was funded under the Innovative Research Call in Explosives and Weapons Detection 2010 initiative. This is a Cross-Government programme sponsored by a number of Departments and Agencies under the UK Government's CONTEST strategy in partnership with the US Department of Homeland Security.

I am also grateful to all my colleagues, and especially my officemates, Deborah Harrison, Ozgur Gulhan and Paraskevi Christogianni, for their help and pleasant breaks, which were often very much needed. Thank you for your patience and endless conversations during these last few months; you have been amazing.

A huge thank you also goes to Katerina, Deborah, Maria, JoJo and Pavlos that have given up their busy schedule to proof read this thesis. Thank you all for helping me!

Finally, I would like to thank my family and friends for their patience and support throughout my studies. Words are not enough to express my gratitude towards my parents and my sister for their help and encouragement all these years. It has not been easy, but your love and support made it possible. Thank you for always being

ACKNOWLEDGEMENTS

there for me to either advise, encourage or motivate me. I am also thankful to all my grandparents for their constant support and for everything they have done for me. A special thank you goes to my good friend Stefani for always being there whenever I needed someone to talk, even when I was boring her with unfamiliar research. Last but not least, I would like to thank Pavlos Mou for his patience and understanding all these years, and for always being next to me, even when being away.

TABLE OF CONTENTS

ABSTRACT	i
ACKNOWLEDGEMENTS	iii
LIST OF FIGURES.....	ix
LIST OF TABLES	xxviii
LIST OF ABBREVIATIONS.....	xxxix
Chapter 1 INTRODUCTION.....	1
1.1 Background	1
1.2 Aims & objectives.....	2
1.3 Thesis outline	2
Chapter 2 AVIATION SECURITY	5
2.1 Bulk detection techniques	8
2.1.1 X-ray transmission systems	9
2.1.2 Dual energy X-ray systems	10
2.1.3 Computed tomography systems.....	11
2.1.4 X-ray diffraction systems	13
2.2 Liquid detection techniques	17
2.2.1 Raman Spectroscopy.....	19
2.2.2 X-ray diffraction	20
2.3 Concluding remarks.....	23
Chapter 3 POWDER X-RAY DIFFRACTION.....	25
3.1 X-ray interactions with matter	25
3.2 Introduction to X-ray diffraction	27
3.2.1 Crystalline materials	27
3.2.2 Fundamental principles of XRD in crystalline materials	29
3.2.2.1 Intensity of diffracted beam.....	30
3.2.2.2 Preferred orientation	31
3.2.2.3 Crystallite size	33
3.2.3 Amorphous materials	34
3.3 Conventional XRD geometries	38
3.3.1 Transmission mode	38
3.3.2 Reflection mode	39
3.3.3 Primary beam profile.....	39
3.4 Comparison between ADXRD and EDXRD	40
3.5 Concluding remarks.....	47

TABLE OF CONTENTS

Chapter 4 CODED APERTURES: INTRODUCTION	49
4.1 Background	49
4.1.1 Analytical description	59
4.2 Encoders	61
4.3 Concluding remarks	64
Chapter 5 FOCAL CONSTRUCT GEOMETRY	65
5.1 Geometry	65
5.2 Previous studies	70
5.3 Research Gap	73
5.4 Concluding remarks	76
Chapter 6 MATERIALS & METHODS	79
6.1 Instrumentation	79
6.1.1 Ray-tracing simulator	80
6.1.2 Empirical approach	81
6.2 Materials	84
6.3 Methodology	89
6.3.1 Alignment	90
6.3.2 Geometric arrangements	91
6.3.2.1 Annular beam arrangement	91
6.3.2.2 Pencil beam arrangement	92
6.3.3 Instrumental broadening	93
6.3.3.1 Comparison of conventional and annular beam geometries	93
6.3.3.2 Collimation system and sample position	93
6.3.3.3 Sample thickness	95
6.3.3.4 Alternative X-ray source (CT system)	95
6.3.4 Analysis of liquid samples	95
6.3.5 Preferred orientation	96
6.3.6 Grain size	98
6.3.7 Randomly orientated planar samples	98
6.3.7.1 Simulation approach	99
6.3.7.2 Empirical approach	100
6.3.8 Multiple scatterers	101
6.4 Data processing	103
Chapter 7 RESULTS	105
7.1 Ray-tracing simulator	105
7.1.1 Single thin planar sample	106
7.1.2 Altering the sample's position	107
7.1.3 Altering the annular beam's wall thickness	107

TABLE OF CONTENTS

7.1.4 Comparison between empirical and simulated data.....	108
7.2 Instrumental broadening.....	110
7.2.1 Comparison of pencil and annular beam geometries.....	110
7.2.2 Collimation optics and sample variations.....	127
7.2.3 Sample thickness.....	129
7.2.4 Alternative X-ray source (CT system).....	135
7.3 Analysis of liquid samples.....	138
7.3.1 Visual inspection.....	138
7.3.2 Analysis of 2D diffraction sequences.....	140
7.3.3 Reproducibility of data.....	145
7.3.4 Comparison between FCG and pencil beam data.....	147
7.4 Preferred orientation.....	149
7.4.1 Theoretical and simulated approach.....	149
7.4.2 Empirical approach.....	152
7.5 Large grain size.....	166
7.5.1 Theoretical and simulated approach.....	166
7.5.2 Empirical approach.....	169
7.6 Randomly orientated planar samples.....	178
7.6.1 Analytical approach.....	179
7.6.2 Simulated data.....	186
7.6.3 Empirical data.....	192
7.6.4 Comparison between empirical data and theory.....	193
7.7 Multiple scatterers.....	197
7.7.1 Same material characteristics.....	198
7.7.2 Different material characteristics.....	201
7.7.3 Comparison between empirical and simulated data.....	203
Chapter 8 CODED APERTURE: EXPERIMENTAL.....	207
8.1 Pre-sample coded aperture.....	208
8.1.1 Simulated data.....	210
8.1.1.1 Proof-of-concept.....	210
8.1.1.2 Two-annulus system.....	219
8.1.1.3 Investigating non-ideal conditions for annular aperture.....	221
8.1.2 Pseudo-empirical data.....	233
8.1.2.1 Preferred orientation.....	237
8.1.2.2 Large grain size.....	239
8.1.3 Empirical FCG data.....	243
8.1.3.1 Non-ideal samples.....	247
8.2 Encoded primary beam.....	250
8.2.1 Simulated data.....	250
8.2.2 Empirical data.....	253

TABLE OF CONTENTS

8.3 Post-sample encoders	255
8.3.1 Linear encoder.....	257
8.3.1.1 Empirical data	264
8.3.2 Archimedean spiral encoder	270
8.3.2.1 Analytical approach	271
8.3.2.2 Empirical approach	277
8.4 Concluding remarks.....	290
Chapter 9 DISCUSSION	291
9.1 Peak broadening	291
9.2 Analysis of liquid samples	298
9.3 Preferred orientation and large grain size.....	301
9.4 Randomly orientated samples	303
9.5 Multiple scatterers	306
9.6 Coded aperture - recovery of Debye rings	308
9.7 Encoders.....	315
9.7.1 Primary beam encoders.....	315
9.7.2 Post-sample encoders.....	317
Chapter 10 CONCLUSIONS & FUTURE WORK.....	323
10.1 Research conclusions	323
10.2 Recommendations for future work.....	327
10.3 Contributions to knowledge	330
REFERENCES	333
APPENDICES.....	347
Appendix A PEAK BROADENING	347
Appendix B MULTIPLE SCATTERERS	355
Appendix C CODED APERTURE	358
Appendix D PUBLICATIONS	360

LIST OF FIGURES

Figure 2.1 An X-ray transmission image of a suitcase under investigation.....	9
Figure 2.2 A dual energy X-ray image of a suitcase under investigation.....	11
Figure 2.3 The densities of a range of threat and non-threat materials often found in a passenger's suitcase [modified from Harding et al. (2012)].....	12
Figure 3.1 The processes (transmission, absorption and scatter) occurring when X-rays are incident upon a material.....	26
Figure 3.2 Characteristic scattering profiles of crystalline solid (a), liquid or amorphous solid (b), monoatomic gas (c), amorphous solid with crystallinity (d) and crystalline solid with air scattering (e) [modified from He (2009)]. ...	28
Figure 3.3 Diagrammatical representation of Bragg's law illustrating the reflection of X-rays from two atomic planes.	29
Figure 3.4 Scattering patterns from a sample with relatively randomly orientated crystallites and small grain size (a), a sample with preferred orientation (b) and a sample with large grain size (c).....	32
Figure 3.5 Diffraction 2D images and corresponding scattering distributions from a crystalline aluminium oxide sample (left) and an amorphous methylated spirit liquid sample (right).	35
Figure 3.6 Illustration of the reference atom and its concentric spheres forming the basis of the radial distribution function [modified from Cote et al. (2001)].	36
Figure 3.7 Schematic illustration of the key features of ADXRD and EDXRD transmission mode arrangements.....	41
Figure 3.8 Scattering profile from cocaine hydrochloride acquired by EDXRD (obtained from Harding (2009)) and by ADXRD (PDF card No. 30-1629).....	42
Figure 4.1 The basic principles of post-sample coded aperture imaging system....	51
Figure 4.2 A graphical representation of a Dirac delta function.	52
Figure 4.3 The autocorrelation plot of a ring-delta function as given by Equation (4.6); for a $r = 8\text{ mm}$ annulus.	56
Figure 4.4 The fundamental concept of tomographic imaging with coded apertures [modified from Chen and Kishimoto (2003)].....	58

LIST OF FIGURES

Figure 4.5 Experimental configuration of a pencil beam coded aperture X-ray scatter imaging system with a comb-like aperture [modified from MacCabe et al. (2012)].	61
Figure 4.6 Experimental arrangement of coded aperture coherent scatter spectral imaging (CACSSI) technique [modified from Greenberg et al. (2013a)].	63
Figure 5.1 A 3D schematic illustration of the focal construct geometry (presenting a limited number of Debye cones). The system is circularly symmetric around the primary beam axis.	66
Figure 5.2 A 2D diagram of the geometrical relationships in a focal construct arrangement.	67
Figure 5.3 Diffraction images from an Al_2O_3 sample measured at 1° less than the 311 convergence point (a), the 311 convergence point (b) (note the high central intensity) and 1° greater than the 311 convergence point (c) [obtained directly from (Rogers et al., 2010)].	68
Figure 5.4 The condensation rings produced by two Bragg's maxima with an annular beam geometry.	68
Figure 5.5 Discretised representation of a continuum of Debye cones forming a converging (a) and diverging (c) condensation ring, and a condensation focus (b). Outer condensation rings are also presented. The red circle represents the primary beam.	69
Figure 5.6 Diffraction image from an aluminium sample with preferred orientation, along with its linear integration at two different azimuthal angles.	71
Figure 5.7 The parallax effect arising from MXAT arrangement.	72
Figure 5.8 A flow diagram illustrating the main research areas of this study along with their aims and objectives.	78
Figure 6.1 Photograph of the FCG instrumentation employed for this work. The red dotted line indicates the primary z-axis of the system.	81
Figure 6.2 The focal construct geometry employed for this work with illustrations of the translational and rotational axes (red arrows) of each instrumentation component.	82
Figure 6.3 Schematic diagram (left) and photograph (right) of the bespoke annular collimator <i>AB1</i> (see Table 6.1).	82

LIST OF FIGURES

Figure 6.4 Photographs of the liquid's sample cells; front view of a 10 mm thick cell (a) and side views of 1.6 mm (b), 5 mm (c) and 10 mm (d) thick cells.....86

Figure 6.5 Photograph of the Al samples positioned in various orientations; *Al_1* (a), *Al_2* (b), *Al_3* (c) and *Al_4* (d).....89

Figure 6.6 Examples of two superimposed images of an aligned annular beam (11.9 mm and 13.8 mm inner radius with 0.3 mm and 0.4 mm wall thickness, respectively) produced by *AB1* collimator (left) and an aligned pencil beam (0.9 mm and 1 mm diameter) produced by *PB2* collimator (right), captured at 190 mm and 220 mm from the X-ray source.....90

Figure 6.7 Schematic illustration of the hollow beam (top) and pencil beam instrumental arrangements (bottom).....92

Figure 6.8 Schematic illustration of the arrangement of FCG with a sample rotation of 40° clockwise around the x-axis (P_x). The X-ray source is considered the origin of the coordinate system, indicated by (0, 0, 0). 100

Figure 7.1 Simulated diffraction images illustrating a single Debye cone (a), two Debye cones (b), four Debye cones (c) and multiple Debye cones (d) converging at a single focal point..... 106

Figure 7.2 Simulated diffraction profiles plotted with respect to the detector's position along the primary axis (A) and 2θ scattering angles (B) from a sample positioned 100 mm, 150 mm, 200 mm and 300 mm away from the X-ray source..... 107

Figure 7.3 Simulated scattering profiles when the annular beam's wall thickness was increased from 0° (A) to 0.1° (B), 0.3° (C) and 0.5° (D). 108

Figure 7.4 Empirical (A) and simulated (B) scattering profiles from Al_2O_3 sample of 0.17 mm thickness when illuminated by an annular beam. 109

Figure 7.5 Empirical FCG data sequence from an Al_2O_3 sample. NB. The non-uniform intensity of the condensation rims is a result of a non-uniform incident beam. 111

Figure 7.6 Scattering profile from an Al_2O_3 sample, obtained by a radial integration of a single FCG image at 24.1 mm (image no. 190) (A) and 16.6 mm (image no. 105) (B) from the sample..... 112

Figure 7.7 Normalised scattering signatures from an Al_2O_3 *S1* plate obtained by the annular beam (A) and pencil beam (B) arrangements and by the Bruker D8-GADDS diffractometer (C)..... 113

LIST OF FIGURES

Figure 7.8 Mean FWHM values of the scattering maxima of Al_2O_3 obtained when illuminated by an annular beam (FCG) and a pencil beam (PB); and when analysed by the benchmark Bruker D8-GADDS diffractometer..... 115

Figure 7.9 Schematic illustration of the width of the diffraction maxima from an infinitely thin sample by pencil beam (top) and annular beam (bottom) arrangements at a certain z-distance. 116

Figure 7.10 The geometric relationships involved in a pencil beam arrangement, with extreme beam divergence for presentation purposes, to determine the widths of the scattering maxima. 117

Figure 7.11 The geometric relationships involved in an FCG arrangement to determine the widths of the scattering maxima. 117

Figure 7.12 Schematic illustration of the width of the diffraction maxima of t thick sample, arising from a pencil beam (top) and annular beam (bottom) arrangement at a certain z-distance. 119

Figure 7.13 The relationships between calculated maximum width of scattering maxima obtained by a pencil beam (PB) and an annular beam geometry, when interpreting around the condensation foci (CF) and condensation rings (CR), with varying scattering angles (A), sample thickness (B), sample's z-position with a fixed sample-to-detector distance (C) and detector's z-position with a fixed sample (D)..... 122

Figure 7.14 Correlation between the calculated maximum width of the scattering maxima obtained by a pencil beam (PB) and an annular beam geometry when integrating around the condensation foci (CF) and condensation rings (CR) with varying beam divergence and beam wall thickness respectively. 123

Figure 7.15 Correlation between the calculated maximum width of the scattering maxima obtained by an annular beam geometry when interpreting around the condensation foci (CF) and condensation rings (CR) with varying angular divergence ϕ_2 (and ϕ_1) and constant beam wall thickness ($\phi_2 - \phi_1$). 124

Figure 7.16 Contribution of 1% increase in all variables (sample thickness, t ; scattering angle, 2θ ; sample position, Z_s ; sample-to-detector distance, D_{SD} ; pencil beam divergence, ϕ_{PB} and beam wall thickness, $\phi_2 - \phi_1$; annular beam divergence ϕ_2) in the width of the scattering maxima. 124

LIST OF FIGURES

Figure 7.17 Scattering signatures from Al₂O₃ (i), synthetic hydroxyapatite (ii) and NaCl (iii) of 1.6 mm (A) and 3 mm (B) thickness, as obtained by an annular beam arrangement..... 129

Figure 7.18 Mean FWHM values of the scattering maxima from Al₂O₃ (i), synthetic hydroxyapatite (ii) and NaCl (iii) powders with 1.6 mm and 3 mm sample thickness, as obtained by an annular beam arrangement..... 131

Figure 7.19 Scattering signatures from Al₂O₃ (i), synthetic hydroxyapatite (ii) and NaCl (iii) of 1.6 mm (A) and 3 mm (B) thickness, as obtained by a pencil beam arrangement..... 133

Figure 7.20 Mean FWHM values of the scattering maxima from Al₂O₃ (i), synthetic hydroxyapatite (ii) and NaCl (iii) powders with 1.6 mm and 3 mm sample thickness, as obtained by a pencil beam arrangement..... 134

Figure 7.21 Sequence of FCG diffraction images obtained from an Al₂O₃ plate within the CT system. The data sequence is displayed from left to right with the condensation focus of 300 reflection in Al₂O₃ illustrated in image no. 18 (red box)..... 136

Figure 7.22 Comparison of the diffraction peak arising from 300 reflection from Al₂O₃, as acquired within the FCG and CT systems. NB. Position offset caused by lack of calibration..... 136

Figure 7.23 Radial integration of diffraction images obtained by the FCG and CT systems, when the 300 reflection from Al₂O₃ was at its focal point..... 137

Figure 7.24 FCG diffraction images of the condensation ring of water (a) and 2-propanol (b) at a 52.2 mm sample-to-detector distance..... 138

Figure 7.25 FCG diffraction images of the condensation ring of coffee (a), methylated spirit (b) and a mixture of the two (c) at a 52.2 mm sample-to-detector distance..... 139

Figure 7.26 FCG diffraction images of the condensation ring of whiskey (a), 2-propanol (b) and a mixture of the two (c) at a 52.2 mm sample-to-detector distance..... 139

Figure 7.27 FCG diffraction images of the condensation ring of water (a), diesel (b) and a mixture of the two (c) at a 52.2 mm sample-to-detector distance. 140

Figure 7.28 FCG diffraction images of the condensation ring of cosmetic foundation cream (a), acetone (b) and a mixture of the two (c) at a 52.2 mm sample-to-detector distance..... 140

LIST OF FIGURES

Figure 7.29 Scattering signatures of all non-threat liquids analysed during this work; including whiskey (A), water (B), coffee (C), cosmetic foundation cream (D) and jam (E).....	141
Figure 7.30 Scattering signatures of all threat liquids analysed during this work; including 2-propanol (A), diesel (B), acetone(C), methylated spirit (D), ethanol (E) and hydrogen peroxide 30% (F).....	141
Figure 7.31 Scattering signatures of water (A), hydrogen peroxide at 3% (B) and 30% (C) concentration.....	143
Figure 7.32 Scattering signatures of 2-propanol and whiskey mixture (A), 2-propanol (B) and whiskey (C).....	144
Figure 7.33 Scattering signatures of methylated spirit and coffee mixture (A), methylated spirit (B) and coffee (C).	144
Figure 7.34 Scattering signatures of acetone and cosmetic foundation cream mixture (A), acetone (B) and cosmetic foundation cream (C).....	144
Figure 7.35 Scattering signatures of diesel and water mixture (A), diesel (B) and water (C).....	144
Figure 7.36 Scattering signatures of methylated spirit acquired after various homing steps and a replaced sample cell (A-G), as well as different sample cell orientation (H) and position (I).....	146
Figure 7.37 Calibrated scattering signatures of methylated spirit acquired after various homing steps, sample translations and dislocations.....	147
Figure 7.38 Scattering signatures of water (i) and methylated spirit (ii) acquired by the annular beam (A) and pencil beam (B) arrangements with 10 seconds time exposure.	148
Figure 7.39 Schematic illustration of an FCG pattern (left) with a condensation focus, a converging condensation ring and a diverging condensation ring produced by Debye cones (top right) of different scattering angles from a sample with extreme preferred orientation.....	149
Figure 7.40 Schematic illustration of an FCG pattern (left) with two converging condensation rings and a diverging condensation ring produced by Debye cones (top right) of different scattering angles from a sample with extreme preferred orientation.....	150
Figure 7.41 Simulated images of a Debye ring from a sample with extreme texture (a), FCG pattern demonstrating a converging condensation ring (b), a	

LIST OF FIGURES

condensation focus (c) and a diverging condensation ring (d) produced by a Debye cone with preferred orientation..... 151

Figure 7.42 Circumferential integration plots of a Debye cone between 2.57-2.65 mm radius (a), an inner converging ring between 0.94-1.02 mm radius (b), an inner diverging ring between 1.22-1.3 mm radius (c) and an outer condensation ring of a condensation focus between 4.8-5.22 mm radius (d). 152

Figure 7.43 Empirical image of a section of the diffraction pattern of Al AS sample obtained by the pencil beam arrangement with collimator *PB1*. 153

Figure 7.44 Complete empirical diffraction pattern of Al AS sample obtained by the pencil beam arrangement with collimator *PB1*. 153

Figure 7.45 Empirical image sequence of the diffraction pattern of Al AS sample obtained by a double-aperture collimator (*AB2*) in the y-direction. 155

Figure 7.46 Empirical image sequence of the diffraction pattern of Al AS sample obtained by a double-aperture collimator (*AB2*) in the x-direction. 156

Figure 7.47 Empirical image sequence of the diffraction pattern of Al AS sample obtained by a quadruple-aperture collimator (*AB3*) in the x and y direction. 157

Figure 7.48 Empirical FCG image sequence of Al AS sample obtained by an annular collimator (*AB1*). 158

Figure 7.49 A simulated annular beam of 1.35 mm inner radius and 0.08 mm thickness (a), simulated image of Debye cones from a sample with preferred orientation representing real-life data (b) and a simulated FCG pattern limited to ~25% of the overall data (c). 159

Figure 7.50 Normalised scattering profiles of an Al sample with extreme preferred orientation obtained from a section of the conventional diffraction pattern (A), from the complete pattern (B) and by FCG (C). 159

Figure 7.51 Empirical diffraction patterns (left) of *Al_1* (a), *Al_2* (b), *Al_3* (c) and *Al_4* (d) samples with their corresponding 3D surface plots (right) as obtained by a pencil beam arrangement. 161

Figure 7.52 Relationship between the transmission coefficient of aluminium and sample thickness for MoK α wavelength ($\rho = 2.7 \text{ gcm}^{-3}$, $\mu/\rho = 5.16 \text{ cm}^2\text{g}^{-1}$) with 0.1° beam divergence. 162

LIST OF FIGURES

Figure 7.53 The relationship between intensity differences (i.e. CN_1) in Debye rings by an angular integration at 17.48° (DC_1), 20.22° (DC_2), 28.74° (DC_3) and 33.84° (DC_4) scattering angles for the empirical PB data from *Al_1* – *Al_4* samples..... 163

Figure 7.54 Scattering signatures of *Al_1* (A), *Al_2* (B), *Al_3* (C) and *Al_4* (D) samples as obtained by FCG..... 164

Figure 7.55 Scattering signatures of *Al_1* sample by FCG (A) and by conventional PB geometry (B) with 10 seconds time exposure. 164

Figure 7.56 Normalised scattering signatures of *Al_1* (i), *Al_2* (ii), *Al_3* (iii) and *Al_4* (iv) samples obtained by an annular (A) and pencil (B) beam arrangement.165

Figure 7.57 Illustration of a converging FCG pattern (left) produced by an annular beam of 33 mm radius and a Debye cone of 14 mm radius consisting of four scattering maxima spots (top right). 167

Figure 7.58 Simulated images of an annular beam of 0.72 mm inner radius and 0.08 mm thickness (a), eight scattering maxima spots spaced at a 3.41 mm radius (b) and their FCG pattern upon convolution (c). 167

Figure 7.59 Simulated images of the Debye cones from a sample with large grain size (a) and its FCG pattern (b). 168

Figure 7.60 Illustration of an FCG pattern (left) with two converging condensation rings and a diverging condensation ring generated by three Debye cones with numerous scattering maxima spots (top right) as in the case of samples with large grain size. 169

Figure 7.61 Empirical diffraction patterns (left) of *Cu_1* (a), *Cu_2* (b), *Cu_3* (c) and *Cu_4* (d) samples with their corresponding 3D surface plots (right) as obtained by a pencil beam arrangement..... 171

Figure 7.62 Representation of the average number of scattering maxima spots present in each Debye ring of each Cu sample (*Cu_2* – *Cu_4*)..... 172

Figure 7.63 Representation of the average size of scattering maxima within a specified integration volume for each Debye ring of each Cu sample (*Cu_2* – *Cu_4*). 173

Figure 7.64 Empirical FCG image sequence of *Cu_4* sample obtained by an annular collimator (*AB1*). 174

Figure 7.65 A single empirical FCG image captured at 20.2 mm from a Cu sample (*Cu_4*) with large grain size. 175

LIST OF FIGURES

Figure 7.66 Scattering signatures of *Cu_1* (A), *Cu_2* (B), *Cu_3* (C) and *Cu_4* (D) samples as obtained by FCG..... 175

Figure 7.67 Scattering signatures of *Cu_1* sample by FCG (A) and by conventional PB geometry (B) with 10 seconds time exposure. 176

Figure 7.68 Normalised scattering signatures of *Cu_1* (i), *Cu_2* (ii), *Cu_3* (iii) and *Cu_4* (iv) samples obtained by an annular (A) and pencil (B) beam arrangement..... 177

Figure 7.69 A 3D view of the annular beam’s footprint onto a clockwise rotated sample around the x-axis, indicating its major and minor axis..... 179

Figure 7.70 The arrangement involved with an annular beam when the sample is rotated by 40° clockwise around the x-axis..... 180

Figure 7.71 Diagrammatical illustration of the geometric relationships involved with an annular beam and a clockwise sample rotation P_x around the x-axis. 181

Figure 7.72 Schematic illustration of the condensation foci formed from 30° and 40° scattering angles when a sample was rotated from (-)70° anticlockwise to (+)70° clockwise in steps of 10° around the x-axis..... 184

Figure 7.73 Graphical representations of the z (a) and y (b) coordinates of the condensation foci at 30° 2θ angle when a sample was rotated from (-)75° anticlockwise to (+)75° clockwise in steps of 1° around the x-axis. 184

Figure 7.74 Schematic illustration of the condensation foci formed from a sample rotated 40° clockwise around the x-axis at a range of 2θ angles from 20°-180° in steps of 10°. 185

Figure 7.75 Graphical representations of the z (a) and y (b) coordinates of the condensation foci formed from a sample rotated 40° clockwise around the x-axis at a range of 2θ angles from 5°-90° in steps of 1°..... 186

Figure 7.76 Simulated diffraction images of a condensation focus when the sample was rotated by 40° anticlockwise (a), 0° (b) and 40° clockwise (c) around the x-axis. The white dotted line is a reference point to mark $y = 0$ 187

Figure 7.77 Simulated diffraction images of a condensation focus when the sample was rotated anticlockwise by 40° around the x-axis (a), 40° around the y-axis (b) and 40° around both x and y axes simultaneously (c). The white dotted lines are a reference point to mark $y = 0$ and $x = 0$ 187

LIST OF FIGURES

Figure 7.78 Simulated diffraction images of a converging (a) and diverging (b) condensation ring from a 40° anticlockwise rotated sample around the x-axis; forming closed curves with a long axis parallel to x and y respectively..... 189

Figure 7.79 Simulated diffraction image of the converging condensation rings from a 40° anticlockwise rotated sample around the x-axis at 19.72° and 25.76° 2θ angles. 191

Figure 7.80 Empirical diffraction images illustrating the formation of a condensation focus when the sample was rotated by 20° anticlockwise (a), 0° (b) and 20° clockwise (c) around the x-axis. The dotted white line is a reference point to mark y = 0. 193

Figure 7.81 Schematic diagrams indicating the condensation foci formed from a sample rotation of 40° anticlockwise (green), 40° clockwise (blue) and 0° (red) at different intersection points of the rotation axes; on (A), above (B) and below (C) the z-axis. 195

Figure 7.82 Diffraction signatures from two Al₂O₃ (S1 and S2) plates separated by 9.4 mm along the z-axis (A), a single Al₂O₃ (S2) plate (B) and a single Al₂O₃ (S1) plate (C). 198

Figure 7.83 Diffraction signatures from two Al₂O₃ (S1 and S2) plates separated by 9.4 mm along the z-axis (A) and a single Al₂O₃ (S2) plate (B). 199

Figure 7.84 Diffraction signatures from two Al₂O₃ (S1 and S2) plates separated by 9.4 mm along the z-axis (A) and a single Al₂O₃ (S1) plate (B). 199

Figure 7.85 Diffraction signatures from an Al₂O₃ (S1) and Al (AS) plates separated by 10.3 mm along the z-axis (A), a single Al (AS) plate (B) and a single Al₂O₃ (S1) plate (C). 201

Figure 7.86 Diffraction signatures from an Al₂O₃ (S1) and Al (AS) plates separated by 10.3 mm along the z-axis (A) and a single Al (AS) plate (B). 202

Figure 7.87 Diffraction signatures from an Al₂O₃ (S1) and Al (AS) plates separated by 10.3 mm along the z-axis (A) and a single Al₂O₃ (S1) plate (B). 202

Figure 7.88 Empirical (A) and simulated (B) scattering signatures of Al₂O₃ (top) and Al (bottom). 204

Figure 7.89 Simulated diffraction signatures from an Al₂O₃ and Al plates separated by 10.3 mm along the z-axis (A), a single Al plate (B) and a single Al₂O₃ plate (C). 205

LIST OF FIGURES

Figure 8.1 The arrangement and procedure involved with a pre-sample annular coded aperture in diffraction space. 209

Figure 8.2 A 2D image (a), a 2-D plot profile (b) and a 3-D surface plot (c) of the $\sim\delta$ -function generated by the auto-correlation of an annular aperture. 210

Figure 8.3 Simulated images of an annular primary beam (a), two Debye rings (b), their FCG pattern (c), the recovered image prior to any processing (d), the processed image after bandpass filtering (e) and the recovered Debye rings after a 175 dc level removal (f). 211

Figure 8.4 Radial integration of simulated image consisting of two Debye rings (A) and corresponding recovered image (B). 212

Figure 8.5 Schematic illustration of the convolution of an annular beam (top left) with two Debye cones (top right) to produce an FCG pattern (bottom). 213

Figure 8.6 Schematic illustration of the convolution (bottom) of an annular beam (top left) with an FCG pattern (top right) to reconstruct the Debye cones. 213

Figure 8.7 Schematic illustration of the convolution of a δ -function approximation (top left) with two Debye cones (top right) to reconstruct the Debye cones and additional rings (bottom). 215

Figure 8.8 Simulated images obtained upon convolution of the Debye rings with the annular beam's SPSF (a), with the outer ring of the annular beam's SPSF (b), and the result of their subtraction (c). 216

Figure 8.9 A simulated image of the annular beam's SPSF (top left) and a 2D plot profile of the image (bottom right) indicating the latter's maximum noise intensity (N_{max}). 217

Figure 8.10 A simulated image of the reconstructed Debye rings (top left) post-filtering (bandpass) and a 2D profile plot of the image (bottom right) indicating the additional dc level of the recovered image. 218

Figure 8.11 A line profile plot across the x pixels of the Debye rings image and the post-processed recovered image. 219

Figure 8.12 Simulated images of the recovered image obtained by the two-annulus system prior (a) and post (b) bandpass filtering and dc removal (85). 220

Figure 8.13 Comparison of the recovered images' cross section profiles along the x-axis for the two-annulus approach (A) and single annulus coded aperture (B), when bandpass filtering was applied and an 85 dc level was subtracted. 220

LIST OF FIGURES

Figure 8.14 Simulated images of an annular primary beam of 1.08 mm inner radius (a), three ideal Debye rings (0.46 mm, 1.08 mm and 2.43 mm inner radius) (b), their FCG pattern (c), the recovered image prior to any processing (d), the processed image after applying a bandpass filter (e) and the recovered Debye rings after a 170 dc level (f). 222

Figure 8.15 Radial integration of the simulated image consisting of three Debye rings (A) and corresponding recovered image (B). 223

Figure 8.16 Simulated image of a noisy FCG pattern (a) and the recovered image via deconvolution (b). 223

Figure 8.17 Simulated images of an annular aperture (a), three Debye rings (b), their convolved FCG pattern (c) and the recovered Debye rings via deconvolution (d). 223

Figure 8.18 Simulated FCG images with increasingly added noise. The FCG images were obtained by convoluting a series of noisy images of three Debye rings (0.46 mm, 1.08 mm and 2.43 mm inner radius and 0.08 mm thickness) with an equivalent series of noisy images of an annular beam of 1.08 mm inner radius and 0.08 mm thickness. 224

Figure 8.19 Reconstructed images of the Debye rings, as obtained by the convolution of noisy FCG images (presented in Figure 8.18) with an annular beam of 1.08 mm inner radius and 0.08 mm thickness. 225

Figure 8.20 Post-processed reconstructed images of the Debye rings, as obtained by the convolution of noisy FCG images with an annular beam of 1.08 mm inner radius and 0.08 mm thickness, after a dc level removal (between 100-180). 225

Figure 8.21 Relationship between PSNR of the diffraction (FCG) data and corresponding recovered Debye cones. The red dotted line is a reference point to mark $y=x$ 226

Figure 8.22 Radial integration of recovered images from noiseless FCG data (A) and from FCG data with a PSNR of 33.79 (B), 18.85 (C), 10.87 (D), 6.45 (E) and 5.97 (F). 227

Figure 8.23 Simulated diffraction images with limited FCG area (top) and corresponding reconstructed images of Debye rings (bottom). Top and bottom images numbered 0 illustrate the complete FCG pattern and the corresponding reconstructed image, respectively. 228

LIST OF FIGURES

Figure 8.24 Radial integration (A-F) of recovered images from a limited area of FCG data (0-5)..... 228

Figure 8.25 Reconstructed (post-processed) images of the Debye rings obtained by the convolution of the diffraction patterns with annular beams of increasing wall thickness. 230

Figure 8.26 Scattering signatures of the recovered Debye rings reconstructed with an annular beam of 0.03 mm (A), 0.08 mm (B), 0.13 mm (C), 0.28 mm (D), 0.48 mm (E), 0.68 mm (F), 0.88 mm (G), 1.08 mm (H) and 1.18 mm (I) wall thickness..... 230

Figure 8.27 Reconstructed (post-processed) images of the Debye rings obtained by the elliptical apertures with their major axis in the x direction. 232

Figure 8.28 Scattering signatures of the Debye rings reconstructed with an annular aperture (A) and with elliptic apertures with x major axis; ellipses number 2 (B), 4 (C), 6 (D), 8 (E), 10 (F) and 11 (G). 232

Figure 8.29 Details on the nature of experiments performed throughout Section 8.1..... 233

Figure 8.30 Empirical diffraction image from an Al_2O_3 sample (S1) illustrating 2θ angles from $\sim 8^\circ$ - 36° (left) and its reconstructed image (right) after convolution with an annular aperture of 14.2 mm inner radius and 0.25 mm wall thickness. 234

Figure 8.31 Scattering signatures of the empirical diffraction image from an Al_2O_3 (S1) sample and of the corresponding reconstructed diffraction pattern. The profile of the reconstructed diffraction image is displayed on a secondary axis for presentation purposes. 235

Figure 8.32 A binary empirical diffraction image from an Al_2O_3 sample (S1) illustrating 2θ angles from $\sim 8^\circ$ - 36° (left) and its reconstructed image (bottom) after convolution with an annular aperture of 14.2 mm inner radius and 0.25 mm wall thickness..... 236

Figure 8.33 Scattering signatures of the empirical binary diffraction image from an Al_2O_3 (S1) sample and of the corresponding reconstructed diffraction pattern. The profile of the reconstructed diffraction image is displayed on a secondary axis for presentation purposes. 236

Figure 8.34 Pseudo-empirical recovered diffraction patterns from *Al_1-Al_4* (rec_a-rec_d) and the corresponding empirical diffraction patterns from *Al_1-*

LIST OF FIGURES

Al_4 samples (a–d). The corresponding scattering signatures of the empirical (A) and recovered (B) diffraction patterns are presented for each Al sample next to their diffraction images. 238

Figure 8.35 The relationship between intensity differences (i.e. CN_1) in Debye rings by an angular integration at 17.48° (DC_1), 20.22° (DC_2), 28.74° (DC_3) and 33.84° (DC_4) scattering angles for the reconstructed diffraction images from *Al_1* – *Al_4* samples. 239

Figure 8.36 Pseudo-empirical recovered diffraction patterns from *Cu1*–*Cu_4* (rec_a–rec_d) and the corresponding empirical diffraction patterns from *Cu_1*–*Cu_4* samples (a–d). The corresponding scattering signatures of the empirical (A) and recovered (B) diffraction patterns are presented for each Cu sample next to their diffraction images. 240

Figure 8.37 Average number of scattering maxima spots present in each recovered Debye ring at 0.209 nm (Ring 1), 0.181 nm (Ring 2) and 0.128 (Ring 3) from each Cu sample *rec_Cu_2* – *rec_Cu_4*..... 242

Figure 8.38 The percentages of average number of scattering maxima spots present in each Debye ring for the empirical diffraction patterns from samples *Cu_2* – *Cu_4* (left) and the recovered patterns *rec_Cu_2* – *rec_Cu_4* (right)..... 242

Figure 8.39 Diagram of the scaling steps followed with empirical FCG data images. 243

Figure 8.40 An FCG image from Al_2O_3 captured at 15 mm from the sample. The canvas size of the image was increased to 3024 x 3024 pixels by an opaque surrounding area..... 244

Figure 8.41 Recovered images of the Debye rings from an FCG sequence at 9 mm, 12 mm, 15 mm, 18 mm, 21 mm, 24 mm, 28 mm, 32 mm, 39 mm and 44 mm sample-to-detector distances..... 245

Figure 8.42 Empirical diffraction image (a) and reconstructed diffraction image (b) from an Al_2O_3 sample, as recovered from a sequence of empirical FCG data. 246

Figure 8.43 Comparison of the diffraction profiles from the recovered diffraction data from Al_2O_3 (A) with a limited sequence of FCG images with the empirical FCG diffraction profile from Al_2O_3 (B)..... 247

Figure 8.44 Recovered diffraction image (top) from a limited sequence of empirical FCG data obtained from an Al sample (*Al_1*). Scattering profiles

LIST OF FIGURES

(bottom) from the recovered diffraction image (A) and from the FCG data (B).
 248

Figure 8.45 Recovered diffraction image (top) from a limited sequence of empirical FCG data obtained from a Cu sample (*Cu_4*). Scattering profiles (bottom) from the recovered diffraction image (A) and from the FCG data (B).
 249

Figure 8.46 Simulated images of an encoded annular aperture of 1.34 mm radius and 0.08 mm thickness (a), two Debye rings of 0.75 mm and 1.65 mm radius and 0.08 thickness (b) and the FCG pattern produced by their convolution (c).
 251

Figure 8.47 A magnified image of the FCG pattern produced by an encoded annular beam illustrating a converging and diverging condensation rings (left); azimuthal integration around the converging (A) and diverging (B) inner condensation rings arising from an encoded annular beam (C) (right). Profile (A) is displayed on a secondary axis for presentation purposes..... 252

Figure 8.48 Simulated images (top) of the self-convolution of an encoded annular beam (i) and the corresponding recovered Debye rings (ii). The radial integration profiles (bottom) of the simulated Debye cones (A) and of the corresponding recovered Debye rings (B) are presented..... 252

Figure 8.49 Empirical image of an encoded annular beam. 253

Figure 8.50 A sequence of empirical FCG diffraction images from an Al₂O₃ sample obtained with an encoded primary beam..... 254

Figure 8.51 The geometry involved with a ‘comb’ harmonic coded aperture (CA) when illuminating a sample with an annular beam..... 255

Figure 8.52 Simulated images of an off-centre linear aperture (a), multiple Debye rings of known radius (b) and the encoded Debye rings (c)..... 258

Figure 8.53 Schematic illustration of ζ angle and α_{LE} distance when using a linear coded aperture. 258

Figure 8.54 The geometric arrangement employed to record the 2D X-ray diffraction data encoded by a single linear encoder (LE), when illuminated by a pencil beam. 259

Figure 8.55 Empirical images of the wire aperture’s footprint on the detector indicating the off-centre distance α_{LE} (a) and the scattering distribution from a single Al₂O₃ sample (b) that has been encoded by a single wire encoder..... 264

LIST OF FIGURES

Figure 8.56 Scattering distribution from a pair of CaCO_3 loaded cellulose sample spatially separated along the primary axis and encoded from a single wire encoder.....266

Figure 8.57 A sequence of empirical FCG diffraction images from an Al_2O_3 sample obtained with an absorbing edge acting as a post-sample coded aperture. ..269

Figure 8.58 The Archimedean spiral encoder (left) and the ambiguity in radius for multiple turns (n) of the spiral (right).....270

Figure 8.59 Simulated images of an Archimedean spiral (a), multiple Debye rings of known radius (b) and the encoded Debye rings (c).271

Figure 8.60 Magnified simulated image of the encoded Debye rings by an Archimedean spiral.272

Figure 8.61 A 2D schematic diagram of a post-sample Archimedean spiral encoder for a pencil beam arrangement (side view). The Archimedean spiral is illustrated in front view.272

Figure 8.62 Graphical illustration of the measured ψ angles against the calculated radii of the Debye cones onto the Archimedean spiral (R_{AS}).274

Figure 8.63 A series of empirical diffraction images captured as a CaCO_3 loaded cellulose sample was translated along the primary beam axis with an Archimedean spiral encoder.....278

Figure 8.64 A series of empirical diffraction images captured as an Al_2O_3 sample was translated along the primary beam axis with an Archimedean spiral encoder.....279

Figure 8.65 Illustration of the encoding caused by the Archimedean spiral for the 104 reflection from CaCO_3 ; at radius R_D and encoded angle ψ . The encoding causes a single intensity minimum for each Debye ring.....280

Figure 8.66 The scattering intensity of a single Debye ring (104 reflection from CaCO_3) around its circumference as the sample was translated along the primary axis.....281

Figure 8.67 Counter plots of the encoding angle on the 104 Debye ring of CaCO_3 (left) and Al_2O_3 (right) samples, as the sample was translated along the primary axis.....281

Figure 8.68 The relationship between measured encoding angles ψ from the diffraction data of a CaCO_3 loaded cellulose and the radii of the Debye cones

LIST OF FIGURES

onto the Archimedean spiral (R_{AS}), as calculated from CaCO_3 's scattering angle 29.4° 282

Figure 8.69 Correlation between calculated sample-to-detector distances obtained from spiral encoding and Debye rings for the 104 Debye ring of CaCO_3 284

Figure 8.70 Comparison of the scattering distribution from a CaCO_3 loaded cellulose sample as recovered by a calibrated Archimedean spiral encoder (A) and from a standard profile of CaCO_3 (PDF card No. 5-586) (B). 284

Figure 8.71 Correlation between calculated sample-to-detector distances obtained from spiral encoding and Debye rings for the 104 Debye ring of Al_2O_3 286

Figure 8.72 A sequence of diffraction images obtained from a pair of CaCO_3 loaded cellulose samples, where one was translated along the primary axis and the other was fixed. The scattering distributions were encoded by an Archimedean spiral (0.055ψ). 287

Figure 9.1 Schematic of the geometry involved with an annular beam and a clockwise-rotated sample around the x-axis. 304

Figure 10.1 A flow diagram illustrating the main research areas of this study along with their key outcomes. 326

Figure 10.2 An Archimedean spiral encoder with an extended structure for FCG experiments. 329

Figure A.1 Relationship between measured widths of Debye rings' wall thickness as the collimator was translated from 129.1 mm – 155.5 mm in steps of 1 mm. Graphs A-F correspond to the six Debye rings from low to high 2θ angles for experiment *DPtr106* (see Table 6.6). 347

Figure A.2 Diffraction images of Al_2O_3 acquired with 0.38° (a) and 0.14° (b) total pencil beam divergence ($2\phi_{PB}$) during experiments *DPtr115* and *DPtr143*, respectively (see Table 6.6). 348

Figure A.3 Scattering profile from Al_2O_3 acquired with 0.38° (A) and 0.14° (B) total pencil beam divergence ($2\phi_{PB}$) during experiments *DPtr115* (A) and *DPtr143* (B). 348

Figure A.4 Mean FWHM values of the scattering maxima of Al_2O_3 obtained with 0.38° and 0.14° total pencil beam divergence ($2\phi_{PB}$) during experiments *DPtr115* and *DPtr143* respectively. 349

LIST OF FIGURES

Figure A.5 Images of the primary beam (top) resulting from collimator *PB5* attached to the X-ray source (a), collimator *PB5* positioned 129.1 mm from the X-ray source (b), collimator *PB6* (c) and collimator *PB7* (d). The corresponding scattering distributions from Al_2O_3 sample are also presented (bottom images). 349

Figure A.6 Scattering profiles of Al_2O_3 when illuminated by a pencil beam of total divergence of 0.38° (A), 0.14° (B), 0.16° (C) and 0.015° (D). 350

Figure A.7 Mean FWHM values of the scattering maxima of Al_2O_3 obtained with 0.38° 0.14° , 0.16° and 0.015° total pencil beam divergence..... 350

Figure A.8 Scattering profiles of Al_2O_3 when illuminated by a pencil beam at 28 mm (A), 38 mm (B), 48 (C), 58 mm(D), 68 mm (E), 78 mm (F) and 88 mm (G) sample-to-detector distances. 351

Figure A.9 Mean FWHM values of the scattering maxima of Al_2O_3 with a sample-to-detector distance from 28-88 mm. 351

Figure A.10 Comparison of the scattering profiles of an Al_2O_3 sample at a different position along the primary axis; 176 mm (A) and 162 mm (B) with similar sample-to-detector distance of 64 mm and 68 mm respectively. 352

Figure A.11 Mean FWHM values of the scattering maxima of Al_2O_3 when positioned 176 mm (DPtr115) and 162 mm (DPtr130) from the X-ray source; at a 64 mm and 68 mm sample-to-detector distance, respectively..... 352

Figure B.1 Diffraction signatures from two Al_2O_3 (*S1* and *S2*) plates separated by 31 mm along the z-axis (A), a single Al_2O_3 (*S2*) plate (B) and a single Al_2O_3 (*S1*) plate (C). 355

Figure B.2 Diffraction signatures from two Al_2O_3 (*S1* and *S2*) plates separated by 31.3 mm along the z-axis (A) and a single Al_2O_3 (*S2*) plate (B). 355

Figure B.3 Diffraction signatures from two Al_2O_3 (*S1* and *S2*) plates separated by 31.3 mm along the z-axis (A) and a single Al_2O_3 (*S1*) plate (B). 356

Figure B.4 Diffraction signatures from an Al_2O_3 (*S1*) and Al (*AS*) plates separated by 11.8 mm along the z-axis (A), a single Al (*AS*) plate (B) and a single Al_2O_3 (*S1*) plate (C). 356

Figure B.5 Diffraction signatures from an Al_2O_3 (*S1*) and Al (*AS*) plates separated by 11.8 mm along the z-axis (A) and a single Al (*AS*) plate (B). 357

Figure B.6 Diffraction signatures from an Al_2O_3 (*S1*) and Al (*AS*) plates separated by 11.8 mm along the z-axis (A) and a single Al_2O_3 (*S1*) plate (B). 357

LIST OF FIGURES

Figure C.1 Representative examples of simulated images of a series of annular apertures when the wall thickness increased to 0.03 mm (1), 0.08 mm (2), 0.13 mm (3), 0.28 mm (6), 0.48 mm (10), 0.68 mm (14), 0.88 mm (18), 1.08 mm (22) and 1.18 mm (24)..... 358

Figure C.2 Simulated images of the elliptical apertures with major axis in the x direction..... 359

LIST OF TABLES

Table 2.1 Non X-ray methods for the detection of illicit substances.....	8
Table 2.2 Electromagnetic methods for the detection of liquid explosives [modified from Kuznetsov and Osetrov (2008)].	19
Table 2.3 Classification scheme of different threat and non-threat liquids for aviation security as provided by Harding et al. (2010).....	22
Table 3.1 Advantages and limitations of ADXRD and EDXRD.	47
Table 6.1 Details on the collimation optics utilised during the experimental work.	83
Table 6.2 The polycrystalline samples analysed during the experimental work.	85
Table 6.3 The liquid samples analysed.....	87
Table 6.4 The liquid mixtures analysed.....	88
Table 6.5 A list of the electrodeposited copper samples employed during the analysis of large grain size with the time and temperature of their heat treatment.....	89
Table 6.6 Details on the experimental arrangements employed with various collimation optics and angular beam divergence.....	94
Table 6.7 Details on the experimental arrangements during the analysis of an Al sample exhibiting preferred orientation.....	97
Table 6.8 A list of the simulated experiments performed with a random sample orientation and details on their rotation around the x and y axes.	99
Table 6.9 Details on the experiments conducted with two overlapping samples by FCG.....	102
Table 7.1 Quantitative comparison of the diffraction maxima positions of Al ₂ O ₃ from the PDF card No. 75-1862, simulation and empirical data.	109
Table 7.2 Quantitative comparison of the diffraction maxima positions and FWHM values from an Al ₂ O ₃ sample; as obtained by the annular beam (FCG) and pencil beam (PB) geometries, and by the Bruker D8-GADDS diffractometer.	114
Table 7.3 Quantitative comparison of Al ₂ O ₃ 's scattering peak areas as obtained by the annular (FCG) and pencil (PB) beam geometries with 10 seconds time exposure.	127

LIST OF TABLES

Table 7.4 The ratio values obtained by the FWHM of empirical data and the calculated maximum length of the condensation foci for Al₂O₃, hydroxyapatite and NaCl samples from 3 mm and 1.6 mm thickness..... 132

Table 7.5 The scattering vector magnitude for all threat and non-threat liquids analysed during this study..... 142

Table 7.6 Scattering vector magnitudes of the mixtures of threat and non-threat liquids analysed. 145

Table 7.7 The coordinates of condensation foci upon sample rotation around different axis. 188

Table 7.8 Analytical, simulation and empirical results of the y and z coordinates of the condensation foci of Al₂O₃ measured at 19.9° 2θ angle when rotated around the x-axis..... 196

Table 7.9 Simulation and empirical radial measurements from the condensation focus (0.206 nm) to the condensation ring (0.235 nm) at circular angles of 0° - 315° in steps of 45°..... 197

Table 8.1 The FWHM values of the Debye rings and the recovered Debye rings. 219

Table 8.2 The results of the measured radii of the Debye cones as captured by the detector (R_D), the measured intersection angle ζ, the calculated radii of the Debye cones when intersected with wire encoder (R_{LE}), the calculated sample-to-detector distances (D_{SD}) using different approaches and the calculated scattering (2θ) angles for Al₂O₃..... 265

Table 8.3 The results of the measured radii of the Debye cones as captured by the detector (R_D), the measured intersection angle ζ, the calculated radii of the Debye cones when intersected with wire encoder (R_{LE}), the calculated sample-to-detector distances (D_{SD}) using different approaches and the scattering (2θ) angles for two sheets of mineral (CaCO₃) loaded cellulose separated along the z-axis..... 267

Table 8.4 Measurements of the radii of the Debye cones at the detector's plane (R_D) when magnified by 1.5, the ψ angle of the opaque points on the Debye cones and the calculated radii of the Debye cones onto the Archimedean spiral, as indicated by R_{AS}=a+bψ. The calculated sample-to-detector distance (D_{SD}) from each Debye cone is given. 274

Table 8.5 Measurements of the radii of the Debye cones (R_D) captured at 180 mm, 190 mm and 200 mm from the X-ray source and their corresponding

LIST OF TABLES

intersection angles ψ obtained from the ray-tracing simulated data when the Archimedean spiral was rotated 20° clockwise around the y-axis. The calculated radii of the Debye cones onto the Archimedean spiral, the sample-to-detector distances and the scattering angles 2θ are presented..... 276

Table 8.6 A list of the calibrated radii of the Debye cone onto the Archimedean spiral calculated via $RAS = 0.00009\psi^2 + 0.0171\psi + 1.304$ and the corresponding calculated sample-to-detector distances and scattering angles (2θ) for CaCO₃ (mineral loaded cellulose)..... 283

Table 8.7 A list of the measured radii of the Debye cones (R_D) and intersection angles ψ at each diffraction image, the calibrated radii of the Debye cone onto the Archimedean spiral calculated via $RAS = 0.00009\psi^2 + 0.0171\psi + 1.304$ and the corresponding calculated sample-to-detector distances and scattering angles (2θ) for Al₂O₃. 285

Table 8.8 A list of the measured radii of the Debye cones (R_D) and intersection angles ψ at each diffraction image, the calibrated radii of the Debye cone onto the Archimedean spiral calculated via $RAS = 0.00009\psi^2 + 0.0171\psi + 1.304$ and the corresponding calculated scattering angles (2θ) for two CaCO₃ loaded cellulose sheets. 287

Table A.1 List of FWHM values of FCG data for Al₂O₃, hydroxyapatite and NaCl with 1.6 mm and 3 mm sample thickness, and corresponding calculated lengths of the condensation foci..... 353

Table A.2 List of FWHM values of conventional XRD data for Al₂O₃, hydroxyapatite and NaCl with 1.6 mm and 3 mm sample thickness. 354

Table C.1 Information on the limitation of the FCG images obtained from two different primary beam annuli in terms of circular and squared area in which the diffraction data are limited to either around the centre of the image (central) or around the outer circumference of the FCG data (peripheral). The percentage of data availability with respect to the complete diffraction pattern is given..... 358

Table C.2 Details on the ellipses employed as a primary beam indicating with x-axis as the major axis and constants (a, b) of each $ax^2 + by^2 = 1$ ellipse..... 359

LIST OF ABBREVIATIONS

AB	Annular beam
ADXRD	Angular dispersive X-ray diffraction
CACSSI	Coded aperture coherent scatter spectral imaging
CAI	Coded aperture imaging
CCD	Charge coupled device
CF	Condensation focus
CR	Condensation ring
CT	Computerised tomography
DC	Debye cone
EDXRD	Energy dispersive X-ray diffraction
ETD	Explosive trace detection
FCG	Focal construct geometry
FWHM	Full width half maximum
FZP	Fresnel zone plate
HME	Home-made explosives
LAG	Liquids, aerosols and gels
MIF	Molecular interference factor
MIFB	Multiple inverse fan beam
MURA	Modified uniformly redundant array
MXAT	Multidirectional X-ray absorption tomography
NIST	National institute of standards and technology
NRA	Non-redundant array
PB	Pencil/pinhole beam
PDF	Powder diffraction file
PSNR	Peak signal-to-noise ratio
PXRD	Powder X-ray diffraction
RDF	Radial distribution function
rTEDDI	Rapid tomographic energy dispersive diffraction imaging
SNR	Signal-to-noise ratio
SORS	Spatially offset Raman spectroscopy
SPSF	System point spread function

LIST OF ABBREVIATIONS

URA	Uniformly redundant array
XDI	X-ray diffraction imaging
XRD	X-ray diffraction

Chapter 1 INTRODUCTION

Outline

This chapter offers an introduction to the research area involved during this study. A novel geometry for X-ray diffraction is presented alongside its key advantages. The aims and objectives of this research are then identified. Finally, the presentation structure of the thesis is outlined.

1.1 Background

X-ray diffraction (XRD) is a non-destructive, material specific analytical technique with applications in a wide range of fields, such as engineering, forensic science, pharmaceutical industries, geological applications and others. XRD is often applied for rapid identification of unknown substances as well as to obtain structural information and characterisation.

This research focused on the development and characterisation of a novel geometry for powder X-ray diffraction (PXRD), referred to as focal construct geometry (FCG), with a variety of non-ideal samples or conditions. FCG is a very promising emerging technique developed and presented by Rogers et al. (2010). Initial research on this novel geometry (Chan et al., 2010, Rogers et al., 2010) has established proof-of-principle, demonstrating the capabilities of FCG to produce conventional diffractograms with higher intensity than traditional XRD techniques. FCG's uniqueness and advantages lie within its hollow conical beam arrangement that 'focuses' multiple diffraction maxima into single condensation foci, along a primary axis, with significantly enhanced intensity. A detailed description of the focal construct geometry and instrumental arrangements are given in Chapter 5.

1.2 Aims & objectives

The aims of this research were to develop, characterise and improve FCG by exploring its full potential with non-ideal samples or near-ideal samples (in terms of preferred orientation and grain size) under non-ideal conditions, with particular respect to aviation security screening. Furthermore, the capabilities of FCG to act as a two-step coded aperture system to recover conventional XRD data was assessed and innovative encoders for spatial discrimination of unknown samples were examined.

The objectives of this research were as listed below:

- Investigate the fundamental differences between scattering maxima arising from conventional XRD and FCG.
- Assessment of peak broadening phenomenon with FCG.
- FCG analysis of non-crystalline samples, such as liquid samples that can be considered as a threat or non-threat to aviation security.
- Identify the potential of FCG in analysing non-ideal samples exhibiting preferred orientation or large grain size and compare them to conventional diffraction patterns.
- Development of FCG with non-ideal sample orientation, e.g. randomly rotated sample.
- Investigation of the effect of multiple scatterers on FCG and determine possible recovery of their individual diffraction patterns.
- Assessment of novel encoders aiming at spatial discrimination and identification of unknown samples within an inspection volume.
- Introduce the concept of an annular beam to act as a pre-sample coded aperture in order to recover conventional diffraction images, i.e. Debye rings, from FCG data and examine its potential under various non-ideal conditions.

1.3 Thesis outline

This research involved the development of FCG through a number of different aspects for main application in security screening. In Chapter 1, an introduction into the research area of this thesis is presented, along with the aims and objectives of

this study. A brief review of the current screening systems and concepts for aviation security is given within Chapter 2. X-ray diffraction (XRD) is identified as one of the most promising conceptual screening techniques for luggage screening. In Chapter 3, the fundamental principles underlying XRD are introduced, including non-ideal samples for XRD, in terms of crystallinity, crystallite preferred orientation and grain size. Chapter 4 provides a systematic literature review on the history and implementation of coded aperture systems, in a non-diffraction space. Coded apertures acting as scattering maxima encoders are then discussed, mainly in relation to XRD and security screening. In Chapter 5, the annular beam geometry referred to as 'focal construct geometry' (FCG) employed throughout this work is presented. The basic principles of FCG as derived from previous studies are explained and the main research gaps are identified. Based on these gaps, the main objectives of this work are presented. The materials and methodology employed in the experimental work presented within this thesis are given in Chapter 6. In Chapter 7, the results obtained from the experimental work aimed at the development of FCG with non-ideal samples or non-ideal sample conditions are presented. The experimental work (including methodology) and corresponding results, performed with coded aperture systems, such as FCG acting as a pre-sample coded aperture as well as novel post-sample encoders, is presented in Chapter 8. A critical discussion of all experimental work performed is given within Chapter 9. Finally, in Chapter 10, the main conclusions drawn from this study are identified and recommendations for future work, directly related to this project, are provided. The key contributions of this research to scientific knowledge are also explained in Chapter 10.

Chapter 2 AVIATION SECURITY

Outline

The main application of the novel beam geometry for XRD developed in this work is identified as security screening of luggage at airports. This chapter highlights the importance of effective luggage screening in aviation security and describes the prominent technologies employed. Screening systems are separated into bulk detection and liquid detection techniques. The main techniques engaged for both categories are presented and compared in terms of significance in aviation security. Finally, a summary of the key features of security screening techniques is given.

Over the last four decades, there has been an increased interest in aviation security worldwide. Alarms were significantly raised when eight commercial aircrafts were affected by terrorist bombings between 1985 and 1997, where almost 1100 people lost their lives as a result of them (Novakoff, 1992, Singh and Singh, 2003). Following these, the events of 9/11, where almost 3500 died, raised the awareness globally and increased the demand of new screening techniques to be developed and employed (Shea and Morgan, 2007, Oster Jr et al., 2013). Research has been focused on the development of pioneering technologies for luggage screening, as they provide one of the primary lines of defence in airports.

Prior to the Pan Am Flight 103 incident in 1988, when a bomb exploded resulting in 270 fatalities (Oster Jr et al., 2013), airport security focused on the detection of weapons such as guns and ammunition, hence high atomic number (Z) metallic objects, rather than explosives (Novakoff, 1992, Murray et al., 1997, Speller, 2001). The necessity for technologies able to detect low Z objects, such as explosives, was then raised. Detection of low Z explosives in highly cluttered checked luggage is however, a more challenging task than the detection of high Z weapons in low clutter carry-on bags (Connelly et al., 1998). Furthermore, the later events of 9/11

demanded all checked luggage to be screened for explosives (100% check policy); whereas prior to that only a small number of checked bags was screened (Leone and Liu, 2005, Lee et al., 2008, Kirschenbaum, 2013, Alards-Tomalin et al., 2014).

Screening systems must therefore fulfil certain requirements in order to be accounted as functional and applicable for aviation security. The core functionalities of a screening technique include high sensitivity in identifying any volumes of threat materials, high specificity to reduce false alarm rates and high throughput in the shortest period of time possible (<5 seconds (Wells and Bradley, 2012)). A false alarm or false positive is the probability of a device to raise alarms for luggage with non-threat contents. In cases of alarm, the luggage must pass several screening levels before it can be cleared for aircraft loading (Candalino jr et al., 2004, Leone and Liu, 2011). Therefore, false positives can prove very costly as they can delay passengers and flights and result in loss of confidence in the system by the operators. Moreover, false negatives (or false clears), where luggage containing threat objects are cleared, are the main reason of illegal substances carried on aircrafts, and can prove extremely dangerous and lethal, as in the case of September 11, 2001.

A suitable screening method will also be required to identify the form and amount of threat material(s) whether in the solid, liquid or gaseous state with low false negative and false positive alarm rates. The London transatlantic bomb plot of 2006 and the “printer cartridge bomb plot” of 2010 may be evidence for the requirement of systems capable of identifying liquids, aerosols and gel explosives (LAGs), and concealed home-made explosives (HMEs), respectively (Harding et al., 2012). Even though the development of contemporary technologies to adapt to expanding potential threats and identify illicit substances is constantly growing, the sophistication of HMEs and their concealment is also increasing (Novakoff, 1992, Klock, 2005, Lee and Jacobson, 2011). Therefore, there is an amplified demand for technologies with high throughput, sensitivity and specificity in order to meet the required low false negatives and false alarm rates and avoid any future disasters in the aviation world (Wells and Bradley, 2012).

The detection method of explosives and other illicit substances, such as drugs, generally depends on the quantity and type of substance present i.e. bulk or trace

(vapour) detection. Further, the detection of explosive devices e.g. bombs and weapons depends on the visualisation of their shape and structure i.e. fine wires in explosive devices (Speller, 2001).

Explosive trace detection (ETD) techniques including mass spectrometry (Yinon, 2007, Cotte-Rodriguez et al., 2008), chemiluminescence (Jimenez and Navas, 2007), ion mobility spectrometry (Ewing et al., 2001, Rondeschagen et al., 2008), immunoassay (Connelly et al., 1998, Rabbany et al., 2000, Singh and Singh, 2003, Shea and Morgan, 2007) and bio-sensor technology (O'Neil), focus on minute concentrations of an illicit substance (less than a microgram) present on the exterior of the luggage or vapours emitting from the substance (Connelly et al., 1998, Singh and Singh, 2003). ETD methods commonly aim to identify any trace residues indicating recent contact with explosives or drugs, but is a slow process with unacceptably low throughput for busy airports (Shea and Morgan, 2007, Wells and Bradley, 2012).

Bulk detection systems, usually referred to as explosive detection systems (EDS), are concentrated in identifying weapons or a volume of illicit substances, such as explosives and drugs of abuse, whilst screening 100% of checked baggage. Bulk detection systems typically focus on capturing an inside image of the luggage under inspection and this can generally be achieved by X-ray based systems, as discussed in the next section. Other screening systems that are non X-ray based include neutron based techniques (Lanza, 2007), nuclear quadrupole resonance (Miller, 2007) and terahertz time domain spectroscopy (Federici et al., 2007). Table 2.1 gives a brief description of the detection methods and capabilities of these techniques.

Table 2.1 Non X-ray methods for the detection of illicit substances.

Technology	Detection	Advantages	Limitations
Neutron based Techniques	Second radiation from interactions of neutron and material's nuclei	High sensitivity and specificity	No detection of metals (e.g. weapons)
	Mainly detects carbon, oxygen and nitrogen	High penetration ability One-side access	Operational safety High cost
Nuclear Quadrupole Resonance	Resonance radiation	High specificity, high selectivity to nitrogen	Low sensitivity (high background noise)
	Detects emitted radio frequency signals from materials' nuclei	One-side access No health risks due to non-ionising radiation	Low throughput
Terahertz Time Domain Spectroscopy	Terahertz waves giving characteristic terahertz spectra	High specificity	Currently unusable for real world application measurements
		Able to see through concealed barriers (except metals) Suitable for personnel screening	Terahertz radiation completely attenuated in bulky samples Does not work in the presence of water vapours

2.1 Bulk detection techniques

This work mostly concentrates on X-ray based bulk detection systems. The most dominant X-ray based screening technologies and concept systems in aviation security are transmission X-ray systems, dual energy X-ray systems, computed tomography (CT) systems and energy dispersive XRD systems.

2.1.1 X-ray transmission systems

Transmission X-ray systems are the conventional method of luggage screening in airports since the 1970s (Connelly et al., 1998, Olapiriyakul and Das, 2007). Figure 2.1 demonstrates a typical X-ray transmission image. The difference in attenuation is causing objects within a luggage to appear in different hues of grey and the contrast in shades is giving the shape of the objects in the transmission image. Materials with densities similar to known explosives are identified as potential threats for further investigation (Wells and Bradley, 2012).

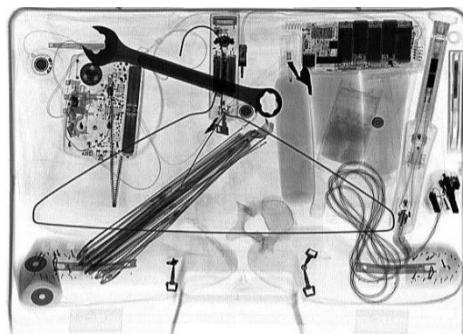


Figure 2.1 An X-ray transmission image of a suitcase under investigation.

Two-dimensional X-ray transmission therefore provides information on the shape, orientation and density of objects (Wells and Bradley, 2012). Identification by shape is effective with knives and weapons, but not significantly informative with explosives and drugs, as many substances have similar shapes. Furthermore, in the presence of two overlapping substances, the attenuation is an addition of the individual linear attenuation coefficients (Connelly et al., 1998), which makes the identification of single objects in high cluttered suitcases an extremely difficult task (Turcsany et al., 2013).

X-ray transmission's main limitation lies within its lack of depth information hence the superimposition of objects in the image (Vogel, 2007, Wells and Bradley, 2012). The transmission images are therefore considered as a representation of the attenuation of each position of the luggage being scanned, rather than an optical image of the suitcase (Connelly et al., 1998). An additional shortcoming of transmission X-ray systems is their inability to distinguish between a thin sheet of

high absorption and a thick slab of low absorption materials as both can attenuate to the same extent (Singh and Singh, 2003).

2.1.2 Dual energy X-ray systems

The appearance of explosives and drugs (low Z materials) demanded new screening systems with greater discrimination power than single energy X-ray transmission was capable (Gang and Dongji, 2009). Dual energy X-ray systems for security scanning were initially introduced in the 1980s. Currently, most European airports employ dual energy X-ray systems as their main bulk explosive detection equipment for cabin baggage (Wetter, 2013). The concept of dual energy systems is based on obtaining images at varying energy levels (high and low energy levels ranging from 30 keV to 200 keV) (Ying et al., 2006).

The high energy : low energy ratio of the linear attenuation coefficients of an object indicates the substance's effective atomic number (Z_{eff}) and it is used for comparison against an existent database (Connelly et al., 1998). Z_{eff} of an object is the atomic number of a single hypothetical element with the same X-ray attenuation value as the object being measured (Ying et al., 2006). The substances are then categorised into organic ($Z_{\text{eff}} < 10$), inorganic ($10 < Z_{\text{eff}} < 18$) or metallic ($Z_{\text{eff}} > 18$), and each category appears in a different colour, as indicated in Figure 2.2. Based on this principle, the thin sheet of high absorption (e.g. steel) and a thick slab of low absorption (e.g. card) that could not be identified by conventional X-ray transmission systems will, in dual energy systems, appear as different colours thus being distinguishable (Connelly et al., 1998).

Even though dual energy X-ray systems offer advantages over conventional X-ray transmission, explosives are not easily distinguished, in contrast to weapons, since most objects within luggage are organic (Connelly et al., 1998). Further, the difficulty with identifying superimposed objects (background overlapping effect) as found in conventional X-ray transmission is not resolved by dual energy X-ray systems (Singh and Singh, 2003, Vogel, 2007). Another limitation of single view dual energy images is that information is obtained only on the material's effective atomic number without any depth information, which does not provide discrimination of substances to a great extent. Multiple views dual energy systems i.e. combination of

single dual energy with a volume imaging system such as computed tomography (Ying et al., 2006, Iovea et al., 2007, Ying et al., 2007), enable 3D views of cluttered environments and determination of the objects' thicknesses, hence mass densities, providing further classification.

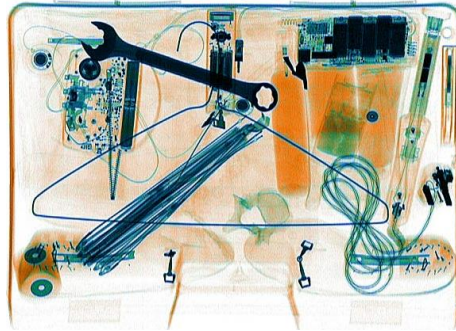


Figure 2.2 A dual energy X-ray image of a suitcase under investigation.

2.1.3 Computed tomography systems

Computed tomography (CT) is typically employed in the medical field for human 3D screening purposes. The 9/11 incidents in 2001 resulted in the introduction of CT by aviation security bodies and it has become one of the USA's main detection techniques (Singh and Singh, 2003, Vogel, 2007).

A CT system is based on X-ray transmission to obtain a sequence of contiguous 2D image slices of the scanned object at varying angles (Kak and Slaney, 1999, Singh and Singh, 2003). Therefore, CT scanning has the ability to reconstruct a 3D view of a luggage under investigation, providing information on the external and internal structure of objects (Kak and Slaney, 1999, Singh and Singh, 2003).

The advantage of CT is that reconstructed 3D images illustrate a volumetric view of the luggage allowing a better appreciation of the objects within it and assisting in the determination of shape, thickness, mass and texture. Moreover, the volumetric view provides the benefit of displaying objects more clearly, even when overlapping, due to the ability of the CT's 3D view to be manipulated and sliced in diverse ways and angles (Kak and Slaney, 1999, Megherbi et al., 2013). Whilst initially the throughput of a typical CT was significantly low, latest CT generations have a higher

throughput of several hundred bags per hour (Wells and Bradley, 2012). CT systems are commonly employed as a level 2 system, i.e. after conventional X-ray scanning for a more detailed inspection of suspected areas within a luggage. CT systems coupled with dual energy X-rays offer greater material discrimination, hence reduced false alarm rates by providing Z_{eff} measurements along with density measurements (Ying et al., 2007, Hao et al., 2013).

Even though CT has great potential and usefulness in security screening due to its density information accompanied by spatial discrimination, it has certain drawbacks. Firstly, the information obtained by CT scanning as well as X-ray transmission and dual energy X-ray systems, is not material specific and cannot discriminate between solids and liquids as stated by Wells and Bradley (2012). Moreover, as stressed by Harding et al. (2012), there is a substantial overlap between the density of some threat and some benign materials (Figure 2.3), which induces further complications in the interpretation of the images obtained by such systems.

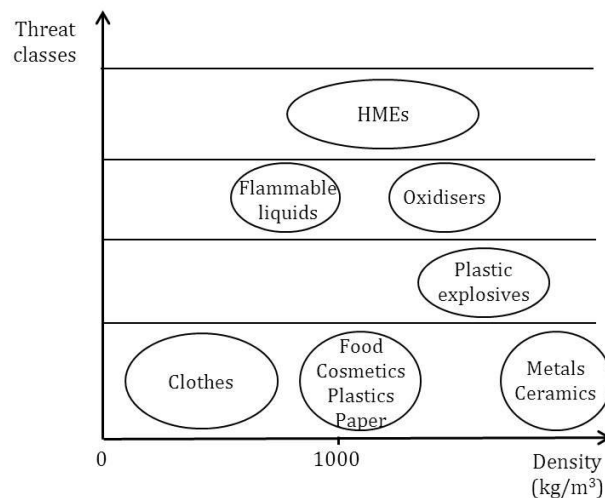


Figure 2.3 The densities of a range of threat and non-threat materials often found in a passenger's suitcase [modified from Harding et al. (2012)].

CT scanners also require very high energy X-rays to be able to fully penetrate luggage and their contents from various angular positions and obtain the high signal-to-noise ratio required for reasonable data resolution (Singh and Singh, 2003,

Evans et al., 2006). Furthermore, CT systems are considered to be 'data hungry', thus several views are needed for reconstruction (Singh and Singh, 2003). Another drawback of CT systems is that they come at a very high cost due to their instrumental and mechanical complexity. It is also worth noting, that X-ray imaging systems suffer from the fact that X-rays cannot penetrate very high density objects, which can therefore provide great concealment for explosives. Additionally, the shape and structure of various electronic devices along with their wires and batteries can look very similar to improvised explosive devices (IEDs) (Wetter, 2013).

Nonetheless, CT systems, as well as dual energy X-ray systems with multi-view, are considered the state-of-the-art for hold luggage screening and are expected to represent the minimum requirements in the future, with faster acquisition times, higher resolution and lower cost (Wetter, 2013).

2.1.4 X-ray diffraction systems

X-ray diffraction (XRD) systems are currently one of the most promising emerging screening methods for identification of threat materials. XRD is considered as a suitable additional (intermediate) level of automated screening, supplementing conventional X-ray imaging systems in identifying illicit substances during luggage inspection (Harding, 2006, Madden et al., 2008). XRD also has the potential to act as a primary detection technology in high security areas, as discussed by Harding (2006).

However, it is important to highlight that XRD screening systems are, at present, concept systems. A single XRD based system (XRD 3500™) commercialised by Morpho (Safran) company is currently implemented in airports for security screening. The XRD 3500™ is a very high cost system (GPB ~0.5 million) utilising high power X-ray sources, hence requiring excessive maintenance. Currently, the XRD 3500™ is employed in a 'system of systems' approach as a secondary screening technique, upon identification of suspicious materials within an inspection volume by CT. Even though this technique is believed to offer high detection and low false alarm rates, to date there are no reports on its performance.

The advantage of XRD over other X-ray based techniques lies within its ability to uniquely identify substances with a high degree of specificity; rather than determining the effective atomic number and density of objects in 2D and 3D, as with dual energy systems and CT, respectively (Beever et al., 1995). XRD in screening is a non-destructive technique that utilises sufficiently high energies to penetrate luggage or parcels containing a variety of attenuating objects (Cook et al., 2009a). The capability of XRD to be highly material specific providing information on the atomic structure of the material under investigation lies within the fundamental principles of crystallography that are discussed in greater depth in Section 3.2.

The effectiveness of XRD technologies vary with angular dispersive (AD) and energy dispersive (ED) XRD techniques; the former producing higher resolution data thus lower false alarms and the latter having a high throughput due to its speed advantage resulting from the static equipment setup. A more detailed description and comparison of ADXRD and EDXRD techniques aimed for security screening is given in Section 3.4.

A number of researchers have investigated the analysis of explosive materials and luggage inspection using coherent X-ray scattering, and specifically EDXRD, due to its material specific characterisation that can uniquely identify objects (Beever et al., 1995, Luggar et al., 1997, Strecker, 1998, Jupp et al., 2000, Madden et al., 2008, Cook et al., 2009a, Pani et al., 2009, Crespy et al., 2010, Sun et al., 2010, Harding et al., 2012, O'Flynn et al., 2013a). However, in this section emphasis is given to the key techniques developed in the last decade.

An EDXRD based imaging technique, termed 'rapid tomographic energy dispersive diffraction imaging' (rTEDDI), has been presented by Cernik et al. (2008). Even though this technique is not aimed for security screening as it utilises a synchrotron radiation, it is an important development of XRD imaging systems. It is based on the principle of EDXRD tomography provided initially by Harding et al. (1990). As explained later on in Section 3.4, an EDXRD system utilises a polychromatic X-ray source and collects diffraction data at a fixed scattering angle by an energy-resolving detector. However, during tomography this arrangement can result in significantly long exposure times.

The uniqueness of rTEDDI lies within the arrays of collimators and energy-sensitive silicon (Si) pixellated detectors that can image a large area of the sample, thus decreasing scanning times (Cernik et al., 2008). Intersection of the incident and scattered beams creates a lozenge area within the sample with a specific gauge volume (Cernik et al., 2008), as also shown in a previous study by Hall et al. (1998). This area can determine the depth spatial resolution of a thick sample along the primary beam axis. For thin samples, as the ones analysed by Cernik et al. (2008), the intersection volume is defined by the sample thickness, and a vertical spatial resolution is provided normal to the primary beam axis. The size of the detectors' array is equal to the size of the collimators' array and each pixel of the detector captures the scattered pattern from the corresponding lozenge volume within the sample (Cernik et al., 2008). Besides the diffraction information obtained that can identify materials present within the sample, an image of the sample is obtained by the total scattering counts which is relative to the density contrast (Cernik et al., 2008). Limitations of rTEDDI rise however from low counting statistics of Si detectors employed at high energies that lead to long acquisition times of ~2-3 hours, and limited sample thickness (Cernik et al., 2008). Lazzari et al. (2009) introduced a reconstruction process for rTEDDI, based on deconvolution algorithm, aimed at the recovery of better resolved images of the object under investigation providing realistic and informative reconstruction of the object.

A multi-generational X-ray diffraction imaging (XDI) technique has been presented by Harding (2009) as a concept system for security screening, combining the ability of X-rays to form an image and to analyse the material under inspection. Although XDI systems can be considered as a promising screening technique, they have the limitation of low speed. The scanning time is over a minute (Harding et al., 2012) restricting XDI from being employed as a security screening technique in airports. XDI systems can therefore be merged in a "system of systems" approach combined with a first stage inspection technique such as CT, similarly to the XRD 3500™.

Inverse fan beam XDI has been improved since it was first introduced by Harding (2005). The latest 3rd generation system is employing a 'multiple inverse fan beam' (MIFB) topology (Harding et al., 2012). MIFB utilises an X-ray multi source consisting of a linear array of 16 focal spots, each activated individually. There are two sets of collimation optics, one on each side of the sample, and there are two

different types of detectors. The first detector type is a conventional transmission detector and the second type is a linear array of energy resolution detectors measuring the scattered energy at a fixed angle, as often the case with EDXRD systems (Section 3.4). Each focal spot produces a collimated fan beam that is directed into specified target points on the detector. The multiple X-ray beams combined with the sequential activation of the focal spots and the collimation optics employed, are causing the X-rays to have their vertex at the detector plane, thus providing the so-called 'inverse beam' topology (Harding et al., 2012). The advantage of this effect is the complete coverage of the object's space and the assignment of the scattered X-rays to their 3D spatial location within the object's space (Harding et al., 2012).

More recent developments in EDXRD for identification of illicit substances are focused on the combination of EDXRD with ADXRD for a greater system specificity and speed (Christodoulou et al., 2011, O'Flynn et al., 2012, O'Flynn et al., 2013a, O'Flynn et al., 2013b). A similar approach was investigated previously by Malden and Speller (2000).

Christodoulou et al. (2011) compared the scattered data obtained from various combinations of samples, all with different concentrations of caffeine, by a polychromatic source (EDXRD) and a pixellated cadmium telluride (CdTe) based detector, at a single, two and four scattered angles (ADXRD) ranging from $\sim 5^\circ$ - 7° . The data collected over 25 minutes exposure time was interpreted through a multivariate partial least squares (PLS) regression statistical test, and the results obtained from the single scattered angle indicated poor correlation to the actual concentrations of caffeine (Christodoulou et al., 2011). In contrast, the best prediction abilities were shown when data from four scattering angles were taken into account, indicating that measurements from multiple scattering angles optimise specificity (Christodoulou et al., 2011). O'Flynn et al. (2012) then demonstrated the simultaneous acquisition of EDXRD and ADXRD data, based on the study of Christodoulou et al. (2011), over a greater range of scattering angles between 0.6° - 15.5° for explosive materials. The area of the pixellated detector corresponding to 6400 individual energy detectors (80 x 80 small area detectors) made the simultaneous acquisition of spatially and energy resolved data feasible with 30-60 minutes time exposure, based on the change in the Debye cones' (Section

3.2.2) radii at isolated energy windows (O'Flynn et al., 2012, O'Flynn et al., 2013b). Data were also captured at shorter acquisition times (10 minutes), but with poor data resolution (O'Flynn et al., 2012).

In a later study, O'Flynn et al. (2013b) compared the diffraction data obtained by the same technique as the one presented by O'Flynn et al. (2012), at 1 second and 1 hour acquisition times for various samples, including explosive materials such as plastic explosives (C4 and Semtex) and an emulsion sample. The 6400 individual energy spectra collected from each sample were converted to a single momentum transfer spectrum by summing them together (O'Flynn et al., 2013b). Even though the data collected at 1 second demonstrated significant noise, the diffraction peaks were still apparent (O'Flynn et al., 2013b). Diffraction data were also collected from a sample with large grain size, hexamine powder, which indicated slight variations in its momentum transfer spectrum from different positions in the sample (O'Flynn et al., 2013b). As it will be discussed later on in Section 5.2, this is an example of the possible inaccuracies of conventional XRD technique when analysing samples with large grain size or preferred orientation.

Moreover, simulants for plastic explosives were analysed by the above technique (O'Flynn et al. (2013b)) at 10 minutes acquisition time (O'Flynn et al., 2013a). The substances consisting of the simulants were successfully identified; however, limitations were raised when analysing thick samples due to peak broadening, that reduces angular resolution and hence specificity (O'Flynn et al., 2013a). O'Flynn et al. (2013a) comment on the small size of the primary beam employed, that would be impractical for security screening and suggest coupling of the technique with conventional imaging methods to examine suspicious areas.

For a detailed review of the current screening systems and decision making principles regarding checked luggage in aviation security the reader may refer to Wells and Bradley (2012). Further, Hudson et al. (2012) provide a brief review of the radiation safety and technical performance of bulk explosives detection systems.

2.2 Liquid detection techniques

Detection of liquids appears to be exceptionally demanding due to the decreased specificity of current screening techniques to identify liquids through their

packaging and the broad range of containers available, operating as means of concealment. The identification of liquids within suitcases using the currently employed detection systems such as transmission X-ray, dual energy X-ray and CT scanning appears to be challenging due to their inability to distinguish between liquids and solids (Harding and Delfs, 2008, Wells and Bradley, 2012).

The 7/7 London bombings and the foiled London transatlantic plot of 2006 raised the awareness regarding the necessity of a satisfactory screening system that would identify threat liquids, such as hydrogen peroxide (BBC, 2006, Wells and Bradley, 2012). Hydrogen peroxide (H_2O_2) combined with acetone was the main HME involved in the shoe bomb plot in 2001 (with PETN explosive), in a failed bombing attempt few days after the 7/7 London bombings in 2005 and in the London transatlantic bomb plot in 2006 (Wells and Bradley, 2012). As it can be deduced from these relatively recent incidents, H_2O_2 in solution is currently the pre-cursor of choice as it is easily and widely accessible (used as bleaching and cleaning agent). It is therefore essential for a screening system to be able to differentiate between H_2O_2 and a non-threat liquid, such as water.

After the 2006 London transatlantic plot, specific regulations have been implemented in airports involving liquids in hand luggage. However, it has been reported that the EU plans to lift this limited liquid policy in the next few years (about 2016) (Loeffen et al., 2011, Wells and Bradley, 2012, European-Commission, 2013). Consequently, this demands the development of mass-screening technologies for carry-on and checked luggage, able to detect HMEs and LAGs (particularly peroxide-based liquids) with low false negatives, high sensitivity and high throughput in order to sustain adequate security (Wells and Bradley, 2012).

Recent studies indicated that liquids can be identified to a certain extent by non-invasive methods including laser based spectroscopy (Gaft and Nagli, 2010) such as Raman spectroscopy (Matousek et al., 2005, Hargreaves and Matousek, 2009, Gaft and Nagli, 2010), laser induced luminescence (Gaft and Nagli, 2010) and spatially offset Raman spectroscopy (SORS) (Matousek et al., 2005, Hargreaves and Matousek, 2009, Buckley and Matousek, 2011), ultra-low-field magnetic resonance imaging (MRI) (Espy et al., 2010), and XRD (Harding and Delfs, 2007, Harding and Delfs, 2008, Harding et al., 2010).

In the following two sections the key characteristics and capabilities of Raman spectroscopy (SORS) and XRD in regards to security screening will be discussed briefly. SORS is one of the leading technologies currently employed in airports for liquid security inspection (Corfield, 2014) and XRD based techniques are of relevance to this work.

Other screening methods employing electromagnetic radiation for the detection of liquid threats are presented in Table 2.2. For a more detailed description of these techniques the reader may refer to Schubert and Kuznetsov (2008).

Table 2.2 Electromagnetic methods for the detection of liquid explosives [modified from Kuznetsov and Osetrov (2008)].

Technology	Detection	Advantages	Limitations
Nuclear Quadruple Resonance	Resonance radiation of nitro group	High selectivity to nitrogen, one-side access	Insensitive to peroxides Does not recognise explosive in metal covering
Terahertz Waves	Transmission spectra	High selectivity	Does not recognise explosive in metal covering
Microwave Radars	Dielectric properties	Standoff inspection, selectivity	Does not recognise explosive in metal covering

2.2.1 Raman Spectroscopy

Raman spectroscopy is believed to be an effective security screening method with high throughput, mainly due to its high material (chemical) specificity, water compatibility, simplicity of experimental setup and portable capacity (Hargreaves and Matousek, 2009). However, interfering fluorescence and Raman signals deriving from the walls of the container are masking the Raman signals from the liquid itself (Hargreaves and Matousek, 2009).

Matousek et al. (2005) who introduced spatially offset Raman spectroscopy (SORS), argue that SORS has the ability of increased sensitivity by suppressing any Raman

signals and fluorescence originating from the wall of the container. This sensitivity arises by SORS's ability to acquire Raman data from spatially offset regions from an illumination area on the sample; thus isolating Raman signals from individual sub-layers within the sample under investigation (Buckley and Matousek, 2011). In the case of a single liquid within a container, Raman signals are collected at zero offset and at a non-zero (e.g. 10 mm) offset (Eliasson et al., 2007, Bloomfield et al., 2010). Once the zero offset is subtracted (scaled) from the spatially offset measurement, the pure Raman spectrum of the liquid can be isolated and compared to a database of known explosive substances obtained in a conventional manner (Eliasson et al., 2007). Eliasson et al. (2007) and Hargreaves and Matousek (2009) demonstrated the ability of SORS to detect 30% H₂O₂ solution concealed in transparent and non-transparent plastic containers, and in 1:1 mixtures with common beverages, respectively. Eliasson et al. (2007) however, comment on the limitation of SORS to detect H₂O₂ in the presence of ethanol, as it will appear as a poorly resolved shoulder on the signal from ethanol.

Even though SORS can be considered as an appropriate technique for liquid detection, it has to be taken into consideration that Raman spectroscopic methods cannot penetrate certain materials, such as metal containers, thus cannot identify liquids within one (Hargreaves and Matousek, 2009, Loeffen et al., 2011). In addition, SORS technique is considered as a Type B LAG screening technology, which requires individual LAGs to be removed from the passengers' bags and placed into the screening system. Inevitably, this single bottle approach decreases throughput and necessitates prior detection of LAGs within carry-on bags by a first stage detection system or by random security checks.

2.2.2 X-ray diffraction

As explained earlier in Section 2.1.4, the employment of XRD screening systems has gained significant interest in the last decade due to XRD's ability to uniquely identify objects by a 'fingerprint' signature in a non-invasive manner. Specificity and sensitivity however, depend on the material's properties and specifically on its crystallinity, as it will be discussed later on in Section 3.2.

Although interpretation of XRD profiles from liquids can be challenging due to the latter's lack of crystalline structure (explained in Section 3.2.3), classification of liquids into different groups is believed achievable by EDXRD as indicated by Harding & Delfs (2007). Harding and Delfs (2007, 2008) demonstrated potential identification of 30% concentration H_2O_2 (an important oxidizer) and pure acetone (a typical hydrocarbon fuel) using XRD, by determining their molecular interference factor (MIF). MIF depends on momentum transfer and it is associated with the radial distribution function (RDF), described in Section 3.2.3 (Harding and Delfs, 2007, Harding and Delfs, 2008). Even though the MIF of acetone and 30% H_2O_2 showed significant differences, the latter's MIF resembled that of water, as this was the main substance in the solution (Harding and Delfs, 2007). Distinction between water and H_2O_2 can be achieved from the considerably higher Z_{eff} of H_2O_2 , as stated by Harding and Delfs (2007).

In a later study, Harding's et al. (2010) developed a classification theme grouping liquids into different threat and non-threat categories for aviation security, as shown in Table 2.3. Approximately 25 liquids (>99% pure) from categories A, B, D and E were analysed by the inverse fan-beam configuration (EDXRD) mentioned previously in Section 2.1.4.

Classification of these liquids was based upon three stages according to Harding's et al. (2010) work: visual inspection of XRD profiles and determination of MIFs and residual MIFs. Residual MIF corresponds to the resulting MIF after subtraction of the water's MIF from that of the investigating liquid (Harding et al., 2010). Harding et al. (2010) assert that the results from these three stages are sufficient in categorising the liquid under investigation. In addition, emphasis is given to the pure isolated nature of the liquid samples analysed and that any effects that could influence the coherent scatter signal would also decrease the detection performance of the system (Harding et al., 2010). Therefore, Harding et al. (2010) suggest that future work should focus on the investigation of threat and non-threat liquids within a variety of common containers.

Table 2.3 Classification scheme of different threat and non-threat liquids for aviation security as provided by Harding et al. (2010).

	Category	Liquid group	Examples
NON-THREAT	A	Dilute aqueous	Tea, coffee
	B	Concentrated aqueous	Cosmetics, drinks, alcoholic beverages
	C	Amorphous	Glass, plastics, fruit preserves (jam)
THREAT	D	1 st threat class (combustible liquids and amorphous hydrocarbons)	Diesel, acetone
	E	2 nd threat class (oxidisers)	Concentrated hydrogen peroxide, nitric acid

Currently, there is an XRD based imaging technique for the detection of liquids, available for implementation at airports referred to as XDi™ (by Morpho). The XDi™ system is based on the work by Harding et al. (2010), with the potential of automated detection of multiple threat liquids within containers and inside carry-on bags (Type D LAG system). Details on performance have not been reported, even though it considers to offer high detection rates with significantly low false negatives.

Furthermore, studies performed by Zhong et al. (2010) and Zhong et al. (2012) demonstrated the acquisition and interpretation of EDXRD data from pure liquids based on their momentum transfer position, shape and intensity. A number of alcohols was analysed, within others, indicating characteristic profiles with a single broad peak arising from CH_x-CH_x correlations from the nearest neighbour carbon chains (Zhong et al., 2012). Slight differences between the diffraction signals arose from the intermolecular correlations of O-O atoms from adjacent -OH groups and from their material properties, such as number of carbons and density (i.e. increase in number of carbons and hence density decreased the diffracted intensity, except for methanol) (Zhong et al., 2012).

One of the aims of this research as mentioned previously in Section 1.2, was to discriminate between threat and non-threat liquids, that are most likely to be present in a passenger's suitcase, by adopting a similar categorisation approach of liquid samples to the work of Harding et al. (2010).

2.3 Concluding remarks

In this chapter, the key characteristics of security screening systems for bulk explosives detection have been discussed. These features include low false negatives (i.e. high sensitivity), low false alarms (i.e. high specificity), high throughput, low operational cost and most importantly the ability to identify a variety of substances, such as plastic explosives, homemade explosives (HMEs) and liquids, aerosols and gel explosives (LAGs).

A description of the main bulk screening systems based on X-rays, that are either currently employed in airports or have great potential in aviation security has been given, along with their advantages and limitations. Such systems include X-ray transmission, dual energy X-rays, computed tomography and X-ray diffraction.

Furthermore, the importance of distinguishing between threat and non-threat liquids has been explained and hydrogen peroxide was identified as one of the main components of currently preferred HMEs. Details were also given on screening technologies aimed at the identification of liquid explosives, such as spatially offset Raman spectroscopy and X-ray diffraction.

Chapter 3 POWDER X-RAY DIFFRACTION

Outline

In this chapter, the key principles involving X-rays and their interactions with matter are introduced, focusing more on coherent scattering, as this is the basis for XRD. Scattering from crystalline substances including materials exhibiting preferred orientation or large grain size is discussed, as well as scattering from non-crystalline substances. A description of conventional XRD arrangements such as transmission and reflection mode is also presented. Finally, a comparison between angular dispersive and energy dispersive XRD is given in terms of security screening.

In the previous chapter, the important role of X-rays, in security screening and imaging techniques, was discussed. It is however, essential to outline the fundamental principles regarding X-rays and their interactions with matter.

X-rays were discovered by the German physicist Röntgen in 1895 and the first diffraction experiments were performed almost two decades later in 1912 by Laue (Cullity, 1978). The wavelength of X-rays lies within the range of 0.1 Å and 100 Å, thus energies of ~100 keV and ~0.1 keV, respectively; whereas the wavelength of X-rays used in diffraction is 0.5-2.5 Å.

3.1 X-ray interactions with matter

When X-rays interact with matter, the X-ray photons are either transmitted through the material with no loss in energy, absorbed by the material with a total loss in energy or scattered elastically (energy is conserved) or inelastically (energy is not conserved). Figure 3.1 illustrates these three processes.

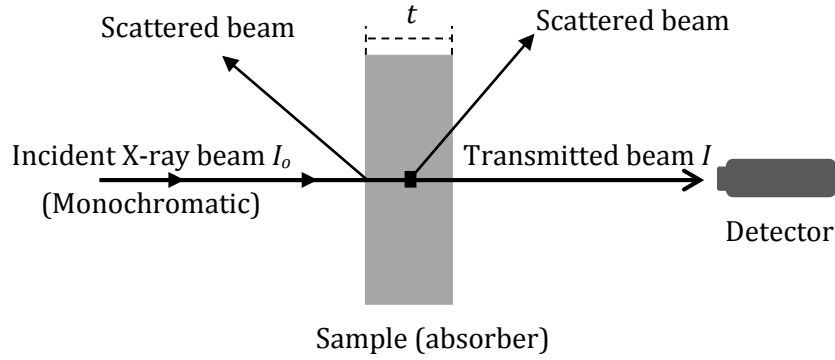


Figure 3.1 The processes (transmission, absorption and scatter) occurring when X-rays are incident upon a material.

When X-ray photons with wavelength λ and initial intensity I_0 are incident upon a material with thickness t , a fraction of the X-ray flux is transferred to the material. This causes the intensity to reduce as a factor of the material's mass attenuation coefficient (μ/ρ), thickness (t) and density (ρ), as shown by the Lambert-Beer law (Equation (3.1)); where μ is the linear attenuation coefficient. The wavelength of the X-rays however remains unchanged.

$$I = I_0 e^{-\frac{\mu}{\rho}(\rho t)} \quad (3.1)$$

The absorption effect of X-rays as they pass through a sample can be determined in terms of transmission coefficient also known as the absorption factor, A , which differs for reflection and transmission (Section 3.3) geometries (He, 2009). As only the transmission arrangement is relevant to this work, the absorption factor for transmission mode XRD (A_T) with angular beam divergence ϕ is given by Equation (3.2).

$$A_T = \frac{\sec\phi(e^{-\mu t \sec\phi} - e^{-\mu t \sec(90^\circ + \phi)})}{\mu(\sec(90^\circ + \phi) - \sec\phi)} \quad (3.2)$$

The optimal sample thickness, t for maximum scattered intensity is given by Equation (3.3);

$$t = \frac{\cos 2\theta \ln \cos 2\theta}{\mu(\cos 2\theta - 1)} \quad (3.3)$$

where 2θ is the sample's scattering angle (discussed in Section 3.2.2).

For a more in depth discussion of the factors affecting X-ray intensities and absorption factors in transmission and reflection mode diffraction, the reader should refer to Woolfson (1997) and He (2009), respectively.

3.2 Introduction to X-ray diffraction

The phenomenon of coherent scattering underpins the theory of X-ray diffraction. X-ray diffraction's practical applications involve the characterisation and identification of unknown compounds or substances, typically polycrystalline, by obtaining structural, chemical and physical information. In order to understand the operation and application of XRD, and why crystals enable X-rays to diffract, it is important to study and establish the fundamental principles of crystallography.

3.2.1 Crystalline materials

A crystal may be defined as "a solid composed of atoms arranged in a pattern periodic in three dimensions" (Cullity, 1978). Materials possessing this essential atomic arrangement periodicity are considered to be crystalline and exhibit a long-range order. In contrast, substances with no regular interior arrangement of atoms are referred to as amorphous (or non-crystalline) and exhibit a short-range order. The majority of natural materials are crystalline, whereas compounds in the liquid or gaseous state are amorphous. Most common forensic substances such as drugs, explosives, soil, paint and bullets possess long-range order, thus frequently analysed by XRD. In contrast, other materials such as glass and polymers typically have a short-range order and are considered to be amorphous.

Even though the way crystalline and amorphous materials scatter X-ray photons differs, this does not imply that XRD cannot be employed in the analysis of

amorphous substances. There is however, a distinct difference in the diffractograms of crystalline and amorphous materials.

Figure 3.2 illustrates a typical scattering distribution from crystalline solids, amorphous solids or liquids, a monoatomic gas and their combinations.

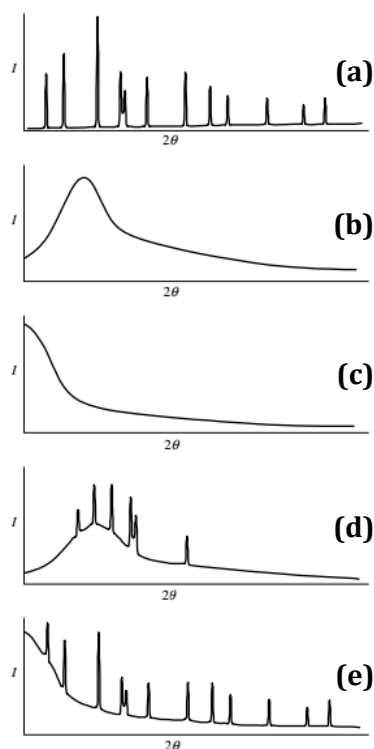


Figure 3.2 Characteristic scattering profiles of crystalline solid (a), liquid or amorphous solid (b), monoatomic gas (c), amorphous solid with crystallinity (d) and crystalline solid with air scattering (e) [modified from He (2009)].

It can be seen that crystalline compounds produce sharp diffraction peaks; whereas the amorphous substances produce a single broad scattering maximum indicating a short-range order. It is important to note that compounds in the liquid or gaseous state are non-crystalline, therefore are expected to produce similar diffraction profiles as with Figure 3.2 (b). Diffraction occurring from amorphous materials is discussed in further detail in Section 3.2.3.

3.2.2 Fundamental principles of XRD in crystalline materials

In a crystalline material or any material with long-range order, coherent scattering will be emitted in spherical waves from adjacent points. These scattering waves will spherically expand in space until they interact with each other, producing constructive (in phase) or destructive (out of phase) interference at certain angles (θ) of view depending on the radiation's wavelength (λ) and on the distance between the crystallographic planes (termed d-spacing) of the crystal (Jenkins and Snyder, 1996). Destructive interference occurs in most scattering directions, but in a few directions, constructive interference arises and diffracted rays are formed (Jenkins and Snyder, 1996). Therefore, diffraction is the constructive interference (in-phase) of coherently scattered radiation within a periodic array of atoms, ions or molecules and is mostly comprehended through Bragg's Law (Equation (3.4));

$$\lambda = 2d_{hkl} \sin \theta \quad (3.4)$$

where λ is the wavelength of the X-ray photons, d_{hkl} is the crystal's interplanar distance and θ is the scattering angle.

Bragg's law is a simplified model considering X-ray scattering as reflection from planes of atoms and demonstrating the relationship between the X-rays' wavelength (λ), the scattering angle (θ) and the perpendicular distances (d_{hkl}) between the crystallographic planes responsible for each reflection (Figure 3.3).

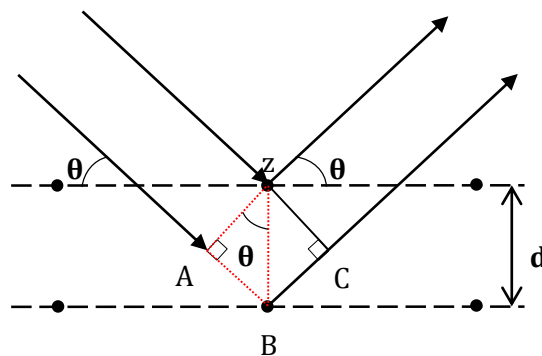


Figure 3.3 Diagrammatical representation of Bragg's law illustrating the reflection of X-rays from two atomic planes.

In diffraction patterns, constructive (greater amplitude) and destructive (smaller amplitude) interference are shown as regions of enhanced and diminished intensities because the intensity of electromagnetic radiation is proportional to the square of the waves' amplitude (Atkins and Paula, 2005). In single crystals, illumination of the crystal from a single orientation would not yield scattering maxima representing all the interplanar distances of the material because not all planes will satisfy Bragg's law. Diffraction data from single crystals is conventionally acquired by rotating the crystal in order for all the atomic planes to fulfil Bragg's geometry.

In the case of polycrystalline materials though, there is not a crystal rotation requirement. Polycrystalline materials are arranged in such a manner that all crystals within them are randomly orientated; thus, a large number of planes simultaneously fulfil Bragg's law. Constructive interference within a periodic array of scattered points will result in the appearance of cones with enhanced intensity, termed Debye cones. The method of collecting diffraction signals from polycrystalline materials is known as powder XRD (PXRD).

The diffracted (2θ) angle of a Debye cone can be measured and applied to Bragg's law. Applying Bragg's Equation (3.4) in empirical data, the interplanar distances within a unit cell thus distances between centres of atoms or ions can be determined, providing distinctive structural information on the material analysed. The spacing values are in the order of 10^{-10} m similar to the wavelength in the X-ray electromagnetic spectrum and are very commonly utilised in uniquely identifying unknown materials through a database of known compounds.

3.2.2.1 Intensity of diffracted beam

The intensity of the diffracted X-ray photons is significantly lower (~99% loss) than the intensity of the incident beam as mathematically illustrated by Woolfson (1997).

The intensity diffracted from a polycrystalline material can be defined by Equation (3.5);

$$I_{hkl} = k_1 \frac{p_{hkl}}{v^2} (LPA) \lambda^3 F_{hkl}^2 e^{(-2M_t - 2M_s)} \quad (3.5)$$

where k_l is an instrument constant scaling between observed and calculated intensities, p_{hkl} is the multiplicity factor of crystal planes (hkl), v is the volume of the unit cell, LPA is the combined correction for the Lorentz, polarisation and absorption factors, F_{hkl} is the structure factor and the term $e^{(-2M_t-2M_s)}$ is the attenuation factor (He, 2009).

As indicated above, Equation (3.2) is a function of the structure factor, $|F_{hkl}|$. The structure factor is a quantitative description of the total scattering from a unit cell and is given by Equation (3.6);

$$F_{hkl} = \sum_{j=1}^m f_j e^{2\pi i(hx_j + ky_j + lz_j)} \quad (3.6)$$

where m is the number of j atoms, x, y and z are the fractional coordinates of the atoms within the unit cell, h, k and l are the indices of reflection and f is the atomic scattering factor.

The intensity of the diffracted beam is a function of the atom's position within the unit cell of the crystal. Therefore, the structure factor is of significant importance when solving crystal structures as it takes into account the atomic positions and gives an intensity value depending on the structure giving rise to that reflection (hkl). For example, if a certain hkl reflection gives a structure factor equal to zero this indicates that the intensity of that hkl is zero.

3.2.2.2 Preferred orientation

In previous sections, it has been assumed that a polycrystalline specimen under investigation has completely randomly orientated crystallites (grains). A sample whose crystallites have a random orientation generates scattering maxima in the form of cones (Debye cones) with a smooth, continuous and uniform intensity around their circumference, as demonstrated by Figure 3.4 (a). There are specimens however, whose crystallites possess a preferred orientation and are hence clustered in one crystallographic orientation, as in the case of mechanically formed samples

(deformation texture) e.g. drawn wires and rolled metal sheets. These samples with non-random crystal orientation are said to exhibit preferred orientation or texture.

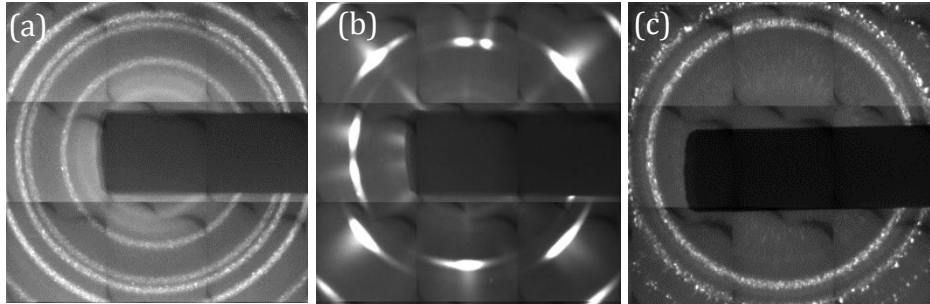


Figure 3.4 Scattering patterns from a sample with relatively randomly orientated crystallites and small grain size (a), a sample with preferred orientation (b) and a sample with large grain size (c).

Preferred orientation is a very common effect typically present in the majority of specimens including natural products, such as rocks. Even though it is not always desired, sometimes it is essential depending on the specimen's intended use due to the effect texture has on the material's physical properties (Wenk and Houtte, 2004). Depending on the degree of preferred orientation of a sample, Debye cones are usually smooth but with a non-uniform intensity around their circumference. Samples with a low degree of preferred orientation give rise to Debye cones with low intensity regions; whereas high levels of preferred orientation generate Debye cones with discontinuities in intensity, similarly to Figure 3.4 (b). These discontinuities appear as arc segments due to the absence of certain orientations in the specimen. An extreme case of preferred orientation is a single crystal.

At this point, it is important to note that with conventional XRD arrangements, where only a portion of the diffraction pattern is captured, certain scattering maxima may be absent from the diffraction images.

There are two widely known and studied types of preferred orientation: fibre and sheet texture. Fibre texture typically involves wires in which their crystallites are orientated with a certain crystallographic direction $[uvw]$ parallel (or nearly parallel) to the wire (or fibre) axis (Cullity, 1978). Fibre texture is considered to be the simplest form of preferred orientation, as it is only in one direction. Materials (commonly sheets) with sheet texture tend to have their crystallites aligned with a

certain crystallographic plane (hkl) parallel (or nearly parallel) to the sheet's surface and with a certain crystallographic direction $[uvw]$ parallel (or nearly parallel) to the rolling direction of the sheet (Klug and Alexander, 1974, Cullity, 1978).

For further details on samples exhibiting preferred orientation and their analysis the reader is referred to Klug and Alexander (1974), Cullity (1978) and He (2009).

3.2.2.3 Crystallite size

Besides the crystallites' orientation, their size is also an important feature especially in metallurgy, as it can influence many of the specimen's properties, such as mechanical strength. For example, an increase in the size of crystallites is associated with a decrease in hardness and strength (Cullity, 1978, He, 2009). Grain growth in metals and alloys, such as copper, can often be induced by heat treatment including annealing (Inami et al., 1999).

Typical crystallite sizes range between 10^4 - 10^5 nm, even though 10^3 - 10^6 nm sizes are encountered in metals and alloys (Cullity, 1978). Analysis of crystallite size by XRD is divided into diffraction line broadening for crystallite sizes less than ~ 100 nm and γ -profile (circumference integration) analysis for sizes between 100 nm and tens of thousands nm (He, 2009). In XRD, the term 'large grain' (crystallite) size commonly refers to crystallite size relative to the incident beam's cross section (Ingham, 2014).

In this study, emphasis is given to large crystallite size when compared to the primary beam, as it is of more relevance to materials requiring analysis during security screening. Materials with grain size ~ 100 -1000 nm tend to have smooth and continuous Debye cones. If the grain size is increased, the Debye cones start becoming discontinuous. For a very coarse grain size, only a small number of crystals will diffract resulting in a diffraction pattern consisting by a few scattering maxima spots (Laue spots), similarly to a single crystal. As the grain size decreases, Debye cones start to form, but with discontinuities, as shown in Figure 3.4 (c). Equations have been derived to associate the number of observed spots around the circumference of the Debye cones (γ -profile analysis) to grain size (He, 2009, Ingham, 2014). Details on this analysis for both transmission and reflection mode diffraction can be found in He (2009). Accurate calibration of the instrumentation

is required for such analysis; involving the incident beam geometry (diameter) and divergence, the sample-to-detector distance and detective area (He, 2009). A common and more accurate approach for determining grain size, considers the acquisition and comparison of diffraction patterns, in terms of scattering maxima intensity, from a series of standard samples with known grain size numbers to an unknown specimen (Cullity, 1978, Ingham, 2014). Further, Ingham (2014) proposes new statistical measurements for quantification of the diffraction maxima spottiness, including average intensity and root mean square intensity analysis from 2D diffraction images.

3.2.3 Amorphous materials

Until now, diffraction from crystalline materials has been examined and discussed. However, gases and liquids, as well as some solids such as glass, do not possess the same periodicity of atoms as crystalline solids; thus are considered to be amorphous. Amorphous materials do not possess the same amount and degree of information as crystalline substances, due to their short-range order. Nonetheless, informative XRD data can still be acquired from such samples. Crystalline materials produce numerous sharp diffraction peaks; whereas amorphous materials generate one or more scattering maxima in the form of broad diffuse halos, as a result of the different way crystalline and amorphous materials scatter X-rays (Klug and Alexander, 1974, Jenkins and Snyder, 1996, He, 2009). Diffraction images and profiles representative of crystalline and amorphous materials are illustrated in Figure 3.5; demonstrating their differences in number and width of scattering maxima.

This section will focus on the analysis of liquid samples as it is of relevance to this research.

Liquids have no fixed structure with respect to an origin due to constant movement of their atoms (Warren, 1990). Liquids however, have a small degree of local order (short-range order), arising from the shortest possible distance between two atoms, which is the sum of their radii (Klug and Alexander, 1974). In liquids, the length of the molecules' bonds and any characteristic angles between them would generate additional fixed intramolecular distances (Klug and Alexander, 1974).

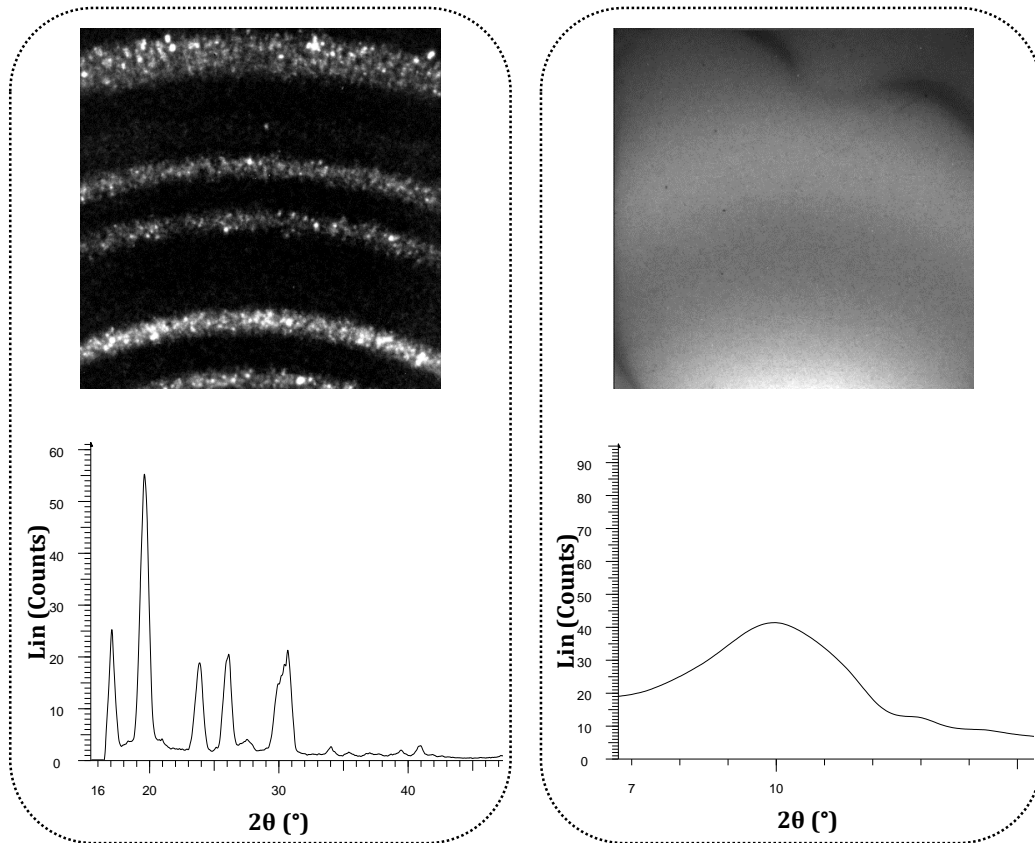


Figure 3.5 Diffraction 2D images and corresponding scattering distributions from a crystalline aluminium oxide sample (left) and an amorphous methylated spirit liquid sample (right).

The atoms of a liquid can be considered to be in the shape of spheres and closely pressed against each other, so that each atom is in contact or almost in contact with a number of neighbouring atoms (Guinier, 1963, Klug and Alexander, 1974). As described by Guinier (1963), constructive interference in liquids arises when the inverse of the minimum distance of a pair of atoms (i.e. sum of their radii) is in the order of $s = (2 \sin \theta) / \lambda$. The scattering distributions from liquids could therefore be interpreted in terms of the magnitude of the scattering vector, s .

In the case of analysing a liquid's structure, where more information is required, the magnitude of the interatomic vectors can be determined. This can be achieved by establishing the radial distribution function (RDF), $g(r)$, which indicates the density of atoms (or electrons) at a certain radial distance from a reference atom (or electron) (Klug and Alexander, 1974).

A better understanding of RDF can be obtained by Figure 3.6, where the red atom is the reference atom and in blue are the atoms surrounding it. The concentric spherical lines have a width of Δr . In simple terms, the RDF is the probability of finding an atom at a distance r and $\Delta r + r$ from the reference atom.

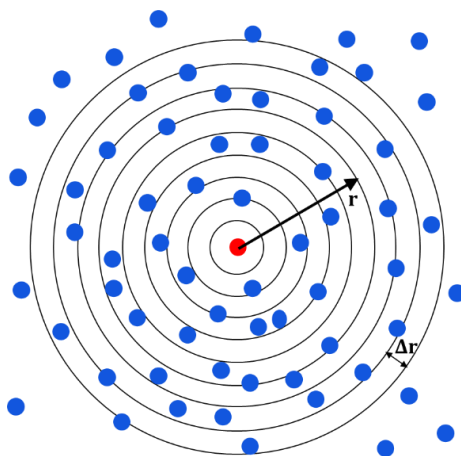


Figure 3.6 Illustration of the reference atom and its concentric spheres forming the basis of the radial distribution function [modified from Cote et al. (2001)].

The RDF is given by Equation (3.7);

$$g(r) = 4\pi^2\rho(r)\Delta r \quad (3.7)$$

where $\rho(r)$ is the number of atoms per unit volume at a distance r from the reference atom and $4\pi^2\rho(r)\Delta r$ is the number of atoms present in a spherical shell of radius r and thickness Δr (Klug and Alexander, 1974).

The intensity of the diffracted rays is converted to electron density and the data are subjected to a number of corrections such as polarisation, incoherent scattering and absorption corrections prior to Fourier transforming it (Klug and Alexander, 1974, Warren, 1990). The data presenting the RDF as a function of distance r can give directly the respective number of certain atom neighbours at several radial

distances r (Klug and Alexander, 1974). For more details on RDF the reader may refer to Klug and Alexander (1974) and Warren (1990).

A liquid that has been widely studied by its scattering distribution is water, mainly due to its importance, abundance and common usage as a solvent for organic liquids (Krishnamurti, 1929, Stewart, 1931, Narten et al., 1967, Huang et al., 2011). Early studies on liquid mixtures analysed by XRD involved their scattering maxima positions (s) as a mean of description (Krishnamurti, 1929, Stewart, 1931, Katzoff, 1934). It was shown that water generates one dominant and two low intensity broad maxima, with Meyer (1930) and Stewart (1931) reporting three maxima at 3.13 Å, 2.12 Å and 1.34 Å, and 3.24 Å, 2.11 Å and 1.13 Å, respectively. Others studies however, indicated just a single scattering maximum from water at varying positions between 3.04-3.27 Å (Stewart, 1931). This arises from the intermolecular interference of the nearest neighbouring oxygen-oxygen (O-O) atoms in water that give rise to a short-range order (Huang et al., 2011). Furthermore, water has shown to have a higher scattering angle i.e. higher magnitude of the scattering vector than organic liquids (Krishnamurti, 1929). Later studies focused on the structure of water, involved determination of its RDF (Katzoff, 1934, Morgan and Warren, 1938, Narten et al., 1967, Huang et al., 2011).

Analysis of aqueous liquid mixtures (1:1 ratio) demonstrated that immiscible mixtures would generate a diffraction pattern consisting of all scattering maxima from both liquids, at the original positions of the pure individual liquids (Krishnamurti, 1929, Stewart, 1931). Solution ratios however, of 1:3 organic liquid:water indicated significantly weak and diffuse halos from the organic liquid, which in some cases was even undetectable (Krishnamurti, 1929). In contrast, when miscible mixtures were analysed, a broad diffuse halo appeared at intermediate angles to that of the pure liquids, depending on their mixture ratios (Krishnamurti, 1929, Stewart, 1931). The scattering maxima from the organic liquid and water would therefore shift to higher and lower angles (referred to as expanding and contracting of the halo) respectively, causing broadened and diffused halos at the edges, resulting in one broad maximum (Krishnamurti, 1929).

3.3 Conventional XRD geometries

The fundamental principles involving PXRD and its geometrical arrangements have long been established (Debye and Scherrer, 1916, Hull, 1917, Barker, 1919, Cullity, 1978). Early systems however suffered from long acquisition times and poor data fidelity (Jenkins and Snyder, 1996). Therefore, later studies, aiming at the acquisition of higher quality and consistency data at shorter exposure times evolved and improved PXRD arrangements (Parrish and Lowitzsch, 1959, Klug and Alexander, 1974, Greenberg, 1993, Jupp et al., 2000, Garrity et al., 2007, Cockcroft and Fitch, 2008).

Two basic geometries for PXRD have prevailed over the years: transmission and reflection mode. In this section, the geometrical arrangements involved with transmission and reflection XRD are presented, along with their main applications, advantages and limitations.

3.3.1 Transmission mode

In transmission mode XRD (or Debye-Scherrer geometry), the instrumental components were initially contained within a cylindrical chamber. A divergent monochromatic pencil beam was employed to illuminate a relatively small amount of sample contained inside a thin cylindrical capillary, normal to the primary beam axis (Aslanov et al., 1998, He, 2009). A photographic film (inside the chamber's circumference) or detector captured sections of the scattering maxima cones arising on a plane normal to the primary beam axis. In modern diffractometers, the divergent beam is focused onto a curved 2θ rotational detector by the use of a curved monochromator, typically a perfect Germanium crystal (Cockcroft and Fitch, 2008).

The Debye-Scherrer geometry is commonly employed when the sample requires sealing in glass capillaries or for cylindrical samples, and for samples with low absorption. Samples prepared in cylindrical capillaries tend to have a more random orientation, thus generating data with more reliable intensities when compared to reflection mode XRD (see below). Moreover, transmission mode lacks systematic errors inducing greater consistency and reliability of the diffraction data acquired, but with a limited angular resolution (Aslanov et al., 1998). The 2θ resolution

mainly depends on the primary beam's size and on the length of the photographic film, which is related to the radius of the cylindrical chamber (He, 2009).

3.3.2 Reflection mode

Reflection mode or focusing plane arrangement is usually referred to the Bragg-Brentano parafocusing geometry. A divergent primary beam passes from the X-ray tube through a divergence slit and illuminates a flat surface sample, over a great area, with an incident angle θ (Aslanov et al., 1998, He, 2009). The scattered X-rays leave the surface of the sample at a 2θ angle from the primary beam, go through an antiscatter slit, and converge on a receiving slit (He, 2009). In Bragg-Brentano geometry, the radial distance between the X-ray source and the sample must be equal to the radial distance between the sample and the receiving slit. In a $\theta:2\theta$ arrangement, the sample is rotated by θ whilst the detector is rotated by 2θ , during data collection. Sample rotation around an axis normal to the surface of the planar sample can also be operated for better powder average (Cockcroft and Fitch, 2008).

Reflection mode XRD provides high intensity scattered rays due to the extended area across the surface of the sample that is illuminated by the incident beam. It is preferred for high angular resolution data, without an increase in exposure time, due to the focusing geometry (Klug and Alexander, 1974, Aslanov et al., 1998, Cockcroft and Fitch, 2008).

Often, reflection mode is chosen over transmission mode, as a long wavelength (i.e. copper) is preferred for a more extended reciprocal space. Analysis of high absorbing materials or samples with increased thickness is restricted by transmission mode XRD, due to limited penetration of such samples by low energies.

3.3.3 Primary beam profile

The profile of the incident beam is of great importance in XRD in order to acquire high quality and resolution data. If a non-collimated X-ray beam illuminates a sample, the diffraction pattern would not be recoverable, due to high scattering in all directions. Therefore, primary beam optics are employed to shape and direct incident X-rays, and to reduce parasitic scattering striking the detector (Aslanov et

al., 1998). Consequently, collimation optics can have an influence on the intensity and angular resolution of diffraction data.

It should be highlighted that the focal spot of an X-ray source also plays an important role, as a small focal spot will generate an incident beam with enhanced intensity and sharper diffraction maxima. Depending on the shape of the focal spot and the X-ray optics, the shape of the primary beam alters from line focus beam, to divergent beam, to highly parallel beam (with the use of Soller slits or parallel polycapillaries) and point beam (He, 2009).

A pinhole collimator is frequently employed to generate a diverging pencil beam as in the case of single crystal analysis and transmission geometries. A slit collimator is also regularly seen in PXRD in order to illuminate a greater area into the powder sample and increase intensity, but at a loss in resolution when compared to pinhole collimators, as indicated by various studies involving EDXRD (Luggar et al., 1997, Malden and Speller, 2000, Madden et al., 2008, Sun et al., 2010).

Further details on the primary beam profiles can be found in Klug and Alexander (1974), Aslanov et al. (1998) and He (2009).

These incident beam profiles are prevalent in XRD and have not been greatly modified over the years. As it is described in detail in Chapter 5, this study focused on the employment of an alternative primary beam profile, an annular beam, for the acquisition of high intensity XRD data.

3.4 Comparison between ADXRD and EDXRD

This section aims to compare the functionality and ability of angular dispersive XRD (ADXRD) and energy dispersive XRD (EDXRD) in terms of security screening.

ADXRD is the conventional laboratory arrangement employed for XRD and it is generally used in material analysis to provide high quality crystallographic data. EDXRD is a relatively recent method that was reported in medical applications by Johns and Yaffe (1983), and then received a distinguishable interest in security screening in the last few decades.

ADXRD utilises a monochromatic X-ray source and a point, line or area detector to measure the intensity of the scattered profile as a function of scattered angle (θ). In contrast, EDXRD uses a polychromatic (white radiation) X-ray source and an energy-resolving detector collects the intensity of the scattered rays at a fixed 2θ angle. Figure 3.7 provides a schematic illustration and comparison of these core features and differences between ADXRD and EDXRD.

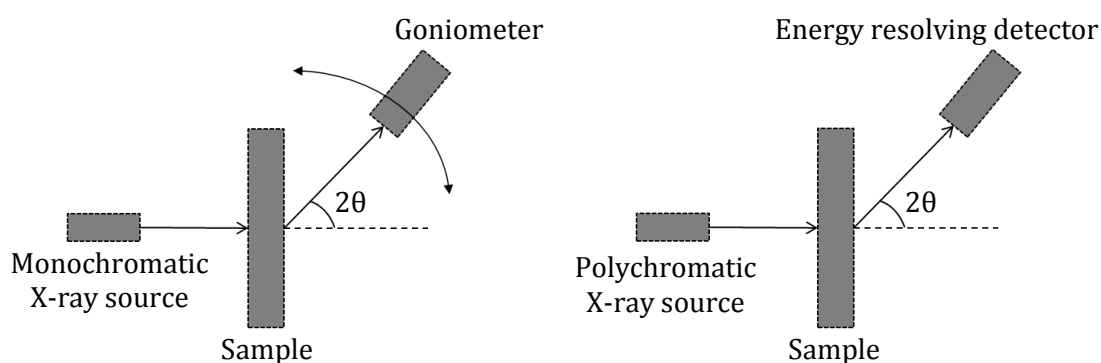


Figure 3.7 Schematic illustration of the key features of ADXRD and EDXRD transmission mode arrangements.

The monochromatic X-ray beam employed for ADXRD has a constant wavelength and the scattered rays are collected over a range of 2θ angles. Bragg's law is then applied to obtain the inter-planar distances (d-spacing) of the sample under investigation. The 2θ angles are typically measured by a point detector that translates at a constant radius around the sample causing an increase in the data collection time, relative to a stationary detector. The acquisition speed can be increased by employing a far more costly area detector, to collect diffraction data simultaneously with no mechanical movement. Jupp et al. (2000) argued that ADXRD can be engaged for security screening and introduced a non-invasive security inspection technique based on ADXRD, with the possibility of differentiating between benign and threat substances at an integration time of 5 seconds. It has been commented that for a full luggage inspection several minutes would be required (Jupp et al., 2000).

Despite the fact that ADXRD analysis dominates in the field of high quality crystallographic data acquisition because of its higher resolution (minimum $\Delta(2\theta)$),

thus greater specificity (see Figure 3.8), EDXRD is more commonly employed in security screening for its speed advantage, as mentioned previously in Section 2.1.4 (Luggar et al., 1997, Strecker, 1998, Malden and Speller, 2000, Cook et al., 2007, Cook et al., 2009b, Sun et al., 2010, Ghammraoui et al., 2012, O'Flynn et al., 2013b).

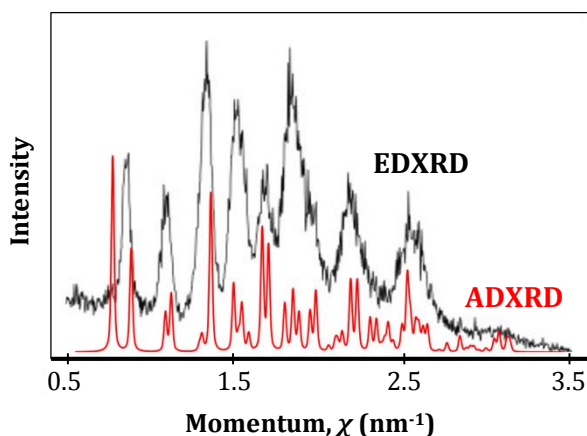


Figure 3.8 Scattering profile from cocaine hydrochloride acquired by EDXRD (obtained from Harding (2009)) and by ADXRD (PDF card No. 30-1629).

In EDXRD, the monochromatic source is replaced by a polychromatic Bremsstrahlung source of typical wavelength between ~ 0.03 - 0.2 nm (Kämpfe et al., 2005) and the scattered rays are measured by an energy resolving detector at a small fixed angle of typically $<10^\circ$ (Luggar et al., 1998, Cook et al., 2007).

In comparison to ADXRD, the EDXRD data are expressed as a function of momentum transfer χ , which is a function of the scattering angle 2θ and the photon energy (E), as indicated by Equation (3.8).

$$\chi = \frac{E}{hc} \sin \theta \quad (3.8)$$

Benchmarked ADXRD diffractometers commonly offer a minimum discrimination of $\sim 0.005^\circ/2\theta$ that is translated to ~ 1.5 eV (at 0.7107 nm molybdenum wavelength). As it will be discussed later on, the highest reported resolution (minimum $\Delta(E)$) offered by energy resolving detectors employed by EDXRD in luggage screening is ~ 700 eV (high purity germanium detectors).

The geometrical components of an EDXRD diffractometer can play a critical role in the acquisition of high energy and angular resolution data. A key feature of EDXRD that can have a major result on the intensity, resolution, energy and momentum space range is the chosen fixed scattering angle (Luggar et al., 1997, Sun et al., 2010).

It is shown that at low scattering angles of $<10^\circ$, coherent scattering dominates over incoherent scattering; hence, the intensity of the resulting diffraction maxima would be much higher at low 2θ angles (Luggar et al., 1997, Luggar and Gilboy, 1999, Cook et al., 2007, Ghammraoui et al., 2012). Incoherent (Compton) scattering involves the inelastic scattering of an X-ray photon from a loosely bounded electron, where the incident photon is re-emitted as an X-ray photon of lower energy (i.e. longer wavelength than the incident beam). Incoherent scattering cannot take part in diffraction since its phase is randomly related to the phase of the incident radiation and no interference effects are produced (Cullity, 1978). This effect typically occurs with light materials of low atomic number as their electrons are loosely bonded to the nucleus. Compton scattering is observed as an undesirable darkening of the background of diffraction patterns.

As the 2θ angle increases, the coherent scattering maxima occur at lower energies, with decreased peak intensity and more dominant attenuation effects (Cook et al., 2007, Ghammraoui et al., 2012). Nevertheless, the energy resolution of the diffraction peaks is higher at high scattering angles i.e. at low energies, as 2θ is inversely proportional to energy as indicated by Equation (3.8) (Luggar et al., 1997). At high 2θ angles (low energy), the momentum space is increased, hence more information can be contained within a limited energy window (Luggar et al., 1997). Luggar et al. (1997) explain that ideally, for a thin sample, a high 2θ scattering angle would be chosen to increase the energy resolution and the d-spacing range acquired. This however, comes to disagreement with the requirement of high energies for security screening in order to penetrate suitcases and thick objects within them. For

this reason, a compromise between high energy resolution and high penetrating X-ray energies has to be reached when it comes to EDXRD and security screening (Luggar et al., 1997).

Moreover, a limitation of EDXRD is that the shape of the energy distribution should be known when interpreting EDXRD data. However, the shape of the energy distribution changes across the thickness of the sample due to beam hardening.

The findings of Luggar et al. (1997) and Lazzari et al. (2009) suggest that 4-5° and 1-5° scattering angle, respectively will be the most suitable for baggage inspection; whereas Cook et al. (2007) identify the optimised 2θ angle for a number of drugs to be 7°. Sun et al. (2010) demonstrated that the optimised scattering angle alters with different threat materials such as TNT or methamphetamine (10° scattered angle) and heroin (12° scattered angle), mainly due to their different elemental composition. In contrast, a study performed by Li et al. (2010) indicated that the optimised scattering angle for methamphetamine (as well as sugar and salt) is 8°, whereas for TNT is 6°. Selection of the most applicable detecting angle for each material is a limitation ADXRD does not have to face, as it collects information from all scattering angles (see below for pixelated energy-resolving detectors).

As mentioned previously in Section 2.1.4, recent developments in EDXRD for security screening have suggested an alternative approach where ADXRD and EDXRD can be combined to utilise advantages from both techniques. An array of scattering collimators and an array of energy sensitive detectors, as well as pixelated detectors, were employed to acquire diffraction data over a range of 2θ angles, similarly to ADXRD (Malden and Speller, 2000, Christodoulou et al., 2011, O'Flynn et al., 2012, O'Flynn et al., 2013a, O'Flynn et al., 2013b). This led to increased counting rates by utilising a higher amount of the scattered beam hence reducing exposure times (Madden et al., 2008). Additionally, Madden et al. (2008) presented a CT system coupled with EDXRD that upon 3D imaging of the suitcase, threat areas were identified for further investigation via EDXRD. Two different scattering angles at 3.2° and 5.1° were employed depending on the density of the possible threat object, as determined by the CT (Madden et al., 2008). For example, analysis of a high density object would require higher energy, therefore the low 2θ angle would be employed and vice versa.

It is also important to note that for EDXRD the incident and scattered collimation apertures play an important role. Optimisation of the geometry can be achieved by a narrow scattered collimator that will increase the angular resolution, thus minimising errors and false alarms, which are of major concern to security screening (Malden and Speller, 2000, Cook et al., 2007, O'Flynn et al., 2013b). For every fixed 2θ angle, there is a small range of scattered angles ($2\theta_1 - 2\theta_2$) that essentially defines the system's angular resolution by $(2\theta_2 - 2\theta_1)/2\theta$ in a simple EDXRD arrangement, as stated by Luggar et al. (1997). Strict scattered collimation will however result in reduced counts due to $\sim 99\%$ loss of the scattered beam flux and increased exposure times (Luggar et al., 1996, Malden and Speller, 2000, O'Flynn et al., 2013b). Even though a wide incident collimation would increase the number of incident X-rays reaching the sample, hence the intensity of the scattered beam, it would also cause a decrease in the angular resolution of the diffraction peaks due to peak broadening. As mentioned previously in Section 3.3.3, studies have shown that a slit collimator offers an increased flux, thus higher signal-to-noise ratio (SNR) when compared to pencil beam collimators, but with a small decrease in the angular resolution (Luggar et al., 1997, Malden and Speller, 2000, Madden et al., 2008, Sun et al., 2010).

Another key aspect of EDXRD is the detector's energy resolution that can affect diffraction profile to a great extent.

Acquisition of EDXRD data has been obtained with significantly shorter times than with ADXRD, with Luggar et al. (1997) and Cook et al. (2007) reporting the collection of EDXRD profiles from explosives and drugs at 1 second but with a low SNR. EDXRD detectors lack however, in energy resolution and often collection times have to be increased for good counting statistics (Luggar et al., 1997). Various energy resolving detectors can be employed for EDXRD with different degrees of energy resolution. Si pixellated detectors indicated low quantum counting at high energies and sodium iodide (NaI) detectors are known to have a low energy resolution of 12% (Cook et al., 2009a). High purity germanium (HPGe) detectors have been proven to provide high energy resolution of 0.7 keV at 59.5 keV, but are expensive and require cooling to liquid nitrogen temperatures (Cook et al., 2009a, Pani et al., 2009). It has been demonstrated that cadmium zinc telluride (CZT) detectors with 4 keV energy resolution at all energies are a good alternative to HPGe detectors; even though

improvement of the formers' energy resolution to 2 keV would be beneficial (Cook et al., 2009a, Cook et al., 2009b, Pani et al., 2009, Ghammraoui et al., 2012). Nonetheless, Crespy et al. (2010) showed that HPGe detectors provide well-resolved peaks that appear as one broad peak with CZT detectors.

Pani et al. (2009) and Cook et al. (2009b) argue that the energy resolution of an EDXRD system is of lower importance when analysing thick samples because of the low angular resolution of the diffraction peaks arising from thick samples, that dominates the overall resolution of the system. Increased sample thickness will cause peak broadening of both EDXRD and ADXRD data, since diffraction maxima will arise throughout the sample (from X-ray source edge to detector edge of the sample), as it is shown later in Section 7.2.

To conclude, both ADXRD and EDXRD have their drawbacks and more or less both techniques suffer from low intensity diffracted X-rays compared to the primary beam (weak diffraction signals). This can cause illicit substances to easily be masked by other substances/structures within luggage. Another major limiting factor of these techniques is their constraint in identifying samples exhibiting preferred orientation or large grain size. Samples with preferred orientation or large grain size often affect the results and interpretation of the raw data. As it will be described later in Chapter 5, the new technique introduced herein, has the ability to overcome the limitations of low intensity profiles, preferred orientation and large grain size.

The key advantages and limitations of ADXRD and EDXRD arrangements are summarised in Table 3.1.

Table 3.1 Advantages and limitations of ADXRD and EDXRD.

ADXRD		EDXRD	
Advantages	Limitations	Advantages	Limitations
High quality crystallographic data	Requires rotation/translation of components	Time effective	Requires narrow and multiple collimation (well-defined 2θ)
No need for spatially filtering the scattered X-ray beam	Long acquisition times	Static equipment setup	High loss of scattered beam flux (long acquisition times)
No need for an energy resolving detector		No need for filtering the incident X-ray beam	Compromise between high energies and good energy resolution
		Possible mobile use	High energy resolution detectors e.g. HPGe are large, expensive and require cryogenic cooling

3.5 Concluding remarks

X-rays interact with matter in various ways, but the most relevant to this work is coherent scattering that offers material characteristic information and is the basis of XRD. Even though scattering can occur from every matter, crystalline materials that possess a long-range order, tend to generate numerous sharp diffraction peaks, in contrast to the broad halos produced by non-crystalline (short-range order) materials. Such materials are liquids and produce one or more broad maxima. Crystalline materials can however, possess certain characteristics that can mislead or complicate the interpretation of their diffraction profiles, such as preferred orientation and large grain size. The leading geometries in the acquisition of scattering distributions, transmission and reflection mode XRD were described

along with the conventional primary beam profiles, including pencil beam geometry. Finally, a comparison between long-established angular dispersive XRD and relatively newly developed energy dispersive XRD was presented, focusing on their differences, advantages and disadvantages in regards to aviation security. It was concluded that even though both arrangements suffer from long acquisition times in demand for good quality data, a combination of both as shown in the literature could be proven beneficial for security screening.

Chapter 4 CODED APERTURES: INTRODUCTION

Outline

A systematic literature review on the history of coded aperture imaging systems is given within this chapter. The foremost coded aperture systems are discussed, mainly in terms of post-sample coded apertures, and the analytical description and fundamental principles of such systems are then presented. Coded aperture analysis is believed to provide an alternative treatment for FCG data interpretation. Finally, coded apertures acting as encoders to obtain spatial discrimination of unknown samples along a primary axis are discussed, in relation to XRD and security screening.

4.1 Background

Part of this work focused on the use of coded aperture systems with focal construct geometry. The importance of coded apertures lies within their potential to offer an alternative approach to FCG data interpretation and their ability to obtain depth information within a volume. It is however important, to first comprehend how coded aperture systems work and identify their abilities and limitations through a brief review of early and current systems.

An early development of a coded aperture system was presented by Mertz and Young (1961) in the form of a Fresnel zone plate (FZP) with a visible-light star camera. The concept of a random array (RA) to act as a coded aperture imaging (CAI) system was introduced later in 1968 in the field of X-ray astronomy by Dicke (1968) and Ables (1968). This notion of randomly arranged multiple holes was introduced due to the need for a system providing high resolution imaging data with a large aperture for X-ray or γ -ray astronomy (Dicke, 1968). Consequently, coded apertures initially consisted of a random arrangement of numerous pinholes of the same diameter (Ables, 1968), as a replacement of the single pinhole system. Even

though a single pinhole would provide the high resolution image required, it possessed an unfeasibly small aperture, thus generating a low SNR (Dicke, 1968).

The major advantage of multi-pinhole coded masks is that the aperture is increased significantly by employing approximately 50% of the area of the aperture, hence increasing the signal-to-noise ratio (SNR) without a decrease in the resolution of the imaging system (Dicke, 1968, Fenimore and Cannon, 1978, Skinner, 1984, Busboom et al., 1997, Gottesman, 2007). The angular resolution of the image is similar to the single small pinhole, but the SNR is increased commensurate with the number of pinholes n of the aperture; \sqrt{n} when a dc background is not subtracted and $\sqrt{n/2}$ when it is subtracted (Ables, 1968, Fenimore, 1978, Fenimore and Cannon, 1978, Fenimore et al., 1978). For X-ray imaging, the advantages of a coded aperture over a pinhole collimator are even greater, due to the weak intensity of the X-ray sources that would require a large aperture to obtain reasonable SNR, sacrificing the angular resolution, as suggested by Fenimore and Cannon (1978). In addition, coded apertures can perform tomography due to the different shadows of the coded aperture arising from different object positions (Fenimore and Cannon, 1978), as will be discussed later on. However, imperfect coded apertures, in terms of non-ideal δ -function autocorrelation as it is explained further on, can cause inherent noise/artefacts in the recovered image (Byard, 2014).

The multi-pinholes aperture masks introduced by Dicke (1968) and Ables (1968) would develop a recorded image consisting of the summation of all the individual images produced by each pinhole in the pattern. Severe overlapping of these images would generate an image with no resemblance to the object under investigation (Fenimore et al., 1978). A decoding procedure involving cross-correlation, by placing the aperture mask on the recorded image, was developed in an attempt to reconstruct the original image of the object (Ables, 1968). Figure 4.1 depicts the above procedure followed during a typical post-sample CAI system.

As demonstrated by Figure 4.1, a coded aperture mask consisting of opaque (0) and transparent (1) elements, is positioned between the object and the detector, hence it is considered as a post-sample aperture. After capturing the encoded image, a decoding procedure follows to recover the original image. This post-processing method involves correlation of the captured image with the coded aperture, based

on the principle that the autocorrelation of the coded mask produces a Dirac δ -function (Gunson and Polychronopoulos, 1976).

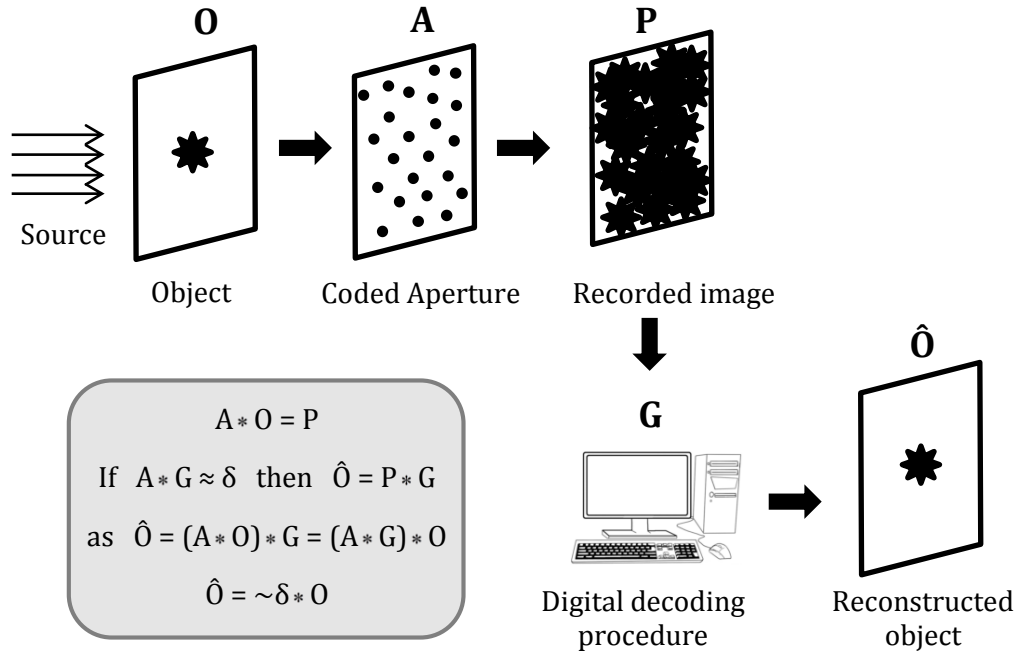


Figure 4.1 The basic principles of post-sample coded aperture imaging system.

It is essential to note here that the terms correlation and convolution are used interchangeable in the literature when the coded mask is circularly symmetric, as convolution is identical to correlation plus a reflection (Silva and Rogers, 1981a, Silva and Rogers, 1981b). However, mathematically, cross-correlation and convolution are distinctly different, as indicated by Equations (4.1) and (4.2), respectively;

$$f(x) \star g(x) = \int_{-\infty}^{\infty} \bar{f}(\tau) g(x + \tau) d\tau \quad (4.1)$$

$$f(x) * g(x) = \int_{-\infty}^{\infty} f(\tau) g(x - \tau) d\tau \quad (4.2)$$

where, \star denotes cross-correlation, $*$ denotes convolution and $\bar{f}(\tau)$ is the complex conjugate of $f(\tau)$.

Details of the mathematical description of coded aperture systems and their decoding procedure are given in Section 4.1.1.

If the autocorrelation of the coded aperture is a perfect Dirac δ -function (see Equation (4.3)), then the object is reconstructed but in the presence of a noise term (Fenimore and Cannon, 1978).

$$\delta(x) = \begin{cases} \infty, & x = 0 \\ 0, & x \neq 0 \end{cases} \quad (4.3)$$

Equation (4.3) indicates that at $x=0$, the δ -function approaches infinity; whereas anywhere else it is equal to zero. This property of the δ -function can be seen in the graphical representation of Figure 4.2. The area under the spike at $x=0$ is always equal to 1 as indicated by Equation (4.4) and $\delta(x)$ can be defined by a number of proper functions, as it is not a true function.

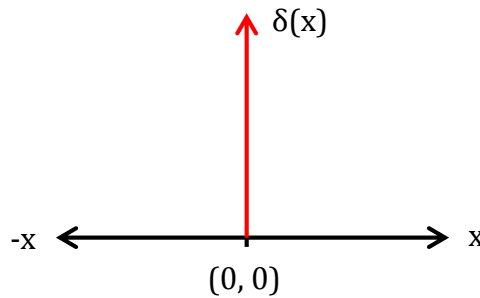


Figure 4.2 A graphical representation of a Dirac delta function.

$$\int_{-\infty}^{\infty} \delta(x) dx = 1 \quad (4.4)$$

However, as it will be discussed later on, most often the autocorrelation nature of the coded mask is not an ideal δ -function. Therefore, artefacts and an inherent noise

are adopted by the reconstructed image, which has a fixed SNR corresponding to the central peak : noise ratio in the auto-correlated function of the coded aperture.

Coded apertures were mainly implemented in X-ray astronomy (Mertz and Young, 1961, Ables, 1968, Dicke, 1968, Skinner, 1984, Busboom et al., 1997) and nuclear medicine (Accorsi et al., 2001, Mu et al., 2009, Martineau et al., 2010) with recent applications in X-ray scattering and security screening (Faust et al., 2009, Olivo et al., 2009, MacCabe et al., 2012). Different mask patterns of coded apertures were evolved over the years commencing with FZP (Mertz and Young, 1961, Barrett, 1972, Cannon and Fenimore, 1980) and random multi-pinhole masks (Ables, 1968, Dicke, 1968, Cannon and Fenimore, 1980), and progressing to non-redundant arrays (NRAs) (Golay, 1971, Weiss, 1975, Vertatchitsch and Haykin, 1986, Finger and Prince, 1995), pseudonoise arrays (MacWilliams and Sloane, 1976, Fenimore and Cannon, 1978, Gottesman and Fenimore, 1989), uniformly redundant arrays (URAs) (Fenimore and Cannon, 1978, Cannon and Fenimore, 1980, Fenimore, 1980, Gottesman and Fenimore, 1989, Busboom et al., 1997, Chen and Kishimoto, 2003) and modified uniformly redundant arrays (MURAs) (Gottesman and Fenimore, 1989, Ballesteros et al., 1996, Gottesman, 2007).

The key criterion on the choice of coded mask, involves the post-processing procedure and which coded aperture's autocorrelation provides the closest approximation to a Dirac δ -function without any sidelobes. The autocorrelation of the coded aperture is described by the system point spread function (SPSF). Nonetheless, most of the proposed systems do not possess a perfect δ -function SPSF, hence the reconstructed object is not a faithful representative of the original object (Fenimore, 1980). In some cases, reconstruction is performed by either correlating the coded image with the coded aperture's convolutional inverse or by correlating the former with the coded mask or a scaled version of it (Fenimore, 1980). In the first case, the decoding array (convolutional inverse) would also enhance any noise present at the certain frequencies of the coded image, thus the reconstructed image would be enhanced by noise (Fenimore, 1980). In the second case of correlation analysis, if the SPSF of the coded aperture is not a perfect δ -function, artefacts would be introduced in the reconstructed image.

The pattern of the FZP autocorrelation function is associated with ripples; whereas the pattern of the random pinhole masks consists of a spike on top of a pyramid and suffers from spurious peaks (fluctuations) (Gunson and Polychronopoulos, 1976, Cannon and Fenimore, 1980, Barrett and Swindell, 1981). NRAs possess an autocorrelation function with a central peak and flat sidelobes equal to unity (Fenimore and Cannon, 1978, Barrett and Swindell, 1981, Skinner, 1984). However, a limitation to NRAs, is the significantly restricted number of holes (maximum ~ 24 holes) due to their associated redundancy that requires each separation (of pair of holes) to occur just once; resulting in a limited increase in the SNR (Fenimore and Cannon, 1978, Skinner, 1984).

URAs are considered as the prevalent coded apertures and were originally proposed by Fenimore and Cannon (1978). URAs belong to a class of arrays referred to as pseudonoise arrays and their uniqueness lies within the constant number of times a particular separation is repeated (Fenimore and Cannon, 1978). During the post-processing procedure of a URA coded aperture system, the coded image can be correlated to a decoding array (also URA) to reconstruct the object. The choice of the decoding array is based on the requirement that upon correlation with the initial URA it will give a perfect δ -function with zero sidelobes (Fenimore and Cannon, 1978). For the SPSF of URAs to be an ideal δ -function, Fenimore and Cannon (1978) state that the post-processing (decoding) array should be the convolutional inverse of the initial URA. It has also been suggested that most post-processing arrays for URAs are equivalent to the initial URA or a scaled version of it (Gottesman and Fenimore, 1989). As proposed by Fenimore and Cannon (1978), zero sidelobes can be achieved either by a single basic URA aperture on a larger detector or by a detector smaller in size than a cyclic-permutation mosaic of URA. By employing only the central region of the URA (single basic array), SPSF with a δ -function nature is achieved (Cannon and Fenimore, 1980). The second method can also be advantageous by providing a larger field of view when small area detectors are employed e.g. X-ray astronomy (Fenimore and Cannon, 1978).

The key advantage URAs have to offer is that they can combine high transmission features often seen by the large open areas of random arrays and ZPL, with the flat sidelobes of the SPSF of NRAs (Fenimore, 1978, Fenimore and Cannon, 1978, Cannon and Fenimore, 1980).

Annular post-sample coded apertures have also been explored, as initially proposed by Walton (1973) and then studied in depth by Simpson (1978). Annular coded apertures belong to the group of dilute apertures together with NRAs, as they have a <50% open fraction; in comparison to the filled apertures (FZP, random pinhole array) that have a ~50% open fraction (Simpson et al., 1975). Similarly to the previously mentioned coded aperture systems, the proposed encoding procedure for annular coded apertures involves correlation of the object with an annulus (coded aperture) with r_1 and r_2 inner and outer radius, respectively. The recorded image is then correlated with the annulus to reconstruct the original object (Walton, 1973, Simpson et al., 1975). The autocorrelation function of the annular coded aperture however, does not represent an ideal δ -function. Instead, there is a central high intensity spike with undesirable ‘wings’ extending out to $2r_2$, and low intensity peaks at $2\bar{r}$ referred to as ‘glitch’ (where \bar{r} is the mean radius of the annulus), as indicated in the literature (Simpson et al., 1975, Simpson, 1978, Silva and Rogers, 1981b). Barrett and Swindell (1981) demonstrated how the annulus can be approximated to a ring-delta function and its autocorrelation has the same characteristics as those proposed by Simpson et al. (1975). The autocorrelation of a ring-delta function (Equation (4.5)) is given by Equation (4.6), over a radial distance r , as shown by Barrett and Swindell (1981). For a more detailed analytical description the reader may refer to Barrett and Swindell (1981).

$$u(r) = \delta(r - \bar{r}) = \delta(|r| - \bar{r}) \quad (4.5)$$

$$u(r) * u(r) = \int_0^\infty d^2r_0 \delta(r_0 - \bar{r}) \delta(|r + r_0| - \bar{r}) = \frac{4\bar{r}^2}{r(4\bar{r}^2 - r^2)^{1/2}} \quad (4.6)$$

Analysis of Equation (4.6), indicates that close to $r=0$, the SPSF has a high fraction value of $4\bar{r}^2$ (i.e. $\frac{4\bar{r}^2}{\sim 0(2\bar{r})}$), whereas at $r=\bar{r}$ is $4/\sqrt{3}$ and at $r=2\bar{r}$ is $2\bar{r}$. When Equation (4.6) is plotted, a central high intensity spike can be seen with a slow decay and ‘glitches’ at $2\bar{r}$ as illustrated in Figure 4.3.

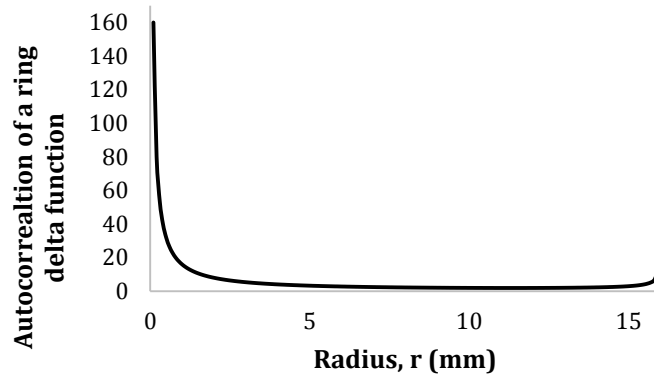


Figure 4.3 The autocorrelation plot of a ring-delta function as given by Equation (4.6); for a $\bar{r} = 8 \text{ mm}$ annulus.

It was suggested by Simpson et al. (1975) that sharpening of the SPSF would improve the quality of the reconstructed image i.e. offering better resemblance to the origin object, but at a possible SNR lost. Simpson et al. (1975) applied certain post-processing filtering to the recovered image, in order to reduce the effect of the slow decaying peak in the annulus SPSF.

As demonstrated by Simpson et al. (1975) and Simpson (1978), this post-processing filtering procedure improved the SPSF in terms of the decaying sidelobes of the central peak, but did not influence the ‘glitch’ at $2r_2$. Filtering eliminated any additional background resulting from the decaying sidelobes, therefore reconstructing the object more effectively. Simpson (1978) determined the increase in SNR from a pinhole to an annulus to be equal to the $\sqrt{\frac{\text{Area of annulus}}{\text{Area of pinhole}}}$ (pinhole is equivalent to pencil beam collimator) prior filtering; with a $\sim 17\%$ decrease in the SNR after filtering.

Simpson (1978) also offers an alternative approach to the annular coded aperture system, aimed to resolve the artefacts introduced by the low intensity peaks at $2r_2$. This approach involved the employment of a two-annulus system with two encoded images. In other words, two annuli of different radius (with an optimum ratio of 1.085 as stated by Simpson (1978)) were convolved with the object to produce two encoded images, that upon certain post-processing would reconstruct the object without the artefacts at $2r_2$. The two encoded images were Fourier transformed and

then added together with appropriate weighting at each frequency (Simpson, 1978). The advantage of this two-annulus system was however eliminated when out-of-focus reconstructions arising from different size shadows of the annular apertures during tomography, re-introduced the artefacts arising from the SPSF at $2r_2$ (Simpson, 1978).

Other researchers (McCrickerd, 1971, Brunol et al., 1978, Silva and Rogers, 1981a, Silva and Rogers, 1981b, Silva and Rogers, 1982) also focused on annulus and twin annulus coded aperture systems. Twin annulus systems involved the application of a single coded aperture consisting of two annuli of different radius.

Early coded aperture systems such as the FZP and random pinhole arrays, as well as all the coded aperture systems discussed in this section up to now, involved post-sample coded masks. However, examples of coded apertures placed prior to the sample, i.e. pre-sample coded aperture, have also been investigated (Klotz et al., 1974, Weiss et al., 1977). In the work presented by Klotz et al. (1974) and Weiss et al. (1977), a non-redundant distribution was examined as a pre-sample coded aperture. Weiss et al. (1977) argue that discrete apertures such as certain point distributions cannot only act as a passive array (post-sample array) but as an active aperture by a distribution of X-ray sources. This distribution of X-ray sources is referred to as a coded source by Barrett and Swindell (1981). The encoded image is obtained by convolution of a non-redundant distribution of X-ray tubes (by simultaneous flashing) with an object. The optical decoding procedure involves correlation and scaling, relevant to the individual layers of the object (Klotz et al., 1974).

A supplementary feature of CAI systems is their tomographic ability, as mentioned previously. The recorded shadow of the coded aperture will be scaled dependently on the distance between the object and the coded aperture (Simpson et al., 1975, Cannon and Fenimore, 1980). Objects close to the coded aperture would produce a larger shadow of the coded mask than objects that are farther away (Chen and Kishimoto, 2003). Additionally, the position of the coded aperture's shadow is dependent on the lateral displacement of the coded aperture (Chen and Kishimoto, 2003, Schultz et al., 2009). These fundamental properties of coded aperture tomographic imaging are illustrated in Figure 4.4.

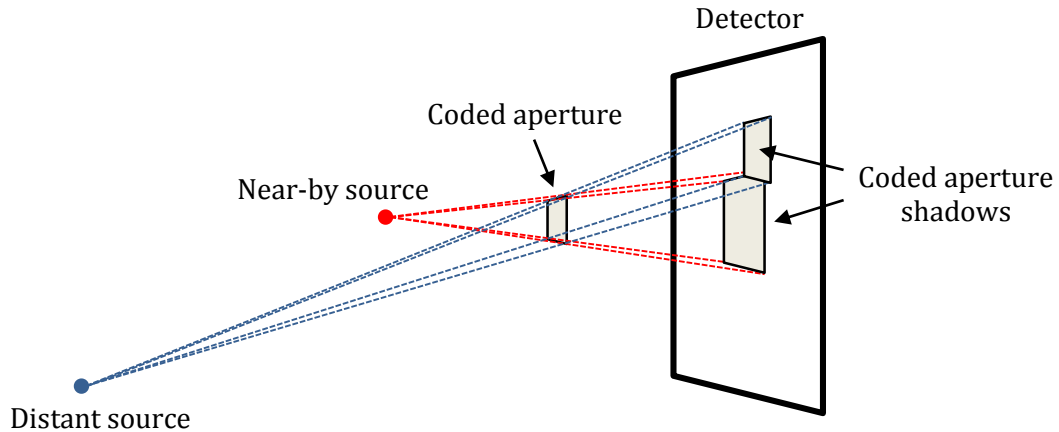


Figure 4.4 The fundamental concept of tomographic imaging with coded apertures [modified from Chen and Kishimoto (2003)].

When imaging 3D objects or multiple objects with a spatial discrimination, the encoded image is the sum of each object plane's correlation with a certain magnification of the coded aperture. Decoding of the image would thus engage correlation of the encoded image with an appropriately magnified decoding array; resulting in only one of the planes to be in-focus, whereas all others would be out-of-focus (Chen and Kishimoto, 2003). Therefore, applications of coded aperture systems do not only purpose an increase in the SNR (without loss of the angular resolution), but also generation of a tomographic effect by acquiring layers of 3D objects (Weiss et al., 1977, Chen and Kishimoto, 2003).

Nonetheless, CAI systems possess certain limitations, specifically in the field of nuclear medicine due to the short distance between the object and the coded aperture camera, such as near-field imaging artefacts with strong background and non-uniform intensities across the field of view (Mu et al., 2009). Artefacts mainly arise during 3D imaging from out-of-focus slices as explained above. Attempts to improve the performance of coded apertures and overcome their limitations resulted in continuous development of different post-processing methods (Accorsi et al., 2001, Mu et al., 2009, Martineau et al., 2010, Zhang et al., 2013, Byard, 2014).

It is important to highlight, that studies on coded apertures, including annular apertures, involved nuclear imaging for medicine as well as X-ray astronomy and

optics, and have been operated in the non-diffractive regime (Simpson et al., 1975, Gottesman, 2007).

4.1.1 Analytical description

In this section, the encoding and decoding procedures involved with a CAI system are presented.

In the spatial domain, let $O(x,y)$ and $A(x,y)$ denote the object and coded aperture, respectively to encode the recorded encoded image by Equation (4.7);

$$P(x,y) = A(x,y) * O(x,y) + N(x,y) \quad (4.7)$$

where $P(x,y)$ is the recorded image, $N(x,y)$ is a noise term and $*$ is the symbol for the 2D correlation operator (or convolution if the coded aperture is circularly symmetric).

One could argue that the object could be recovered by simply deconvolving the recorded image $P(x,y)$ with the coded aperture $A(x,y)$. Even though this would work for ideal noise-less data, in the presence of noise $N(x,y)$ deconvolution fails to recover the object under investigation.

When the cross-correlation (or convolutional inverse) decoding procedure is applied, the reconstructed object, $\hat{O}(x,y)$, is obtained by cross-correlation of the recorded image with a decoding array, $G(x,y)$, as illustrated by Equation (4.8);

$$\hat{O}(x,y) = P(x,y) * G(x,y) \quad (4.8)$$

which when substituted into Equation (4.7) gives Equation (4.9);

$$\hat{O} = [A(x,y) * O(x,y)] * G(x,y) + G(x,y) * N(x,y) \quad (4.9)$$

hence,

$$\hat{O} = [A(x,y) * G(x,y)] * O(x,y) + G(x,y) * N(x,y) \quad (4.10)$$

The reconstructed image is thus arising from the correlation of the object with the correlated coded aperture and decoding array $G(x,y)$ plus a noise term. The following requirements are therefore essential for a perfect reconstruction of the object:

$$A(x,y) * G(x,y) = \delta \quad \text{and} \quad G(x,y) * N(x,y) = 0$$

As mentioned previously, in the case of URAs, the post-processing operator $G(x,y)$ is the convolutional inverse of $A(x,y)$ and is typically a scaled version of $A(x,y)$; whereas for FZP and NRAs, $G(x,y)$ is identical to the coded aperture $A(x,y)$ (Fenimore and Cannon, 1978, Cannon and Fenimore, 1980). In cases of a mismatched decoder $G(x,y)$, i.e. non-identical to the coded aperture $A(x,y)$ (also known as balanced correlation method), where $A(x,y)$ is represented by 1's (transparent elements i.e. pinholes) and 0's (opaque elements), the decoding array would consist of 1's and -1's respectively (Simpson, 1978, Cannon and Fenimore, 1980, Ballesteros et al., 1996).

The decoding procedure is based on the property of $A * G \approx \delta$ (or $A * A \approx \delta$), thus when correlated with the object it generates its reconstruction. Ideally, $A * G$ would be an exact δ -function with zero sidelobes as in the case of URAs (Fenimore, 1978, Fenimore and Cannon, 1978, Chen and Kishimoto, 2003). If however, $A * G$ produces sidelobes with a constant value, a dc background is added to the reconstructed image, which can be removed during post-processing (Fenimore and Cannon, 1978). Sidelobes though, are not usually constant and give rise to inherent noise in the reconstructed object. As mentioned previously, SPSF (Equation (4.11)), which is the autocorrelation function of the coded aperture ($A * A$ or $A * G$) gives an indication on the ability of the coded aperture to recover the original object (Fenimore and Cannon, 1978). The closer the SPSF is to a δ -function the higher the SNR of the reconstructed object.

$$\text{SPSF} = A(x,y) * G(x,y) \quad (4.11)$$

4.2 Encoders

An alternative and more recent approach to CAI systems is to employ the coded mask as an encoder, in order to extract depth information, i.e. tomographic data (MacCabe et al., 2012). This gives rise to the combination of coded apertures with a variety of techniques, such as phase contrast imaging (Olivo and Speller, 2007, Olivo and Speller, 2008a, Olivo and Speller, 2008b, Olivo et al., 2009, Ignatyev et al., 2011, Olivo et al., 2011) and X-ray diffraction (MacCabe et al., 2012, Greenberg et al., 2013b, Greenberg et al., 2014a, Greenberg et al., 2014b). Recent developments on CAI systems tend to focus on their employment in security screening for the detection of explosives and improvised explosive devices (Faust et al., 2009, Olivo et al., 2009, Greenberg et al., 2013a, Greenberg et al., 2014b).

This section will focus on encoders coupled with coherent scattering, as it is of relevance to this work.

A coded aperture composed of a periodic array of lead bars constructed in a comb-like structure has been initially suggested by MacCabe et al. (2012) to act as a post-sample encoder. This ‘coded aperture X-ray scatter imaging’ (CAXSI) system aimed at the recovery of spatial information and identification of unknown substances along a primary axis with a single snapshot. A primary aperture was positioned between the X-ray source and the sample to shape the primary beam into a pencil beam, as illustrated in Figure 4.5.

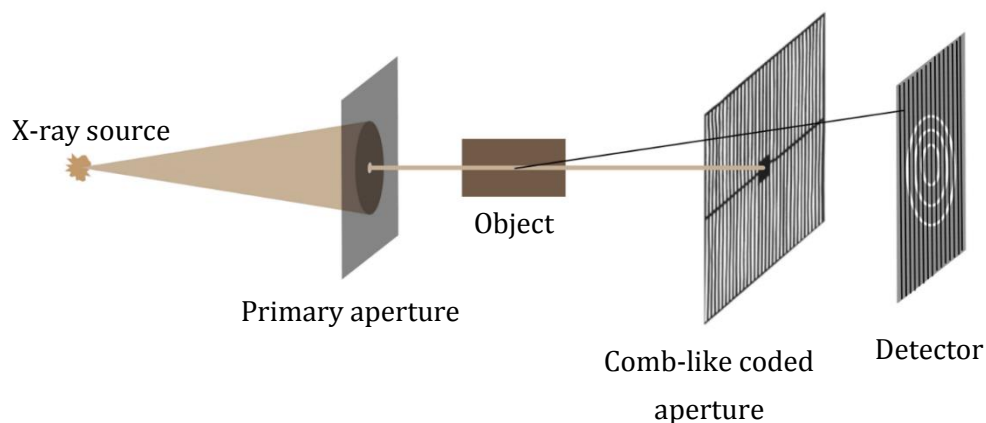


Figure 4.5 Experimental configuration of a pencil beam coded aperture X-ray scatter imaging system with a comb-like aperture [modified from MacCabe et al. (2012)].

A secondary aperture, the comb-like encoder (see Figure 4.5), was placed between the sample and a 2D detector array in order to encode the resulting scattering maxima (MacCabe et al., 2012). The coded aperture and detector array were placed perpendicular to the primary beam's axis, similarly to a transmission mode ADXRD arrangement (see Sections 3.3.1 and 3.4). Once the sample was penetrated by the pencil beam, scattering maxima (Debye cones) struck the coded aperture at certain angles (radius). Scattered X-rays were either transmitted or absorbed by the coded aperture. The Debye cones were therefore modulated in an unambiguous manner by the reference structure proposed by the coded aperture, relevant to the formers' radii, possessing a spatial frequency encoding. The encoded structure of the Debye rings was resolved by an analytical decoding procedure, as designated by MacCabe et al. (2012).

This allowed determination of the sample's position along the primary axis and hence identification of the substance, based on its diffraction characteristics. Moreover, the work was extended to multiplex sampling, comprising of two crystalline powders at different spatial ranges, in order to test the ambiguity of the technique (MacCabe et al., 2012). MacCabe et al. (2012) assert that the results indicated a clear modulation to the geometry of the Debye cones that led in the successful determination of the individual samples and multiplex samples' positions along the primary axis, with an average error of 1.5% and 1.3% respectively, in a single snapshot. Therefore, the samples were identified with an average 0.3% error (MacCabe et al., 2012). The experimental analysis took into account *a priori* knowledge of the samples' positions along the primary beam axis to act as a comparison tool for validation purposes. MacCabe et al. (2012) also proposed that a coded aperture with a finer structure would improve the spatial and momentum transfer resolution of the system. In a later study, the ability of a coded aperture comprised of a sequence of alternating opaque and transparent line blocks of different widths (in the vertical direction) to acquire snapshot tomography with a fan beam geometry was presented (MacCabe et al., 2013).

Greenberg et al. (2013a) combined EDXRD with the coded aperture ADXRD method proposed by MacCabe et al. (2012) to resolve depth and material characteristic information of unknown samples at unknown locations. This technique is referred to as 'coded aperture coherent scatter spectral imaging' (CACSSI). A similar comb-

like encoder to MacCabe et al. (2012) was placed in the path of the scattered X-rays and a linear array of energy-sensitive detector pixels was employed, as shown in Figure 4.6 (Greenberg et al., 2013a). The position-dependent magnification of the coded aperture induces a spatial encoding on the scattering maxima allowing recovery of their position along the primary beam axis through a reconstruction algorithm proposed by Greenberg et al. (2013a).

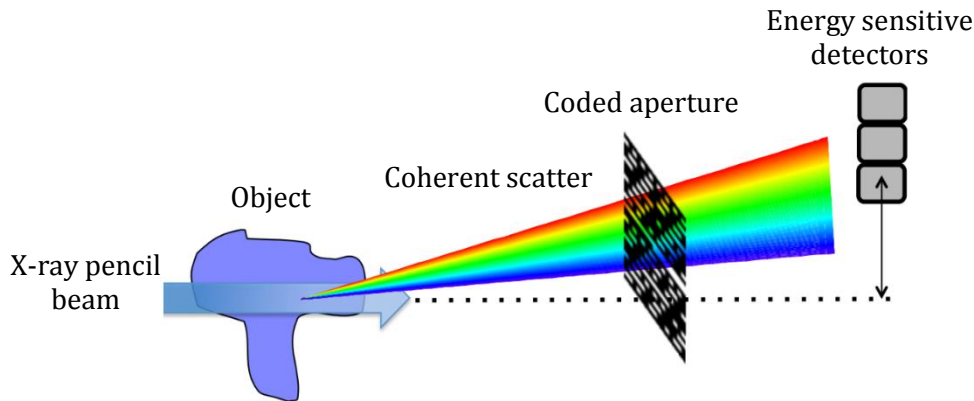


Figure 4.6 Experimental arrangement of coded aperture coherent scatter spectral imaging (CACSSI) technique [modified from Greenberg et al. (2013a)].

CACSSI was also attempted with liquid samples indicating potential discrimination between water and 50% concentration of H_2O_2 (Greenberg et al., 2013a). However, the momentum transfer resolution of CACSSI was reduced when the complexity of the objects increased during multiplex sampling (Greenberg et al., 2013a). Furthermore, Greenberg et al. (2014a) demonstrated the application of CACSSI with a single energy-sensitive pixel detector of sufficient energy resolution to detect the modulation in the scattered rays.

In a later study, Greenberg et al. (2014b) employed a similar encoder to that of CACSSI as a pre-sample coded aperture aiming to enhance source efficiency. This technique is termed 'structure illumination coherent scatter imaging' (SICSI) and implements at least one polychromatic X-ray source. A coded aperture consisting of a periodic series of holes was positioned between the X-ray source and the object (Greenberg et al., 2014b). The coded aperture served two causes: to decrease the required incident beam flux and to induce a position-dependent modulation on the scattered X-rays (Greenberg et al., 2014b). The object was translated relative to the

X-ray source in order to be illuminated by a multiple number of different incident angles, resulting in lower required incident beam flux or shorter acquisition times (Greenberg et al., 2014b). A single energy-sensitive pixel detector was employed to obtain time measurements (to determine object's position along the translational x-axis) and energy-resolved measurements (modulated for different object positions along the primary z-axis) of the scattered rays (Greenberg et al., 2014b). A reconstruction process was then applied to extract the encoded information.

Greenberg et al. (2014b) suggest that the results indicated reasonable estimations of the object's position and material characteristics, despite the presence of some artefacts. It was noted that only $\sim 0.1\%$ of the coherent scattering was acquired by the detector, signifying that a larger detector could reduce time exposure (Greenberg et al., 2014b).

4.3 Concluding remarks

In this chapter, a review on the history of coded aperture systems was given, whilst focusing more on the dominant URAs and the relevant to this work, annular coded apertures. The key characteristics and ability of the annular coded apertures to reconstruct objects were discussed alongside proposed post-processing procedures for more efficient reconstructions.

The main advantages of coded aperture systems were identified to be the increased SNR when compared to pinhole apertures and good angular resolution. Additionally, CAI systems have been notably developed for their tomographic capabilities, specifically for nuclear medicine.

Recent developments on coded apertures involve their application in XRD, mainly as post-sample encoders. Their purpose is to modulate the scattered X-rays in a position-dependent manner in order to determine the position of unknown substances along a primary axis and enable material identification. This serves in the characterisation of unknown substances with no *a priori* knowledge of their spatial range, which within other applications, could be implemented in the identification of hidden explosives.

Chapter 5 FOCAL CONSTRUCT GEOMETRY

Outline

In this chapter, the novel 'focal construct geometry' (FCG) developed during this work is introduced and described in detail. The theory underlying an annular beam geometry with its fundamental principles and key concepts are explained. Details are given on previous studies performed with this geometric arrangement and examples of such XRD data are presented. Lastly, the main gaps in research involving FCG and the objectives of this study are identified.

Focal construct geometry is the scientific and technological basis of a new method for high speed acquisition of angular dispersive X-ray diffraction data with enhanced intensity. The theoretical considerations underlying FCG were first presented by Rogers et al. (2010).

FCG is an emerging novel geometry for powder X-ray diffraction that utilises an annular beam instead of the conventional pencil beam arrangement. Proof-of-concept for this innovative technology has been established by previous research (Chan et al., 2010, Rogers et al., 2010), demonstrating the capability of FCG to provide diffractograms of much higher intensity than conventional XRD techniques. In addition, FCG has the advantage of utilising a greater cross-section of the interrogating sample area when compared to traditional XRD techniques, without increasing the flux density, within security screening where the approach integrates a larger volume simultaneously.

5.1 Geometry

FCG's fundamental property is the employment of an annular beam (hollow conical beam) instead of the conventional pencil beam arrangement. FCG is employed

usually in transmission mode angular dispersive powder XRD, where the sample and detector are normal to the primary axis. Figure 5.1 illustrates a 3D schematic diagram of the FCG arrangement. An annular collimation optic is placed between the X-ray source and the sample to shape the primary beam into a hollow cone. The circular footprint of the primary beam onto the sample can theoretically be considered to consist of an infinite number of pencil beams around its circumference. A Debye cone will therefore be generated from each pencil beam around the circumference of the annular beam, hence causing the formation of multiple Debye cones. Since these Debye cones occupy the same radius, at certain distances they will converge into single points along the primary axis.

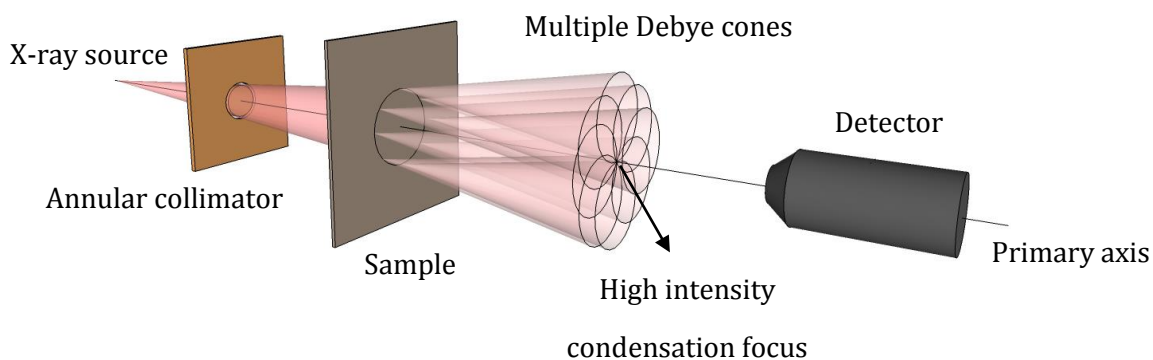


Figure 5.1 A 3D schematic illustration of the focal construct geometry (presenting a limited number of Debye cones). The system is circularly symmetric around the primary beam axis.

These focal points are termed ‘condensation foci’ and have enhanced intensity due to the concentration of multiple Debye cones, as demonstrated in Figure 5.1. Translation of an area detector along the primary axis acquires the location of the condensation foci, which can be converted into conventional 2θ angles by Equation (5.1);

$$2\theta = \phi_m + \tan^{-1}\left(\frac{R_s}{D_{SD}}\right) \quad (5.1)$$

where ϕ_m is the mean angular divergence, R_s is the radius of the primary beam's footprint on the sample and D_{SD} is the sample-to-detector distance, as depicted in Figure 5.2.

The scattering 2θ angles can then be translated into d-spacing values by employing Bragg's law Equation (3.4).

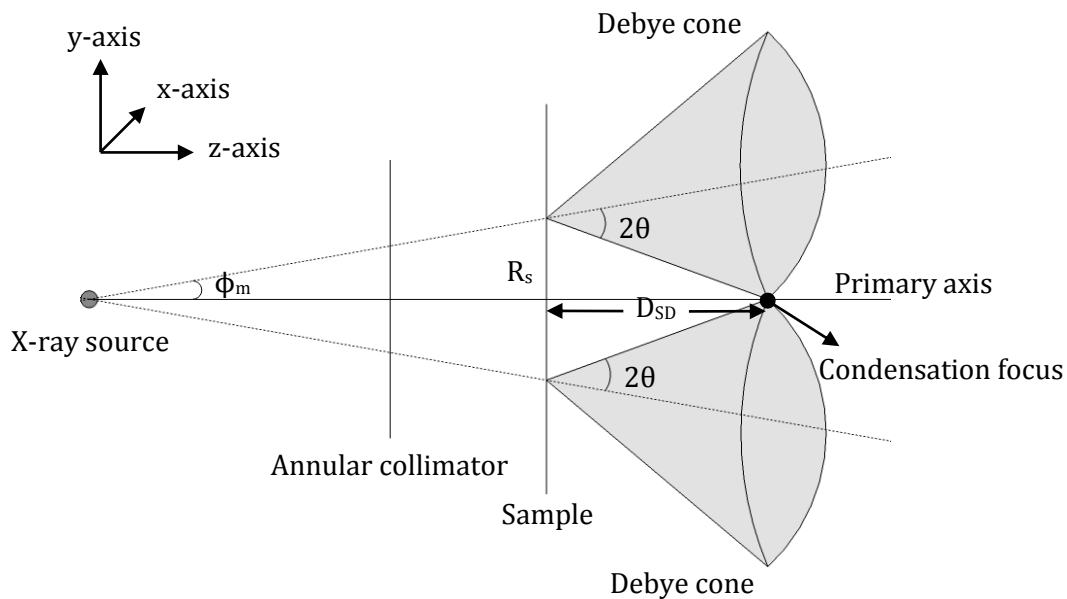


Figure 5.2 A 2D diagram of the geometrical relationships in a focal construct arrangement.

An example of the high intensity condensation focus can be observed in Figure 5.3 (b), in which empirical diffraction (FCG) patterns produced from an aluminium oxide (Al_2O_3) plate along the primary axis are presented. Figure 5.3 (a) and (c) illustrate the diffraction patterns at $\sim 1^\circ$ 2θ angle at either side of the Bragg maximum. Converging condensation rings prior to their condensation into a focal point are shown in Figure 5.3 (a); whereas in Figure 5.3 (c), the condensation focus had already been formed and it is now in the shape of a diverging condensation ring.

It is important to note that these rings present in the FCG pattern are not Debye rings. They are condensation rings caused by the convergence and divergence of multiple Debye cones into and from condensation foci respectively, and they show

the same enhanced intensity as the condensation foci. The bright FCG patterns can therefore be referred to as diffraction caustics as defined by Evans et al. (2014).

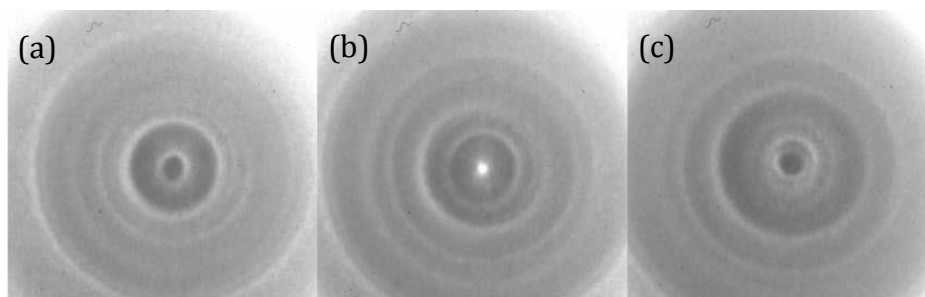


Figure 5.3 Diffraction images from an Al_2O_3 sample measured at 1° less than the 311 convergence point (a), the 311 convergence point (b) (note the high central intensity) and 1° greater than the 311 convergence point (c) [obtained directly from (Rogers et al., 2010)].

A better understanding of the formation of the condensation rings can be provided by Figure 5.4. The condensation rings coloured in green and blue are formed from the convergence of multiple Debye cones into condensation foci labelled '1' and '2', respectively.

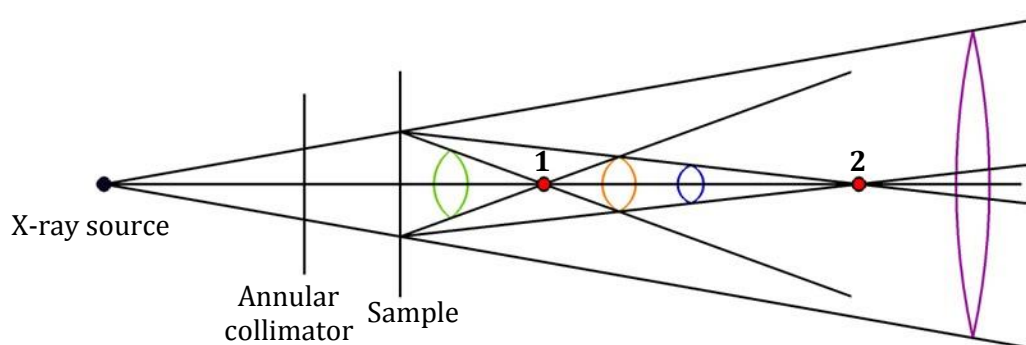


Figure 5.4 The condensation rings produced by two Bragg's maxima with an annular beam geometry.

The condensation ring in orange colour is an overlap/combination of the convergence of the Debye cones forming condensation focus '2' and the divergence of the Debye cones forming condensation focus '1'. Therefore, for the example given

in Figure 5.4, at each detector's z-location prior condensation focus '1', two converging rings are captured; whereas in between condensation foci '1' and '2', one diverging and one converging condensation rings are observed. After the focal point of both scattering maxima, two diverging condensation rings are recorded. The ring coloured in purple is the annular primary beam that is generally greater than the area of the detector; therefore, it is experimentally non-observable.

The schematic illustration of the condensation focus and rings depicted in Figure 5.5 shows FCG diffraction caustics generated from conventional scattering maxima. In Figure 5.5, scattering maxima from a single 2θ angle are considered with a fixed annular beam (red ring).

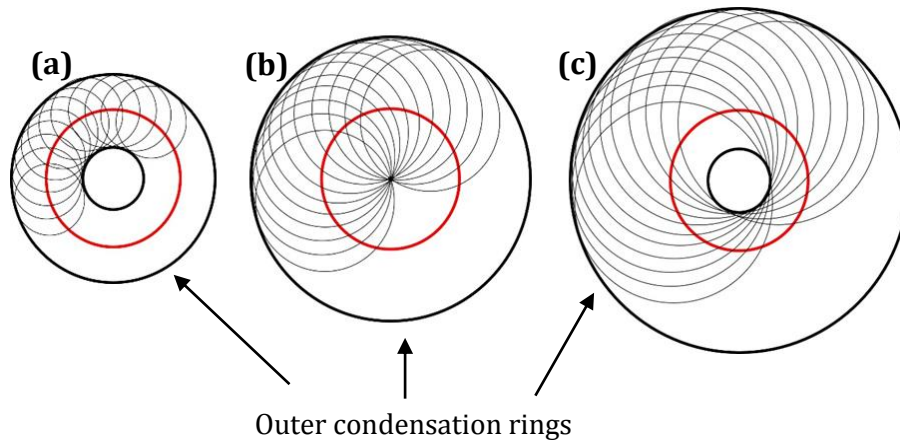


Figure 5.5 Discretised representation of a continuum of Debye cones forming a converging (a) and diverging (c) condensation ring, and a condensation focus (b). Outer condensation rings are also presented. The red circle represents the primary beam.

Essentially, FCG patterns can be considered a result of the convolution of the Debye cones with the annular primary beam, as seen in Figure 5.5. The convergence and divergence of these Debye cones, as their radius increases is illustrated in Figure 5.5 (a) and (c), respectively. Figure 5.5 (b) demonstrates the condensation focus formed when the Debye cones have the same radius as the primary beam. The outer condensation rings are also shown, indicating that their radius increases proportionally to the radius of the Debye cones.

5.2 Previous studies

Previous research (Chan et al., 2010, Rogers et al., 2010) illustrated the fundamental principles underpinning FCG, theoretically and experimentally. Empirical diffraction patterns have been acquired successfully by FCG and the enhanced intensity of the condensation foci has been experimentally confirmed. The intensity of the FCG diffraction maxima has been calculated to be a factor of $\sim 8R_s/W_T$ greater than the intensity of the scattering signatures obtained from an equivalent pinhole of W_T diameter, as indicated by Rogers et al. (2010). The relationship of the absolute intensities of FCG and conventional diffraction maxima will be described in greater depth later in Section 7.2.1. The relative intensities however, of the diffraction caustics differ to those from conventional XRD data, mainly due to intensity corrections (e.g. Lorentz factor that varies with diffraction geometry) applied to the latter, as commented by Rogers et al. (2010).

It has also been demonstrated (Chan et al., 2010, Evans and Rogers, 2011) that FCG can identify illicit substances and materials of varying thicknesses within a very short period of time when compared to other XRD techniques, as well as being able to identify samples under non-ideal conditions (i.e. beam occlusion). FCG has been proven to identify substances that are partly covered by placing an absorber in between either the sample and the detector or the X-ray source and the sample. The successful identification of partly covered materials is of significant benefit, especially when dealing with security screening of luggage in airports, where structures may be overlapping or camouflaged.

In addition, FCG is believed to have the capability of identifying substances having preferred orientation and/or large grain size, which is a major drawback of traditional XRD analysis, since any of these effects can influence the raw data and its interpretation (Chan et al., 2010, Evans et al., 2010, Rogers et al., 2010). Conventional XRD techniques typically capture a section of the Debye rings. If the material analysed exhibits preferred orientation, there is a high possibility that some of the Debye rings will be absent at that section, giving rise to misinterpreted results as illustrated in Figure 5.6.

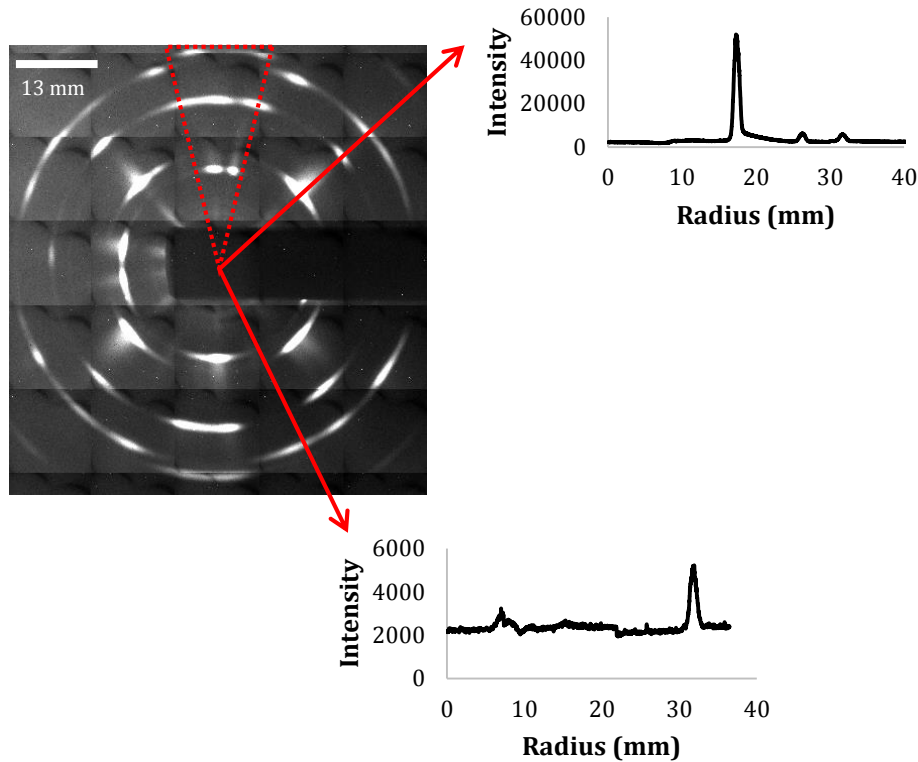


Figure 5.6 Diffraction image from an aluminium sample with preferred orientation, along with its linear integration at two different azimuthal angles.

A simulation algorithm has also been developed to reproduce experimental data and aid the development of FCG. Simulation work has determined the potential hit rate i.e. sensitivity and the false alarm rate i.e. specificity of FCG (Evans and Rogers, 2011). The results were derived from 200 trials for each threat material including a variety of explosives and drugs of abuse of different relative compositions. The performance of FCG was shown to be poorer than that of the benchmark laboratory diffractometer's, but this was expected taking into account the early developing stages of FCG. The sensitivity of FCG was proven to be very high as it did not produce any false positives for the threat materials analysed, except for TNT (Evans and Rogers, 2011).

Furthermore, previous research has established the development of a novel imaging technique, referred to as multidirectional X-ray absorption tomography (MXAT) (Evans, 2010). MXAT utilises the annular beam geometry to capture absorption information and provide 3D view images of the scanned object. A typical

arrangement for MXAT is shown in Figure 5.7. As in the case of FCG, a monochromatic X-ray source is utilised with an annular collimation system forcing the X-ray photons to strike the sample in the shape of a hollow cone. A transmission area detector or a ring detector (line detector in the shape of a ring) can be used to measure the attenuation of the objects within the volume. The X-ray beam and the detector are translated simultaneously in x and y directions as shown in Figure 5.7, raster scanning the suitcase. Taking a closer look at the arrangement of MXAT, it can be seen that a parallax effect is being produced, providing depth information. This parallax effect, as demonstrated in Figure 5.7, is being formed when the annular beam is translated along the scanned item, providing information on the depth difference between two overlapping (same x and y positions but different z position) objects. This produces a sequence of images, viewed as a video, that can impart a vivid appearance of relative depth (Evans and Rogers, 2010).

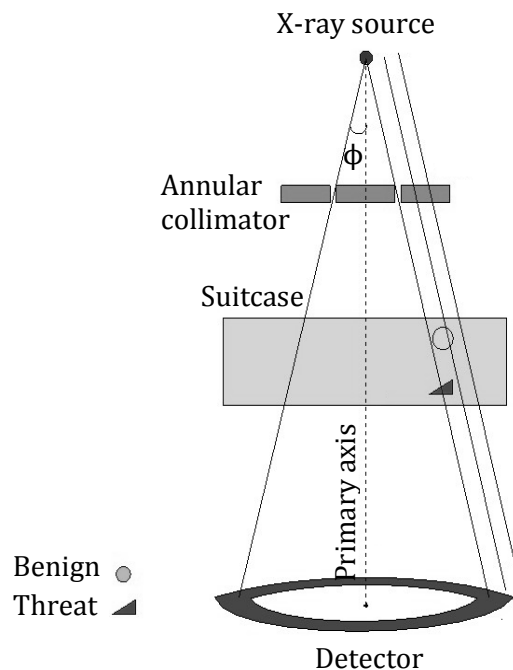


Figure 5.7 The parallax effect arising from MXAT arrangement.

A brief summary of the key findings of previous research and indications for further reading are given below:

1. High intensity diffractograms (Chan et al., 2010, Evans et al., 2010, Rogers et al., 2010).
2. Identification of substances having preferred orientation / large grain size (Chan et al., 2010, Evans et al., 2010, Rogers et al., 2012).
3. Rapid identification of a range of materials and illicit substances (Chan et al., 2010, Evans et al., 2010, Rogers et al., 2010, Evans and Rogers, 2011).
4. Identification of partly covered substances under different conditions (Chan et al., 2010, Evans and Rogers, 2011).
5. Technique's potential hit rate (sensitivity) and false alarm rate (specificity) tested (Evans and Rogers, 2011).
6. Simulation algorithm developed to re-create and compare experimental data (Evans and Rogers, 2011).
7. Simulation of samples with preferred orientation and large grain size and comparison with empirical data (Rogers et al., 2012).
8. On-going development of a novel imaging technique (MXAT) based on the same annular beam geometry as FCG (Evans and Rogers, 2010, Evans et al., 2014).

5.3 Research Gap

Focal construct geometry is an emerging technique with a wide field of areas yet to be explored. Some of the key areas in need of further research are explained below.

- ***Instrumental development***

FCG is still in development stages and it has great potential of improvement, especially in terms of specificity. The scattering maxima currently obtained by FCG, possess a broadening phenomenon that is not yet fully appreciated. The acquisition of diffraction signals from FCG and conventional XRD techniques have to be further explored and compared in order to identify possible FCG peak broadening or instrumental broadening. Future experiments aiming to decrease the width of the diffraction peaks thus increase the resolution, could involve investigation into the

effect of a variety of collimation optics, sample alterations and alternative X-ray sources and detectors. The shape, length and wall thickness of the collimation optic could be altered to decrease beam thickness and angular divergence in order to increase the technique's specificity. Additionally, different X-ray sources and/or detectors could provide greater angular resolution with shorter acquisition times, thus making FCG more practical for security screening.

- ***Non-ideal samples***

Previous research was focused on the appreciation and detection of Bragg's maxima with near-ideal polycrystalline samples, in terms of preferred orientation and grain size. Even though the acquisition of diffraction maxima from single non-ideal samples exhibiting preferred orientation and large grain size has been successfully achieved by Rogers et al. (2012), the relationship between their Debye cones and their diffraction caustics has not been demonstrated. It is important to examine such samples in detail in order to understand their effect on FCG.

Furthermore, non-crystalline samples such as liquids that are of significant value to aviation security have not been previously analysed by FCG. Identification of such samples and discrimination between threat and benign liquids would be extremely beneficial for the world of security screening.

- ***Random sample orientation***

FCG has been established with planar samples, normal to the primary axis. This however, is a special case of sample arrangement for FCG. A more generalised scenario of the geometry involved, would possess a sample randomly orientated with respect to the primary axis. For example, in suitcases that undergo security checks it is very unlikely that the long axis (surface) of all objects would be normal to the FCG system's primary axis. It is therefore essential to examine different sample orientations and assess their effect on FCG diffraction caustics.

- ***Multiple samples***

Clustering of objects within suitcases is another limitation for screening techniques. Previous studies involved the determination of partly covered substances by high absorbing materials. It is however important to establish the ability of FCG to identify substances when present in a clustered environment by low absorbing materials. For example, in the case of multiple scatterers when an explosive substance is overlapped by an organic material. This is essential for security screening as often explosives are camouflaged and cluttered with other common objects within suitcases.

- ***X-ray penetration of bulk objects***

The energy employed during the FCG analysis of samples by previous studies is limited to ~ 17 keV (molybdenum). Any system aimed for aviation security screening must be able to have X-rays of sufficient energy in order to penetrate suitcases and objects within them. For this reason, it would be valuable to merge FCG with higher energies (e.g. tungsten) than that of previous use.

- ***FCG coupled with an imaging technique***

A successful screening technology would have the ability to provide shape, material and depth information with high sensitivity and specificity. For this reason, combination of FCG with an imaging technique would be extremely advantageous in the field of security screening. Current research is focusing on the development of an imaging technique based on the same annular beam geometry as FCG. This technique aimed to combine diffraction data and shape information is termed HALO. HALO is an innovative material specific imaging technique, initially developed in 2010 by collaboration of Cranfield University and Nottingham Trent University (Evans, 2010, Evans et al., 2014). HALO utilises the focal construct beam geometry to combine XRD and the novel MXAT imaging technique mentioned previously in Section 5.2. HALO enables the acquisition of a material specific volumetric image of the scanned object. Further development and improvement of HALO is an essential aspect of the FCG technology to act as a screening technique, as material

characteristics without depth (and shape) information can occasionally be proven insufficient.

- ***Coded aperture***

Previous works have not considered the possibility of FCG acting as a coded aperture imaging system. An annulus can be treated as a coded aperture as illustrated by a number of researchers (Simpson, 1978, Barrett and Swindell, 1981, Silva and Rogers, 1981b) due to its unique shape with the capacity to recover an image of the objects under investigation; which in this case are the Debye cones. However, previous studies on annular coded apertures were performed in non-diffractive space.

Establishment of an annular aperture system with XRD can prove very beneficial for FCG, as it would recover conventional XRD images of any sample, without compromising the enhanced intensity of the scattering maxima provided by FCG. In addition, conventional interpretation methods could therefore be employed for the reconstructed data if needed.

5.4 Concluding remarks

In this chapter, the novel primary beam geometry (FCG) investigated throughout this work was presented and explained. The geometrical arrangement and XRD data obtained by FCG were rationalised and explained in detail. Furthermore, the key features and importance of an annular primary beam, especially for security screening, were highlighted with reference to previous studies. Former research, as well as on-going studies, were reported along with important reference points for the reader, and the current research gaps were identified. Based on previous research and limited development of FCG in certain areas, the intentions of this work were determined as:

- Investigate the current limitation of FCG in terms of data specificity resulting from peak broadening. Identify if it is an outcome of the annular beam geometry or the instrumentation employed.

- Identify the potential of FCG to analyse non-crystalline samples such as liquids and investigate potential differentiation between threat and benign liquids for aviation security.
- Explore and understand the diffraction caustic data generated from samples exhibiting preferred orientation or large grain size and identify any advantages of FCG when analysing such samples.
- Study a more generalised case of sample orientation with respect to the system's primary axis and determine if FCG data with enhanced intensity could still be acquired.
- Identify if analysis of multiple samples is feasible with FCG and determine possible recovery of their individual diffraction patterns.
- Study FCG in terms of convolution of the primary beam and Debye cones, and identify their relationships with the resulting FCG diffraction maxima (condensation rings).
- Investigate the potential of an annular (pre-sample) coded aperture system aiming at the recovery of conventional XRD data from single FCG images at significantly short acquisition times.
- Finally, study the effect of novel post-sample encoders in order to acquire spatial information and identify unknown samples with conventional XRD and FCG.

A summary of the key research areas along with the corresponding aims and objectives are given in Figure 5.8. The experimental work and the outcomes of this study, presented in Chapter 6-Chapter 8, are outlined in the same order as indicated by Figure 5.8. Moreover, a supplementary diagram to Figure 5.8 is provided as a concluding remark in Chapter 10 (Figure 10.1), where the aims and objectives are replaced with the main conclusions drawn from this research.

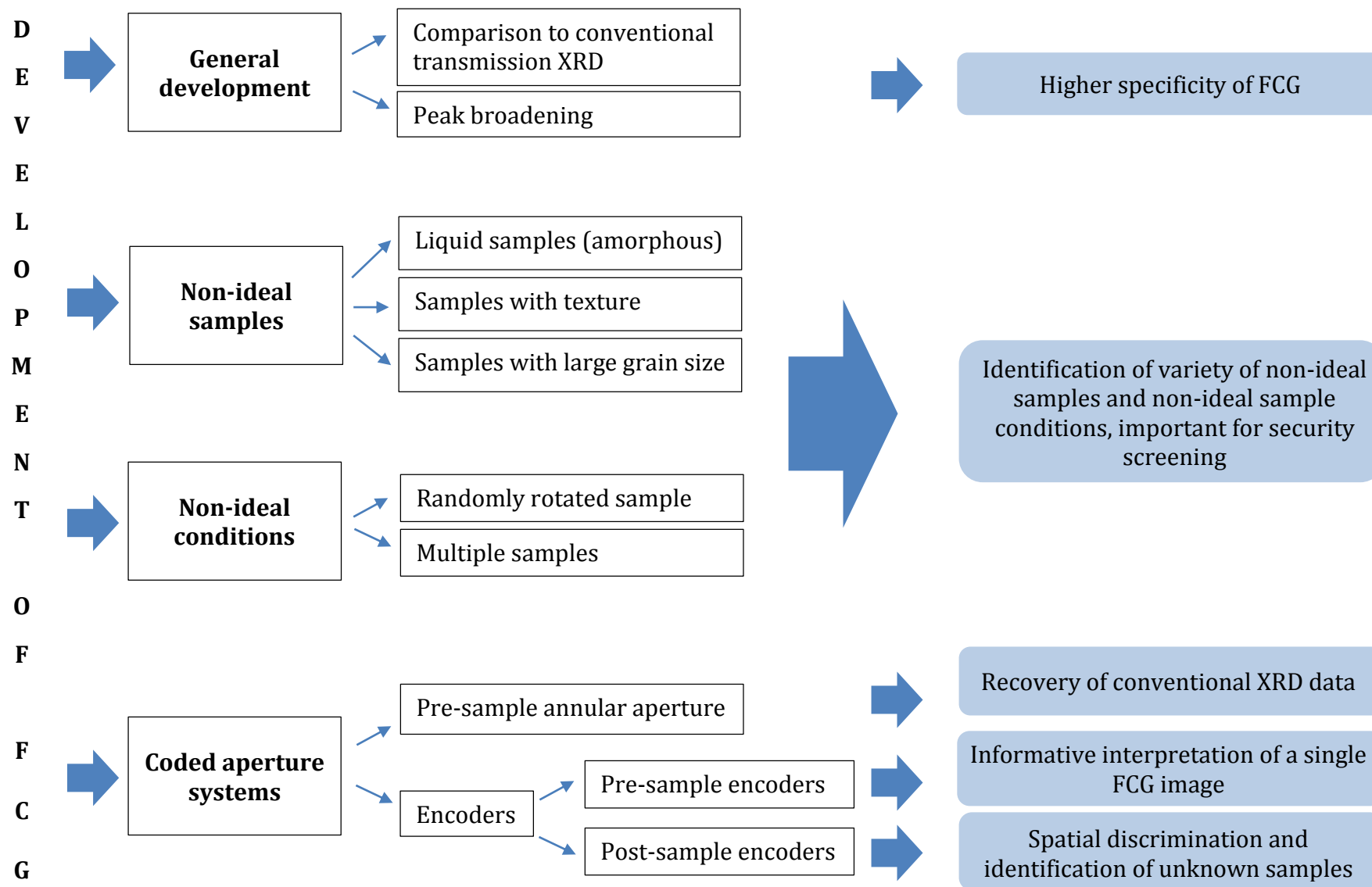


Figure 5.8 A flow diagram illustrating the main research areas of this study along with their aims and objectives.

Chapter 6 MATERIALS & METHODS

Outline

In this chapter, the instrumentation and materials utilised during the experimental work are presented. Experiments were performed in a simulated and empirical manner. A ray-tracing simulator is introduced and the instrumentation used to collect the empirical data is described. Furthermore, the methodology employed for each series of experiments is given and the post-processing analysis of the collected data is explained. The experimental work is divided into five main research studies involving the analysis of non-ideal samples with an annular beam arrangement. Initially, a comparison between the annular and pencil beam geometries is provided, in terms of peak broadening. The effect of the focal construct geometry on the width of diffraction peaks, as well as the instrumental broadening was examined. Non-crystalline samples such as liquids were investigated. The identification of two major groups of non-ideal samples with significant value to security screening systems was explored, including samples exhibiting preferred orientation and large grain size. Additionally, the effect of a different sample arrangement for focal construct geometry was studied, where the sample was placed in a random orientation with respect to the primary axis. Finally, experiments were performed with the presence of multiple samples, both normal to the primary axis but with different primary axis' position, characteristic of objects within luggage.

6.1 Instrumentation

The majority of the experimental work in this study was focused on the focal construct geometry (FCG) described in Chapter 5. In several experiments however, a conventional pencil beam geometry was employed to act as either a comparative or a supplementary tool to the diffraction caustic data (see Chapter 5). The instrumentation employed (except the collimation optics) remained the same for

both geometric arrangements; whereas the experimental methodology and analysis were modified depending on beam geometry.

The majority of experimental work was performed through two different approaches, i.e. simulation and empirical. Simulated experiments mainly operated as a confirmatory and comparative approach to empirical data. Moreover, a simulator was employed to facilitate the design, as well as to assist and predict empirical experiments and the behaviour of X-rays with various non-ideal sample conditions.

6.1.1 Ray-tracing simulator

An in-house 3D ray tracing simulator package was developed in Matlab® to assist the optimisation and development of FCG. In the simulator, X-ray photons were represented by rays that were emitted from an ideal point source and their path was recorded as they passed through a specified volume i.e. a sample. For optimisation, rays were emitted at a specified angle ϕ (or angles) around the primary z-axis (Figure 5.2); rather than being emitted isotropically and collimated. Sample objects of any size and shape were designed in Google SketchUp (version 8.0.16846) and imported into the simulator's volume at any desirable distance from the X-ray source. The wavelength was set at 0.07107 nm for a molybdenum target X-ray source and the user could then assign a mass attenuation coefficient value (Section 3.1) to the sample, as well as scattering maxima positions (2θ angles), thus introducing material specific characteristics. Once the rays entered a voxel within the sample, the behaviour of the rays was modified; either in terms of attenuation (reducing the intensity of the rays) or direction (diffraction according to the pre-specified scattering angles). Images were formed on a plane normal to the primary axis at any given distance from the source. It should be noted that the ray-tracing simulator is limited by inaccurate relative intensities of the diffraction maxima and lack of accountability for air and Compton scattering.

6.1.2 Empirical approach

The instrumental set-up included a molybdenum (Mo) target X-ray tube, bespoke collimators (either annular or pinhole), a sample and a CCD detector (Figure 6.1 and Figure 6.2). A detailed description of each of these components is provided below.

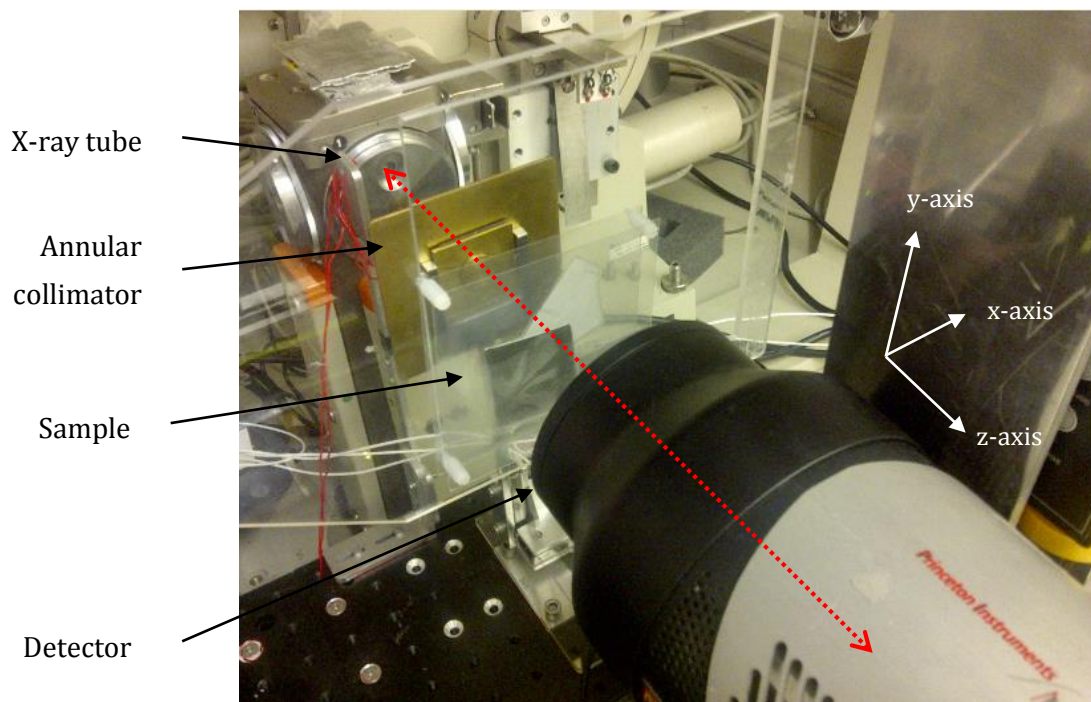


Figure 6.1 Photograph of the FCG instrumentation employed for this work. The red dotted line indicates the primary z-axis of the system.

- ***Panalytical XRD Glass Tube***

The X-ray source employed was a standard water cooled sealed monochromatic glass tube (40 kV, 30 mA) with a molybdenum (Mo) target of 0.7107 \AA ($\sim 17.5 \text{ keV}$) and a zirconium (Zr) filter. The take-off angle of the X-ray source was set at 6° with a long fine focus spot of $0.4 \times 12 \text{ mm}$.

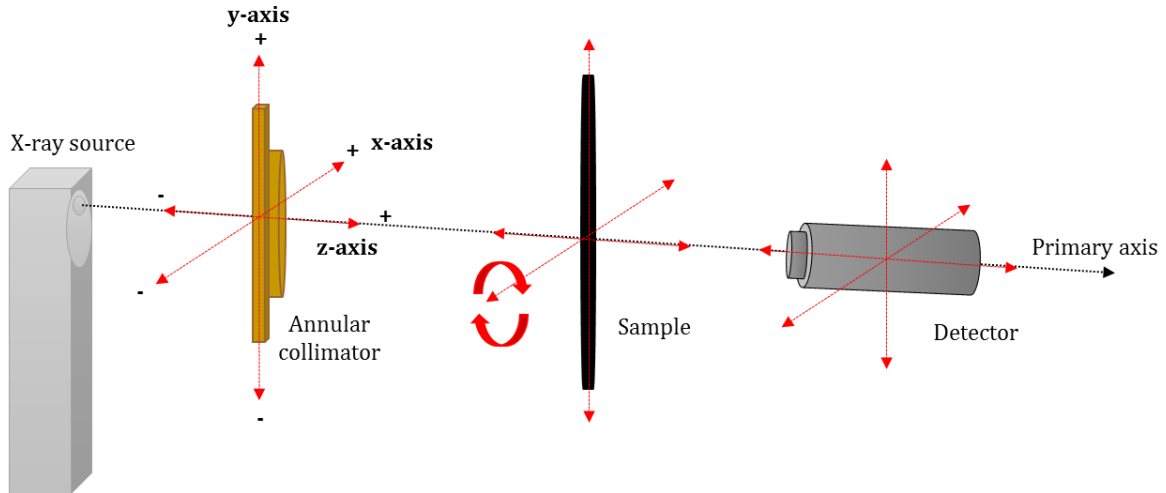


Figure 6.2 The focal construct geometry employed for this work with illustrations of the translational and rotational axes (red arrows) of each instrumentation component.

- ***Collimation optics***

An annular collimator (*AB1*) made from brass was employed during FCG experiments. Figure 6.3 illustrates the dimensions of the collimator, including both the solid circular disc of 17.5 mm diameter and the rectangular plate with an annular aperture of 18 mm diameter. The disc and plate were attached by adhesive tape to form collimator *AB1*, as shown in Figure 6.3.

The bespoke annular, pencil beam and pinhole collimation optics utilised during the experimental work are given in Table 6.1.

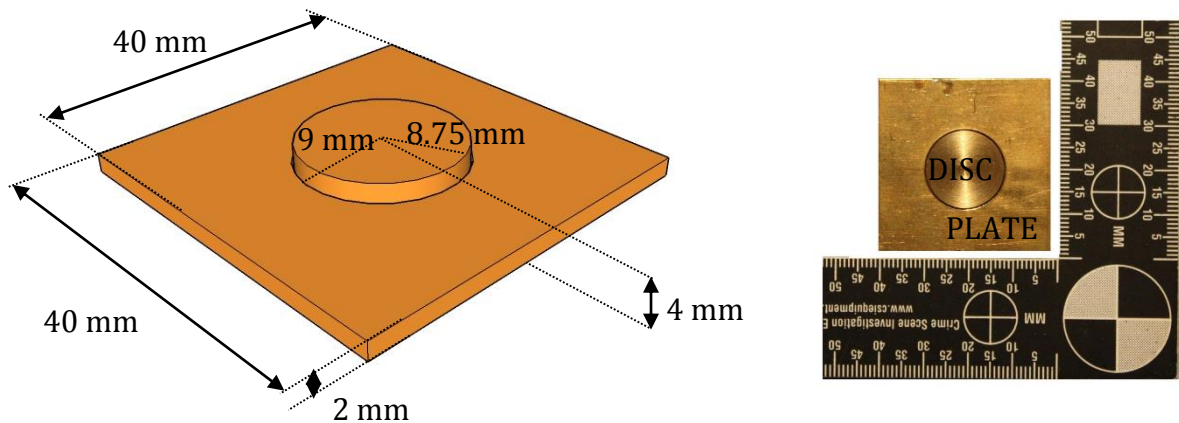


Figure 6.3 Schematic diagram (left) and photograph (right) of the bespoke annular collimator *AB1* (see Table 6.1).

Table 6.1 Details on the collimation optics utilised during the experimental work.

Collimator	Aperture shape	Diameter (mm)		Dimensions (mm)	Inner separation distance (mm)	Thickness / Length (mm)	
		Inner	Outer			Plate	Disc
<i>AB1</i>	annular	17.5	18	-	-	2	4
<i>AB2</i>	2 rectangles	-	-	1.9 x 1.4; 1.4 x 1.25	11.3	~4	-
<i>AB3</i>	4 rectangles	-	-	3 x 0.95; 3.5 x 0.95; 3.15 x 0.95; 2.6 x 0.95	11.9	~5	-
<i>PB1</i>	pinhole	-	~0.55	-	-	4	-
<i>PB2</i>	pinhole	-	0.66	-	-	4	-
<i>PB3</i>	pinhole	-	0.66	-	-	2	-
<i>PB4</i>	1 rectangle	-	-	1.5 x 1	-	3	-
<i>PB5</i>	pencil beam	-	0.5	-	-	75	-
<i>PB6</i>	pencil beam	-	0.5	-	-	175	-
<i>PB7</i>	pencil beam	-	0.05	-	-	190	-

- ***Detector***

A Princeton Instruments 13.3 x 13.3 mm area detector with 1024 x 1024 pixels (13 x 13 μm) CCD (2D Gadox – Princeton Instrument PIXIS 1024), thermoelectrically cooled to $\sim 233\text{ K}$ ($\sim -40^\circ\text{C}$). The detector consisted of a $\text{Gd}_2\text{O}_2\text{S:Tb}$ phosphor screen (for 17 keV) to convert X-ray photons into visible light. The captured data were saved as 16-bit non-compressed images.

- ***Translation stages***

The collimator and sample holders were mounted onto three axes miniature SmarACT GmbH computer controlled translation stages with precise positioning capability of $\pm 1\ \mu\text{m}$ in x, y and z directions; except for the x and y directions of the sample holder with $\pm 4\ \mu\text{m}$ precise positioning capability. The detector was mounted on motorised Thorlabs linear translation stages with $\pm 4\ \mu\text{m}$ precise positioning and $\pm 13\ \text{mm}$ movement capability in the x and y directions. A rotational stage was attached to the sample's translation stages allowing the sample to rotate 360° around the x-axis with a $\pm 0.02^\circ$ precision ability. The translational and rotational axes available for each instrumentation are illustrated in Figure 6.2.

6.2 Materials

As this research mainly involved the examination of FCG with non-ideal samples, a wide range of samples was employed. The materials examined during the experimental work are divided into four main groups as follows:

(a) Polycrystalline samples

- i) Sintered aluminium oxide (Al_2O_3) plates of various thicknesses (Table 6.2). A NIST standard SRM 1976 (only in one form) made of Al_2O_3 with small grain size and low preferred orientation. Al_2O_3 naturally occurs in its crystalline phase, also known as corundum and has a density of $\sim 4\ \text{gcm}^{-3}$.

Table 6.2 The polycrystalline samples analysed during the experimental work.

Sample	Material	Thickness (mm)
<i>S1</i>	Al ₂ O ₃ plate	0.17
<i>S2</i>	Al ₂ O ₃ plate	0.24*
<i>S3</i>	Al ₂ O ₃ plate	1.53

*NIST standard

(ii) Three powder samples were utilised to study the effect of sample thickness on FCG. Powders were placed in cylindrical cells (Figure 6.4) utilised for liquid samples (see Section 6.2(b)), with 1.6 mm and 3 mm thickness. The powders analysed were:

- Aluminium oxide (Al₂O₃)
- Synthetic hydroxyapatite (Ca₁₀(PO₄)₆(OH)₂)
- Sodium chloride (NaCl)

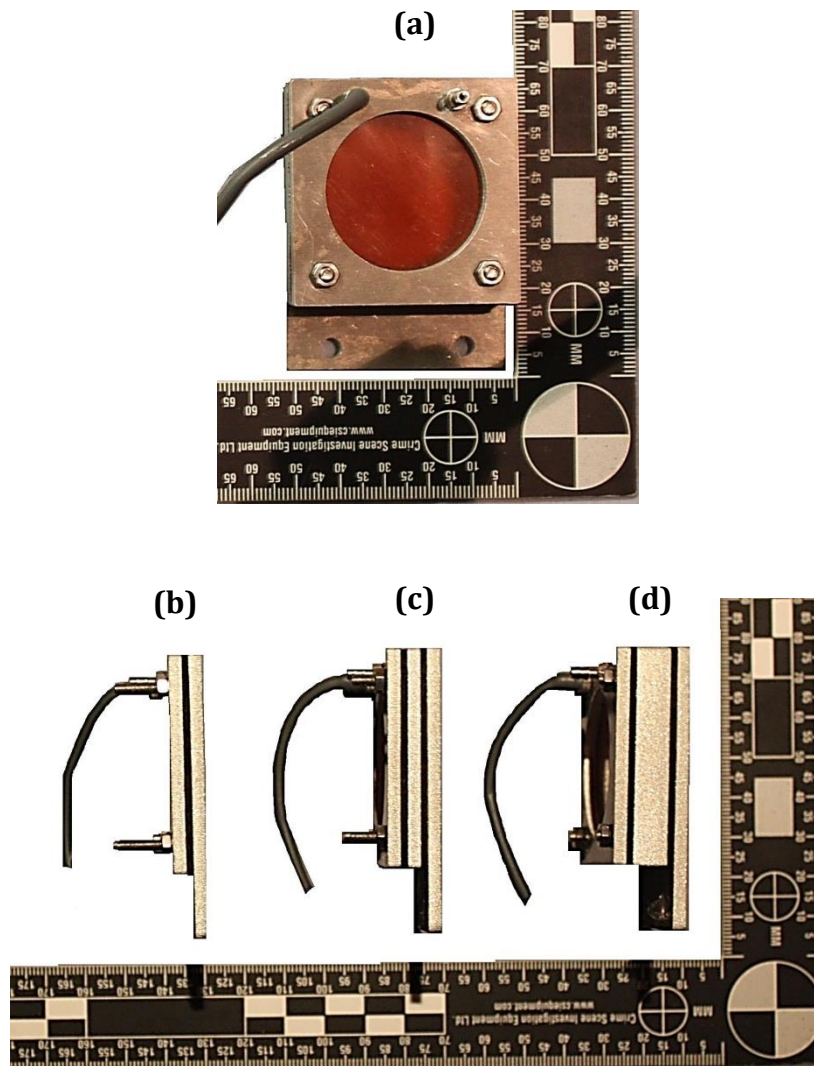


Figure 6.4 Photographs of the liquid's sample cells; front view of a 10 mm thick cell (a) and side views of 1.6 mm (b), 5 mm (c) and 10 mm (d) thick cells.

(b) Liquid samples

The liquid samples investigated in this study were classified into five different groups based on the study of Harding et al. (2010) that was discussed in Section 2.2.2. There are two main categories for threat liquids; first class (Category A) and second class (Category B) threat liquids that involve combustible fuels (and amorphous hydrocarbons) and liquid oxidisers, respectively. Category C includes a third class, which contains liquids that can be considered as threat liquids when accumulated at high concentrations, such as low concentration hydrogen peroxide

(3% H₂O₂). The last two categories include concentrated (Category D) and diluted (Category E) aqueous solutions. Categorised liquids analysed for proof-of-concept purposes are listed in Table 6.3.

Table 6.3 The liquid samples analysed.

Category A	Category B	Category C	Category D	Category E
1st class threats	2nd class threats	3rd class threats	Concentrated aqueous	Diluted aqueous
Diesel (>94%)	Hydrogen peroxide (30%)	Hydrogen peroxide (3%, - hair bleach)	Whiskey	Water
Acetone (99%)		Methylated spirit (ethanol 89%, methanol 5%, water 6%)	Cosmetic foundation cream	Coffee
		Ethanol (99%)	Jam	
		2-propanol (>95%)		

Table 6.4 presents different mixtures of liquids (miscible and immiscible) investigated in a 1:1 volume ratio.

Table 6.4 The liquid mixtures analysed.

Threat liquid + Non-threat liquid		
Miscible	<i>Mixture 1</i>	Methylated spirit + Coffee
	<i>Mixture 2</i>	2-propanol + Whiskey
Immiscible	<i>Mixture 3</i>	Acetone + Cosmetic foundation cream
	<i>Mixture 4</i>	Diesel + Water

A bespoke cylindrical cell formed from a pair of parallel polyimide window sheets (Kapton) was employed to contain the liquid samples. The cylindrical cell had a 10 mm thickness (except for the cosmetic foundation cream and jam samples that were placed in a 5 mm thick cell) and 35 mm window diameter, as illustrated in Figure 6.4. Therefore, the liquid sample cell accommodated the full diameter of the incident beam as produced by the annular collimation optics.

(c) Samples exhibiting preferred orientation

An aluminium sheet (AS) of 0.25 mm thickness was initially employed to study the phenomenon of preferred orientation with an annular beam.

Another aluminium (Al) sample was also analysed, in which the degree of preferred orientation was gradually decreased by combining a number of Al sheets at different orientations. An Al sheet (79.3 mg/cm²) of 0.3 mm thickness was divided into ~25 mm x 25 mm pieces. The first Al sample (Al_1) analysed was a single individual sheet. The second sample (Al_2) was two sheets, one placed 90° degrees to the other; whereas sample Al_3 and sample Al_4 were made of three and four Al sheets respectively, placed at random orientations with respect to each other, as illustrated in Figure 6.5. This aimed to induce a more random orientation of the crystallites, hence reducing the sheet texture within the samples.

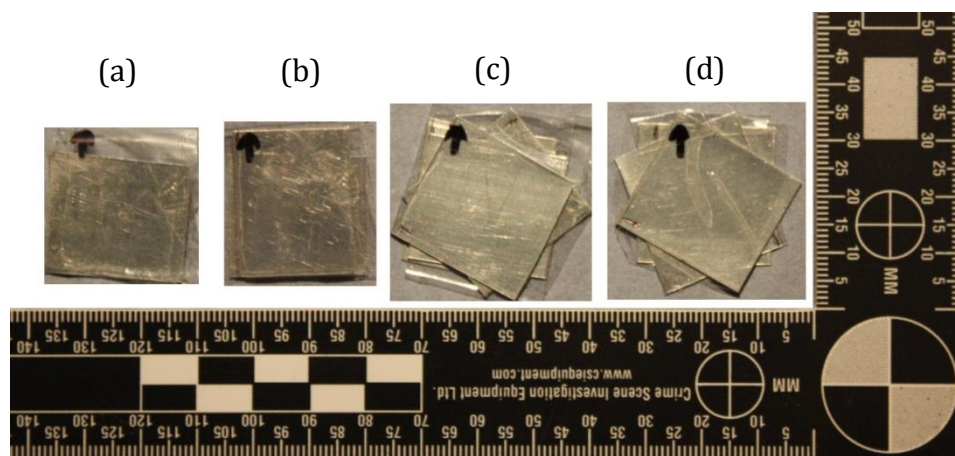


Figure 6.5 Photograph of the Al samples positioned in various orientations; *Al_1* (a), *Al_2* (b), *Al_3* (c) and *Al_4* (d).

(d) Samples with large grain size

An electrodeposited copper (Cu) foil (99.95% purity) of 0.035 mm thickness was employed for this series of experiments. The electrodeposited Cu foil was divided into four ~20 mm x 20 mm pieces and each piece was heat-treated, as indicated by Table 6.5, to induce grain growth.

Table 6.5 A list of the electrodeposited copper samples employed during the analysis of large grain size with the time and temperature of their heat treatment.

Sample	Temperature (°C)	Time (min)
<i>Cu_1</i>	-	-
<i>Cu_2</i>	500	30
<i>Cu_3</i>	600	30
<i>Cu_4</i>	700	45

6.3 Methodology

In this section, the methodology followed for each set of empirical experiments is described. The beam geometry as well as the arrangement and/or translation of the collimation optics, the sample and the detector varied between experiments.

6.3.1 Alignment

Prior to any empirical work, a standard equipment setup was necessary. The sample, collimation and detector stages were homed for accurate positioning. The collimator was then aligned in such position, that the primary beam was in the centre of the coordinate system along the primary axis. Such an alignment is essential for FCG in order for the condensation foci (i.e. Bragg's maxima) to occur at the same x and y positions during the linear translation of the detector along the primary z-axis. For the FCG arrangement, the collimator was aligned by raster scanning the detector along the x and y axes to capture an image of the primary beam, at two different detector positions. Superimposition of the two images and assessment of their radial differences assisted in aligning the collimator along the x and y axes in order for the distance between the two rings to remain as close to constant as possible along their circumference, i.e. concentric circles (Figure 6.6).

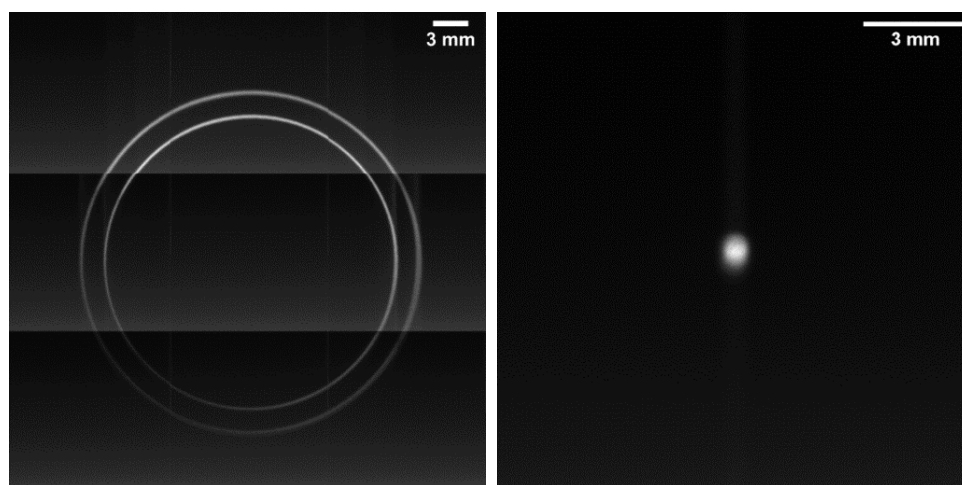


Figure 6.6 Examples of two superimposed images of an aligned annular beam (11.9 mm and 13.8 mm inner radius with 0.3 mm and 0.4 mm wall thickness, respectively) produced by *AB1* collimator (left) and an aligned pencil beam (0.9 mm and 1 mm diameter) produced by *PB2* collimator (right), captured at 190 mm and 220 mm from the X-ray source.

During the employment of the pencil beam arrangement, the collimator was aligned by adjusting it along the x and y axes and capturing single images of the primary beam at two different z-distances from the X-ray source. The collimator was considered aligned when the primary beam's footprint onto the detector completely overlapped for the two images (Figure 6.6).

All images of the primary beam were captured at 20 kV and 10 mA at 1 second time exposure and with a steel plate (1.9 mm thickness) in front of the X-ray source to act as an absorber.

6.3.2 Geometric arrangements

Two main beam geometries were established during the course of this study: the focal construct geometry described in Chapter 5 utilising a hollow conical beam and a conventional pencil beam (pinhole) geometry. The typical methodology employed for both beam geometries during the experimental work is described below.

6.3.2.1 Annular beam arrangement

An annular collimator such as *AB1* (Table 6.1) was employed for the annular beam arrangement. A hollow conical beam was produced as illustrated in Figure 6.7, forcing the Debye cones to converge at certain condensation foci along the primary z-axis. A sequence of such diffraction data was recorded through a linear translation of the detector along the primary axis, over a maximum range of 112 mm in steps of 0.1 mm. A sequence of bright field background images was also recorded for each experiment.

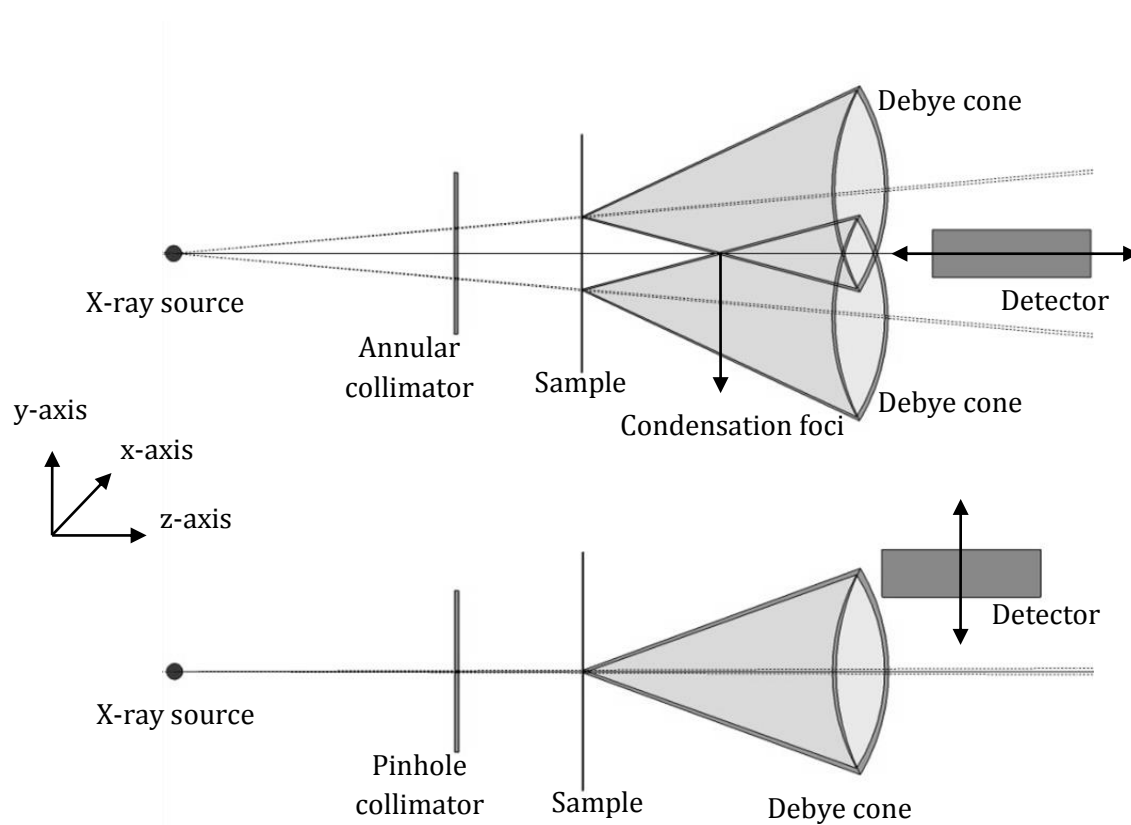


Figure 6.7 Schematic illustration of the hollow beam (top) and pencil beam instrumental arrangements (bottom).

6.3.2.2 Pencil beam arrangement

A pencil beam geometry was generated by a pinhole (or pencil beam) collimation optic, typically collimator *PB2* (Table 6.1). The captured image represented either a section of the Debye rings or the complete diffraction pattern. A section of the diffraction pattern was acquired by translating the detector along the *y*-axis, as indicated by Figure 6.7, in steps of 13 mm. In order to capture the complete Debye rings, a 65 x 65 mm matrix was acquired by raster scanning the detector along the *x* and *y* axes in steps of 13 mm. A metal rod (8.3 mm diameter) was placed in front of the detector to block the primary beam. Bright field background data were also captured by the same procedure.

6.3.3 Instrumental broadening

As mentioned in Section 5.3, FCG has been shown to produce broad diffraction peaks. For this reason, the peak broadening phenomenon of FCG was examined to determine its cause and identify whether it is a result of the focal construct geometry or of the instrumentation employed. Additionally, the capabilities of each of the instrumentation's components and their contribution to diffraction peaks' broadening were explored.

6.3.3.1 Comparison of conventional and annular beam geometries

Peak broadening was initially assessed by obtaining the diffraction pattern from an Al_2O_3 sample (*S1*) plate by FCG (*AB1* collimator – experiment *DPtr1089*) and by the conventional pencil beam geometry (*PB1* collimator – experiment *DPtr1098*) with the same instrumentation. The same collimator and sample positions were employed for both experiments. Details on the arrangement of these experiments are presented in Table 6.6.

The same sample was also examined by an independent XRD system, a Bruker D8 GADDS for comparison purposes. Conventional diffractograms were plotted for all three experiments and compared, in order to evaluate the performance of FCG and the instrumentation employed.

6.3.3.2 Collimation system and sample position

The effect of the collimation optics on the width of the diffraction peaks was investigated. A number of pencil beam collimators of varying lengths and aperture diameters were employed to explore the impact of beam divergence on peak broadening. A list of the experiments performed and details on their arrangement and collimation optics utilised are given in Table 6.6. In all cases, the collimators were aligned with respect to the X-ray source and the detector for optimisation reasons.

Table 6.6 Details on the experimental arrangements employed with various collimation optics and angular beam divergence.

Experiment index	Collimator	Sample	Position / Movement (mm)				Angular divergence (°)	Sample-detector distance (mm)	Exposure time (s)
			Collimator	Sample	Detector				
			z-axis	z-axis	y-axis	z-axis			
<i>DPtr1089</i>	<i>AB1</i>	<i>S1</i>	140	153.8	-7.1	160-240 (0.1 mm steps)	3.58/3.68	6.2-86.2 (0.1 mm steps)	10
<i>DPtr1098</i>	<i>PB1</i>	<i>S1</i>	140	153.8	7-33 (13 mm steps)	190	0.22	36.2	600
<i>DPtr106</i>	<i>PB4</i>	<i>S1</i>	129.5-155.5 (1 mm steps)	160	13-26 (13 mm steps)	170	0.66-0.56 (0.005 steps)	10	60
<i>DPtr115</i>	<i>PB5</i>	<i>S1</i>	mounted on X-ray tube	176	13-65 (13 mm steps)	240	0.38	64	300
<i>DPtr130</i>	<i>PB5</i>	<i>S1</i>	mounted on X-ray tube	162	13-65 (13 mm steps)	190-250 (10 mm steps)	0.38	28-88 (10 mm steps)	300
<i>DPtr143</i>	<i>PB5</i>	<i>S1</i>	129.1	218	13-65 (13 mm steps)	270	0.14	52	300
<i>DPtr145</i>	<i>PB6</i>	<i>S1</i>	mounted on X-ray tube	226	13-65 (13 mm steps)	270	0.16	44	300
<i>DPtr148</i>	<i>PB5</i>	<i>S1</i>	129.1	226	13-65 (13 mm steps)	270	0.14	44	300
<i>DPtr272</i>	<i>PB7</i>	<i>S1</i>	mounted on X-ray tube	246	5-18 (13 mm steps)	272	0.015	26	600

6.3.3.3 Sample thickness

The effect of sample thickness on FCG diffractograms was studied with powder samples (listed in section 6.2 (a)) of two different thicknesses: 1.6 mm and 3 mm. FCG patterns were obtained over a range of 87 mm in 0.1 mm steps with 2 seconds exposure time.

The same samples were also interrogated by the pencil beam arrangement (*PB2* collimator) for comparison purposes. Diffraction data were captured over a 39 mm linear translation of the detector along the y-axis. The time exposure for the 1.6 mm thick samples was 300 seconds (except for NaCl that was 200 seconds); whereas for the 3 mm thick samples it was 600 seconds.

6.3.3.4 Alternative X-ray source (CT system)

In order to investigate the effect of the sealed source X-ray tube spot size on broadening the diffraction peaks, an alternative X-ray source was sought. Therefore, the X-ray source within a Nikon XTH225 METRIS micro-CT system with a focal spot of approximately 10 microns was employed. The same Princeton Instruments (PIXIS) detector (see Section 6.1) as with all previous experiments was used to collect diffraction data within the CT system. An annular collimator (*AB1*) was mounted on the end of a 90 mm long hollow brass tube of 30 mm diameter. The Princeton Instruments detector was mounted on the CT stage and diffraction data were captured from an Al₂O₃ (*S1*) sample over a range of 3 mm in 0.1 mm steps. Each step had a time exposure of 30 seconds and the voltage and current were 50 kV and 1000 uA respectively, with a Mo target (and a zirconium filter). The CT system was limited to a single stage, thus causing movement restrictions when the FCG arrangement was employed and inaccurate measurements, mainly in the positions of the collimator and sample along the primary axis.

6.3.4 Analysis of liquid samples

The liquid samples listed in Table 6.3 and Table 6.4 were analysed by both FCG and conventional pencil beam arrangement. FCG analysis (*AB1* collimator) was performed over a 95 mm range (0.1 mm step size) along the primary axis, as

described in Section 6.3.2.1. Conventional pencil beam data (*PB2* collimator) were acquired by the procedure described in Section 6.3.2.2, over a 26 mm range along the y-axis. The sample-to-detector distance was 70 mm.

The repeatability of these experiments and the precision with which the diffraction maxima positions could be determined were investigated by acquiring the diffraction pattern of methylated spirit, whilst altering the sample loading procedure. The sample stage was either homed or not, prior or post positioning the sample cell and the FCG scattering profile from methylated spirit was acquired at the end of each step. Furthermore, scattering profiles were obtained at different sample positions and with a second sample cell (containing methylated spirit).

This series of experiments aimed to assess the reproducibility of the FCG data when moving the sample or replacing it with a new sample cell without homing the stage between different samples. The reason for this was the stage's inability of homing while the sample cell was attached to it due to space restrictions; thus, giving rise to the possibility of intra-experimental errors.

All FCG data acquired in this section were interpreted by identifying the condensation foci's positions along the primary axis and integrating over a circular area of ~ 25 pixels around the condensation foci. A conventional diffractogram illustrating the magnitude of scattering vector versus intensity was then plotted for each sample using Equation (6.1).

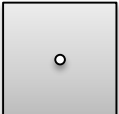
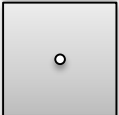
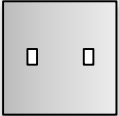
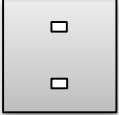
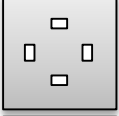

$$s = \frac{2 \sin \left[\frac{\phi_m + \tan^{-1}(R_s/D_{SD})}{2} \right]}{\lambda} \quad (6.1)$$

6.3.5 Preferred orientation

A theoretical approach into the study of samples exhibiting preferred orientation and their effect on FCG was explored by simulating the diffraction pattern of such samples by convolution.

Empirical data were also obtained with an Al sheet (*AS* – Section 6.20), exhibiting preferred orientation, via five different beam arrangements as shown in Table 6.7.

Table 6.7 Details on the experimental arrangements during the analysis of an Al sample exhibiting preferred orientation.

Collimator	Sample-detector distance (mm)	Detector's translation range (mm)			Time exposure (seconds)	
		x-axis	y-axis	z-axis		
	<i>PB2</i>	64	-	26 (13 mm steps)	-	180
	<i>PB2</i>	47	65 (13 mm steps)	65 (13 mm steps)	-	180
	<i>AB2</i>	7	-	-	40 (0.1 mm steps)	10
	<i>AB2</i>	7	-	-	40 (0.1 mm steps)	10
	<i>AB3</i>	7	-	-	40 (0.1 mm steps)	3
	<i>AB1</i>	20	-	-	40 (0.1 mm steps)	8

Following the initial assessment of this phenomenon, the aluminium samples *Al_1*-*Al_4* with varying degrees of preferred orientation, as mentioned in Section 6.2 (c), were examined by the pencil beam (Section 6.3.2.2) and hollow beam (Section 6.3.2.1) geometries.

6.3.6 Grain size

The effect of large grain size (relative to the primary beam) on FCG was examined through a simulated approach, by convolution. FCG diffraction caustics were also simulated to assist the visualisation of the occurrence of the condensation foci and condensation rings when a sample exhibits large grain size.

A series of Cu samples (Table 6.5) was analysed by a pencil beam arrangement and FCG as described in Section 6.3.2.2 and Section 6.3.2.1, respectively.

6.3.7 Randomly orientated planar samples

The effect of random sample orientation on FCG was investigated in an analytical, simulated and empirical manner.

The term randomly orientated sample is referred to the physical orientation of a planar sample and it should not be confused with samples exhibiting preferred or random crystallite orientation. Throughout the experimental work with a randomly orientated sample, an ideal sample, in terms of preferred orientation and grain size was examined.

The analytical approach involved the geometric analysis of the effect and determination of mathematical equations to explain the location of the condensation foci and the shape of the condensation rings. Simulations aimed at the visualisation of random sample orientations on scattering distributions and at the comparison of simulated data with empirical data and analytical approach. Finally, the empirical method aided the verification of the analytical and simulated data and vice versa, and it provided a better understanding of the effect.

6.3.7.1 Simulation approach

The 3D ray-tracing simulation package described in Section 6.1.1 was employed for the simulated experiments. The effect of random sample orientation on scattering distributions was initially studied with the least parameters possible for simplicity purposes. The annular beam was produced with an opening angle ϕ of 3.63° around the primary axis. A series of 50 x 50 mm planar samples (0.17 mm thickness) with the same material characteristics (a single scattering angle of 25.76° was specified) but varying orientations relative to the simulator's coordinates was placed between the X-ray source and the detector. A list of the sample orientations examined is given in Table 6.8. Images were recorded over a number of distances along the primary axis since the location of the condensation foci was not constant, but a typical range was 100 mm in steps of 0.1 mm.

Table 6.8 A list of the simulated experiments performed with a random sample orientation and details on their rotation around the x and y axes.

Sample	Rotation	
	x-axis	y-axis
SIM_1	-60°	0°
SIM_2	-40°	0°
SIM_3	-20°	0°
SIM_4	0°	0°
SIM_5	$+20^\circ$	0°
SIM_6	$+40^\circ$	0°
SIM_7	$+60^\circ$	0°
SIM_8	0°	-60°
SIM_9	0°	-40°
SIM_10	0°	-20°
SIM_12	0°	$+20^\circ$
SIM_13	0°	$+40^\circ$
SIM_14	0°	$+60^\circ$
SIM_15*	$+40^\circ$	$+40^\circ$
SIM_16	$+40^\circ$	$+20^\circ$
SIM_17	$+40^\circ$	-20°
SIM_18	-40°	-20°

*xy and yx rotations

6.3.7.2 Empirical approach

The empirical experiments involved capturing standard FCG data sequences with various rotated planar samples. An Al_2O_3 sample (*S1*) was rotated around the x-axis from $(-)$ 20° anticlockwise to $(+)$ 20° clockwise in steps of 5°, as illustrated in Figure 6.8. Furthermore, the sample was rotated \sim 20° clockwise and anticlockwise around the y-axis. At each angle, the detector was translated along the primary axis over a range of 30 mm in 0.1 mm steps at 30 seconds time exposure. In addition, the sample was translated by \pm 3 mm along the y-axis and the above procedure was repeated at $(-)$ 20° anticlockwise, 0° and $(+)$ 20° clockwise sample rotation around the x-axis.

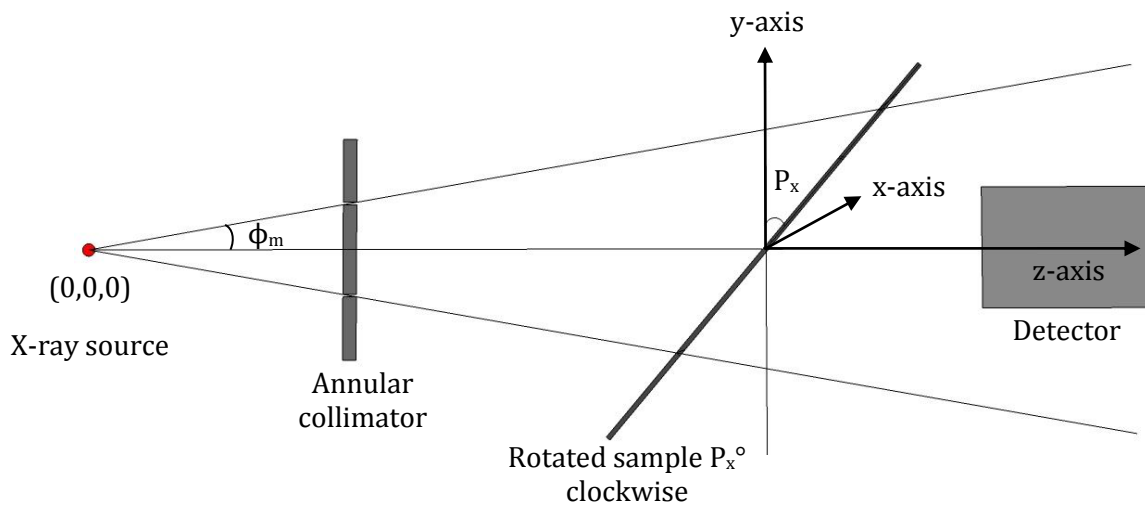


Figure 6.8 Schematic illustration of the arrangement of FCG with a sample rotation of 40° clockwise around the x-axis (P_x). The X-ray source is considered the origin of the coordinate system, indicated by (0, 0, 0).

Simulated and empirical experiments were also performed with the same parameters for direct comparison. The parameters set for these empirical experiments were 3.39° opening angle ϕ , 11.82°, 16.15°, 17.54°, 19.77°, 24.13°, 26.16°, 30.29°, 34.75° 2θ scattering angles and a recording range from 185-272 mm in 0.1 mm steps. The sample was initially normal to the primary axis and then rotated $(-)$ 20° anticlockwise and $(+)$ 20° clockwise around the x-axis.

6.3.8 Multiple scatterers

This series of experiments (presented in Table 6.9.) was performed in order to determine the ability of FCG to identify overlapping samples, i.e. samples with the same x and y positions but different z positions, when planar samples were normal to the primary axis. The experiments were divided into two main groups.

The first group included the analysis of two samples with the same material characteristics (Al_2O_3), but with slightly different thicknesses (*S1* and *S2* samples from Table 6.2); whereas the second group involved the examination of two samples with different material characteristics (Al_2O_3 and Al – Section 6.20). Details on the experimental setups are given in Table 6.9.

These experiments were also simulated by the ray-tracing simulator. The simulator's opening angle ϕ was set at 3.65° and each sample's scattering angles were employed. The images were recorded from 200 – 270 mm in steps of 0.1 mm.

Table 6.9 Details on the experiments conducted with two overlapping samples by FCG.

Experiment index	Collimator	Sample	Position / Movement z-axis (mm)			Exposure time (s)
			Collimator	Sample	Detector	
<i>DPtr325</i>	<i>AB1</i>	<i>S2</i>	140	177.4	190 - 270 (0.1 mm steps)	3
<i>DPtr328</i>	<i>AB1</i>	<i>S1 & S2</i>	140	168 (<i>S1</i>); 177.4 (<i>S2</i>)	190 - 270 (0.1 mm steps)	3
<i>DPtr329</i>	<i>AB1</i>	<i>S1</i>	140	168	190 - 270 (0.1 mm steps)	3
<i>DPtr331</i>	<i>AB1</i>	<i>S1</i>	140	146.1	190 - 270 (0.1 mm steps)	3
<i>DPtr332</i>	<i>AB1</i>	<i>S1 & S2</i>	140	146.1 (<i>S1</i>); 177.4 (<i>S2</i>)	190 - 270 (0.1 mm steps)	3
<i>DPtr344</i>	<i>AB1</i>	<i>S1</i>	140	150.2	173 - 263 (0.1 mm steps)	3
<i>DPtr345</i>	<i>AB1</i>	<i>AS</i>	140	160.5	173 - 263 (0.1 mm steps)	3
<i>DPtr346</i>	<i>AB1</i>	<i>S1 & AS</i>	140	150.2 (<i>S1</i>); 160.5 (<i>AS</i>)	173 - 263 (0.1 mm steps)	3
<i>DPtr349</i>	<i>AB1</i>	<i>S1</i>	140	162.4	173 - 263 (0.1 mm steps)	3
<i>DPtr350</i>	<i>AB1</i>	<i>AS</i>	140	150.6	173 - 263 (0.1 mm steps)	3
<i>DPtr351</i>	<i>AB1</i>	<i>S1 & AS</i>	140	162.4 (<i>S1</i>); 150.6 (<i>AS</i>)	173 - 263 (0.1 mm steps)	3

6.4 Data processing

In all data collected, bright field background images were subtracted from the raw data prior to further analysis for both annular beam and pencil beam arrangements.

The raw FCG data sequence was initially viewed and integrated by an optimal circular area of typically $\sim 0.13 - 0.2$ mm ($\sim 10 - 15$ pixels) radius around the condensation foci, approximately at the centre of the image. Background subtraction and circular integration around the condensation foci were the only pre-processing procedures performed on the raw FCG data. The integrated intensity was then plotted against the detector's location along the primary axis. Equation (5.1) (Section 5.1) was applied to calculate the scattering maxima positions in 2θ angles and were then converted into d-spacing values by Bragg's law equation (Equation (3.4), Section 3.2.2).

XRD data acquired by conventional pencil beam geometry were analysed using ImageJ software (version 1.48v) only in the case where a section of the Debye rings was captured. Interpretation of complete diffraction patterns was performed using Datasqueeze (version 3.0.0). The centre of each image was determined by fitting a ring around a Debye cone and the complete diffraction pattern was integrated from $0^\circ - 360^\circ$.

In both cases of FCG and conventional XRD analysis, data were imported into DIFFRAC^{plus} EVA (version 14,0,0,0) software for uniformity purposes and for a background correction if background data were not available. The scattering maxima positions and their corresponding errors were acquired via DIFFRAC^{plus} TOPAS (version 4.1) software. Broadening of diffraction peaks was assessed in terms of full width half maximum (FWHM), attained via DIFFRAC^{plus} TOPAS software.

The PDF card numbers of the samples utilised were obtained from the International Centre for Diffraction Data (ICDD) through Crystallographica Search-Match (version 2,1,1,1) software.

Chapter 7 RESULTS

Outline

In this chapter, the results obtained from the experimental work performed during this research study are presented. Firstly, the results for the in-house ray-tracing simulator are shown and a comparison between simulated and empirical FCG diffraction data is performed. Analysis of both conventional pencil beam arrangement and FCG is achieved for direct comparison and benchmarking with FCG. The FCG instrumentation is then assessed in terms of peak broadening with various collimators (mainly by conventional XRD) and sample thicknesses. The FCG diffraction caustics attained from an alternative X-ray source within a micro-CT system are presented and compared to corresponding data from the FCG system.

Analysis of non-crystalline samples (such as liquids) by FCG and conventional XRD is then presented. The effect of other non-ideal samples with preferred orientation and large grain size on FCG data is theoretically and empirically assessed.

Further, the analysis of samples under non-ideal conditions is investigated. A polycrystalline sample with random orientation with respect to the primary axis is examined in an analytical, simulated and empirical manner. Finally, the acquisition of FCG data in the presence of multiple scatterers is simulated and empirically investigated.

7.1 Ray-tracing simulator

The ray-tracing simulator was typically employed to facilitate the development of FCG, mainly by reproducing experimental data and acting as a comparison tool. In this section, the basic abilities of the simulator are demonstrated for proof-of-concept purposes.

7.1.1 Single thin planar sample

A single planar sample of 0.2 mm thickness was employed to simulate the formation of an FCG condensation focus and assist in the visualisation and better comprehension of the annular beam geometry. Figure 7.1 illustrates a pictorial essay of the process of forming a single Debye cone to the formation of a condensation focus, as previously depicted in Figure 6.7.

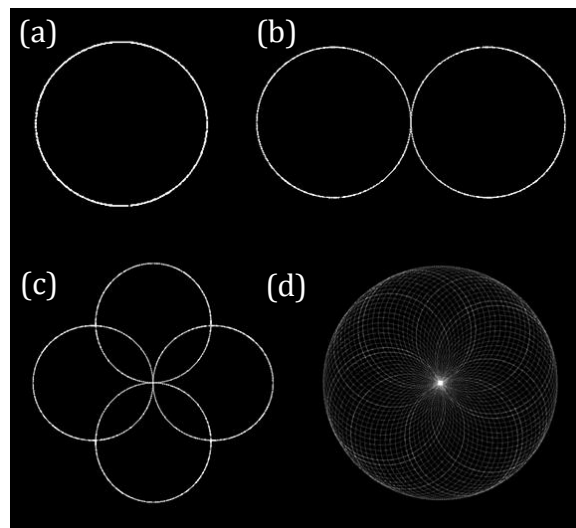


Figure 7.1 Simulated diffraction images illustrating a single Debye cone (a), two Debye cones (b), four Debye cones (c) and multiple Debye cones (d) converging at a single focal point.

In Figure 7.1 (a), a single Debye cone arising from a conventional pencil beam (PB) arrangement is observed. Figure 7.1 (b) and (c) demonstrate the congregation of two and four Debye cones respectively, at the centre of the image. The Debye cones of Figure 7.1 (b) and (c) were produced by rays separated by 180° and by 90° ; corresponding to collimators with two and four diametrically opposed pinholes, respectively. Lastly, Figure 7.1 (d) demonstrates the convergence of multiple Debye cones (acquired in radial increments of 3°) in order to produce a high intensity condensation focus, similarly to the results of an annular collimator.

7.1.2 Altering the sample's position

The ray-tracing simulator was assessed by acquiring FCG diffraction caustics (Chapter 5) from a sample (specified 15° and 20° 2θ angles) at various positions along the primary axis. The sample was positioned at 100 mm, 150 mm, 200 mm and 300 mm from the X-ray source and FCG diffraction patterns were acquired over a range of detector positions. As observed in Figure 7.2 (A), an increase in the sample's z-position caused the scattering maxima to occur further along the primary axis. Calibration of the scattering patterns, in terms of 2θ , with each sample's z-position generated profiles with diffraction signals at the specified 15° and 20° 2θ angles (Figure 7.2 (B)).

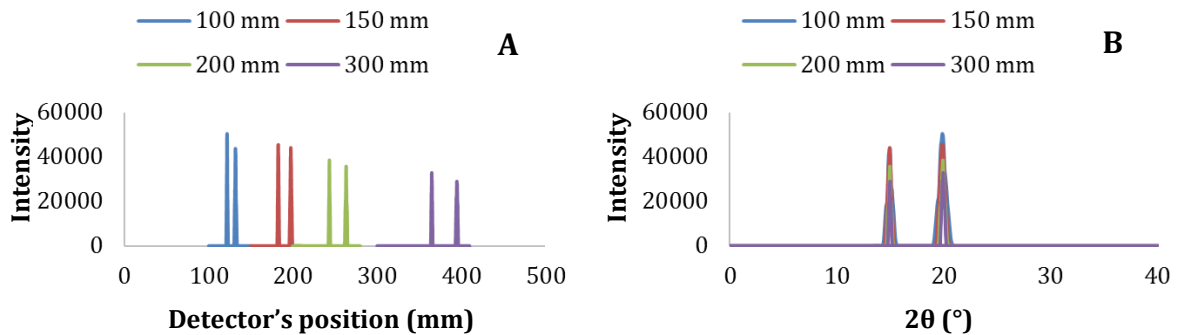


Figure 7.2 Simulated diffraction profiles plotted with respect to the detector's position along the primary axis (A) and 2θ scattering angles (B) from a sample positioned 100 mm, 150 mm, 200 mm and 300 mm away from the X-ray source.

7.1.3 Altering the annular beam's wall thickness

Simulated experiments were also performed with a 0.1 mm thick sample at specified scattering angles (15° and 20°) over a range of annular beam wall thicknesses, to assess the effect of an increased beam wall thickness on FCG diffraction caustics.

Initially, the minimum and maximum beam divergences were set at 3.5° with an infinitely thin wall thickness (referred to as 0°). The minimum beam divergence remained fixed while the maximum beam divergence was increased by 0.1° , 0.3° and 0.5° . The resulting scattering profiles are presented in Figure 7.3, where it is clearly

seen that the width of the diffraction signals increased significantly when the wall thickness of the annular beam was increased beyond 0.1° .

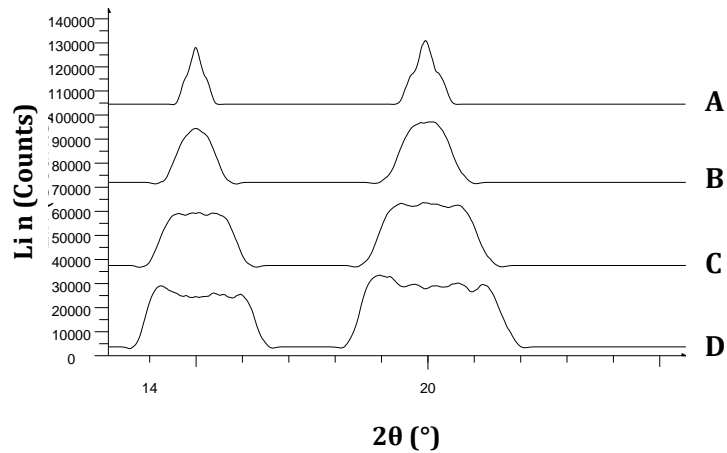


Figure 7.3 Simulated scattering profiles when the annular beam's wall thickness was increased from 0° (A) to 0.1° (B), 0.3° (C) and 0.5° (D).

7.1.4 Comparison between empirical and simulated data

A quantitative comparison of the simulated and empirical FCG data was accomplished, in terms of scattering maxima positions along the primary axis. An Al_2O_3 sample of 0.17 mm thickness was employed for the empirical experiments and a representative sample (0.17 mm thickness) was designed for the ray-tracing simulations. The scattering profiles from Al_2O_3 obtained from simulated and empirical experiments are illustrated in Figure 7.4. A numerical evaluation of their scattering maxima positions is presented within Table 7.1 and compared to the powder diffraction file (PDF) card No. 75-1862.

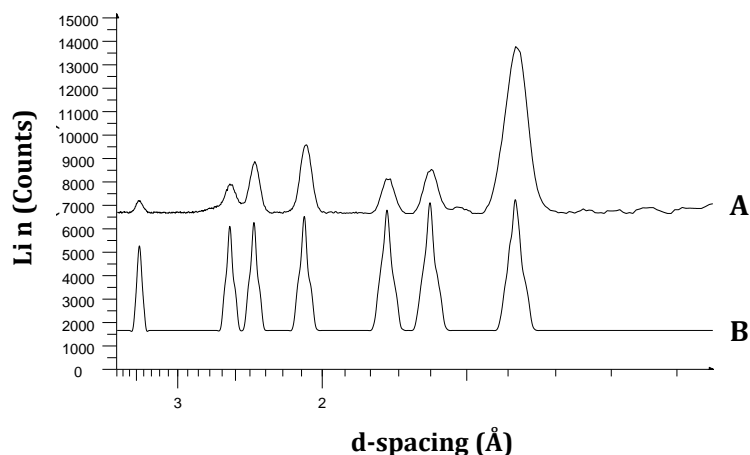


Figure 7.4 Empirical (A) and simulated (B) scattering profiles from Al_2O_3 sample of 0.17 mm thickness when illuminated by an annular beam.

Table 7.1 Quantitative comparison of the diffraction maxima positions of Al_2O_3 from the PDF card No. 75-1862, simulation and empirical data.

PDF card No. 75-1862 (nm)	Simulation (nm)	Empirical (nm)
0.138	$0.139 \pm 2.96 \times 10^{-5}$	$0.138 \pm 6.77 \times 10^{-6}$
0.160	$0.160 \pm 6.06 \times 10^{-5}$	$0.160 \pm 3.09 \times 10^{-5}$
0.174	$0.174 \pm 2.09 \times 10^{-5}$	$0.174 \pm 3.09 \times 10^{-5}$
0.209	$0.209 \pm 4.86 \times 10^{-4}$	$0.208 \pm 1.97 \times 10^{-5}$
0.238	$0.238 \pm 7.86 \times 10^{-5}$	$0.238 \pm 4.01 \times 10^{-5}$
0.255	$0.255 \pm 8.56 \times 10^{-5}$	$0.254 \pm 1.01 \times 10^{-4}$
0.348	$0.348 \pm 1.18 \times 10^{-4}$	$0.348 \pm 2.30 \times 10^{-4}$

The differences in the diffraction maxima positions are within experimental errors, thus indicating a good agreement between simulated and empirical data. The ray-tracing simulator can therefore be considered as a good representative tool of empirical data.

7.2 Instrumental broadening

As observed in previous studies discussed in Chapter 5 involving the acquisition of FCG diffraction data, the resulting maxima appear relatively broad. Hence, this peak broadening phenomenon of FCG was investigated to determine its cause and identify whether it is a result of the annular beam geometry or of the instrumentation employed. Additionally, the capabilities of each of the instrumentation's components and their accountability on peak broadening were explored.

7.2.1 Comparison of pencil and annular beam geometries

Annular and pencil beam geometries were compared in terms of scattering maxima position, width and intensity. Beforehand however, a typical FCG data sequence obtained from an Al_2O_3 sample is presented in Figure 7.5. The high intensity condensation foci discussed in Chapter 5 are illustrated, as highlighted by a red box in image number 150 (Figure 7.5). The enhanced converging condensation rings can also be observed as they approach their condensation focus and then diverge in the opposite directions to form diverging condensation rings (Section 5.1). The condensation focus shown in image number 150 corresponds to the 300 reflection from Al_2O_3 at 0.138 nm.

FCG data are interpreted in terms of a circular integration around the condensation foci over a sequence of diffraction images, as previously explained in Section 5.1. Nonetheless, FCG data could also be interpreted by a radial integration of a single image (i.e. integrating the condensation rings), as illustrated in Figure 7.6. In Figure 7.6 (A) the radial integration of an FCG image illustrating a condensation focus is presented; whereas Figure 7.6 (B) represents the radial integration of a non – condensation focus FCG image.

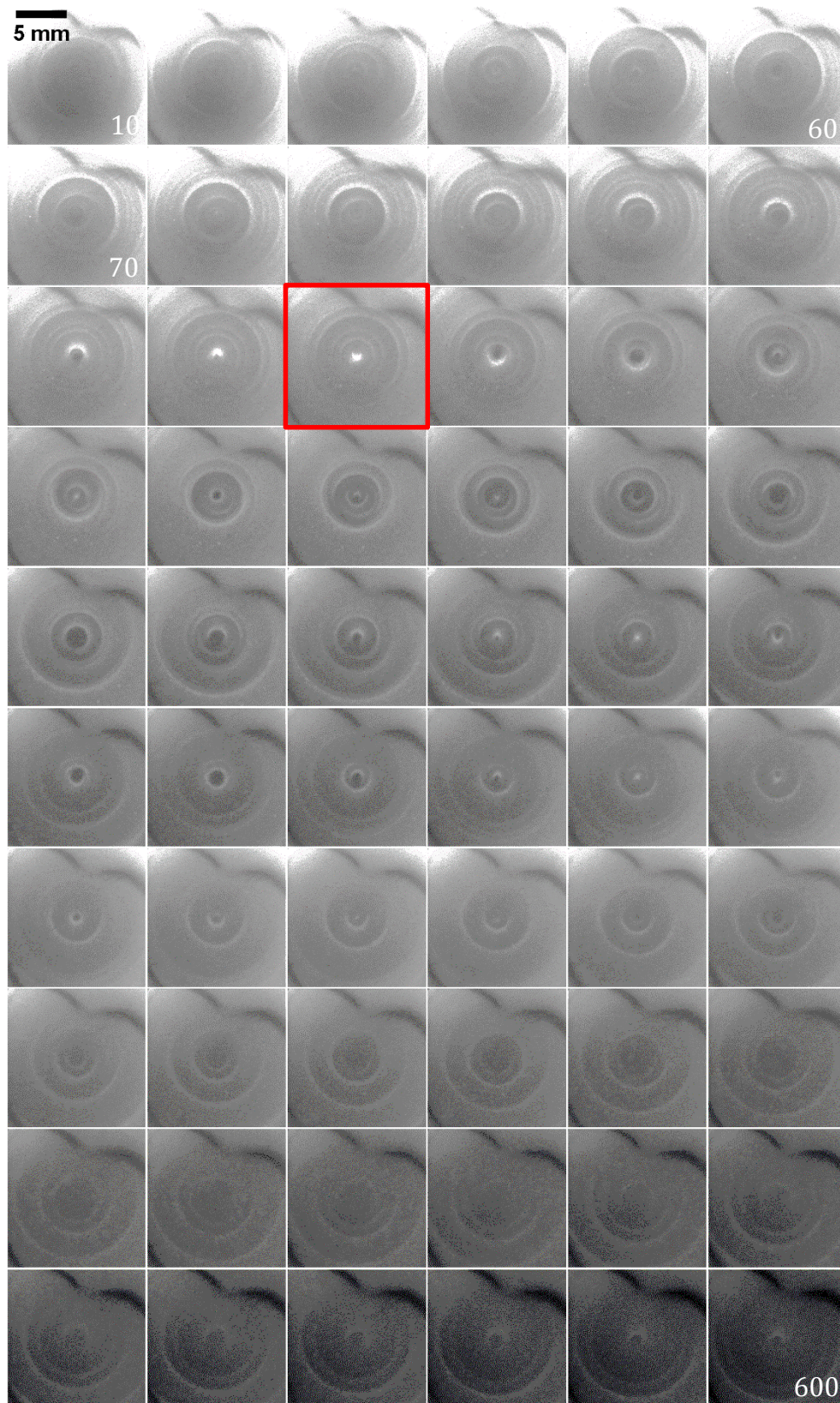


Figure 7.5 Empirical FCG data sequence from an Al_2O_3 sample. NB. The non-uniform intensity of the condensation rims is a result of a non-uniform incident beam.

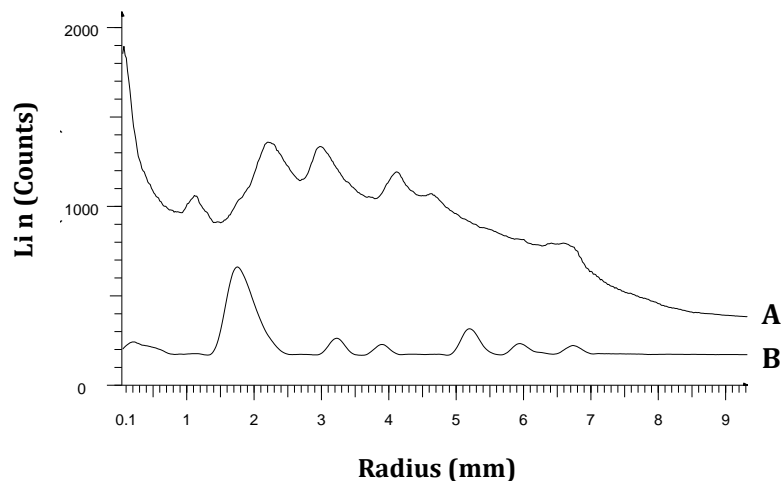


Figure 7.6 Scattering profile from an Al_2O_3 sample, obtained by a radial integration of a single FCG image at 24.1 mm (image no. 190) (A) and 16.6 mm (image no. 105) (B) from the sample.

The advantage of this interpretation method lies clearly within its ability to obtain FCG diffraction profiles from a single image, rather than a sequence of images. However, as seen in Figure 7.6, the radius of the scattering maxima was not simply increased as the sample-to-detector distance increased. This is due to the simultaneous presence of converging and diverging condensation rings, that complicates the interpretation of radially integrated images into meaningful unit measurements, such as 2θ or d-spacing values. This effect will be discussed in greater detail later on in this section (page 125).

Integration around the condensation foci from a sequence of FCG images was therefore employed throughout this work. Figure 7.7 (A) and (B) presents the scattering profiles from an Al_2O_3 sample, when illuminated by an annular X-ray beam and a pencil X-ray beam respectively, with the same instrumentation components (see Table 6.6). The diffraction profile from Al_2O_3 as obtained by a standard laboratory-based diffractometer, Bruker D8-GADDS, is also illustrated in Figure 7.7 (C) for comparison purposes.

Visual inspection of the three diffractograms in Figure 7.7 shows good agreement of their diffraction maxima positions. A quantitative comparison of the diffraction maxima positions and widths of Al_2O_3 as obtained via the different arrangements is

given in Table 7.2. The positions of their diffraction signals are within experimental errors with each other and with the d-spacing values obtained from aluminium oxide's PDF card (No. 75-1862).

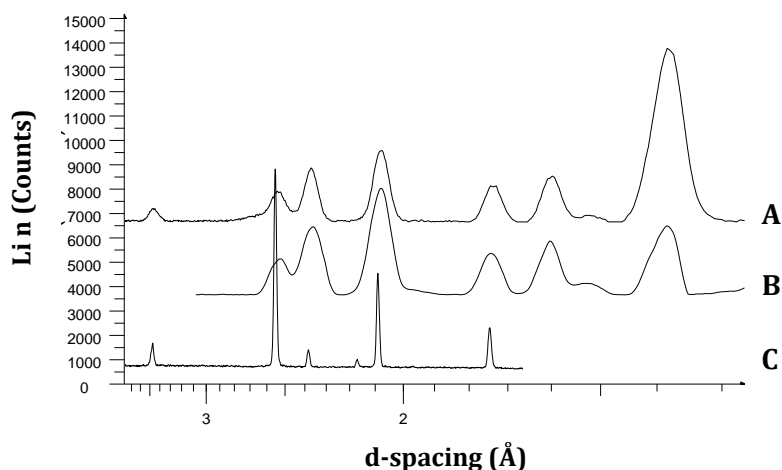


Figure 7.7 Normalised scattering signatures from an Al_2O_3 S1 plate obtained by the annular beam (A) and pencil beam (B) arrangements and by the Bruker D8-GADDS diffractometer (C).

Correlation plots of the mean FWHM values of the scattering maxima from Al_2O_3 , as obtained by the annular and pencil beam geometries within the FCG system, as well as from the benchmark Bruker D8-GADDS diffractometer are presented and compared in Figure 7.8.

As illustrated in Figure 7.8, the widths of the diffraction signals acquired by the Bruker D8-GADDS diffractometer are significantly narrower than those obtained within the FCG system. However, FCG gave rise to sharper diffraction peaks than PB geometry when the same instrumentation was employed. This may be a result of the different beam divergence employed for each geometry, as explained in depth later in this section.

Table 7.2 Quantitative comparison of the diffraction maxima positions and FWHM values from an Al₂O₃ sample; as obtained by the annular beam (FCG) and pencil beam (PB) geometries, and by the Bruker D8-GADDS diffractometer.

PDF card No. 75-1862 (nm)	FCG		PB		Bruker D8-GADDS	
d-spacing (nm)	d-spacing (nm)	FWHM (nm)	d-spacing (nm)	FWHM (nm)	d-spacing (nm)	FWHM (nm)
0.138	$0.138 \pm 6.77 \times 10^{-6}$	$0.0029 \pm 7.37 \times 10^{-6}$	$0.138 \pm 5.07 \times 10^{-5}$	$0.0025 \pm 5.87 \times 10^{-5}$	-	-
0.152	$0.152 \pm 3.08 \times 10^{-4}$	$0.0022 \pm 2.41 \times 10^{-4}$	$0.152 \pm 8.88 \times 10^{-4}$	$0.0039 \pm 1.45 \times 10^{-3}$	-	-
0.160	$0.160 \pm 3.09 \times 10^{-5}$	$0.0024 \pm 4.38 \times 10^{-5}$	$0.160 \pm 1.17 \times 10^{-4}$	$0.0026 \pm 1.40 \times 10^{-4}$	-	-
0.174	$0.174 \pm 3.09 \times 10^{-5}$	$0.0026 \pm 3.58 \times 10^{-5}$	$0.174 \pm 1.16 \times 10^{-4}$	$0.0031 \pm 1.21 \times 10^{-4}$	$0.174 \pm 1.92 \times 10^{-5}$	$0.0005 \pm 1.93 \times 10^{-5}$
0.209	$0.208 \pm 1.97 \times 10^{-5}$	$0.0033 \pm 2.22 \times 10^{-5}$	$0.208 \pm 7.27 \times 10^{-5}$	$0.0044 \pm 8.71 \times 10^{-5}$	$0.209 \pm 1.55 \times 10^{-5}$	$0.0006 \pm 1.54 \times 10^{-5}$
0.238	$0.238 \pm 4.01 \times 10^{-5}$	$0.0038 \pm 4.93 \times 10^{-5}$	$0.236 \pm 1.74 \times 10^{-4}$	$0.0057 \pm 2.45 \times 10^{-4}$	$0.238 \pm 6.19 \times 10^{-5}$	$0.0008 \pm 6.66 \times 10^{-5}$
0.255	$0.254 \pm 1.01 \times 10^{-4}$	$0.0050 \pm 1.27 \times 10^{-4}$	$0.254 \pm 3.07 \times 10^{-4}$	$0.0053 \pm 3.60 \times 10^{-4}$	$0.256 \pm 1.49 \times 10^{-5}$	$0.0009 \pm 1.42 \times 10^{-5}$
0.348	$0.348 \pm 2.30 \times 10^{-4}$	$0.0056 \pm 2.84 \times 10^{-4}$	-	-	$0.348 \pm 1.35 \times 10^{-4}$	$0.0018 \pm 1.51 \times 10^{-4}$

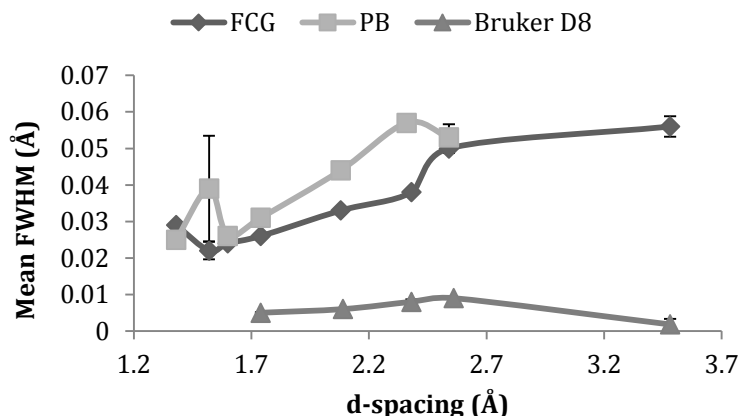


Figure 7.8 Mean FWHM values of the scattering maxima of Al_2O_3 obtained when illuminated by an annular beam (FCG) and a pencil beam (PB); and when analysed by the benchmark Bruker D8-GADDS diffractometer.

The annular and pencil beam geometries were also assessed analytically in terms of their contribution to the width of the diffraction signals. A schematic illustration of the Debye cones produced via the annular and pencil beam arrangements is given in Figure 7.9; and the measured widths of the Debye cones for each geometry are illustrated at the same z coordinate. W_{PB} and W_{FCG} , as indicated in Figure 7.9, correspond to the width of the Debye cones arising from pencil beam and FCG arrangements, respectively. The wall divergence of the annular beam is equal to the overall beam divergence of the pencil beam for comparative data.

If the diffraction maxima arising from the two different geometries were to be recorded along the same axis, then their widths would be more comparable. However, each arrangement possesses a different measurement axis. W_{PB} is recorded along the y -axis, whereas W_{FCG} is measured along the z -axis.

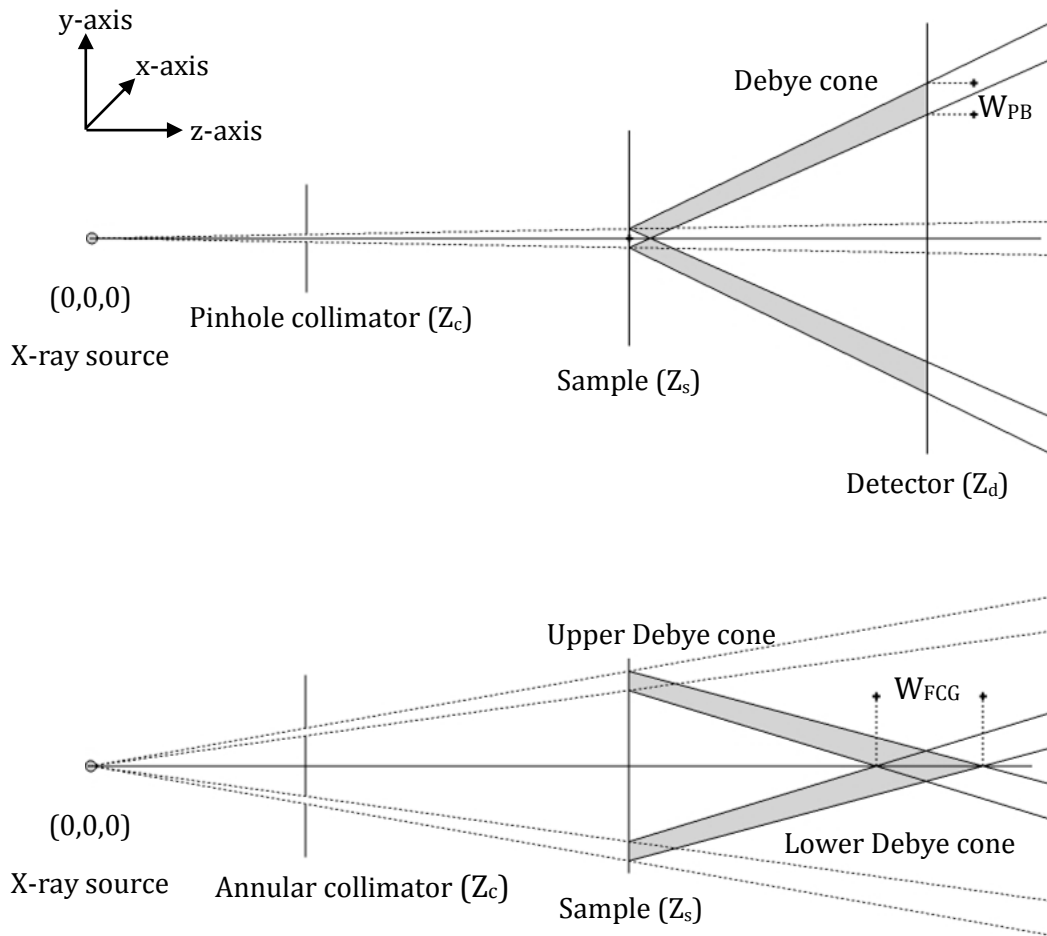


Figure 7.9 Schematic illustration of the width of the diffraction maxima from an infinitely thin sample by pencil beam (top) and annular beam (bottom) arrangements at a certain z-distance.

Based on the geometric relationships shown in Figure 7.10, the width of the Debye cones of an infinitely thin sample arising from a PB arrangement can be calculated by Equation (7.1). Further, as indicated by the schematic diagram of Figure 7.11 the length of the condensation focus i.e. width of the diffraction signal arising from the FCG arrangement can be calculated by Equation (7.2). Equations (7.1) and (7.2) are valid when $\phi < 2\theta < 90^\circ$.

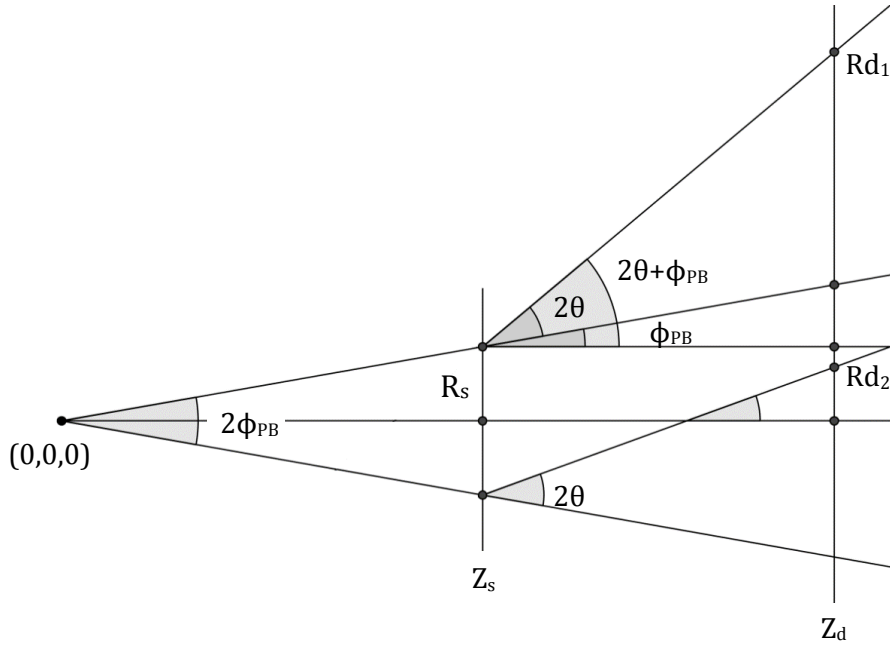


Figure 7.10 The geometric relationships involved in a pencil beam arrangement, with extreme beam divergence for presentation purposes, to determine the widths of the scattering maxima.

$$R_{d1} - R_{d2} = (Z_d - Z_s)[\tan(2\theta + \phi_{PB}) - \tan(2\theta - \phi_{PB})] + 2Z_s \tan \phi_{PB} \quad (7.1)$$

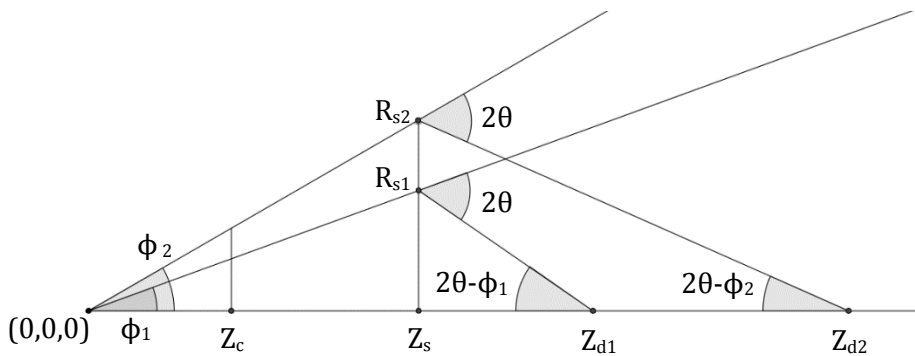


Figure 7.11 The geometric relationships involved in an FCG arrangement to determine the widths of the scattering maxima.

$$Z_{d2} - Z_{d1} = \frac{Z_s \tan \phi_2}{\tan(2\theta - \phi_2)} - \frac{Z_s \tan \phi_1}{\tan(2\theta - \phi_1)} \quad (7.2)$$

An example is considered where the overall PB divergence ($2\phi_{PB}$) is 1° , the annular beam's divergence ϕ_1 and ϕ_2 are 3° and 4° respectively, the sample (Z_s) and detector's (Z_d) z-coordinates are 150 mm and 200 mm respectively, the radius of the pencil beam's footprint on the sample ($R_s = Z_s \tan \phi_{PB}$) is 1.31 mm and the sample's 2θ scattering angle is 25° . W_{PB} (i.e. $R_{d1} - R_{d2}$) is calculated to be 3.68 mm (Equation (7.1)), whereas W_{FCG} (i.e. $Z_{d2} - Z_{d1}$) is calculated to be 7.87 mm (Equation (7.2)). This indicates that there is a 2.1 factor of increase, corresponding to 114% increase in the width/length (mm) of the diffraction maxima by FCG. However, as the radius of the annular collimator decreases (hence FCG beam divergence decreases), the length of the condensation focus is reduced, even if the beam's wall thickness remains the same.

Even though an infinitely thin sample was considered until now, the sample's thickness plays an important role in broadening the scattering maxima. If a finite sample of t thickness is taken into account, the width of the diffraction peaks is expected to increase for both geometries.

Figure 7.12 depicts the effect of sample thickness on the width of the scattering signals for the annular and pencil beam geometries employed during this work. The diffracted rays coloured in red indicate the minimum and maximum limits of the diffraction maxima. The length of the condensation foci is considerably greater than the width of the Debye cones, for the same beam divergence ($2\phi_{PB}$) and wall thickness ($\phi_2 - \phi_1$) i.e. $2\phi_{PB} = \phi_2 - \phi_1$, as illustrated in Figure 7.12. The width of the diffraction maxima of a sample with thickness t , for a pencil beam and annular beam arrangement can be calculated by Equations (7.3) and (7.4), respectively.

If the same experimental parameters were implemented as with the above example, but with a sample thickness of 1 mm and Z_{s1} at 149.5 mm, then the width of the diffraction peaks would be 4.15 mm for the PB arrangement and 9.02 mm for FCG. The FCG:PB width ratio is 2.2 (117% increase), which is slightly higher than the calculated width ratio for an infinitely thin sample. This indicates that an increase in the sample's thickness would affect the length of the condensation foci to a greater extent than the width of the Debye cones.

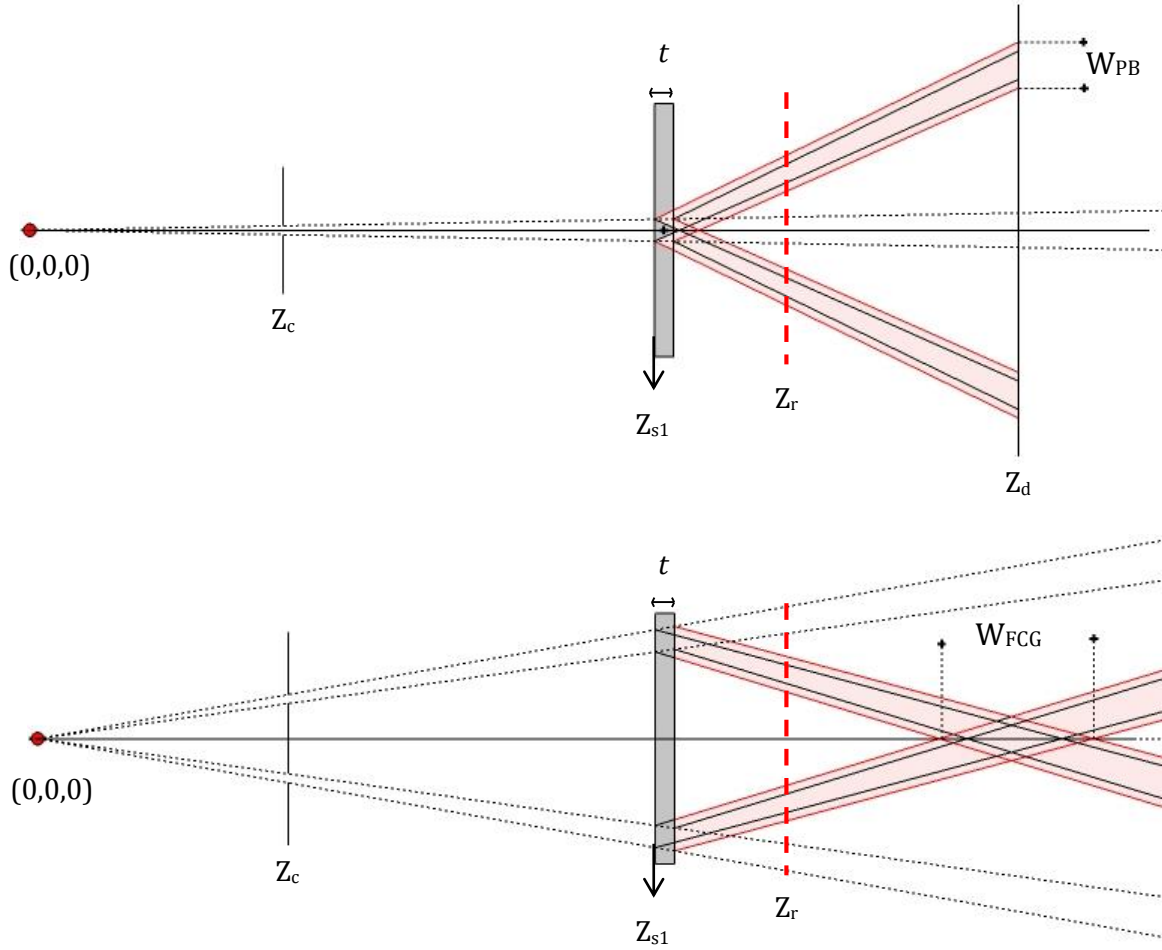


Figure 7.12 Schematic illustration of the width of the diffraction maxima of t thick sample, arising from a pencil beam (top) and annular beam (bottom) arrangement at a certain z -distance.

$$(R_{d1} - R_{d2})_t = (Z_d - Z_{s1}) \tan(2\theta + \phi_{PB}) - (Z_d - Z_{s1} - t) \tan(2\theta - \phi_{PB}) + (2Z_{s1} + t) \tan \phi_{PB} \quad (7.3)$$

$$(Z_{d2} - Z_{d1})_t = \frac{(Z_{s1} + t) \tan \phi_2}{\tan(2\theta - \phi_2)} - \frac{Z_{s1} \tan \phi_1}{\tan(2\theta - \phi_1)} + t \quad (7.4)$$

When the same parameters are applied as with the empirical experiments presented in Figure 7.7, the calculated width of the diffraction peak for the 300 reflection in Al_2O_3 at 0.138 nm ($29.84^\circ 2\theta$), for both the pencil and annular beam geometries,

based on Equations (7.3) and (7.4), is 0.820 mm and 0.827 mm, respectively. The measured FWHM of the diffraction profiles (FCG and PB) of Figure 7.7, are given in Table 7.2. The ratio of the FCG:PB width of the diffraction signal at 29.84° as obtained experimentally is 1.16; which is, within experimental errors and analytical approximations, similar to the 1.01 ratio of the analytically determined widths.

It is important to note at this point, that the analytical tool developed was aimed at determining comparative values on maximum width of scattering signals when various parameters were applied. It is a simplified model that did not propose the direct comparison of calculated values with measured FWHM of scattering peaks. For this reason, calculated values of maximum widths of diffraction maxima are given in different units than measured FWHM values of diffraction peaks. Therefore, the relative values of calculated and measured widths (i.e. ratios) were compared.

As discussed earlier, an alternative approach to interpreting FCG data is to perform a radial integration around the condensation rings. Figure 7.12 illustrates by a red dotted line at Z_r , that if the detector is positioned at a condensation ring z-coordinate, the width of the condensation rings would account for the width of the diffraction peaks. The width of the condensation ring (W_r) would then be more comparable to the width of the PB Debye cones, as indicated in Figure 7.12. Equation (7.8) indicates the width of the condensation rings at a certain Z_r detector position;

$$W_r = R_{s2} - R_{s1} + (Z_r - Z_{s1}) \tan(2\theta - \phi_1) - (Z_r - Z_{s1} - t) \tan(2\theta - \phi_2) \quad (7.5)$$

where $R_{s2} = (Z_{s1} + t) \tan \phi_2$ and $R_{s1} = Z_{s1} \tan \phi_1$.

If the same example is used as in page 118, then W_r is calculated to be 0.399 mm at 170 mm z-position (Z_r); whereas for the PB arrangement at the same z-position is 0.709 mm. This is an indication of the potential of the condensation rings to provide sharper diffraction peaks than conventional PB arrangement.

However, there are a number of variables such as 2θ , sample and detector positions, beam divergence and beam's wall thickness that can affect the width of the scattering maxima. A comparison of the width of the diffraction peaks arising from

PB and FCG (condensation foci and rings) arrangements, in respect to these variables, was performed using Equations (7.3), (7.4) and (7.5), respectively. The constant values employed when alternative variables were examined were $2\theta = 29.84^\circ$, $\phi_{PB} = 0.1^\circ$, $\phi_1 = 3.58^\circ$, $\phi_2 = 3.68^\circ$, $Z_s = 153.72$ mm, $Z_d = 170$ mm and $t = 0.17$ mm; similarly to the empirical data.

Figure 7.13 illustrates the relationship of the calculated width of scattering maxima as obtained by the radial integration of PB and FCG data, and by the linear integration of FCG condensation foci, when the scattering angle, sample thickness and sample and detector z-positions were altered. An increase in the sample's thickness and the sample's z-position (constant sample-to-detector distance) indicates a positive linear relationship (different gradients) with the width of the scattering maxima, for all three data interpretation methods (Figure 7.13 (B) & (C)). Their different gradients suggest that the condensation foci are influenced the most by an increased sample thickness and sample z-position, whereas the condensation rings the least.

It is important to note at this point, that as indicated by Equation (7.4), the length of the condensation foci is independent of the detector's position along the z-axis. Figure 7.13 (D) demonstrates that as the detector's z-coordinate increases (with a fixed sample), the width of the condensation rings and the PB Debye cones increase linearly, with the former generating narrower diffraction peaks.

In contrast, the relationship between the width of the scattering maxima and the sample's scattering angles illustrates a rapid growth at $\sim 80^\circ$ for the width of the Debye cones and the condensation rings, and a rapid growth below $\sim 20^\circ$ for the length of the condensation foci (Figure 7.13 (A)).

Figure 7.14 compares the increase of the pencil beam's divergence and the annular beam's wall thickness with the width of the scattering maxima. In all cases, the width of the diffraction maxima increases, but follows a linear relationship for the Debye cones and condensation rings; whereas for the condensation foci it follows a more rapid increase.

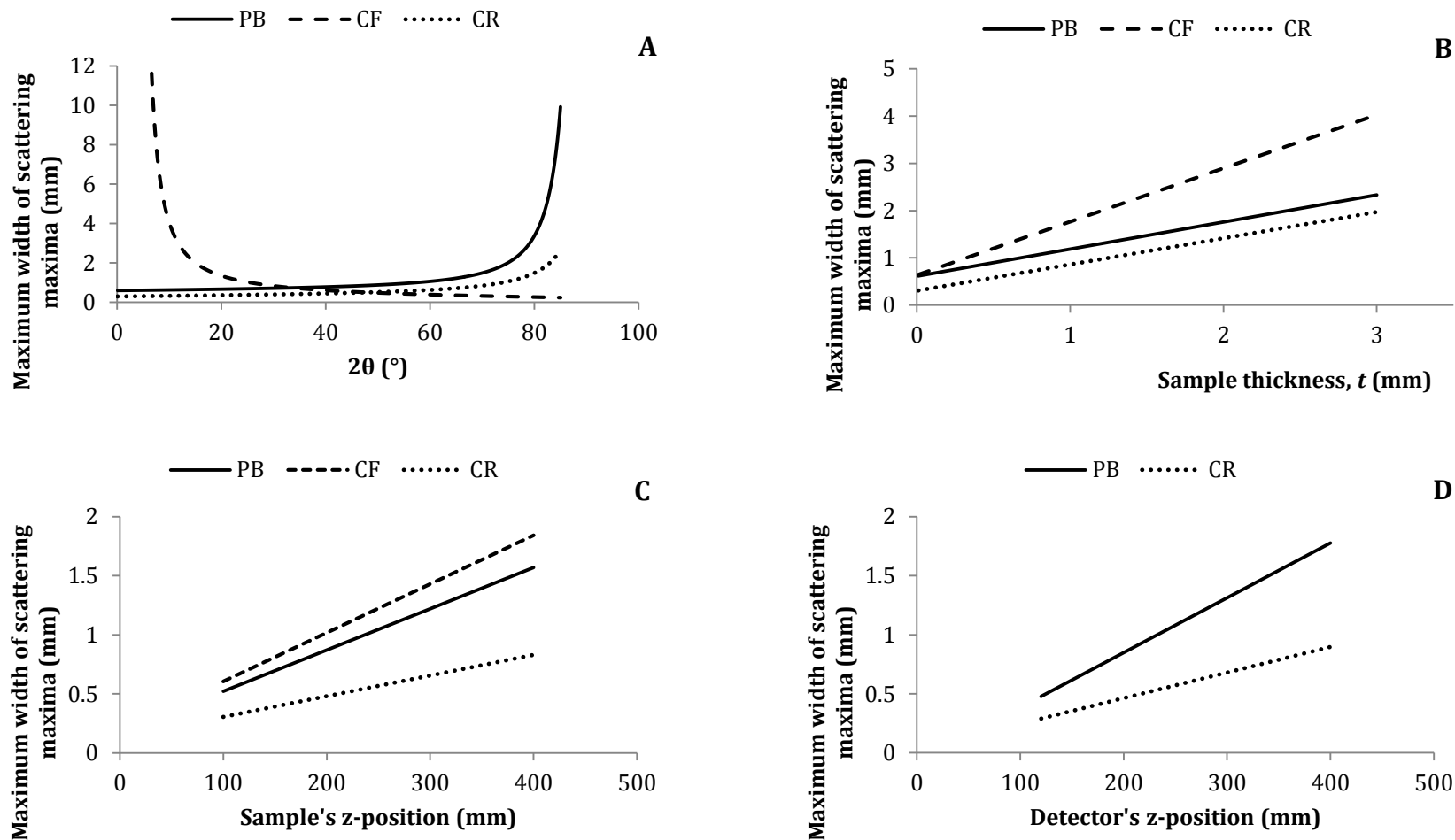


Figure 7.13 The relationships between calculated maximum width of scattering maxima obtained by a pencil beam (PB) and an annular beam geometry, when interpreting around the condensation foci (CF) and condensation rings (CR), with varying scattering angles (A), sample thickness (B), sample's z-position with a fixed sample-to-detector distance (C) and detector's z-position with a fixed sample (D).

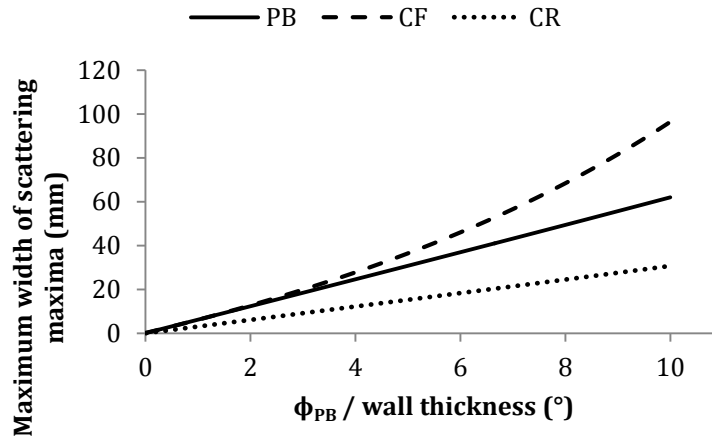


Figure 7.14 Correlation between the calculated maximum width of the scattering maxima obtained by a pencil beam (PB) and an annular beam geometry when integrating around the condensation foci (CF) and condensation rings (CR) with varying beam divergence and beam wall thickness respectively.

Lastly, the length/width of the condensation foci and rings were assessed with respect to the annular beam's opening angle (ϕ_2)[†], as seen in Figure 7.15. The length of the condensation foci is greater than the width of the condensation rings, with the latter increasing at a minute rate (linearly) and the former increasing at a greater rate (non-linearly).

A 1% increase in all variables (from typical empirical values) demonstrates that the width of the condensation rings suffers the least from peak broadening, as shown in Figure 7.16. Moreover, comparison of each component's contribution to peak broadening (except 2θ angles) showed that the width of the PB scattering maxima is affected the most by the sample-to-detector distance (D_{SD}) and beam divergence; whereas the length of the condensation foci is affected mostly by the sample's position along the z-axis and by the beam's wall thickness. The greatest contribution on the width of the condensation rings arose from the D_{SD} distance and beam wall thickness.

[†] The same relationship is observed with ϕ_1 .

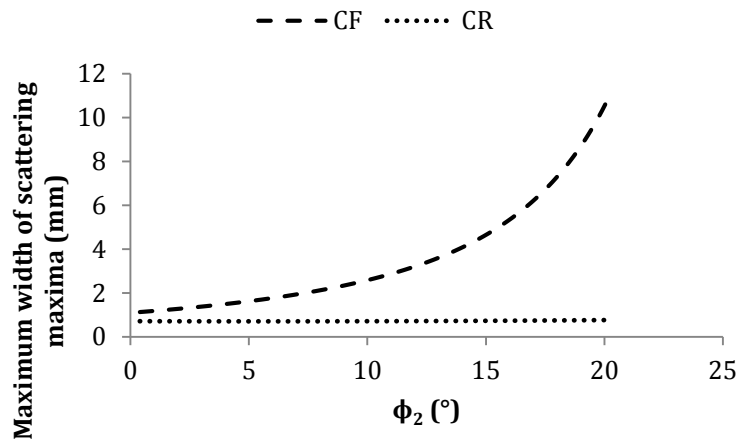


Figure 7.15 Correlation between the calculated maximum width of the scattering maxima obtained by an annular beam geometry when interpreting around the condensation foci (CF) and condensation rings (CR) with varying angular divergence ϕ_2 (and ϕ_1) and constant beam wall thickness ($\phi_2 - \phi_1$).

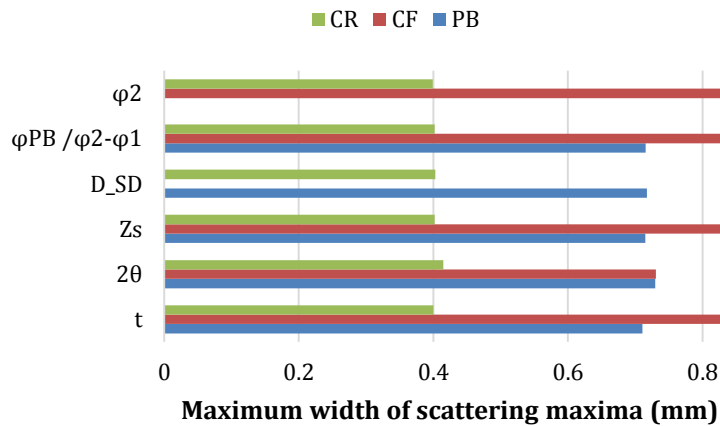


Figure 7.16 Contribution of 1% increase in all variables (sample thickness, t ; scattering angle, 2θ ; sample position, Z_s ; sample-to-detector distance, D_{SD} ; pencil beam divergence, ϕ_{PB} and beam wall thickness, $\phi_2 - \phi_1$; annular beam divergence ϕ_2) in the width of the scattering maxima.

In summary, it was analytically shown that the width of the condensation rings was significantly lower than the width of the Debye cones and length of condensation foci, whilst the latter demonstrated the highest peak broadening effect.

The condensation rings can therefore be employed during FCG data analysis for sharper diffraction peaks. However, when an FCG image is radially integrated, the radii of the condensation rings have to be translated into 2θ scattering angles. This conversion procedure differs for converging and diverging condensation rings. Equations (7.6) and (7.7) relate the radius of the converging and diverging rings, respectively to the sample's scattering angles ($2\theta_{cr}$ and $2\theta_{dr}$);

$$2\theta_{cr} = \tan^{-1} \left(\frac{Z_s \tan \phi_m - R_{cr}}{Z_r - Z_s} \right) + \phi_m \quad (7.6)$$

$$2\theta_{dr} = \tan^{-1} \left(\frac{Z_s \tan \phi_m + R_{dr}}{Z_r - Z_s} \right) + \phi_m \quad (7.7)$$

where R_{cr} and R_{dr} are the radii of the converging and diverging condensation rings, respectively.

This requires the FCG image to be comprised of either converging or diverging rings in order to determine the scattering angles. However, FCG images commonly consist of both converging and diverging condensation rings. Discrimination between these condensation rings is of great importance when acquiring a single FCG image. This requirement will be considered in greater depth in Section 8.2 and Section 8.3.

Scattering maxima obtained from both geometries (FCG and PB) were also assessed in terms of peak intensity. The total intensity of the condensation rings around their circumference is the same as the intensity of the corresponding condensation foci. For this reason, only the intensity of the condensation foci is taken into account in the following comparison.

Initially, the intensity of the scattering maxima as obtained by the annular and pencil beam arrangements was analytically assessed and compared. The condensation foci possess a considerably enhanced intensity that corresponds to $\sim 8R_s/W_T$ (see

Section 5.2), as indicated by Rogers et al. (2010). The relationship between the intensities of conventional and FCG data was re-considered in order to provide a more accurate comparison.

If an annular collimator of r_1 and r_2 inner and outer radius, respectively is considered, the area of the annulus is $\pi(r_2^2 - r_1^2)$. The area of a pinhole of diameter W_T is $\pi\left(\frac{W_T}{2}\right)^2$. The annulus area : pinhole area ratio is given by Equation (7.8).

$$I_{FCG_1:PB_2} = \frac{4(r_2^2 - r_1^2)}{W_T^2} \quad (7.8)$$

If the pinhole's diameter is the same as the annulus' thickness, i.e. $W_T = r_2 - r_1$, then Equation (7.8) can be simplified to Equation (7.9);

$$I_{FCG_1:PB_1} = \frac{8\bar{r}}{W_T} \quad (7.9)$$

where \bar{r} is the mean radius of the annular collimator.

Empirical data were also considered in order to compare the intensity of FCG and conventional scattering maxima. It should be noted that during the acquisition of conventional XRD data the time exposure was significantly higher (60 times) than that employed for the FCG experiment.

The area under the diffraction peaks from Al_2O_3 arising from both the annular and pencil beam geometries was obtained, assuming the same time exposure (10 seconds), and are presented in Table 7.3. The measured $I_{FCG_1:PB_2}$ ratio ranges from 22.47 to 134.21. The calculated $I_{FCG_1:PB_2}$ ratio (Equation (7.8)), corresponding to the empirical data, is ~ 71 (when R_1 and R_2 are 8.75 mm and 9 mm (*AB1* collimator), respectively, and W_T is 0.5 mm (*PB1* collimator)), which is within the empirical values.

As explained previously in Section 5.2, the relative intensities of the diffraction signals arising from an annular beam geometry differ from the intensities of conventional XRD signals. This may explain the inconsistencies in FCG:PB ratio determined from empirical data.

Table 7.3 Quantitative comparison of Al₂O₃'s scattering peak areas as obtained by the annular (FCG) and pencil (PB) beam geometries with 10 seconds time exposure.

PDF card No. 75-1862 d-spacing (nm)	Peak area		FCG:PB ratio
	FCG	PB	
0.138	656 ± 2.3	4.9 ± 0.6	133.9
0.152	18 ± 6.1	0.8 ± 0.9	22.5
0.160	76 ± 4.6	1.8 ± 0.8	42.2
0.174	49 ± 0.8	1.3 ± 0.1	37.7
0.209	61 ± 0.3	2.1 ± 0.1	29.0
0.238	28 ± 0.8	0.9 ± 0.1	31.1
0.255	24 ± 0.8	0.3 ± 0.1	80
0.348	2 ± 0.1	-	-

Following the initial comparison of the two different geometries, the effect of FCG system's components, including the collimation optics, sample thickness, and X-ray source, on peak broadening were investigated.

7.2.2 Collimation optics and sample variations

The effect of beam divergence on the width of scattering maxima was analysed via conventional XRD for simplicity purposes. As indicated previously by Figure 7.14, the effect of beam divergence on peak broadening is similar for conventional and FCG arrangements. However, since the relationship between collimation optics and beam divergence and their effect on peak broadening are well known and widely studied, the outcomes are reported briefly. Detailed results from each experimental procedure are given in Appendix A.

Initially, the effect of increased beam divergence on the width of the Debye cones was assessed by translating a pencil beam collimator along the primary axis. It was shown that as the X-ray source-to-collimator distance increases (hence beam divergence decreases), the width of the diffraction peaks decreases (Appendix A.1.1). Comparison of their FWHM indicated an average minor decrease of $\sim 0.01^\circ$ in the width of the diffraction peaks when the angular divergence was decreased from 0.38° to 0.14° (see Appendix A.1.1, Figure A.4).

Further examination of collimation optics involved a decrease of the pinhole diameter, in addition to an increase of the collimator's length or distance from the X-ray source. This indicated that narrower diffraction peaks arise from the collimator with the longest length and smaller pinhole diameter, i.e. smaller angular divergence (see Appendix A.1.2).

The effect of sample-to-detector distance on peak broadening was also investigated. Although the widths of the diffraction peaks were expected to increase as the sample-to-detector distance increased (as shown in Figure 7.13 (D)), the peaks appeared slightly narrower (Appendix A.2 – Figure A.8 and Figure A.9). This is believed to be due to the better resolved scattering maxima as the sample-to-detector increases, especially at a limited low 2θ range.

Examination of the X-ray source-to-sample distance at a fixed sample-to-detector distance confirmed that as the sample is translated further away from the X-ray source, the widths of the diffraction peaks increase (Figure A.10 and Figure A.11). The farther the sample is from the X-ray source, the greater the dimensions of the primary beam's footprint onto the sample, hence the broader the diffraction peaks, as theoretically assessed in Section 7.2.1.

In summary, it was demonstrated that a smaller beam divergence would generate narrower diffraction peaks. However, even with low beam divergence, diffraction profiles obtained by the FCG system, but with a conventional pencil beam arrangement, were not as sharp as the diffraction peaks obtained by standard diffractometers.

7.2.3 Sample thickness

The effect of increased sample thickness on FCG was investigated with powder samples of two different thicknesses. Figure 7.17 presents the scattering signatures obtained from Al_2O_3 , hydroxyapatite and NaCl powders with a sample thickness of 1.6 mm and 3 mm.

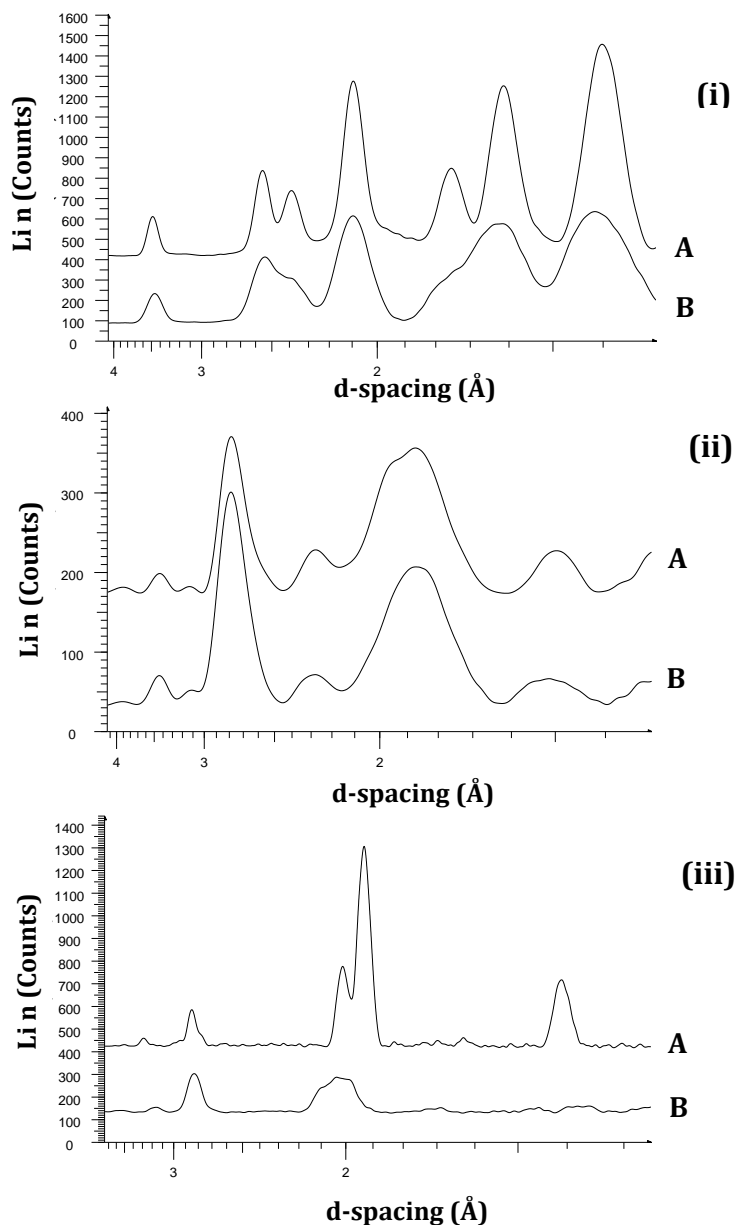


Figure 7.17 Scattering signatures from Al_2O_3 (i), synthetic hydroxyapatite (ii) and NaCl (iii) of 1.6 mm (A) and 3 mm (B) thickness, as obtained by an annular beam arrangement.

Diffraction profiles obtained from 1.6 mm thick samples illustrate narrower diffraction peaks, especially for Al_2O_3 . As seen in Figure 7.17 (i), the diffraction peaks at 0.239 nm and 0.256 nm of diffractogram A started to merge into one broad peak with a shoulder when the sample thickness increased (diffractogram B). For the scattering profiles of 1.6 mm and 3 mm thick hydroxyapatite samples, no significant differences were observed. The scattering maxima of NaCl indicate a distinctive decrease in the signal-to-noise ratio (SNR) when the sample thickness was increased to 3 mm.

The average optimal thickness for maximum scatter intensity for Al_2O_3 , hydroxyapatite and NaCl over a 10° - 40° 2θ range was calculated by Equation (3.3) to be 0.71 mm, 0.45 mm and 0.62 mm, respectively. The higher optimal thickness of Al_2O_3 over hydroxyapatite and NaCl may explain the higher resolution and intensity diffraction data obtained from Al_2O_3 .

Figure 7.18 presents the FWHM values obtained by the scattering signatures from Al_2O_3 , hydroxyapatite and NaCl with 1.6 mm and 3 mm sample thickness, when illuminated by an annular beam ($\phi_1 = 3.58^\circ$ and $\phi_2 = 3.68^\circ$), in terms of d-spacing. FWHM values with associated errors for each sample analysed are given in Appendix A.4.1 (Table A.1).

It is observed that as the thickness of the sample increases so does the width of the diffraction peaks, specifically for Al_2O_3 and NaCl; whereas for hydroxyapatite the width of the peaks arising from both sample thicknesses varied. A general trend is illustrated in Figure 7.18, indicating an increase in the FWHM as the 2θ angle decreases (d-spacing increases), even though they were exceptions; as also determined by Equation (7.4) (Figure 7.13 (A)).

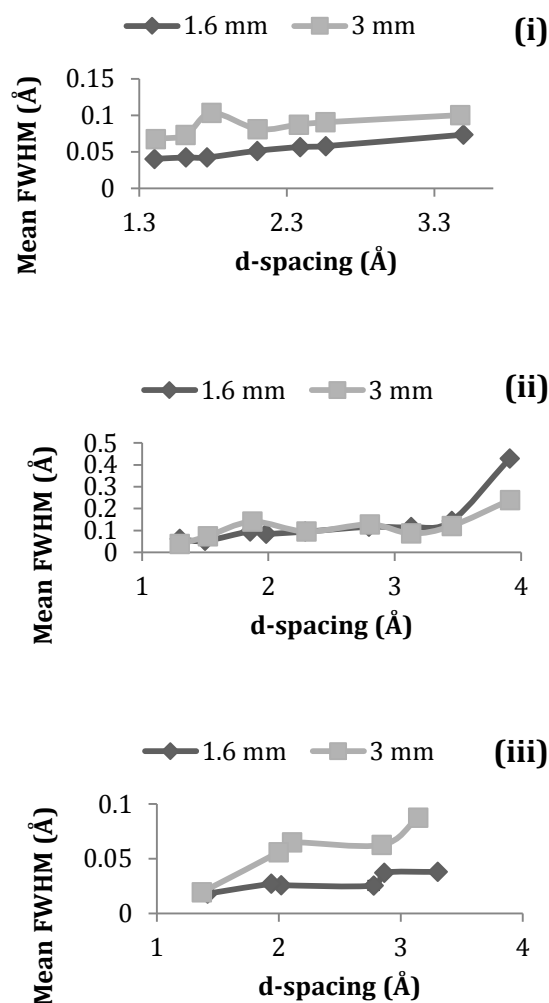


Figure 7.18 Mean FWHM values of the scattering maxima from Al₂O₃ (i), synthetic hydroxyapatite (ii) and NaCl (iii) powders with 1.6 mm and 3 mm sample thickness, as obtained by an annular beam arrangement.

The length of the corresponding condensation foci for all samples was calculated by Equation (7.4). The FWHM and the length of the condensation foci are not directly comparable (as explained in Section 7.2.1); therefore, the ratio of the FWHM values for 1.6 mm and 3 mm sample thickness were obtained and compared to the ratio of the condensation foci lengths for 1.6 mm and 3 mm sample thickness. The ratios are listed in Table 7.4.

Table 7.4 The ratio values obtained by the FWHM of empirical data and the calculated maximum length of the condensation foci for Al_2O_3 , hydroxyapatite and NaCl samples from 3 mm and 1.6 mm thickness.

	Ratio (3 mm : 1.6 mm sample thickness)	
	Empirical FWHM	Calculated condensation focus length
Al_2O_3	1.36	1.37
	1.57	1.47
	1.54	1.49
	1.58	1.53
	2.44	1.59
	1.73	1.59
	1.68	1.63
$\text{Ca}_{10}(\text{PO}_4)_6(\text{OH})_2$	0.56	1.34
	0.84	1.38
	0.75	1.41
	1.10	1.45
	1.01	1.51
	1.65	1.50
	1.46	1.57
	1.42	1.62
NaCl	0.61	1.65
	1.23	1.44
	1.45	1.53

The ratio values indicate an agreement between the empirical FWHM and calculated maximum length of the condensation foci, even though there are some inconsistencies between the ratio values, mainly due to the broader scattering maxima from 1.6 mm hydroxyapatite.

Conventional XRD data (Figure 7.19) were also acquired from the powder samples with 1.6 mm and 3 mm thickness. Similarly to the FCG profiles, the width of the diffraction peaks increases as the sample thickness increases, especially for Al_2O_3 (Figure 7.19 (i)).

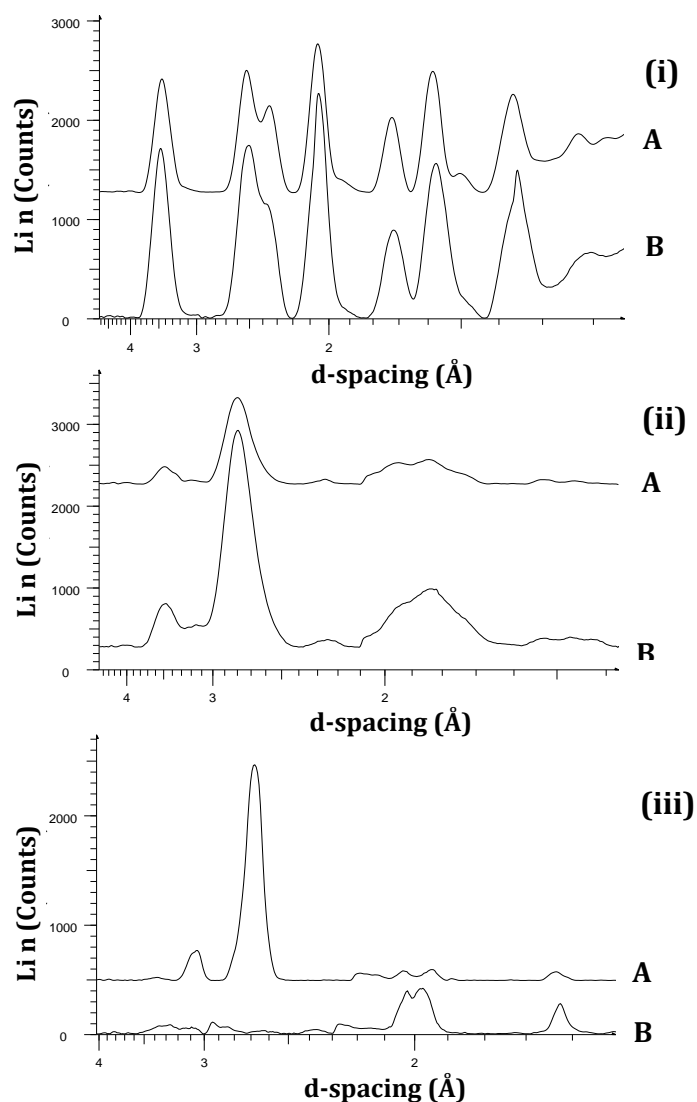


Figure 7.19 Scattering signatures from Al_2O_3 (i), synthetic hydroxyapatite (ii) and NaCl (iii) of 1.6 mm (A) and 3 mm (B) thickness, as obtained by a pencil beam arrangement.

The scattering profiles of NaCl (Figure 7.19 (iii)), a sample with large grain size, is of interest as its scattering maxima arising from reflections 111 and 200 are not observed with the 3 mm thick sample. This is an example of misleading XRD data that can be acquired with samples exhibiting large grain size, when capturing only a section of the diffraction pattern. Plots illustrating the relationship between FWHM of the scattering signals of each sample as their thickness increases are

presented in Figure 7.20 for conventional XRD (list of FWHM tabulated in Table A.2, Appendix A.4.2).

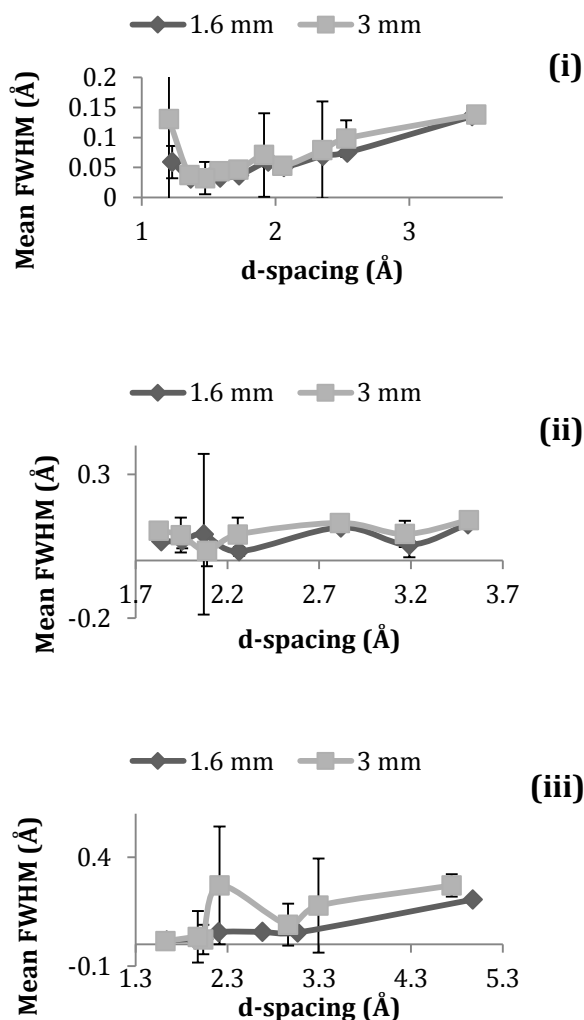


Figure 7.20 Mean FWHM values of the scattering maxima from Al_2O_3 (i), synthetic hydroxyapatite (ii) and NaCl (iii) powders with 1.6 mm and 3 mm sample thickness, as obtained by a pencil beam arrangement.

The FWHM values of the 3 mm thick samples tend to be higher than the FWHM value of the 1.6 mm thick samples, with considerably higher errors. It is noteworthy, that the errors of the FWHM values for the conventional data for both sample thicknesses are significantly higher than the associated errors of the FCG data.

7.2.4 Alternative X-ray source (CT system)

An alternative X-ray source (see Section 6.3.3.4 for X-ray source specifications) was employed to determine its effect on FCG diffraction patterns, mainly in terms of peak broadening. The Panalytical X-ray tube has a focal spot with physical dimensions of 0.4 x 12 mm and a target to beam angle of 6°, as mentioned in Section 6.1.2. Even though the area of the resultant focal spot is compatible with the requirement of a focal spot of less than 1 mm² for the production of high quality diffraction signals (Cullity, 1978), the large physical dimensions of the focal spot can cause an increase in the beam divergence and an enhanced geometric unsharpness.

The X-ray source within a CT system was therefore engaged and evaluated in terms of diffraction peaks' widths. Even though the acquisition of FCG diffraction patterns within the CT system is currently at very early stages, a series of 30 diffraction frames was successfully captured (Figure 7.21). The data sequence demonstrates the convergence of a condensation ring at its condensation focus and its divergence, as illustrated in Figure 7.21. This scattering maximum arises from the 300 reflection in Al₂O₃ with an interplanar distance of 0.138 nm. The diffraction peak was compared to its equivalent diffraction peak acquired by the original FCG system, as illustrated in Figure 7.22.

It is observed that the diffraction peak obtained by the CT system is slightly narrower (FWHM of $0.0057 \pm 4.39 \times 10^{-4}$ nm) than the diffraction peak from the original FCG system (FWHM of $0.0067 \pm 2.12 \times 10^{-4}$ nm); indicating a ~15% decrease in FWHM.

Moreover, Figure 7.23 provides a comparison between the widths of the condensation rings acquired by the FCG system and the CT system. It is indicated that the width of the condensation rings captured within the CT system are narrower when compared to the FCG system's data.

It should be noted that the intensity of the diffraction profiles obtained by the two systems (Figure 7.22 and Figure 7.23) is not comparable due to different time exposures, voltage and current values employed.

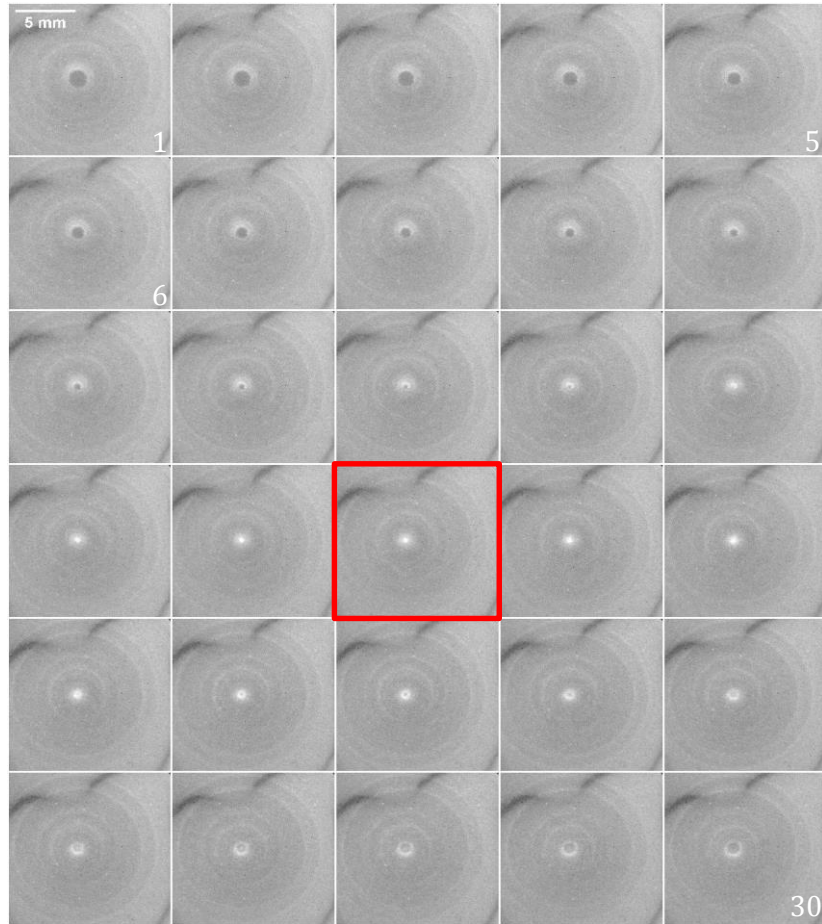


Figure 7.21 Sequence of FCG diffraction images obtained from an Al_2O_3 plate within the CT system. The data sequence is displayed from left to right with the condensation focus of 300 reflection in Al_2O_3 illustrated in image no. 18 (red box).

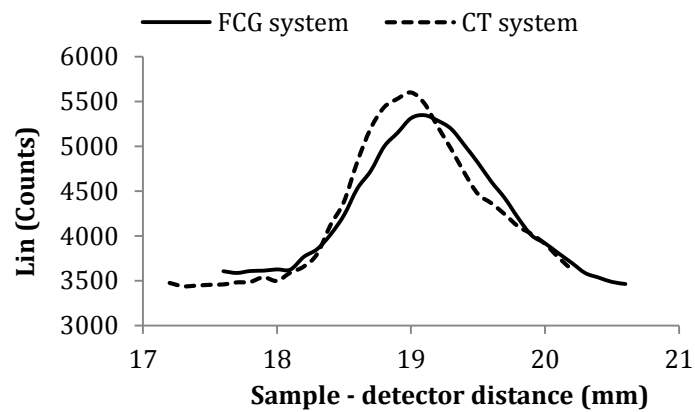


Figure 7.22 Comparison of the diffraction peak arising from 300 reflection from Al_2O_3 , as acquired within the FCG and CT systems. NB. Position offset caused by lack of calibration.

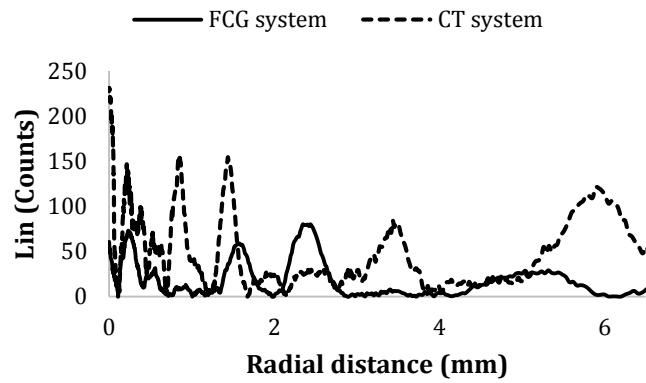


Figure 7.23 Radial integration of diffraction images obtained by the FCG and CT systems, when the 300 reflection from Al_2O_3 was at its focal point.

In summary, broadening of the diffraction peaks was shown to be dependent upon instrumentation components, as well as the beam geometry employed. Peak broadening (B_p) can therefore be described by Equation (7.10);

$$B_p = \sigma(S_{FS}) + \sigma(PB_S) + \sigma(\phi_{PB}) + \sigma(t) + \sigma(Z_s) + \sigma(Z_d) + \sigma(D_{PSF}) \quad (7.10)$$

where $\sigma(S_{FS})$ is the peak broadening of the diffraction peaks (in $^\circ/2\theta$) caused by the X-ray source's focal spot, $\sigma(PB_S)$ and $\sigma(\phi_{PB})$ are the peak broadening of the diffraction peaks (in $^\circ/2\theta$) caused by the shape and angular divergence of the primary beam respectively, $\sigma(t)$ is the peak broadening of the diffraction peaks (in $^\circ/2\theta$) caused by the sample thickness, $\sigma(Z_s)$ and $\sigma(Z_d)$ the peak broadening of the diffraction peaks (in $^\circ/2\theta$) caused by the sample and detector's position along the primary axis and $\sigma(D_{PSF})$ the peak broadening of the diffraction peaks (in $^\circ/2\theta$) caused by the point spread function of the detector.

Nonetheless, in all cases, the widths of the diffraction peaks acquired within the FCG system (or CT system) were not in the same order as the widths of diffraction peaks obtained by a standard diffractometer (Bruker D8-GADDS).

7.3 Analysis of liquid samples

Analysis of liquid samples involved the discrimination between threat and benign liquids for aviation security (Section 2.2.2). Scattering maxima from a variety of liquid samples (Table 6.3) were acquired using both the annular beam and conventional pencil beam arrangements. The results presented in this section were initially examined by a qualitative inspection of the diffraction images and then by a quantitative comparison of their scattering distributions.

7.3.1 Visual inspection

Representative scattering distributions of threat and benign liquids, as obtained by FCG at single detector positions along the primary axis are shown in Figure 7.24. Images (a) and (b) of Figure 7.24 were acquired at a sample-to-detector distance of 52.5 mm, illustrating the difference in the dominant scattering distributions between water and 2-propanol; a non-threat and a 3rd class threat liquid, respectively (classified in Section 6.2 (b) as indicated by Harding et al. (2010)). The higher scattering angle of water emerges close to a condensation focus at a 52.5 mm sample-to-detector distance, in comparison to the lower scattering angle of 2-propanol that forms a distinguishable condensation ring.

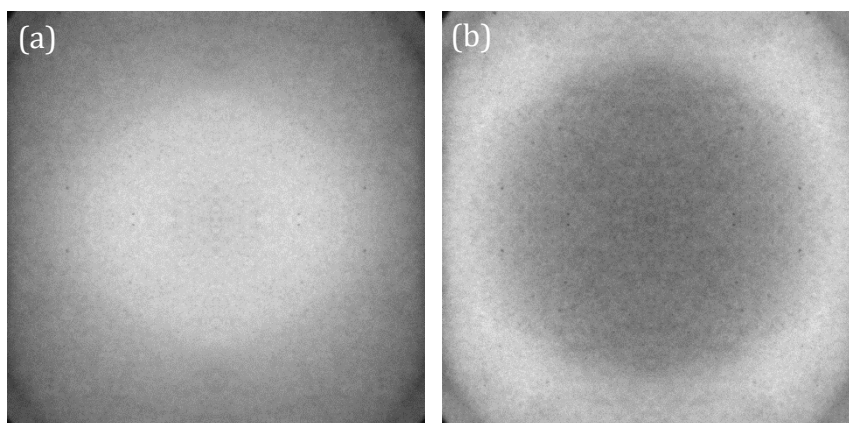


Figure 7.24 FCG diffraction images of the condensation ring of water (a) and 2-propanol (b) at a 52.2 mm sample-to-detector distance.

All benign liquids analysed, illustrated similar intensity maxima to water (Figure 7.24 (a)); whereas the condensation ring formed by the scattering maxima of all threat liquids (except hydrogen peroxide) appeared at a greater radius, similarly to 2-propanol (Figure 7.24 (b)); indicating a lower scattering angle. Therefore, a visual inspection of the scattering image of a liquid could assist in the identification of a threat liquid.

Single scattering images of miscible and immiscible liquid mixtures, as listed in Table 6.4, were obtained and compared to the scattering images of the individual liquids. Analysis of 2D diffraction images illustrated in Figure 7.25 and Figure 7.26, as obtained by miscible mixtures, indicated a single dominant condensation ring of an approximately amid radius. In the case of immiscible mixtures, the diffraction image possessed two condensation rings, as seen in Figure 7.27 and Figure 7.28, each corresponding to the individual liquid.

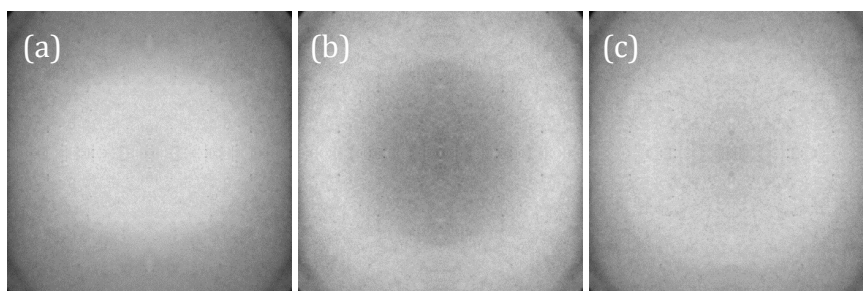


Figure 7.25 FCG diffraction images of the condensation ring of coffee (a), methylated spirit (b) and a mixture of the two (c) at a 52.2 mm sample-to-detector distance.

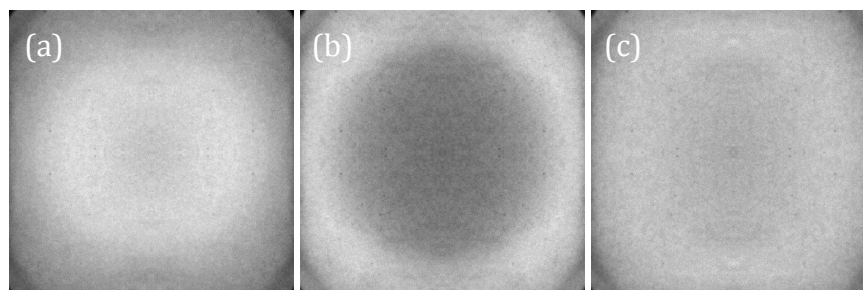


Figure 7.26 FCG diffraction images of the condensation ring of whiskey (a), 2-propanol (b) and a mixture of the two (c) at a 52.2 mm sample-to-detector distance.

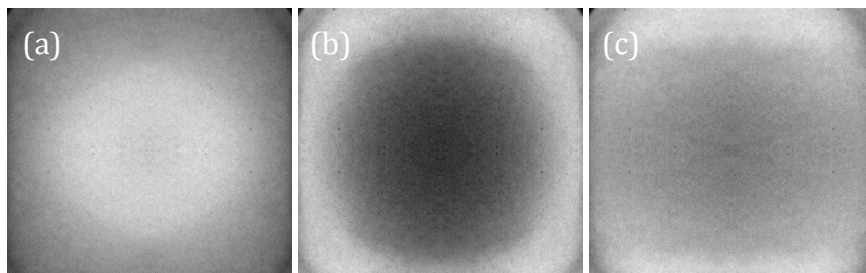


Figure 7.27 FCG diffraction images of the condensation ring of water (a), diesel (b) and a mixture of the two (c) at a 52.2 mm sample-to-detector distance.

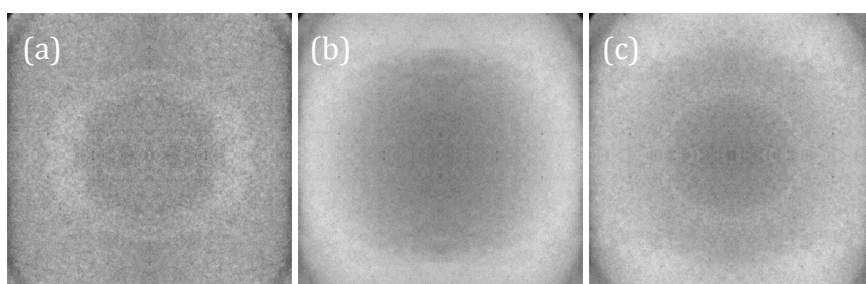


Figure 7.28 FCG diffraction images of the condensation ring of cosmetic foundation cream (a), acetone (b) and a mixture of the two (c) at a 52.2 mm sample-to-detector distance.

7.3.2 Analysis of 2D diffraction sequences

As mentioned earlier in Section 6.3.4, the scatter intensity maxima of liquids can be calculated via Equation (6.1). All benign liquids produced diffractograms with a single diffraction signal between 0.325-0.354 nm (Figure 7.29); except the cosmetic foundation cream that produced an additional weak signal at 0.42 nm. The diffractograms of all threat liquids (with the exception of hydrogen peroxide) demonstrated scatter maxima between 0.401-0.442 nm (Figure 7.30). Additionally, the intensity of the signals arising from threat liquids was significantly higher than the intensity of the diffraction signals of the benign liquids. Table 7.5 presents the scattering vector magnitude for each threat and non-threat liquid analysed with their corresponding error values.

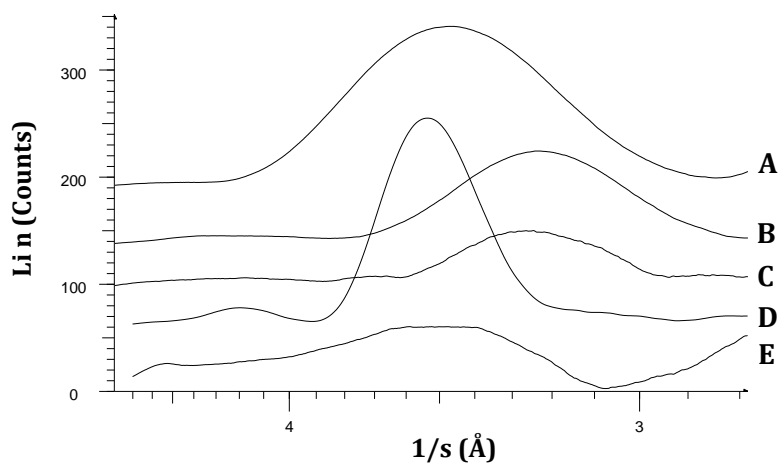


Figure 7.29 Scattering signatures of all non-threat liquids analysed during this work; including whiskey (A), water (B), coffee (C), cosmetic foundation cream (D) and jam (E).

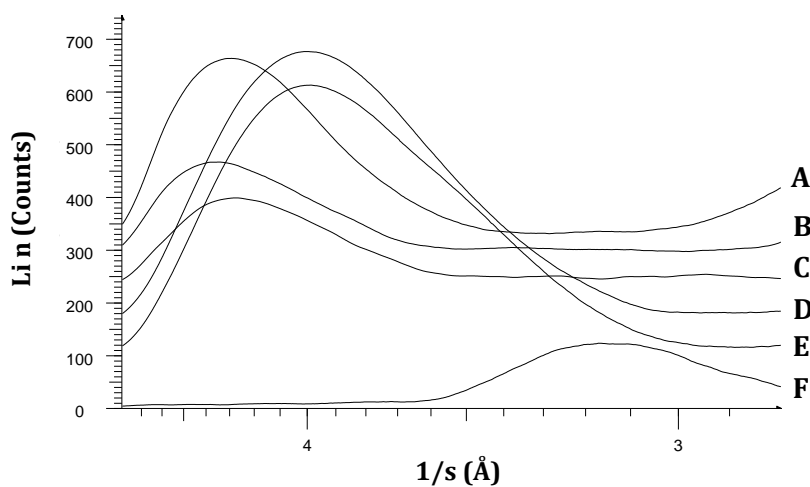


Figure 7.30 Scattering signatures of all threat liquids analysed during this work; including 2-propanol (A), diesel (B), acetone (C), methylated spirit (D), ethanol (E) and hydrogen peroxide 30% (F).

Table 7.5 The scattering vector magnitude for all threat and non-threat liquids analysed during this study.

	Category*	Sample	$1/s = \lambda / (2\sin\theta)$ (nm)
Threat	A	Diesel	$0.442 \pm 1.50 \times 10^{-3}$
	A	Acetone	$0.431 \pm 5.52 \times 10^{-4}$
	B	Hydrogen peroxide (30%)	$0.317 \pm 3.91 \times 10^{-4}$
	C	Hydrogen peroxide (3%)	$0.325 \pm 1.30 \times 10^{-3}$
	C	Methylated spirit	$0.401 \pm 3.21 \times 10^{-4}$
	C	Ethanol	$0.402 \pm 7.85 \times 10^{-4}$
	C	2-propanol	$0.436 \pm 6.33 \times 10^{-4}$
Non-threat	D	Whiskey	$0.348 \pm 6.83 \times 10^{-4}$
	D	Cosmetic foundation cream	$0.420 \pm 3.42 \times 10^{-3}$
			$0.354 \pm 4.52 \times 10^{-4}$
	D	Jam	$0.353 \pm 9.96 \times 10^{-4}$
	E	Water	$0.325 \pm 6.79 \times 10^{-4}$
	E	Coffee	$0.325 \pm 4.09 \times 10^{-4}$

*As categorised in Section 6.2(b)

Hydrogen peroxide (H₂O₂) was analysed in two different concentrations: 3% and 30%. The scattering maxima from 3% H₂O₂ occurred at 0.325 nm similarly to that of water; whereas 30% H₂O₂ produced a diffraction signal with a lower inverse scattering vector magnitude of 0.317 nm, as illustrated in Figure 7.31. The lower inverse scattering vector magnitude of 30% H₂O₂ can be explained by the higher density of H₂O₂ (1.11 gcm⁻³ for 30% H₂O₂ and 1.45 gcm⁻³ for pure H₂O₂), when compared to the density of water (1 gcm⁻³) (Wells and Bradley, 2012).

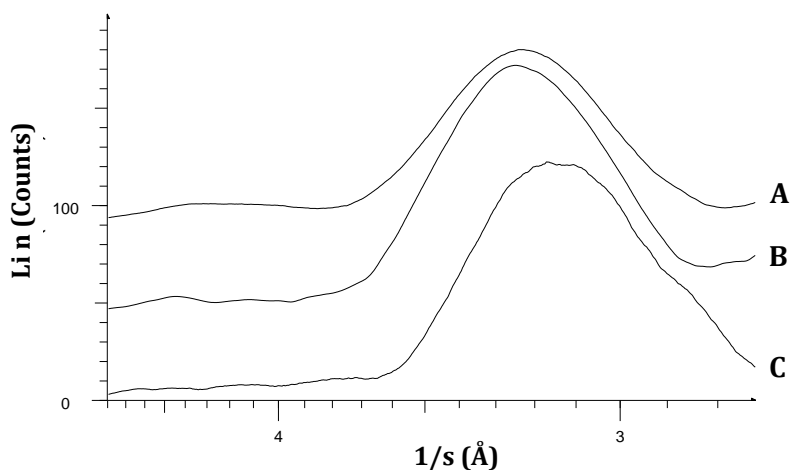


Figure 7.31 Scattering signatures of water (A), hydrogen peroxide at 3% (B) and 30% (C) concentration.

In summary, analysis of restricted (limited d-spacing) FCG data sequences indicated determination between threat and non-threat liquids based on their scattering maxima positions.

Diffraction images from mixtures of threat and non-threat liquids were also analysed to determine possible discrimination between the distinct liquids. The solutions were mixed in a 1:1 ratio, as described in Section 6.2(b); therefore, each liquid was present at equal volumes. The scattering distributions arising from such mixtures indicated the presence of either one or two dominant signals, depending on the miscibility of the two solutions. For example, miscible mixtures such as 2-propanol with whiskey (Figure 7.32) and methylated spirit with coffee (Figure 7.33) produced a single dominant scattering maximum. The scattering vector magnitude of the diffraction signal arising from miscible samples was between the values from the individual liquids.

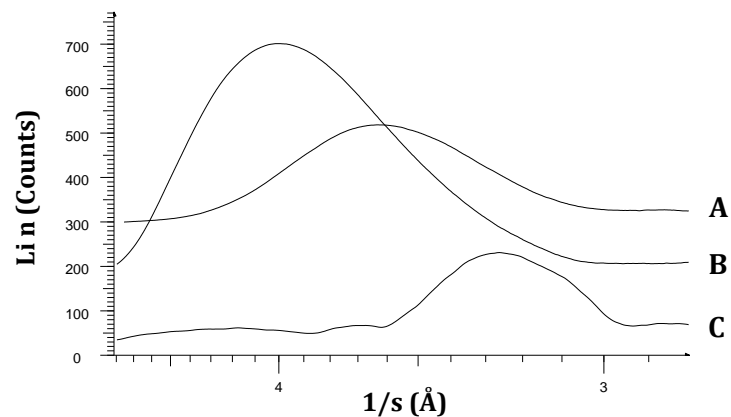


Figure 7.33 Scattering signatures of methylated spirit and coffee mixture (A), methylated spirit (B) and coffee (C).

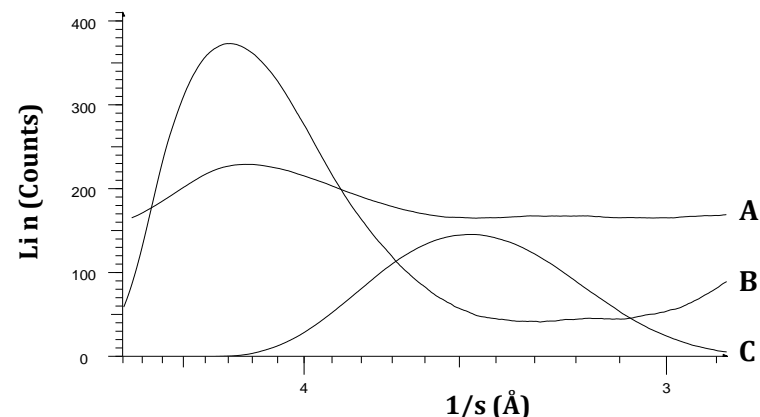


Figure 7.32 Scattering signatures of 2-propanol and whiskey mixture (A), 2-propanol (B) and whiskey (C).

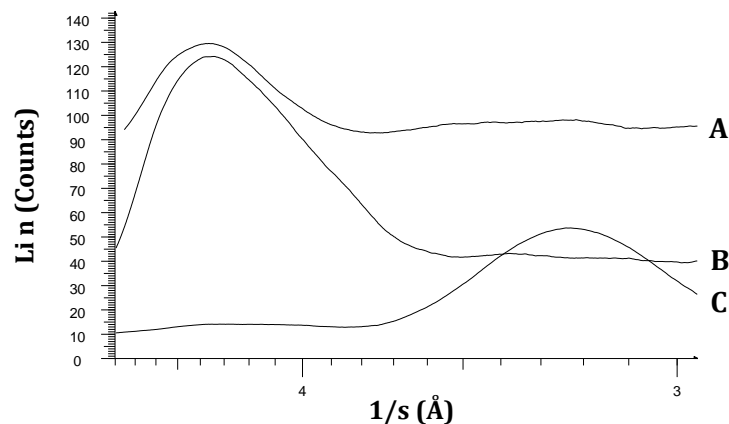


Figure 7.35 Scattering signatures of diesel and water mixture (A), diesel (B) and water (C).

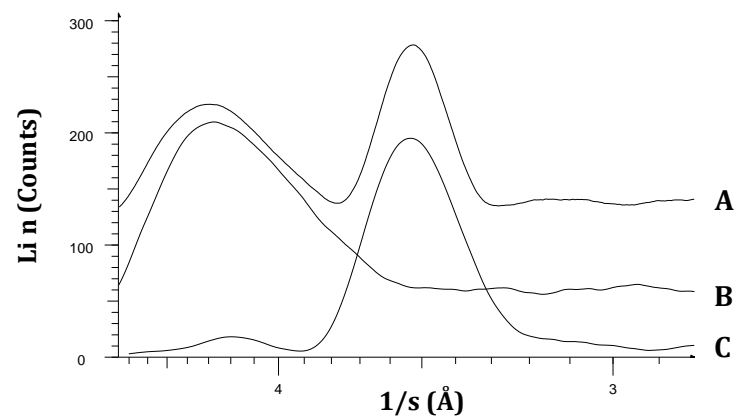


Figure 7.34 Scattering signatures of acetone and cosmetic foundation cream mixture (A), acetone (B) and cosmetic foundation cream (C).

However, in the case of immiscible mixtures, two dominant scattering maxima were produced, each arising from the individual liquid. As observed in Figure 7.34, the mixture of acetone and the cosmetic foundation cream yielded two diffraction signals at 0.354 nm and 0.434 nm; corresponding to the cosmetic foundation cream and acetone, respectively.

The cosmetic foundation cream has an additional peak of low intensity at 0.420 nm (Figure 7.34 (C)) which overlaps with the dominant diffraction signal of acetone at 0.431 nm (Figure 7.34 (B)) in the diffractogram of their mixture solution, thus producing a broader signal at 0.434 nm (Figure 7.34 (A)).

Similarly, the mixture of diesel and water yielded a dominant scattering maximum at 0.442 nm arising from diesel and a very weak signal at ~ 0.317 nm resulting from water, as illustrated in Figure 7.35.

Table 7.6 presents the scattering vector magnitudes of the mixtures analysed.

Table 7.6 Scattering vector magnitudes of the mixtures of threat and non-threat liquids analysed.

Mixtures	$1/s = \lambda/(2\sin\theta)$ (nm)
Methylated spirit + Coffee	$0.363 \pm 4.20 \times 10^{-4}$
2-propanol + Whiskey	$0.424 \pm 7.69 \times 10^{-4}$
Acetone + Cosmetic foundation cream	$0.434 \pm 9.40 \times 10^{-1}, 0.354 \pm 5.01 \times 10^{-4}$
Diesel + Water	$0.442 \pm 2.78 \times 10^{-3}, 0.317 \pm 3.83 \times 10^{-2}$

7.3.3 Reproducibility of data

Since the diffraction signals from the liquid samples are significantly broadened when compared to the diffraction peaks of crystalline materials, the reproducibility of the FCG patterns was evaluated. The scattering maximum position of methylated spirit was acquired a number of times after various instrumental movements and calibration arrangements, as described in Section 6.3.4.

As seen in Figure 7.36, the scattering signatures acquired after various homing steps, appear (within experimental errors) at the same detector's distance along the

primary axis. Nonetheless, the data sequences captured after employing a different sample cell orientation and cell position, demonstrated scattering maxima at a shorter distance from the X-ray source. During the last two steps, the direction of the sample cell was inverted and the position of the cell was slightly dislocated; hence altering the sample-to-detector distance. A minor change of ~ 5 mm in the sample's z-distance indicates significant differences in the scattering maxima positions, which can be resolved with accurate calibration of the instrumentation, as indicated in Figure 7.37.

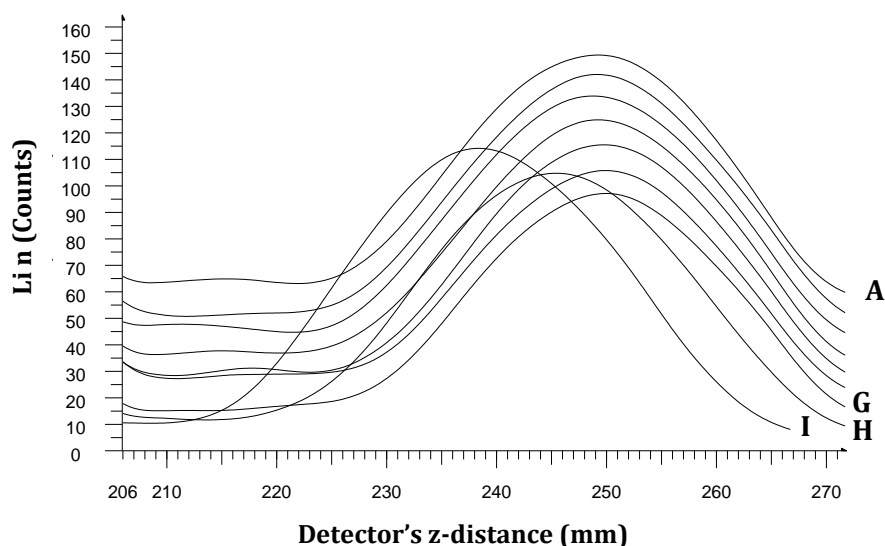


Figure 7.36 Scattering signatures of methylated spirit acquired after various homing steps and a replaced sample cell (A-G), as well as different sample cell orientation (H) and position (I).

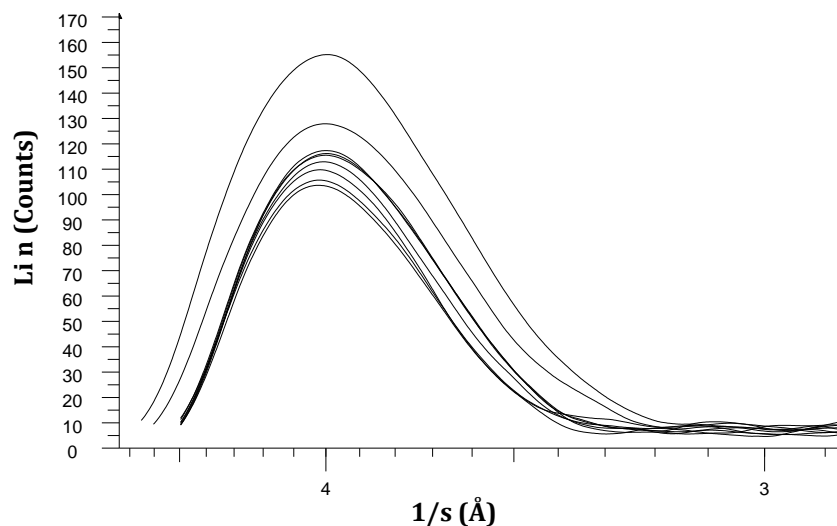


Figure 7.37 Calibrated scattering signatures of methylated spirit acquired after various homing steps, sample translations and dislocations.

7.3.4 Comparison between FCG and pencil beam data

A comparative study was performed with all non-threat and threat liquids analysed during this work. The aim was to determine the differences in the scattering distributions from amorphous substances between FCG and conventional XRD data.

Even though the pencil beam geometry produced scattering distributions of similar peak widths as FCG, the intensity of the diffraction maxima from the pencil beam arrangement was significantly lower, as expected (see Sections 5.2 and 7.2.1). FCG diffraction signals were acquired at a time exposure of 10 seconds; whereas conventional diffraction maxima were captured at 10 minutes time exposure for an analogous degree of discrimination.

Figure 7.38 (i) illustrates the diffraction signatures of water, a representative benign liquid, as obtained by the annular and pencil beam geometries. As shown, both diffraction signals occupy a broad distribution with $0.027 \pm 1.79 \times 10^{-3}$ nm and $0.037 \pm 1.85 \times 10^{-3}$ nm FWHM values for FCG and PB arrangements, respectively. The scattering maximum of water acquired by an annular beam occupies a significantly enhanced intensity generating a better-defined diffraction maximum signal at a

lower position associated error. FCG produced a scattering maximum with a $\sim 24\%$ greater area than the scattering maximum from the pencil beam geometry.

The same observations were seen with the analysis of threat liquids. A representative example is given within Figure 7.38 (ii), where the diffraction maxima of methylated spirit obtained by FCG and by the conventional pencil beam arrangement are compared. Similarly to benign liquids, the FCG diffraction maximum indicates a higher resolution with $0.052 \pm 6.84 \times 10^{-4}$ nm FWHM when compared to $0.060 \pm 7.43 \times 10^{-2}$ nm FWHM of the conventional XRD data. Furthermore, the intensity (area) of FCG scattering maximum is significantly higher than that from conventional PB geometry.

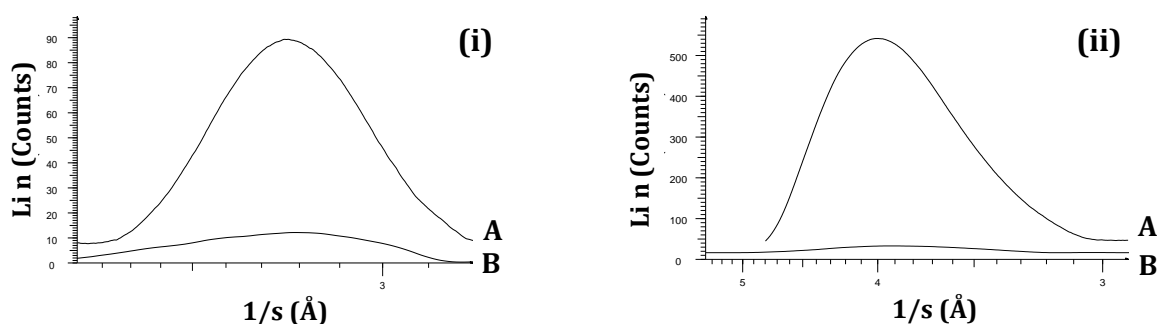


Figure 7.38 Scattering signatures of water (i) and methylated spirit (ii) acquired by the annular beam (A) and pencil beam (B) arrangements with 10 seconds time exposure.

To summarise, it was demonstrated that FCG data analysis can distinguish between threat and benign liquids based on the position of their scattering maxima. Discrimination between water and 30% H_2O_2 was also achieved. Mixtures of miscible and immiscible liquids were also analysed and similar results to Krishnamurti (1929) were observed (see Section 3.2.3). The reproducibility of the FCG system was tested and verified with methylated spirits, a threat liquid. In addition, comparison of FCG and conventional XRD data from threat and non-threat liquids indicated enhanced intensity of the former, hence more effective data interpretation.

7.4 Preferred orientation

The phenomenon of preferred orientation was examined with FCG, initially through a theoretical and simulated approach and then in an empirical manner.

7.4.1 Theoretical and simulated approach

Theoretical and simulated analysis of FCG data involved convolution of an annular primary beam with either a single or a set of Debye rings to simulate an FCG pattern, as previously illustrated in Section 5.1. Further analysis of convolved FCG patterns is presented later on in Section 8.1.

Simulated FCG patterns were produced following the theoretical basis of diffraction maxima arising from an infinite number of pencil beams around the circumference of the annular beam. A Debye cone with the same radius as the primary beam was employed as well as two Debye rings, one with a smaller radius than the primary beam and the other with a greater radius. The Debye cones arose from a sample exhibiting extreme preferred orientation; hence appear as discontinuous Debye arcs. The different radii of the Debye rings enabled the formation of a condensation focus, a converging condensation ring and a diverging condensation ring, as illustrated in Figure 7.39.

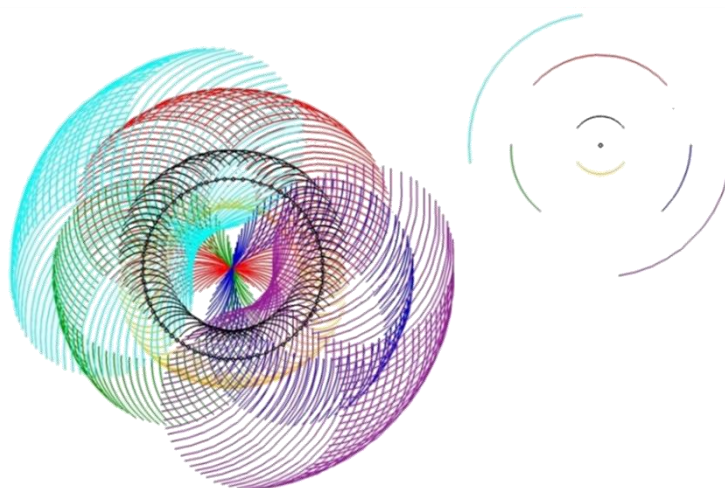


Figure 7.39 Schematic illustration of an FCG pattern (left) with a condensation focus, a converging condensation ring and a diverging condensation ring produced by Debye cones (top right) of different scattering angles from a sample with extreme preferred orientation.

The Debye arcs coloured in black and yellow, with a smaller radius than the primary beam, produced a converging ring with the opposite geometry than the Debye arcs. The yellow arc formed the top part of the converging ring, whereas the black arc formed the bottom part of the converging ring. This effect can be seen more clearly in Figure 7.40 with the green, red and blue Debye arcs forming a converging ring close to a condensation focus position, where the geometry of the arcs has been inverted.

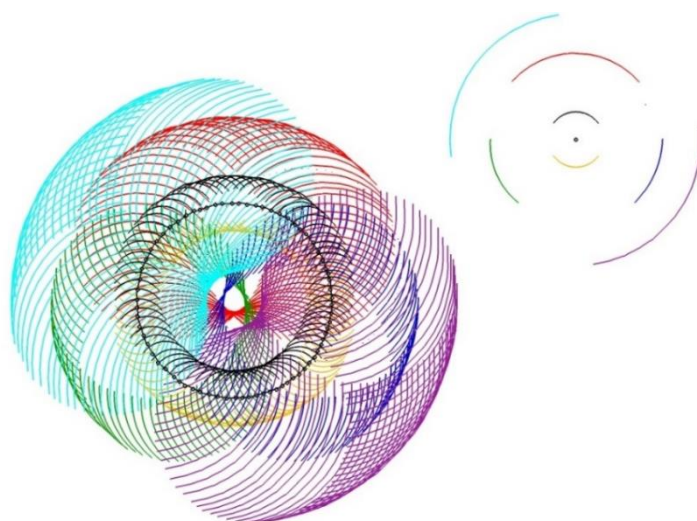


Figure 7.40 Schematic illustration of an FCG pattern (left) with two converging condensation rings and a diverging condensation ring produced by Debye cones (top right) of different scattering angles from a sample with extreme preferred orientation.

The outer condensation ring formed by this Debye arc possesses the exact same geometry as the latter. In fact, it was determined that all outer condensation rings formed by Debye cones of any scattering angle will have the same geometry as the initial Debye arcs. Moreover, the diverging condensation rings illustrated in Figure 7.39 and Figure 7.40 (coloured in light blue and purple) possess the same geometry as the initial Debye arcs, since the arcs converge with an inverse geometry to a condensation focus and then diverge in the opposite direction to create the same geometry as the initial Debye arcs.

The geometry of the Debye arcs and their corresponding condensation rings was then examined via the convolution of a simulated image of a single Debye ring (Figure 7.41(a)) with simulated images of three annular beams of varying radius.

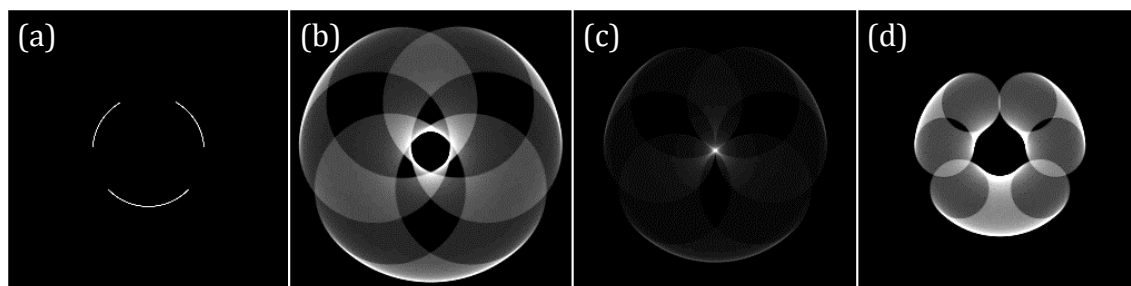


Figure 7.41 Simulated images of a Debye ring from a sample with extreme texture (a), FCG pattern demonstrating a converging condensation ring (b), a condensation focus (c) and a diverging condensation ring (d) produced by a Debye cone with preferred orientation.

In Figure 7.41 (b), the converging condensation ring of an FCG pattern produced by an annular beam of a greater radius than the Debye cone is shown. When comparing the geometry of the Debye arcs presented in Figure 7.41 (a) with the geometry of the converging ring in Figure 7.41 (b), it is evident that the geometry of the Debye arcs is inverted; whereas the outer ring of the FCG pattern retains the original geometry. Moreover, the outer rings of Figure 7.41 (c) and (d) possess the initial geometry of the Debye arcs, as well as the diverging ring demonstrated in Figure 7.41 (d). This relationship between the Debye arcs and the condensation arcs can also be observed through a circumferential integration around the Debye cone and around each inner and outer condensation rings, as illustrated in Figure 7.42. Simulated data are therefore in agreement with the theoretical predictions.

To summarise, converging condensation rings occupy an inverted geometry to that of the initial Debye cones; whereas diverging condensation rings occupy the same geometry. All outer condensation rings possess the same geometry as the Debye rings.

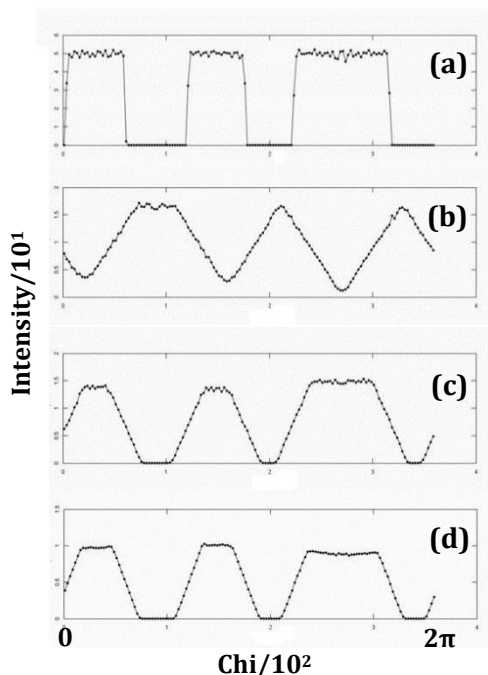


Figure 7.42 Circumferential integration plots of a Debye cone between 2.57-2.65 mm radius (a), an inner converging ring between 0.94-1.02 mm radius (b), an inner diverging ring between 1.22-1.3 mm radius (c) and an outer condensation ring of a condensation focus between 4.8-5.22 mm radius (d).

7.4.2 Empirical approach

The effect of preferred orientation on FCG was also examined empirically to support the theoretical predictions and establish the geometry of the condensation rings, with respect to the corresponding Debye cones. In addition, these experiments intended to demonstrate the differences between diffraction data obtained by conventional PB arrangement and FCG.

Initially, an Al sample (AS) with preferred orientation was analysed by the conventional PB arrangement by capturing a section of the Debye cone, as indicated in Figure 7.43.

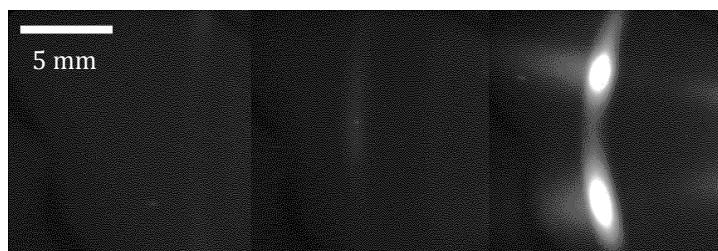


Figure 7.43 Empirical image of a section of the diffraction pattern of Al AS sample obtained by the pencil beam arrangement with collimator *PB1*.

The complete diffraction pattern from the Al sample was also captured to reveal the overall geometry of the Debye cones/arcs (Figure 7.44). The dotted red box in Figure 7.44 corresponds to the section of diffraction pattern presented in Figure 7.43. Comparison of the two images illustrates the absence of three Debye rings in Figure 7.43 due to strong preferred orientation, which causes discontinuities in the intensity of the Debye rings around their circumference. Thus suggesting, that acquisition of a section of the diffraction pattern from samples with preferred orientation, by conventional XRD, can be misleading.

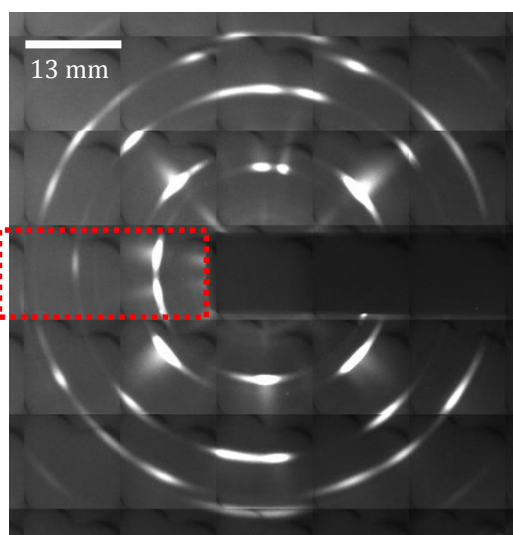


Figure 7.44 Complete empirical diffraction pattern of Al AS sample obtained by the pencil beam arrangement with collimator *PB1*.

The convergence and divergence of Debye cones, in the y-direction and x-direction, were acquired in the form of image sequences with a double-aperture collimator (*AB2*), as demonstrated in Figure 7.45 and Figure 7.46, respectively. In Figure 7.45, the lower arc of a Debye cone (top part of each diffraction frame up until image number ~ 221) converges with the upper arc of the same Debye cone (bottom part of each diffraction frame up until image number ~ 221) to intersect at image number 246 and diverge in the opposite direction. The same effect is observed in Figure 7.46, but with the Debye arcs that appear along the x-direction of the diffraction pattern shown in Figure 7.44. In Figure 7.47, a combination of the diffraction patterns illustrated in Figure 7.45 and Figure 7.46 is observed, as four apertures (*AB3*) were employed; two in the x-direction and two in the y-direction. It is therefore shown that different Debye arcs contribute to an FCG pattern.

In order to complete the study, the sample was illuminated by an annular beam to capture the FCG data presented in Figure 7.48. As illustrated in Figure 7.48, the FCG data do not resemble the same pattern as with an ideal sample (in terms of preferred orientation), where continuous circular condensation rings are observed. The FCG pattern of a sample with preferred orientation appears to have various arcs at certain directions that converge to a condensation focus and diverge in opposed directions. Even though, the pattern is not formed by continuous circular condensation rings, converging and diverging maxima can still be distinguished.

Comparison of the empirical data with the theoretical/simulated FCG patterns as presented in the previous section, suggests that their appearance is not similar. This is due to the decreased number of Debye arcs of extended length used for the simulated data (for simplicity purposes), compared to the short and numerous Debye arcs that are produced by a sample with preferred orientation. Furthermore, the active area of the detector employed during the experimental work is capturing only a limited area of the FCG pattern around the primary axis. A simulated FCG example produced with various short Debye arcs is presented in Figure 7.49. The FCG pattern is limited to $\sim 25\%$ of the complete diffraction data around the primary axis, similarly to empirical data. It can be now seen that Figure 7.49 (c) displays greater similarities with Figure 7.48 than previously presented empirical FCG images.

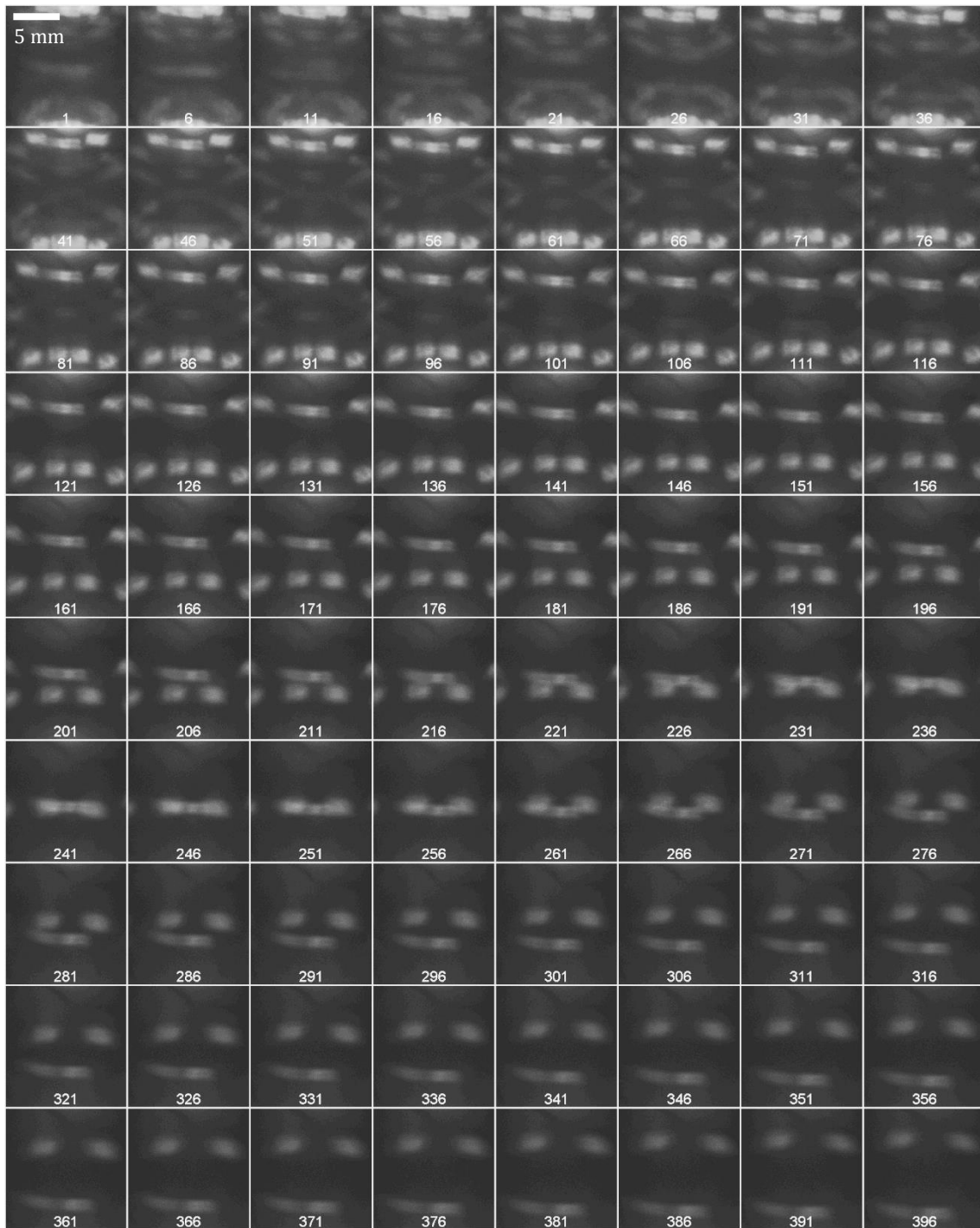


Figure 7.45 Empirical image sequence of the diffraction pattern of Al AS sample obtained by a double-aperture collimator (*AB2*) in the *y*-direction.

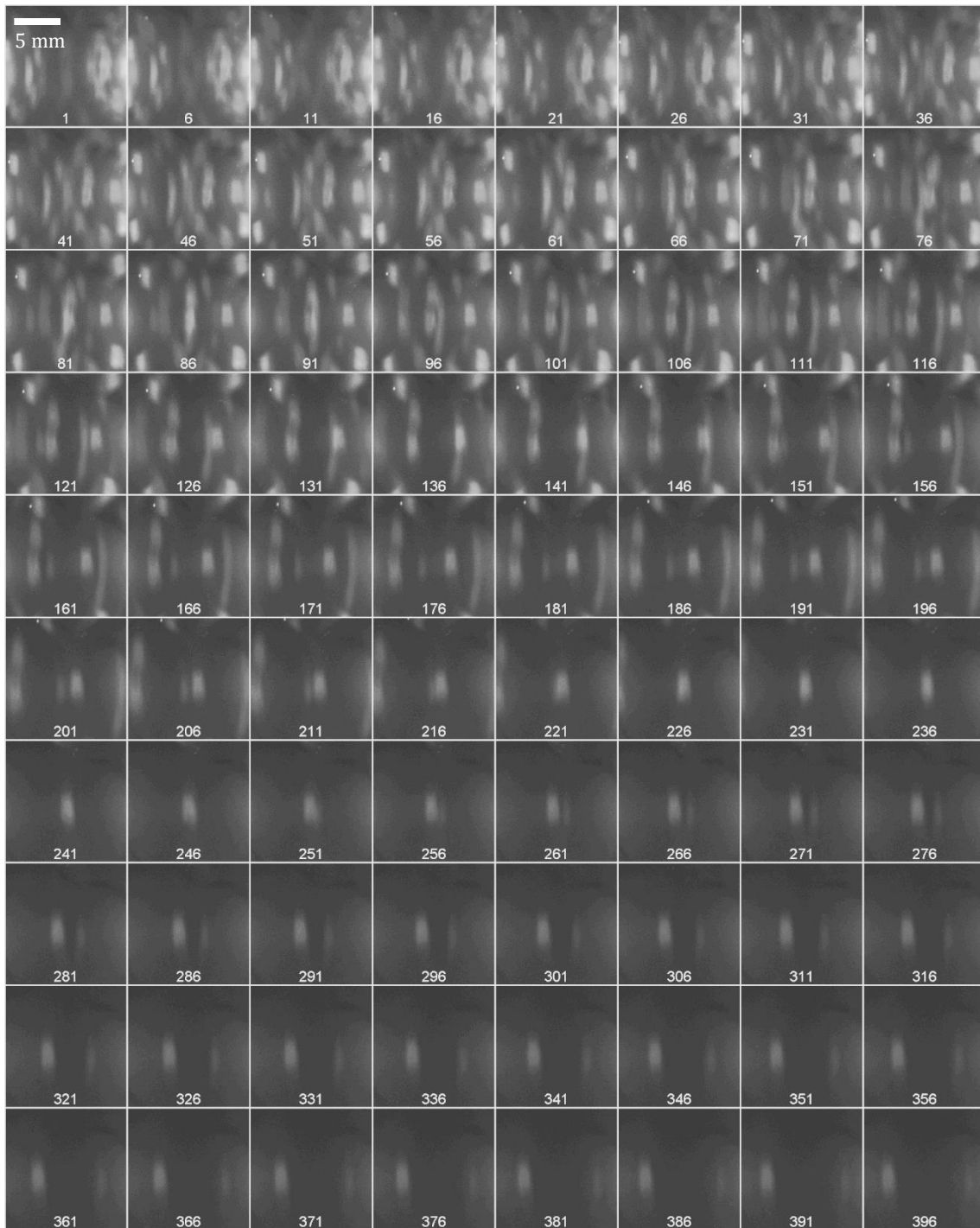


Figure 7.46 Empirical image sequence of the diffraction pattern of Al AS sample obtained by a double-aperture collimator (*AB2*) in the x-direction.

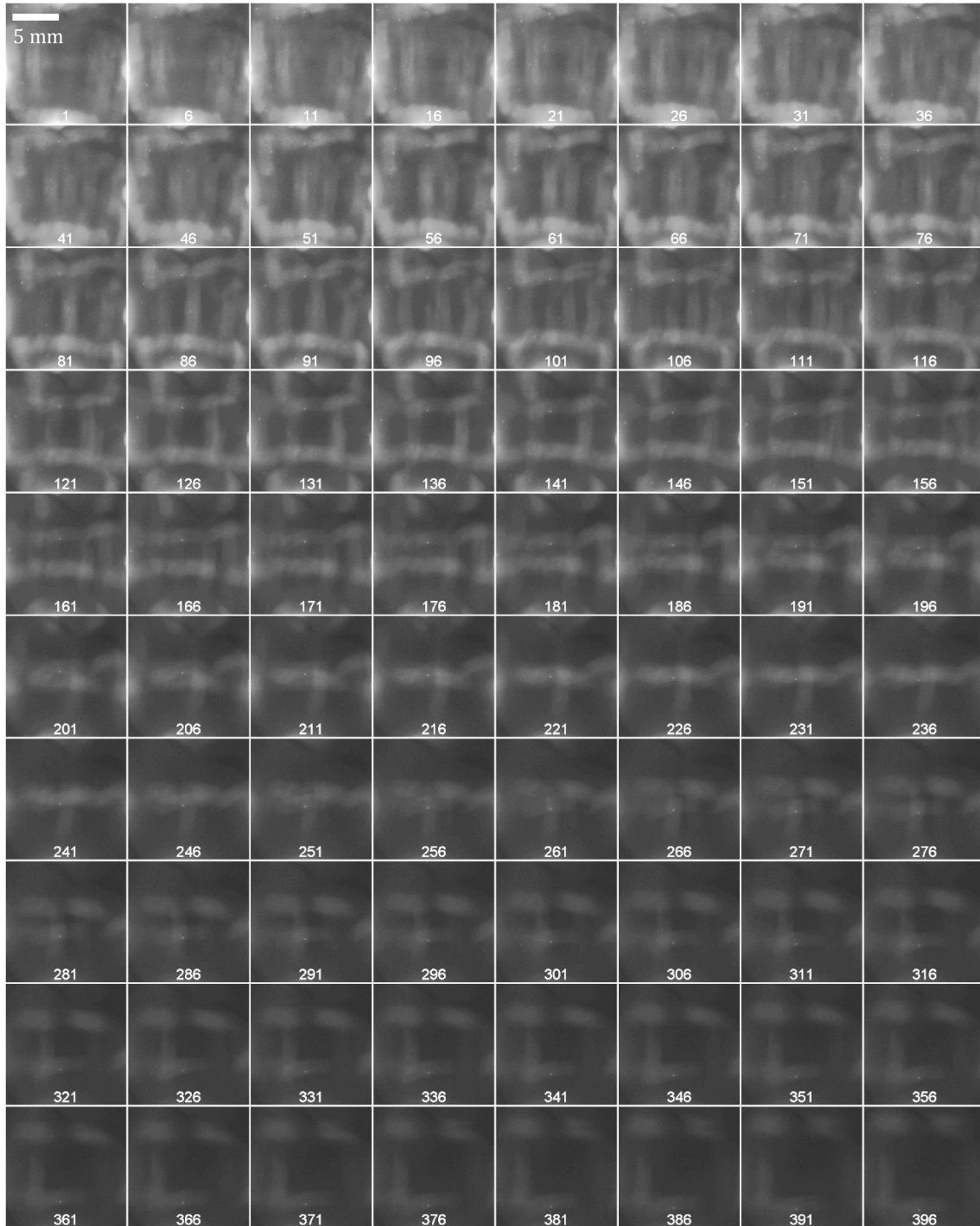


Figure 7.47 Empirical image sequence of the diffraction pattern of Al AS sample obtained by a quadruple-aperture collimator (AB3) in the x and y direction.

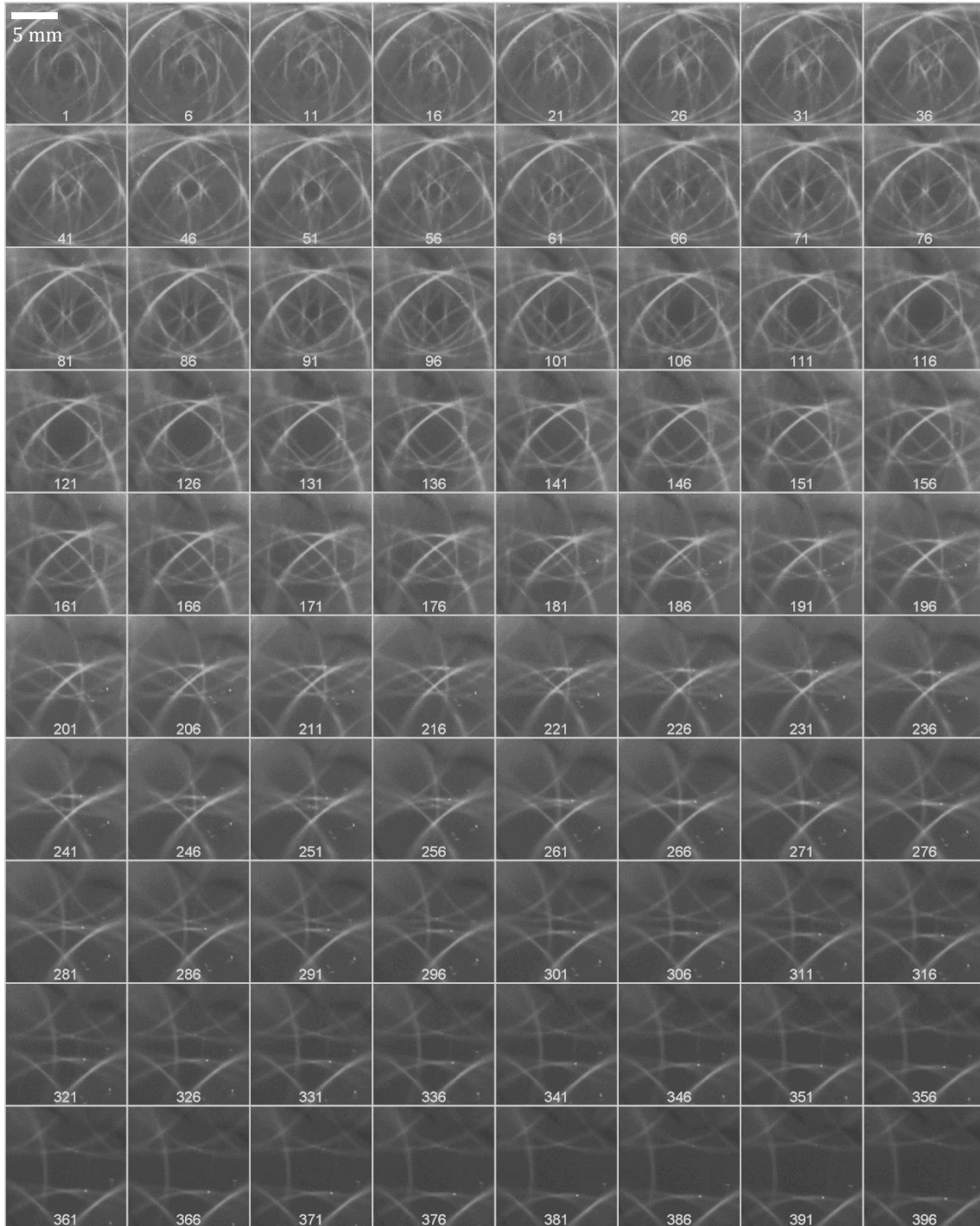


Figure 7.48 Empirical FCG image sequence of Al AS sample obtained by an annular collimator (AB1).

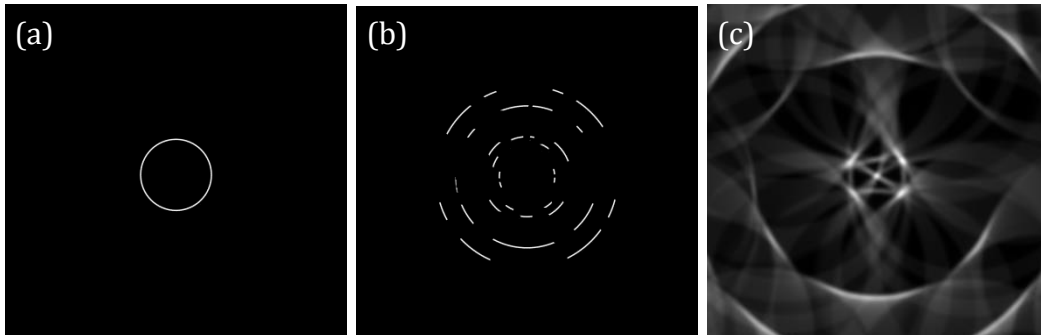


Figure 7.49 A simulated annular beam of 1.35 mm inner radius and 0.08 mm thickness (a), simulated image of Debye cones from a sample with preferred orientation representing real-life data (b) and a simulated FCG pattern limited to ~25% of the overall data (c).

Figure 7.50 compares the scattering profiles from the Al sample as obtained by conventional XRD (seen in Figure 7.43 and Figure 7.44) and by FCG. The data obtained showed that, when the sample was illuminated by a pencil beam and a section of the diffraction pattern was acquired, only a single peak was recorded by the detector; therefore, preventing effective identification of unknown samples.

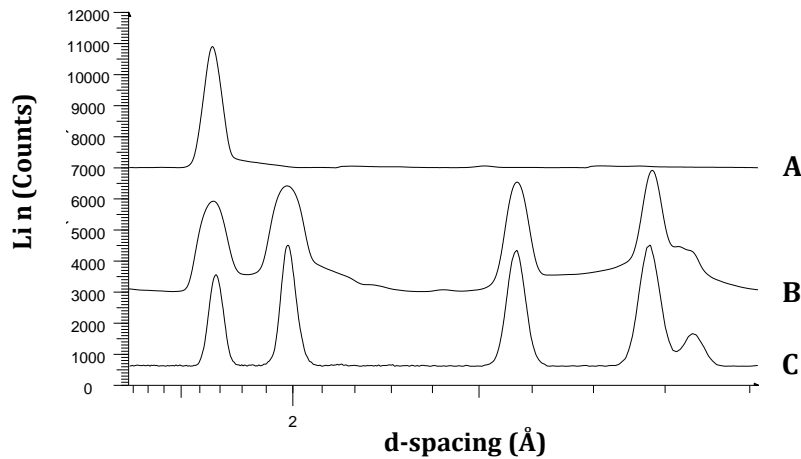


Figure 7.50 Normalised scattering profiles of an Al sample with extreme preferred orientation obtained from a section of the conventional diffraction pattern (A), from the complete pattern (B) and by FCG (C).

Complete pencil beam patterns revealed the same scattering maxima as with FCG, but with broader widths, as illustrated in Figure 7.50 (B) and (C). This is believed to be a result of different angular beam divergence during FCG and PB experiments. Furthermore, the FCG profile was obtained at a significantly shorter exposure time (~23 times) than the PB data.

Additional work on samples exhibiting preferred orientation involved the acquisition of complete diffraction patterns from a series of Al samples (*Al_1* – *Al_4*) with different degrees of preferred orientation. Figure 7.51 illustrates conventional XRD data from these samples. The intensity of the diffraction data decreases from *Al_1* to *Al_4* samples as more Al sheets were added (Section 6.20), hence the overall thickness of the sample increases. When the transmitted beam passes through an Al sample of 0.3 mm (*Al_1*), 0.6 mm (*Al_2*), 0.9 mm (*Al_3*) and 1.2 mm (*Al_4*) thickness, its intensity decreases to 98.8%, 97.6%, 96.4% and 95.2% respectively, as calculated by Equation (3.1) (Section 3.1). The optimal thickness of this Al sample derived from Equation (3.3), for a 2θ range of 15° - 55° , is calculated to be between 0.7 - 0.5 mm (Figure 7.52).

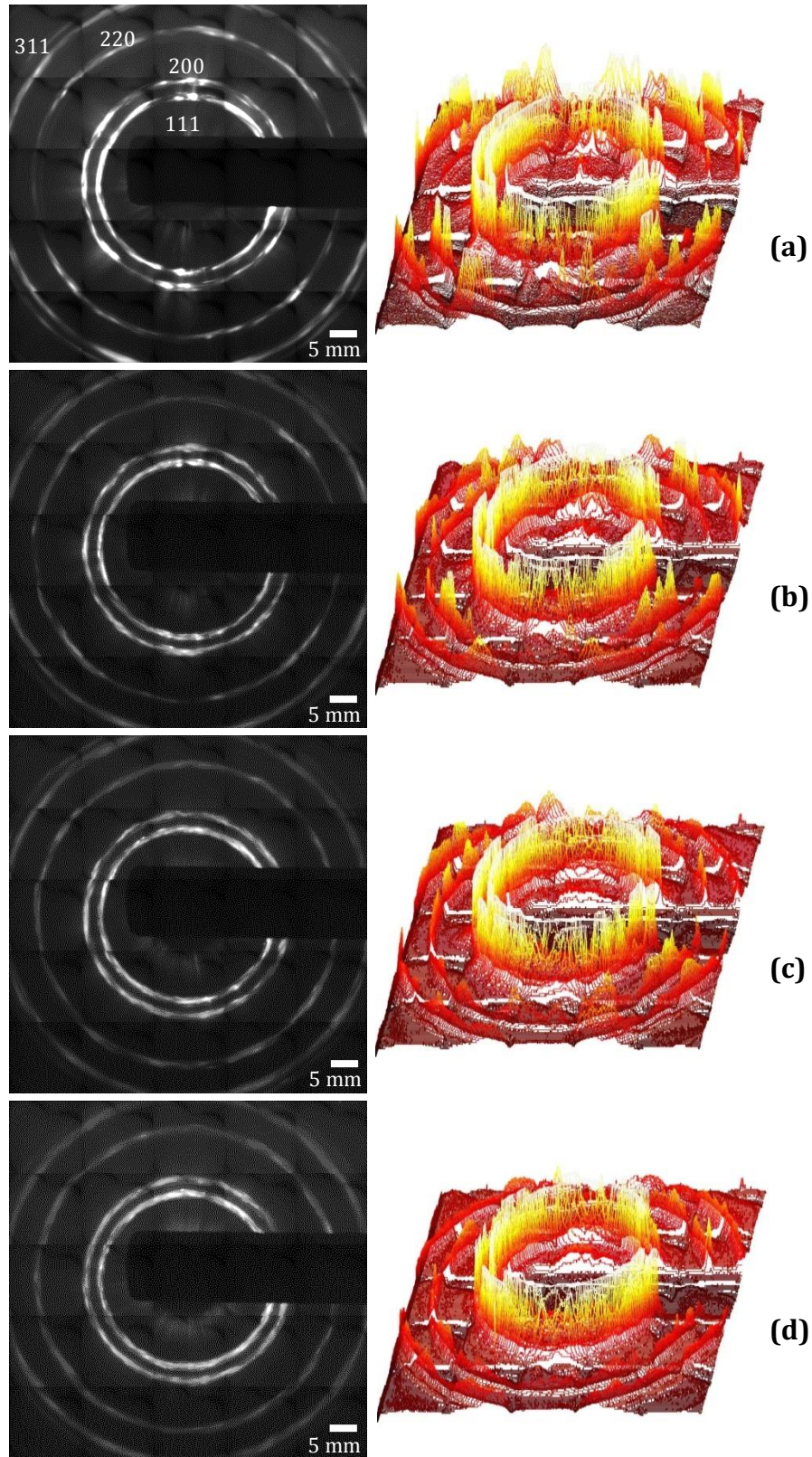


Figure 7.51 Empirical diffraction patterns (left) of *AL₁* (a), *AL₂* (b), *AL₃* (c) and *AL₄* (d) samples with their corresponding 3D surface plots (right) as obtained by a pencil beam arrangement.

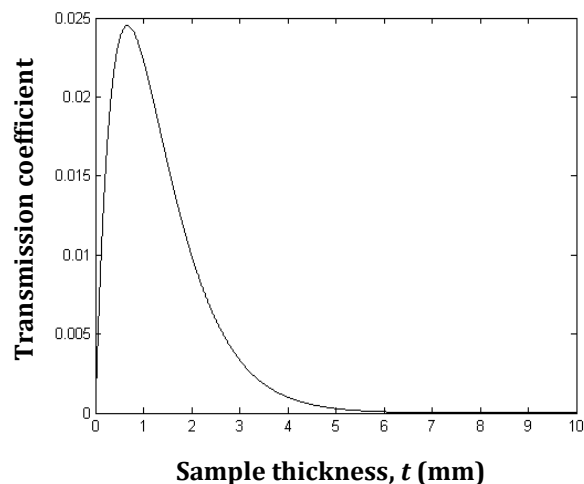


Figure 7.52 Relationship between the transmission coefficient of aluminium and sample thickness for MoK α wavelength ($\rho = 2.7 \text{ gcm}^{-3}$, $\mu/\rho = 5.16 \text{ cm}^2\text{g}^{-1}$) with 0.1° beam divergence.

Quantitative comparison of the Al samples' texture was achieved by an integration around the circumference of each of the four Debye rings at 17.48° , 20.22° , 28.74° and 33.84° 2θ angles (corresponding to 111, 200, 220 and 311 reflections from Al, respectively), and the average intensity from each Debye cone's circumferential integration was calculated. The sum of the absolute difference between the average intensity ($I_{\text{angular average}}$) and each angular position's intensity value ($I_{\text{angular position}}$) for every Debye cone of each Al sample was determined (Equation (7.11)).

$$CN_1 = \sum_{i=0}^{2\pi} |I_{\text{angular average}} - I_{\text{angular position}}| \quad (7.11)$$

A CN_1 value equal to zero represents a constant intensity around the circumference of the Debye rings, whereas a high CN_1 value indicates a high degree of preferred orientation.

Implementation of Equation (7.11) revealed a decrease in intensity as the thickness of the sample was increased, and a decrease in the intensity uniformity around the circumference of each Debye ring, as presented in Figure 7.53.

The comparison number CN_1 of the Debye rings' intensity uniformity, decreased by >63% in all Debye rings when the second sheet of Al was added (i.e. from Al_1 to Al_2), as illustrated in Figure 7.53. When the third Al sheet was randomly placed, there was a decrease between 14-43%; whereas when the fourth Al sheet was added the uniformity of intensity around the Debye rings was reduced by 13-33%. This indicates a more uniform intensity distribution around the Debye rings as more Al sheets of random orientation were added, hence decreasing the preferred orientation of the specimen's crystallites.

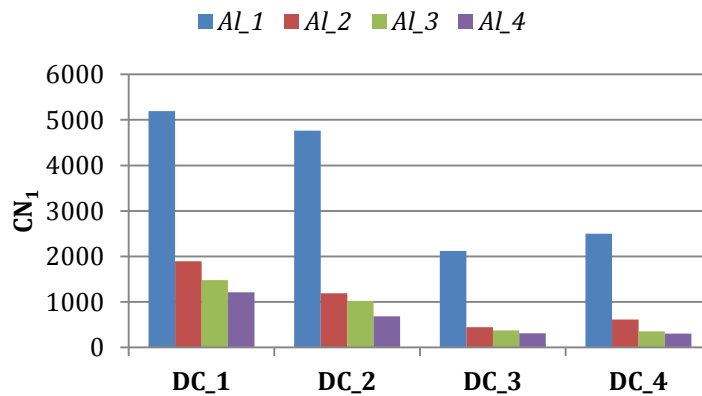


Figure 7.53 The relationship between intensity differences (i.e. CN_1) in Debye rings by an angular integration at 17.48° (DC_1), 20.22° (DC_2), 28.74° (DC_3) and 33.84° (DC_4) scattering angles for the empirical PB data from Al_1 - Al_4 samples.

FCG data sequences were also acquired for each Al sample and their scattering signatures are illustrated in Figure 7.54. The width of the diffraction peaks increases as the sample thickness increases from sample Al_1 to sample Al_4 ; thus causing a decrease in peak resolution and specificity, as illustrated by the scattering maxima at 0.122 nm in Figure 7.54 (A) and (D).

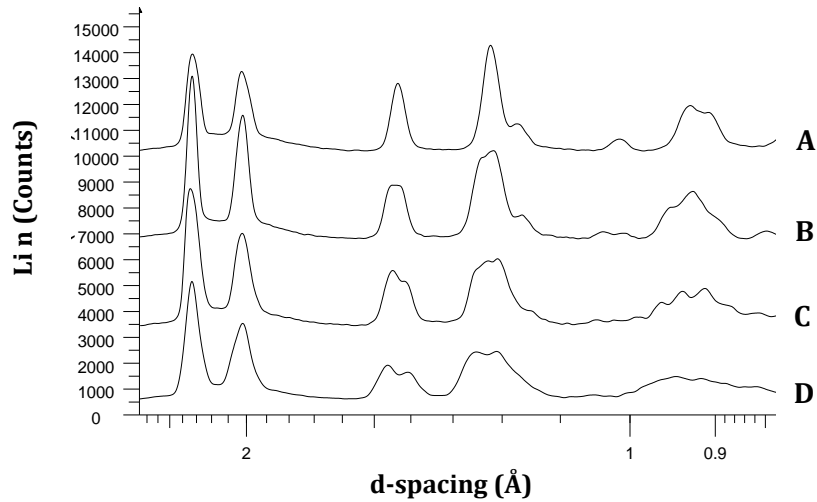


Figure 7.54 Scattering signatures of Al_1 (A), Al_2 (B), Al_3 (C) and Al_4 (D) samples as obtained by FCG.

A representative example comparing the scattering profiles of the four Al samples attained by the annular and pencil beam arrangements with 10 seconds time exposure is demonstrated in Figure 7.55. The FCG data possess a significantly enhanced intensity when compared to the pencil beam diffraction signatures. Figure 7.56 compares the FCG and PB scattering profiles of $Al_1 - Al_4$ samples with normalised intensities over a limited d-spacing range.

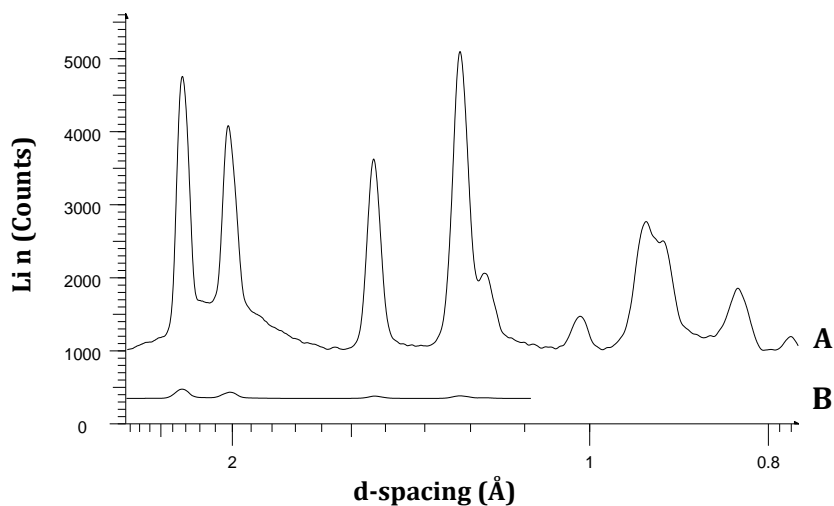


Figure 7.55 Scattering signatures of Al_1 sample by FCG (A) and by conventional PB geometry (B) with 10 seconds time exposure.

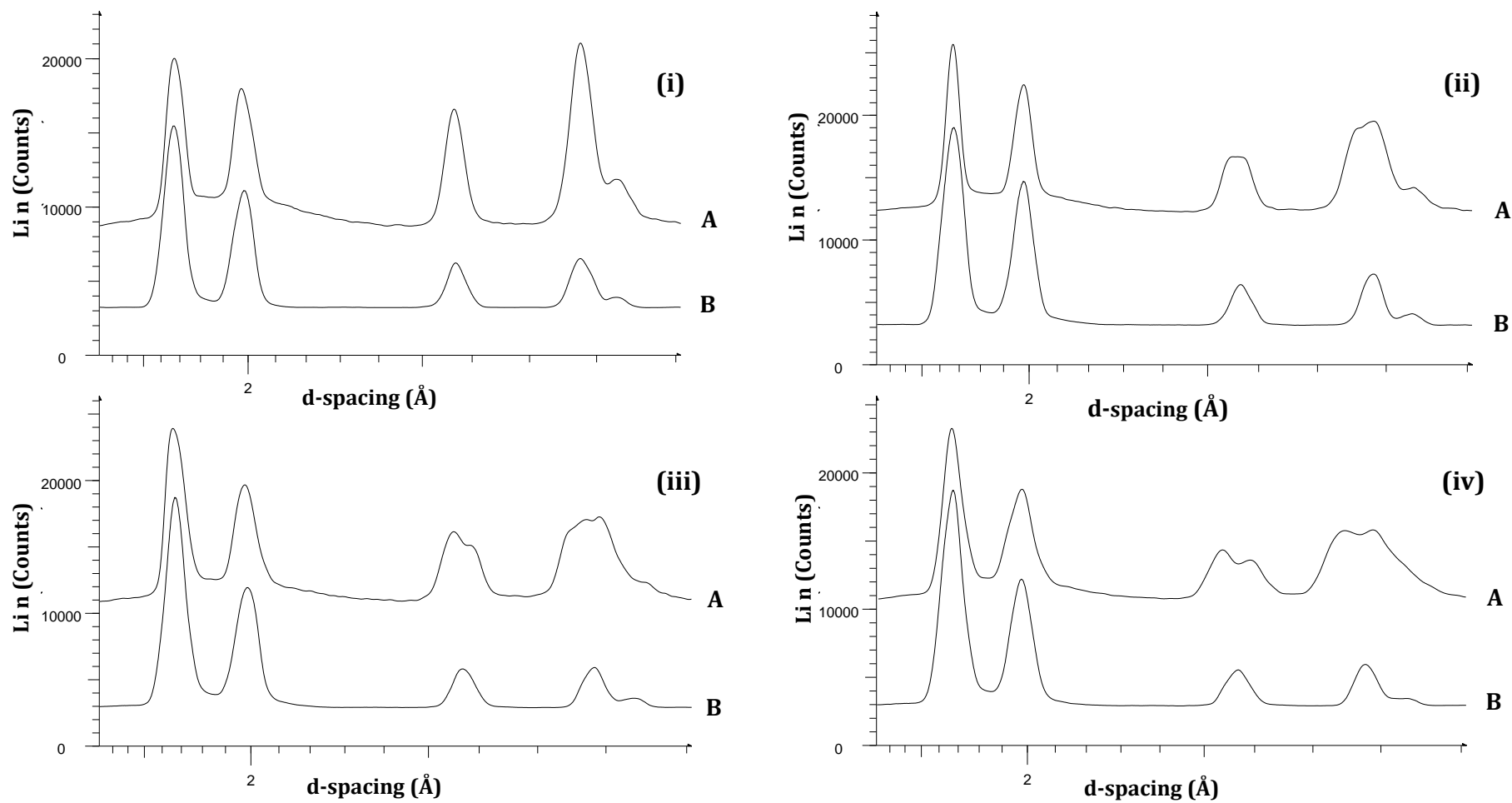


Figure 7.56 Normalised scattering signatures of AL₁ (i), AL₂ (ii), AL₃ (iii) and AL₄ (iv) samples obtained by an annular (A) and pencil (B) beam arrangement.

As seen in Figure 7.56, the FCG scattering profiles are in agreement with the conventional XRD data. However, in Figure 7.56 (iii) and (iv), an additional peak at ~ 0.14 nm is observed in the FCG diffractograms that is not present in the pencil beam profiles.

In summary, data suggests, that for samples exhibiting preferred orientation, discrimination between converging and diverging condensation rings can be achieved based on their intensity geometry around their circumference. Acquisition of FCG data from samples with different degrees of texture was attained, and demonstrated to be superior to conventional XRD when only a section of the diffraction pattern is captured. Further, collection of FCG data has been achieved at a shorter exposure time and with enhanced intensity when compared to traditional XRD.

7.5 Large grain size

Diffraction caustics produced by samples with large grain size were investigated in a simulated and empirical manner to understand the effect of large grain size on FCG.

7.5.1 Theoretical and simulated approach

Similarly to the theoretical approach of preferred orientation (Section 7.4.1), a diagrammatic simulation of the convolution of an annular beam with only four diffraction maxima at the same 2θ angle is shown in Figure 7.57. The scattering maxima spots form new rings whose centres are in the original position of the scattering maxima spots, with an equal radius to that of the annular beam (R_{AB}). The inner and outer condensation rings possess the same geometry as FCG data from samples with texture (see Section 7.4.1).

Figure 7.58 illustrates a simulated FCG pattern from a sample with large crystallites (similarly to a single crystal). The resulting FCG pattern appears to be the outcome of the convolution of the annular beam with eight δ -functions (eight scattering maxima) i.e. producing eight annular beams with their centre at the scattering

maxima spots' positions, as illustrated in Figure 7.58 (c). Intersection of these rings at a certain radius produces intensity maxima (Figure 7.58 (c)).

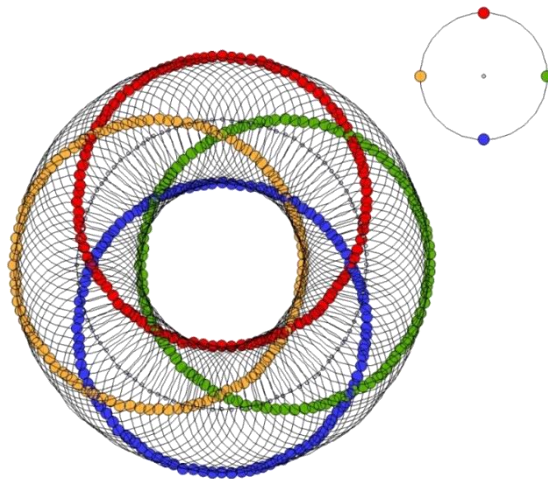


Figure 7.57 Illustration of a converging FCG pattern (left) produced by an annular beam of 33 mm radius and a Debye cone of 14 mm radius consisting of four scattering maxima spots (top right).

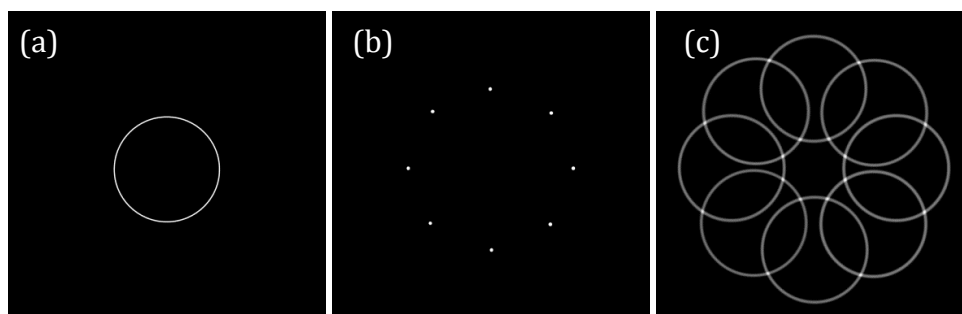


Figure 7.58 Simulated images of an annular beam of 0.72 mm inner radius and 0.08 mm thickness (a), eight scattering maxima spots spaced at a 3.41 mm radius (b) and their FCG pattern upon convolution (c).

Nonetheless, the appearance of the above examples is not representative of the real-life diffraction maxima arising from a sample with large grains. The empirical Debye rings of such samples consist of a significant number of scattering maxima spots, similarly to Figure 7.59.

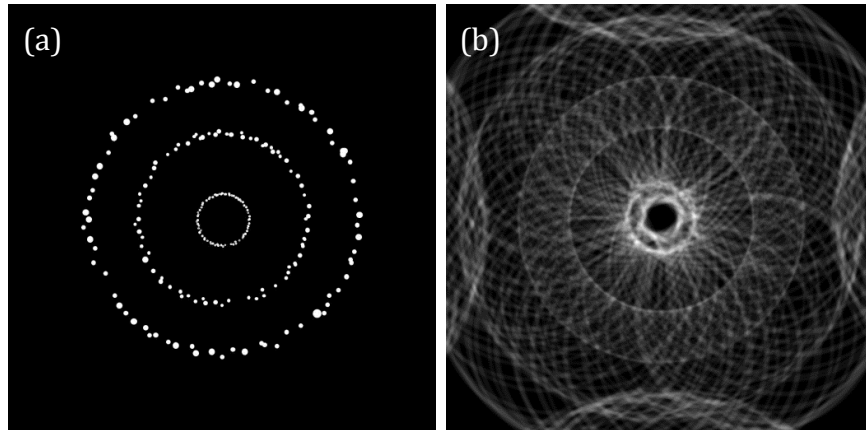


Figure 7.59 Simulated images of the Debye cones from a sample with large grain size (a) and its FCG pattern (b).

The relatively large number of scattering maxima spots and their scattering over a limited range of 2θ angles, increase the intersection points of the newly formed rings; hence complicating the appearance of the FCG pattern even further. Although, scattering maxima spots arising from a certain scattering angle cluster together at specified locations forming condensation rings, the scattering maxima spots are distributed throughout the FCG pattern, as demonstrated in Figure 7.60.

This makes the determination of the number of scattering maxima spots with the same 2θ angle that contribute to the formation of a condensation ring in the FCG pattern impractical. The pattern could be resolved by deconvolution with the primary beam; however, deconvolution is ineffective in the presence of noise as shown later on in Section 8.1.1.3 (a). A coded aperture analysis can provide an alternative interpretation method to such FCG patterns, as illustrated in Section 8.1.2.2.

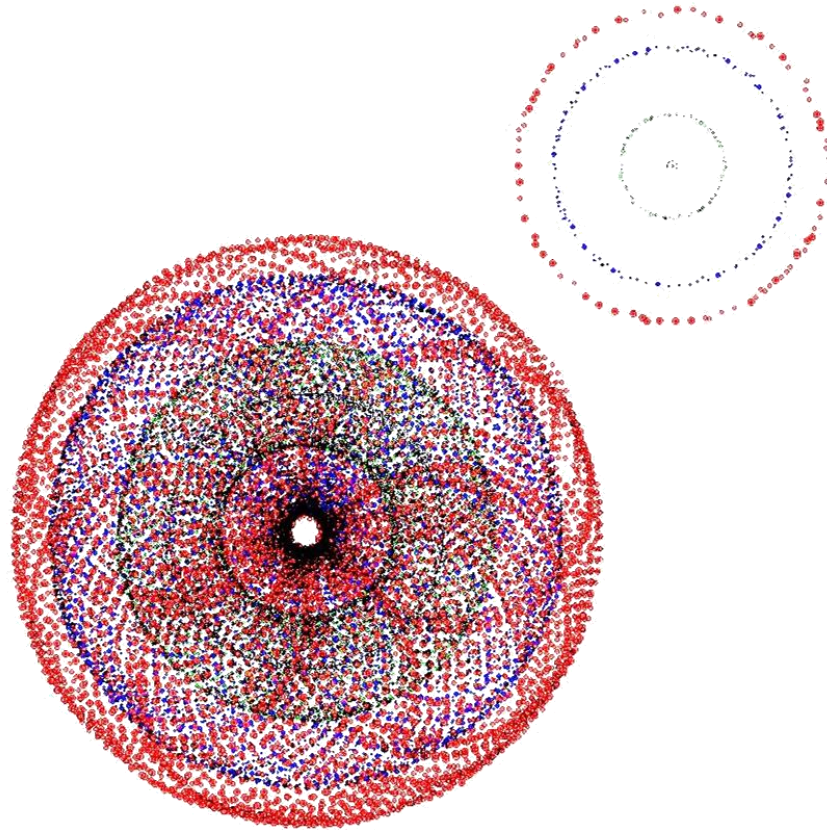


Figure 7.60 Illustration of an FCG pattern (left) with two converging condensation rings and a diverging condensation ring generated by three Debye cones with numerous scattering maxima spots (top right) as in the case of samples with large grain size.

7.5.2 Empirical approach

Samples with large grain size were analysed empirically to establish a better understanding of the effect of large grains on FCG patterns, and compare them to the simulated outcomes and to conventional XRD data.

Diffraction patterns from a series of heat-treated Cu samples (*Cu_1* – *Cu_4*, Section 6.2(d)) with an increasing grain size were examined, when illuminated by either a pencil beam or an annular beam. The results of conventional XRD analysis are given in Figure 7.61. From the diffraction patterns, it is revealed that, the unheated Cu sample (*Cu_1*) has a uniform intensity around the circumference of the Debye rings; arising from reflections 111, 200, 220 and 331 corresponding to 0.209 nm, 0.181

nm, 0.128 and 0.109 nm, respectively. The heat-treated Cu samples show additional scattering maxima at 0.243 nm and 0.149 nm arising from 111 and 220 reflections from Cu₂O. Moreover, *Cu_3* and *Cu_4* samples gave rise to an additional diffraction signal at 0.232 nm from the 111 reflection from CuO. Cu₂O and CuO were formed as a black deposit on the surface of the samples due to oxidation upon heating.

Visual comparison of the diffraction patterns shown in Figure 7.61, indicates that the *Cu_4* sample (which was heated at the highest temperature and for the longest time; 700°C, 45 minutes) has a fewer number of diffraction maxima but of a larger size. As illustrated by the diffraction pattern of *Cu_4* in Figure 7.61 (d), an increase in the grain size of the additional scattering maxima arising from Cu₂O and CuO can also be observed.

Relative quantification of the diffraction patterns of *Cu_2*–*Cu_4* was performed by counting the number of scattering maxima spots at each d-spacing, as indicated by Costas and Yang (2009) in a non-XRD scenario, using the ‘*Analyze Particles*’ function of ImageJ software. This procedure was repeated 10 times for each Debye ring of each sample and the average number of scattering maxima spots was calculated. Figure 7.62 compares the average number of diffraction maxima spots present in each Debye ring of samples *Cu_2*, *Cu_3* and *Cu_4*. Sample *Cu_1* and the additional scattering maxima of *Cu_2*–*Cu_4* samples (from Cu₂O and CuO) were not quantitatively analysed due to their intensity uniformity.

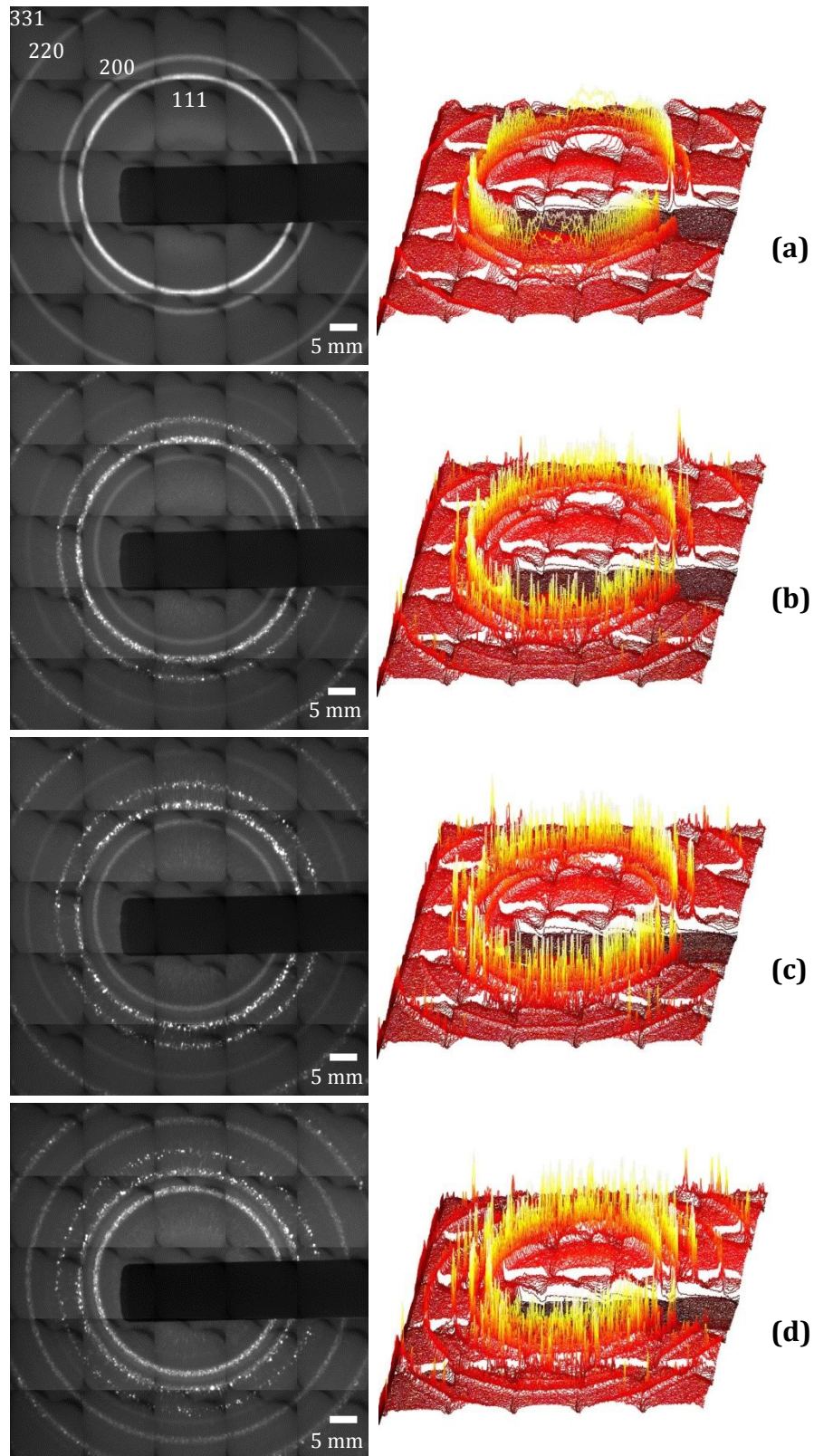


Figure 7.61 Empirical diffraction patterns (left) of *Cu_1* (a), *Cu_2* (b), *Cu_3* (c) and *Cu_4* (d) samples with their corresponding 3D surface plots (right) as obtained by a pencil beam arrangement.

As demonstrated in Figure 7.62, the average number of scattering maxima spots decreases as the temperature of the heat-treatment was increased, indicating an induced grain growth. Furthermore, Figure 7.62 illustrates that reflections 111 (Ring 1) and 200 (Ring 2) from Cu samples have a significantly larger number of scattering maxima spots when compared to reflection 220 (Ring 3). The average number of scattering maxima spots decreased from *Cu_2* sample to *Cu_3* and *Cu_4* samples for all three Debye rings, according to Figure 7.62.

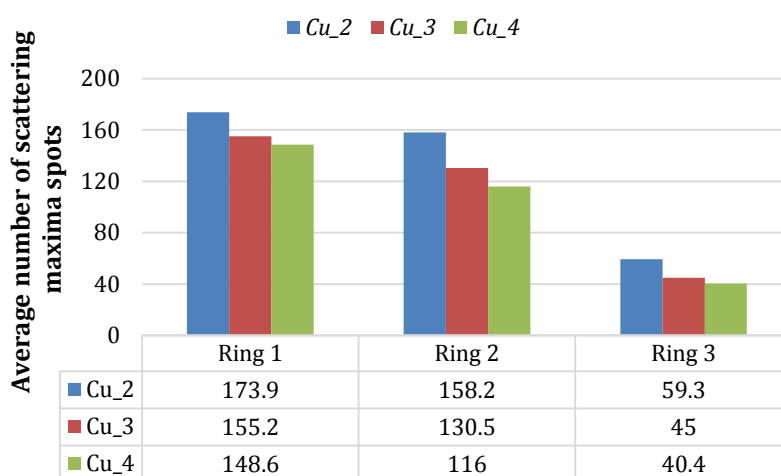


Figure 7.62 Representation of the average number of scattering maxima spots present in each Debye ring of each Cu sample (*Cu_2* – *Cu_4*).

A relative comparison number of the average size of the scattering maxima spots was calculated by dividing the number of the scattering maxima in each Debye ring by the integration area of the corresponding Debye ring. The average size of the scattering maxima within a specified volume for each 2θ angle is presented in Figure 7.63, which compares the changes in average size between the different Cu samples. As expected, the average scattering maxima size increases as the Cu samples were heated at a higher temperature, except for the scattering maxima from 200 reflection (Ring 2) from *Cu_4* sample.

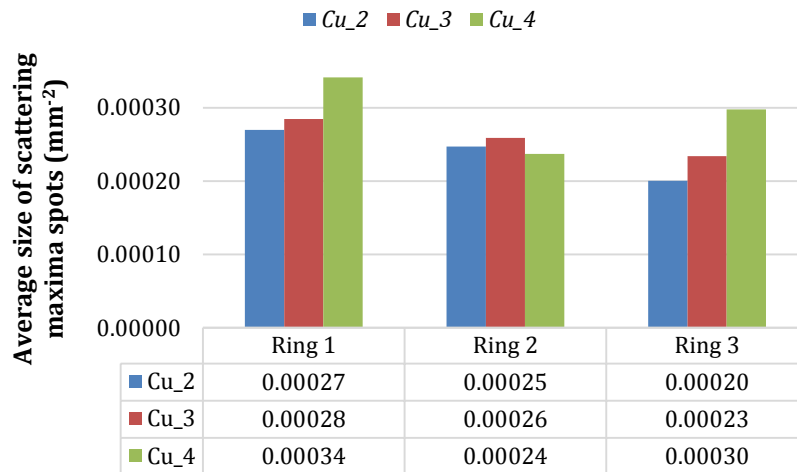


Figure 7.63 Representation of the average size of scattering maxima within a specified integration volume for each Debye ring of each Cu sample (*Cu_2* - *Cu_4*).

The Cu samples were also analysed by FCG, and a representative data sequence obtained by the *Cu_4* sample is presented in Figure 7.64. This data sequence indicates that, the scattering maxima spots converge to a condensation focus and then diverge in opposite directions, as with near-ideal samples. The FCG pattern consists of scattering maxima spots that even though clustered at certain 2θ angles, it is difficult to distinguish between them. A single FCG image is shown in Figure 7.65 in order to visualise scattering maxima spots in the FCG pattern, and compare it to the simulated patterns shown in Section 7.5.1 (Figure 7.59 and Figure 7.60). Empirical FCG data resemble the simulated data in terms of the diffraction caustics that consist of numerous scattering maxima.

It should be noted that the continuous Debye rings present in Figure 7.64 and Figure 7.65 correspond to Cu_2O and CuO that were introduced upon heat treatment.

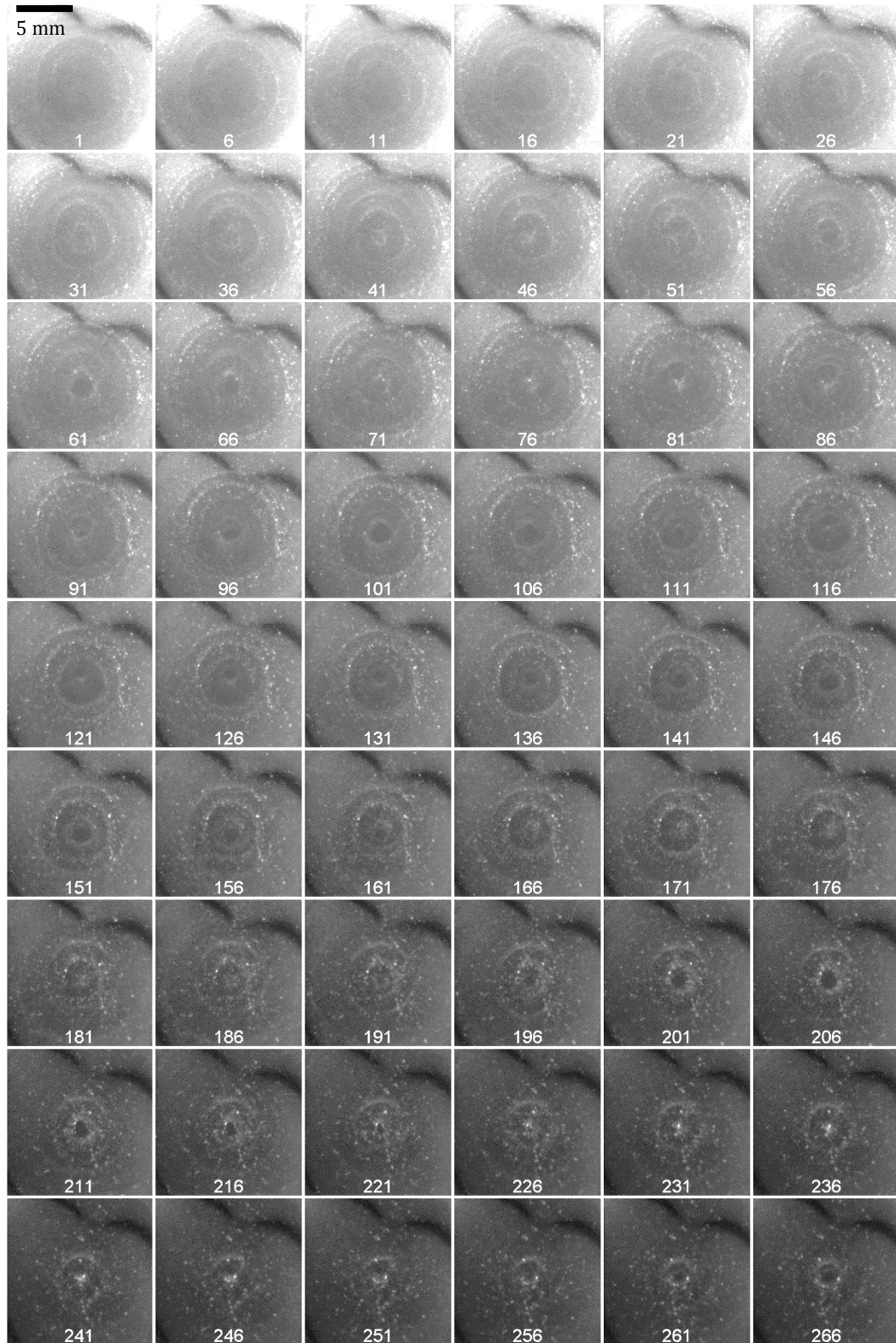


Figure 7.64 Empirical FCG image sequence of Cu₄ sample obtained by an annular collimator (AB1).

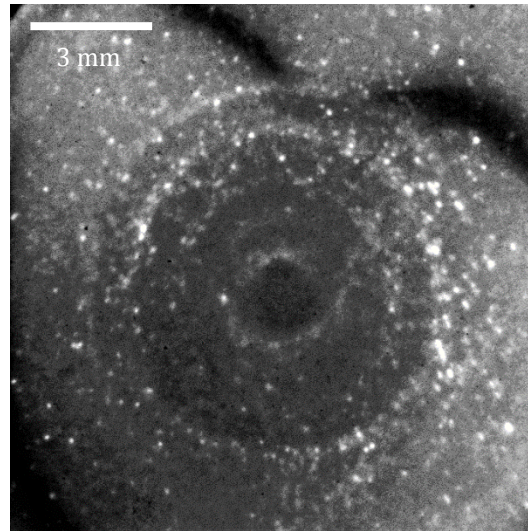


Figure 7.65 A single empirical FCG image captured at 20.2 mm from a Cu sample (*Cu_4*) with large grain size.

FCG scattering signatures from the different Cu samples are presented in Figure 7.66. As explained above, as the heating temperature of the samples increased, scattering maxima arising from Cu_2O and CuO were introduced (see Figure 7.66 (C) and (D)).

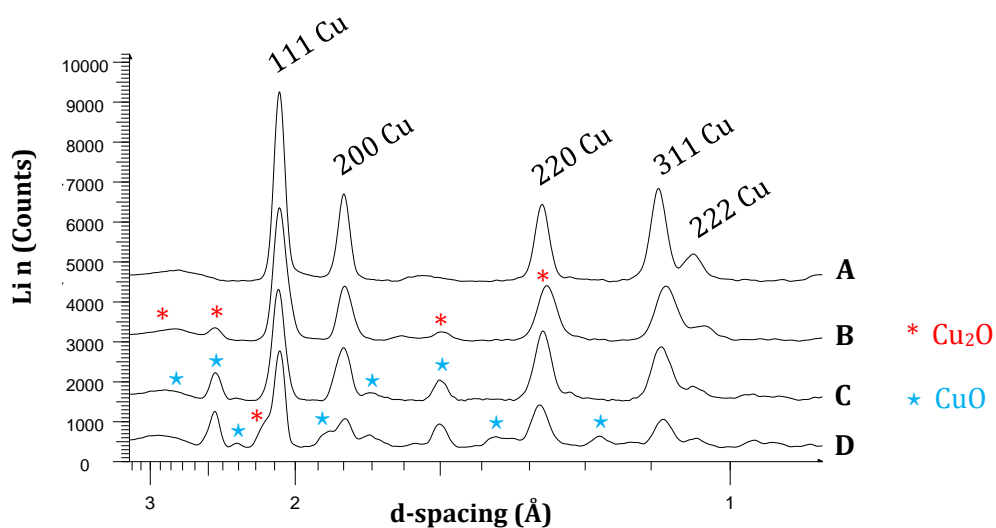


Figure 7.66 Scattering signatures of *Cu_1* (A), *Cu_2* (B), *Cu_3* (C) and *Cu_4* (D) samples as obtained by FCG.

As with the Al samples illustrated in Section 7.4.2, the intensity of the scattering maxima obtained from the Cu samples by the annular beam geometry was significantly higher, when compared to the intensity of the pencil beam scattering maxima (Figure 7.67).

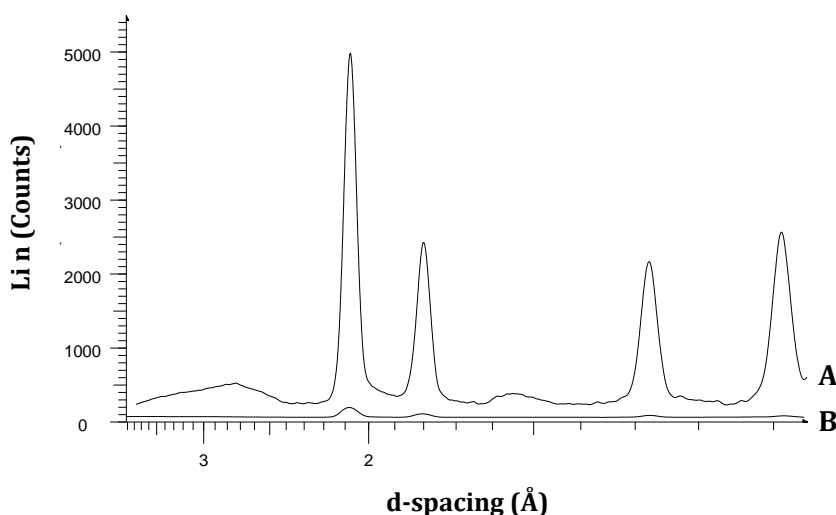


Figure 7.67 Scattering signatures of *Cu_1* sample by FCG (A) and by conventional PB geometry (B) with 10 seconds time exposure.

Normalised scattering profiles from *Cu_1* – *Cu_4* samples when incident by an annular beam and a pencil beam are compared in Figure 7.68. FCG scattering profiles are in agreement with PB diffraction profiles. However, the FCG diffractograms shown in Figure 7.68 demonstrate a higher sensitivity than the conventional pencil beam data. This is more apparent in Figure 7.68 (iv), where additional low intensity diffraction signals are present in the FCG data at 0.186 nm, 0.158 nm and at the 0.1-0.13 nm region arising from CuO. Moreover, the width of the FCG diffraction peaks is narrower than that of the pencil beam data, as displayed in Figure 7.68 (iv) at 0.232 nm (111 reflection from CuO).

Similarly to the scattering distributions from Al samples, FCG diffraction data from Cu samples were captured at a significantly shorter time exposure by a factor of 60.

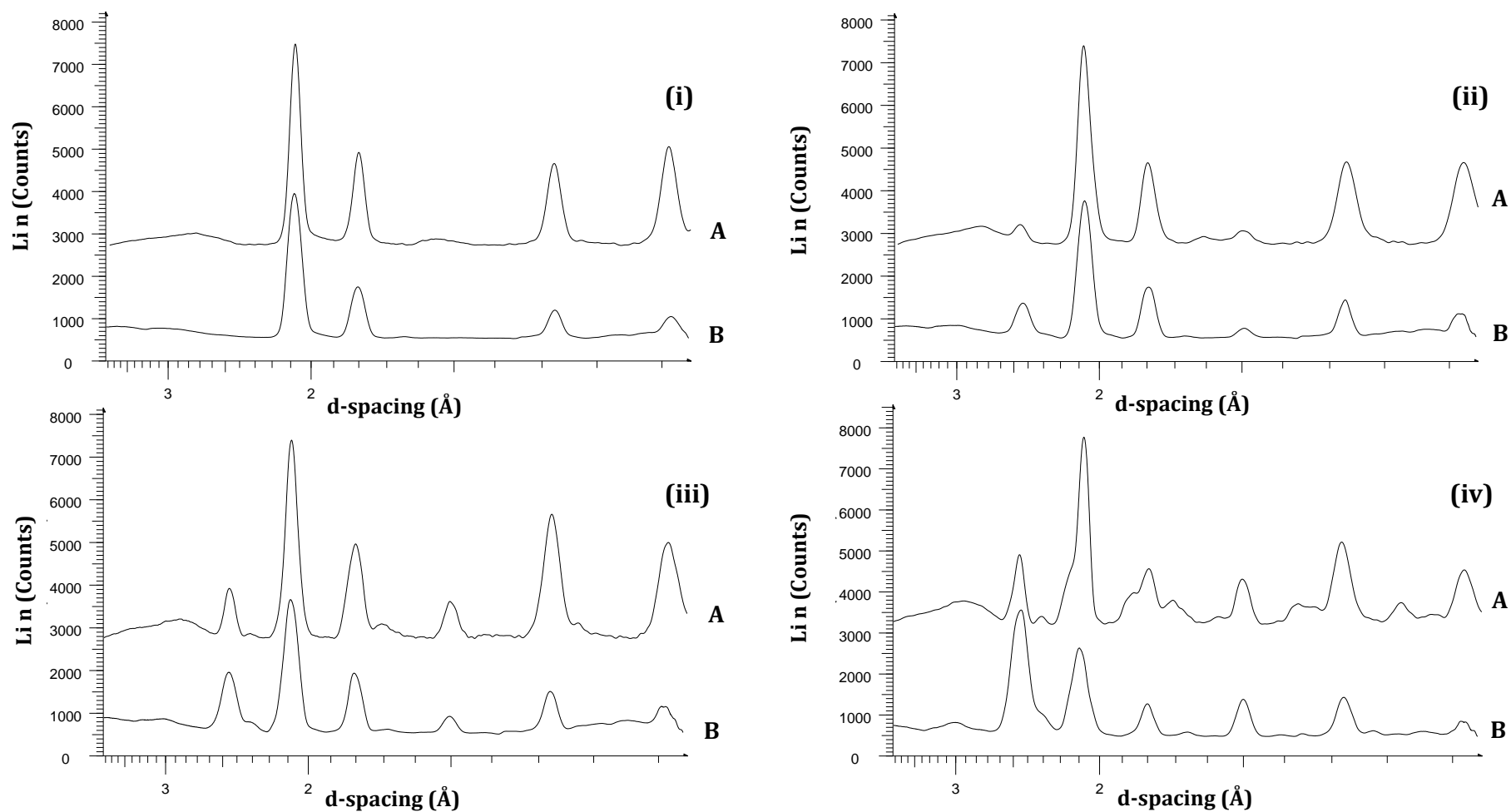


Figure 7.68 Normalised scattering signatures of *Cu_1* (i), *Cu_2* (ii), *Cu_3* (iii) and *Cu_4* (iv) samples obtained by an annular (A) and pencil (B) beam arrangement.

To summarise, in Sections 7.4 and 7.5, the ability of FCG to analyse samples exhibiting preferred orientation or large grain size was demonstrated. FCG's higher intensity was confirmed with such non-ideal samples. Moreover, FCG was shown to consider the intensity distributions around the circumference of Debye rings; therefore providing more informative diffraction data than when a section of the diffraction pattern is captured by conventional XRD.

7.6 Randomly orientated planar samples

The focal construct geometry described in detail in Chapter 5 was explained initially with a sample normal to the primary axis. This however, is a special case of FCG. A more general sample arrangement for FCG involves a sample with a random orientation with respect to the primary z-axis, as illustrated in Figure 6.8 (Section 6.3.7.2).

As previously discussed, when considering the exceptional situation of a sample normal to the z-axis, the footprint of the primary beam onto the sample will be an annulus of $Z_s \tan \phi_m$ radius. Since the centre of the primary beam's footprint is located at $(0,0,z)$, then the condensation rings will converge into condensation foci at specific distances along the z-axis at $x=0$ and $y=0$.

In the general case of a randomly rotated sample, the circular symmetry of the primary beam's footprint on the sample will be distorted relative to the direction of sample rotation. In addition, the sample-to-detector distance along the surface of the rotated sample and hence the circumference of the primary beam's footprint onto the sample will vary. In case where the sample is rotated clockwise around the x-axis, the upper part of the sample will occupy a shorter sample-to-detector distance than the lower part of the sample. Combination of the distorted symmetry of the primary beam and the variation in the sample's distance from the detector (and X-ray source), will cause a short continuum of condensation foci to occur further away from the sample than with ideal sample orientation (sample normal to z-axis), and at different x and y coordinates. This continuum of condensation foci will be referred to as a single condensation focus for simplicity purposes.

Further to the modification of the condensation foci's location, the shape of the condensation rings will be distorted. This alteration in the shape of the condensation rings is explained later on in Section 7.6.2.

Analysis of the effect of sample rotation with FCG was approached and presented herein in three different manners: analytically, simulated and empirically.

7.6.1 Analytical approach

An analytical approach to the effect of sample rotation with FCG was undertaken in a 2D right handed Cartesian coordinate system, as indicated in Figure 6.8. Any sample orientation can be resolved into a combination of rotations around the x and/or y axes.

Initially, a sample with clockwise rotation around the x-axis ($+P_x$) is considered. In the scenario presented in Figure 7.69, the sample is rotated clockwise by 40° around the x-axis, causing the annular beam's footprint onto the sample to elongate towards the y-direction. The x-axis of the primary beam's footprint retained the symmetry and length as if the sample was normal to the primary axis, i.e. $2Z_s \tan \phi_m$. However, the direction of the major axis has been rotated from the y-axis by 40° clockwise around the x-axis ($+P_x$).

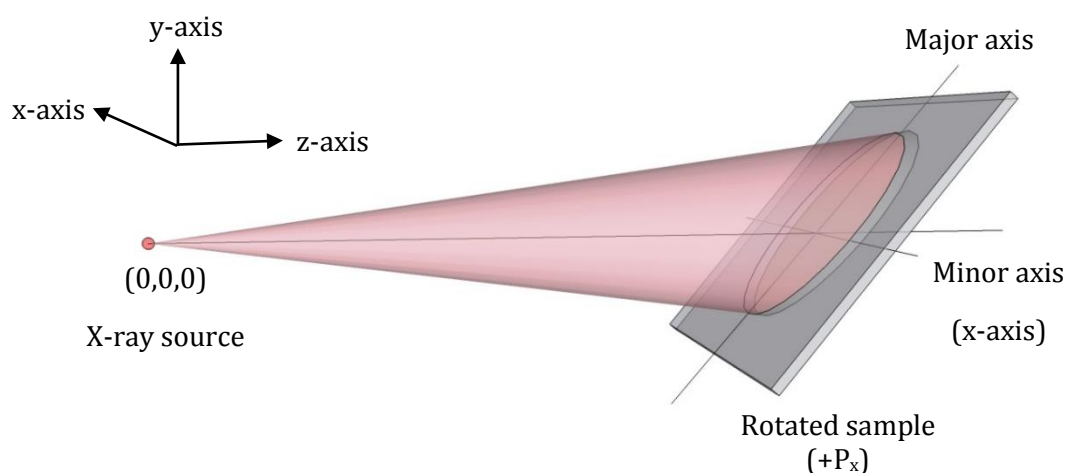


Figure 7.69 A 3D view of the annular beam's footprint onto a clockwise rotated sample around the x-axis, indicating its major and minor axis.

The dimension of the major axis (A_{major}) is given by Equation (5.1), where $P_{x/y}$ is the sample's rotation either around the x or y axis.

$$A_{major} = \frac{Z_s \tan \phi_m}{\cos(90^\circ - P_{x/y})} \left(\frac{1}{\tan(90^\circ - P_{x/y}) + \tan \phi_m} + \frac{1}{\tan(90^\circ - P_{x/y}) - \tan \phi_m} \right) \quad (7.12)^\ddagger$$

Scattering maxima arising from around the circumference of the distorted primary beam will converge at $(0, y_i, z_i)$, as indicated in Figure 7.70. The location of the condensation focus along the y and z axes when the sample occupies a rotation around the x-axis can be determined based on the geometrical scheme and calculations presented in Figure 7.71.

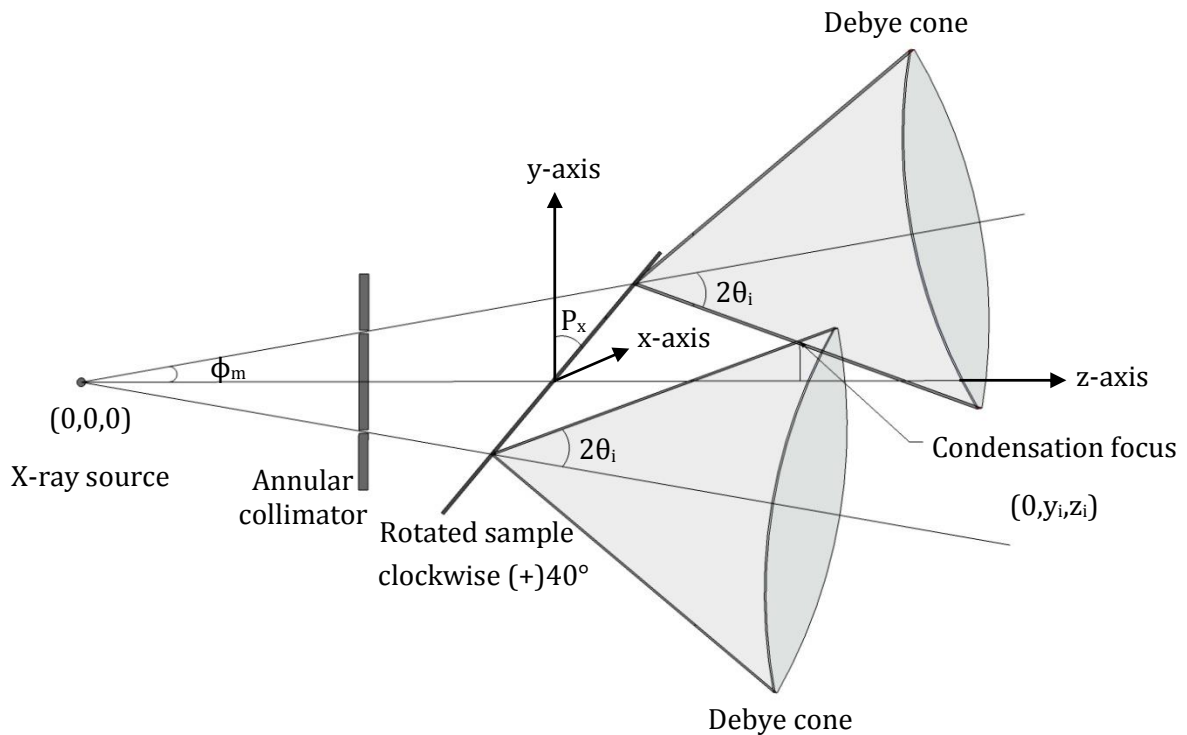


Figure 7.70 The arrangement involved with an annular beam when the sample is rotated by 40° clockwise around the x-axis.

[‡] For symbols Z_s and ϕ_m refer to Section 5.1 or Figure 7.70.

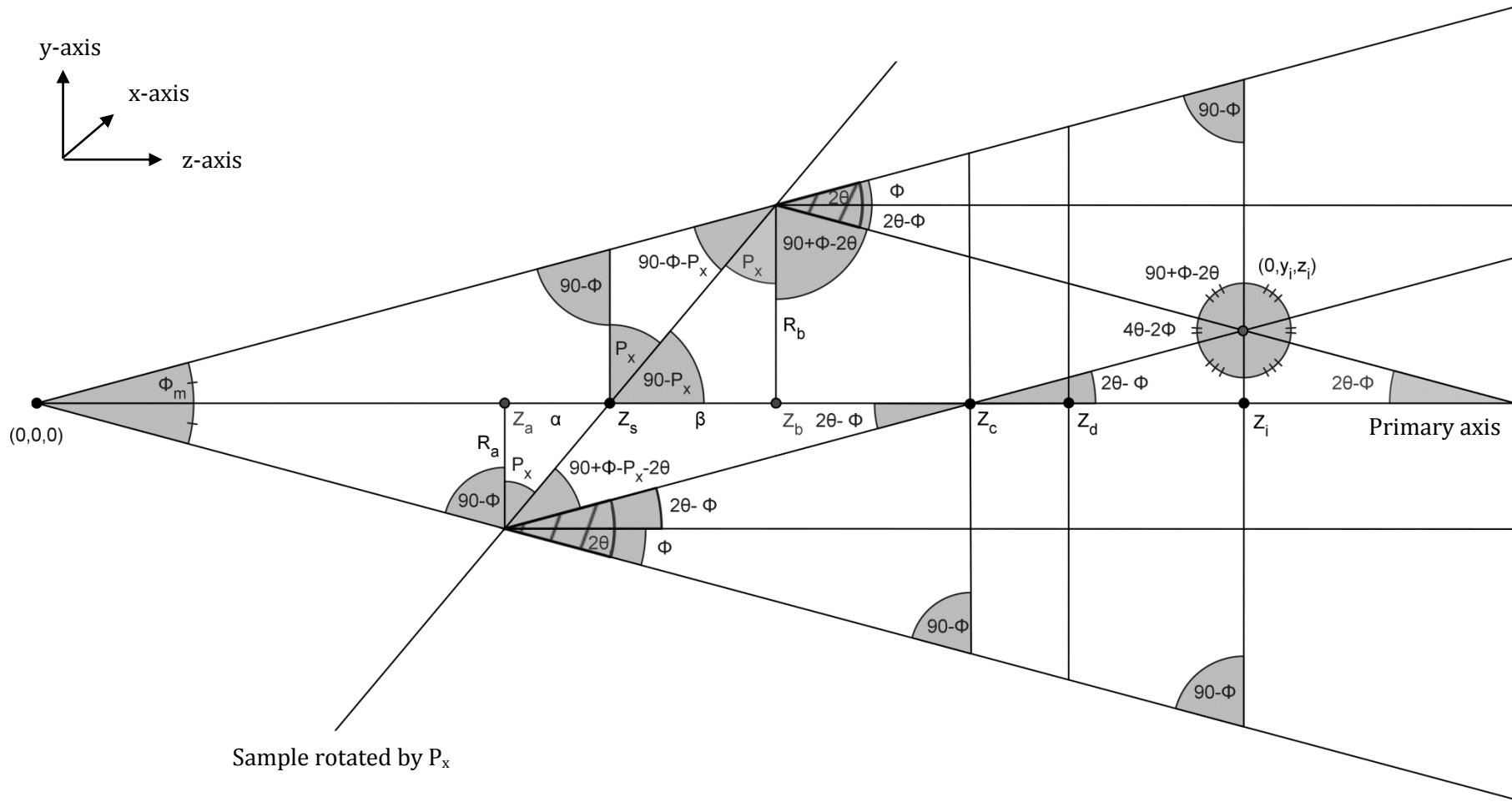


Figure 7.71 Diagrammatic illustration of the geometric relationships involved with an annular beam and a clockwise sample rotation P_x around the x-axis.

The z coordinates (Z_i) of the condensation foci as defined for the i^{th} condensation focus can be calculated as follows:

$$Z_i = \frac{Z_c + Z_d}{2} \quad (7.13)$$

where,

$$Z_c = Z_a + \frac{R_a}{\tan(2\theta_i - \phi_m)} \quad (7.14)$$

and

$$Z_d = Z_b + \frac{R_b}{\tan(2\theta_i - \phi_m)} \quad (7.15)$$

where,

$$R_a = Z_a \tan \phi_m \quad (7.16)$$

$$R_b = Z_b \tan \phi_m \quad (7.17)$$

and

$$Z_a = \frac{Z_s}{\tan P_x \tan \phi_m + 1} \quad (7.18)$$

$$Z_b = \frac{-Z_s}{\tan P_x \tan \phi_m - 1} \quad (7.19)$$

hence,

$$Z_i = \frac{-Z_s [\tan \phi_m + \tan(2\theta_i - \phi_m)]}{(\tan^2 P_x \tan^2 \phi_m - 1) \tan(2\theta_i - \phi_m)} \quad (7.20)$$

The y coordinates, Y_i , (or x coordinates, X_i , if the rotation is around the y-axis) of the i^{th} condensation foci are given by $Y_i = (Z_i - Z_c) \tan(2\theta_i - \phi_m)$; hence Equation (7.21).

$$Y_i = Z_i \tan(2\theta_i - \phi_m) - \frac{Z_s[\tan \phi_m + \tan(2\theta_i - \phi_m)]}{\tan P_x \tan \phi_m + 1} \quad (7.21)$$

Equations (7.20) and (7.21) can however only be fulfilled when $P_x \neq 90^\circ - \phi_m$ (or $P_y \neq 90^\circ - \phi_m$ for rotation around the y-axis).

It is important to note that if the sample was rotated around the y-axis, the z coordinate of the condensation focus would still be determined by Equation (7.20); whereas the x coordinate would be calculated by Equation (7.21); replacing Y_i with X_i and P_x with P_y , as seen below.

$$\text{if } \left. \begin{array}{l} 0^\circ < P_x < 90^\circ \text{ but } P_x \neq 90^\circ - \phi_m \\ 0^\circ < P_y < 90^\circ \text{ but } P_y \neq 90^\circ - \phi_m \end{array} \right\} \begin{array}{l} Y_i = \text{Equation (7.21)} \\ X_i = \text{Equation (7.21)} \end{array}$$

The location of the condensation focus along the remaining coordinate e.g. x coordinate if the rotation is around the x-axis, would be equal to zero e.g. (0, Y_i , Z_i).

Nevertheless, the location of the condensation focus is not only dependent on the rotation axes. As indicated by Equations (7.20) and (7.21), Z_i and Y_i (or X_i) depend on the degree of sample rotation and on the sample's scattering 2θ angles. Figure 7.72 illustrates the location of the condensation foci arising from a sample that was rotated from (-)70° anticlockwise to (+)70° clockwise around the x-axis at specified scattering angles of 30° and 40°. Condensation foci occurring from $\pm 80^\circ$ sample rotation are not presented within Figure 7.72, due to their extended distance away from the main axes. It is evident that all condensation foci, arising from either a clockwise or an anticlockwise sample rotation, are formed further away from the X-ray source than the condensation focus from a sample normal to the z-axis. However, when the sample is rotated clockwise, the condensation foci occur above the primary axis; whereas when the sample is rotated anticlockwise, the condensation foci occur below the primary axis.

The relationship between the angle of rotation and the location of the condensation foci on the z and y axes is graphically demonstrated in Figure 7.73, where the sample was rotated from -75° to +75° in steps of 1° around the x-axis. The z-locations of the

condensation foci follow a rapid increase when the sample is rotated by approximately $>\pm 60^\circ$. The y coordinates of the condensation foci possess a sigmoidal-like trend when the sample is rotated clockwise from an anticlockwise direction.

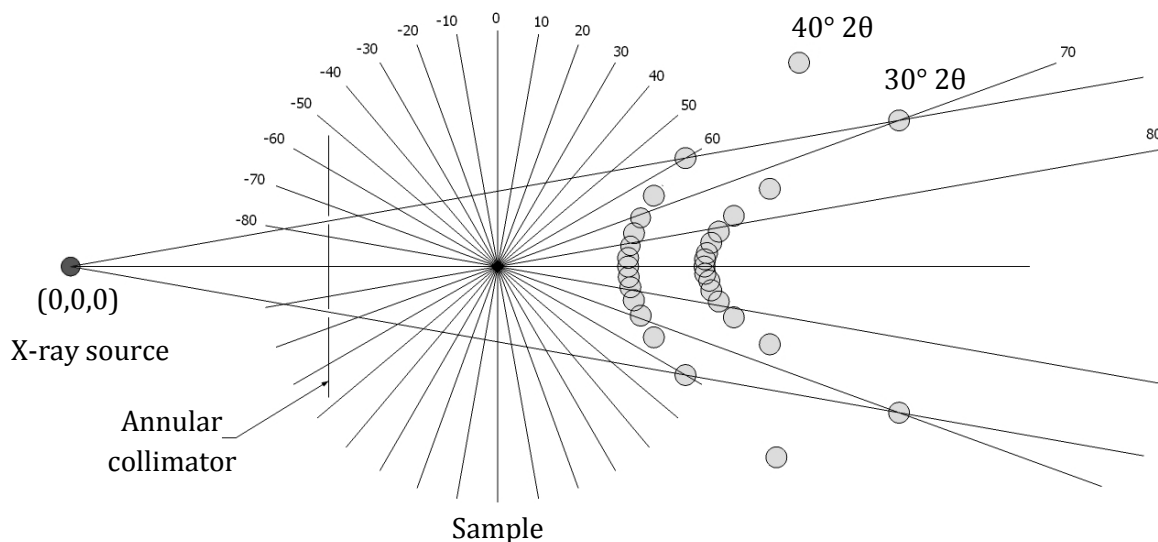


Figure 7.72 Schematic illustration of the condensation foci formed from 30° and 40° scattering angles when a sample was rotated from (-)70° anticlockwise to (+)70° clockwise in steps of 10° around the x-axis.

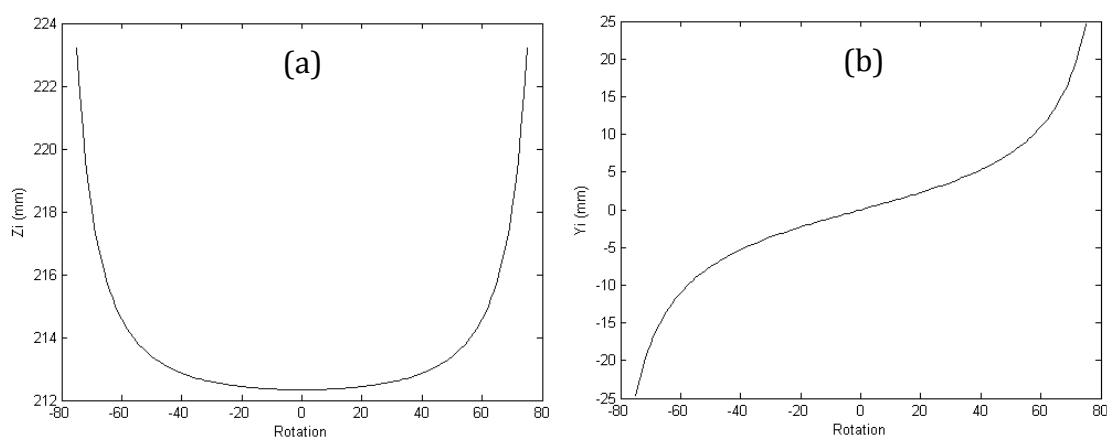


Figure 7.73 Graphical representations of the z (a) and y (b) coordinates of the condensation foci at $30^\circ 2\theta$ angle when a sample was rotated from (-)75° anticlockwise to (+)75° clockwise in steps of 1° around the x-axis.

Additionally, the location of the condensation foci is altered depending on the scattering angles of the sample. As indicated by Figure 7.74, the scattering maxima arising from 2θ angles up to 90° , converge above the primary axis; whereas condensation foci of higher 2θ angles occur below the primary axis.

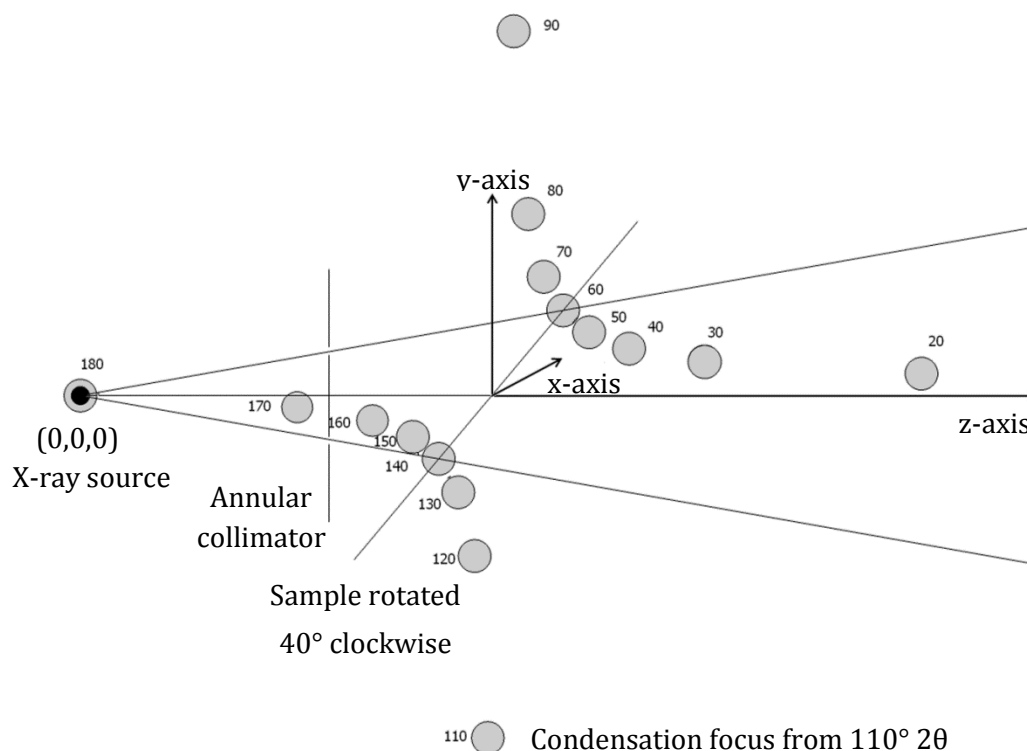


Figure 7.74 Schematic illustration of the condensation foci formed from a sample rotated 40° clockwise around the x-axis at a range of 2θ angles from 20° - 180° in steps of 10° .

The location of the condensation foci along the y and z axes and its relationship to the scattering angles of the sample are illustrated in the graphical representations in Figure 7.75. The y and z coordinates of the condensation foci arising from 5° - 90° 2θ angles, when the sample was rotated by $+40^\circ$ around the x-axis, were determined and plotted against the corresponding 2θ angle. The location of the condensation foci along the z-axis displays a rapid ($< \sim 20^\circ$) decay until $\sim 100^\circ$, followed by a rapid

(> $\sim 170^\circ$) growth until 180° . The y coordinate increases rapidly between $\sim 75^\circ$ - $\sim 100^\circ$ and then decreases in an analogous trend.

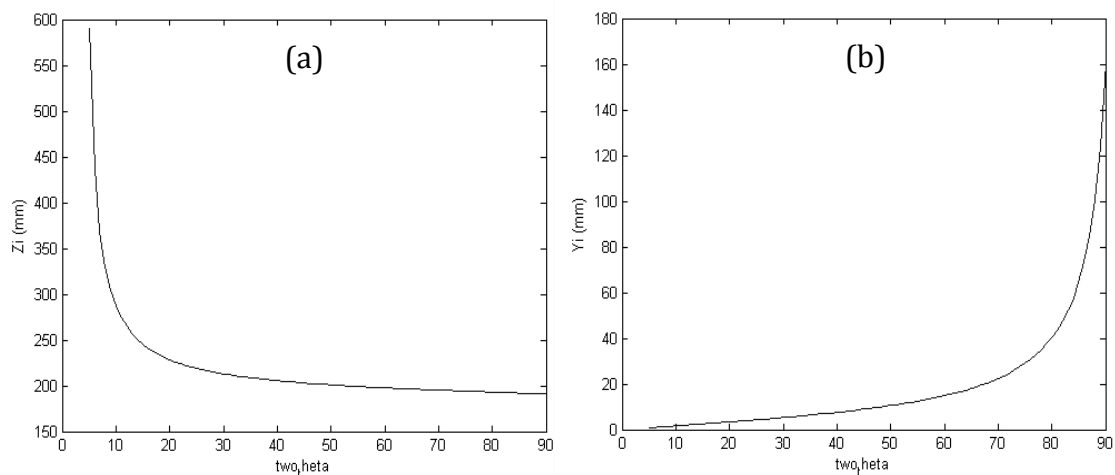


Figure 7.75 Graphical representations of the z (a) and y (b) coordinates of the condensation foci formed from a sample rotated 40° clockwise around the x-axis at a range of 2θ angles from 5° - 90° in steps of 1° .

7.6.2 Simulated data

Simulated diffraction images were obtained with random sample rotations for a better appreciation of the effect, as well as to obtain supplementary data and aid further investigation.

Figure 7.76 illustrates representative examples of simulated condensation foci obtained from a sample that was rotated by 40° anticlockwise (a), 40° clockwise (c) and with a sample normal to the primary axis (b). The condensation focus for both $\pm 40^\circ$ sample rotations was formed at 174.7 mm away from the X-ray source; whereas the condensation focus arising from a sample with no rotation (0°) occurred at a 0.5 mm shorter distance, at 173.9 mm. Additionally, as seen in Figure 7.76, the condensation focus from the samples that were rotated 40° clockwise and anticlockwise around the x-axis converged at 3.7 mm above and below the primary axis, respectively. In contrast, the sample normal to the primary axis produced a condensation focus at $x=0$ and $y=0$. Simulated data indicated a consistency with the analytical approach, in the z and y coordinates of the condensation focus.

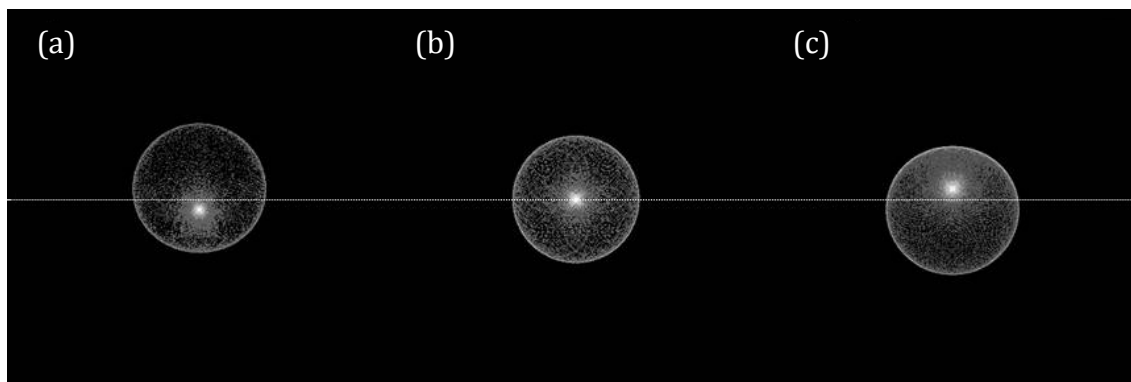


Figure 7.76 Simulated diffraction images of a condensation focus when the sample was rotated by 40° anticlockwise (a), 0° (b) and 40° clockwise (c) around the x-axis. The white dotted line is a reference point to mark $y = 0$.

Similarly, when the sample was rotated around the y-axis, the condensation focus' location along the z and y axes differed to that of a sample with no rotation, as indicated by Figure 7.77 (b). The coordinates of the condensation focus occurring from -40° around the y-axis were $(-3.7, 0, 174.7)$.

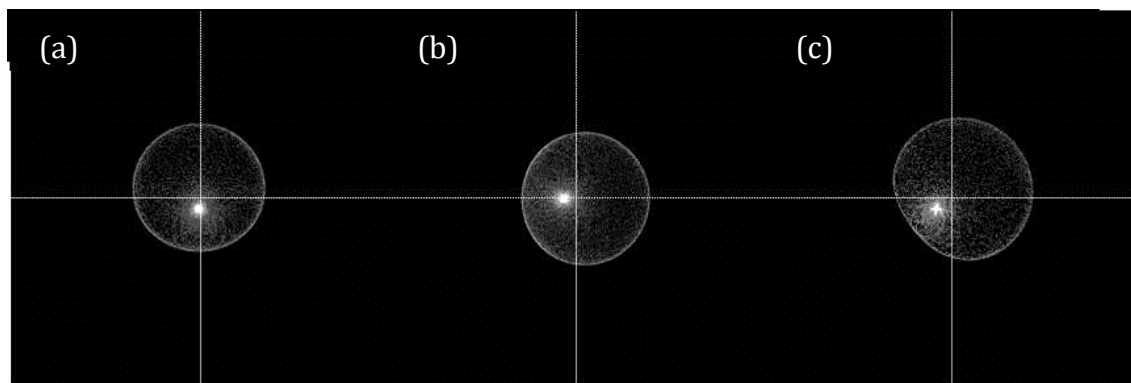


Figure 7.77 Simulated diffraction images of a condensation focus when the sample was rotated anticlockwise by 40° around the x-axis (a), 40° around the y-axis (b) and 40° around both x and y axes simultaneously (c). The white dotted lines are a reference point to mark $y = 0$ and $x = 0$.

In cases where the sample was randomly rotated around both x and y axes simultaneously, a summation of the results of the individual rotations occurred resulting to a condensation focus with $x \neq 0$ and $y \neq 0$ coordinates. However, the

location of the condensation focus depends on which rotation occurred first when the sample is rotated by the same degree around both axes. For instance, if the sample was rotated first around the x-axis and then around the y-axis (by the same angle), then the y coordinate of the condensation focus would be given by Equation (7.21); whereas the x coordinate would be greater than Equation (7.21). Moreover, the z coordinate of the condensation focus would be greater than that given by Equation (7.20). For the particular example shown in Figure 7.77 (c), the coordinates of the condensation focus occurring from a simultaneous anticlockwise sample rotation around the x and then y axis were (-4.9, -3.7, 176.8).

A summary of the coordinates of condensation focus when the sample is rotated solely either around x or y axes, and both axes simultaneously is provided in Table 7.7.

Table 7.7 The coordinates of condensation foci upon sample rotation around different axis.

Rotation axis	x-coordinate*	y-coordinate	z-coordinate
x	0	Y_i	Z_i
y	X_i	0	Z_i
xy	$>X_i$	Y_i	$>Z_i$
yx	X_i	$>Y_i$	$>Z_i$

* For X_i (and Y_i) and Z_i coordinates refer to Equations (7.21) and (7.20), respectively.

Further to the dislocation of condensation foci due to sample rotation, close examination of the shape of condensation rings indicated variation of their symmetry as adjacent to their condensation focus. When the sample was rotated anticlockwise by 40° around the x-axis, the converging ring approached its focus point in a closed curve profile with its long axis parallel to the x-axis, as indicated in Figure 7.78 (a). The condensation focus then diverged into a condensation ring (caustic) with its long axis parallel to the y-axis, as seen in Figure 7.78 (b).

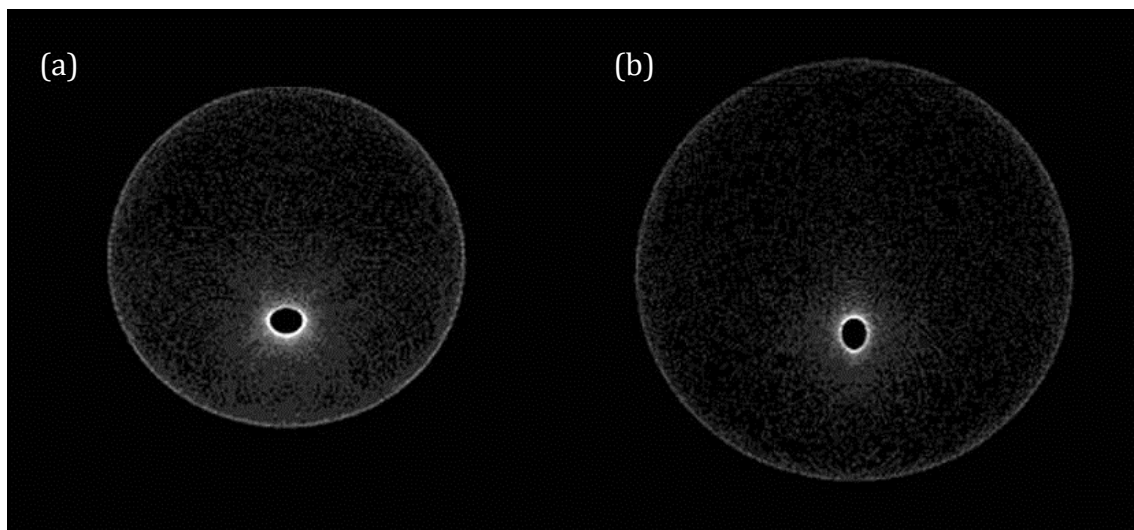


Figure 7.78 Simulated diffraction images of a converging (a) and diverging (b) condensation ring from a 40° anticlockwise rotated sample around the x-axis; forming closed curves with a long axis parallel to x and y respectively.

This systematic distortion of the condensation rings' profile can be explained by the non-circular footprint of the primary beam on the sample and the variation in sample-to-detector distance along the surface of the sample, as previously described.

Consider diametrically opposed points on the primary beam's footprint on the sample. The change in the radius of the Debye cones from each point as the detector's z-distance increases is only equal to its opposed point when both points lie on the rotation axis (e.g. x-axis). For the example given in Figure 7.78, the increase in the radius of the Debye cones arising from the points on the sample where $y=0$, with z distance, is at a mid-way rate between the extremes. Extreme changes in the radii of Debye cones arise from upper and lower Debye cones that are scattered from different parts on a rotated sample. In the example presented herein, the anticlockwise rotated sample has a shorter sample-to-detector distance at $y<0$. This causes the Debye cones arising from this part of the sample to start emerging after the Debye cones from $y>0$ of the sample. Combination of this with the greater change in the radius of lower Debye cones, over the same z-distance (see Equation (7.27)), causes the converging ring to approach its focus as a closed curve with a long axis parallel to x. Upper and lower Debye cones then diverge in opposite

directions prior to the convergence of the Debye cones arising from $y=0$ points on the sample. This creates a short continuum of condensation foci due to the convergence of the Debye cones arising from $y>0$ and $y<0$ from opposed points on the sample and then from $y=0$. When the upper and lower Debye cones then diverge simultaneously from a condensation focus, a closed curve with long axis parallel to the y -axis is formed, due to the greater change in the radius of the lower Debye cones over the same z -distance. The relationship between the change in the radii of the lower and upper Debye cones over the same z -distance is given by Equation (7.22);

$$\frac{\Delta r_u}{\Delta r_l} = \left(\frac{r_u \text{ at } Z_i}{r_u \text{ at } Z_d} \right) / \left(\frac{r_l \text{ at } Z_i}{r_l \text{ at } Z_d} \right) \quad (7.22)$$

where Δr_u and Δr_l is the change in the radius of the upper (r_u) and lower (r_l) Debye cones respectively, over distance $Z_i - Z_d$, Z_d is any z -coordinate of the detector given $\frac{cZ_s}{1-c} < Z_d < Z_i$ and $c = \tan P_x \tan \phi_m$.

Equation (7.22) could be resolved into Equation (7.23), when considering the geometrical scheme illustrated in Figure 7.71;

$$\begin{aligned} & \frac{\Delta r_u}{\Delta r_l} \\ &= \left[\frac{(Z_i - Z_b)(\tan \phi_m + \tan(2\theta_i - \phi_m))}{(Z_d - Z_b)(\tan \phi_m + \tan(2\theta_i - \phi_m))} \right] / \left[\frac{(Z_i - Z_a)(\tan \phi_m + \tan(2\theta_i - \phi_m))}{(Z_d - Z_a)(\tan \phi_m + \tan(2\theta_i - \phi_m))} \right] \end{aligned} \quad (7.23)$$

where $Z_b = Z_s + \beta$ and $Z_c = Z_s - \alpha$.

Therefore,

$$\frac{\Delta r_u}{\Delta r_l} = \left(\frac{Z_i - Z_s - \beta}{Z_d - Z_s - \beta} \right) / \left(\frac{Z_i - Z_s + \alpha}{Z_d - Z_s + \alpha} \right) \quad (7.24)$$

Equation (7.24) could then be rearranged and expanded with β and α as given below to give Equation (7.27).

$$\beta = \frac{Z_s \tan P_x \tan \phi_m}{1 - \tan P_x \tan \phi_m} \quad (7.25)$$

$$\alpha = \frac{Z_s \tan P_x \tan \phi_m}{1 + \tan P_x \tan \phi_m} \quad (7.26)$$

$$\frac{\Delta r_u}{\Delta r_l} = \left(\frac{Z_i - Z_s - \frac{cZ_s}{1-c}}{Z_d - Z_s - \frac{cZ_s}{1-c}} \right) \times \left(\frac{Z_d - Z_s + \frac{cZ_s}{1+c}}{Z_i - Z_s + \frac{cZ_s}{1+c}} \right) \quad (7.27)$$

Analysis of simulated diffraction patterns produced from rotated samples with more than one scattering maxima indicated the presence of non-circular condensation rings. As previously explained by Figure 7.74 and Figure 7.75, condensation foci arising from different scattering (2θ) angles occupy a different y coordinate, when the rotation is around the x-axis. For instance, the centre of condensation rings from high 2θ angles would appear further along the y and/or x axes (depending on sample rotation axis) than the centre of condensation rings from low 2θ angles. This causes a centre misalignment of the condensation rings resulting in non-equal radial distances among them, in the y (or/and x) direction. This is observed as a distortion of the circular symmetry of condensation rings as illustrated in Figure 7.79.

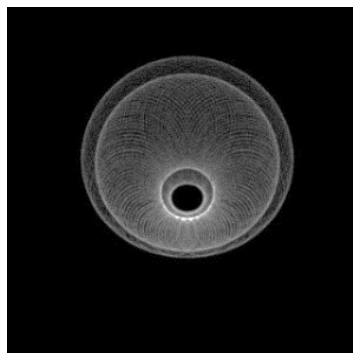


Figure 7.79 Simulated diffraction image of the converging condensation rings from a 40° anticlockwise rotated sample around the x-axis at 19.72° and 25.76° 2θ angles.

The ratio of the radial distances ($ratio_{rd}$) of two non-circular condensation rings corresponding to different scattering maxima is derived by:

$$ratio_{rd} = \frac{R_{l2\theta_2} - R_{l2\theta_1}}{R_{u2\theta_2} - R_{u2\theta_1}} \quad (7.28)$$

where $R_{l2\theta_2}$, $R_{u2\theta_2}$, $R_{l2\theta_1}$ and $R_{u2\theta_1}$ are the radii of the lower and upper Debye cones of a $2\theta_2$ and $2\theta_1$ scattering angles, respectively. Equation (7.28) could be translated into Equation (7.29), based on Figure 7.71 and then expanded to Equation (7.30);

$$ratio_{rd} = \frac{Z_d - Z_s + \alpha}{Z_d - Z_s - \beta} \quad (7.29)$$

$$ratio_{rd} = \left(\frac{Z_d - Z_s + Z_d \tan P_x \tan \phi_m}{1 + \tan P_x \tan \phi_m} \right) \times \left(\frac{1 - \tan P_x \tan \phi_m}{Z_d - Z_s - \tan P_x \tan \phi_m} \right) \quad (7.30)$$

where the detector's distance can be defined by $Z_d = \left(\frac{Z_s(\tan \phi_m + \tan(2\theta_i - \phi_m))}{(1 + \tan P_x \tan \phi_m) \tan(2\theta_i - \phi_m)} \right)$.

7.6.3 Empirical data

The empirical experiments performed, verified the predictions and outcomes of the analytical approach and simulated data. The location of condensation foci varied depending primarily on the direction and angle of sample rotation. Clockwise rotation of an Al_2O_3 plate around the x-axis from an anticlockwise direction of -20° to $+20^\circ$ resulted in the translation of its condensation foci along the y-axis, from below to above the primary axis.

Figure 7.80 illustrates the convergence of the Debye cones from the 113 reflection from Al_2O_3 to a condensation focus when the sample was rotated $\pm 20^\circ$ around the x-axis, and when the sample was normal to the z-axis. Clockwise and anti-clockwise rotated samples produced condensation foci at 0.1 mm further along the primary axis than the sample with no rotation. Moreover, as illustrated by Figure 7.80 (a) and (c), the y coordinates of the condensation focus from an anticlockwise and

clockwise sample rotation were relocated at -1.5 mm and +1.5 mm, respectively; whereas the x coordinates remained at 0. The translation and direction of movement of the condensation foci indicated consistency with the theoretical predictions.

In addition, the distorted shape of the condensation rings shown in Figure 7.80 is in agreement with the distorted condensation rings demonstrated by the simulated data in Figure 7.79 and verified by the analytical description given by Equation (7.30).

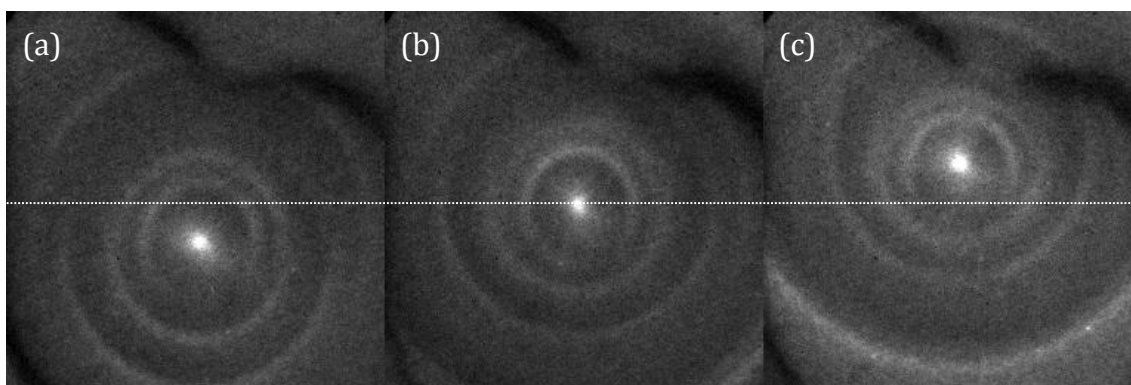


Figure 7.80 Empirical diffraction images illustrating the formation of a condensation focus when the sample was rotated by 20° anticlockwise (a), 0° (b) and 20° clockwise (c) around the x-axis. The dotted white line is a reference point to mark $y = 0$.

7.6.4 Comparison between empirical data and theory

A qualitative and semi-quantitative comparison of the analytical, simulated and empirical approaches has been exemplified above, verifying their consistency and agreement. The correspondence between theoretical predictions and experimental data obtained from randomly rotated samples was qualitatively achieved by comparing the simulated images of Figure 7.76 and Figure 7.79 with the empirical data shown in Figure 7.80.

The coordinates of the condensation foci were then analytically, simulated and empirically determined when the sample was rotated by $\pm 20^\circ$ around the x-axis and

when the sample was normal to the primary axis. This was achieved by considering three different intersection points for the rotation axes.

The relative distances between the condensation foci arising from samples rotated anticlockwise and clockwise differ depending on the rotation axes' intersection point, as indicated in Figure 7.81. When the intersection point of the rotation axes is at $(0, 0, Z_s)$, the condensation foci from a sample that has been rotated clockwise and anticlockwise by the same angle, would occupy the same location on the z-axis and the same distance on the y-axis in opposite directions (Figure 7.81 (A)).

However, if the rotation axes' intersection point is at $(0, >0, Z_s)$ as in Figure 7.81 (B), then the condensation foci from the anticlockwise rotated sample will occur further along the primary axis than the condensation foci of the clockwise rotated and non-rotated sample. Furthermore, the scattering maxima of the clockwise rotated sample will converge at a closer distance to the X-ray source along the z-axis, than the sample with no rotation. The Y_i location of the condensation foci of the anticlockwise rotated sample will be below the primary axis; whereas for the clockwise rotated sample it will be above the primary axis at a shorter y-distance.

If the intersection point is at $(0, <0, Z_s)$ the z and y coordinates of the condensation foci arising from a clockwise and anticlockwise rotated sample would be vice versa to $(0, >0, Z_s)$ intersection point, as indicated in Figure 7.81 (C).

The values of the Y_i and Z_i positions of the condensation foci from clockwise and anticlockwise rotated samples with different intersection points of their rotation axes were obtained analytically, simulated and empirically. The results are presented and compared in Table 7.8. The differences in the z and y coordinates obtained from the three different approaches are within experimental errors, thus demonstrating a quantitative agreement between theoretical and empirical data. The difference in Y_i position varied when the rotation axes' intersection point was above or below the primary axis, as calculated by the analytical descriptions, but the variation was not measurable for the simulated and empirical data.

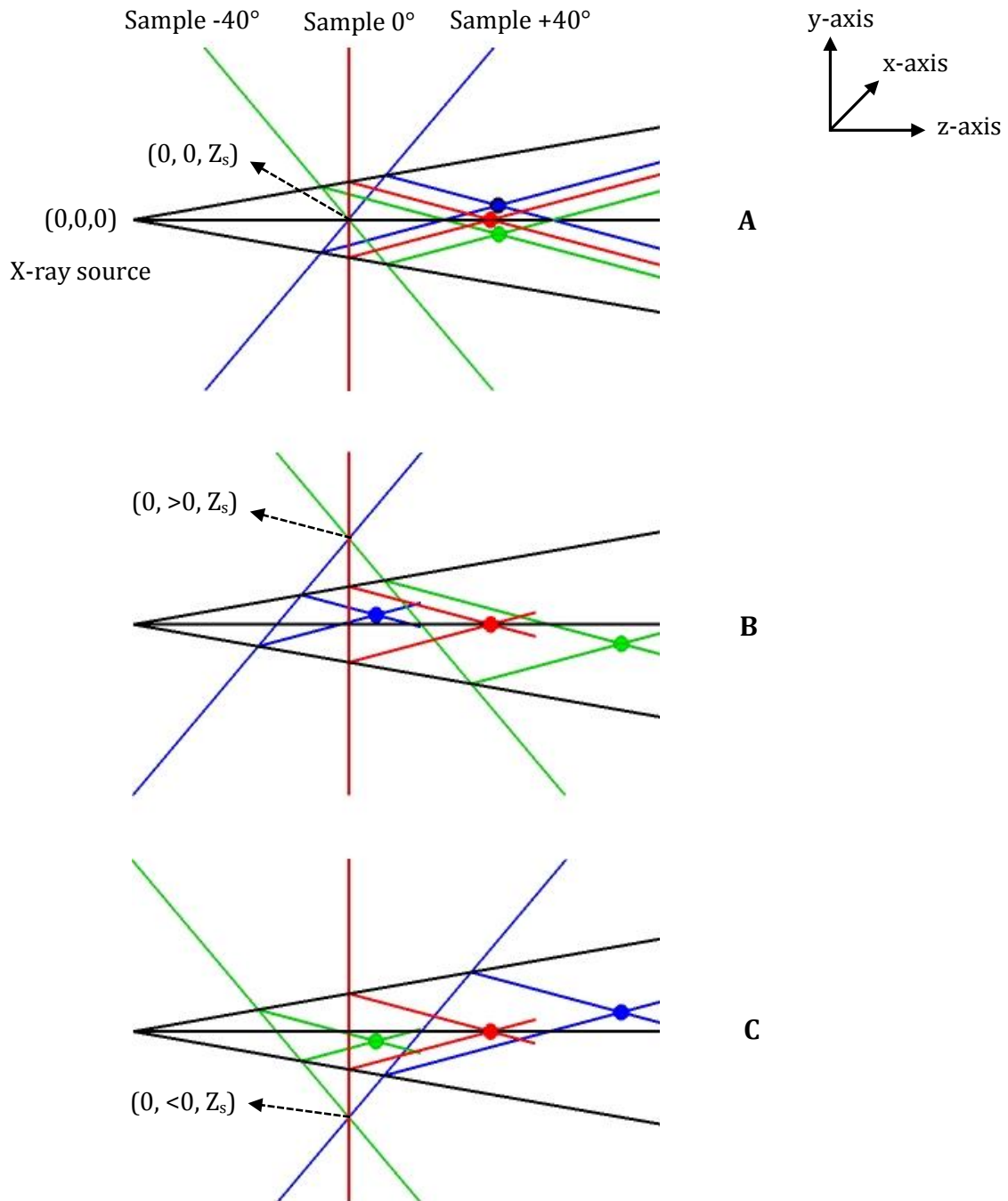


Figure 7.81 Schematic diagrams indicating the condensation foci formed from a sample rotation of 40° anticlockwise (green), 40° clockwise (blue) and 0° (red) at different intersection points of the rotation axes; on (A), above (B) and below (C) the z-axis.

Table 7.8 Analytical, simulation and empirical results of the y and z coordinates of the condensation foci of Al_2O_3 measured at 19.9° 2θ angle when rotated around the x-axis.

Rotation axes' intersection point	Sample rotation*	Analytical		Simulation		Empirical	
		Z _i (mm)	Y _i (mm)	Z _i (mm)	Y _i (mm)	Z _i (mm)	Y _i (mm)
(0, > 0, Z _s)	-20°	230.53	-1.47	230.8	-1.5	230.8	-1.5
	0°	229.12	0	229.2	0	229.3	0
	+20°	227.92	1.46	228.2	1.5	228.1	1.5
(0, 0, Z _s)	-20°	229.22	-1.46	229.7	-1.5	229.4	-1.5
	0°	229.12	0	229.2	0	229.3	0
	+20°	229.22	1.46	229.7	1.5	229.4	1.5
(0, < 0, Z _s)	-20°	227.92	-1.46	228.2	-1.5	228.1	-1.5
	0°	229.12	0	229.2	0	229.3	0
	+20°	230.53	1.47	230.8	1.5	230.8	1.5

*Anticlockwise rotation (-); Clockwise rotation (+)

In addition, simulated and empirical outcomes were further assessed by a quantitative comparison of the radial distances from the condensation foci at ~ 0.207 nm to the condensation ring at ~ 0.235 nm when the sample was rotated by $\pm 20^\circ$ and 0° around the x-axis. The radial measurements were taken at angular increments from 0° - 315° in steps of 45° . The results from the empirical and simulated measurements are presented in Table 7.9, and are within experimental errors, in agreement with each other.

The radial distance of the diffraction maxima, when the sample was normal to the primary axis maintained at 1.8 mm throughout the circumference of the condensation ring for both empirical and simulated data. However, for both simulated and empirical experiments, when the sample was rotated anticlockwise, the radial distances decreased systematically as approached 180° angular increment and then increased again to the initial value. The opposite effect was observed with the clockwise rotated sample. This comes to support the observation of non-circular condensation rings described in the previous sections. In addition,

as indicated by the radial measurements, the major and minor axes of the distorted condensation rings are inverted accordingly to the direction of sample rotation.

Table 7.9 Simulation and empirical radial measurements from the condensation focus (0.206 nm) to the condensation ring (0.235 nm) at circular angles of 0° - 315° in steps of 45°.

		Radial distance (mm)							
		<i>Circular angle</i>							
Sample rotation*		0°	45°	90°	135°	180°	225°	270°	315°
Simulation	-20°	2	1.9	1.8	1.7	1.6	1.7	1.8	1.9
	0°	1.8	1.8	1.8	1.8	1.8	1.8	1.8	1.8
	+20°	1.6	1.7	1.8	1.9	2	1.9	1.8	1.7
Empirical	-20°	2	1.9	1.7	1.7	1.7	1.7	1.8	1.9
	0°	1.8	1.8	1.8	1.8	1.8	1.8	1.8	1.8
	+20°	1.7	1.7	1.8	1.9	1.9	1.9	1.8	1.7

*Anticlockwise rotation (-); Clockwise rotation (+)

In summary, in this section it was shown that when a sample is rotated around the x or y axis, the xyz coordinates of the condensation foci alter; depending on the degree, direction and axis of sample rotation, as well as on the sample's scattering angles. Furthermore, the symmetry of the condensation rings is distorted as they are approaching their focal point. Comparison of analytical, simulated and empirical data indicated strong agreement between all three approaches.

7.7 Multiple scatterers

Analysis of multiple scatterers occupying the same x and y coordinates but different z coordinate, i.e. spatially distributed along the primary axis, was achieved using samples with the same material characteristics and with different material characteristics (Table 6.9, Section 6.3.8).

7.7.1 Same material characteristics

Scattering maxima from two Al_2O_3 samples separated by 9.4 mm were recorded (Figure 7.82 (A)) and presented along with their individual diffractograms (Figure 7.82 (B) and (C)).

The diffraction patterns were initially plotted against the detector's position along the primary axis. The scattering pattern from both scatterers is a combination of their individual patterns, as illustrated by Figure 7.82 (A).

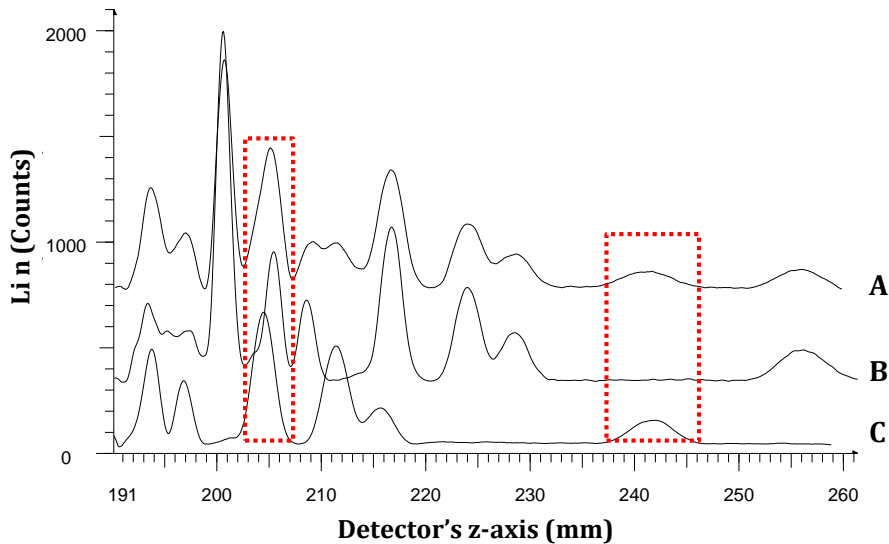


Figure 7.82 Diffraction signatures from two Al_2O_3 (*S1* and *S2*) plates separated by 9.4 mm along the z-axis (A), a single Al_2O_3 (*S2*) plate (B) and a single Al_2O_3 (*S1*) plate (C).

For example, the peak at ~205 mm is caused by an overlapping of the scattering maxima from *S1* and *S2* samples at ~204.5 mm and ~205.5 mm, respectively, as seen in Figure 7.82 (A). Besides the overlapping peaks, the diffractogram shown in Figure 7.82 (A) has additional peaks corresponding to a combination of the individual diffractograms of Al_2O_3 at different z-positions, as illustrated by the signal at ~241.5 mm.

The diffraction maxima from multiple scatterers were then interpreted in terms of d-spacing values, taking into account each sample's z coordinate (Figure 7.83 and Figure 7.84). In Figure 7.83, diffractogram A possesses additional peaks at 0.108 nm, 0.124 nm, 0.188 nm and 0.3 nm that are not from sample S2. Interpretation of the diffraction maxima arising from both samples simultaneously, with S1 sample's z-position (Figure 7.84 (A)), indicates the actual d-spacing values of these signals at 0.161 nm, 0.178 nm, 0.241 nm and 0.347 nm; corresponding to 116, 024, 110 and 012 reflection in Al_2O_3 , respectively (Figure 7.84 (B)).

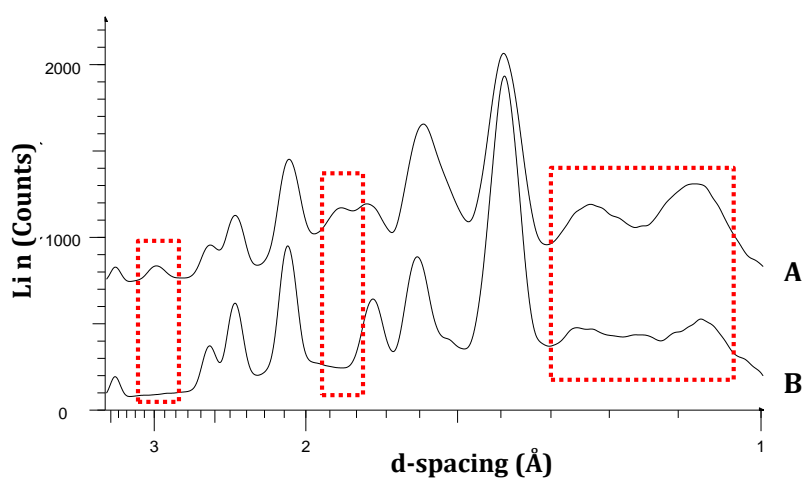


Figure 7.83 Diffraction signatures from two Al_2O_3 (S1 and S2) plates separated by 9.4 mm along the z-axis (A) and a single Al_2O_3 (S2) plate (B).

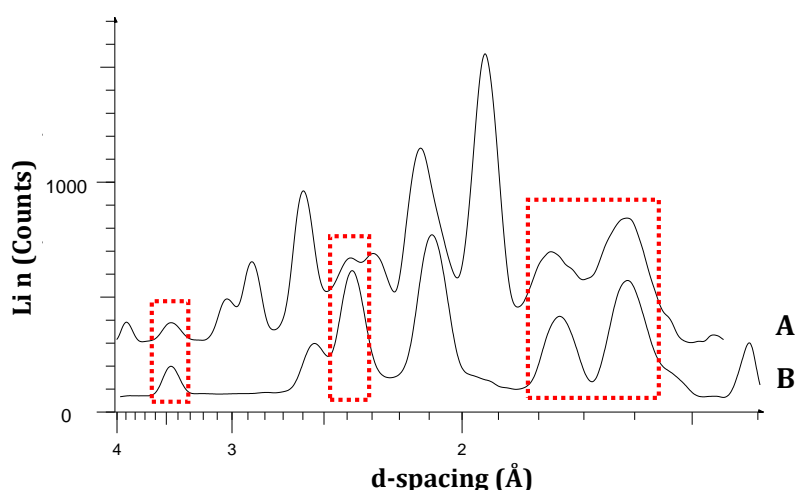


Figure 7.84 Diffraction signatures from two Al_2O_3 (S1 and S2) plates separated by 9.4 mm along the z-axis (A) and a single Al_2O_3 (S1) plate (B).

Interpretation of the combined diffraction profile at each sample's position along the primary axis could therefore identify both samples as Al_2O_3 .

Similarly, the same observations were detected when the spatial discrimination of the samples along the z-axis increased to 31.3 mm (see Appendix B.1).

It is therefore concluded, that once the position of a sample along the primary axis is known, the sample can be identified even in the presence of additional scatterers.

In addition, it was demonstrated that the resolution of the diffraction peaks depends on the spatial distance between multiple samples. For samples with same material characteristics, the mean distance between FCG scattering maxima $(Z_{d2}-Z_{d1})_m$, from two infinitely thin samples separated by $Z_{s2}-Z_{s1}$ distance along the primary axis, is calculated by Equation (7.31).

$$(Z_{d2} - Z_{d1})_m = \frac{(Z_{s2} - Z_{s1})[\tan(2\theta - \phi_m) + \tan \phi_m]}{\tan(2\theta - \phi_m)} \quad (7.31)^\S$$

For direct comparison purposes, the mean distance between the scattering maxima $(R_1-R_2)_m$ from two samples separated by $Z_{s2}-Z_{s1}$ distance for conventional XRD is given by Equation (7.32).

$$(R_1 - R_2)_m = (Z_{s2} - Z_{s1}) \tan 2\theta \quad (7.32)$$

For example, for 1 mm spatial discrimination between two scatterers, the FCG peaks would be separated by $\frac{[\tan(2\theta-\phi_m)+\tan \phi_m]}{\tan(2\theta-\phi_m)}$ (e.g. 1.21 mm for $2\theta=20^\circ$ and $\phi_m=3.5^\circ$) and pencil beam peaks would be separated by $\tan 2\theta$ (e.g. 0.36 mm for $2\theta=20^\circ$). Therefore, it is evident that FCG maxima are resolved by a ~ 3.5 greater distance than conventional pencil beam maxima from samples with the same 2θ angles.

[§] For symbol ϕ_m refer to Section 5.1.

7.7.2 Different material characteristics

Similarly to multiple scatterers with same material characteristics, the scattering maxima obtained from Al_2O_3 and Al simultaneously, were a combination of their individual diffraction signals. When the two samples were separated by 10.3 mm along the z-axis, with the Al sample closer to the detector, four dominant diffraction maxima were acquired arising from Al (Figure 7.85). The additional peaks arose from Al_2O_3 , which caused broadening or appeared as shoulders to the main peaks; except the low intensity peak at ~ 217 mm.

Interpretation of the multiple scatterers' profile in terms of d-spacing, as determined from each sample's z-position, is presented in Figure 7.86 and Figure 7.87. In Figure 7.86, there are additional signals at 0.184 nm and 0.303 nm, as well as a peak shoulder at 0.156 nm, which are not present in the diffractogram of Al. The actual d-spacing values of these scattering maxima are 0.210 nm, 0.237 nm and 0.351 nm corresponding to the 113, 110 and 012 reflections in Al_2O_3 , respectively (Figure 7.87).

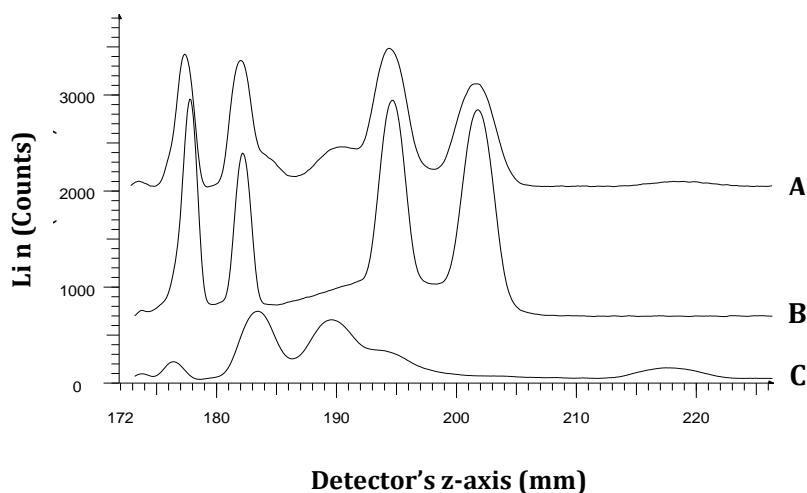


Figure 7.85 Diffraction signatures from an Al_2O_3 (S1) and Al (AS) plates separated by 10.3 mm along the z-axis (A), a single Al (AS) plate (B) and a single Al_2O_3 (S1) plate (C).

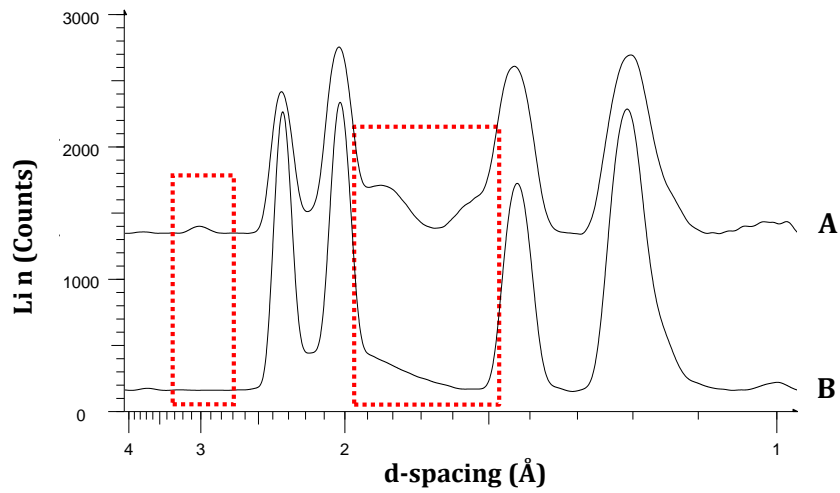


Figure 7.86 Diffraction signatures from an Al_2O_3 (S1) and Al (AS) plates separated by 10.3 mm along the z-axis (A) and a single Al (AS) plate (B).

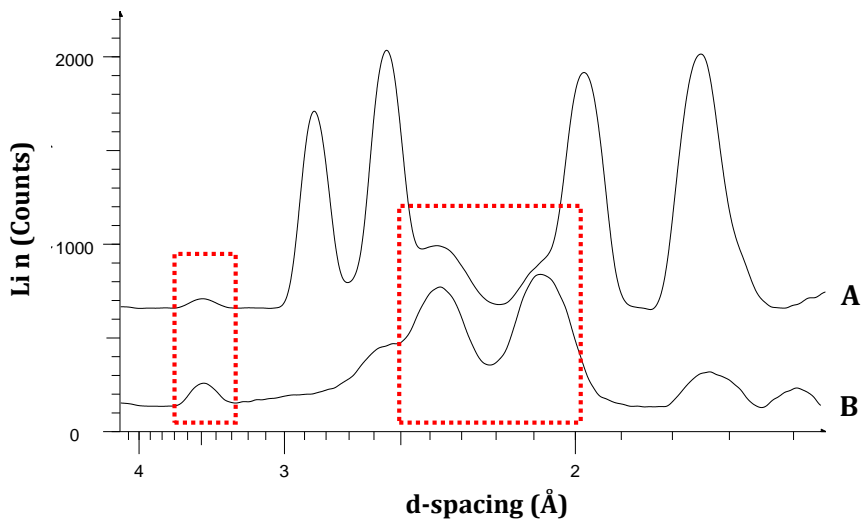


Figure 7.87 Diffraction signatures from an Al_2O_3 (S1) and Al (AS) plates separated by 10.3 mm along the z-axis (A) and a single Al_2O_3 (S1) plate (B).

When the z locations of the Al and Al_2O_3 plates were inverted i.e. Al further away from the detector, only two diffraction maxima arising from Al were observed in the combined diffractogram (see Appendix B.2) due a greater sample-to-detector distance.

Likewise to the samples with same material characteristics, the distance between FCG scattering maxima $(Z_{d2}-Z_{d1})_m$ and the distance between conventional scattering maxima $(R_2-R_1)_m$ for samples with different material characteristics (separated by $Z_{s2}-Z_{s1}$), can be determined by Equation (7.33) and Equation (7.34), respectively.

$$(Z_{d2} - Z_{d1})_m = (Z_{s2} - Z_{s1}) + \frac{Z_{s2} \tan \phi_m}{\tan(2\theta_2 - \phi_m)} - \frac{Z_{s1} \tan \phi_m}{\tan(2\theta_1 - \phi_m)} \quad (7.33)**$$

$$(R_1 - R_2)_m = (Z_d - Z_{s1}) \tan 2\theta_1 - (Z_d - Z_{s2}) \tan 2\theta_2 \quad (7.34)$$

Equations (7.33) and (7.34) require $2\theta_1 > 2\theta_2$ and $Z_{d2} > Z_{d1}$ (or $R_1 > R_2$ for Equation (7.34)); otherwise the absolute value of these equations should be used.

For an example where $Z_{s2}-Z_{s1}=1$ mm, $Z_{s2}=151$ mm, $Z_{s1}=150$ mm, $Z_d=200$ mm, $2\theta_1=20^\circ$, $2\theta_2=15^\circ$ and $\phi_m=3.5^\circ$, the distance between FCG scattering maxima is calculated to be 15.42 mm and between conventional maxima 5.07 mm. Thus, it was demonstrated that for both $2\theta_1=2\theta_2$ and $2\theta_1 \neq 2\theta_2$ FCG diffraction maxima are separated by a greater spatial distance than conventional Debye cones.

7.7.3 Comparison between empirical and simulated data

Simulated diffraction data were acquired from multiple scatterers as well as individual samples at the same z-coordinates as with the empirical experiments. This intended to determine the correspondence between empirical and simulated data in the presence of multiple scatterers.

Representative examples of simulated scattering patterns of Al_2O_3 and Al, when compared to the empirically obtained patterns are presented in Figure 7.88. Both simulated samples were assigned specified thicknesses according to the actual Al_2O_3 and Al samples employed in Section 7.7.2.

** For symbol ϕ_m refer to Section 5.1.

The positions of the simulated diffraction maxima are, within experimental errors, consistent with the positions of the empirical signals. However, the width of the simulated diffraction peaks is significantly narrower than the width of the empirically obtained peaks.

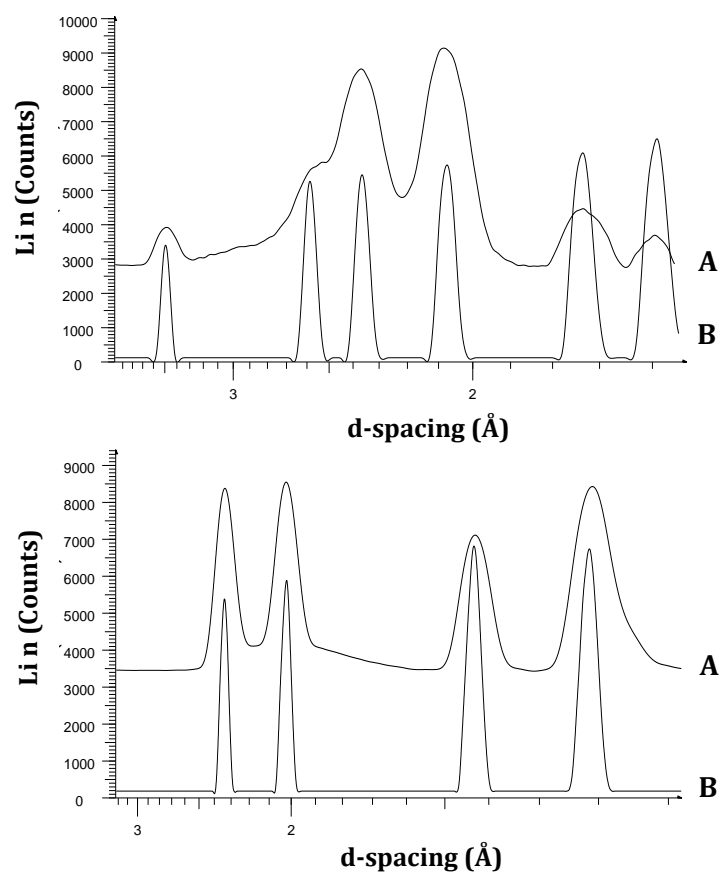


Figure 7.88 Empirical (A) and simulated (B) scattering signatures of Al_2O_3 (top) and Al (bottom).

In Figure 7.89, the scattering profile obtained from both samples simultaneously is a combination of their individual diffraction maxima similarly to the empirical data. It should be noted that due to the narrower width of the simulated peaks, the latter appear better resolved than the empirical peaks (see Figure 7.89 and Figure 7.85).

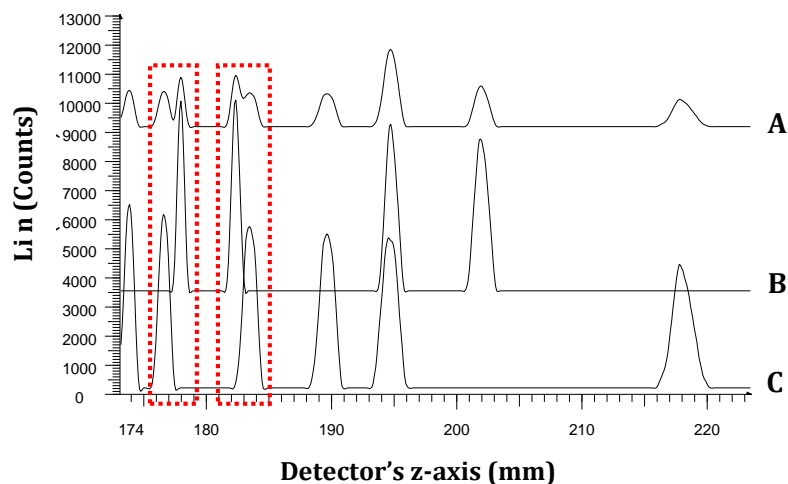


Figure 7.89 Simulated diffraction signatures from an Al_2O_3 and Al plates separated by 10.3 mm along the z-axis (A), a single Al plate (B) and a single Al_2O_3 plate (C).

To summarise, in this section, spatial discrimination of samples along the primary axis was shown to give rise to scattering maxima at different z-coordinates depending on each sample's position. It has been analytically determined that FCG generates diffraction maxima from multiple samples, along the primary axis, with a greater spatial discrimination between the diffraction peaks than conventional XRD.

It was also demonstrated that the identification of multiple unknown materials with a spatial discrimination along a primary axis is feasible only with *a priori* knowledge of their positions along the axis. However, in certain applications, such as luggage screening in airports, prior knowledge of the sample's position is unusual. In such systems, there is a need to determine depth information of unknown substances for material identification. This requirement is addressed in the next chapter (Section 8.3) with coded aperture encoders.

Chapter 8 CODED APERTURE: EXPERIMENTAL

Outline

In this chapter, theoretical and experimental data on coded aperture systems are presented. Initially, the annular beam of FCG is treated as a pre-sample coded aperture with the aim of recovering conventional XRD data. The effects of several non-ideal conditions of either the primary beam or FCG data are investigated in order to identify their influence on the coded aperture system. Proof-of-principle is then demonstrated in a simulated and pseudo-empirical approach, and the optimised methodology is employed for non-ideal samples exhibiting preferred orientation or large grain size. Furthermore, the theory and preliminary FCG data obtained with an encoded annular beam are introduced and explained. Finally, two novel encoders, a linear wire and an Archimedean spiral, are assessed in their performance and ability to act as post-sample encoders, with conventional XRD data and preliminary FCG data, to determine sample spatial information.

Early developments of coded aperture systems (Ables, 1968, Dicke, 1968, Fenimore and Cannon, 1978, Simpson, 1978), as well as recent studies on coded masks (MacCabe et al., 2012, Greenberg et al., 2014b) discussed in Chapter 4, involved post-sample coded apertures. However, in particular studies, such as that of Weiss et al. (1977), a distribution of X-ray sources was established as a type of pre-sample coded aperture (Section 4.1).

In this chapter, the annular beam employed by FCG is considered as a type of coded aperture. The annular collimator presented in this work was placed between the X-ray source and the sample, hence considered as a pre-sample coded aperture. As previously explained in Section 4.1, the coded aperture imaging systems are based on the convolution of the object with the coded mask in order to obtain a complicated image with no resemblance to the object. This image is then convolved

with a post-processing array, typically the coded mask, to reconstruct the object. Therefore, the annular aperture of FCG was employed in a post-processing procedure aimed at the reconstruction of the desired object.

8.1 Pre-sample coded aperture

In diffraction space, the sample is not the required object for reconstruction, but the material specific characteristics of the sample, i.e. the Debye rings observed in a conventional diffraction pattern are the desired object.

This chapter aims to examine the diffraction data obtained by a hollow beam arrangement through a coded aperture approach. As illustrated in Figure 8.1, the annular mask is acting as a primary collimator to produce a hollow conical beam, that while passing through the sample it scatters diffraction caustics (see Chapter 5). The image produced (the FCG pattern) is a combination of single (pencil beam) Debye cones, which are the required object for reconstruction. If this procedure is viewed from a coded aperture system prospective, then the FCG patterns can be considered the result of the convolution of an annular beam with a single or numerous Debye cones. A second convolution of the FCG pattern with the annular coded aperture should therefore reconstruct the Debye rings as indicated by Figure 8.1; thus enabling the treatment of diffraction patterns obtained via a hollow beam arrangement in a conventional manner. At this point, it is important to note that in this study, the term reconstruction of Debye rings is referred to the recovery of their radii.

Reconstruction of Debye rings by an annular coded aperture relies within the auto-convolution function (SPSF) of the annular beam. The coded aperture presented herein is similar to the annular coded aperture examined in detail by Simpson (1978) in non-diffraction space, as explained in Section 4.1. The analytical description and auto-convolution of an annular coded aperture is given by a ring-delta function, as seen by Equation (4.6). As previously demonstrated in Figure 4.3, the SPSF of an annulus has a high intensity peak at $r=0$ but with a slow decay down to $r=2\bar{r}$, at which point the intensity increases slightly.

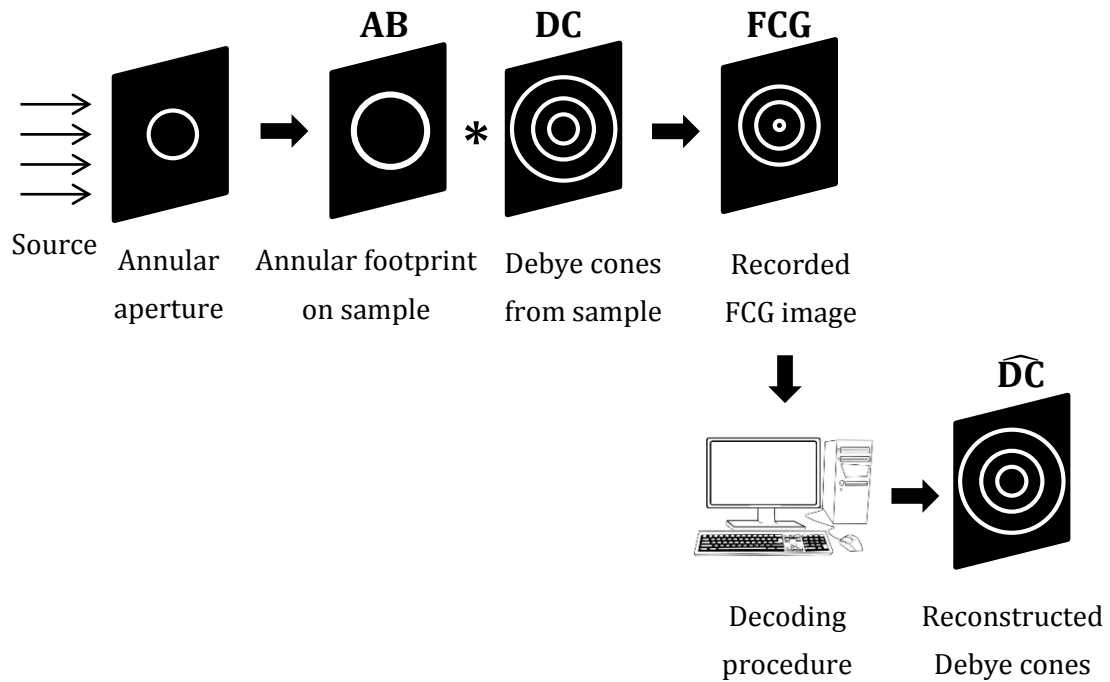


Figure 8.1 The arrangement and procedure involved with a pre-sample annular coded aperture in diffraction space.

A simulated example of the SPSF of an annulus (1.34 mm inner radius and 0.08 mm wall thickness) is presented in Figure 8.2 and comes in agreement with the SPSF reported by Simpson (1978) and Barrett and Swindell (1981). Similarly to a Dirac δ -function, the self-convolution of a circle produces a high intensity focus at the centre of the image ($x=0$). However, there is also a lower intensity distribution radially to the focus between $0 < x < 2\bar{r}$, that increases slightly at $2\bar{r}$ (where \bar{r} is the mean radius of the annulus). Therefore, even though the central spike of the self-convolution of a circle denotes a δ -function, the low intensity outer ring and the distribution of noise in between indicate an approximation to a δ -function.

In the example given in Figure 8.2, the central spike has ~ 20 times and ~ 65 times higher intensity than the outer ring (sidelobe spike) and inherent noise (sidelobe), respectively. Even though the difference in intensity changes significantly depending on the annulus' parameters, e.g. thickness, the general relationship between the intensity of these three main features remains the same.

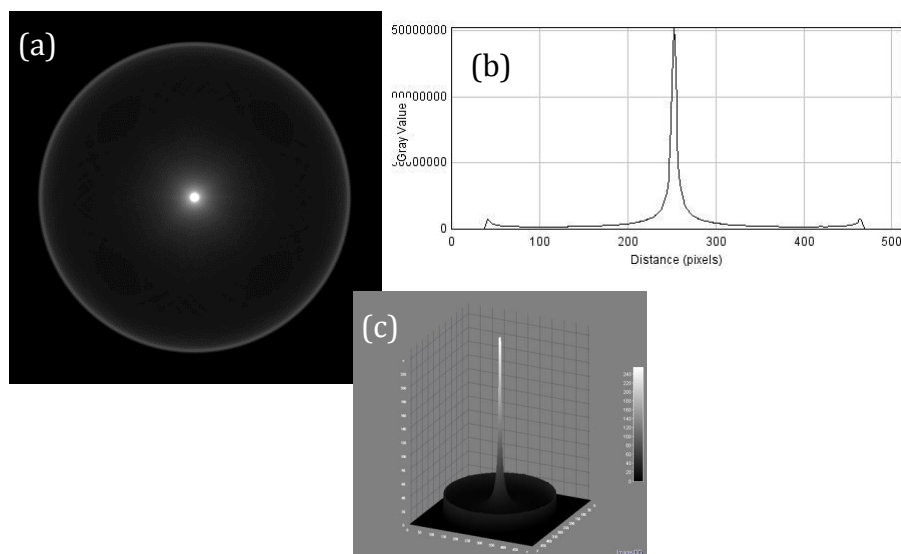


Figure 8.2 A 2D image (a), a 2-D plot profile (b) and a 3-D surface plot (c) of the $\sim\delta$ -function generated by the auto-correlation of an annular aperture.

8.1.1 Simulated data

The ability of the annular aperture to reconstruct the Debye rings of conventional diffraction patterns, as illustrated in Figure 8.1, was initially examined in a simulated approach using ImageJ software's *Convolve* function. Simulated data enabled the establishment of an annular coded aperture concept with an ideal sample, in terms of preferred orientation and grain size, and assess its potential.

8.1.1.1 Proof-of-concept

An ideal (noise-less) FCG image (Figure 8.3 (c)) was produced by convolving an annular beam (AB) of 1.34 mm inner radius and 0.08 mm thickness with two simulated Debye rings of 0.75 mm (0.292 nm d-spacing) and 1.65 mm (0.155 nm d-spacing) inner radius and 0.08 mm thickness, as illustrated in Figure 8.3. The radii of the Debye rings were selected deliberately to generate an FCG pattern consisting of both converging and diverging condensation rings. It should be noted that all simulated images were comprised of opaque (0) and transparent (255) elements.

The resulting FCG image was then convolved with the annulus to reconstruct the Debye cones (DC). As discussed in Section 4.1, if the self-convolution of the coded aperture does not produce a perfect δ -function, then the image of the recovered object suffers from inherent artefacts. As indicated in Figure 8.2, the self-convolution of an annulus produces an approximation to a δ -function due to the additional noise surrounding the central high intensity focus. Consequently, the reconstructed image suffered from inherent artefacts in the form of additional rings, shown in Figure 8.3 (d). An optimised post-processing procedure was then applied, involving bandpass filtering of large structures down to 40 pixels and small structures up to 3 pixels; hence narrowing the spatial frequencies' range (Figure 8.3 (e)), and a dc level removal, as initially indicated by Fenimore and Cannon (1978). Visual inspection of the resulting post-processed image shown in Figure 8.3 (f) indicates reconstruction of the Debye rings of Figure 8.3 (b).

Comparison of the scattering profiles of the Debye rings and the reconstructed image verifies the effective recovery of the desirable scattering angles, as indicated in Figure 8.4.

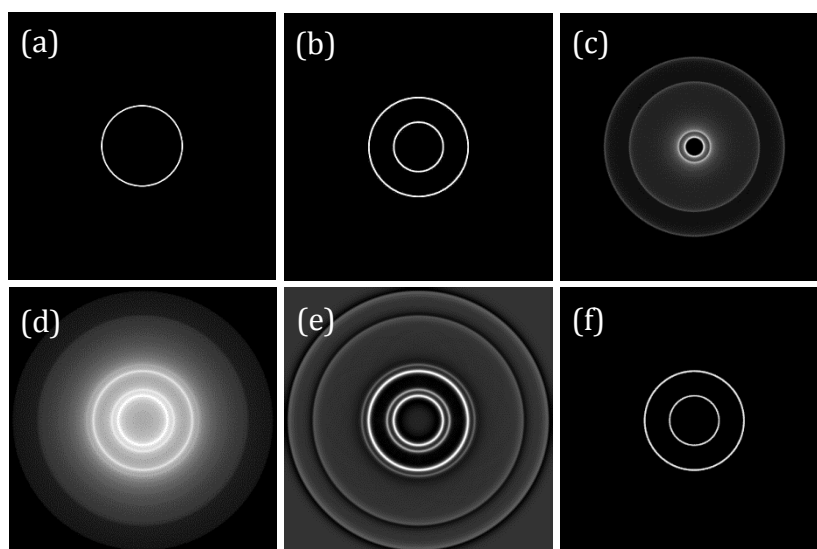


Figure 8.3 Simulated images of an annular primary beam (a), two Debye rings (b), their FCG pattern (c), the recovered image prior to any processing (d), the processed image after bandpass filtering (e) and the recovered Debye rings after a 175 dc level removal (f).

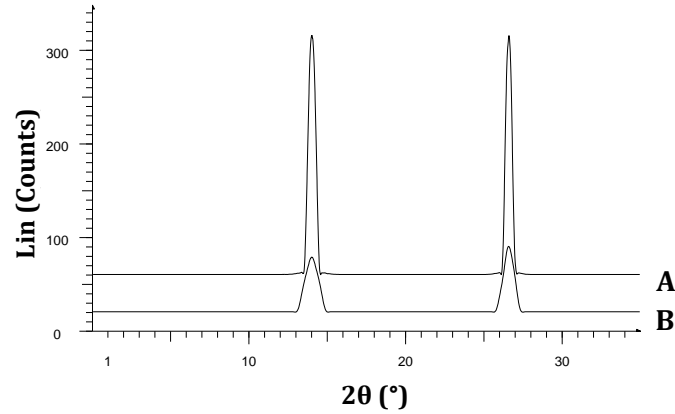


Figure 8.4 Radial integration of simulated image consisting of two Debye rings (A) and corresponding recovered image (B).

Even though deconvolution of the FCG pattern with the annular beam would also reconstruct the Debye rings, this process can be particularly challenging when dealing with non-ideal images that suffer from noise (Fenimore and Cannon, 1978), as shown in Section 8.1.1.3 (a).

Looking at the additional rings in the recovered image prior post-processing (Figure 8.3 (d)), they represent an example of the inherent artefacts found when attempting to reconstruct Debye rings. Additional rings arise from the convolution of the four condensation rings present in the FCG pattern (Figure 8.3 (c)) with the annulus (Figure 8.3 (a)). A better illustration of this effect can be seen in Figure 8.5 and Figure 8.6, where a schematic illustration of the coded aperture procedure has been outlined. Figure 8.5 - Figure 8.7 are analytically described as:

$$AB * DC = FCG \quad \rightarrow \quad \text{see Figure 8.5}$$

$$FCG * AB = \widehat{DC} \quad \rightarrow \quad \text{see Figure 8.6}$$

$$(AB * AB) * DC = \widehat{DC} \quad \rightarrow \quad \text{see Figure 8.7}$$

Convolution of an annulus (annular beam, AB) with two Debye rings (DC) of smaller and greater radius than the former, results in four condensation rings with specific associations to the annulus and Debye rings, as indicated in Figure 8.5.

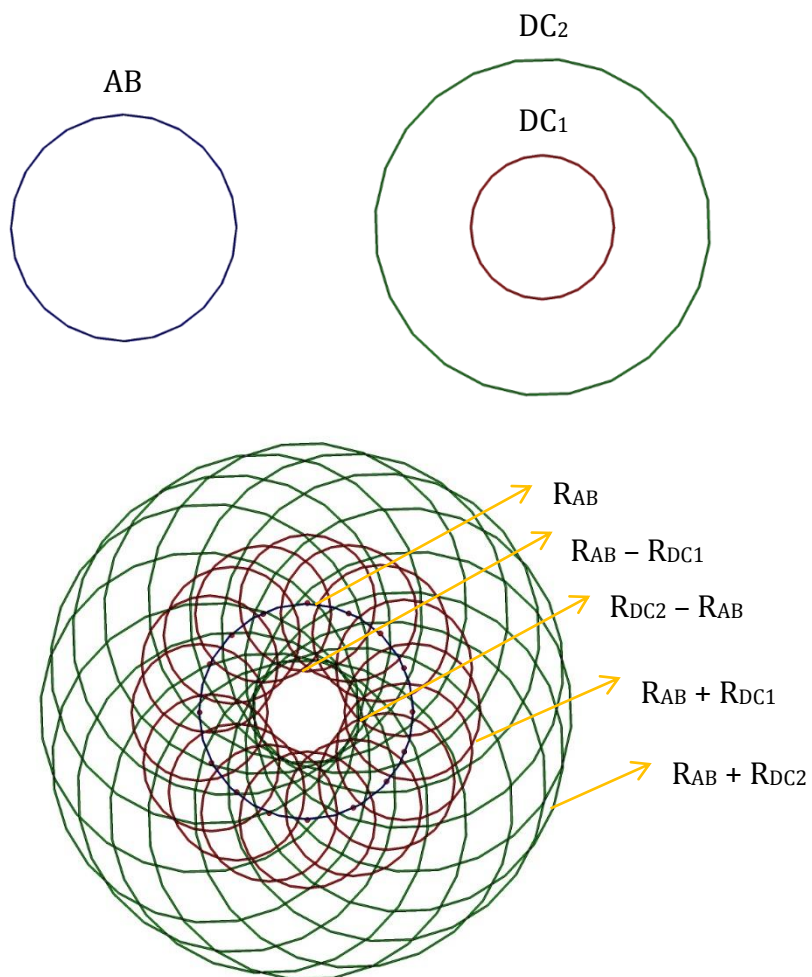


Figure 8.5 Schematic illustration of the convolution of an annular beam (top left) with two Debye cones (top right) to produce an FCG pattern (bottom).

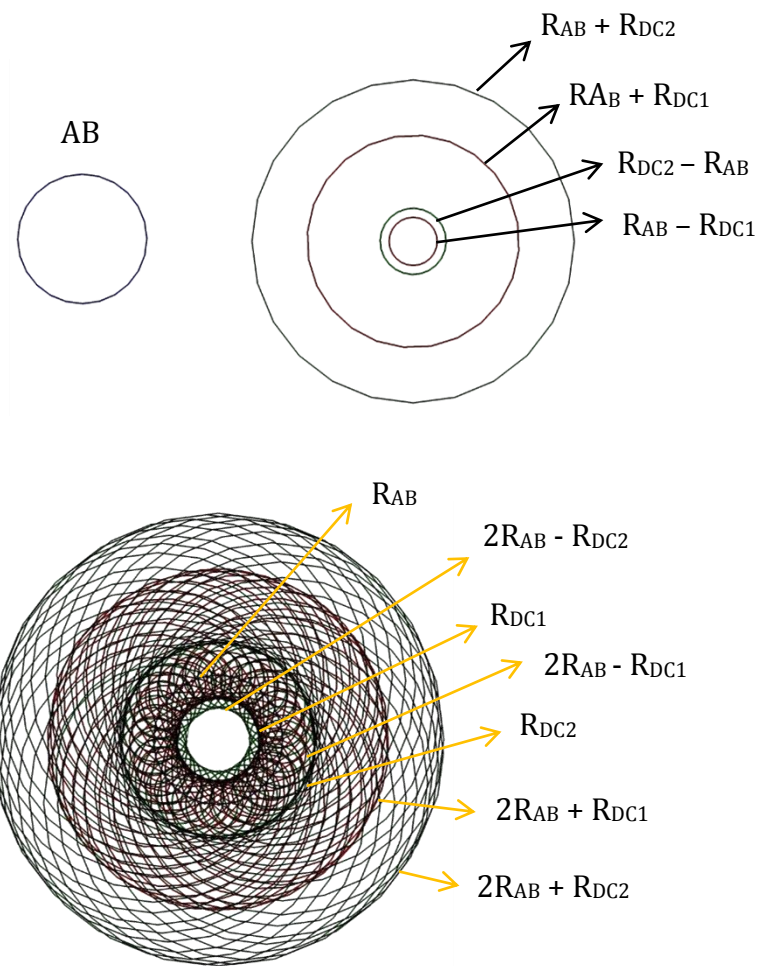


Figure 8.6 Schematic illustration of the convolution (bottom) of an annular beam (top left) with an FCG pattern (top right) to reconstruct the Debye cones.

Condensation rings satisfying $R_{AB}+R_{DC}$, where R_{DC} is the radius of the Debye ring and R_{AB} the radius of the annulus, are referred to as outer condensation rings; whereas condensation rings at $R_{DC}-R_{AB}$ and $R_{AB}-R_{DC}$ are referred to as inner condensation rings. For every inner condensation ring in the FCG pattern, two relationships could be satisfied, $R_{DC}-R_{AB}$ and $R_{AB}-R_{DC}$; but only one of them would be valid depending on the converging or diverging nature of the condensation ring.

For the example illustrated in Figure 8.5 and Figure 8.6, four condensation rings in the FCG diffraction pattern (corresponding to two Debye cones) will reconstruct an image with six associated rings (four of them of low intensity), as illustrated in Figure 8.6. This pattern consists of the reconstructed Debye rings and four additional rings, which are considered as artefacts. The radii of the additional four rings correspond to $2R_{AB} \pm R_{DC}$ (Figure 8.6). It should be noted, that even though the primary beam is illustrated in Figure 8.6, it is not apparent in the reconstructed images.

A schematic diagram illustrating the convolution of an annulus' SPSF with two Debye rings is presented in Figure 8.7, in order to demonstrate the associative property of convolution on which coded aperture systems are based on, as shown in Section 4.1.1. Comparison of Figure 8.6 and Figure 8.7 ascertains that the same reconstructed pattern is observed when convolving an FCG pattern with the annular beam as when convolving the δ -function approximation (annulus' SPSF) with the Debye cones.

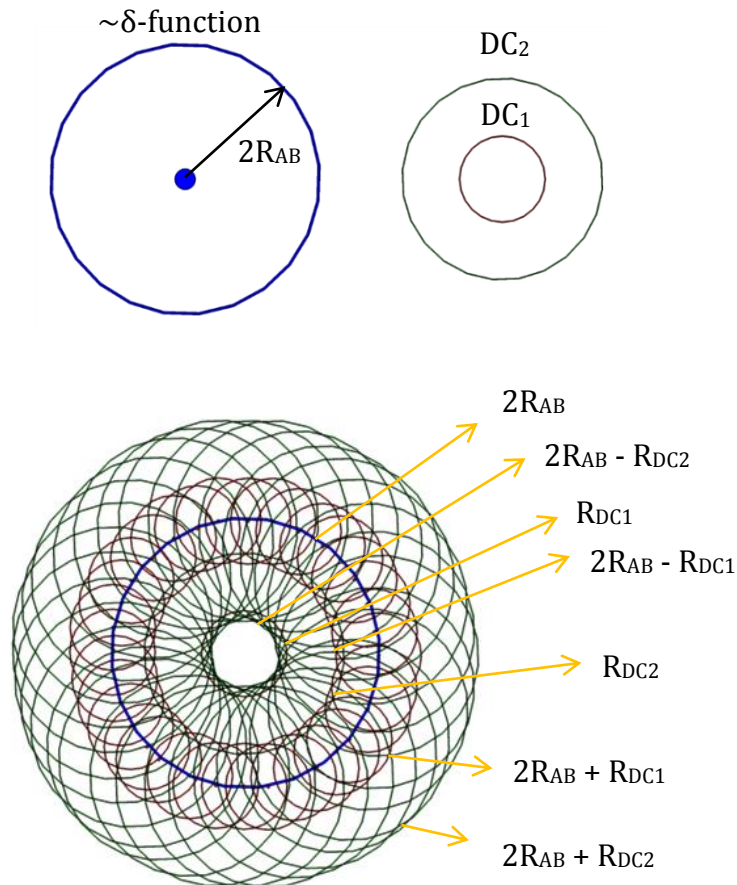


Figure 8.7 Schematic illustration of the convolution of a δ -function approximation (top left) with two Debye cones (top right) to reconstruct the Debye cones and additional rings (bottom).

Figure 8.8 (a) illustrates the image obtained by convolving the Debye rings presented in Figure 8.3 (b) with the self-convolution of the primary beam of Figure 8.3 (a). If the annulus' SPSF consisted just by the low intensity circle at $2\bar{r}$, its convolution with the Debye rings would generate the rings shown in Figure 8.8 (b). These rings are identical to the additional rings of Figure 8.8 (a). Visual inspection and comparison of the two images (Figure 8.8 (a) and (b)), as well as determination of the radii of each ring can identify the Debye rings. Furthermore, subtraction of the additional rings (Figure 8.8 (b)) from the recovered image of the Debye rings and additional rings (Figure 8.8 (a)) should result in an image with just the two Debye rings (Figure 8.8 (c)). Figure 8.8 (c) shows that there are only two high intensity rings with the same radius as the Debye rings. This verifies that the

additional rings observed in the reconstructed image are indeed a result of the low intensity peak at $2\bar{r}$ of the annulus' non-ideal δ -function SPSF.

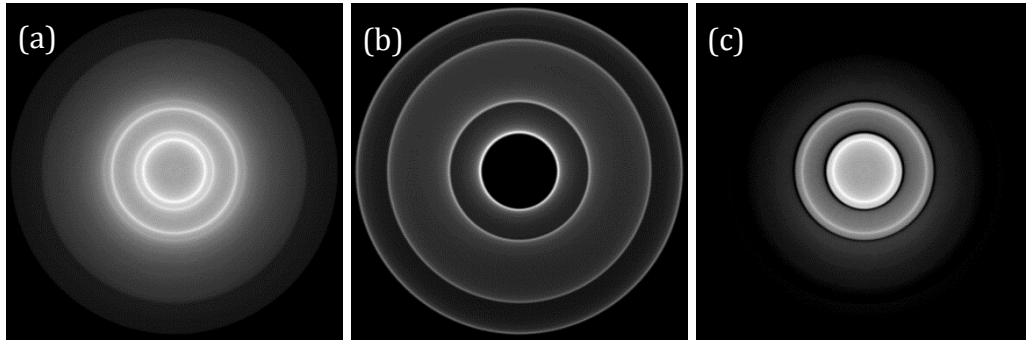


Figure 8.8 Simulated images obtained upon convolution of the Debye rings with the annular beam's SPSF (a), with the outer ring of the annular beam's SPSF (b), and the result of their subtraction (c).

The low intensity of the inherent artefacts in the reconstructed image can be observed as a dc level addition. Without any prior knowledge on the Debye cones, the approximate dc level needed to be subtracted from the recovered image can be

calculated by $\frac{N_{\max}}{\%N_{\text{total}}}$; where N_{\max} is the maximum value of noise (artefacts in non-

deal δ -function – see Figure 8.9) present in the self-convolved image of the annular aperture after bandpass filtering and $\%N_{\text{total}}$ is the self-convolved image's total percentage of noise. For the example illustrated in Figure 8.3, the maximum intensity of noise is 11 and the total noise percentage is 6.24%, as calculated by the profile plot in Figure 8.9; hence, a value of ~ 176 should be subtracted from the filtered image to successfully reconstruct the Debye rings. Visual comparison of the known Debye rings and the reconstructed image revealed that if a value within the range of 174-254 was subtracted from the reconstructed image, the Debye rings were recovered effectively, as illustrated in Figure 8.3 (f).

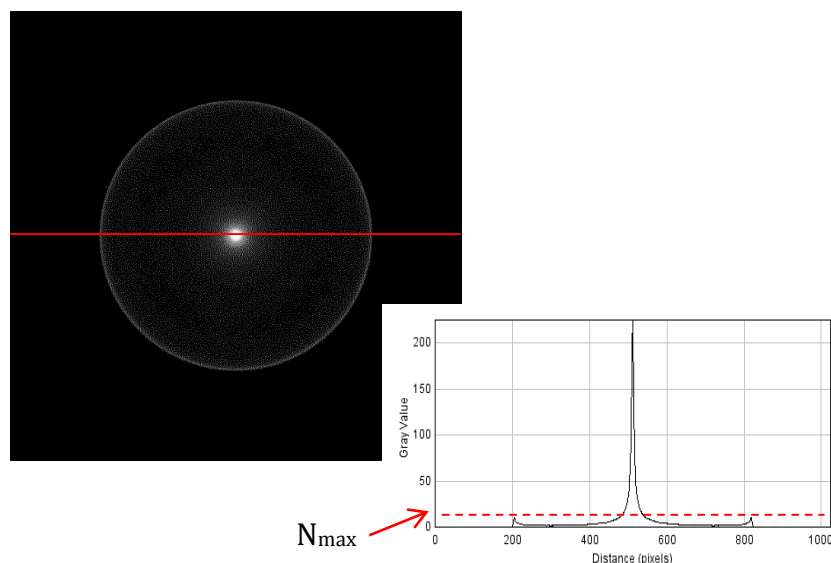


Figure 8.9 A simulated image of the annular beam's SPSF (top left) and a 2D plot profile of the image (bottom right) indicating the latter's maximum noise intensity (N_{max}).

In order to determine the dc level, which was required to be removed, an alternative approach is considered by a linear profile plot of the filtered image (e.g. Figure 8.3 (e)). Since, FCG images allow determination of the number of Debye rings needed to be recovered, the corresponding number of peaks with the highest intensity in the filtered recovered image can be identified as the Debye rings' peaks. The highest intensity value of the remaining peaks corresponds to the additional dc level present in the recovered image. Taking in consideration the previous example, the FCG image identifies the presence of only two Debye cones. Figure 8.10 illustrates the filtered recovered image and its corresponding plot profile across the centre of the pattern (as indicated by the red solid line). The highest intensity of the additional rings (besides the Debye rings) corresponds to the required dc level and it was identified from the profile plot (Figure 8.10) as ~ 170 .

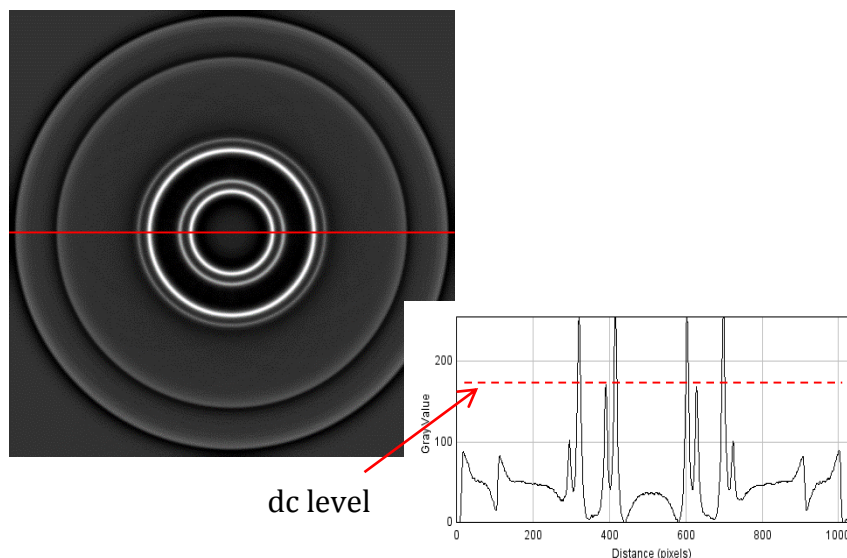


Figure 8.10 A simulated image of the reconstructed Debye rings (top left) post-filtering (bandpass) and a 2D profile plot of the image (bottom right) indicating the additional dc level of the recovered image.

For the example shown in Figure 8.3, comparison of the line profiles of the Debye rings (Figure 8.3 (b)) and of the recovered Debye rings (Figure 8.3 (f)) indicates a strong correlation between the two images in terms of Debye rings' intensity (Figure 8.11). The intensity of the recovered Debye rings is equivalent to the intensity of the initial Debye rings when the subtracted dc level is re-added to the recovered image, as demonstrated by Figure 8.11.

FWHM were calculated for the particular peaks illustrated in Figure 8.11, for both the Debye rings and the recovered Debye rings. The Debye rings had a thickness of 0.052 mm, whereas the thickness of the recovered Debye rings was increased to 0.065 mm. The FWHM were also calculated in a 2θ ($^\circ$) scale; representing an average of $\sim 88\%$ increase in the width of the recovered Debye rings (see Table 8.1).

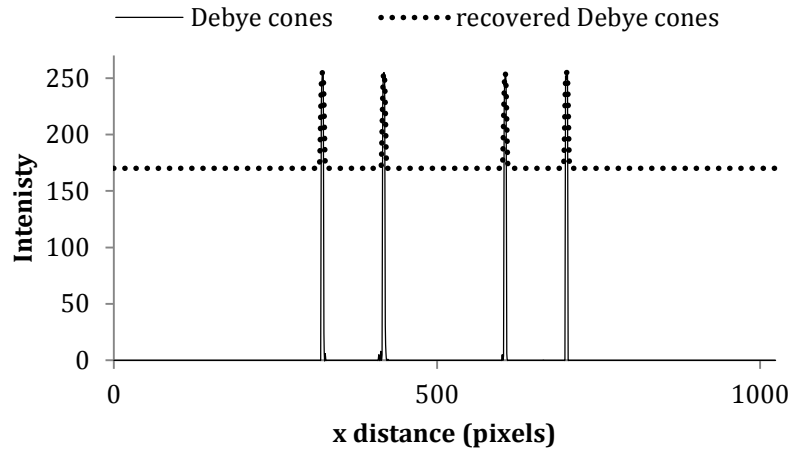


Figure 8.11 A line profile plot across the x pixels of the Debye rings image and the post-processed recovered image.

Table 8.1 The FWHM values of the Debye rings and the recovered Debye rings.

FWHM (°)	
Debye rings	Recovered Debye rings
0.22	0.43
0.20	0.36

8.1.1.2 Two-annulus system

A supplementary approach to the above post-processing procedure is proposed, based on the two-annulus concept (in non-diffraction space) of Simpson (1978) (see Section 4.1), to examine its capabilities and potential advantages. The same annular coded aperture and Debye rings as the ones employed in Section 8.1.1.1 (i.e. Figure 8.3) were utilised for these simulated experiments.

The radius of the second annulus was increased by 1.085, as suggested by Simpson (1978), to 1.45 mm inner radius and 0.08 mm thickness. The reconstruction procedure adopted throughout Section 8.1.1.1 was carried out for both annular beams individually, without any post-processing. Once the recovered images were obtained, they were added together, and went through bandpass filtering and dc removal. The recovered Debye rings prior and post additional reconstruction

processing (i.e. bandpass filtering and dc removal) are presented in Figure 8.12 (a) and (b), respectively.

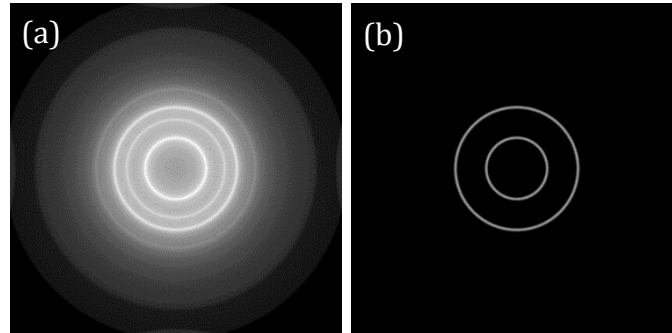


Figure 8.12 Simulated images of the recovered image obtained by the two-annulus system prior (a) and post (b) bandpass filtering and dc removal (85).

Cross-section profile plots along the horizontal x-axis of the recovered image, as well as the recovered image from a single annulus (described in the previous section) are compared in Figure 8.13. The same post-processing was applied for both recovered images.

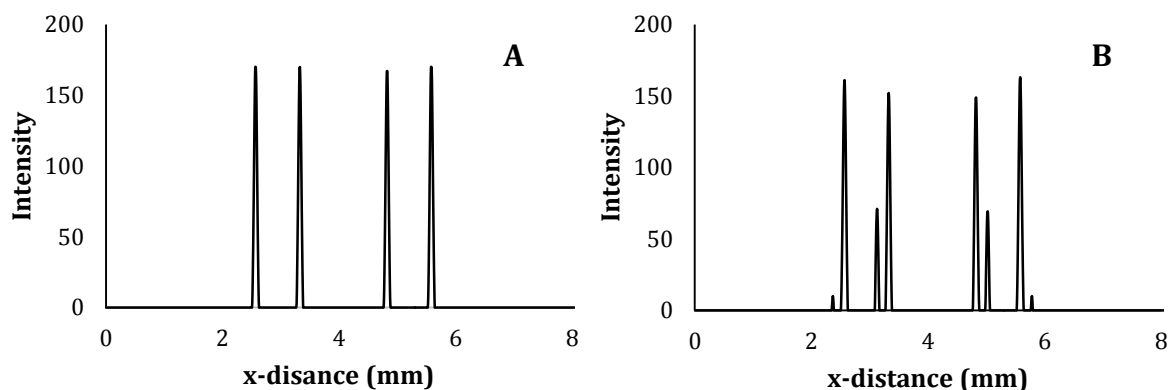


Figure 8.13 Comparison of the recovered images' cross section profiles along the x-axis for the two-annulus approach (A) and single annulus coded aperture (B), when bandpass filtering was applied and an 85 dc level was subtracted.

From the data obtained, the two-annulus system showed more effective recovery of the Debye rings, in terms of intensity. The scattering maxima were reconstructed in the same positions, within experimental errors, from both approaches. However, the two-annulus system introduced an enhanced intensity to the recovered Debye rings, whilst reducing the intensity of additional rings, which are regarded as artefacts. This is clearly demonstrated by the absence and presence of the additional rings in Figure 8.13 (A) and (B) respectively, when the exact same post-processing procedure was applied to both recovered images.

The key feature of the two-annulus system is based on the fact that inherent artefacts in the reconstructed images from two different annuli correspond to different additional rings. Thus, their intensity is reduced upon addition of the reconstructed images. In contrast, the Debye rings remain the same; hence, their intensity is enhanced once the two recovered images are added together. Even though the two-annulus system was proven to be superior to the single annulus approach, the latter was employed throughout this work for simplicity, since there was no difference in the reconstruction of the diffraction maxima positions.

8.1.1.3 Investigating non-ideal conditions for annular aperture

The effectiveness of the annular aperture was examined by applying various alterations either to the simulated FCG images or to the annular mask, in order to assess their effect on the recovery of the Debye rings.

Simulated images of three Debye rings (0.448 nm, 0.207 nm and 0.107 nm d-spacing) and an annular primary beam (1.08 mm inner radius and 0.08 mm thickness) were employed throughout this analysis, as illustrated in Figure 8.14 (b) and (a), respectively. The radii of the Debye rings and annulus were specifically chosen in order to generate an FCG pattern with a condensation focus, a converging condensation ring and a diverging converging ring (Figure 8.14 (c)).

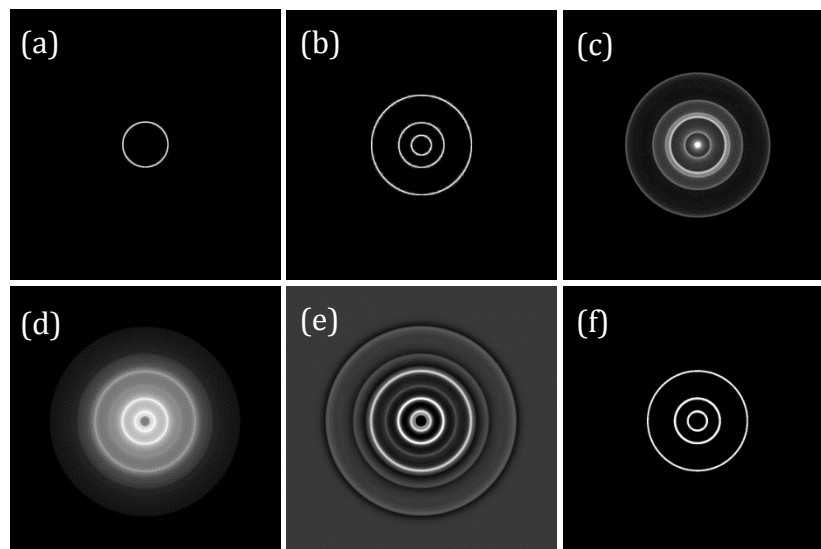


Figure 8.14 Simulated images of an annular primary beam of 1.08 mm inner radius (a), three ideal Debye rings (0.46 mm, 1.08 mm and 2.43 mm inner radius) (b), their FCG pattern (c), the recovered image prior to any processing (d), the processed image after applying a bandpass filter (e) and the recovered Debye rings after a 170 dc level (f).

As developed in Section 8.1.1.1, the Debye rings were recovered by convolving single FCG images with the annular beam (Figure 8.14 (d)) and applying bandpass filtering (Figure 8.14 (e)) and removal of a dc level (Figure 8.14 (f)).

The images presented in Figure 8.14 were considered as the ‘ideal’ simulated data that acted as a mean of comparison to the reconstructed Debye rings obtained under non-ideal conditions. A quantitative comparison of the Debye rings and the recovered Debye rings is displayed in Figure 8.15. The scattering maxima positions of the recovered data are, within experimental errors, consistent to the scattering angles of the diffraction data at 9.1° , 19.8° and 38.7° . Assessment of the successful recovery of Debye rings obtained within this section will focus on the diffraction maxima positions, due to the various conditions under investigation.

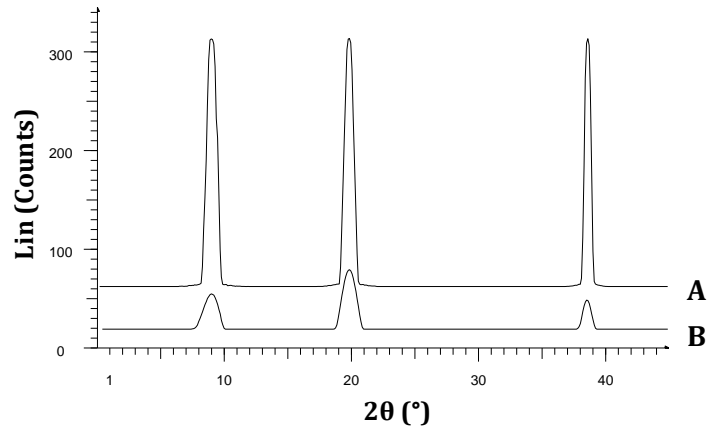


Figure 8.15 Radial integration of the simulated image consisting of three Debye rings (A) and corresponding recovered image (B).

(a) Addition of noise

As previously discussed, an image can be recovered by deconvolution of the convolved image (see Figure 8.17). However, when a noise distribution is introduced to the image, deconvolution is proven problematic for the recovery of the original image, as shown in Figure 8.16. Deconvolution was performed using ImageJ software's *'Deconvolve'* function.

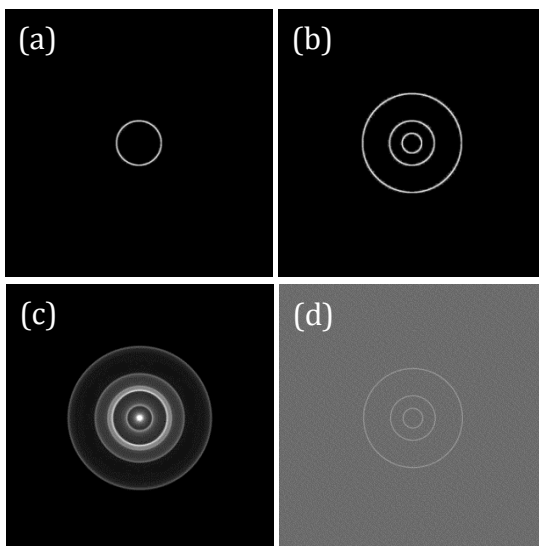


Figure 8.17 Simulated images of an annular aperture (a), three Debye rings (b), their convolved FCG pattern (c) and the recovered Debye rings via deconvolution (d).

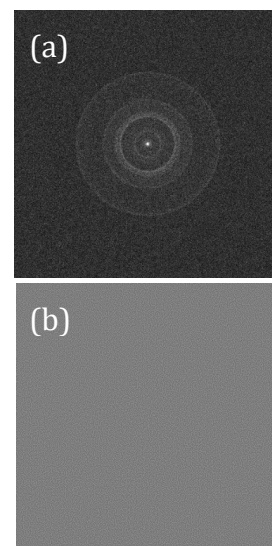


Figure 8.16 Simulated image of a noisy FCG pattern (a) and the recovered image via deconvolution (b).

Therefore, the effect of noise on the reconstruction procedure developed in Section 8.1.1.1 was investigated. A normally distributed (Gaussian) random noise with $\bar{\mu}=0$ and $\sigma=25$, as provided by the built-in 'Add Noise' function of ImageJ software, was gradually added to the simulated annular aperture and Debye rings (prior convolution) for a better resemblance to the empirical data (Figure 8.18).

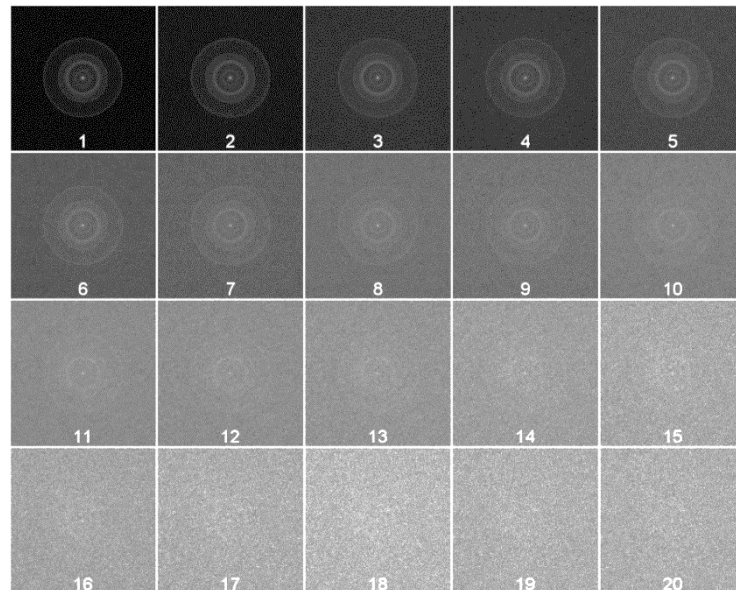


Figure 8.18 Simulated FCG images with increasingly added noise. The FCG images were obtained by convoluting a series of noisy images of three Debye rings (0.46 mm, 1.08 mm and 2.43 mm inner radius and 0.08 mm thickness) with an equivalent series of noisy images of an annular beam of 1.08 mm inner radius and 0.08 mm thickness.

As observed in Figure 8.18, the FCG patterns are significantly obscured by noise, especially after image number 11. However, upon convolution with the annular mask, the Debye rings were recovered even in the presence of extreme noise, as demonstrated in Figure 8.19 and Figure 8.20.

Visual inspection of the recovered Debye rings, prior processing as shown in Figure 8.19, indicates great resemblance to the recovered Debye rings obtained from noiseless data. Post-processed images have random discontinuities in the intensity of the recovered Debye rings around their circumference, especially after image number 5 (Figure 8.20). This is a result of the added (random) noise in the FCG data,

that interferes with the structure of the Debye rings and once a dc level was removed, the intensity of the Debye rings appeared non-uniform.

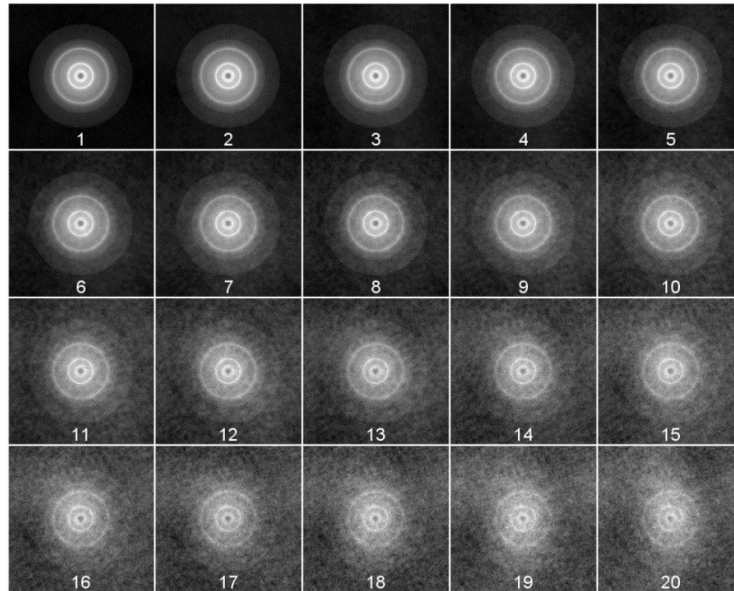


Figure 8.19 Reconstructed images of the Debye rings, as obtained by the convolution of noisy FCG images (presented in Figure 8.18) with an annular beam of 1.08 mm inner radius and 0.08 mm thickness.

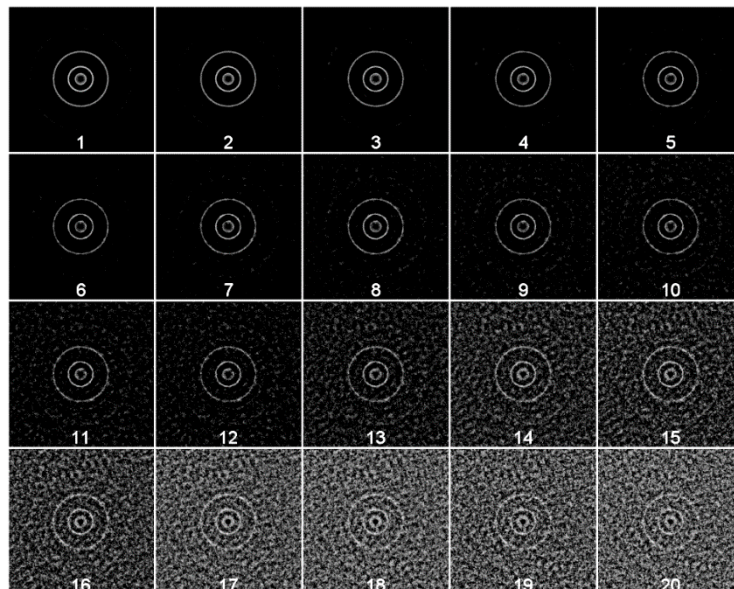


Figure 8.20 Post-processed reconstructed images of the Debye rings, as obtained by the convolution of noisy FCG images with an annular beam of 1.08 mm inner radius and 0.08 mm thickness, after a dc level removal (between 100-180).

Quantification of the noise added to the diffraction data and the noise present in the recovered Debye rings prior to any further processing was achieved by calculating their peak signal to noise ratio (PSNR). The relationship between PSNR of FCG and recovered data is presented in Figure 8.21. The PSNR of the recovered images is considerably higher than the PSNR of the diffraction images (with some exceptions), indicating that the Debye rings were reconstructed effectively even from diffraction data with significantly low SNR.

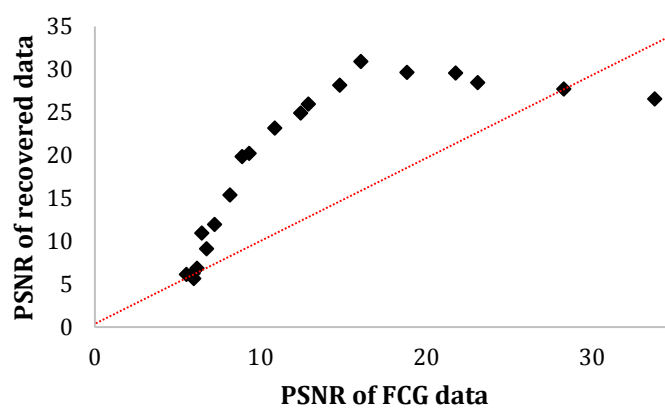


Figure 8.21 Relationship between PSNR of the diffraction (FCG) data and corresponding recovered Debye cones. The red dotted line is a reference point to mark $y=x$.

The recovery of scattering maxima positions was assessed by comparing the scattering angles of the recovered Debye rings as obtained from noiseless data, and from a series of FCG data with increasing random noise. Figure 8.22 illustrates the differences in the scattering maxima as the SNR decreases, indicating a consistency in the 2θ angles. However, the intensity of the peaks decreases with lower SNR.

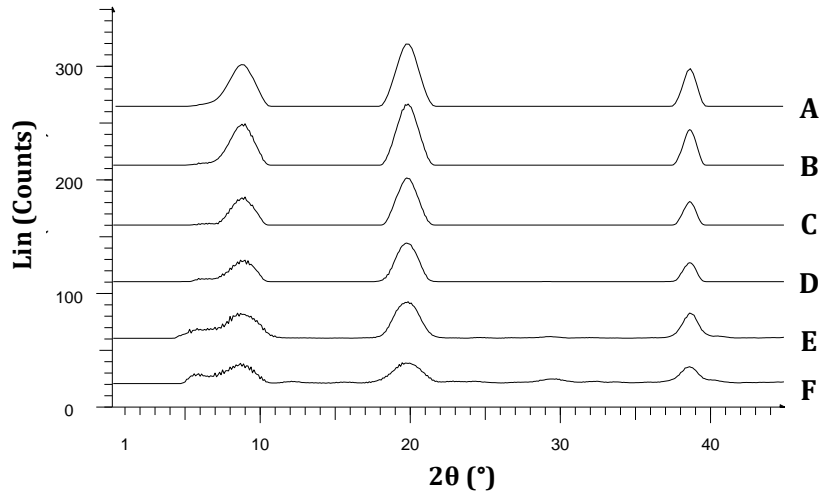


Figure 8.22 Radial integration of recovered images from noiseless FCG data (A) and from FCG data with a PSNR of 33.79 (B), 18.85 (C), 10.87 (D), 6.45 (E) and 5.97 (F).

In this section, it was shown that the scattering maxima positions can be recovered by coded aperture analysis, even in the presence of extreme noise, in contrast to deconvolution.

(b) Limited area of FCG data

During a typical FCG experiment (empirical), the detector area is limited. For example in this study, a detector with $\sim 13 \times 13$ mm active area was employed; hence the diffraction data available for the reconstruction of the Debye rings was usually between ~ 23 - 28% of the complete FCG pattern, within a 2θ range of 10° - 60° . It is noteworthy, that for this reason the inner condensation rings are the only ones captured during a typical FCG experiment and none of the outer condensation rings.

Thus, FCG diffraction patterns were limited to specified circular and rectangular areas, either centrally or peripherally to the central axis, by removing all data from these areas. This aimed at the examination of the effect of incomplete data to the recovery of conventional XRD data. The limitations applied to each FCG image indicating the available data area and its percentage, with respect to the complete diffraction pattern are listed in Appendix C.1 (Table C.1).

A representative example of the limited patterns with their corresponding recovered Debye rings is seen in Figure 8.23. Comparison of the scattering profiles of the recovered images was achieved by their radial integrations, as presented in Figure 8.24.

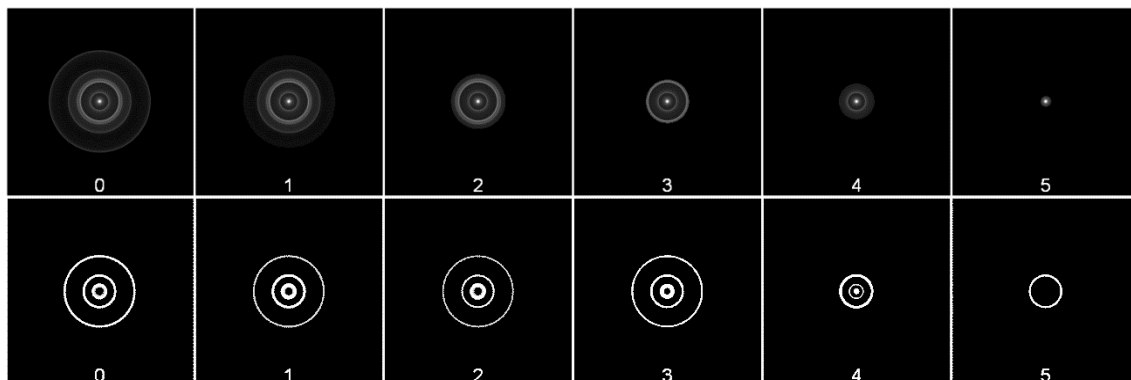


Figure 8.23 Simulated diffraction images with limited FCG area (top) and corresponding reconstructed images of Debye rings (bottom). Top and bottom images numbered 0 illustrate the complete FCG pattern and the corresponding reconstructed image, respectively.

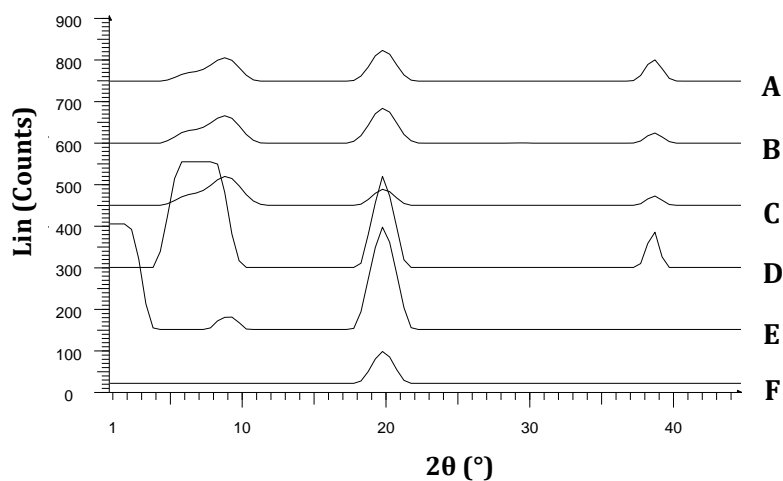


Figure 8.24 Radial integration (A-F) of recovered images from a limited area of FCG data (0-5).

Recovered images indicated that the Debye cone at 19.8° 2θ angle (0.207 nm) could be reconstructed even with the lowest data availability of $\sim 1\%$, which corresponds to a condensation focus, as indicated by the reconstructed image number 5 in Figure 8.23 and its scattering profile in Figure 8.24 (F).

Processing of all reconstructed images obtained from limited data area, circular or square, centrally or peripherally to the primary axis, indicated that scattering maxima positions were reconstructed effectively when the complete pattern of either the inner or outer condensation ring was available in the diffraction data, including the condensation focus.

In summary, it was shown that the scattering maxima can be reconstructed even with limited FCG data in the presence of either a condensation focus, an inner condensation ring or an outer condensation ring.

(a) Increased thickness of the annulus

Further investigation into this annular coded aperture system was achieved by examining various alterations to the thickness and circular symmetry (next section (d)) of the annular mask.

An initial annulus of 0.03 mm wall thickness and 1.18 mm outer radius was employed. The wall thickness of the annulus was increased progressively in steps of 0.05 mm up to a solid disc aperture (Appendix C.2, Figure C.1). The effect of a thicker annulus on the reconstructed image was visually assessed and the scattering angles of the reconstructed images were quantitatively evaluated by plotting their radial integrations.

The Debye rings were reconstructed effectively, until a certain annulus' wall thickness. All three Debye rings were recovered when the wall thickness of the annular aperture was 0.28 mm or smaller. However, the two condensation rings at 9.1° and 19.8° 2θ angles, started to merge into a broad ring when the wall thickness of the annular beam increased beyond 0.28 mm, preventing the reconstruction of the smallest Debye cone as demonstrated by Figure 8.25 and Figure 8.26.

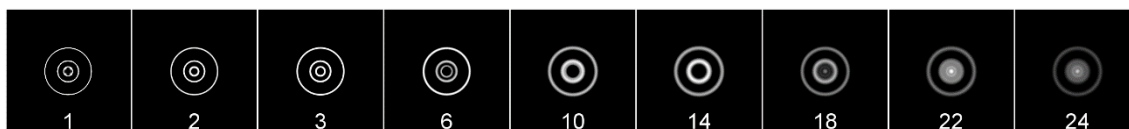


Figure 8.25 Reconstructed (post-processed) images of the Debye rings obtained by the convolution of the diffraction patterns with annular beams of increasing wall thickness.

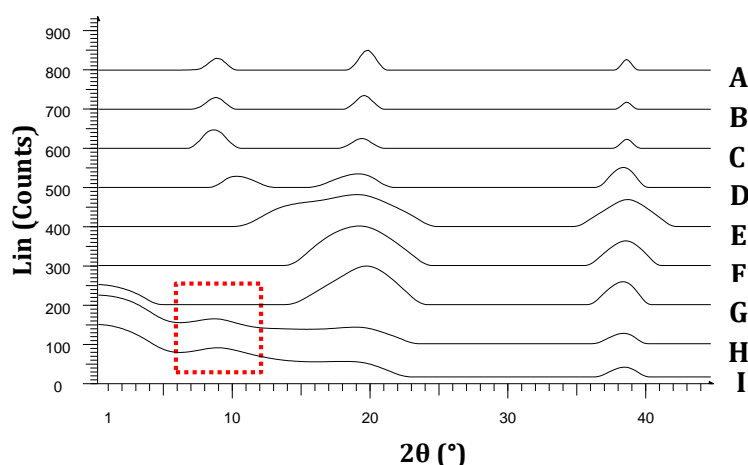


Figure 8.26 Scattering signatures of the recovered Debye rings reconstructed with an annular beam of 0.03 mm (A), 0.08 mm (B), 0.13 mm (C), 0.28 mm (D), 0.48 mm (E), 0.68 mm (F), 0.88 mm (G), 1.08 mm (H) and 1.18 mm (I) wall thickness.

As observed from the scattering signatures of the recovered Debye rings in Figure 8.26, before merging of the two peaks at 9.1° and 19.8° into one broad signal, the peaks shifted towards higher and lower 2θ angles, respectively (Figure 8.26 (D)). In addition, at 0.28 mm wall thickness of the primary beam (Figure 8.26 (D)), the high angle Debye cone shifted from 38.7° towards lower 2θ angle ($\sim 38.4^\circ$). However, when the primary beam's wall thickness was increased beyond 0.68 mm, the Debye ring at 19.8° was recovered successfully (Figure 8.26 (F-I)).

Taking into account that the Debye cone with the largest radius was separated by the mid-radius Debye cone by more than 50% of the distance the latter was separated by the Debye cone with the smallest radius. For this reason, the high 2θ

Debye cone was reconstructed even when the annulus' wall thickness was increased significantly (up to a disc). However, when the annular beam's thickness increased to an extent that the aperture appeared more similar to a broad δ -function (after image number 18 Figure 8.25; 0.88 mm wall thickness), the smallest Debye cone was also reconstructed, as seen in image number 24 of Figure 8.25. The diffractogram obtained from image number 24 is presented in Figure 8.26 (I), where the diffraction signal of the smallest Debye cone at $\sim 9.1^\circ$ is apparent (see red dotted box).

In summary, the scattering maxima were reconstructed effectively even with annuli of significantly increased wall thickness, although up to a certain extent. A considerably high wall thickness caused broadening and merging of adjacent scattering peaks. However, when the annulus approached a solid disc, it acted as a form of extremely broad δ -function with some reconstruction abilities.

(b) Elliptical aperture

Alternatively to an annular aperture, an elliptical aperture of varying degrees (Appendix C.3, Table C.2) was employed in order to investigate the effect of circular distortion on the reconstruction abilities of the annular coded aperture.

The circular symmetry of a 2.43 mm radius annular aperture was distorted to create elliptical apertures with major axis in the x direction (Appendix C.3, Figure C.2). The Debye rings (Figure 8.14 (b)) were convolved with each elliptical beam to generate an FCG diffraction pattern that was then convolved with the corresponding elliptical beam to reconstruct the initial Debye cone image.

The Debye rings were reconstructed even with severe distortion of the annulus' circular symmetry, as illustrated in Figure 8.27. The scattering profiles of the reconstructed Debye rings obtained by radial integration of the recovered images are presented in Figure 8.28.

The reconstruction was more effective when the dimensions of the elliptical apertures were greater than the diameter of the Debye rings. In cases where the ellipses' dimensions were smaller than the diameter of the Debye rings (e.g. ellipses

number 8 - 11), interference between the ellipse and the Debye rings was observed that influenced the recovery (intensity distribution) of the latter.

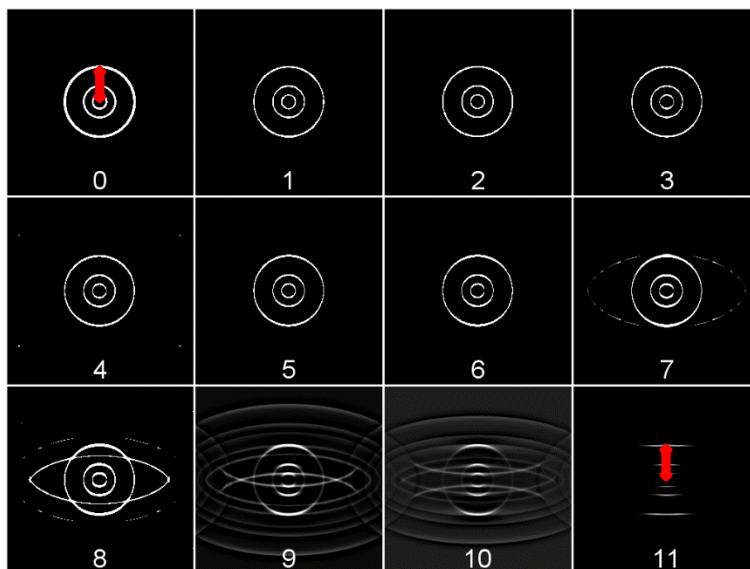


Figure 8.27 Reconstructed (post-processed) images of the Debye rings obtained by the elliptical apertures with their major axis in the x direction.

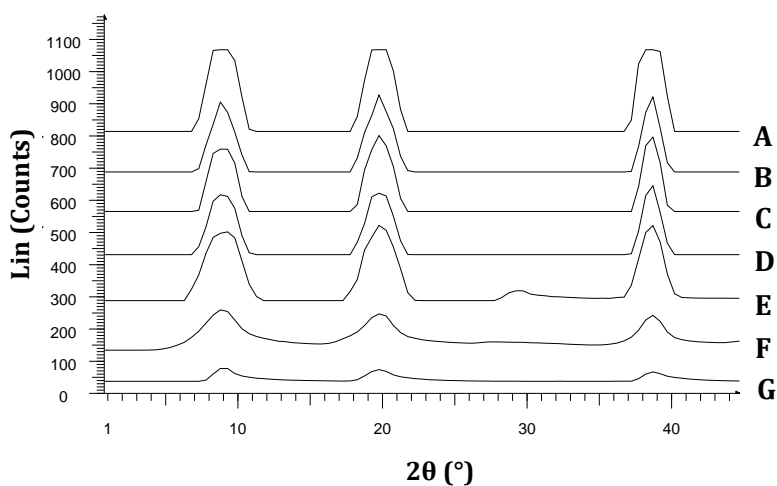


Figure 8.28 Scattering signatures of the Debye rings reconstructed with an annular aperture (A) and with elliptic apertures with x major axis; ellipses number 2 (B), 4 (C), 6 (D), 8 (E), 10 (F) and 11 (G).

When the interference occurred at severe levels, it prohibited the recovery of the overall shape of the Debye rings (Figure 8.27). Nonetheless, the radius of the Debye rings and thus their scattering angles can be determined by measuring the distance between the three horizontal lines (6 mirror-imaged lines) shown in image number 11 in Figure 8.27. These distances correspond to the radius of the Debye rings as indicated by the red arrows in Figure 8.27 (images number 0 and 11). Recovery of the scattering maxima from an extreme elliptical aperture was also confirmed by their positions. The positions of the recovered scattering maxima were (within experimental errors) the same as the original diffraction data, as indicated in Figure 8.28 (G).

To summarise, the Debye rings were efficiently recovered even with significant elliptical distortion of the circular symmetry of the annulus. Nevertheless, interference with the structure of the Debye rings was observed when the elliptical apertures' minor axis was shorter than the Debye rings' diameter. Even in these particular cases, the scattering maxima positions were yet recovered.

8.1.2 Pseudo-empirical data

The previous section established the ability of an annular coded aperture with simulated experiments. A pseudo-empirical approach into the recovery of Debye rings is presented in this section, while Section 8.1.3 examines empirical FCG data. Figure 8.29 provides a brief description of the nature of experiments performed in Section 8.1.1 – Section 8.1.3.

Section 8.1.1 simulated data

Section 8.1.2 (simulated AB) * (empirical DC) = pseudo-empirical FCG

(pseudo-empirical FCG) * (simulated AB) = pseudo-empirical \widehat{DC}

Section 8.1.3 (empirical FCG) * (simulated AB) = pseudo-empirical \widehat{DC}

Figure 8.29 Details on the nature of experiments performed throughout Section 8.1.

Pseudo-empirical data involved convolution of an empirical diffraction image with a simulated image of an annular aperture to produce pseudo-empirical FCG patterns. The resulting FCG image was then convolved with the simulated annular beam to recover the Debye rings (Figure 8.29). Recovered images were then processed in terms of bandpass filtering and dc level removal, as developed in Section 8.1.1.1. These experiments acted as a step towards the recovery of Debye rings from empirical FCG data.

A conventional diffraction pattern from an Al_2O_3 sample (*S1*) was acquired by a pinhole collimator, as described in Section 6.3.2.2. An annular aperture of 14.2 mm inner radius and 0.25 mm wall thickness was employed to recover the Debye rings illustrated in Figure 8.30 (left). The reconstructed image presented in Figure 8.30 (right) demonstrates recovery of the empirical Debye rings.

Comparison of the scattering profile of the reconstructed image to the initial empirical image is presented in Figure 8.31. It seems that there is a significant correspondence between the diffraction maxima positions of the reconstructed image and the empirical diffraction image. However, some of the low intensity peaks at $\sim 21.7^\circ$ and $\sim 27.6^\circ$ 2θ of the empirical diffraction image were not recovered.

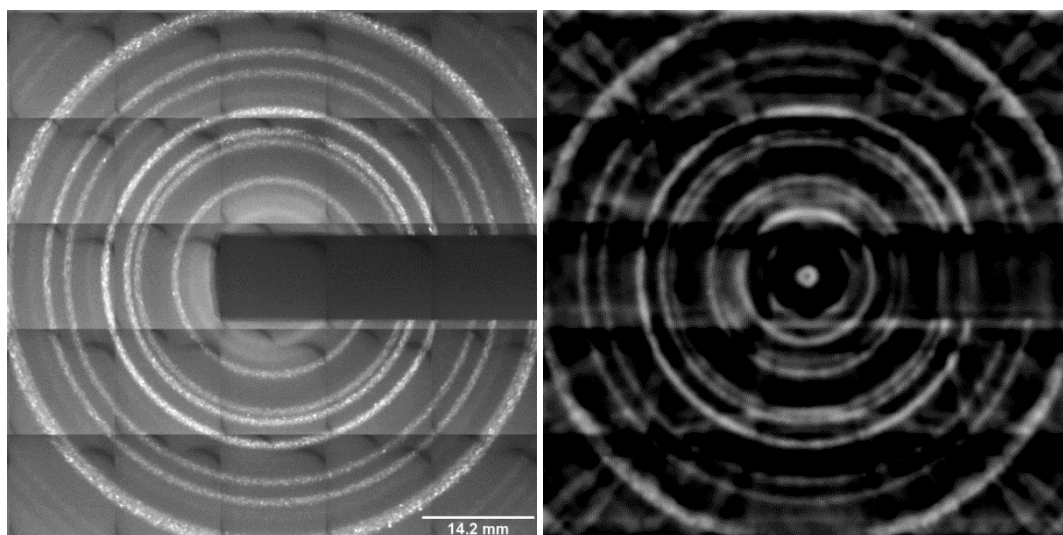


Figure 8.30 Empirical diffraction image from an Al_2O_3 sample (*S1*) illustrating 2θ angles from $\sim 8^\circ$ - 36° (left) and its reconstructed image (right) after convolution with an annular aperture of 14.2 mm inner radius and 0.25 mm wall thickness.

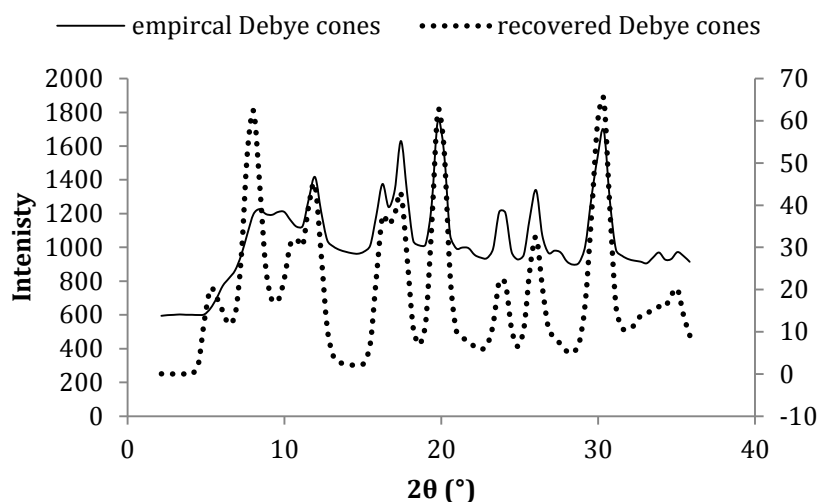


Figure 8.31 Scattering signatures of the empirical diffraction image from an Al_2O_3 (S1) sample and of the corresponding reconstructed diffraction pattern. The profile of the reconstructed diffraction image is displayed on a secondary axis for presentation purposes.

Even though there is an additional peak at 5.28° 2θ angle for the reconstructed image (Figure 8.31), the detector was only able to capture scattering angles between $\sim 8^\circ - 36^\circ$, as previously discussed, due to the primary beam stopper blocking the low 2θ angles. Therefore, any peaks outside this 2θ range are considered as artefacts.

As described earlier in this chapter, the inherent artefacts in the reconstructed image are in the form of additional rings that can generally be removed by the post-processing procedure. However, with empirical data, the intensity of Debye rings differs around the circumference. Therefore, the effect of non-uniform intensity around the circumference of the Debye rings on their recovery was investigated by converting the empirical diffraction image of Al_2O_3 into a binary image (Figure 8.32 (left)). The same decoding procedure was followed as with the raw data (described above) and the recovered image is presented in Figure 8.32 (right)). Comparison of reconstructed images as obtained by a raw diffraction image and by a binary diffraction image of Al_2O_3 , indicates good agreement between their scattering maxima positions (of the high intensity peaks). The additional ring at 5.28° 2θ angle is also present in the reconstructed Debye rings arising from the binary diffraction

image. This can be clearly observed from a radial integration of the reconstructed image (binary) illustrated in Figure 8.33.

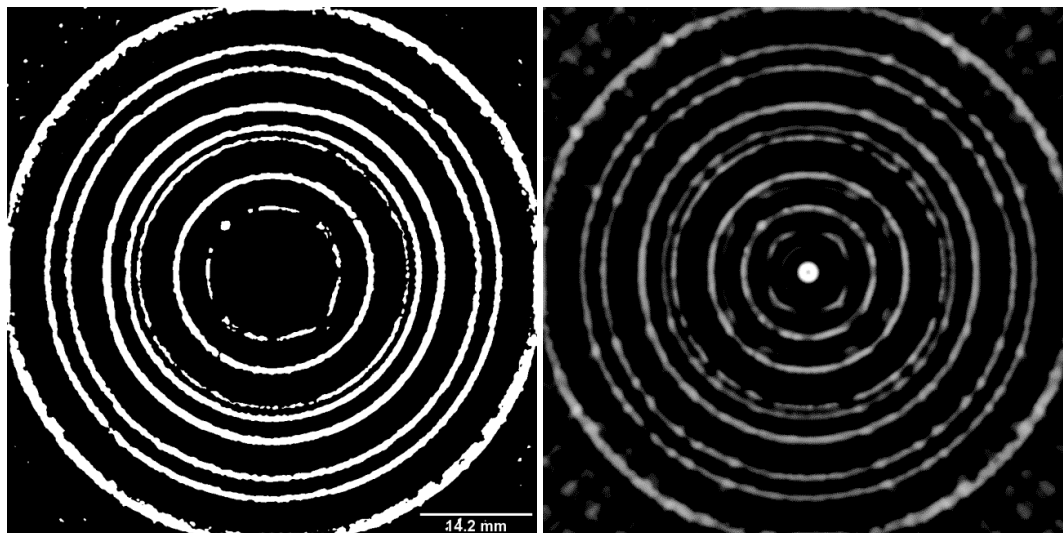


Figure 8.32 A binary empirical diffraction image from an Al_2O_3 sample (S1) illustrating 2θ angles from $\sim 8^\circ$ - 36° (left) and its reconstructed image (bottom) after convolution with an annular aperture of 14.2 mm inner radius and 0.25 mm wall thickness.

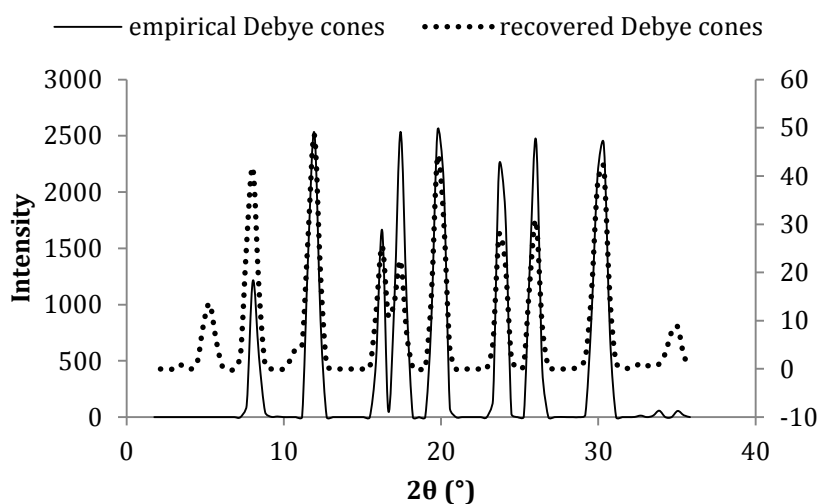


Figure 8.33 Scattering signatures of the empirical binary diffraction image from an Al_2O_3 (S1) sample and of the corresponding reconstructed diffraction pattern. The profile of the reconstructed diffraction image is displayed on a secondary axis for presentation purposes.

8.1.2.1 Preferred orientation

Recovery of Debye rings from samples with preferred orientation was attempted in a similar manner to the recovery of aluminium oxide's Debye rings from pseudo-empirical data.

Complete diffraction patterns of each Al sample (*Al_1* – *Al_4*) analysed in Section 7.4.2, were convolved with a simulated annular beam of 8.8 mm inner radius and 0.4 mm thickness. The resulting images (i.e. FCG patterns) were when convolved with the annular beam to reconstruct the initial empirical diffraction patterns of Al samples. The reconstructed images of the Debye rings after post-processing are presented in Figure 8.34 (rec_a-rec_d).

Visual observation and comparison of the reconstructed diffraction patterns to the empirically obtained patterns (Figure 8.34 (a-d)), suggest effective recovery of the scattering maxima number, position and geometry. All five Debye rings are present in the recovered data at the same scattering maxima positions (within experimental errors) and without the presence of additional peaks, as demonstrated by the diffractograms in Figure 8.34. It is also noteworthy, that the relative intensities of the scattering maxima were approximately recovered (Figure 8.34).

As more sample orientations were introduced to the specimen, the uniformity of the intensity around the recovered Debye rings was increased, similarly to the empirically obtained diffraction patterns. Additionally, when discontinuous Debye rings were present, for instance in the Debye ring with the lowest scattering angle, emphasised by a dotted red circle in Figure 8.34 (a), the geometry of the Debye arcs was recovered in the reconstructed image (Figure 8.34 (rec_a)).

Equation (7.11) (see Section 7.4.2) was employed to quantify and characterise the uniformity of each Debye cone for the reconstructed images, and the results are presented in Figure 8.35.

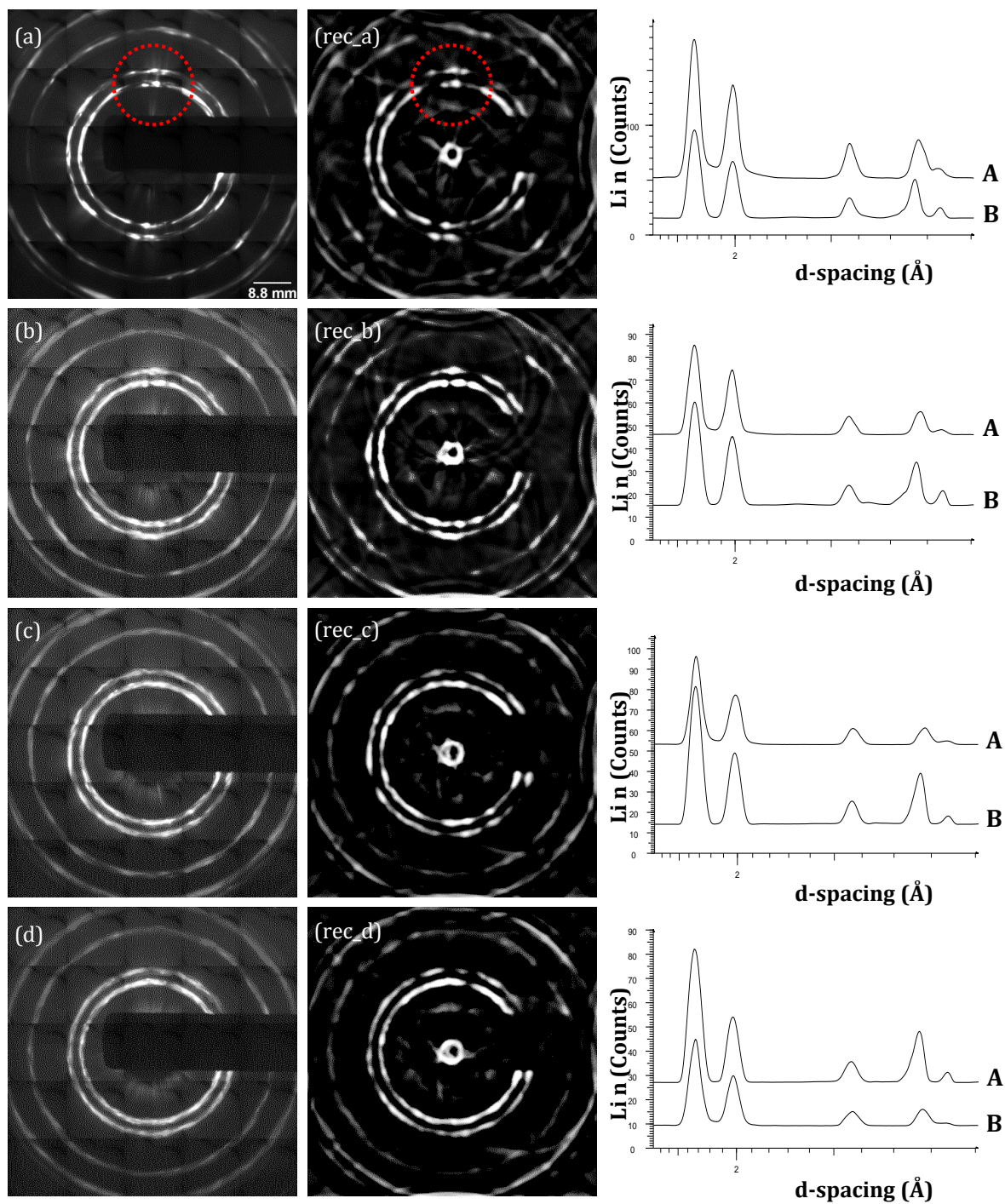


Figure 8.34 Pseudo-empirical recovered diffraction patterns from *AL_1-AL_4* (rec_a-rec_d) and the corresponding empirical diffraction patterns from *AL_1-AL_4* samples (a-d). The corresponding scattering signatures of the empirical (A) and recovered (B) diffraction patterns are presented for each Al sample next to their diffraction images.

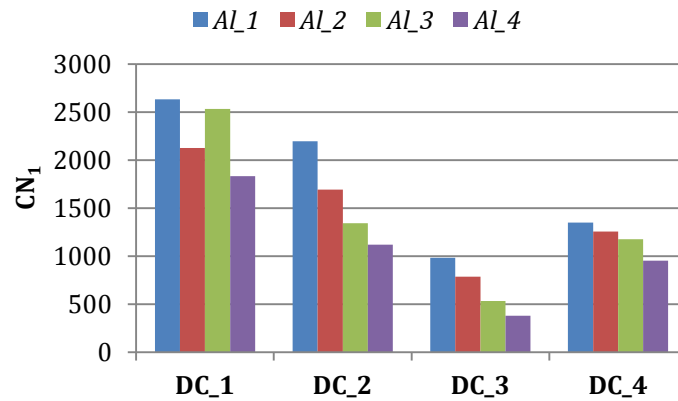


Figure 8.35 The relationship between intensity differences (i.e. CN_1) in Debye rings by an angular integration at 17.48° (DC_1), 20.22° (DC_2), 28.74° (DC_3) and 33.84° (DC_4) scattering angles for the reconstructed diffraction images from $Al_1 - Al_4$ samples.

Quantitative comparison of the intensity uniformity of each Debye ring, demonstrates an increase in the uniformity (decrease in CN_1), as more samples were added at a random orientation (Section 6.2 (c)), except for the diffraction ring at 17.48° 2θ angle for Al_3 sample. Comparing Figure 8.35 with Figure 7.53 (Section 7.4.2), where the conventional XRD data were analysed in the same manner (Equation (7.11)), the recovered data seem to possess greater intensity uniformity than original diffraction data. This however, may be a result of blurring around the Debye rings, which increases the intensity distribution.

8.1.2.2 Large grain size

Conventional diffraction patterns of a series of Cu samples, presented in Figure 7.61 (Section 7.5.2), were convolved with a simulated image of an annular beam (10 mm radius and 0.4 mm thickness). Pseudo-empirical FCG patterns were then convolved with the annular beam to reconstruct the empirical image of the Debye rings. Figure 8.36 presents the empirical diffraction images of samples $Cu_1 - Cu_4$ (a-d) and the corresponding reconstructed images (rec_a-rec_d).

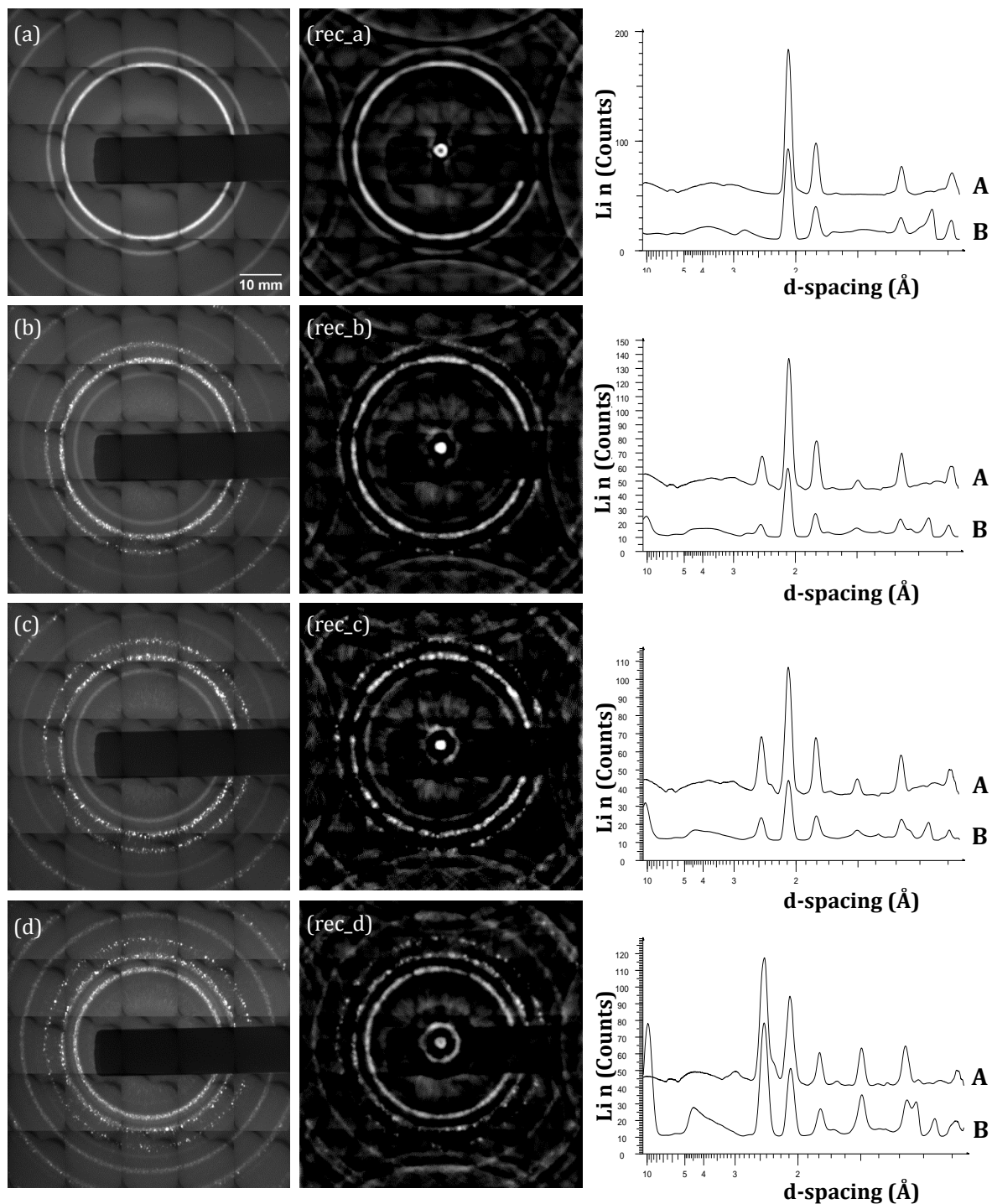


Figure 8.36 Pseudo-empirical recovered diffraction patterns from *Cu*₁-*Cu*₄ (rec_a-rec_d) and the corresponding empirical diffraction patterns from *Cu*₁-*Cu*₄ samples (a-d). The corresponding scattering signatures of the empirical (A) and recovered (B) diffraction patterns are presented for each Cu sample next to their diffraction images.

Original and recovered images are shown to be similar. Their diffraction profiles suggest recovery of scattering maxima at the same positions, within experimental errors, to original diffraction data (see diffractograms in Figure 8.36). Similarly to recovered data from Al samples, the relative intensities of the scattering maxima from Cu samples were also recovered to some extent, especially for the high intensity peaks (Figure 8.36).

There is an additional peak in the recovered data at ~ 0.118 nm due to the inherent artefacts of the reconstruction procedure, arising from $2R_{AB} + R_{DC[331]}$ as rationalised in Figure 8.6; where $R_{DC[331]}$ is the radius of the Debye cone corresponding to the 331 reflection from Cu at 0.109 nm. Moreover, similarly to Al_2O_3 and Al, low 2θ peaks at >10 nm (not shown in the diffractograms) can be seen in the recovered data (Figure 8.36 (rec_a-rec_d)) as a consequence of the reconstruction process. However, similarly to the integration of Al_2O_3 and Al samples in the previous sections, the measurable 2θ angle range was restricted between $\sim 8^\circ - 36^\circ$; hence, any rings outside this region are considered reconstructed artefacts.

Further comparison of the scattering maxima and recovered images, indicated good agreement, in terms of grain size increase, as the heating temperature increased. Correspondence between recovered Debye rings and empirical Debye rings was quantitatively assessed by determining the average number and size of their scattering maxima spots from 10 repeated measurements, similarly to Section 7.5.2. The results of the average number of scattering maxima are presented in Figure 8.37.

The average number of scattering maxima decreases for each reconstructed Debye cone as the heat treatment's temperature and time increased i.e. from *Cu_2* to *Cu_4*. Comparison of the average number of scattering maxima of empirical (Figure 7.62) and reconstructed (Figure 8.37) data demonstrated a decrease in the average number of recovered maxima by $\sim 50\%$. This is thought to be as a result of blurring in the recovered images, causing scattering maxima spots to merge.

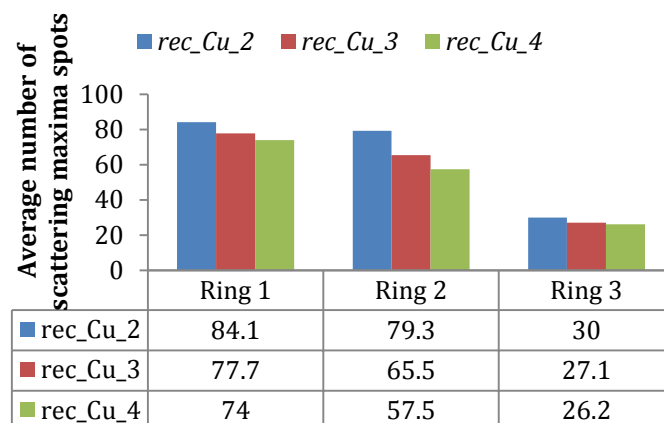


Figure 8.37 Average number of scattering maxima spots present in each recovered Debye ring at 0.209 nm (Ring 1), 0.181 nm (Ring 2) and 0.128 (Ring 3) from each Cu sample *rec_Cu_2* - *rec_Cu_4*.

The relationship between the scattering maxima of empirical and reconstructed data was then assessed by comparing their percentage decrease from *Cu_3* to *Cu_4*, as illustrated in Figure 8.38. Maximum percentage i.e. 100% of scattering maxima was appointed to the Debye rings of *Cu_2* sample, since the latter possessed the greatest uniformity in intensity, due to the highest number of scattering maxima spots. The scattering maxima labelled as 'Ring 2' at 0.181 nm (200 reflection from Cu) revealed greater resemblance to the original diffraction patterns than the scattering maxima labelled 'Ring 1' (0.209 nm 111 reflection from Cu) and 'Ring 3' (0.128 nm 220 reflection from Cu). This may be due to software errors and its inability to analyse fine or large particles as effectively as mid-size particles (e.g. in the case of scattering maxima at 0.181 nm).

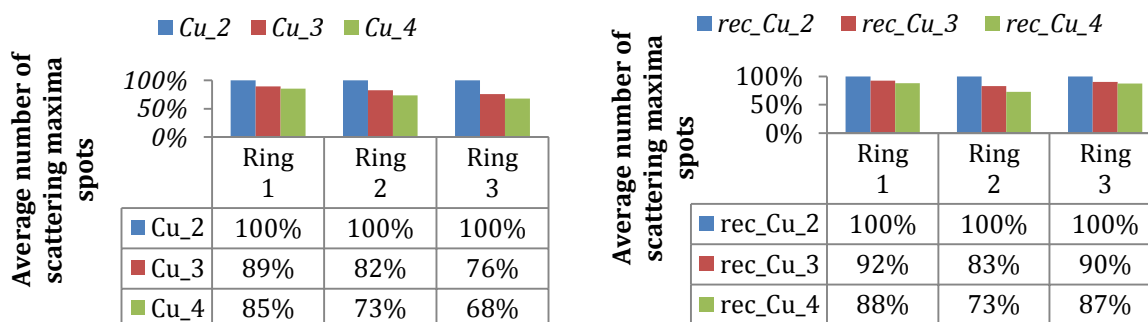


Figure 8.38 The percentages of average number of scattering maxima spots present in each Debye ring for the empirical diffraction patterns from samples *Cu_2* - *Cu_4* (left) and the recovered patterns *rec_Cu_2* - *rec_Cu_4* (right).

8.1.3 Empirical FCG data

The ability of the annular coded aperture to recover conventional XRD data was also assessed with empirical FCG data.

This involved the acquisition of a series of empirical diffraction caustic patterns, following the procedure described in Section 6.3.2.1. Each FCG image was convolved with a simulated primary beam, corresponding to the empirical primary beam's footprint on the sample, in terms of radius and thickness. The centre of the simulated primary beam was adjusted to correspond to the centre of the FCG pattern. Acquisition of the primary beam's footprint at the sample's position was not possible due to the limited translation capabilities of the detector.

It is important to take into consideration that decoding of FCG data and reconstruction of Debye rings can involve a single diffraction image, consisting of condensation rings corresponding to the desired recovered Debye rings. However, employment of a limited sequence of FCG images and appropriate summation of their recovered data can be considered as an analogous approach to the two-annulus system demonstrated in Section 8.1.1.2.

Therefore, a sequence of FCG images, typically 10 images, was captured over a range of sample-to-detector positions. The images were re-scaled as indicated by Figure 8.39.

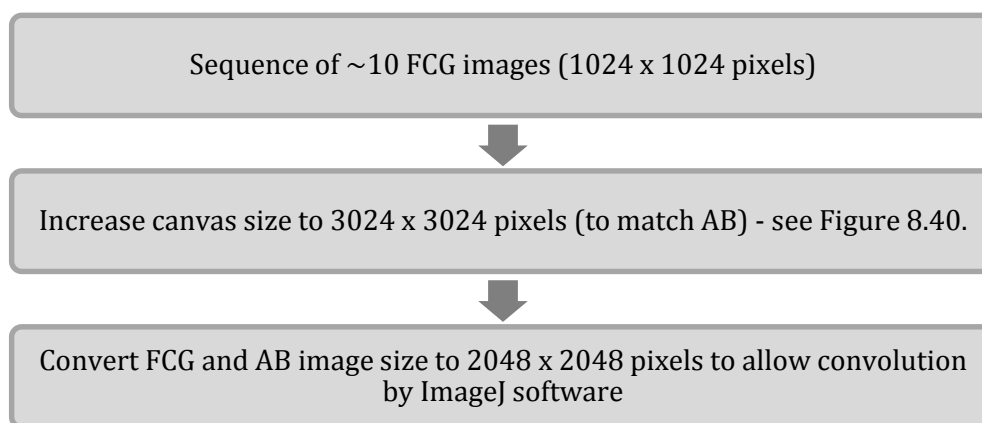


Figure 8.39 Diagram of the scaling steps followed with empirical FCG data images.

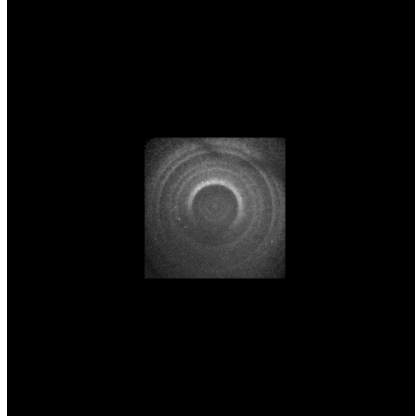


Figure 8.40 An FCG image from Al_2O_3 captured at 15 mm from the sample. The canvas size of the image was increased to 3024 x 3024 pixels by an opaque surrounding area.

This ‘multiple FCG images’ approach requires determination of the radius of the Debye cones at certain sample-to-detector distances and scaling of the recovered images to the greatest image size, in order to add all recovered images together. Consequently, once each FCG image was convolved with the primary beam, the recovered images were scaled to the size of the last image with the greatest sample-to-detector distance (D_{SD}). The scaling procedure was achieved by using Equation (8.1) to calculate the radius of the Debye rings for each recovered image (R_{DC_FCG}).

$$R_{DC_FCG} = D_{SD} [\tan(2\theta + \phi_m) + (\tan(2\theta - \phi_m))] \quad (8.1)^{\dagger\dagger}$$

The radius of Debye rings of every recovered image was divided by the radius of the Debye cone at the greatest sample-to-detector distance to obtain their scaling ratio. This ratio is independent of the scattering angle employed during the calculations.

^{††} For symbol ϕ_m refer to Section 5.1.

The scaled images were then all adjusted to the same canvas size for comparative purposes, as seen in Figure 8.41. The red dotted annular area indicates the Debye cone at $29.84^\circ 2\theta$ for all images (up to image number 28). The post-processing procedure described in Section 8.1.1.1 was employed (bandpass filter and dc level removal) for all recovered images presented in Figure 8.41. However, additional rings were still present in the recovered images and the diffractograms appeared noisy.

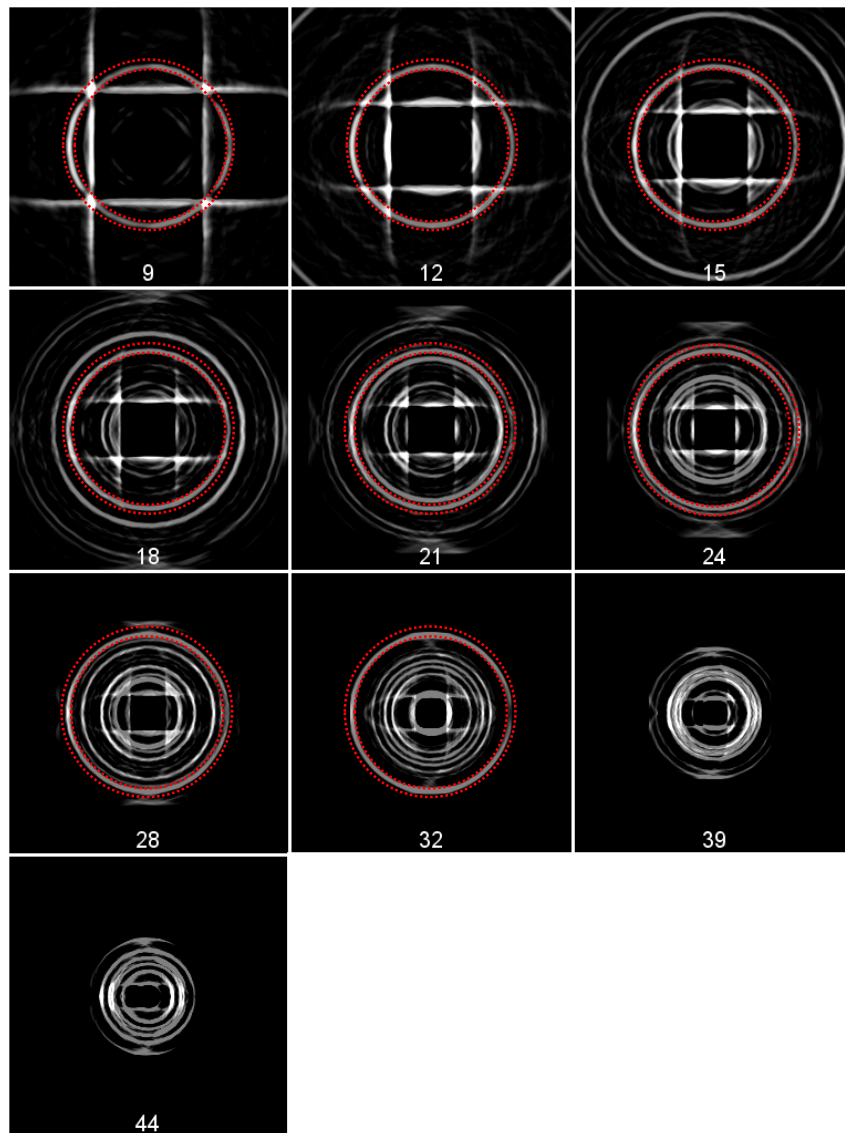


Figure 8.41 Recovered images of the Debye rings from an FCG sequence at 9 mm, 12 mm, 15 mm, 18 mm, 21 mm, 24 mm, 28 mm, 32 mm, 39 mm and 44 mm sample-to-detector distances.

The single recovered images were then added together, prior processing, to increase the SNR and produce a single enhanced image of the recovered Debye rings. Next, bandpass filtering and dc removal were applied to the resulting image. The post-processed reconstructed image was then added to a 180° rotated image of itself. This was performed in order to eliminate intensity variations around the circumference of the Debye rings induced by the empirical primary beam of non-uniform intensity. The final reconstructed image was compared to the empirical diffraction image of Al_2O_3 , as shown in Figure 8.42.

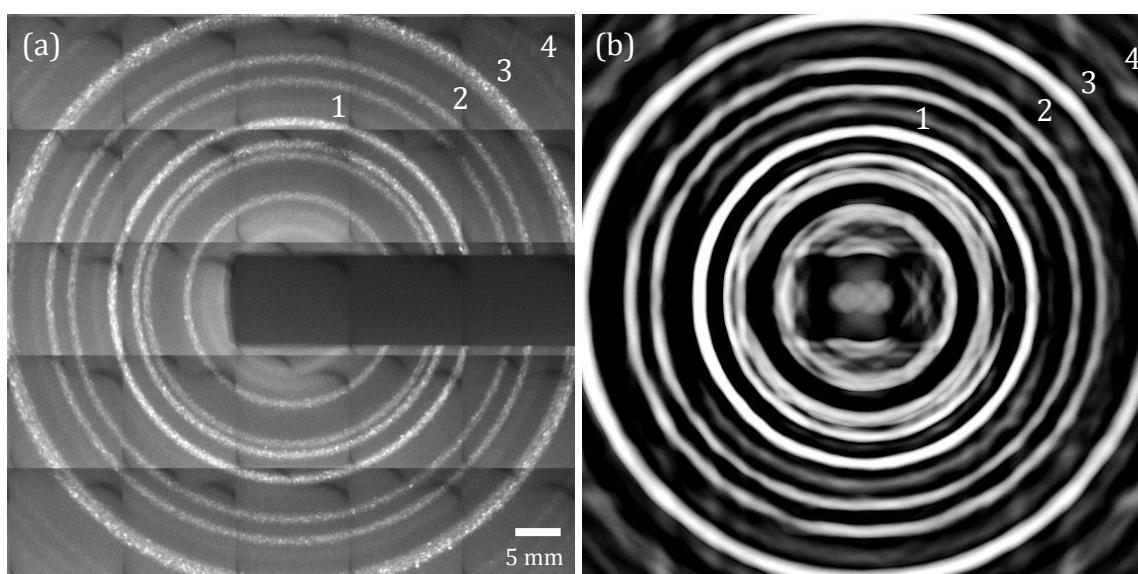


Figure 8.42 Empirical diffraction image (a) and reconstructed diffraction image (b) from an Al_2O_3 sample, as recovered from a sequence of empirical FCG data.

Qualitative comparison between the empirical diffraction image of Al_2O_3 and the recovered image signifies a good agreement of their scattering maxima. Even the low intensity Debye rings indicated by the numbers 1-4 in Figure 8.42 (a) were recovered effectively in the reconstructed image (Figure 8.42 (b)). It is important to highlight here, that Figure 8.42 (b) corresponds to a conventional diffraction image of 5024 x 5024 pixels size acquired at 10 minutes time exposure, and it was reconstructed from a limited number of 1024 x 1024 pixels FCG images, captured at 10 seconds time exposure.

Figure 8.43 provides a quantitative comparison of the scattering maxima positions, indicating a disagreement between the empirical and recovered data. Even though the scattering maxima from Al_2O_3 are present in the reconstructed image, there is a disparity in their positions. As it will be discussed later in Section 9.6, this is assumed to be either as a result of a number of inaccuracies in the instrumentation components' positions along the primary axis or due to the various conversion steps followed during reconstruction.

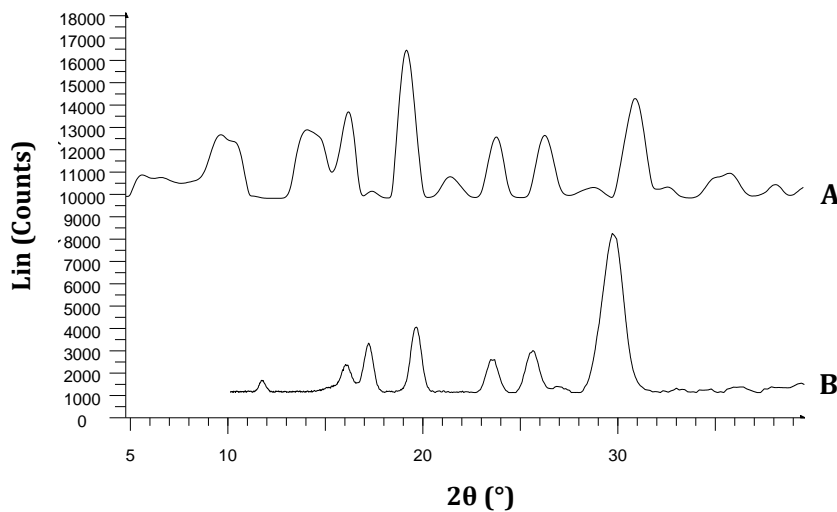


Figure 8.43 Comparison of the diffraction profiles from the recovered diffraction data from Al_2O_3 (A) with a limited sequence of FCG images with the empirical FCG diffraction profile from Al_2O_3 (B).

8.1.3.1 Non-ideal samples

The same procedure as described above was performed to recover conventional diffraction maxima from a limited number of FCG images from an Al sample (*AL_1*) exhibiting preferred orientation and from a Cu sample (*Cu_4*) with large grain size.

Figure 8.44 and Figure 8.45 illustrate the recovered diffraction images and scattering profiles from an Al and a Cu sample, respectively. As seen in Figure 8.44, the reconstructed diffraction pattern of Al resembles that of Figure 8.34 (a) to some extent. At the lower part of the image, highlighted by red dotted boxes, the non-uniform intensity geometry of the Debye rings, due to sample's preferred

orientation, is reconstructed similarly to the empirical diffraction pattern Figure 8.34 (a).

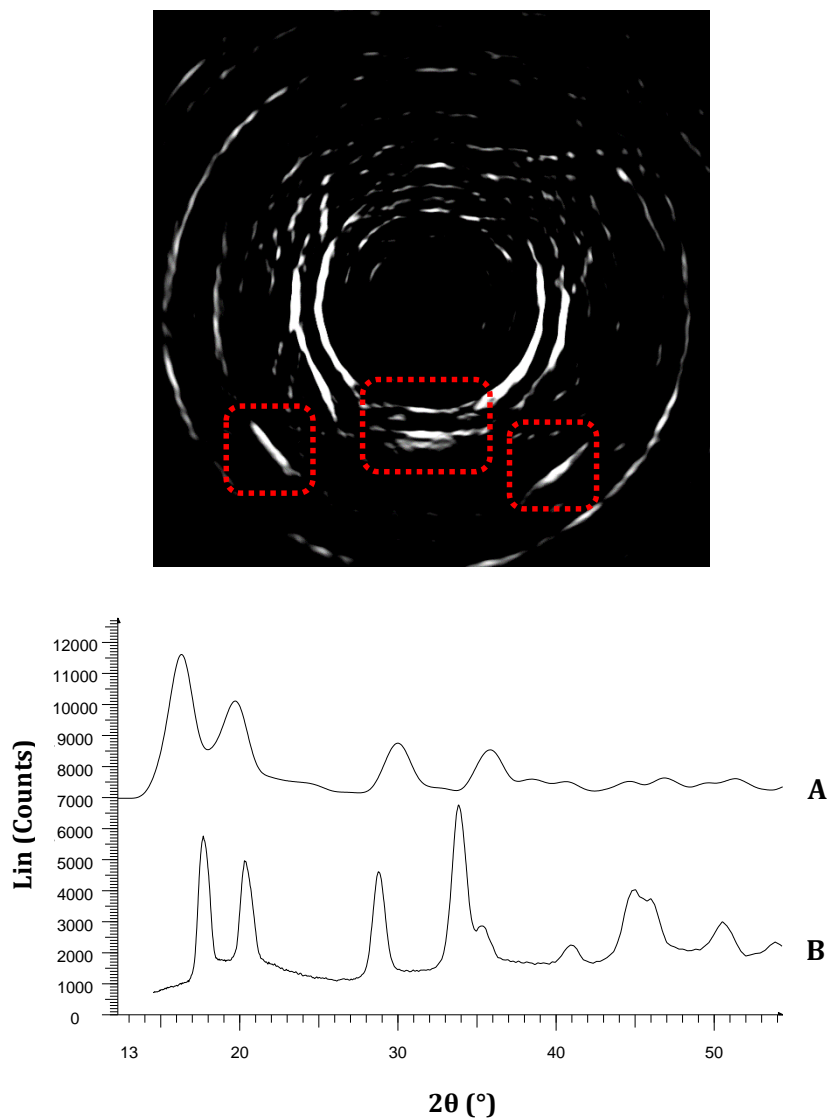


Figure 8.44 Recovered diffraction image (top) from a limited sequence of empirical FCG data obtained from an Al sample (*Al_1*). Scattering profiles (bottom) from the recovered diffraction image (A) and from the FCG data (B).

The lower part of the diffraction pattern was reconstructed more effectively than the upper part, due to the difference in intensity around the circumference of the empirical primary beam, that induced an additional pseudo preferred orientation effect to the FCG data. Quantitative comparison (Figure 8.44) of the scattering

signatures between empirical and reconstructed data show similar disagreements as with Al_2O_3 (Figure 8.43). Furthermore, the high scattering angles of Al were not reconstructed.

The recovered diffraction image of Cu (Figure 8.45) did not resemble the spottiness of the original Debye rings (Figure 8.36 (d)). However, all high intensity scattering maxima were reconstructed effectively, as seen in Figure 8.45. The scattering maxima positions of the recovered data do not come in agreement with that of the original data, similarly to the previously recovered images from empirical FCG data.

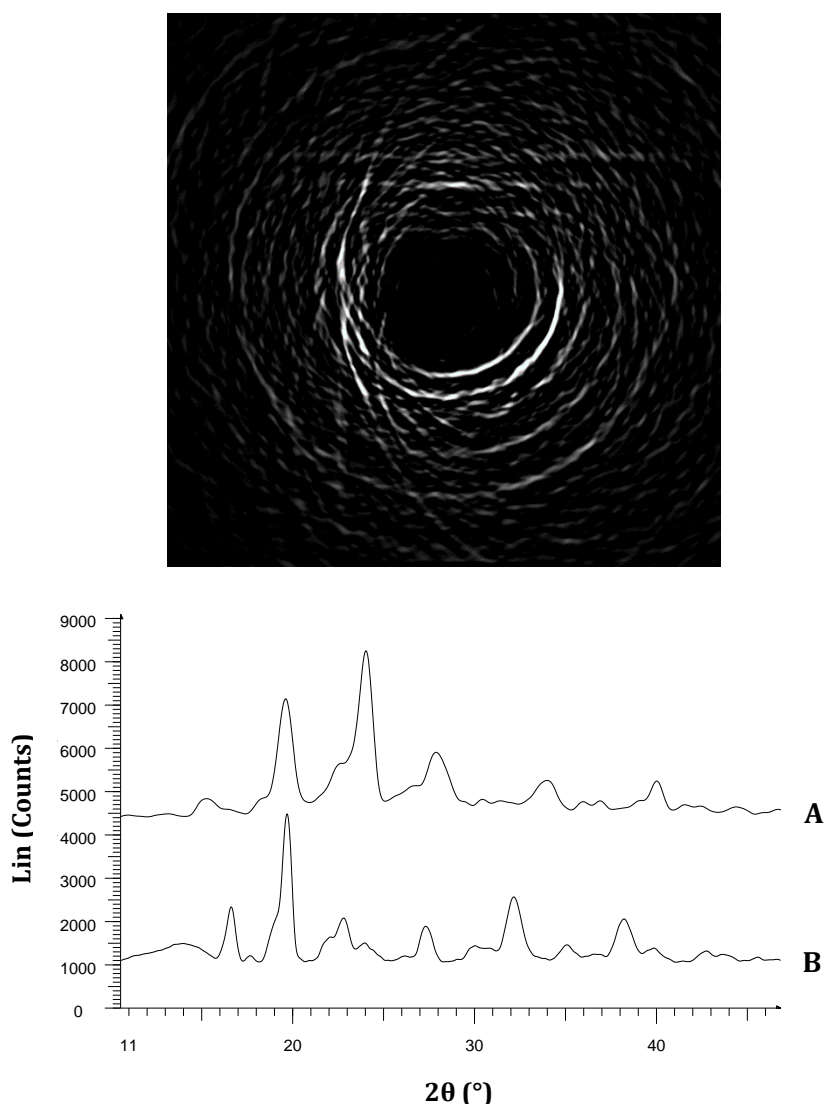


Figure 8.45 Recovered diffraction image (top) from a limited sequence of empirical FCG data obtained from a Cu sample (*Cu_4*). Scattering profiles (bottom) from the recovered diffraction image (A) and from the FCG data (B).

In summary, the ability of FCG to be treated as a pre-sample coded aperture was investigated. From the data obtained, it was shown that an annular pre-sample coded aperture system has the potential to recover conventional diffraction images from a restricted number of FCG images. The scattering maxima were effectively reconstructed and in some cases with details on their structure; however, their positions were not in agreement with conventional XRD data. The importance of this coded aperture system to recover Debye rings from single or several FCG data images was emphasised, as it has the ability to reconstruct a large diffraction area from a limited small data area.

8.2 Encoded primary beam

In this section, an encoded annular primary beam was considered as a pre-sample coded aperture; aiming to differentiate between converging and diverging condensation rings present in single FCG images.

An encoded primary beam includes an annular beam that possesses specific intensity characteristics around its circumference. This could involve a single or numerous, low or high intensity segments, arranged asymmetrically around the circumference of the annular beam. The asymmetric arrangement of these sections provides the encoded property of the aperture. When an encoded primary beam forces multiple Debye cones from a sample to merge, the latter will form a characteristic profile associated with the encrypted beam that specifies certain information on the scattering angle of the Debye cones.

8.2.1 Simulated data

Consider an encoded annular beam (Figure 8.46 (a)) and a set of Debye rings (Figure 8.46 (b)) of the same radius and thickness as with the example shown in Figure 8.3 (Section 8.1.1.1). Convolution of the encoded annular beam with the Debye rings generates an FCG pattern with coded condensation rings, as illustrated in Figure 8.46 (c). Both outer condensation rings possess the same structural profile with low intensity (or opaque) sections, at the same polar angles, as the primary beam's encoding (Figure 8.46). However, encoding of the inner condensation rings differs depending on their converging or diverging nature.

The rationale behind this is similar to the FCG patterns generated by samples exhibiting preferred orientation described in Section 7.4.1.

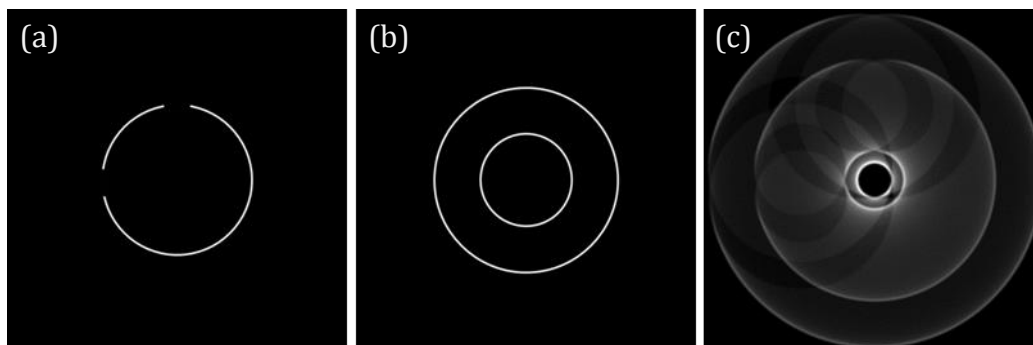


Figure 8.46 Simulated images of an encoded annular aperture of 1.34 mm radius and 0.08 mm thickness (a), two Debye rings of 0.75 mm and 1.65 mm radius and 0.08 thickness (b) and the FCG pattern produced by their convolution (c).

Figure 8.47 provides a close-up examination of the shape of the condensation rings produced by an encoded annular beam. The converging condensation ring was encoded similarly to the encoded primary beam; whereas the diverging ring occupies an inverted encoding geometry to that of the primary beam. This relationship is also verified by an azimuthal integration around the encoded annular beam and around the inner condensation rings, as shown in Figure 8.47 (right).

However, an encoded beam will result in an encoded SPSF, which would reconstruct Debye rings with similar intensity geometry to that of the annular beam, as illustrated in Figure 8.48. Nonetheless, Figure 8.48 indicates that recovery of scattering maxima positions is not affected by their intensity discontinuities.

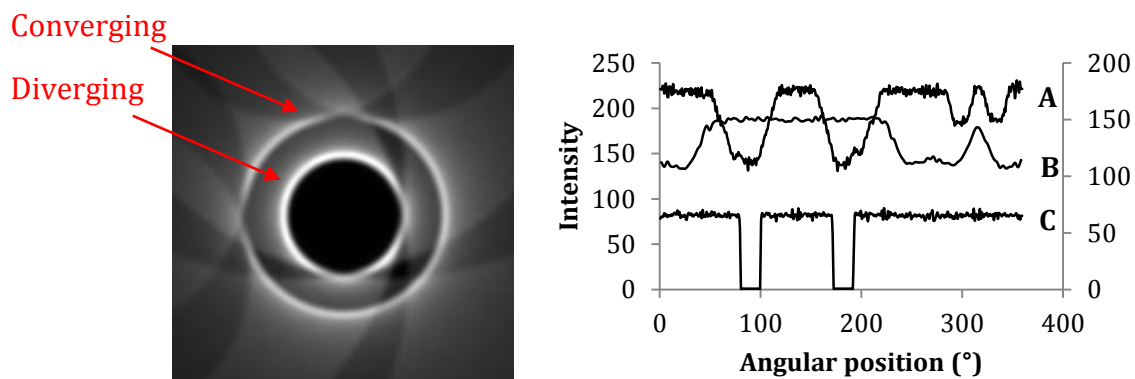


Figure 8.47 A magnified image of the FCG pattern produced by an encoded annular beam illustrating a converging and diverging condensation rings (left); azimuthal integration around the converging (A) and diverging (B) inner condensation rings arising from an encoded annular beam (C) (right). Profile (A) is displayed on a secondary axis for presentation purposes.

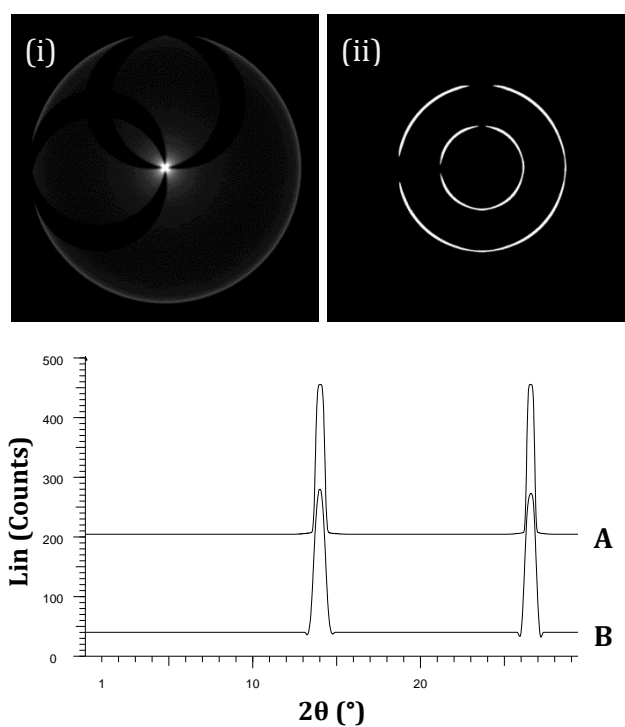


Figure 8.48 Simulated images (top) of the self-convolution of an encoded annular beam (i) and the corresponding recovered Debye rings (ii). The radial integration profiles (bottom) of the simulated Debye cones (A) and of the corresponding recovered Debye rings (B) are presented.

8.2.2 Empirical data

The proof-of-concept of an encoded annular beam was achieved by obscuring approximately the lower half of an annular collimator (*AB1* – see Table 6.1), as illustrated in Figure 8.49. The diffraction pattern from an Al_2O_3 sample was acquired over a range of 75 mm in steps of 0.5 mm with 30 seconds frame exposure (Figure 8.50).

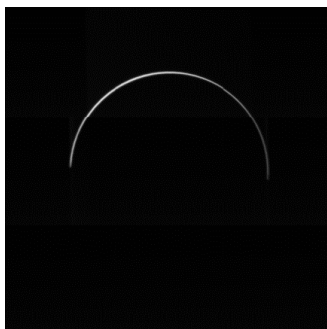


Figure 8.49 Empirical image of an encoded annular beam.

Figure 8.50 demonstrates converging condensation rings only on the upper half of the diffraction images, similarly to the shape of the primary beam; whereas diverging condensation rings appear on the lower half of the image. This can be clearly seen by the converging ring from 300 reflection from Al_2O_3 indicated by the red arrow in images number 1-10. The 300 converging ring is only observed in the upper half of the images, and as it is approaching its condensation focus at image number 10, it diverges in the opposite direction (see image number 13). The 300 diverging ring is then only apparent in the lower half of images 13-43. Images in which condensation rings are observed in both halves, signify the presence of both converging and diverging condensation rings, which may have the same radius at certain locations, as previously explained in Section 5.1.

To summarise, in this section, the ability of an encoded annular primary beam to distinguish between converging and diverging condensation rings was demonstrated both simulated and empirically. This is extremely useful when analysing single FCG images and the pre or post condensation focus nature of condensation rings is undetermined.

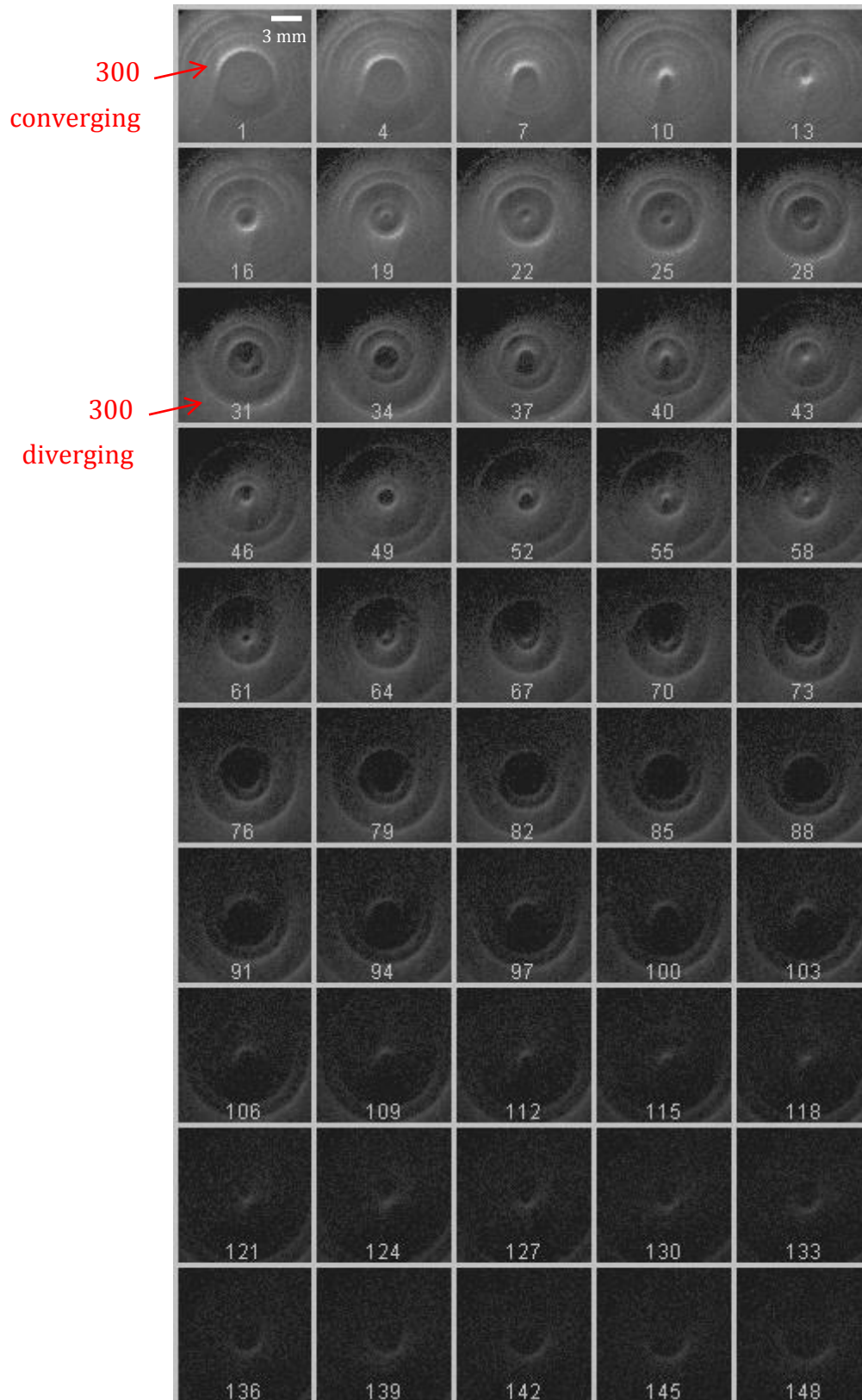


Figure 8.50 A sequence of empirical FCG diffraction images from an Al_2O_3 sample obtained with an encoded primary beam.

8.3 Post-sample encoders

Post-sample coded apertures may be employed for the identification of unknown materials with no spatial information along a primary axis. As described earlier in Section 4.2, coded apertures such as the ‘comb’ harmonic encoder, suggested by MacCabe et al. (2012), offer spatial discrimination of samples along a primary axis; hence identification of unknown materials by encoding the Debye cones with respect to their radius. However, the symmetry of the comb-like encoder induces a certain ambiguity when employed with FCG. As illustrated in Figure 8.51, when the sample is illuminated with an annular beam, the encoding of a single condensation ring would be the same for two different detector positions.

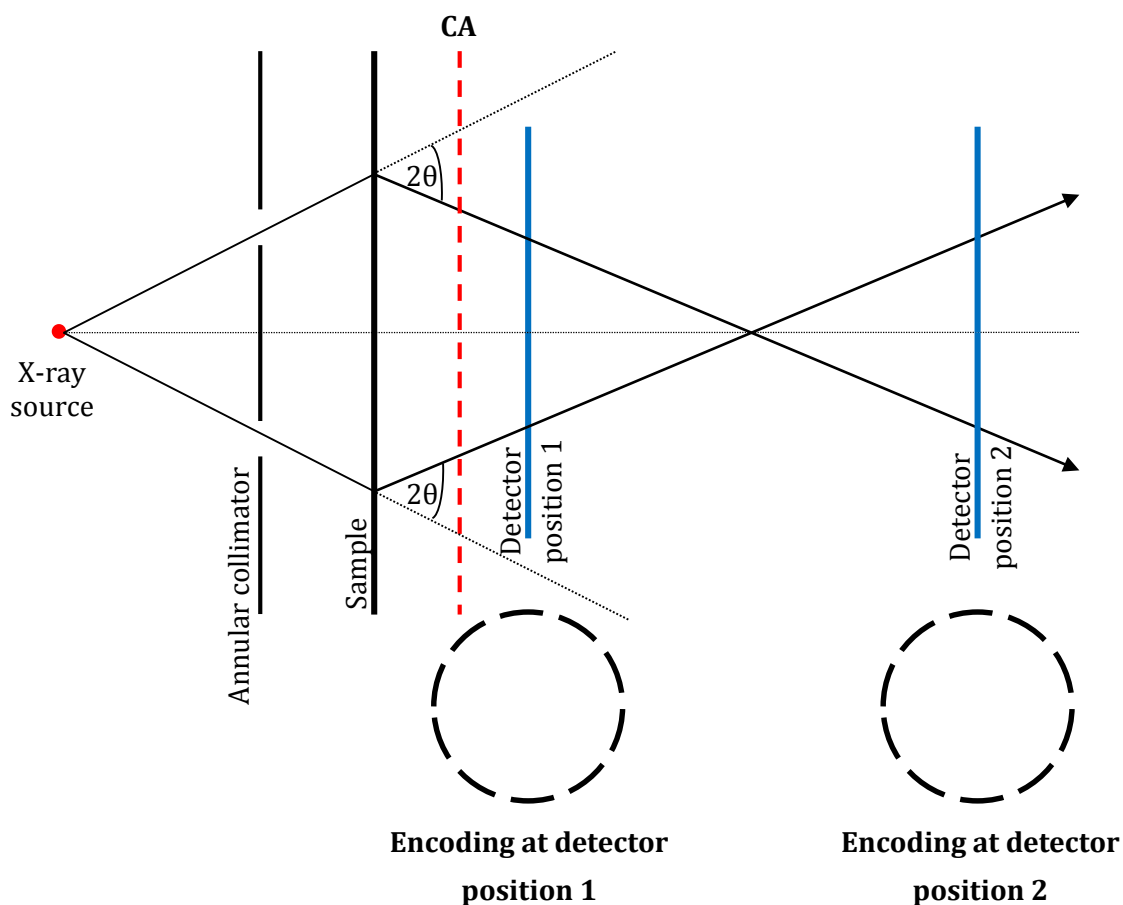


Figure 8.51 The geometry involved with a ‘comb’ harmonic coded aperture (CA) when illuminating a sample with an annular beam.

For certain detector positions, the radius of the converging and diverging condensation ring would be identical, as explained previously in Section 5.1. Therefore, a converging and a diverging condensation ring arising from the same scattering angle would possess the same spatial frequency encoding. This results in an ambiguity in determining the sample-to-detector distance, as well as the scattering angles of the sample from FCG data. This could be resolved by discrimination between converging and diverging condensation rings.

This discrimination is essential, as determination of the sample-to-detector distance and 2θ angles depends on the position of the detector relative to the condensation focus, i.e. whether it is a converging or diverging condensation ring, as explained in Section 7.2.1. The sample-to-detector distance for a converging (D_{SD_cr}) and diverging (D_{SD_dr}) condensation ring can be calculated by Equation (8.6) and (8.3), respectively;

$$D_{SD_cr} = \frac{R_{CA}Z_{d1} - R_{d1}Z_{CA}}{(Z_{d1} - Z_{CA}) \tan \phi_m + R_{CA} - R_{d1}} \quad (8.2)$$

$$D_{SD_dr} = \frac{R_{CA}Z_{d2} + R_{d2}Z_{CA}}{(Z_{d2} - Z_{CA}) \tan \phi_m + R_{CA} + R_{d2}} \quad (8.3)$$

where R_{CA} is the radius of the condensation ring at the coded aperture position, R_{d1} and R_{d2} are the radii of the converging and diverging condensation rings at detector positions 1 and 2 respectively, Z_{CA} is the position of the coded aperture along the primary axis, Z_{d1} and Z_{d2} are the detector positions along the primary axis and ϕ_m is the average annular beam divergence.

Even though the scattering angles of the sample can be calculated by Equations (8.4) and (8.5) independently of sample position, discrimination between converging and diverging rings is essential due to their different analytical descriptions and data analysis calculations.

$$2\theta_{cr} = \tan^{-1} \left(\frac{R_{CA} - R_{d1}}{Z_{d1} - Z_{CA}} \right) + \phi_m \quad (8.4)$$

$$2\theta_{dr} = \tan^{-1} \left(\frac{R_{CA} + R_{d1}}{Z_{d1} - Z_{CA}} \right) + \phi_m \quad (8.5)$$

Consequently, discrimination between converging and diverging rings is not possible with symmetric coded apertures such as the ‘comb’ harmonic encoder proposed by MacCabe et al. (2012), due to their symmetry that will encode converging and diverging rings in an indistinguishable manner. Moreover, the ~50% open fraction of comb-like apertures results in ~50% loss of scattered rays.

Herein, two novel post-sample encoders are introduced for the first time, which have the potential to encode unambiguously pencil beam and annular beam diffraction data. This approach is similar to that of MacCabe et al. (2012); where a pencil beam (primary collimation) illuminates the sample and a coded aperture is placed between the sample and a 2D detector. However, instead of a ‘comb’ harmonic coded aperture, the potential of a linear wire and an Archimedean spiral to act as post-sample encoders was investigated. Both encoders were initially assessed for a pencil beam geometry.

8.3.1 Linear encoder

A linear wire was employed to act as a post-sample encoder. The key feature of such an encoder is its off-centre location that will give rise to unique polar angles with respect to the radius of the Debye cones. As shown in Figure 8.52 (a), the wire encoder is 0.576 mm ($x=-0.576$) away from the centre of the image along the x-axis. This off-centre distance will be referred to as distance α_{LE} . When the wire encoder was superimposed on multiple Debye rings (Figure 8.52 (b)), the wire encoder intersected the Debye rings as indicated in Figure 8.52 (c). Encoding of the Debye rings arises from these intersection angles ζ (as shown in Figure 8.53), that can be determined by measuring their polar angles ($\zeta = 180 - \text{polar angle}$).

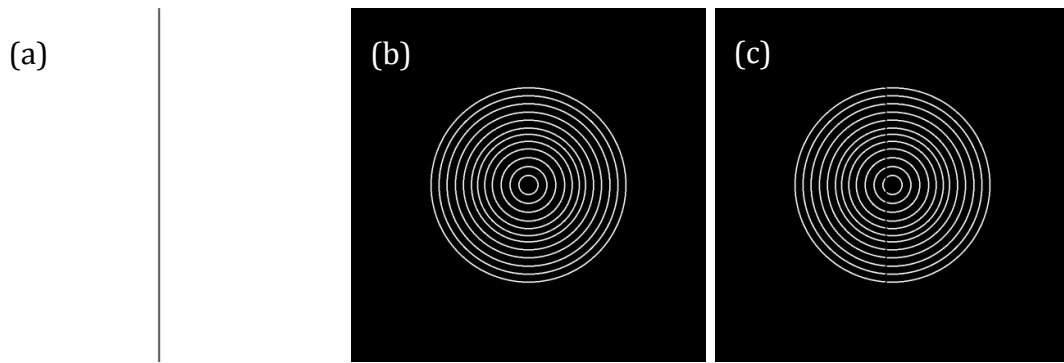


Figure 8.52 Simulated images of an off-centre linear aperture (a), multiple Debye rings of known radius (b) and the encoded Debye rings (c).

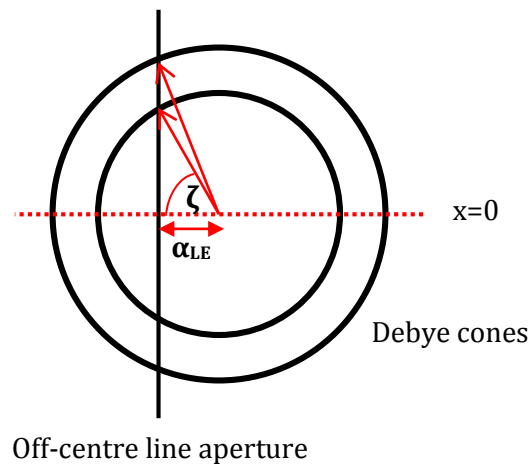


Figure 8.53 Schematic illustration of ζ angle and α_{LE} distance when using a linear coded aperture.

The radius of the Debye cones at the encoder plane (R_{LE}) corresponding to each ζ angle can be determined by Equation (8.6).

$$R_{LE} = \frac{\alpha_{LE}}{\cos \zeta} \quad (8.6)$$

The relationship between calculated radius R_{LE} and angle of intersection ζ follows a rapid growth, as indicated by Equation (8.6). As the off-centre distance α_{LE} of the wire encoder increases, the resolution and thus the specificity of the coded aperture

system increase. However, a large α_{LE} distance would result in limited encoding of Debye cones with small radii.

In contrast to the encoding of Debye cones arising from different scattering angles (same sample) illustrated in Figure 8.52 (c) and Figure 8.53, encoding of a single Debye cone at different sample-to-detector distances does not possess the same off-centre position of the encoder along the x-axis. An illustration of the arrangement involved with a wire encoder is presented in Figure 8.54. A wire encoder intersects the Debye cone on the detector's plane at a different distance (α_D) from the x-centre of the image than the actual α_{LE} distance of the linear encoder.

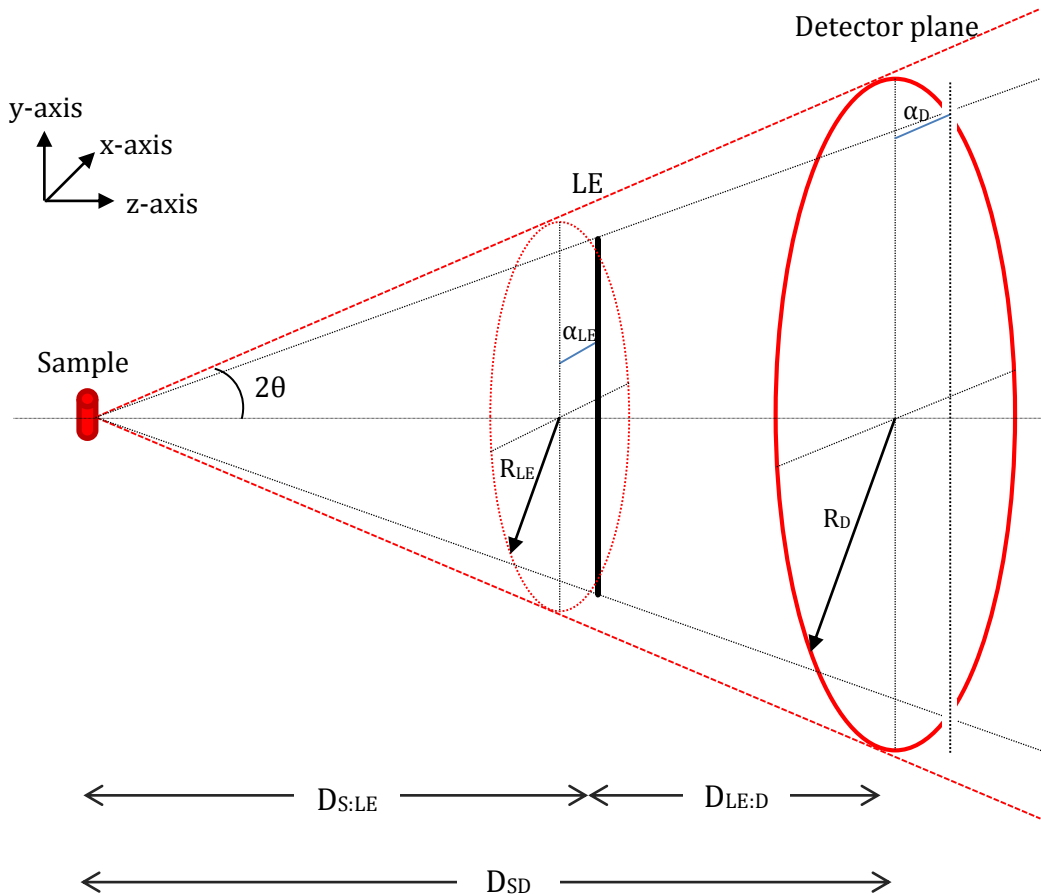


Figure 8.54 The geometric arrangement employed to record the 2D X-ray diffraction data encoded by a single linear encoder (LE), when illuminated by a pencil beam.

Encoding of the Debye cones at the detector plane occurs from the absorption of the scattering distribution by the wire encoder, which appears as intersection points on the Debye rings. The radius of the Debye cone as acquired by the detector (R_D) and the intersection angle ζ can be measured from the diffraction data.

The radius of the Debye cone at the wire encoder's plane (R_{LE}) can be determined by Equation (8.7).

$$R_{LE} = \frac{\alpha_{LE} R_D}{\alpha_D} \quad (8.7)$$

If the scattering angle 2θ of the sample is taken into account, then Equation (8.8) can be considered;

$$\tan 2\theta = \frac{R_{LE}}{D_{S:LE}} = \frac{R_D}{D_{S:LE} + D_{LE:D}} \quad (8.8)$$

where $D_{S:LE}$ is the distance between the sample and the wire encoder along a primary axis and $D_{LE:D}$ is the known distance between the wire encoder and the detector along a primary axis.

Combination of Equation (8.7) and Equation (8.8) results in Equation (8.9), determining the sample-to-detector distance (D_{SD}).

$$D_{SD} = D_{LE:D} + \frac{\alpha_{LE} D_{LE:D}}{\alpha_D - \alpha_{LE}} \quad (8.9)$$

Sample-to-detector distance can also be calculated by Equation (8.10), where R_D and intersection angle ζ are taken into account for each Debye cone.

$$D_{SD} = D_{LE:D} + \frac{D_{LE:D}(\alpha_{LE}/\cos \zeta)}{R_D - \alpha_{LE}/\cos \zeta} \quad (8.10)$$

Furthermore, the sample's scattering angles could be determined independently from the sample-to-detector distance by Equation (8.11).

$$2\theta = \tan^{-1} \left(\frac{R_D - \alpha_{LE}/\cos \zeta}{D_{LE:D}} \right) \quad (8.11)$$

The associated errors for each variable when determining the sample-to-detector distance and the scattering angles via Equations (8.9), (8.10), (8.8) and (8.11), and their interpretations, can be calculated by Equations (8.12), (8.13), (8.14) and (8.15), respectively.

$$\sigma^2(D_{SD}) = \left(\frac{dD_{SD}}{dD_{LE:D}} \right)^2 \sigma^2(D_{LE:D}) + \left(\frac{dD_{SD}}{d\alpha_{LE}} \right)^2 \sigma^2(\alpha_{LE}) + \left(\frac{dD_{SD}}{d\alpha_D} \right)^2 \sigma^2(\alpha_D) \quad (8.12)$$

$$\begin{aligned} \sigma^2(D_{SD}) &= \left(1 + \frac{\alpha_{LE}}{\alpha_D - \alpha_{LE}} \right)^2 \sigma^2(D_{LE:D}) \\ &+ \left(\frac{D_{LE:D}}{\alpha_D - \alpha_{LE}} + \frac{\alpha_{LE} D_{LE:D}}{(\alpha_D - \alpha_{LE})^2} \right)^2 \sigma^2(\alpha_{LE}) \\ &+ \left(\frac{-\alpha_{LE} D_{LE:D}}{(\alpha_D - \alpha_{LE})^2} \right)^2 \sigma^2(\alpha_D) \end{aligned}$$

$$\begin{aligned} \sigma^2(D_{SD}) &= \left(\frac{dD_{SD}}{dD_{LE:D}} \right)^2 \sigma^2(D_{LE:D}) + \left(\frac{dD_{SD}}{d\alpha_{LE}} \right)^2 \sigma^2(\alpha_{LE}) \\ &+ \left(\frac{dD_{SD}}{d\chi} \right)^2 \sigma^2(\chi) + \left(\frac{dD_{SD}}{dR_D} \right)^2 \sigma^2(R_D) \end{aligned} \quad (8.13)$$

$$\begin{aligned}
 & \sigma^2(D_{SD}) \\
 &= \left(1 + \frac{\alpha_{LA}}{\cos \zeta \left(R_D - \frac{\alpha_{LE}}{\cos \zeta} \right)} \right)^2 \sigma^2(D_{LE:D}) \\
 &+ \left(\frac{D_{LE:D}}{\cos \zeta \left(R_D - \frac{\alpha_{LE}}{\cos \zeta} \right)} + \frac{\alpha_{LE} D_{LE:D}}{\cos^2 \zeta \left(R_D - \frac{\alpha_{LE}}{\cos \zeta} \right)^2} \right)^2 \sigma^2(\alpha_{LE}) \\
 &+ \left(\frac{\alpha_{LE} D_{LE:D} \sin \zeta}{\cos^2 \zeta \left(R_D - \frac{\alpha_{LE}}{\cos \zeta} \right)} \right. \\
 &\left. + \frac{\alpha_{LE}^2 D_{LE:D} \sin \zeta}{\cos^3 \zeta \left(R_D - \frac{\alpha_{LE}}{\cos \zeta} \right)^2} \right)^2 \sigma^2(\zeta) + \left(\frac{-\alpha_{LE} D_{LE:D}}{\cos \zeta \left(R_D - \frac{\alpha_{LE}}{\cos \zeta} \right)^2} \right)^2 \sigma^2(R_D)
 \end{aligned}$$

$$\sigma^2(2\theta) = \left(\frac{d_{2\theta}}{dR_D} \right)^2 \sigma^2(R_D) + \left(\frac{d_{2\theta}}{dD_{SD}} \right)^2 \sigma^2(D_{SD}) \quad (8.14)$$

$$\sigma^2(2\theta) = \left(\frac{D_{SD}}{R_D^2 + D_{SD}^2} \right)^2 \sigma^2(R_D) + \left(\frac{-R_D}{R_D^2 + D_{SD}^2} \right)^2 \sigma^2(D_{SD})$$

$$\begin{aligned}
 \sigma^2(2\theta) &= \left(\frac{d_{2\theta}}{dR_D} \right)^2 \sigma^2(R_D) + \left(\frac{d_{2\theta}}{d\alpha_{LE}} \right)^2 \sigma^2(\alpha_{LE}) + \left(\frac{d_{2\theta}}{d\zeta} \right)^2 \sigma^2(\zeta) \\
 &+ \left(\frac{d_{2\theta}}{dD_{LE:D}} \right)^2 \sigma^2(D_{LE:D})
 \end{aligned} \quad (8.15)$$

$$\begin{aligned}
\sigma^2(2\theta) = & \left(\frac{D_{LE:D}}{\left(R_D - \frac{\alpha_{LE}}{\cos \zeta}\right)^2 + D^2} \right)^2 \sigma^2(R_D) \\
& + \left(\frac{-D_{LE:D}}{\cos \zeta \left[\left(R_D - \frac{\alpha_{LE}}{\cos \zeta}\right)^2 + D^2 \right]} \right)^2 \sigma^2(\alpha_{LE}) \\
& + \left(\frac{-D_{LA:D} \alpha_{LE} \sin \chi}{\cos^2 \zeta \left[\left(R_D - \frac{\alpha_{LE}}{\cos \zeta}\right)^2 + D^2 \right]} \right)^2 \sigma^2(\zeta) \\
& + \left(\frac{\frac{\alpha_{LE}}{\cos \zeta} - R_D}{\left(R_D - \frac{\alpha_{LE}}{\cos \zeta}\right)^2 + D^2} \right)^2 \sigma^2(D_{LE:D})
\end{aligned}$$

For instance, the error in the calculated D_{SD} distance ($\sigma(D_{SD})$) based on Equations (8.12) and (8.13) was calculated to be ± 1.85 mm and ± 2.12 mm respectively, for a linear encoder example with $D_{LE:D} = 39$ mm, $\alpha_{LE} = 6$ mm, $\alpha_D = 17.4$ mm, $\zeta = 46.78^\circ$ and $R_D = 25.1$ mm[‡]. The standard deviation errors employed were $\sigma(D_{LE:D}) = \pm 1$ mm, $\sigma(\alpha_{LE}) = \pm 0.1$ mm, $\sigma(\alpha_D) = \pm 0.5$ mm, $\sigma(\zeta) = \pm 3^\circ$ and $\sigma(R_D) = \pm 0.5$ mm. It was determined that the greatest variation in the calculated D_{SD} distance comes from the encoder-to-detector distance ($D_{LE:D}$).

For the above example, the error in the calculated scattering angles ($\sigma(2\theta)$) based on Equations (8.14) and (8.15) was calculated to be $\pm 0.53^\circ$ (with $D_{SD} = 59.8$ mm and $\sigma(D_{SD}) = \pm 1$ mm) and $\pm 0.93^\circ$, respectively. The radius of the Debye cones at the detector plane (R_D) was the highest contributed factor to this error.

When a 1% error was applied to all variables of Equations (8.12) and (8.13), the greatest errors for the sample-to-detector distance, $\sigma(D_{SD}) = \pm 0.74$ mm and $\sigma(D_{SD}) = \pm 0.80$ mm respectively, arose from $D_{LE:D}$ distance. However, the highest errors for

[‡] Values obtained from empirical experiments described later in Section 8.3.1.1.

the scattering angle with 1% error in all variables, emerged from R_D radius for Equation (8.15) ($\sigma(2\theta) = \pm 0.40^\circ$); whereas for the conventional Equation (8.14) the error ($\sigma(2\theta) = \pm 0.29^\circ$) was equally divided between R_D radius and D_{SD} distance.

8.3.1.1 Empirical data

Proof-of concept for a linear encoder was initially investigated with a pencil beam arrangement using a Bruker D8-GADDS diffractometer.

A metallic wire encoder made from lead with an off-centre distance (α_{LE}) of 6 mm was employed for this series of experiments at 39 mm ($D_{LE:D}$) from the detector, and its footprint onto the sample is illustrated in Figure 8.55 (a). In Figure 8.55 (b), the diffraction pattern from Al_2O_3 is displayed and the encoding arising from the intersection points of the wire encoder with the Debye rings are apparent.

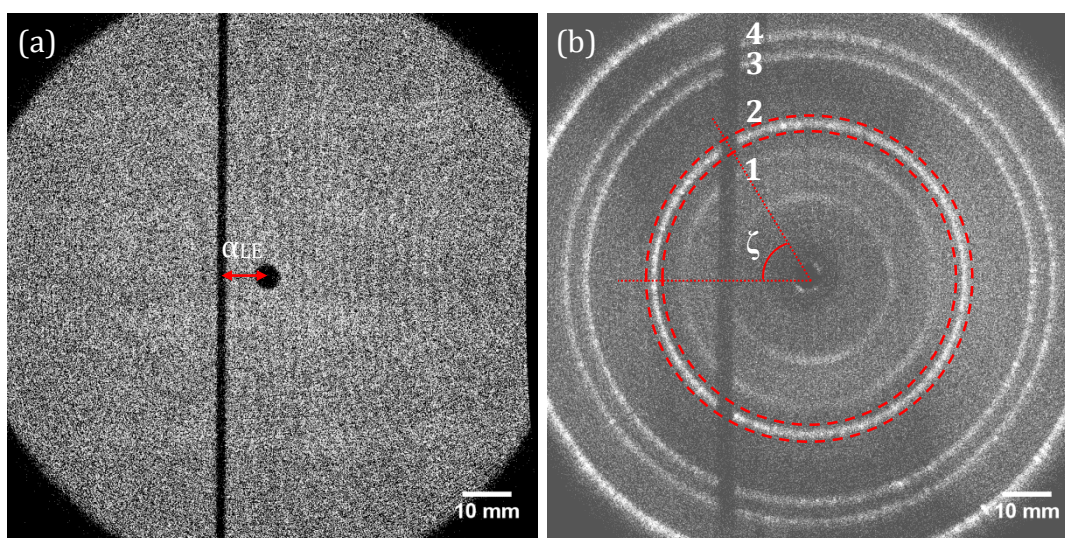


Figure 8.55 Empirical images of the wire aperture's footprint on the detector indicating the off-centre distance α_{LE} (a) and the scattering distribution from a single Al_2O_3 sample (b) that has been encoded by a single wire encoder.

The sample-to-detector distance D_{SD} was initially calculated by Equation (8.9) to be 61 mm. Measurements were then taken from four encoded Debye rings as illustrated in Figure 8.55 (b). Table 8.2 presents the results obtained from Figure 8.55 (b). The D_{SD} distance was re-calculated by Equation (8.10) with a mean value

of 61.75 mm, indicating a strong correlation between the two approaches. The scattering angles were calculated via both Equations (8.8) and (8.11), giving similar values, within experimental errors. Table 8.2 tabulates the scattering angles calculated by Equation (8.8) with a D_{SD} of 61.75 mm, as it was determined to have a lower error (see Section 8.3.1) than Equation (8.11).

Table 8.2 The results of the measured radii of the Debye cones as captured by the detector (R_D), the measured intersection angle ζ , the calculated radii of the Debye cones when intersected with wire encoder (R_{LE}), the calculated sample-to-detector distances (D_{SD}) using different approaches and the calculated scattering (2θ) angles for Al_2O_3 .

Debye rings	Measured R_D (mm)	Measured ζ angle (°)	Calculated R_{LE} (mm) Equation (8.6)	Calculated D_{SD} (mm) Equation (8.9)*	Calculated D_{SD} (mm) Equation (8.10)	Calculated 2θ (°) Equation (8.8)
1	26	49	9	61	61	23
2	32	59	12	61	62	27
3	45	69	17	61	62	36
4	50	71	18	61	62	39

*The off-centre α_D distance was 16.8 mm.

The diffraction pattern of two $CaCO_3$ loaded cellulose samples with a spatial separation along the primary axis was also obtained with a single wire encoder ($\alpha_{LE}=6$ mm, $D_{LE:D}=39$ mm). As demonstrated in Figure 8.56, there are two footprints of the wire encoder in the diffraction image, each corresponding to a different sample-to-detector distance. Each wire encoder's footprint at the detector plane intersects only Debye rings corresponding to the sample-to-detector distance related with the specific footprint of the wire encoder. Therefore, one can differentiate between scattering maxima arising from multiple samples.

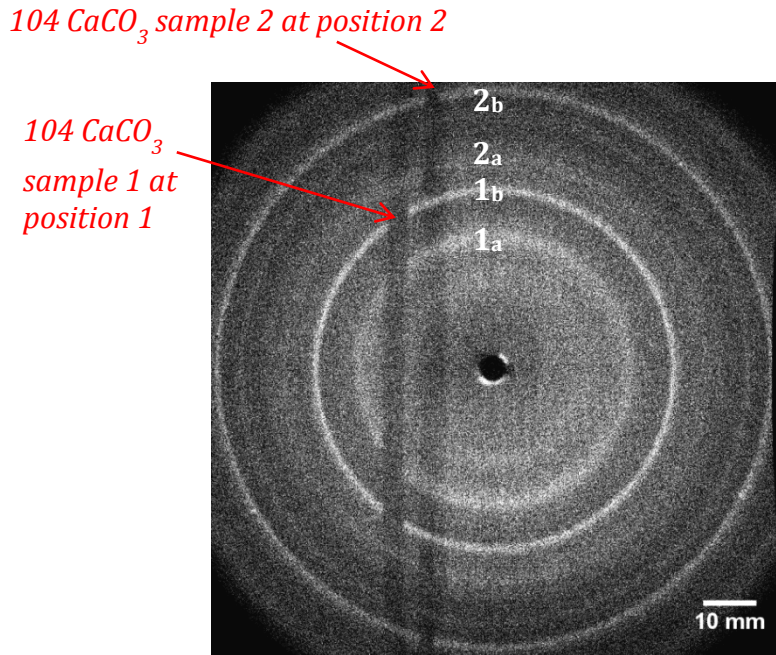


Figure 8.56 Scattering distribution from a pair of CaCO_3 loaded cellulose sample spatially separated along the primary axis and encoded from a single wire encoder.

Table 8.3 tabulates the results obtained from two sheets of CaCO_3 loaded cellulose, as calculated by Equations (8.9) and (8.10). The average sample-to-detector distances of the two mineral loaded cellulose sheets were determined to be 60 mm and 92 mm, indicating a 32 mm distance between the two samples.

Results obtained from empirical data without *a priori* knowledge of the samples' material characteristics, were then verified by taking into account the samples' scattering angles for comparison and confirmatory purposes, similarly to MacCabe et al. (2012). The Debye rings of Figure 8.56, designated 1_a and 2_a, arise from a scattering angle of 22.77° (Cu target Bruker D8-GADDS) from cellulose (0.390 nm); whereas Debye rings 1_b and 2_b correspond to 29.39° 2θ from CaCO_3 (0.304 nm). D_{SD} distance can therefore be calculated by $R_D/\tan(2\theta)$. For Debye rings 1_a and 1_b, arising from the same sample as indicated from their encoding in Figure 8.56, the average sample-to-detector distance was calculated to be 60 mm; whereas for the Debye rings 2_a and 2_b was calculated to be 92 mm. Thus, the samples were separated by 32 mm.

Table 8.3 The results of the measured radii of the Debye cones as captured by the detector (R_D), the measured intersection angle ζ , the calculated radii of the Debye cones when intersected with wire encoder (R_{LE}), the calculated sample-to-detector distances (D_{SD}) using different approaches and the scattering (2θ) angles for two sheets of mineral ($CaCO_3$) loaded cellulose separated along the z-axis.

Debye rings	Measured R_D (mm)	Measured ζ angle ($^\circ$)	Calculated R_{LE} (mm) Equation (8.6)	Calculated D_{SD} (mm) Equation (8.9)	Calculated D_{SD} (mm) Equation (8.10)	Calculated 2θ ($^\circ$) Equation (8.8)
1_a*	25	47	9	60	60	23
1_b	34	59	12	60	60	29
2_a	39	75	22	92	93	23
2_b	52	78	30	92	91	29

*The 1st and 2nd footprint of the line aperture on the detector had a α_D of 10.4 mm and 17.4 mm, respectively.

Comparing this value (32 mm) with the D_{SD} distance value obtained with no *a priori* knowledge of the samples' scattering angles (32 mm), indicates good agreement between the two. Therefore, verifying that a linear encoder can act as a post-sample coded aperture to recover spatial information and identify unknown samples.

Following the establishment of a linear encoder as a post-sample coded aperture with conventional XRD, proof-of-concept was attempted with FCG. For the purposes of this research, combination of the annular beam with a wire encoder aimed at differentiating between converging and diverging condensation rings. This was based on the fact that when converging rings approach their condensation focus, they then diverge in opposed directions with an inverted geometry (as shown previously with an encoded primary beam in Section 8.2).

Annular beam experiments were performed using the FCG system with a PIXIS detector of $\sim 13 \times 13$ mm active area (Section 6.1.2). For this reason, a very fine wire was required for clear and precise encoding of the condensation rings. However, a wire with this required diameter, suffered from low absorption as the FCG system utilises a higher energy (~ 17 keV) than the Bruker D8-GADDS (~ 8 keV). Therefore, an absorbing edge was employed for proof-of-principle purposes. An FCG data

sequence from an Al_2O_3 plate (S1, Table 6.2) was captured over a range of 80 mm in steps of 0.2 mm with 30 seconds time exposure (Figure 8.57).

As illustrated in Figure 8.57 (image number 1), the absorbing edge was obstructing the right hand side of the detector, allowing only the left hand side of the diffraction caustics to be observed. However, when converging rings approached their focal point (condensation focus) and diverged in the opposite direction, diverging rings were observed in the right hand side of the detector.

In Figure 8.57 image number 1, only the converging rings are apparent; whereas in image number 241 only the diverging rings are evident. However, for instance, in image number 57 both converging (left hand side) and diverging (right hand side) condensation rings are present. Hence, converging and diverging condensation rings can be differentiated based on which side of the detector they appear (with respect to the encoder); similarly to an encoded primary beam presented in Section 8.2.2.

To summarise, from the results obtained, it was demonstrated that a linear (wire) encoder could be employed with conventional XRD to acquire spatial information of multiple samples along a primary axis and identify unknown samples. Furthermore, it was shown that an absorbing edge and essentially a wire encoder could be utilised with FCG to discriminate between converging and diverging condensation rings. Once converging condensation rings are discriminated from diverging condensation rings or *vice versa*, Equations (8.4) and (8.5) could be used for determination of the sample's scattering angles and hence acquisition of a diffraction profile from a single FCG image.

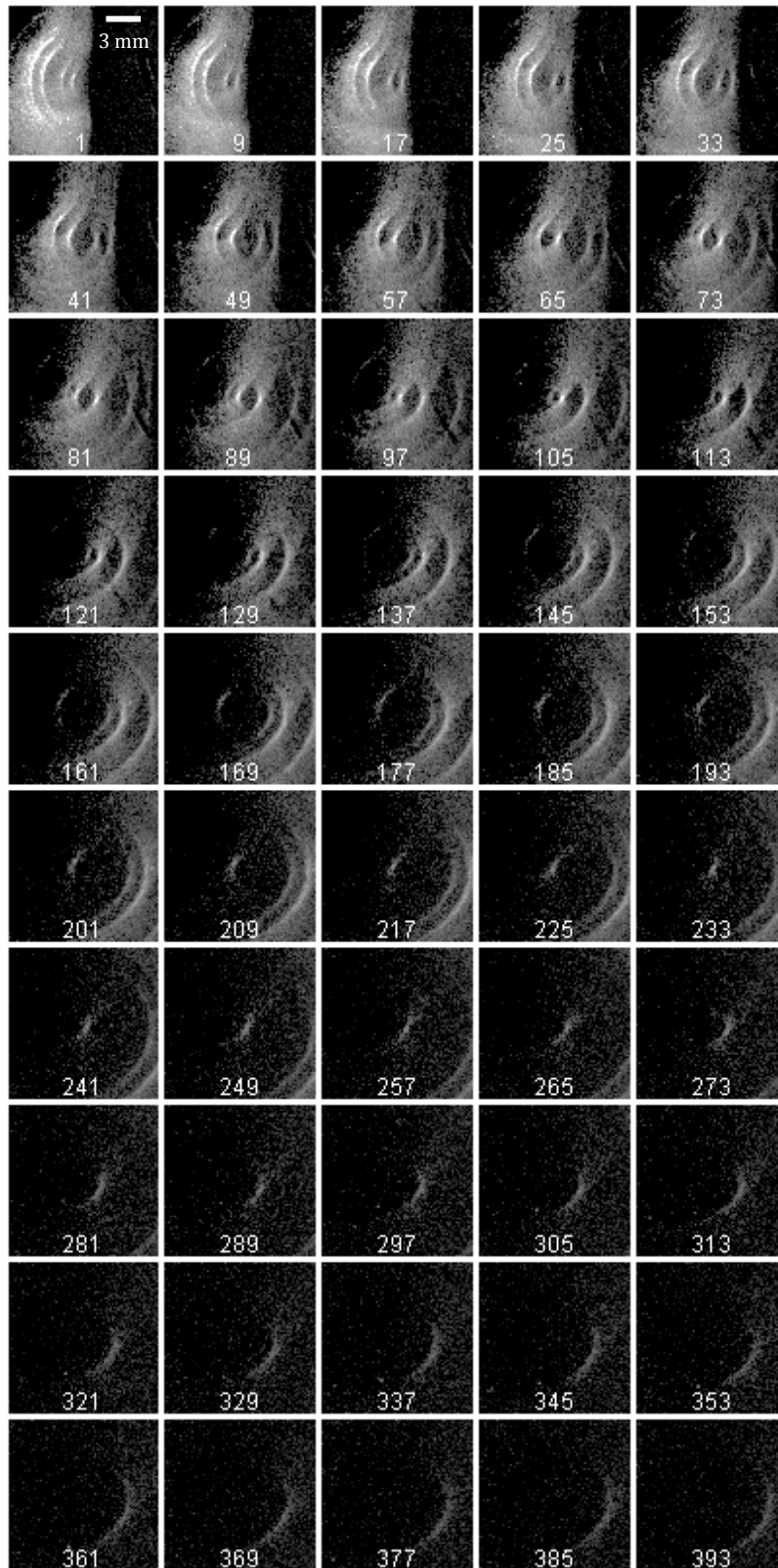


Figure 8.57 A sequence of empirical FCG diffraction images from an Al_2O_3 sample obtained with an absorbing edge acting as a post-sample coded aperture.

8.3.2 Archimedean spiral encoder

A spiral, such as an Archimedean spiral, can also be considered as a post-sample encoder. An Archimedean spiral (Figure 8.58) can be analytically described by Equation (8.16);

$$R_{AS} = a + b\psi \quad (8.16)$$

where R_{AS} is the radial distance, ψ is the polar angle, and a and b are real numbers. An increase in a will turn the spiral by dislocating its centre positively along the x -axis; whereas an increase in b will increase the distance between successive turns.

Likewise to a linear wire, the aim of this spiral encoder is to recover the 2θ angles of any material under investigation with no spatial information on the sample along the primary axis. In order to do so, the Archimedean spiral employed has to consist of $n=1$ turns, as indicated in Figure 8.58. An Archimedean spiral with multiple turns ($n>1$) would result in a single encoding angle ψ corresponding to multiple radii, thus inducing certain encoding ambiguities. For this reason, a single turn Archimedean spiral, $n=1$ from 0° - 360° , was considered during this study. Moreover, the $(0,0)$ coordinate of the Archimedean spiral should be positioned at the centre of the diffraction pattern for accurate encoding.

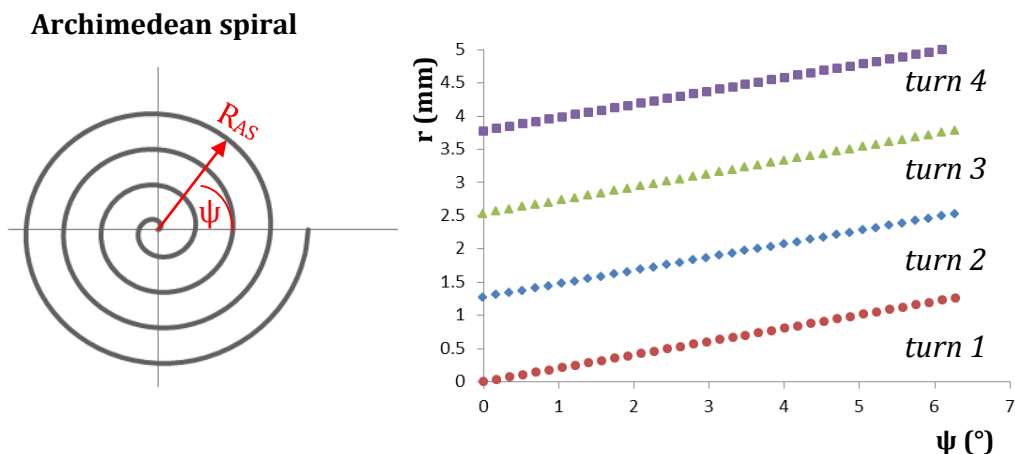


Figure 8.58 The Archimedean spiral encoder (left) and the ambiguity in radius for multiple turns (n) of the spiral (right).

8.3.2.1 Analytical approach

Initially, a single sample was analysed by a pencil beam geometry. If an Archimedean spiral is placed after the sample, the radius of the Debye cones on the spiral plane can be determined by Equation (8.16). An Archimedean spiral made of a high absorption material e.g. metallic wire (Figure 8.59 (a)) would block the scattering of Debye cones (Figure 8.59 (b)) of certain radius occupying specific ψ angles, similarly to a linear encoder, as illustrated in Figure 8.59 (c). This characteristic opaque discontinuities will occur at specific ψ ($\psi=(R_{AS}-a)/b$) angles on the Debye cones; hence encoding the captured diffraction data.

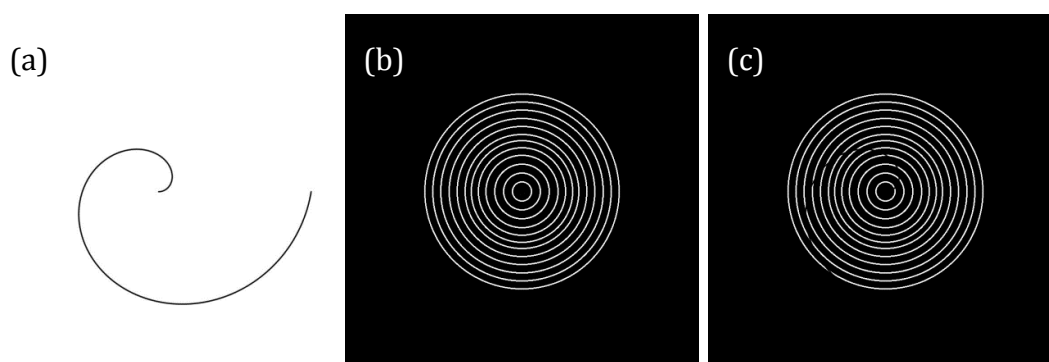


Figure 8.59 Simulated images of an Archimedean spiral (a), multiple Debye rings of known radius (b) and the encoded Debye rings (c).

However, a representative example of the empirical data involves magnification of Figure 8.59 (c), due to the increased radii of the Debye cones when captured by the detector, as illustrated in Figure 8.60. The radius of the Debye cones at the detector plane (R_D) increases depending on sample-to-detector distance (D_{DS}) and beam divergence (ϕ_{PB}). Therefore, it is essential to determine a relationship between the diffraction data's encoding and the sample-to-detector distance.

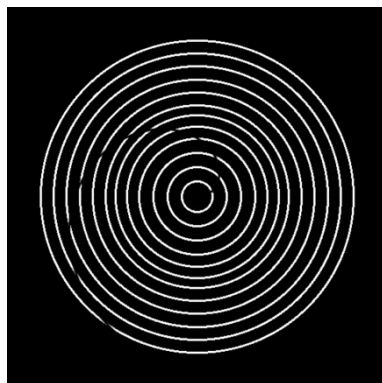


Figure 8.60 Magnified simulated image of the encoded Debye rings by an Archimedean spiral.

Figure 8.61 illustrates a pencil beam arrangement employing an Archimedean spiral as a post-sample encoder.

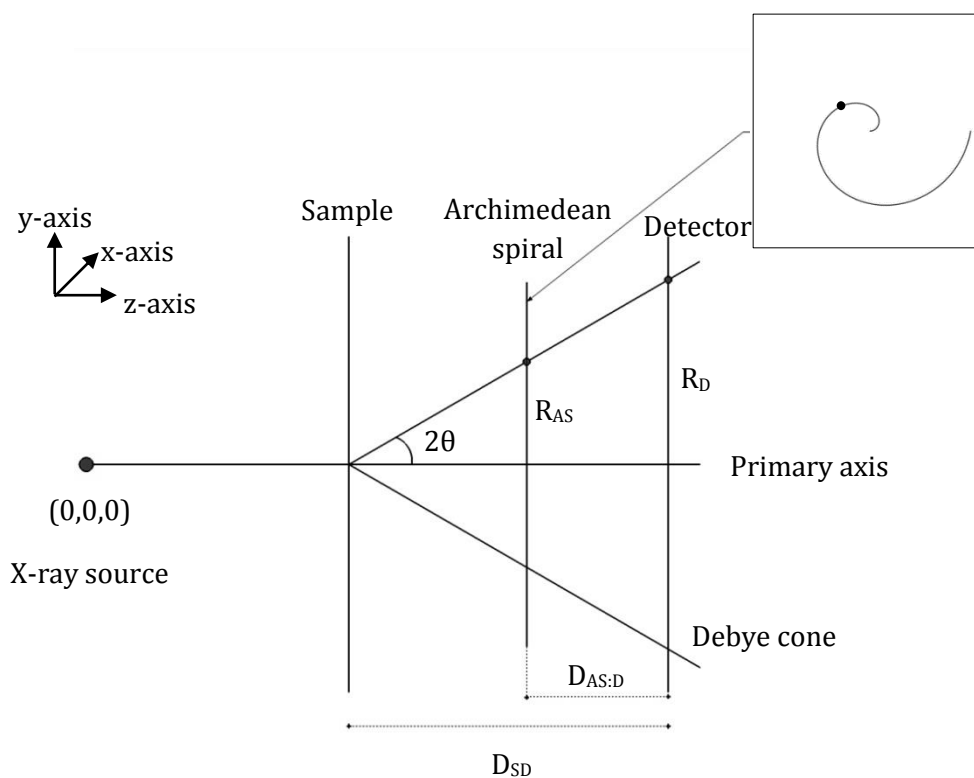


Figure 8.61 A 2D schematic diagram of a post-sample Archimedean spiral encoder for a pencil beam arrangement (side view). The Archimedean spiral is illustrated in front view.

As determined from Figure 8.61, the sample-to-detector distance (D_{SD}) can be calculated by Equation (8.17);

$$D_{SD} = D_{AS:D} + \frac{D_{AS:D}(a + b\psi)}{R_D - a - b\psi} \quad (8.17)$$

where $D_{AS:D}$ is the distance between the Archimedean spiral and the detector, R_D is the radius of the Debye cone at the sample plane, a and b are the values used to create the spiral and ψ is the measured polar angle of the intersection point of the spiral and the Debye cone.

The scattering angles of the sample could be determined by Equation (8.18).

$$2\theta = \tan^{-1}\left(\frac{R_D - a - b\psi}{D_{AS:D}}\right) \quad (8.18)$$

The results obtained from interpretation of the magnified image shown in Figure 8.60, are presented in Table 8.4. The range of D_{SD} distances, as calculated from each Debye cone (Table 8.4), varies over 1 mm with a standard deviation of 0.3 that can be considered to be within experimental errors. The average D_{SD} distance was calculated to be 26 mm.

The measured intersection angles ψ were plotted against the calculated R_{AS} radii, demonstrating a positive linear relationship (Figure 8.62), as indicated by the Archimedean spiral's equation.

Table 8.4 Measurements of the radii of the Debye cones at the detector's plane (R_D) when magnified by 1.5, the ψ angle of the opaque points on the Debye cones and the calculated radii of the Debye cones onto the Archimedean spiral, as indicated by $R_{AS}=a+b\psi$. The calculated sample-to-detector distance (D_{SD}) from each Debye cone is given.

Measured R_D (mm)	Measured ψ angle ($^\circ$)	Calculated R_{AS} (mm) Equation (8.16)	Calculated D_{SD} (mm) Equation (8.17)
3	20	1	25
6	42	1	26
10	66	2	26
13	89	3	26
16	109	4	26
18	125	4	26
20	139	5	26
23	156	5	26
26	173	6	26
29	193	7	26
32	213	7	26
35	235	8	26
Mean			26
Standard deviation			0.3

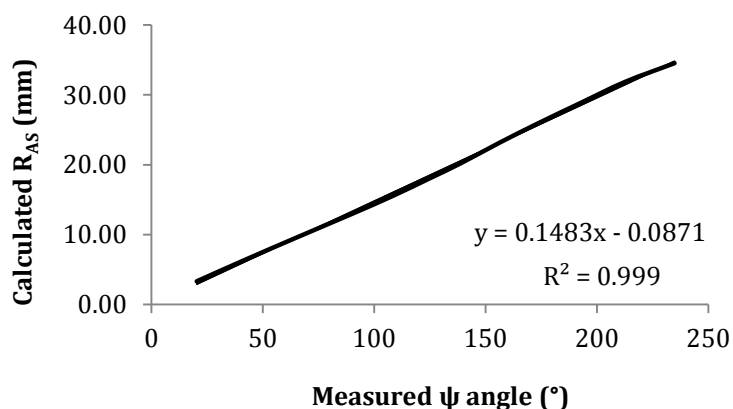


Figure 8.62 Graphical illustration of the measured ψ angles against the calculated radii of the Debye cones onto the Archimedean spiral (R_{AS}).

The sensitivity of an Archimedean spiral in recovering spatial information was assessed by distorting its shape either by changing a and b values or by rotating the spiral around the y -axis.

(a) Altering a and b values

The effect of a uniformly distorted Archimedean spiral was examined by employing a $0.005+0.038\psi$ spiral for the simulated data. The analytical approach however, considered a $0+0.035\psi$ spiral. This resulted in an average calculated D_{SD} distance of 25.5 mm introducing an error of $\sim 2\%$ from the previously calculated 26 mm D_{SD} distance. A non-uniform distortion along the spiral would result in greater intra-errors when calculating the D_{SD} distance from different Debye cones arising from a single sample; hence generating a greater range of calculated D_{SD} distances.

(b) Archimedean spiral rotation

Rotation of the Archimedean spiral is thought to result in inherent experimental errors because of two hypothetical reasons. Firstly, due to alteration of its structure and secondly due to different sample-to-spiral and spiral-to-detector distances along the surface of the spiral. This effect was simulated using the ray-tracing simulator described in Section 6.1.1.

Initially, a perfect Archimedean spiral with no rotation was considered. A sample of 0.1 mm thickness with 10° , 20° and 25° scattering angles was positioned 150 mm away from the X-ray source. An Archimedean spiral ($a=0$ and $b=0.035$) normal to the primary axis was initially employed at $(0,0,170)$ coordinates. The radius of the Debye rings and their encoding angles ψ at 180 mm, 190 mm and 200 mm away from the sample were measured. Assuming no prior knowledge on the sample's position, the sample-to-detector distances were calculated by Equation (8.17).

The results indicated that the average D_{SD} distances were 30 mm, 40 mm and 50 mm when the detector was at 180 mm, 190 mm and 200 mm away from the X-ray source, respectively. The sample was known to be at 150 mm from the X-ray source, hence signifying that accurate D_{SD} distances could be determined in an ideal case of an Archimedean spiral encoder.

The spiral was then rotated 20° clockwise around the y-axis, with its centre at (0,0,170). The sample and detector remained at the same positions.

The data obtained are presented in Table 8.5. The calculated D_{SD} distances for the same detector positions vary by 1-2 mm (i.e. 2-6.7% error) from the calculated distances with no spiral rotation. Consequently, this induced errors in the calculated scattering angles. The average scattering angles were calculated to be 10°, 20° and 25° with no rotation and 10°, 21° and 26° with 20° spiral rotation. This indicates that rotating the spiral would result in additional errors signifying a shorter sample-to-detector distance (~4% mean error) and higher scattering angles (~2% mean error).

Table 8.5 Measurements of the radii of the Debye cones (R_D) captured at 180 mm, 190 mm and 200 mm from the X-ray source and their corresponding intersection angles ψ obtained from the ray-tracing simulated data when the Archimedean spiral was rotated 20° clockwise around the y-axis. The calculated radii of the Debye cones onto the Archimedean spiral, the sample-to-detector distances and the scattering angles 2θ are presented.

Detector's z-distance (mm)	Measured R_D (mm)	Measured ψ angle (°)	Calculated R_{AS} (mm) Equation (8.16)	Calculated D_{SD} (mm) Equation (8.17)	Calculated 2θ (°) Equation (8.18)
180	5	99	3	29	10
	11	371	13	28	21
	14	374	13	28	26
190	7	99	3	39	10
	15	374	13	38	21
	19	379	13	39	26
200	9	99	3	49	10
	18	378	13	49	20
	23	383	13	49	25

Analysis of the experimental errors arising from the different variables of Equations (8.17) and (8.18), including the encoder-to-detector distance as well as the a and b

values of the Archimedean spiral, are presented further on in Section 8.3.2.2 (page 288).

In summary, a non-ideal Archimedean spiral structure or rotation of the Archimedean spiral could result in inaccuracies in the calculated sample-to-detector distance and scattering angles of a sample under investigation. These errors may be overcome by calibration corrections. A data sequence can be collected with a known sample and the intersection angles ψ can be plotted against the radii of the Debye cones at the spiral's plane (R_{AS}), as calculated by $D_{S:AS} \tan 2\theta$; where $D_{S:AS}$ is the sample-to-spiral distance. Ideally, this should indicate a positive linear relationship, as previously discussed and illustrated in Figure 8.62. However, if the Archimedean spiral is distorted or rotated, then this relationship would alter and the calculated R_{AS} , and hence calculated D_{SD} distance and 2θ angles would no longer be accurate. This inherent error may be resolved by applying a new equation retrieved by a ' ψ angle against R_{AS}' (from known 2θ) plot to calibrate the data.

8.3.2.2 Empirical approach

The concept of employing an Archimedean spiral as a post-sample encoder was empirically investigated with a pencil beam arrangement using a Bruker D8-GADDS diffractometer.

A metallic (lead) spiral approximating the Archimedean equation $0+0.055\psi$ was employed for this series of experiments. Initially, single samples, mineral (CaCO_3) loaded cellulose and Al_2O_3 , at unknown z-coordinates were utilised. Each sample was translated in steps of 1 mm, over a range of 22 mm along the primary axis. The sample-to-spiral and sample-to-detector distances therefore varied between 7-29 mm and 61-83 mm, respectively ($D_{AS:D}=54$ mm).

2D diffraction images acquired for a mineral loaded cellulose and an Al_2O_3 sample are presented in Figure 8.63 and Figure 8.64, respectively. Images number 1 (Figure 8.63 and Figure 8.64) were obtained with the sample close to the detector, whilst images number 23 were obtained with the sample close to the X-ray source.

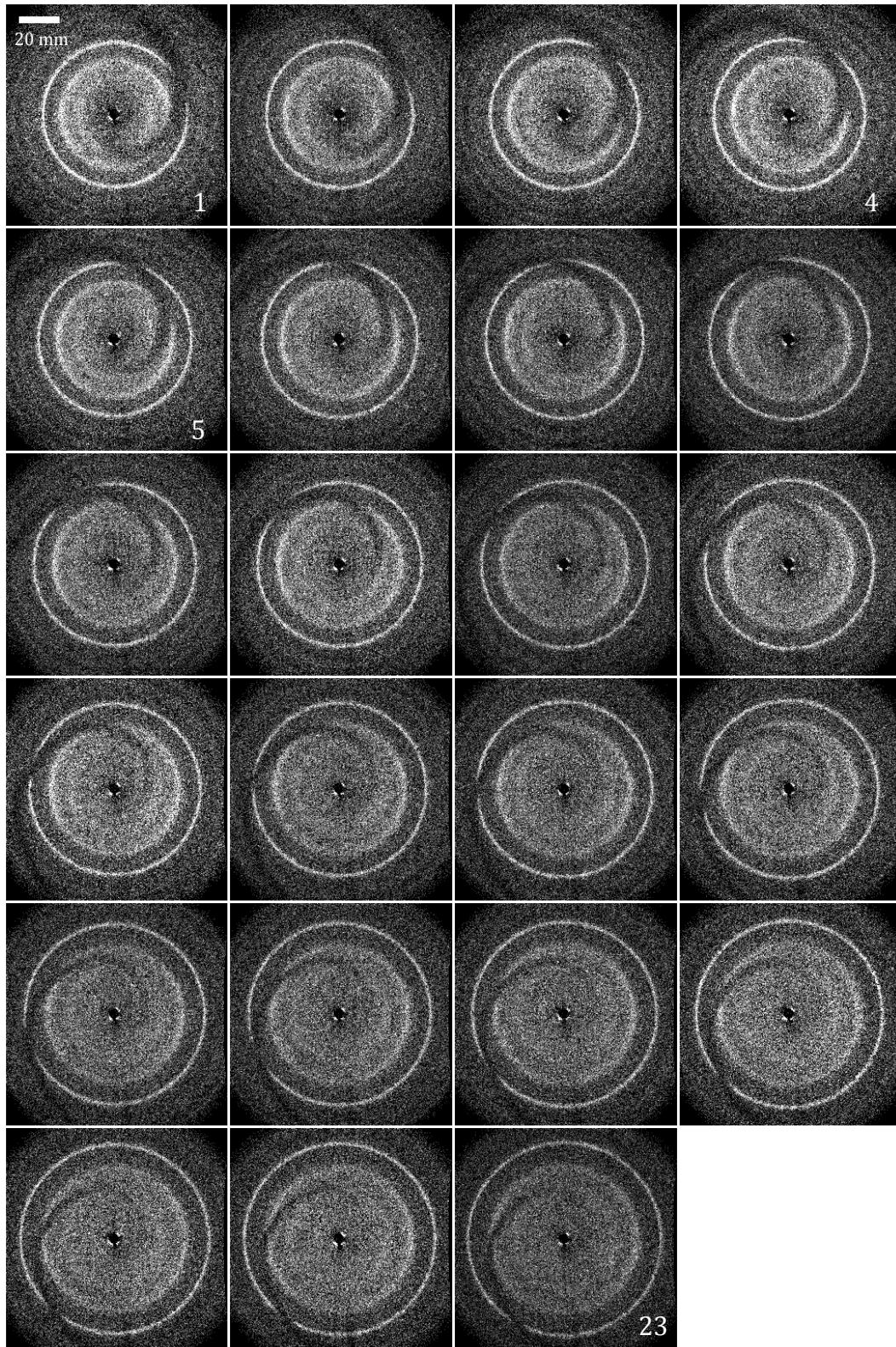


Figure 8.63 A series of empirical diffraction images captured as a CaCO_3 loaded cellulose sample was translated along the primary beam axis with an Archimedean spiral encoder.

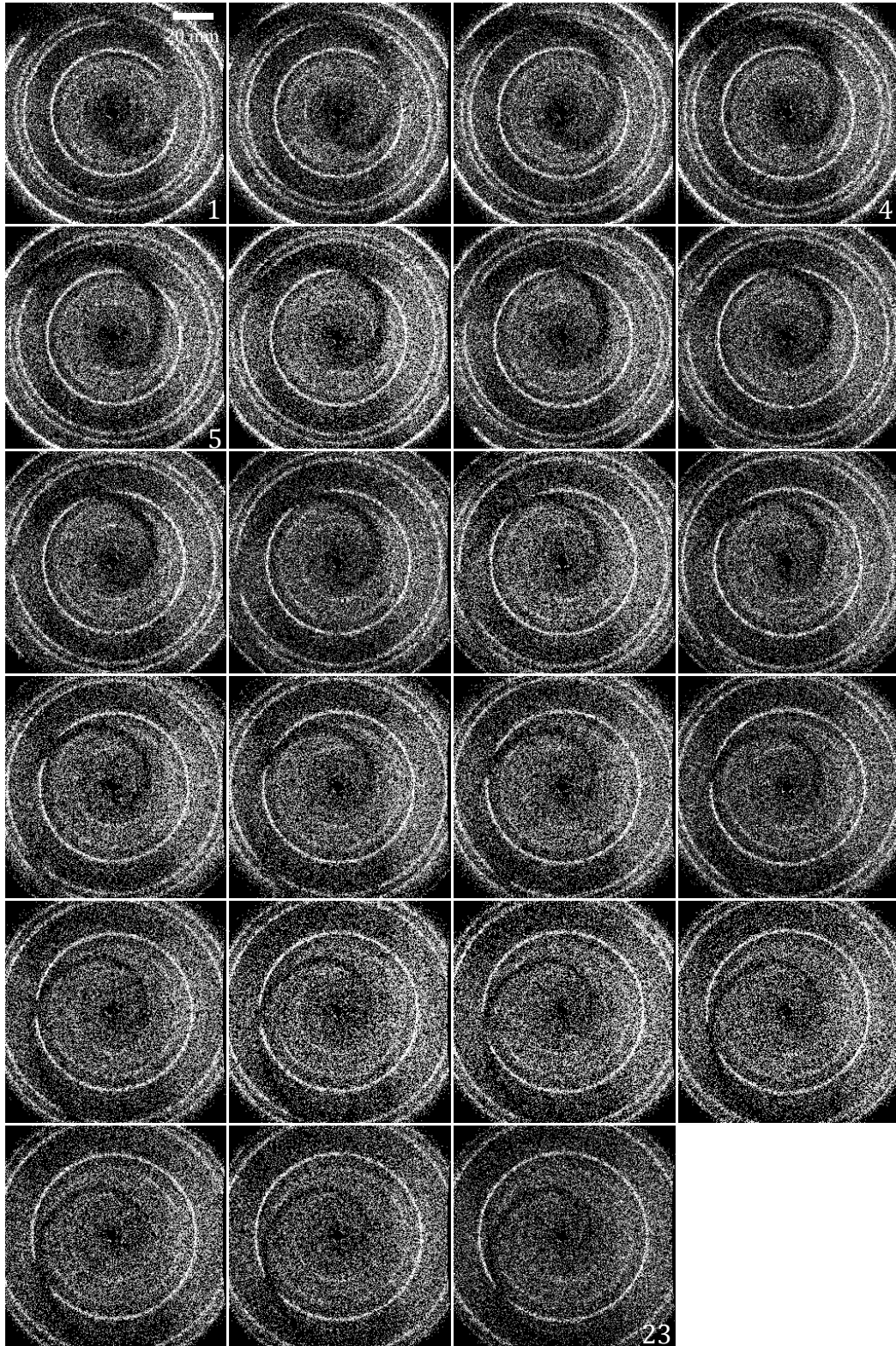


Figure 8.64 A series of empirical diffraction images captured as an Al_2O_3 sample was translated along the primary beam axis with an Archimedean spiral encoder.

As observed, the radius of the Debye rings increases as the sample is translated further away from the detector (from images 1 to images 23); whereas the dimensions of the Archimedean spiral decrease. The latter is a magnification effect resulting from incoherent scattering.

Encoding of the Debye rings occurred at single unique locations along their circumference, relative to the radius. The encoded points arose from the scattered beam's absorption by the Archimedean spiral. Analysis of the recorded diffraction images and interpretation of their encoding involved determination of the Debye ring's radius at the detector plane (R_D) and the encoded angle (ψ), as indicated in Figure 8.65.

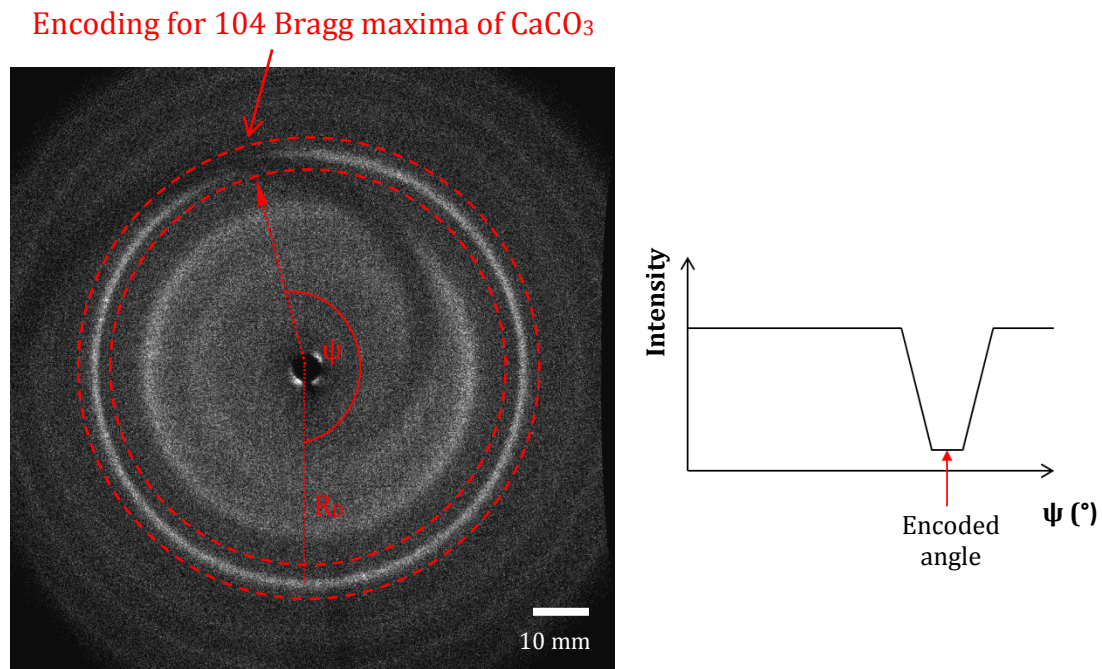


Figure 8.65 Illustration of the encoding caused by the Archimedean spiral for the 104 reflection from CaCO_3 ; at radius R_D and encoded angle ψ . The encoding causes a single intensity minimum for each Debye ring.

Evaluation of the scattering profiles' encoding was achieved by an integration around the circumference of each Debye cone, as the sample was translated along the primary axis, over a finite range of 2θ angles, and the intensity was plotted as a function of the encoded angle ψ (Figure 8.66).

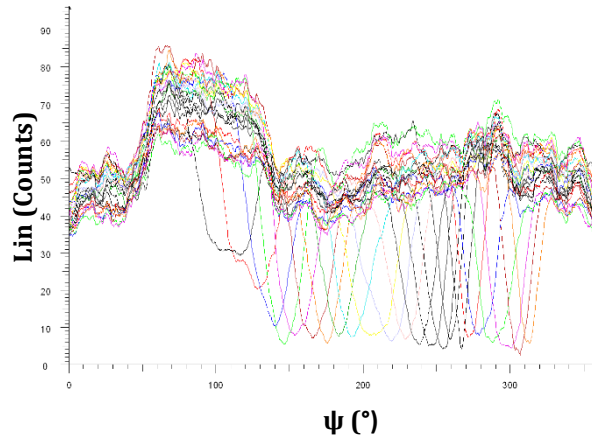


Figure 8.66 The scattering intensity of a single Debye ring (104 reflection from CaCO_3) around its circumference as the sample was translated along the primary axis.

Counter plots indicating correlation of the sample's linear translation along the primary axis with the encoded angle ψ are given in Figure 8.67. The rotation of the encoding point along the 104 Debye ring of CaCO_3 and Al_2O_3 samples is demonstrated, as the sample is translated along the primary axis. For both samples, there is a clear deviation from the linear relationship, indicating a polynomial trend.

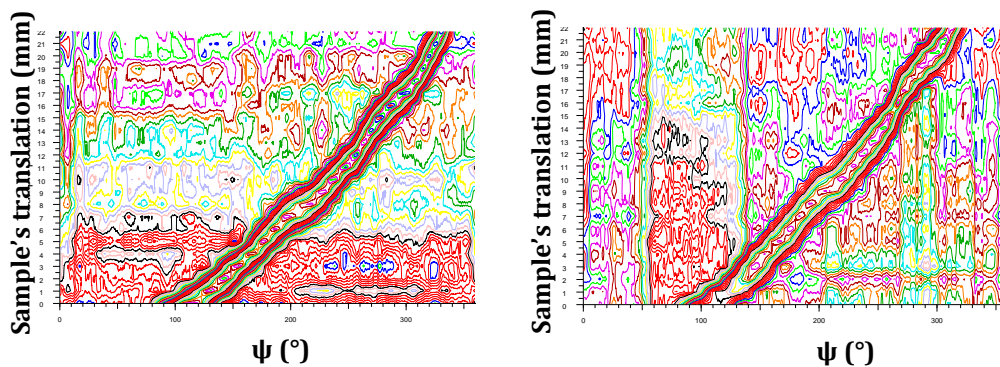


Figure 8.67 Counter plots of the encoding angle on the 104 Debye ring of CaCO_3 (left) and Al_2O_3 (right) samples, as the sample was translated along the primary axis.

For this reason, the radius of the Debye cones onto the spiral (R_{AS}) was calculated based on the known 2θ angle of CaCO_3 (29.4°) in order to determine the relationship between R_{AS} and the intersection angles as previously explained (Section 8.3.2.1).

Figure 8.68 represents the relationship between the encoding angles and the radii of the Archimedean spiral employed for these empirical experiments. The relationship follows a polynomial trend, instead of the linear inclination specified by the spiral's $R_{AS}=a+b\psi$ equation. This is an indication of a non-uniform distortion and perhaps incorrect alignment of the Archimedean spiral during the experimental work. The R_{AS} radii and hence the D_{SD} distance and 2θ angles of the mineral (CaCO_3) loaded cellulose were calculated using the polynomial equation $R_{AS} = 0.00009\psi^2 + 0.0171\psi + 1.304$, as obtained by the relationship shown in Figure 8.68.

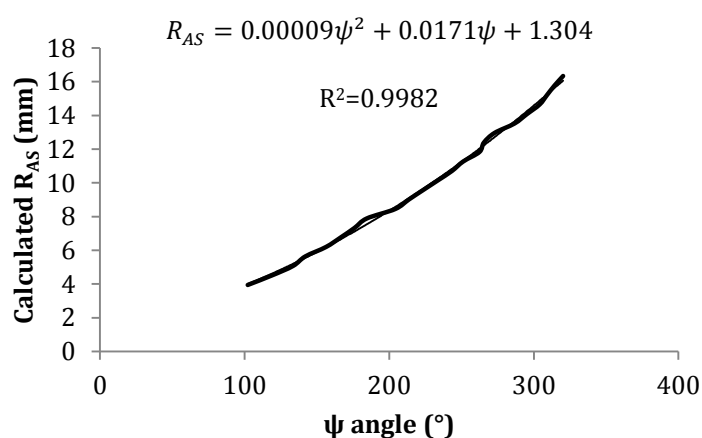


Figure 8.68 The relationship between measured encoding angles ψ from the diffraction data of a CaCO_3 loaded cellulose and the radii of the Debye cones onto the Archimedean spiral (R_{AS}), as calculated from CaCO_3 's scattering angle 29.4° .

Calibrated sample-to-detector distances and scattering angles at each diffraction images are presented in Table 8.6. The sample-to-detector distances were calculated to range between 61-83 mm and the average scattering angle of the sample was determined to be 29° . These values come in agreement (within experimental errors) with the known distances (61-83 mm) and 2θ angle of CaCO_3 (29.4°).

Correlation between the calculated sample-to-detector distances, as determined by the spiral's encoding and by the Debye cone's radius (from known 2θ angle) for the 104 reflection from CaCO_3 , is shown in Figure 8.69. The calculated sample-to-

detector distances indicate a relatively linear relationship, demonstrating successful calibration of the Archimedean spiral encoding.

Table 8.6 A list of the calibrated radii of the Debye cone onto the Archimedean spiral calculated via $R_{AS} = 0.00009\psi^2 + 0.0171\psi + 1.304$ and the corresponding calculated sample-to-detector distances and scattering angles (2θ) for CaCO_3 (mineral loaded cellulose).

Image number	Measured R_D (mm)	Measured ψ angle ($^\circ$)	Calculated R_{AS} (mm)	Calibrated D_{SD} (mm)	Calculated 2θ ($^\circ$)
1	35	102	4	61	30
2	35	119	5	62	30
3	36	133	5	63	30
4	36	142	6	64	30
5	37	156	6	65	30
6	37	166	7	66	30
7	38	176	7	66	30
8	38	184	8	67	30
9	39	204	9	69	29
10	39	214	9	70	29
11	40	223	10	71	29
12	41	233	10	72	29
13	41	243	11	73	29
14	42	251	11	74	29
15	42	262	12	76	29
16	43	265	12	76	29
17	43	273	13	77	29
18	44	287	14	79	29
19	44	295	15	80	29
20	45	304	15	82	29
21	45	309	16	82	29
22	46	314	16	83	29
23	46	320	16	83	29
Mean					29
Standard deviation					0.3

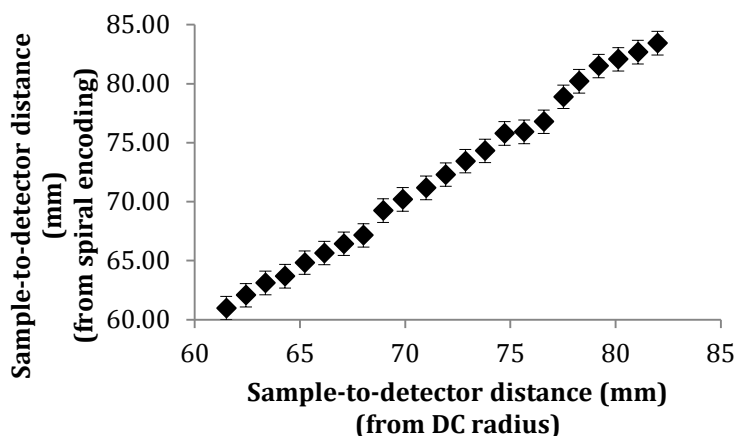


Figure 8.69 Correlation between calculated sample-to-detector distances obtained from spiral encoding and Debye rings for the 104 Debye ring of CaCO_3 .

The determined scattering angle, 29° , was then used to calibrate the scattering profile from a CaCO_3 loaded cellulose sample and compare it to the standard profile of CaCO_3 , as illustrated in Figure 8.70. As seen, there is a good agreement between measured and standard scattering signatures from CaCO_3 .

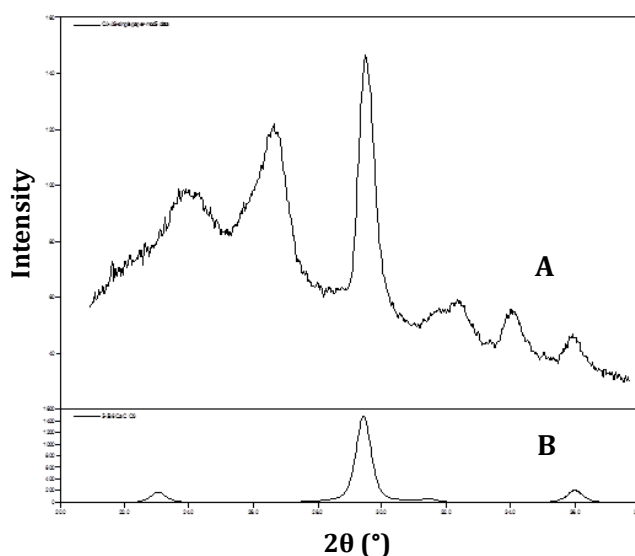


Figure 8.70 Comparison of the scattering distribution from a CaCO_3 loaded cellulose sample as recovered by a calibrated Archimedean spiral encoder (A) and from a standard profile of CaCO_3 (PDF card No. 5-586) (B).

The same calibration equation was then applied to the empirical data obtained from Al_2O_3 and the results are presented in Table 8.7. The average scattering angle for the highest intensity Debye ring (116 reflection from Al_2O_3 at 0.160 nm) used for data analysis was calculated to be 26° , which corresponds to the scattering maxima from Al_2O_3 at 25.57° .

Table 8.7 A list of the measured radii of the Debye cones (R_D) and intersection angles ψ at each diffraction image, the calibrated radii of the Debye cone onto the Archimedean spiral calculated via $R_{AS} = 0.00009\psi^2 + 0.0171\psi + 1.304$ and the corresponding calculated sample-to-detector distances and scattering angles (2θ) for Al_2O_3 .

Image number	Measured R_D (mm)	Measured ψ angle ($^\circ$)	Calibrated R_{AS} (mm)	Calculated D_{SD} (mm)	Calculated 2θ ($^\circ$)
1	30	99	4	62	26
2	30	110	4	63	26
3	31	125	5	64	26
4	31	136	5	65	26
5	32	146	6	66	26
6	32	157	6	67	26
7	33	165	7	68	26
8	33	174	7	68	26
9	34	184	8	70	26
10	34	195	8	71	26
11	35	205	9	72	26
12	35	217	9	73	26
13	35	225	10	74	25
14	36	233	10	76	26
15	37	241	11	77	26
16	37	246	11	77	26
17	37	254	12	78	26
18	38	260	12	79	26
19	38	266	12	80	26
20	39	276	13	81	26
21	39	286	14	83	25
22	40	295	14	84	25
23	40	301	15	86	25
Mean					26
Standard deviation					0.2

A correlation plot between the sample-to-detector distances calculated from known 2θ (Debye rings' radius) and from the spiral encoding for Al_2O_3 is presented in Figure 8.71; indicating a relatively linear trend as expected.

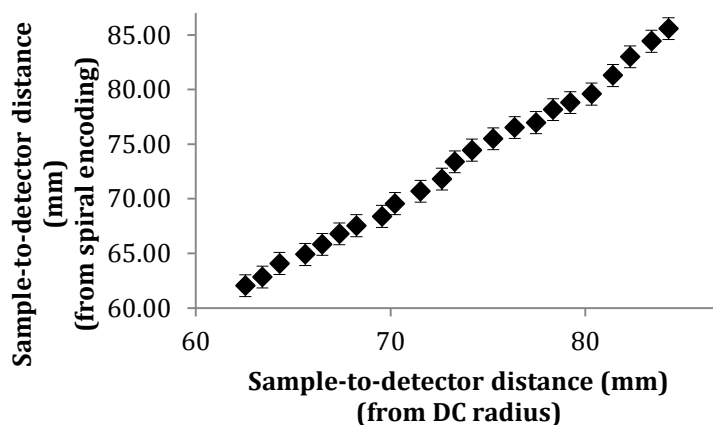


Figure 8.71 Correlation between calculated sample-to-detector distances obtained from spiral encoding and Debye rings for the 104 Debye ring of Al_2O_3 .

A series of diffraction data (Figure 8.72) was also acquired from a pair of CaCO_3 loaded cellulose samples that were spatially separated along the primary axis. One sample remained fixed, whilst the other was translated along the primary axis. As demonstrated in Figure 8.72, the radius and intersection angle of one of the two Debye rings under examination remained constant (red solid box), as the sample was translated; whereas the radius and intersection angle of the other altered (red dotted box). The radii of the Debye rings (from CaCO_3) and encoding ψ angles were measured, and the scattering angles of the samples were determined after applying the calibration procedure described previously. The results are given in Table 8.8.

As seen in Table 8.8, the calculated 2θ angle for the sequence of diffraction images determined via the Archimedean spiral encoder is 29° , for both fixed and translated samples. Both scattering values are, within experimental errors, in agreement with the scattering angle of CaCO_3 at 29.4° .

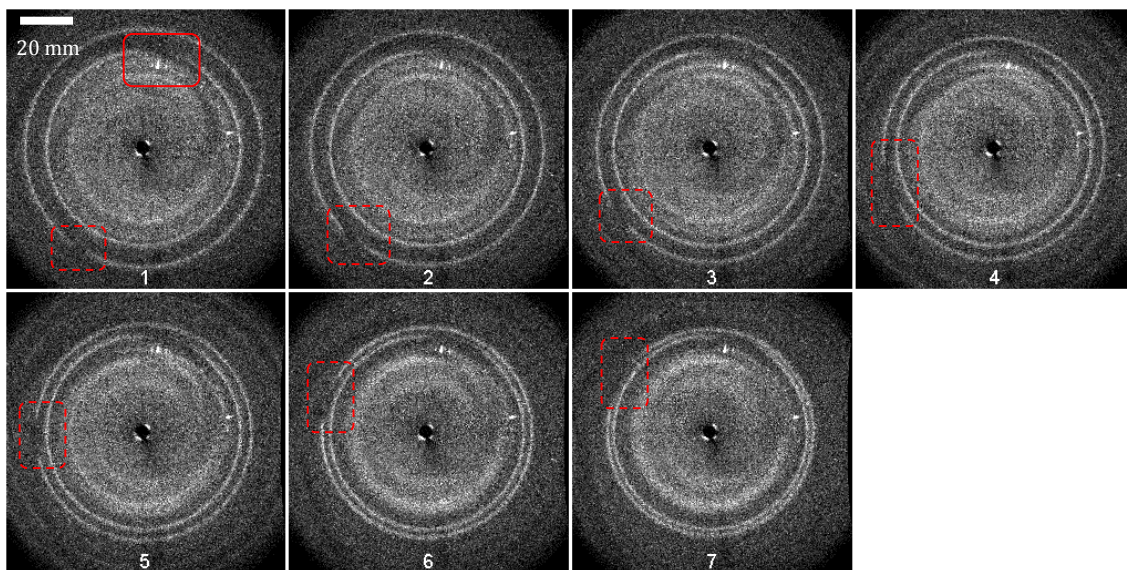


Figure 8.72 A sequence of diffraction images obtained from a pair of CaCO_3 loaded cellulose samples, where one was translated along the primary axis and the other was fixed. The scattering distributions were encoded by an Archimedean spiral (0.055ψ).

Table 8.8 A list of the measured radii of the Debye cones (R_D) and intersection angles ψ at each diffraction image, the calibrated radii of the Debye cone onto the Archimedean spiral calculated via $R_{AS} = 0.00009\psi^2 + 0.0171\psi + 1.304$ and the corresponding calculated scattering angles (2θ) for two CaCO_3 loaded cellulose sheets.

Image number	Measured R_D (mm)	Measured ψ angle ($^\circ$)	Calibrated R_{AS} (mm)	Calculated 2θ ($^\circ$)
1	37	165	7	29
1	46	312	16	29
2	45	304	15	29
3	44	289	14	29
4	42	268	13	29
5	41	254	12	29
6	40	234	10	29
7	39	217	9	29
Mean				29
Standard deviation				0.1

The errors associated with the D_{SD} distance (Equation (8.17)) and 2θ angles (Equation (8.18)) equations for an unknown sample with an Archimedean spiral encoder were assessed by applying Equations (8.19) and (8.20), respectively.

$$\begin{aligned} \sigma^2(D_{SD}) = & \left(\frac{dD_{SD}}{dD_{AS:D}} \right)^2 \sigma^2(D_{AS:D}) + \left(\frac{dD_{SD}}{da} \right)^2 \sigma^2(a) + \left(\frac{dD_{SD}}{db} \right)^2 \sigma^2(b) \\ & + \left(\frac{dD_{SD}}{d\psi} \right)^2 \sigma^2(\psi) + \left(\frac{dD_{SD}}{dR_D} \right)^2 \sigma^2(R_D) \end{aligned} \quad (8.19)$$

$$\begin{aligned} \sigma^2(D_{SD}) = & \left(1 + \frac{a + b\psi}{R_D - a - b\psi} \right)^2 \sigma^2(D_{AS:D}) \\ & + \left(\frac{D_{AS:D}}{R - a - b\psi} + \frac{D_{AS:D}(a + b\psi)}{(R_D - a - b\psi)^2} \right)^2 \sigma^2(a) \\ & + \left(\frac{\psi D_{AS:D}}{R - a - b\psi} + \frac{\psi D_{AS:D}(a + b\psi)}{(R_D - a - b\psi)^2} \right)^2 \sigma^2(b) \\ & + \left(\frac{b D_{AS:D}}{R - a - b\psi} + \frac{b D_{AS:D}(a + b\psi)}{(R_D - a - b\psi)^2} \right)^2 \sigma^2(\psi) \\ & + \left(\frac{-D_{AS:D}}{(R_D - a - b\psi)^2} \right)^2 \sigma^2(R_D) \end{aligned}$$

$$\begin{aligned} \sigma^2(2\theta) = & \left(\frac{d(2\theta)}{dD_{AS:D}} \right)^2 \sigma^2(D_{AS:D}) + \left(\frac{d(2\theta)}{da} \right)^2 \sigma^2(a) + \left(\frac{d(2\theta)}{db} \right)^2 \sigma^2(b) \\ & + \left(\frac{d(2\theta)}{d\psi} \right)^2 \sigma^2(\psi) + \left(\frac{d(2\theta)}{dR_D} \right)^2 \sigma^2(R_D) \end{aligned} \quad (8.20)$$

$$\begin{aligned}
\sigma^2(2\theta) = & \left(\frac{a + b\psi - R_D}{(R_D - a - b\psi)^2 + D_{AS:D}^2} \right)^2 \sigma^2(D_{AS:D}) \\
& + \left(\frac{-D_{AS:D}}{(R_D - a - b\psi)^2 + D_{AS:D}^2} \right)^2 \sigma^2(a) \\
& + \left(\frac{-\psi D_{AS:D}}{(R_D - a - b\psi)^2 + D_{AS:D}^2} \right)^2 \sigma^2(b) \\
& + \left(\frac{-b D_{AS:D}}{(R_D - a - b\psi)^2 + D_{AS:D}^2} \right)^2 \sigma^2(\psi) \\
& + \left(\frac{D_{AS:D}}{(R_D - a - b\psi)^2 + D_{AS:D}^2} \right)^2 \sigma^2(R_D)
\end{aligned}$$

Equations (8.19) and (8.20) were solved for a simulated Archimedean spiral arrangement; where $D_{AS:D} = 10$ mm, $a = 0$, $b = 0.055$, $\psi = 207.5^\circ$ and $R_D = 10.9$ mm. The standard deviations used of each variable were $\sigma(D_{AS:D}) = \pm 1$ mm, $\sigma(a) = \pm 0.1$, $\sigma(b) = \pm 0.03$, $\sigma(\psi) = \pm 5^\circ$ and $\sigma(R_D) = \pm 0.5$ mm. The errors $\sigma(D_{SD})$ and $\sigma(2\theta)$ were determined to be ± 1.03 mm and $\pm 1.42^\circ$, respectively. The greatest error for the calculated sample-to-detector distance arises from the spiral-to-detector distance ($D_{AS:D}$); whereas the greatest error for the scattering angles comes from the radius of the Debye cones at the detector plane (R_D). It is however important to note, that the second and third greatest errors arise from the b and a values of the Archimedean spiral respectively, and minor variations of these values can have a major effect on the calculated errors, especially on the D_{SD} distance.

Similarly to the wire encoder, when a 1% error was employed to all variables, the greatest errors for D_{SD} distance ($\sigma(D_{SD}) = \pm 0.1$ mm) and 2θ angles ($\sigma(2\theta) = \pm 0.32^\circ$), originated from $D_{AS:D}$ distance and R_D radius, respectively.

To summarise, it was shown that an Archimedean spiral could be employed as a post-sample encoder to acquire spatial discrimination of either a single or multiple samples along a primary axis and determine their diffraction profile. However, minor variations in the Archimedean spiral's structure either by rotation or by non-ideal manufacturing could result in additional experimental errors. Calibration of the Archimedean spiral's encoding equation with a standard sample could provide

a more accurate estimation of measurements. The greatest errors when calculating sample-to-detector distance and 2θ angles arise from inaccuracies in the spiral-to-detector distance and Debye cones radius at the detector plane, respectively.

8.4 Concluding remarks

In this chapter, the concept of innovative pre- and post-sample coded apertures was introduced.

An annular beam employed for FCG experiments was considered as a pre-sample coded aperture, aiming at the recovery of conventional XRD data from FCG patterns. The proof-of-concept was presented with simulated data and the coded aperture was assessed under various non-ideal conditions in a simulated manner. Optimised procedures were applied to pseudo-empirical and empirical FCG data. The methodology was also applied to recover Debye rings from FCG data from samples exhibiting preferred orientation or large grain size. Even though reconstruction of conventional XRD data from simulated and pseudo-empirical data was successful, recovery of accurate scattering maxima positions from empirical FCG data was not achieved.

An encoded annular beam was then considered as a type of pre-sample encoder and its ability to discriminate between converging and diverging condensation rings in an FCG pattern was demonstrated.

Lastly, the concept of two different post-sample encoders, a linear wire and an Archimedean spiral, for conventional transmission diffraction geometries was investigated. The encoders were initially assessed in an analytical and simulated approach. The proof-of-principle was then established empirically with a pencil beam arrangement, demonstrating successful determination of the scattering angles of unknown samples with no *a priori* knowledge on their positions along a primary axis. The capability of a linear encoder was also examined with an annular beam arrangement, by an absorbing edge, indicating effective discrimination between converging and diverging condensation rings.

Chapter 9 DISCUSSION

Outline

In this chapter, a critical discussion of the key findings of this research is presented. The chapter is divided into seven main studies, involving: (1) comparison of FCG with conventional XRD techniques (2) analysis of threat and benign liquids for aviation security and comparison to previous studies, (3) analysis of non-ideal samples in terms of preferred orientation and large grain size by FCG, (4) investigation of the effect of a random sample orientation with respect to FCG's primary axis, (5) FCG analysis of multiple samples with a spatial discrimination along a primary axis, (6) employment of an annular beam as a pre-sample coded aperture aimed at the recovery of conventional XRD data and (7) employment of pre-sample and post-sample encoders to either discriminate between converging and diverging condensation rings or obtain spatial information of unknown samples along a primary axis.

9.1 Peak broadening

Peak broadening may be considered one of the main limitations of FCG, as it decreases specificity and in extreme cases, it can restrict sample identification. It was therefore essential to determine the origin of this effect. One of the aims of this study was to identify which component contributed the most to diffraction peak broadening. Initially, FCG was analytically compared to conventional transmission XRD by exploiting their differences in peak broadening and absolute intensities of scattering maxima. Following that, data obtained from empirical experiments were utilised to compare the width and intensities of diffraction peaks acquired from both geometries. Lastly, peak broadening was investigated by altering various instrumentation components.

FCG data has been typically interpreted by a circular integration around condensation foci over a sequence of diffraction caustics, as initially proposed by Rogers et al. (2010). In Section 7.2.1, it was demonstrated that FCG data could be interpreted in terms of both condensation foci and condensation rings. Both approaches, integration around a condensation focus and radial integration of condensation rings (0° - 360° azimuthal integration), possess the same enhanced intensity when compared to conventional XRD data, since condensation foci consist of converged condensation rings. However, acquisition of a scattering profile from condensation foci requires a sequence of FCG images. In contrast, acquisition of scattering signatures from a radial integration employs a single FCG image. This advantage of radially integrated FCG images can be extremely important within areas in need of rapid identification such as security screening, as a single FCG image can be captured at 1 second time exposure. Even though informative data are acquired at 1 second, high quality data requires longer exposure times of ~ 10 seconds with the FCG laboratory arrangement, as shown in Figure 7.7. Acquisition of FCG data in real-life scenarios, such as screening at airports, may require longer exposure times due to clustering of objects within an inspection volume under various non-ideal conditions e.g. sample crystallinity, sample thickness and orientation. This study focused on the investigation and development of FCG under such non-optimised conditions, in a controlled environment.

As discussed throughout Chapter 2 and Section 3.4, screening techniques for aviation security require short acquisition times to offer a high throughput. Technologies based on ADXRD are traditionally limited by long acquisition times, mainly due to translation or rotation requirements. EDXRD techniques however, do not have this limitation but suffer from low quality data due to high degrees of collimation; hence need to increase exposure times, which effectively leads to long acquisition times. A current technique, initially proposed by Christodoulou et al. (2011), aimed to acquire high quality crystallographic data in short exposure times by combining EDXRD with ADXRD, as described in Section 2.1.4. More recent studies on this technique indicated that acquisition time is limited to 10 minutes as indicated by O'Flynn et al. (2013a), which is significantly high for aviation security. Moreover, the small size of the incident beam causes further limitations when a large area requires investigation, as explained in Section 2.1.4.

FCG however, employs an annular beam that can interrogate a greater surface area than conventional pencil beam geometries. It is important to note here, that if an annular beam illuminates a sample smaller than the beam's diameter, then no significant intensity advantage would be observed, compared to a pencil beam of the same diameter as the annular beam's wall thickness. Similarly, if a pencil beam with a cross-section area equal to the cross-section area of the annular beam was employed, there would be no difference in intensity of the scattering maxima. However, a significantly large pencil beam divergence would result in considerably broad (non-informative) diffraction peaks. FCG combines the high intensity gained from an increased incident beam area with its property to pseudo-focus scattering maxima. Therefore, FCG has the advantage of acquiring informative diffraction profiles (in terms of peaks' widths) with enhanced intensity.

As demonstrated throughout Chapter 7, FCG generated scattering maxima with enhanced intensity at significantly shorter exposure times than conventional XRD. In this work, a typical exposure time of 10 seconds was employed for FCG data, whereas for conventional XRD data a 10 minutes exposure time was typically employed. This considerably shorter time exposure can be a major advantage for FCG, especially when a single image is required, as in the case of radially integrating condensation rings. When however FCG data are interpreted in terms of condensation foci i.e. sequence of hundreds of data images, acquisition time increases significantly to ~2 hours, even though the exposure time is low (10 seconds). It is therefore critical to be able to interpret single FCG images to meaningful diffractograms in order to identify an unknown material.

Another advantage of radially integrating FCG images is the narrower diffraction peaks arising from the condensation rings, when compared to either conventional XRD data or FCG condensation foci data. This advantage lies within the pseudo-focusing property of condensation rings. Narrower diffraction peaks translate into better resolved peaks and higher system specificity, which is a key factor for security screening as it reduces false alarm rates (Chapter 2). This outcome was based on the theoretical predictions described in Section 7.2.1, that intended a direct comparison of maximum widths of conventional and FCG scattering maxima (condensation foci and rings). Even though peak broadening for conventional XRD

is widely known, analytical descriptions were provided in Section 7.2.1 for benchmarking with FCG.

It was demonstrated that in all cases when various parameters were altered, such as scattering angle, sample thickness, angular beam divergence, beam wall thickness, sample position and sample-to-detector distance, radial integration of condensation rings provided significantly narrower diffraction peaks, even when compared to conventional XRD. Nonetheless, an increase in all variables individually, causes an increase in the width of the diffraction peaks independent of data interpretation approach. A significant trend in the discriminating power of scattering maxima was however noticed as the scattering angle increased, as suggested by Rogers et al. (2010). Condensation foci tend to produce narrower diffraction peaks at high 2θ angles, whereas pencil beam XRD generates narrower peaks at low 2θ angles. Even though Rogers et al. (2010) commented on this phenomenon, there was no reference to FCG condensation rings. Theoretical analysis of peak broadening when integrating condensation rings revealed a similar trend to conventional XRD, i.e. narrower peaks at low 2θ angles. Furthermore, the widths of the scattering maxima are shown to be narrower than that of pencil beam XRD (see Figure 7.13 (A)). It should be highlighted, that such direct comparison of pencil and annular beam geometries requires a pinhole of the same diameter as the wall thickness of an annulus (Section 7.2.1).

Even though radial integration of single FCG images offers major advantages, it suffers from the simultaneous presence of converging and diverging condensation rings in single images. Meaningful interpretation of condensation rings lies within their converging or diverging nature, as indicated in Section 7.2.1. Therefore, different equations were established to convert radial distances of converging and diverging condensation rings to conventional diffractograms. Consequently, it was not possible to interpret single FCG images into informative scattering signatures in practise, as converging and diverging rings were indistinguishable in single FCG images. This could be resolved by either capturing a limited sequence of FCG images or by encoding the condensation rings in an unambiguous manner. In this work, this particular limitation was targeted by pre-sample and post-sample encoders, as demonstrated in Section 8.2 and Section 8.3, respectively, and it is discussed in greater depth later in Section 9.7.

Analytical predictions on approximated intensity enhancement offered by FCG over pinhole beam arrangement were previously determined by Rogers et al. (2010) and Chan et al. (2010) for an annular collimator with the same wall thickness as a pinhole's diameter. A more accurate description of the intensity gain when employing an annular beam was provided in Section 7.2.1, by comparing it to a pinhole of either equal or non-equal diameter size to the annulus' wall thickness. This provided a more precise interpretation of the intensity enhancement, able to compare even non-equivalent collimation optics. However, it should be noted that the analytical predictions use a simplified model aiming to provide a mathematical description of the typical intensity gain of FCG without taking into account any intensity correction factors, such as the Lorentz and polarisation factors. Consequently, the relative intensities of FCG and conventional XRD differ significantly, hence predicted and measured FCG:pinhole intensity ratios are not in absolute agreement. Furthermore, it is important to note that small changes in either the diameter of the pinhole or the radii (inner or outer) of the annular collimator would affect the intensity of the diffraction peaks considerably. For example, a ± 0.01 mm change in collimation (annulus of 17.5 mm and 18 mm inner and outer diameter, respectively or pinhole of 0.66 mm diameter) measurements would have an effect of $\sim \pm 4\%$ in intensity. Therefore, when comparing calculated and measured intensity values, it is important to be aware of the limitations arising from inaccurate collimation measurements.

Returning to the matter of peak broadening, initial investigation of empirical diffraction profiles from an Al_2O_3 sample by FCG and conventional XRD (by FCG system and by an independent diffractometer) indicated that the diffractograms obtained by the FCG system were comprised of broad diffraction peaks, regardless of the geometry employed (see Figure 7.7). Peak broadening can therefore be considered a result of a single or a combination of instrumentation components, such as the X-ray source's focal spot, collimation optics, beam divergence, sample thickness and detector. Collimation optics and sample thickness can have a major effect on beam divergence (incident or scattered, respectively), which is considered as a key parameter in peak broadening. In addition to beam divergence, peak broadening can also be a consequence of unsharpness of the diffraction signal that can be caused either due to a large focal spot size of the X-ray source (geometric

unsharpness), movement of one of the system's instrumentation or due to the detector's ability to diffuse light and convert X-rays into visible light signal (point spread function).

The effect of the X-ray source's focal spot on peak broadening was investigated by an alternative X-ray source with a smaller focal spot (micro-CT system). Preliminary experiments (Section 7.2.4) indicated that diffraction signals obtained from the CT system appeared to have a greater specificity, in terms of narrower diffraction peaks. It is important to note, that even though the same collimation optics and detector were employed for both experimental procedures, the beam divergence employed for the experiments performed within the CT system was greater, due to different collimator and sample positions (Section 7.2.2). Even though, an increased beam divergence was expected to broaden the diffraction peaks, the FWHM of the diffraction maximum obtained within the CT system decreased by ~15%. This can be considered a result of the smaller dimensions of the focal spot of the CT's X-ray source, which reduces geometric blurring of diffraction signals. It can therefore be suggested, that if the same collimator and sample z-positions were retained for both arrangements, the widths of scattering signals obtained within the CT-system would have been even narrower.

The ability to collect high quality diffraction profiles within the CT system is very promising and shows great potential for security screening. Future development of FCG could consider utilising the CT system, as it has the ability to employ higher X-ray energies e.g. W target; thus being able to penetrate suitcases and objects within them, which is essential for security screening.

The effect of sample thickness on peak broadening was also investigated with FCG, indicating that the width of the diffraction peaks increases and the peaks become less resolved as the sample thickness increases beyond an optimum value. As suggested in Section 3.1, each scatterer has an optimal thickness that can be calculated by Equation (3.3). Even though the sample thickness of the materials analysed was significantly greater than their optimal thickness as indicated in Section 7.2.3, characteristic scattering profiles were obtained, especially from the thinner samples. It should be noted that when the thickness of NaCl powder was increased, certain scattering maxima were not observed (or possessed significantly

low intensity). This effect was expected with the thinner sample as a decrease in the sample volume would accommodate less number of grains. When NaCl was analysed by conventional XRD, the scattering profiles arising from different sample thicknesses varied significantly. As it was indicated in Section 5.2 (Figure 5.6) with a sample exhibiting preferred orientation, when a section of the diffraction pattern (pencil beam) from such non-ideal samples (with texture or large grain size) is integrated, it is possible to disregard certain scattering maxima, in contrast to FCG (see Section 7.4.2 and Section 7.5.2).

To conclude, FCG has the potential of narrower diffraction peaks with ideal instrumentation that could offer low beam divergence and low geometric blurring. It was demonstrated that peak broadening is not a significant effect of FCG when the primary beam's wall thickness is low, but most probably of the instrumentation employed. It was determined that even though beam divergence, X-ray source focal spot, sample thickness, sample and detector position and beam geometry play an important role in peak broadening, diffraction peaks obtained by the FCG system (independent of beam geometry) were not in the same order as diffraction peaks acquired by a benchmarked diffractometer (Bruker D8 GADDS). This can either be a combination of non-optimised instrumentation components or due to the lack of optimised software to interpret diffraction data from FCG's detector. As it will be discussed in Section 10.2, another aspect that should be targeted in future work is the employment of a diffracting annular collimator to essentially narrow the width of scattered rays.

Ideally, radial integration of single FCG images should be employed, as this has been theoretically determined (Section 7.2.1) to provide sharper diffraction peaks than conventional XRD. This can exhibit major advantages and potential of FCG in security screening as it would employ high quality ADXRD data at short acquisition times with enhanced intensity. However, in order to engage such an approach, discrimination between converging and diverging condensation rings is essential and it will be discussed later in Section 9.7.

9.2 Analysis of liquid samples

Analysis of non-crystalline materials was performed with liquid samples, which may be determined as either a threat or a non-threat to aviation security. Categorisation of threat and benign liquids was based on the work of Harding et al. (2010), as listed in Table 2.3 (Section 2.2.2). This classification was slightly altered to include 3rd class threat liquids, including low concentration chemicals such as 3% H₂O₂ that can be considered dangerous when accumulated in higher concentrations. This resulted in expanding the variety of threat liquids analysed, as more chemicals are considered hazardous with increasing intelligence of HMEs, as explained in Chapter 2. Additionally, in this study, fruit preserves such as jam were included within the concentrated aqueous category, rather than in the amorphous category suggested by Harding et al. (2010); as all liquids studied are assumed to be amorphous. It should be noted that experimental data illustrated that jam possessed a higher degree of order than other liquids examined in this work.

As explained previously in Section 3.2.3, interpretation of X-ray coherent scattering from amorphous substances such as liquids can be challenging, as they do not yield the same degree of information as crystalline substances. Early studies such as that performed by Luggar et al. (1997) suggested that identification of explosives could be based on their crystallinity, and substances that generated broad featureless diffraction patterns were differentiated from explosives. Nowadays, this is not the case, as there is an increased development of liquid explosives and they are widely known to produce broad halos due to their lack of crystallinity. Nonetheless, Harding et al. (2010) have shown that discriminative data can be obtained from liquid samples if their MIF and RDF are considered, as described in Section 2.2.2. In this work, it has been demonstrated that identification and discrimination of threat and benign liquids can be achieved solely on the position of their dominant scattering maximum, without the need of subtracting water's MIF from each liquid's MIF (residual MIF), as suggested by Harding et al. (2010). This may be a result of the angular dispersive arrangement employed during FCG analysis, in contrast to EDXRD engaged by Harding et al. (2010). As demonstrated in Section 3.4 (Figure 3.8), ADXRD offers data of higher specificity when compared to EDXRD.

Therefore, FCG enabled discrimination between threat and non-threat liquids by the region of their scattering maxima position. Threat liquids were determined to have

a scattering maximum position between 0.401- 0.442 nm, with the exception of H₂O₂ (3% and 30%); whereas the scattering signal of benign liquids emerged at a lower scattering vector magnitude (Section 7.3.2). It should also be noted, that FCG analysis of liquid samples was performed over a limited 2 θ range to enable more rapid data acquisition.

The scattering maximum position of water at 0.325 nm is in agreement with previous studies mentioned in Section 3.3.3, reporting a single dominant peak within the range of 0.304-0.327 nm. Other researchers such as Stewart (1931) state that water generates a dominant peak at 0.324 nm, similarly to this study, but with two additional maxima of low intensity at higher scattering angles. The absence of the additional scattering maxima in the data presented herein may be due to the limited 2 θ range acquired by the detector. Nevertheless, successful discrimination of liquids was based entirely on the dominant maximum from innocuous and threat liquids, hence additional maxima were not required.

As discussed in Section 2.2, H₂O₂ is considered to be a major threat liquid oxidiser, especially after the London transatlantic plot of 2006. Previous research performed by Harding et al. (2010) demonstrated discrimination between 30% concentration of H₂O₂ and acetone, but limited discrimination between H₂O₂ and water based on Z_{eff} measurements. Herein, discrimination between water and 30% H₂O₂, as well as 30% and 3% concentration of H₂O₂, has been presented. It was demonstrated that FCG has the potential to distinguish between 30% H₂O₂ and water by a shift in the former's scattering maximum position to higher scattering angles. It is believed that if the concentration of H₂O₂ is increased beyond 30%, its discrimination from water would be more distinctive, similarly to other threat liquids that were in pure form. 3% H₂O₂ was not distinguished from water by its scattering maximum position due to the low concentration of H₂O₂. Discrimination between water and 30% H₂O₂ is considered a key feature for any screening technique, as the latter is the current precursor of choice for terrorists (see Section 2.2). Moreover, it is extremely important for a screening tool to distinguish H₂O₂ from water, as it would reduce false alarm rates significantly.

The higher scattering angle of 30% H₂O₂ when compared to water and other liquids can be explained by its denser nature i.e. lower intermolecular distances. The higher

density of non-threat liquids and H₂O₂ can also explain the lower intensity of their scattering maxima. Lower intensity of non-threat liquids has also been supported by Zhong et al. (2012), as discussed in Section 2.2.2. Threat liquids have a higher electron density and a lower linear absorption coefficient (Section 3.1). For example, hydrogen peroxide, water and ethanol have a linear absorption coefficient (μ) value of 1.8202 cm⁻¹, 1.2067 cm⁻¹ and 0.6559 cm⁻¹, respectively. This explains the larger area of their scattering maxima as their linear absorption coefficient decreases (see Figure 7.29 and Figure 7.30). This change in intensity between innocuous and threat (except H₂O₂) liquids can act as a supplementary feature for discrimination, under controlled conditions (benchmarked). However, in security screening, where the volume of the liquid under inspection is usually unknown, discrimination of liquids based on their scattering maxima intensity may be misleading.

In addition to single liquids, this work expanded in the analysis of miscible and immiscible mixtures of threat and non-threat liquids. The observations were consistent with those reported initially by Krishnamurti (1929) and Stewart (1931). Liquid mixtures caused alterations in either the number of scattering maxima or their position (s) depending on their miscibility (Section 7.3). Therefore, it was shown that the presence of a threat liquid can be identified when mixed with a benign liquid in equal volumes, either by additional peaks (immiscible mixture) or by an intermediate scattering angle to that of threat and non-threat liquids (miscible mixture). It should be noted that all liquid mixtures were analysed in a 1:1 ratio. A solution of 30% concentration of H₂O₂, however, can be considered to be a miscible mixture of H₂O₂ and water in a 3:10 ratio; which is similar to the 1:3 ratio reported by Krishnamurti (1929), demonstrating significantly weak maxima at intermediate distances of the individual liquids. Therefore, this can support the suggestion of more effective discrimination when the concentration of H₂O₂ is increased beyond 30%.

In order to establish the accuracy of the outcomes, the reproducibility of FCG data with liquid samples was evaluated with a threat liquid. It was demonstrated that upon accurate calibration of the system, specifically of sample-to-detector distance, scattering maxima positions were reproduced successfully, within experimental errors.

Furthermore, FCG data were compared to conventional XRD data from both benign and threat liquids. It was verified that even with non-crystalline materials, the enhanced intensity of FCG was retained, signifying better discrimination between threat and non-threat liquids. Moreover, FCG scattering signatures from liquid samples are not limited by peak broadening, as they are already significantly broad halos even with standard XRD techniques.

9.3 Preferred orientation and large grain size

FCG's potential to analyse samples exhibiting either preferred orientation or large grain size was investigated. A series of samples with preferred orientation and a series of samples with large grain size were examined by both FCG and pencil beam geometry. This aimed to assess the ability of FCG to analyse such types of samples compared to conventional XRD. This work did not intend to investigate or develop quantitative methods for analysing such samples by FCG. Quantitative assessment of preferred orientation or grain size for the samples analysed was performed for relative comparison purposes and verification of increasing /decreasing texture or grain size.

It was shown in Section 7.4 and Section 7.5 by both simulated and empirical data, that characteristic FCG caustics are produced from samples with preferred orientation and samples with large grain size. Converging condensation rings possess an inverted (intensity) geometry to that of the Debye rings; whereas diverging condensation rings possess the same intensity geometry as the Debye rings. The term 'inverted intensity geometry' of the condensation rings refers to the distribution of the scattering maxima with respect to the latter's distribution as shown by the captured Debye rings. This encoding phenomenon of condensation rings depending on their converging or diverging nature initiated further exploration into encoding either the annular primary beam (pre-sample encoders) or scattering signatures (post-sample encoders), as it will be discussed later on in Section 9.7.

Further analysis of such samples indicated that FCG offers greater sensitivity and specificity when compared to pencil beam XRD. During conventional acquisition of XRD data, where a section of the diffraction profile was integrated, revealed a single

scattering maximum; whereas FCG revealed five scattering maxima. Acquisition of the complete conventional diffraction pattern required long experimental times and yielded broader peaks, possibly due to the greatest pinhole diameter compared to the annulus wall thickness.

A series of samples with decreasing degree of preferred orientation was analysed by both geometries, demonstrating the ability of FCG to analyse samples with preferred orientation at short exposure times. The intensity gain offered by FCG was not affected by the non-ideal nature of the sample. Additionally, a simplistic method for quantitative comparison of the relative degree of preferred orientation exhibited by a series of samples was introduced. It was based on average intensity differences of each Debye cone around its circumference, as similarly suggested by Ingham (2014), for statistical assessment of diffraction maxima from samples with large grain size.

FCG diffraction caustics generated by samples with large grain size were investigated in a similar manner to samples with preferred orientation. Scattering maxima spots from samples with large grain size consequently generate spotty FCG patterns. Analogously to samples with preferred orientation, a series of samples with varying grain size was analysed by FCG and conventional XRD. The samples analysed did not suffer from extreme large grain size (as for example with a single crystal), compared to the primary beam, hence conventional XRD interpretation could have been applied without any major inconsistencies in the number of scattering maxima. The ability of FCG to analyse samples with large grain size was demonstrated effectively without affecting its advantage of enhanced intensity (see Section 7.4.2, Figure 7.55). The relative grain size of the sample series analysed was quantitatively compared by counting the number of scattering maxima present in certain Debye rings in conventional diffraction data. A comparison number for the grain size was obtained by dividing the number of scattering maxima with the interrogated area. Unfortunately, comparison of conventional (Figure 7.61 (d)) and FCG scattering maxima (Figure 7.65) to establish a relationship between the two was not achievable due to the diffuse 2θ range of FCG scattering maxima. The occurrence of FCG scattering maxima spots was broadly diffused and the condensation rings' termini were unidentifiable, as illustrated in Figure 7.65. Future

work should aim at determining the relationship between conventional and FCG scattering maxima spots.

During this work, the potential of FCG to interrogate a series of non-ideal samples exhibiting preferred orientation or large grain size was established. It was also shown that FCG offers certain advantages over traditional XRD techniques when analysing such samples, besides its enhanced intensity. An annular beam has the ability to take into account the whole circumference of a Debye cone. Therefore, FCG data effectively consists of complete Debye rings considering all possible irregularities along their circumference, hence generating more accurate and informative diffractograms. Furthermore, if the sample is heterogeneous, FCG offers greater analytical capabilities due to the larger interrogated area along the surface of the sample offered by its annular beam profile.

It is also important to note that the coded aperture offered by FCG's annular beam (discussed in Section 9.6), has the potential to recover conventional XRD data even from samples with preferred orientation or large grain size, without compromising FCG's main advantages, as shown in Section 8.1.2. Even though simulated, as well as pseudo-empirical experiments were shown to be very promising with such non-ideal samples, empirical data were unable to recover details on the geometry or characteristics of their scattering maxima. Nonetheless, further development of an annular coded aperture could provide positive outcomes and an alternative interpretation method for FCG data acquired from such non-ideal samples. The ability of an annular coded aperture system will be discussed in greater detail in Section 9.6.

9.4 Randomly orientated samples

Up to date, FCG has been reported with samples normal to the primary axis (Chapter 5). Similarly, conventional XRD geometries, such as transmission and reflection arrangements described in Section 3.3, utilise specific sample orientations, i.e. either normal to the incident beam or at a θ angle from the incident beam, respectively.

A more generalised scenario of FCG would involve a sample with a random orientation with respect to the primary axis. As is often the case in inspection

volumes such as suitcases, the sample is randomly positioned without a specific orientation. One could assume that if the sample is not normal to the primary axis, then condensation foci may not be formed; hence, the main advantage of FCG, its enhanced intensity, would be lost. Therefore, this work aimed at examining the effect of a random sample orientation to FCG and its scattering caustics.

Analysis of this effect was performed in three stages, analytical, simulated and empirical, in order to fully appreciate the geometry involved and the resulting scattering rays. The results from all three approaches were, within experimental errors, in good agreement. The key feature of the geometry involved with an annular beam and a rotated sample lies within the non-symmetric footprint of the primary beam on the sample and on the non-equal distances between the sample, detector and X-ray source along the surface of the sample (see Figure 9.1). It was demonstrated that a short continuum of high intensity condensation foci is generated when the sample is not normal to the primary axis.

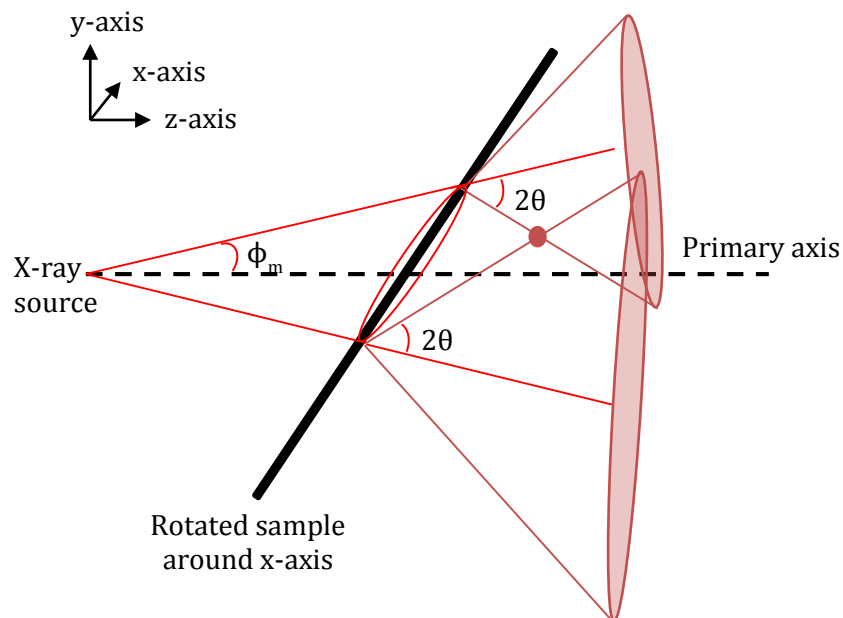


Figure 9.1 Schematic of the geometry involved with an annular beam and a clockwise-rotated sample around the x-axis.

The xyz coordinates of the condensation foci alter depending on the degree, direction and axis of sample rotation, as well as on the sample's scattering angles. An example of the alteration in the location of the condensation foci is shown in Figure 9.1, where a sample with a 2θ angle of 45° is rotated by 35° clockwise around the x-axis. The condensation focus' coordinates were analytically described for any sample orientation either around the x or y axes (Table 7.7) and are in agreement with experimental data. However, simultaneous rotation around both x and y axes by the same angle is more complicated, as explained in Section 7.6.2. Unfortunately, due to unavailability of rotational y-axis within the FCG system, this effect could not be investigated further in order to compare empirical data with theoretical predictions.

If the sample's orientation with respect to the primary axis is unknown, this variation in the condensation foci's coordinates can influence the interpretation of FCG data in an automated system. However, visual inspection of the diffraction patterns can identify the xy coordinates of the condensation foci and enable integration of FCG data at the appropriate coordinates.

Besides the translation of the condensation focus along the x or y axes and z-axis depending on sample rotation, the shape of condensation rings is altered when approaching its focal point (Figure 7.78), as explained thoroughly in Section 7.6.2. Additionally, condensation rings arising from different 2θ angles from a rotated sample occupy different x or y coordinates depending on the rotation axis. This results in a centre misalignment of condensation rings with different 2θ angles that is observed as a circular symmetry distortion, in both simulated and empirical diffraction images (Figure 7.79 and Figure 7.80). Therefore, radial integration of condensation rings would give rise to certain complications, since the centre of each condensation ring would differ, depending on its scattering angle.

It was also demonstrated, that the intersection point of the rotation axes plays a significant role in the location of the condensation foci, as illustrated in Figure 7.81. As discussed extensively, sample rotation will translate the z coordinates of the condensation focus positively along the z-axis, whereas the x or y coordinates (depending on rotation axis) will translate either above or below the x or y axis depending on the direction of sample rotation (clockwise or anticlockwise

respectively). This however is only the case when the intersection point of the rotation axes is at $(0,0,Z_s)$. When the intersection point is translated for example to $(0,>0,Z_s)$ or $(0,<0,Z_s)$ then the xyz coordinates of the condensation foci are altered, as explained in Section 7.6.4. This was illustrated for analytical, simulated and empirical data. It is therefore important to evaluate the intersection point of the rotation axes prior to data interpretation and be aware of this phenomenon, specifically when analysing empirical data that the intersection point can vary for a non-standardised diffraction system.

Comparing FCG with conventional geometries, such as transmission and reflection arrangements described in Section 3.3, FCG can be considered to have a greater sensitivity to sample mis-orientation, due to the shape of the cross-section profile of the incident beam. Conventional XRD arrangements typically utilise a pencil beam profile that strikes the sample at a 'single' location along its surface. In contrast, FCG utilises an annular beam that incidents on a larger area on the sample's surface. Hence, sample rotation would affect the shape of the incident's beam footprint on the sample, as well as the sample-to-detector distance along the surface of the sample, to a greater extent than conventional XRD geometries. It was shown however, that the enhanced intensity of scattering maxima generated by FCG was not influenced by a random sample orientation. Nonetheless, as previously mentioned, the xyz coordinates of scattering maxima were altered relatively to the sample rotation axis, degree and direction, depending on their 2θ angle. Therefore, when the sample is not normal to the primary axis, integration around condensation foci is recommended, as radial integration of condensation rings may result to inaccuracies due to their centre misalignment. For employment of FCG as an automated screening system, it would therefore be essential to couple it with an imaging technique in order to assess the orientation of suspicious objects, hence the xy location of the condensation foci.

9.5 Multiple scatterers

Analysis of multiple scatterers was performed in order to explore the potential of FCG in obtaining scattering data and identify unknown substances that are spatially distributed along the primary axis. It was demonstrated that FCG is capable of

identifying the presence of additional scatterers if their diffraction signals are within the 2θ range captured by the detector (Section 7.7). Multiple samples are acknowledged by the presence of additional scattering maxima that appear in the diffractogram as supplementary peaks or alter the shape of certain peaks when generated at similar positions. Determination of multiple samples was shown to be independent of the material characteristics i.e. same or different samples, but highly dependent upon the sample's position. Moreover, it was theoretically predicted, that FCG scattering maxima possess a greater spatial discrimination than pencil beam scattering maxima (see Section 7.7.1 and 7.7.2). This can be considered as an advantage of FCG over conventional transmission mode beam geometries, as FCG would generate better resolved diffraction peaks from multiple scatterers. On the other hand, this can also be a limitation of FCG if the scattering distribution is greatly extended, and requires acquisition of a larger number of FCG data images (condensation foci) along the primary axis.

Meaningful interpretation of these diffractograms for phase identification requires *a priori* knowledge of each sample's position. This is also often the case in security screening, where the key intention is to determine threat substances that may be superimposed or camouflaged by benign substances with unknown spatial discrimination. There are a few different approaches to overcome this limitation.

One of the solutions would be to generate an extensive database by collecting diffraction profiles from a broad range of threat and perhaps benign materials (commonly found in suitcases) at different distances from the detector along the primary axis. This would provide a database of all current threat materials at any depth within a suitcase, thus being capable of identification. This could be performed in a simulated manner, which is more time effective. As illustrated in Section 7.7.3, the ray-tracing simulator provided an effective representation of empirical data with higher specificity. This approach however, can be very time consuming and it will not have the ability to identify substances that have not been recorded at varying distances.

A second approach involves coupling FCG with an imaging technique, hence determining spatial information of unknown substances prior to material identification. Ideally, the imaging technique would employ the same beam

geometry as FCG to limit instrumentation components and system complexity. Such an imaging technique is discussed in Section 5.2, referred to as MXAT. The annular beam geometry is employed to obtain both tomographic and material characteristic information. MXAT has the capability of providing a tomographic 3D view of the suitcase under investigation; thus determining depth information of unknown objects. A simultaneous “system of systems” approach can be adapted with MXAT acting as an initial screener, determining shape and position of substances within a luggage and FCG as a material specific technique, identifying unknown substances as either threat or innocuous. Development of MXAT to the tomographic imaging technique proposed by Evans et al. (2014) offers depth information of unknown substances at unknown positions based on their diffraction caustics, which are optically encoded with shape and position information of crystalline materials.

A third approach that is more relevant to this work, involves an encoding system, similarly to MacCabe et al. (2012), as discussed in Section 4.2. Encoding of scattering signatures can be utilised to determine depth information of unknown substances along a primary axis prior to their identification. However, symmetric encoders such as the comb-like aperture proposed by MacCabe et al. (2012) generate certain ambiguities to FCG caustics due to the same radius of a condensation ring when it converges or diverges, as mentioned previously in Section 8.3. For this reason, novel encoders were employed during this work to assess their potential and unambiguous capabilities with FCG (Section 8.3). The outcomes of these post-sample encoding systems are discussed in Section 9.7.2.

9.6 Coded aperture - recovery of Debye rings

Coded aperture imaging systems were introduced a few decades ago aiming at capturing an image of an object, through a coded mask and a reconstruction process, as described in Section 4.1. FCG’s annular beam was considered as a pre-sample coded aperture in order to aid the interpretation of FCG data.

Commonly in the literature, coded apertures involve a post-sample coded mask with the exception of coded sources that consist of a distribution of X-ray sources. Herein, a pre-sample coded aperture with an annular mask was introduced for the first time. There are two main differences between this annular mask and previous annular

coded apertures examined (see Section 4.1). Firstly, the annular mask presented in this work is a pre-sample coded aperture i.e. it is positioned between the X-ray source and the sample. Secondly, this coded aperture system is utilised in near-field diffraction space; therefore, the object requiring reconstruction is not essentially the sample under investigation but the sample's Debye cones are; i.e. conventional XRD data. Therefore, the purpose of this work was to recover conventional XRD data from single FCG images of enhanced intensity acquired at a shorter period of time than traditional diffraction profiles.

The unique feature of an annular mask that allows it to act as a coded aperture lies within the δ -function approximation of its SPSF (Section 8.1). The inherent artefacts in reconstructed images from an annular coded aperture, appear as additional rings, which is unfortunate since the required object of recovery are also in the shape of rings (Debye rings). Nonetheless, the known structure of the required object (i.e. ring) is a major advantage. The presence and radii of additional rings were rationalised in a simulated manner verifying them as a result of the non-ideal δ -function nature of an annular beam's SPSF. However, it is important to note, that even in the presence of additional rings, a threat material such as an explosive would still be identified by its unique scattering signature.

Proof-of-concept as well as a methodology for an annular coded aperture system was established and developed in a simulated manner. An optimised methodology for the recovery of conventional data from simulated images initially involved convolution of an annular beam with a set of Debye rings to generate simulated FCG data. Convolution of FCG data with the annular beam recovered the desired Debye rings plus additional noise that was removed by applying bandpass filtering and dc level subtraction. Two alternative approaches were provided to calculate the amount of dc level required to be removed in order to successfully recover only the required rings (Section 8.1.1.1). The first approach was based on the annular beam's SPSF, by calculating the relation between maximum noise and percentage of total noise present within its SPSF image upon bandpass filtering. The second approach involved determining the number of scattering maxima from visual inspection of the FCG image and measuring the maximum intensity value of the additional rings in the recovered filtered image. Even though both approaches were able to calculate the required dc level to be removed, the first approach is considered more unbiased as

it does not involve the reconstructed image, but is solely based on the annular mask's SPSF.

It should be highlighted at this point, that this annular coded aperture system is at early stages and this work mostly focused on the recovery of conventional scattering maxima in terms of their positions. Even though proof-of-concept indicated effective recovery of the intensity of scattering maxima (when dc level was re-added, Figure 8.11), certain simulated reconstructions revealed differences in the relative intensities of scattering maxima. This however, does not affect the purpose of this study, which is material discrimination, as intensity is not the primary identifier.

An alternative post-processing approach of recovered data was also investigated based on the two-annulus system proposed by Simpson (1978) (see Section 4.1). A similar methodology to that employed by Simpson (1978) was followed and analogous outcomes were observed. Artefacts introduced by the non-ideal δ -function of an annulus' SPSF were eliminated more effectively with a two-annulus system, as also reported by Simpson (1978). Even though Simpson (1978) did not focus further on this approach due to its inability to deal with tomographic imaging as discussed in Section 4.1, this system is believed to be extremely beneficial for the coded aperture system examined herein. Its main advantage lies within its capability to suppress inherent noise and enhance Debye rings by adding reconstructed images consisting of the same recovered Debye rings but of different artefacts. Different artefacts are arising from reconstructed additional rings of various radii, as they were reconstructed from different annular masks. For simplicity, throughout this work a single annulus approach was employed; however, the superiority of a two-annulus system is apparent. An analogous tactic to that of a two-annulus system was established with empirical data, as discussed further on.

Simulated data with a single annulus system demonstrated successful recovery of scattering maxima positions without the presence of additional rings (Figure 8.3). The effect of various non-ideal conditions to either the annular beam or FCG data was then investigated to assess the potential of an annular mask to recover Debye rings under these non-optimised circumstances (Section 8.1.1.3). FCG data or annular mask was altered in a way similar to real-life empirical data that commonly suffer from noise, limited detector active area and non-ideal circular beam. An

annular coded aperture system was able to recover Debye rings even in the presence of extreme noise or with a limited area of the FCG pattern. Reconstruction of conventional XRD data in the presence of noise is considered as one of the key advantages of coded aperture systems, as previously discussed in Section 4.1; especially when compared to deconvolution approaches (Figure 8.16). Moreover, the ability of an annular coded aperture to recover conventional XRD data from a limited area of an FCG pattern is of significant importance, as only a relatively small percentage of the total FCG pattern was captured by the detector during this study (Section 8.1.1.3 (b)). Combination of these two non-ideal conditions was considered with empirical FCG data, which commonly suffer from noise and a limited active area of the detector. As it will be discussed further on, successful recovery of the Debye rings from empirical FCG data was achieved, but with incorrect scattering angles. Nonetheless, as explained later in this section, this is not believed to be an effect of noise or limited area of the FCG pattern.

Additionally, the thickness and shape of an annular mask were altered, individually, to assess their effect on Debye rings recovery. Alterations to the annular beam were expected to have a more significant effect to the coded aperture system, as the SPSF of the annulus would effectively be altered. However, it was demonstrated that even with an increased annular wall thickness (Section 8.1.1.3(a)) or in extreme cases of circular symmetry distortion of the annulus (elliptical distortion, Section 8.1.1.3 (b)), scattering maxima positions were recovered effectively.

At this point, the key difference between an increased annulus' thickness and an increased Debye rings' thickness should be clarified. Convolution's commutative property signifies that the resulting FCG pattern would be the same if either the annulus or the Debye rings' thickness is increased. However, recovery of the Debye rings is only affected if the thickness of the annulus is increased (Section 8.1.1.3 (a)). Alterations in the thickness of the Debye rings should not influence the reconstruction procedure, since Debye rings are the desired object to be recovered and any changes in their geometry should not affect the coded aperture system. On the other hand, alterations in the thickness of the annulus would have a significant result in the reconstruction property of an annular coded aperture. This is because the SPSF of the coded aperture would be altered when the annulus' thickness is

increased; hence, the δ -function approximation may alter, inducing different artefacts in the reconstructed images.

A systematic approach to empirical data involved convolving empirical conventional diffraction patterns with a simulated annular beam to generate pseudo-empirical FCG images. Pseudo-empirical experiments (Section 8.1.2) were conducted with an ideal sample in terms of preferred orientation and grain size, a series of samples with decreasing preferred orientation and a series of samples with increasing grain size (same samples as in Section 7.4.2 and Section 7.5.2, respectively). In all cases, it was determined that not only the scattering maxima positions were recovered effectively, but the geometry of the Debye rings was also recovered. Reconstructed diffraction patterns from samples with preferred orientation possessed similar degree of texture as conventional data. Moreover, reconstructed Debye rings from samples with large grain size consisted of similar spottiness to the empirical diffraction patterns. In all cases, an additional ring of high intensity was generated at significantly low scattering angles as a result of inherent artefacts. Its low scattering angle however, excluded it from the diffraction pattern as it was close to the incident beam's area, from which scattering data was not captured. Reconstructed patterns from samples with large grains possessed an additional ring of low intensity. However, even in the presence of these additional rings, the samples were identifiable as all their scattering maxima were reconstructed successfully. Recovered data were quantitatively assessed in the same way as their corresponding empirical patterns in Section 7.4.2 and Section 7.5.2. It was shown that even though the general trend of decreasing degree of texture (except for the low scattering angle Debye ring from sample *Al_3*) and increasing grain size was observed similarly to empirical data, their absolute values did not agree. This is believed to be an effect of convolution, which is a smearing function and caused blurring of the reconstructed images.

Recovery of conventional XRD data from empirical FCG data followed a similar approach to that of a two-annulus system suggested by Simpson (1978) for better reconstruction of the Debye rings. However, not the exact same enhancement effect was achieved, as with the two-annulus approach. As previously discussed, the key advantage of this system lies within the different SPSF of the two annuli. Hence, the different reconstruction artefacts are compressed upon addition of the two images.

Since a sequence of FCG images is captured by translation of the detector, even though the sample-to-detector distance is altered, the sample's position remains the same. Therefore each FCG image is convolved with the same annular beam, hence inherent noise remains the same but in a different scale. It is recommended that in future work, a sequence of FCG images should be captured whilst translating the sample in order to apply a multiple-annulus system approach. However, this will give rise to additional complexities due to sample movement, especially with an inaccurately calibrated system.

A visual assessment of the reconstructed data, specifically from the ideal sample (Al_2O_3) indicated strong correlation to their empirical diffraction patterns. Furthermore, even low intensity maxima were recovered effectively in the reconstructed image from Al_2O_3 . In contrast to the reconstructed images from simulated and pseudo-empirical data, the geometry and spottiness of scattering maxima from samples with preferred orientation and large grain size, respectively were not recovered. Moreover, comparison of the recovered scattering maxima to the sample's scattering maxima indicated poor agreement in their positions. It appears as if the reconstructed profiles were re-scaled (extended). This could be a result of one of two effects or their combination, as explained below:

1. FCG system employed throughout this work suffered from lack of accurate calibration due to position inaccuracies either occurring from the initial placement of translation stages or missed steps during their translation.
 - Experiments presented herein were all calibrated in terms of sample-to-detector position with known samples (for condensation foci analysis). However, radial integration of condensation rings takes into account the detector's position along the primary axis in order to scale the recovered images, as described in Section 8.1.3. If the detector's precise position is unknown, then there would be inaccuracies in the scaled images. This would appear as blurred scattering maxima upon addition of the images. However, blurring of the added recovered image was not observed to a great extent, indicating that scaling of the recovered images is not at fault.

- Inaccurate positioning of the collimator and sample can have a major effect, as the simulated annular beam would not be a truthful representation of the empirical beam, thus altering the annulus' SPSF.
2. Recovery of Debye rings from empirical data involved various transformation and conversion steps (see Section 8.1.3).
- Required steps to increase the dimensions of the FCG image and enable their convolution with an annular beam.
 - Scaling and re-sizing of the recovered images was then essential prior to their addition.
 - These steps may have resulted in inherent alterations of the distances between recovered scattering maxima. If this was the case, it would explain systematic inaccuracies to the recovered data since the same post-processing procedure was followed for each sample. It should be noted that all recovered diffraction profiles appear as if they were expanded indicating error consistency.

It is also important to highlight, that the simulated primary beam employed for this series of experiments, may have induced further artefacts or noise in the recovered images. This is due to the non-uniform intensity of the empirical primary beam that resulted in an induced 'preferred orientation' appearance of the scattering maxima, even from samples with no preferred orientation. This effect is similar to an encoded primary beam discussed in Section 9.7.1. As explained in Section 8.1.3, an empirical primary beam could not be employed during this study for practical reasons. However, it is believed, that convolution of empirical FCG patterns with an empirical primary beam may have reduced this effect. Consequently, this could have led to reconstructed data of higher resemblance to empirical data, in terms of Debye rings' intensity uniformity around their circumference.

Moreover, it is essential to note, that effective recovery of a conventional XRD image requires *a priori* knowledge of the sample's position. *A priori* knowledge of the sample's position along the primary axis is essential for an annular coded aperture system, as it is based on the fundamental principle of convolving FCG data with the annular beam's footprint on the sample. It is therefore necessary to know the

sample's position in order to determine the annular beam's radius at that plane. Moreover, in all XRD experiments, information on the sample's position is required in order to identify unknown samples. As previously mentioned, a solution to this requirement was provided through a coded aperture encoder system, as it is discussed in Section 9.7.2.

To summarise, an annular coded aperture system can have great advantages upon further development, as listed below:

- (a) Recovery of conventional XRD data
- (b) Recovery of conventional XRD data in the presence of noise, limited FCG data, thick annulus, thick samples and non-circular annulus
- (c) Interpretation of all FCG data, including that from samples with preferred orientation or large grain size, in a conventional manner
- (d) Acquisition of conventional XRD at low time exposures
- (e) Acquisition of a significantly large diffraction space by capturing only a limited region of it by a limited active area detector

9.7 Encoders

Pre- or post-sample encoders studied in this work served two purposes: (i) to discriminate between converging and diverging rings and (ii) to obtain spatial information of unknown substances along a primary axis. The former aimed to establish an effective approach for interpretation of single FCG images by a radial integration and reduce acquisition times significantly. The latter intended to obtain depth information of unknown substances in order to identify them by XRD. This was performed by establishing various pre (encoded annular beam) or post (wire and Archimedean spiral) sample encoders.

9.7.1 Primary beam encoders

A primary beam encoder was assessed in its ability to discriminate between converging and diverging condensation rings. As initially observed by samples exhibiting preferred orientation, converging and diverging condensation rings are encoded in an inverted manner when the Debye cones possess certain non-

symmetric geometries. Since convolution has a commutative property, encoding of the annular beam should also encode converging and diverging condensation rings unambiguously. However, non-symmetric encoding of the incident beam has opposite effects to that of Debye cone's encoding (i.e. discontinuous intensity from samples with preferred orientation).

It was shown that converging condensation rings occupy the same intensity geometry as the encoded primary beam, whereas diverging condensation rings occupy an inverted geometry. In addition, encoding of the annular beam did not influence its capability to act as a coded aperture in recovering conventional scattering maxima. Nevertheless, recovered Debye cones possessed the same intensity geometry as the encoded annular beam. Even though when analysing unknown samples this encoding can be observed as an indication of preferred orientation, misinterpretation of data can be avoided by the known geometry (encoding) of the annular beam. When however, a sample with preferred orientation is analysed this encoding may cause further complications to FCG data and reconstructed conventional data.

Proof-of-principle for an encoded annular beam was established with an absorbing edge covering approximately half of the primary beam. A linear encoder could not be employed with FCG for practical purposes as explained in Section 8.3.1.1. Theoretical predictions were supported by empirical data establishing that an encoded annular beam could be employed to discriminate between converging and diverging condensation rings. This can be proven extremely important, as it would enable interpretation of single FCG images to identify unknown substances. However, encoding of the annular beam with an absorbing edge involves obscuring approximately half of the incident beam hence decreasing the intensity of the condensation foci significantly. If however a fine structure was to be employed, the decrease in scattered intensity would not be substantial. Future work could focus on manufacturing such a structure and assessing its capabilities as an annular beam encoder. Moreover, if the encoder is placed after the sample the incident beam is not affected, but the scattered rays are encoded, as shown in Section 8.3.

9.7.2 Post-sample encoders

Post-samples encoders aim at the identification of unknown substances with no *a priori* knowledge of their location within an inspection volume, as discussed in Section 4.2.

Similarly to the study of MacCabe et al. (2012), two novel encoders were presented herein (Section 8.3) to obtain spatial discrimination of unknown samples along a primary axis, hence enabling phase identification. Symmetric encoders, such as the comb-like encoder proposed by MacCabe et al. (2012), could not be employed with FCG as it would result in certain ambiguities due to its symmetric structure (Section 8.3, Figure 8.51). If however, a non-symmetric encoder, with respect to circular structures (i.e. condensation rings) is utilised, the latter would be encoded in an unambiguous manner. Moreover, a comb-like encoder presented by MacCabe et al. (2012) results in $\sim 50\%$ loss of scattered intensity as it is absorbed by the $\sim 50\%$ open fraction of the encoder structure. The linear wire and the Archimedean spiral encoders possess a significantly larger open fraction ($\sim 90\%$); hence, allowing the acquisition of higher percentage of scattered rays.

Proof-of-principle of a linear post-sample encoder was demonstrated with a pencil beam arrangement indicating successful determination of the sample's position along the primary axis with $\sim 1\%$ precision.

Two approaches for determining the sample's z-position were identified and established during this work. Sample-to-detector distance can be calculated by the off-centre distance α_{LE} and α_D (Section 8.3.1), without taking into account the radius of the Debye cones or their intersection angles with the line aperture. The second approach engages the radius of Debye cones on the detector plane, as well as their encoding angles. It should be noted that information on coded aperture-to-detector distance along the primary axis is required for both approaches.

The first method can be considered as more straightforward and time effective when dealing with multiple samples and scattering angles, since only a single measurement of α_D is required per sample. However, this can also be a limitation due to a limited number of measurements prohibiting cross-examination of calculated values. Moreover, as the dimensions of the linear encoder increase at short sample-to-coded aperture distances, greater human and experimental errors

occur, thus lower system specificity. At this point, it should be highlighted that the off-centre distance α_{LE} of the line encoder plays a significant role. As illustrated in Section 8.3.1, an increase in α_{LE} causes an increase in the encoder's sensitivity for spatial discrimination since differences in encoding angles would be more perceptible. This however, would affect encoding of low scattering angle maxima, as they will not be intersected by the encoder. A high α_{LE} distance would position the encoder at a greater radial distance than the radial distance of certain scattering maxima occurring at low 2θ angles. Therefore, a compromise between high sensitivity and specificity should be attained.

The second method, which involved measurement of Debye cones' radii and their intersection angles χ , can verify calculated sample positions by obtaining numerous measurements from different diffraction maxima arising from the same sample. The average sample-to-detector value can then be determined. However, if the structure of the wire encoder has imperfections, i.e. if it is not linear, this can cause additional errors in the measured encoding angles, leading to erroneous calculations of the sample-to-detector distance.

It was analytically assessed that the greatest errors in the calculated sample-to-detector distances and 2θ angles are arising from errors in the encoder-to-detector distance ($D_{LE:D}$) and Debye cones' radius on the detector plane (R_D), respectively. Therefore, inaccurate measurements specifically of $D_{LE:D}$ due to experimental position imprecisions, were expected to affect calculated sample-to-detector distances, hence scattering angles. It should be noted that the work presented herein is an initial study on coded aperture encoders and the diffractometer employed was not designed to sustain accurate positioning of additional structures, such as an encoder.

Nonetheless, preliminary data presented in Section 8.3.1.1, confirmed the theoretical predictions and indicated good consistency, in terms of determined sample-to-detector distances and 2θ angles, between the two approaches. The outcomes of a linear encoder were verified by comparing the sample-to-detector distance calculated from a known sample. Even though this study aimed to identify samples at unknown positions along a primary axis, as often is the case in luggage

screening, *a priori* knowledge on the sample's position was employed to act as a confirmatory tool in order to assess the ability and accuracy of a linear encoder.

Consequently, the concept of a linear encoder was also investigated with an annular beam. However, unavailability of a fine high absorbing wire structure did not allow employment of a linear encoder for the practical reasons described in Section 8.3.1.1. Even though combination of FCG with a post-sample encoder has the potential for spatial discrimination of unknown samples similarly to conventional XRD, this practical limitation, restricted the purpose of the experiments. FCG experiments aimed at the discrimination between converging and diverging condensation rings, as it is an essential requirement for obtaining spatial discrimination of samples from FCG diffraction data. This was also the main reason why a symmetric encoder such as that proposed by MacCabe et al. (2012) could not be employed with FCG and alternative encoders were pursued. Moreover, as previously discussed in Section 9.1, discrimination between converging and diverging condensation rings is extremely significant when radially integrating single FCG images. As explained throughout this work, interpretation of single FCG images is important for both higher specificity (narrower diffraction peaks) and speed purposes.

A high absorbing edge obscuring less than half of the detector active area, demonstrated possible differentiation between converging and diverging condensation rings (Figure 8.57). The edge encoder intersected diffraction caustics similarly to conventional Debye cones, discriminating between converging and diverging condensation rings, based on the position they appeared on the detector plane. This suggests that a linear encoder would be able to determine sample position by encoding condensation rings, of which their converging or diverging nature would be identified by the location of their encoding angles, with respect to the encoder. It is recommended, that future work should focus on manufacturing a fine high absorbing linear structure to act as a post-sample encoder with FCG. This would assist in assessing theoretical predictions of spatially discriminating samples along a primary axis by combining FCG with a linear encoder.

The ability of an alternative encoder, an Archimedean spiral, was also evaluated as a post-sample encoder. The basic principle of encoding scattering maxima by an

Archimedean spiral is similar to that of a linear encoder. Scattering maxima arising from a sample are encoded at specified polar angles, relative to the sample's location along a primary axis. Analytical descriptions of this encoding were established during this work enabling determination of the sample's position and hence its scattering profile.

Calibration of the Archimedean spiral encoder was performed with a known sample to eliminate high experimental errors arising from either imperfect manufacturing or inaccurate positioning of the Archimedean spiral. As previously explained, the Archimedean spiral employed in this study was designed (inaccurately) to approximate a given equation (Section 8.3.2.1); therefore, inherent errors were expected to arise during data analysis. Moreover, simulated analysis of the developed mathematical model confirmed the assumptions of induced errors in the calculated sample-to-detector distances when the structure of the spiral was altered. This was shown to be due to imprecise manufacturing or non-parallel positioning of the spiral to the detector plane. Both effects result in a different spiral equation than that employed during calculations. Thus, it is suggested, that when employing a post-sample encoder with a specific geometry is critical to ensure its design accuracy by calibrating the system prior to any data analysis.

It was also determined that similarly to a linear encoder, the greatest errors in determining the sample's position and scattering angles arise from the encoder-to-detector distance and radius of Debye cones on the detector plane, respectively. It was also assessed that inaccuracies in the structure of the Archimedean spiral (i.e. a and b values) result in high errors in the calculated sample-to-detector distances. When comparing 1% error in all variables for both linear and Archimedean spiral encoders, it was shown that the latter possesses lower experimental errors specifically in the calculated sample-to-detector distance (~7.5 times lower). Therefore, an accurately manufactured Archimedean spiral has the ability to obtain reliable spatial discrimination of unknown samples. However, this is a preliminary study indicating great potential of an Archimedean spiral and linear encoders yet to be explored, requiring precise manufacturing and development of a diffractometer to support a post-sample encoder accurately, in order to avoid high experimental errors.

It should be highlighted that these post-sample encoders require further development, specifically with FCG. Accurate designs of a wire and an Archimedean spiral should be manufactured with a high absorbing material to assess their potential with FCG. An Archimedean spiral encoder could be employed with FCG by extending the spiral's structure, as discussed later in Section 10.2.

Further work on the establishment of such coded aperture systems should also be performed with samples exhibiting preferred orientation and/or large grain size with both FCG and conventional XRD. Even though, experimental data suggested effective spatial discrimination and identification of samples with either a linear wire or an Archimedean spiral, only ideal samples, in terms of preferred orientation and grain size were examined. In cases of extreme preferred orientation or large grain size, the diffraction patterns would comprise of opaque areas, where the intensity of Debye cones is discontinued; hence possibly complicating the identification of their encoding angles. Possible limitations of post-sample encoders with such samples should be assessed in the future for a more accurate representation of their ability. However, it should be noted that this is not a limitation specifically to linear and Archimedean spiral encoders but to all post-sample encoders relying on encoding of scattering maxima. Moreover, diffraction patterns acquired with encoders of a low open fraction (e.g. ~50% of comb-like encoders) are expected to be affected to a greater extent by samples exhibiting preferred orientation or large grain size, than high open fraction encoders (i.e. linear wire and Archimedean spiral).

Chapter 10 CONCLUSIONS & FUTURE WORK

Outline

Conclusions drawn from this work are presented, in addition to recommendations for future work. Finally, an explanation of the key contributions of this research to general knowledge and specifically to the development of this novel beam geometry is provided.

10.1 Research conclusions

During this research, a novel beam geometry (FCG) for powder XRD was investigated and developed with both non-ideal samples and samples under non-ideal conditions.

Initially, an annular beam arrangement was compared to conventional pencil beam XRD, in terms of scattering maxima widths and intensity. FCG has the significant advantage of enhanced intensity by ‘focusing’ multiple scattering maxima at single condensation foci along a primary axis. Therefore, a considerably lower exposure time was employed during all FCG experiments, when compared to conventional XRD.

Broadening of diffraction peaks was observed for FCG and pencil beam scattering maxima, when acquired by the FCG system. Even though a decrease in beam divergence, sample thickness and X-ray source’s focal spot size decreased the width of diffraction peaks, no significant advantage was observed.

It was suggested that even though FCG data are commonly interpreted by an integration around the condensation foci over an extended image sequence, radial integration of a single FCG image is not only more time effective but it also provides narrower diffraction peaks. Both speed and high specificity are extremely

important in various areas in need of rapid identification of unknown substances. However, radial integration of FCG images requires discrimination between converging and diverging condensation rings, which was pursued with either pre-sample or post-sample encoders. The latter was also employed in obtaining spatial information of unknown substances along a primary axis.

Non-ideal samples in terms of preferred orientation and grain size were analysed by FCG and compared to conventional XRD data. Scattering maxima from samples with preferred orientation or large grain possess a different FCG pattern to ideal samples. Preferred orientation effects caused diffraction caustics to retain a certain geometry relative to the geometry of the Debye cones, whereas samples with large grain size generated spotty FCG images. It was demonstrated that FCG offers greater advantages over pencil beam geometry, where only a section of the diffraction patterns is captured.

Moreover, analysis of non-ideal amorphous samples was performed with liquid samples, which were categorised into threat and non-threat groups based on their risk to aviation security. It was demonstrated that threat liquids could be discriminated from benign liquids based on the formers' lower scattering angles. It was also shown that it is possible to differentiate between water and 30% concentration hydrogen peroxide, which is currently considered one of the most important threat liquids in aviation security.

Previous research on FCG involved a specific sample arrangement. A more general scenario of random sample orientation by rotating the sample was investigated to determine its effect on FCG caustics. It was illustrated analytically, empirically and through simulations that condensation foci of enhanced intensity are still formed even with a sample non-normal to the primary axis. However, the xyz coordinates of condensation foci are dependent upon their scattering angle as well as degree, direction and axis of sample rotation. Additionally, successful FCG analysis of multiple samples, normal to the primary axis, was achieved when the samples' position along the beam axis was known, as with all XRD experiments.

Two novel post-sample encoders (linear wire and Archimedean spiral) were investigated to recover spatial information of unknown materials along a primary axis. Proof-of-principle for both encoders was established with conventional XRD

due to practical limitations with FCG. A calibration method was provided to overcome experimental errors arising from imprecise designing and positioning of the encoders. An absorbing edge was utilised with FCG, similarly to a linear encoder demonstrating possible discrimination between converging and diverging condensation rings. This could enable both spatial discrimination of unknown samples with FCG, and interpretation of single FCG images at significantly short acquisition times and possibly with higher specificity.

Finally, the concept of a pre-sample coded aperture to aid interpretation of FCG data was examined. FCG's annular beam was considered as a pre-sample coded aperture aiming at the recovery of conventional XRD data from single FCG images. Simulated and pseudo-empirical data demonstrated great potential of this coded aperture system in reconstructing the radii and geometry of Debye cones from ideal and non-ideal samples, in terms of texture and grain size. However, empirical data indicated a limited ability of the annular aperture in recovering precise scattering maxima positions.

A flow diagram illustrating the key research areas investigated during this study is presented in Figure 10.1, along with their main outcomes.

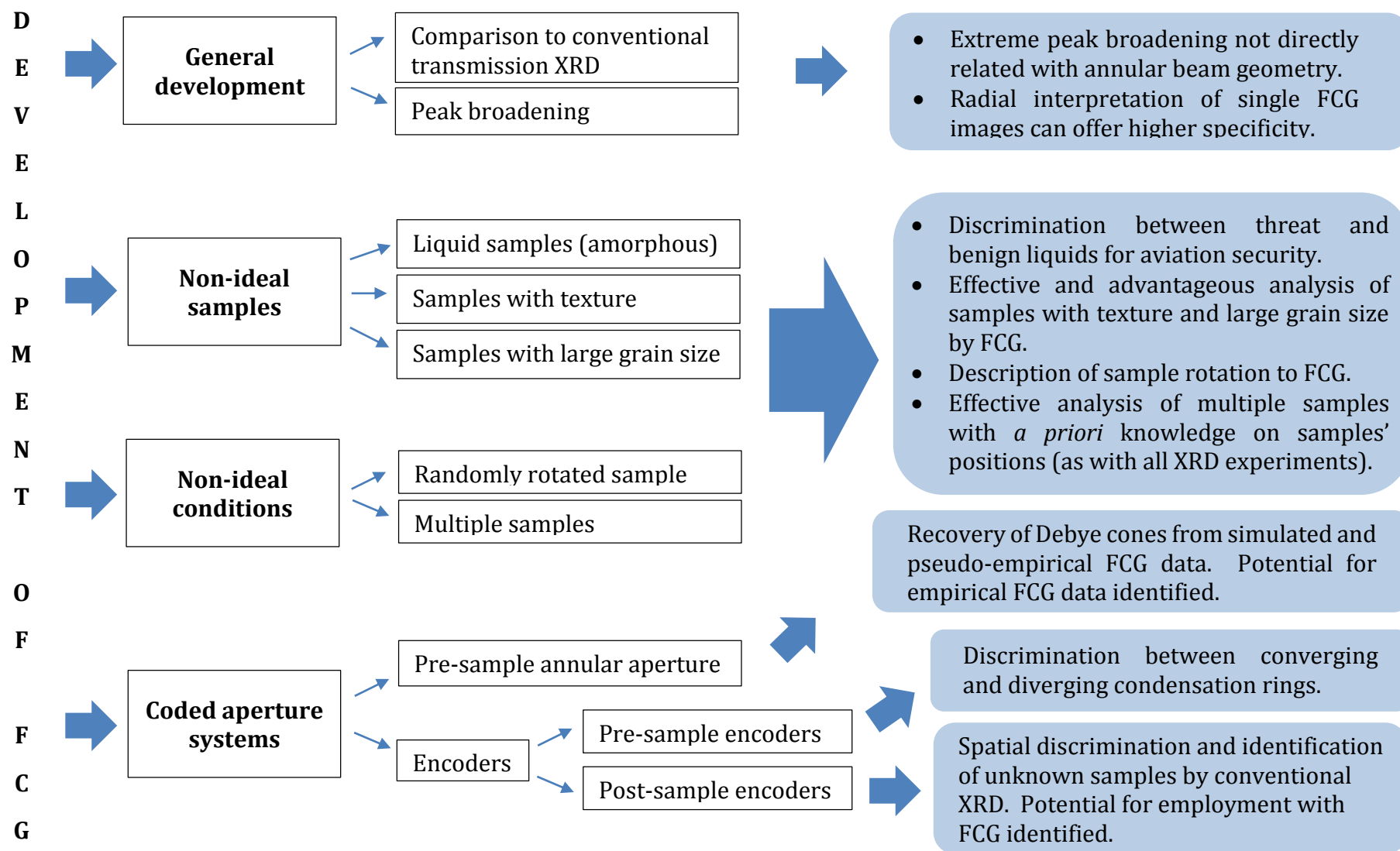


Figure 10.1 A flow diagram illustrating the main research areas of this study along with their key outcomes.

10.2 Recommendations for future work

FCG is a relatively new technique with potential in various fields yet to be explored. Future work could focus on a number of different areas as discussed and described earlier in Section 5.3. In this section, only the key areas in need of further development that are directly related to this research are considered.

- **FCG system development**

Peak broadening of scattering maxima obtained by FCG should be investigated further. FCG should be employed by an independent diffractometer to assess any possible differences in the widths of diffraction peaks. An X-ray source with a small focal spot should also be considered in future development. Moreover, unconventional collimation optics such as long hollow tube collimators designed by 3D printing and polycapillary collimators could also be utilised to determine their effect on the width of diffraction peaks. 3D printing collimators have the advantage of being formed as a single unit rather than multiple units attached together, thus causing the primary beam to have a greater uniformity and perhaps lower angular and wall divergence. Pencil beam polycapillary collimators have the unique arrangement of multiple long tapered pinholes that force incident rays to exit the collimator with a very constrained beam divergence. A similar approach to annular collimators would decrease angular beam divergence significantly, by employing a more parallel beam, hence generating narrower diffraction peaks.

Additionally, precise positioning and translation of all stages should be established for more accurate results. Once an optimised collimator is chosen, precise alignment of the annular collimator should be established for all experiments to avoid induced non-uniformity effects on the intensity of scattered rays.

The effect of a diffracting collimator should be assessed in terms of peak broadening. A secondary annular collimator would be positioned between the sample and the detector. Initially, a stationary collimator of smaller diameter of that of the incident beam's footprint on the sample should be investigated, and then translation of the diffracting collimator could be explored. Initial theoretical valuations suggest utilising an annulus with a radius equal to half of the radius of the incident's beam

footprint on the sample. Such a diffracting collimator requires translation along the primary axis independently to the detector, by a step size half of the latter's. It is believed that a diffracting collimator could reduce the width of the diffraction peaks.

- **Pre-sample coded aperture**

Proof-of-concept of an annular beam coded aperture has been established with simulated and pseudo-empirical data (see Section 8.1), indicating that a significantly large area of conventional diffraction patterns can be recovered from a limited active area detector (Section 9.6). However, further research into the recovery of conventional XRD data from empirical data is required. A pilot study into post-processing empirical FCG images to recover standard diffraction patterns was provided. The limitations of the current study arising from its inability to recover accurate scattering maxima positions, along with possible reasons were explained (Section 9.6). Future work should focus on determining a more suitable post-processing procedure that could possibly involve a single or a restricted number of FCG images. An appropriate software for automated or multi-processing of FCG images should be identified or developed for a more time effective analysis, hence enabling system optimisation. Moreover, besides recovery of accurate scattering maxima positions, reconstruction of Debye rings from samples with preferred orientation or large grain size would be beneficial. This would enable interpretation of any FCG data in a conventional manner without compromising FCG's enhanced intensity and hence speed advantage. In addition, as discussed in Section 9.6, significantly large diffraction areas could be acquired with small compact detectors.

- **Post-sample encoders with FCG**

A linear wire and an Archimedean spiral have been established herein as post-sample encoders with conventional XRD. Future work could focus on establishing their proof-of-concept with FCG. This would require manufacturing bespoke encoders in order to reduce experimental errors and achieve greater accuracy in determining spatial information and identifying unknown substances. Precise designing may be achieved by 3D printing, with a high absorbing material, thus enabling encoding of FCG data. A linear encoder would act similarly to an absorbing

edge described in Section 8.3.1.1, which would simultaneously spatially encode and discriminate converging and diverging condensation rings. An Archimedean spiral could also be employed with FCG in a similar manner to a linear encoder, as indicated in Figure 10.2. The fundamental geometry of the Archimedean spiral is not altered, but the extended line would assist in differentiating between converging and diverging condensation rings as their encoding will appear on opposed sides, similarly to an absorbing edge.

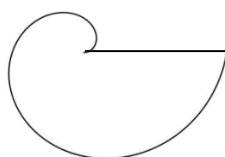


Figure 10.2 An Archimedean spiral encoder with an extended structure for FCG experiments.

The extended structure will however result in an additional encoding angle for each scattering maxima. However, since the extended line passes through the centre of the spiral and hence the centre of the diffraction pattern, it would encode all scattering rings at the same angle.

Combination of FCG with an encoder essentially couples a pre-sample coded aperture with a post-sample coded aperture. A system that would enable simultaneous presence of an annular mask with an encoder would have the potential to recover conventional data from a single FCG image whilst spatially discriminating and identifying unknown samples. Therefore, any unknown samples with *no a priori* knowledge of their position could be identified in a short period of time by a single FCG image in a conventional manner.

10.3 Contributions to knowledge

The key contributions of this research to knowledge are as follows:

- Further development of a novel geometry referred to as 'focal construct geometry' (FCG) for power X-ray diffraction utilising an annular beam. This geometry enables acquisition of enhanced intensity data at short time exposures due to 'focusing' of multiple scattering maxima at single locations. Advantages of an alternative data interpretation method have been identified for narrower diffraction peaks at shorter acquisition times. Moreover, solutions to practical limitations arising from this method have been determined, including a beam encoder and post-sample encoders.
- Development of FCG with non-ideal samples. This involved non-crystalline materials such as liquid samples, as well as samples with preferred orientation or large grain size. FCG data analysis has been proposed for effective discrimination between threat and non-threat liquids for aviation security. Discrimination of threat liquids present in 1:1 volume mixtures with benign liquids has been determined depending on their miscibility. Moreover, FCG analysis of a series of samples with increasing preferred orientation and a series of samples with increasing grain size has been established. Comparison between FCG and conventional data from such samples has been accomplished identifying FCG's advantages. The main benefit from analysing samples with preferred orientation or large grain size with an annular beam geometry lies within its 'focusing' property that concentrates multiple Debye cones by taking into account their complete circumference.
- Development of FCG with ideal samples under non-ideal conditions. This experimental work focused on analysis of ideal samples (in terms of crystallinity, preferred orientation and grain size) which were positioned under non-ideal orientations. Previous studies on FCG employed a single planar sample placed normal to the primary axis. The scenario of a more general sample orientation with respect to the primary axis was investigated. The effect of sample rotation around x and/or y axes on FCG diffraction

caustics has been determined and presented in an analytical, simulated and empirical approach. Theoretical predictions were in agreement with empirical outcomes. Therefore, mathematical models describing this effect have been developed to predict the behaviour of FCG scattering maxima at any random sample orientation and assist experimental data. Additionally, the effect of multiple samples, placed normal to the primary axis, on FCG scattering maxima was investigated. Similarly, to all XRD data analysis, *a priori* knowledge of the samples' positions was required in order to simultaneously identify multiple samples. Suggestions and empirical data demonstrating possible resolution of this requirement were given by post-sample encoders.

- Development of a pilot study of a coded aperture system with FCG. FCG's annular beam was established as a pre-sample coded aperture aiming at the recovery of conventional XRD data. The potential of an annular coded aperture was demonstrated mainly through a simulated approach. A developed methodology along with alternative post-processing procedures was presented for effective recovery of Debye cones from simulated and pseudo-empirical FCG data. The potential of an annular coded aperture with empirical FCG data was also demonstrated, although further work is required for accurate recovery of scattering maxima positions and intensity geometry. Development of this system also proposes an alternative approach to the analysis of FCG data from samples with preferred orientation or large grain size. Additionally, the potential of an annular pre-sample coded aperture to recover information on a significantly larger diffraction pattern to that acquired by a small area detector was identified.
- Establishment of two novel post-sample encoders for spatial discrimination of unknown samples along a primary axis. Proof-of-principle of a linear encoder and an Archimedean spiral encoder was established with conventional XRD. This demonstrated effective recovery of either a single sample or multiple samples' position along the primary axis. In turn, this enabled determination of samples' scattering angles. These post-sample encoders could be applied by any conventional XRD geometries, as well as

FCG. Identification of any material by XRD analysis requires *a priori* knowledge of sample position. Therefore, in cases where there is no information available on samples under investigation, i.e. luggage screening techniques, post-sample encoders could be employed. Similar encoders proposed by other studies have two main disadvantages: (1) there is ~50% loss of scattered rays due to their ~50% open fraction structure, and (2) they cannot be engaged by FCG due to ambiguity limitations arising from their inability to distinguish between FCG's converging and diverging condensation rings.

- Discrimination between FCG's converging and diverging condensation rings. Two alternative approaches have been presented in this work for effective discrimination of condensation rings. Firstly, an annular beam (pre-sample) encoder was employed to encode converging and diverging condensation rings in opposed angles, depending on the encoder's position. Secondly, post-sample encoders mentioned above, were suggested to encode converging and diverging condensation rings, similarly to a primary beam encoder. Proof-of-concept for FCG was established for a linear encoder with an absorbing edge. Employment of post-sample encoders with FCG has the ability to discriminate between converging and diverging condensation rings, as well as enabling acquisition of depth information of unknown samples along a primary axis. Discrimination between converging and diverging condensation rings is significant for FCG, as it would allow informative interpretation of single FCG images captured at considerably low acquisition times, offering narrower diffraction peaks i.e. higher specificity. FCG's high intensity along with high specificity and speed advantage is extremely important for areas in need of rapid material identification, such as security screening or *in-situ* crime scene analysis.

REFERENCES

- ABLES, J. G. 1968. Transform photography: A new method for X-ray astronomy. *Proceeding of the Astronomical Society of Australia*, 1, 172-173.
- ACCORSI, R., GASPARINI, F. & LANZA, R. C. 2001. Optimal coded aperture patterns for improved SNR in nuclear medicine imaging. *Nuclear Instruments and Methods in Physics Research A*, 474, 273-284.
- ALARDS-TOMALIN, D., ANSONS, T. L., REICH, T. C., SAKAMOTO, Y., DAVIE, R., LEBOE-MCGOWAN, J. P. & LEBOE-MCGOWAN, L. C. 2014. Airport security measures and their influence on enplanement intentions: Responses from leisure travelers attending a Canadian University. *Journal of Air Transport Management*, 37, 60-68.
- ASLANOV, L. A., FETISOV, G. V. & HOWARD, J. A. K. 1998. *Crystallographic instrumentation*, New York, Oxford University Press.
- ATKINS, P. & PAULA, J. 2005. *Elements of Physical Chemistry* Oxford, Oxford University Press.
- BALLESTEROS, F. J., SANCHEZ, F., REGLERO, V., PORRAS, E., PEREZ, F. & ROBERT, A. Imaging in X-ray with coded-aperture masks. Proceedings 2nd INTEGRAL Workshop 'The Transparent Universe', 1996 St. Malo, France. 357-360.
- BARKER, T. V. 1919. Crystallography. *Annual Reports on the Progress of Chemistry*, 16, 197-220.
- BARRETT, H. H. 1972. Fresnel zone plate imaging in nuclear medicine. *The Journal of Nuclear Medicine*, 13, 382-385.
- BARRETT, H. H. & SWINDELL, W. 1981. *Radiological Imaging: The theory of image formation, detection, and processing*, New York, Academic Press.
- BBC. 2006. 'Airlines terror plot' disrupted [Online]. <http://news.bbc.co.uk/1/hi/uk/4778575.stm>: BBC News. [Accessed 13th January 2012].
- BEEVOR, S. P., SANDER, J., RAITT, I., BURROWS, J. D. & MANN, K. 1995. Non-invasive inspection of baggage using coherent X-ray scattering. *European Convention on Security and Detection*. Brighton.
- BLOOMFIELD, M., LOEFFEN, P. W. & MATOUSEK, P. Detection of concealed substances in sealed opaque plastic and coloured glass containers using SORS. 2010. 783808-783808-15.
- BRUNOL, J., FONROGET, J. & LOWENTHAL, S. 1978. Deconvolution analogique en imagerie par ouverture codee appliquee a la medecine nucleaire. *Optica Acta*, 25, 113-124.
- BUCKLEY, K. & MATOUSEK, P. 2011. Non-invasive analysis of turbid samples using deep Raman spectroscopy. *Analyt*, 136, 3039-3050.

REFERENCES

- BUSBOOM, A., SCHOTTEN, H. D. & ELDERS-BOLL, H. 1997. Coded aperture with multiple measurements. *Journal of Optical Society of America*, 14, 1058-1065.
- BYARD, K. 2014. Fast decoding algorithms for coded aperture systems. *Nuclear Instruments and Methods in Physics Research Section A: Accelerators, Spectrometers, Detectors and Associated Equipment*, 754, 36-41.
- CANDALINO JR, T. J., KOBZA, J. E. & JACOBSON, S. H. 2004. Designing optimal aviation baggage screening strategies using simulated annealing. *Computers & Operations Research*, 31, 1753-1767.
- CANNON, T. M. & FENIMORE, E. E. 1980. Coded aperture imaging: many holes make light work. *Optical Engineering*, 19, 283-289.
- CERNIK, R. J., KHOR, K. H. & HANSSON, C. 2008. X-ray colour imaging. *Journal of the Royal Society Interface*, 5, 477-481.
- CHAN, J., EVANS, P., WANG, X., GODBER, S., PEATFIELD, I., ROGERS, K., ROGERS, J. & DICKEN, A. 2010. Scatter enhanced 3D X-ray imaging for materials identification. *Security Technology (ICCST), 2010 IEEE International Carnahan Conference*.
- CHEN, Y. W. & KISHIMOTO, K. 2003. Tomographic resolution of uniformly redundant arrays coded aperture. *Review of Scientific Instruments*, 74, 2232-2235.
- CHRISTODOULOU, C., REID, C. B., O'FLYNN, D., WILSON, M., VEALE, M., CERNIK, R. J., SELLER, P. & SPELLER, R. D. 2011. Multivariate analysis of pixellated diffraction data. *Journal of Instrumentation*, 6, C12027.
- COCKCROFT, J. K. & FITCH, A. N. 2008. *Powder diffraction: Theory and practice*, Cambridge, RSC.
- CONNELLY, J. M., CURBY, W. A., FOX, F. T. & HALLOWELL, S. F. 1998. Detection of hidden explosives. In: BEVERIDGE, A. (ed.) *Forensic investigation of explosions*. London: Taylor & Francis
- COOK, E., FONG, R., HORROCKS, J., WILKINSON, D. & SPELLER, R. 2007. Energy dispersive X-ray diffraction as a means to identify illicit materials: A preliminary optimisation study. *Appl. Radiat. Isot.*, 65, 959-967.
- COOK, E. J., A., G. J., M., K., C., G., S., P., HORROCKS, J. A., L., G., S., H. & SPELLER, R. 2009a. Illicit drug detection using energy dispersive x-ray diffraction. In: BLACKBURN, B. W. (ed.) *Non-Intrusive Inspection Technologies II*. 7310, 73100I ed.: Proc. of SPIE.
- COOK, E. J., PANI, S., GEORGE, L., HARDWICK, S., HORROCKS, J. A. & SPELLER, R. D. 2009b. Multivariate data analysis for drug identification using energy-dispersive X-ray diffraction. *IEEE Transactions on Nuclear Science*, 56, 1459-1464.
- CORFIELD, R. 2014. Liquid explosives detectors entering service at airports. *Chemistry world*. Royal Society of Chemistry.

REFERENCES

- COSTAS, C. M. & YANG, S. 2009. Counting pollen grains using readily available, free image processing and analysis software. *Annals of Botany*, 104, 1005-1010.
- COTE, A. S., SMITH, B. & LINDAN, P. J. D. 2001. *A Molecular Dynamics tutorial* [Online]. Daresbury Laboratory. Available: <http://www.compsoc.man.ac.uk/~lucky/Democritus/Theory/rdf.html> [Accessed 9th April 2012].
- COTTE-RODRIGUEZ, I., HERNANDEZ-SOTO, H., CHEN, H. & COOKS, R. G. 2008. In situ trace detection of peroxide explosives by desorption electrospray ionization and desorption atmospheric pressure chemical ionization. *Anal. Chem.*, 80, 1512-1519.
- CRESPY, C., DUVAUCHELLE, P., KAFTANDJIAN, V., SOULEZ, F. & PONARD, P. 2010. Energy dispersive X-ray diffraction to identify explosive substances: Spectra analysis procedure optimization. *Nuclear Instruments and Methods in Physics Research A*, 623, 1050-1060.
- CULLITY, B. D. 1978. *Elements of X-ray diffraction* USA, Addison-Wesley.
- DEBYE, P. & SCHERRER, P. 1916. Interferenzen an regellos orientierten Teilchen im Röntgenlicht. *Physikalische Zeitschrift*, 17, 277-283.
- DICKE, R. H. 1968. Scatter-hole cameras for X-rays and gamma rays. *The astrophysical journal*, 153, L101-105.
- ELIASSON, C., MACLEOD, N. A. & MATOUSEK, P. 2007. Noninvasive detection of concealed liquid explosives using Raman spectroscopy. *Anal Chem*, 79, 8185-9.
- ESPY, M., FLYNN, M., GOMEZ, J., HANSON, C., KRAUS, R., MAGNELIND, P., MASKALY, K., MATLASHOV, A., NEWMAN, S., OWENS, T., PETERS, M., SANDIN, H., SAVUKOV, I., SCHULTZ, L., URBAITIS, A., VOLEGOV, P. & ZOTEV, V. 2010. Ultra-low-field MRI for the detection of liquid explosives. *Supercond. Sci. Technol.*, 23, 1-8.
- EUROPEAN-COMMISSION. 2013. *Air: Liquids, aerosols and gels* [Online]. European Commission. Available: http://ec.europa.eu/transport/modes/air/security/aviation-security-policy/lags_en.htm [Accessed 19 August 2014].
- EVANS, J. P. O. 2010. GB patent application.
- EVANS, J. P. O., LIU, Y., CHAN, J. W. & DOWNES, D. 2006. View synthesis for depth from motion 3D X-ray imaging. *Pattern Recognition Letters* 27, 1863-1873.
- EVANS, P. & ROGERS, K. 2008. *Detection of X-ray scattering*. International Patent patent application.
- EVANS, P. & ROGERS, K. 2010. 3D X-ray Diffraction Imaging for Materials ID. *Technologies for Homeland Security (HST), 2010 IEEE International Conference*.

REFERENCES

- EVANS, P. & ROGERS, K. 2011. Final Report: HotSpot X-ray Diffraction Imaging for Materials ID. *Innovative ideas for explosives and weapons detection R&D (2007 call)*. Nottingham Trent University; Cranfield University.
- EVANS, P., ROGERS, K., CHAN, J., ROGERS, J. & DICKEN, A. 2010. High intensity x-ray diffraction in transmission mode employing an analog of Poisson's spot. *Applied Physics Letters*, 97, 204101-1 - 204101-3.
- EVANS, P., ROGERS, K., DICKEN, A., GODBER, S. & PROKOPIOU, D. 2014. X-ray diffraction tomography employing an annular beam. *Optics Express*, 22, 11930-11944.
- EWING, R. G., ATKINSON, D. A., EICEMAN, G. A. & EWING, G. J. 2001. A critical review of ion mobility spectrometry for the detection of explosives and explosive related compounds. *Talanta*, 54, 515-529.
- FAUST, A. A., ROTHSCCHILD, R. E., LEBLANC, P. & MCFEE, J. E. 2009. Development of a coded aperture X-ray backscatter imager for explosive device detection. *IEEE Transactions on Nuclear Science*, 56, 299-307.
- FEDERICI, J. F., GARY, D., BARAT, R. & MICHALOPOULOU, Z. H. 2007. Detection of explosives by tetrahertz imaging. *In: YINON, J. (ed.) Counterterrorist Detection Techniques of Explosives*. 1st ed. Oxford: Elsevier.
- FENIMORE, E. E. 1978. Coded aperture imaging: predicted performance of uniformly redundant arrays. *Applied Optics*, 17, 3562-3570.
- FENIMORE, E. E. 1980. Coded aperture imaging: the modulation transfer function for uniformly redundant arrays. *Applied Optics*, 19, 2465-2471.
- FENIMORE, E. E. & CANNON, T. M. 1978. Coded aperture imaging with uniformly redundant arrays. *Applied Optics*, 17, 337-347.
- FENIMORE, E. E., CANNON, T. M. & MILLER, E. L. 1978. Comparison of Fresnel zone plates and uniformly redundant arrays. *SPIE Application of Digital Image Proceedings*, 149, 232-236.
- FINGER, M. H. & PRINCE, T. A. 1995. Useful classes of redundant arrays for imaging applications in Imaging. *In: BASSANI, L. & COCCO, G. D. (eds.) High energy astronomy*.
- GAFT, M. & NAGLI, L. Liquid explosives detection in transparent containers. *In: HARMON, S. R., HOLLOWAY, J. H. & BROACH, J. T., eds. Detection and Sensing of Mines, Explosive Objects, and Obscured Targets XV, 2010. Proc. SPIE*.
- GANG, T. & DONGJI, F. 2009. The research & application of the detection capability of dangerous goods in dual-energy X-ray security equipment. *Second Conference on Intelligent Computation Technology and Automation*.
- GARRITY, D. J., JENNESON, P. M. & VINCENT, S. M. 2007. Transmission geometry X-ray diffraction for materials research. *Nuclear Instruments and Methods in Physics Research A*, 580, 412-415.

REFERENCES

- GHAMMRAOUI, B., TABARY, J., POUGET, S., PAULUS, C., MOULIN, V., VERGER, L. & DUVAUCHELLE, P. 2012. New software to model energy dispersive X-ray diffraction in polycrystalline materials. *Nuclear Instruments and Methods in Physics Research A*, 664, 324-331.
- GOLAY, M. J. E. 1971. Point arrays having compact, nonredundant autocorrelations. *Journal of the Optical Society of America*, 61, 272-273.
- GOTTESMAN, S. R. 2007. Coded apertures: past, present, and future applications and design. *Proceedings of SPIE*, 6714, 671405-1 - 671405-11.
- GOTTESMAN, S. R. & FENIMORE, E. E. 1989. New family of binary arrays for coded aperture imaging. *Applied Optics*, 28, 4344-4352.
- GREENBERG, B. 1993. *Advances in X-ray analysis*, New York, Plenum Press.
- GREENBERG, J., KRISHNAMURTHY, K. & BRADY, D. 2014a. Compressive single-pixel snapshot x-ray diffraction imaging. *Optics Letters*, 39, 111-114.
- GREENBERG, J. A., HASSAN, M., KRISHNAMURTHY, K. & BRADY, D. 2014b. Structured illumination for tomographic X-ray diffraction imaging. *Analyst*, 139, 709-713.
- GREENBERG, J. A., KRISHNAMURTHY, K. & BRADY, D. 2013a. Snapshot molecular imaging using coded energy-sensitive detection. *Optics Express*, 21, 25480-25491.
- GREENBERG, J. A., KRISHNAMURTHY, K., LAKSHMANAN, M., MACCABE, K., WOLTER, S., KAPADIA, A. & BRADY, D. 2013b. Coding and sampling for compressive x-ray diffraction tomography. *Proceedings of SPIE*, 8858, 885813-1 - 885813-11.
- GUINIER, A. 1963. *X-Ray Diffraction In Crystals, Imperfect Crystals and Amorphous Bodies*, San Francisco, W. H. Freeman and Company.
- GUNSON, G. F. & POLYCHRONOPULOS, B. 1976. Optimum design of a coded mask X-ray telescope for rocket applications. *Monthly Notices of the Royal Astronomical Society*, 177, 485-497.
- HALL, C., BARNES, P., COCKCROFT, J. K., COLSTON, S. L., HÄUSERMANN, D., JACQUES, S. D. M., JUPE, A. C. & KUNZ, M. 1998. Synchrotron energy-dispersive X-ray diffraction tomography. *Nuclear Instruments and Methods in Physics Research Section B: Beam Interactions with Materials and Atoms*, 140, 253-257.
- HAO, J., KANG, K., ZHANG, L. & CHEN, Z. 2013. A novel image optimization method for dual-energy computed tomography. *Nuclear Instruments and Methods in Physics Research Section A: Accelerators, Spectrometers, Detectors and Associated Equipment*, 722, 34-42.
- HARDING, G. The design of direct tomographic energy-dispersive x-ray diffraction imaging (XDI) systems. 2005. *Proceedings of SPIE*, 59230R-59230R-9.

REFERENCES

- HARDING, G. Effective density and atomic number determined from diffraction profiles. 2006. Proceedings of SPIE, 631910-631910-9.
- HARDING, G. 2009. X-ray diffraction imaging - A multi-generational perspective. *Appl. Radiat. Isot.*, 67, 287-295.
- HARDING, G. & DELFS, J. Liquids identification with x-ray diffraction. *In: DOTY, F. P., BARBER, H. B. & ROEHRIG, H., eds. Penetrating Radiation Systems and Applications VIII, 2007. 67070T-1 -12.*
- HARDING, G. & DELFS, J. 2008. Identifying liquids for security screening purposes. *SPIE* [Online]. [Accessed 15th November 2011].
- HARDING, G., FLECKENSTEIN, H., KOSCIESZA, D., OLESINSKI, S., STRECKER, H., THEEDT, T. & ZIENERT, G. 2012. X-ray diffraction imaging with the Multiple Inverse Fan Beam topology: Principles, performance and potential for security screening. *Applied Radiation and Isotopes*, 70, 1228-1237.
- HARDING, G., FLECKENSTEIN, H., OLESINKI, S. & ZIENERT, G. Liquid detection trial with x-ray diffraction. *In: DOTY, F. P., BARBER, H. B., ROEHRIG, H. & SCHIRATO, R. C., eds. Proc. SPIE 7806, Penetrating Radiation Systems and Applications XI, 2010 San Diego, California.*
- HARDING, G., NEWTON, M. & KOSANETZKY, J. 1990. Energy-dispersive x-ray diffraction tomography. *Physics in Medicine and Biology*, 35, 33-41.
- HARGREAVES, M. D. & MATOUSEK, P. Threat detection of liquid explosive precursor mixtures by Spatially Offset Raman Spectroscopy (SORS). *In: LEWIS, C., ed. Optics and Photonics for Counterterrorism and Crime Fighting V, 2009. Proc. SPIE.*
- HE, B. B. 2009. *Two-dimensional X-ray diffraction*, New Jersey, John Wiley & Sons.
- HUANG, C., WIKFELDT, K. T., NORDLUND, D., BERGMANN, U., MCQUEEN, T., SELBERG, J., PETERSON, L. G. & NILSSON, A. 2011. Wide-angle X-ray diffraction and molecular dynamics study of medium-range order in ambient and hot water. *Physical Chemistry Chemical Physics* 13, 19997-20007.
- HUDSON, L., BATEMAN, F., BERGSTROM, P., CERRA, F., GLOVER, J., MINNITI, R., SELTZER, S. & TOSH, R. 2012. Measurements and standards for bulk-explosives detection. *Applied Radiation and Isotopes*, 70, 1037-1041.
- HULL, A. W. 1917. X-ray crystal analysis. *Physical Review*, 10, 661-696.
- IGNATYER, K., MUNRO, P. R. T., SPELLER, R. D. & OLIVO, A. 2011. Phase contrast imaging with coded apertures using laboratory-based X-ray sources. *AIP Conference Proceedings*, 1365, 254-257.
- INAMI, T., KOBIYAMA, M., OKUDA, S., MAETA, H. & OHTSUKA, H. 1999. Grain size measurement of nanocrystalline gold by X-ray diffraction method. *Nanostructured Materials*, 12, 657-660.

REFERENCES

- INGHAM, B. 2014. Statistical measures of spottiness in diffraction rings. *Journal of Applied Crystallography*, 47, 166-172.
- IOVEA, M., NEAGU, M., DULIU, O. G. & MATEIASI, G. 2007. High accuracy X-ray dual-energy experiments and non-rotational tomography algorithm for explosives detection technique in luggage control. *International Symposium on Digital industrial Radiology and Computed Tomography*. Lyon, France.
- JENKINS, R. & SNYDER, R. L. 1996. *Introduction to X-ray powder diffractometry*, New York, Wiley.
- JIMENEZ, A. M. & NAVAS, M. J. 2007. Detection of explosives by chemiluminescence. In: YINON, J. (ed.) *Counterterrorist Detection Techniques of Explosives*. 1st ed. Oxford: Elsevier.
- JOHNS, P. C. & YAFFE, M. J. 1983. Coherent scatter in diagnostic radiology. *Medical Physics*, 10, 40-50.
- JUPP, J., DURRANT, P. T., RAMSDEN, D., CARTER, T., DERMODY, G., PLEASANTS, I. B. & BURROWS, D. 2000. The Non-Invasive Inspection of Baggage Using Coherent X-ray Scattering. *IEEE Transactions on Nuclear Science*, 47, 1987-1994.
- KAK, A. C. & SLANEY, M. 1999. *Principles of computerized tomographic imaging*, New York, IEEE Press.
- KÄMPFE, B., LUCZAK, F. & MICHEL, B. 2005. Energy dispersive X-ray diffraction. *Particle & Particle Systems Characterization*, 22, 391-396.
- KATZOFF, S. 1934. XRay studies pf the molecular arrangement in liquids. *Journal of Chemical Physics*, 2, 841-851.
- KIRSCHENBAUM, A. 2013. The cost of airport security: The passenger dilemma. *Journal of Air Transport Management*, 30, 39-45.
- KLOCK, B. A. Test and evaluation report for X-ray detection of threats using different X-ray functions. Security Technology, 2005. CCST '05. 39th Annual 2005 International Carnahan Conference on, 11-14 Oct. 2005 2005. 182-184.
- KLOTZ, E., LINDE, R. & WEISS, H. 1974. A new method for deconvoluting coded aperture images of three dimensional X-ray objects. *Optics Communications*, 12, 183-187.
- KLUG, H. P. & ALEXANDER, L. E. 1974. *X-ray Diffraction Procedures: For Polycrystalline and Amorphous Materials*, USA, John Wiley & Sons.
- KRISHNAMURTI, P. 1929. X-ray diffraction in liquid mixtures. *Indian Journal of Physics and Proceedings of the Indian Association for Cultivation of Science*, 3, 331-355.

REFERENCES

- KUZNETSOV, A. V. & OSETROV, O. I. 2008. Overview of liquid explosives' detection. *In: SCHUBERT, H. & KUZNETSOV, A. (eds.) Detection of Liquid Explosives and Flammable Agents in Connection with Terrorism*. The Netherlands: Springer
- LANZA, R. C. 2007. Neutron techniques for detection of explosives. *In: YINON, J. (ed.) Counterterrorist Detection Techniques of Explosives*. 1st ed. Oxford: Elsevier.
- LAZZARI, O., JACQUES, S., SOCHI, T. & BARNES, P. 2009. Reconstructive colour X-ray diffraction imaging - a novel TEDDI imaging method. *Analyst*, 134, 1802-1807.
- LEE, A. J. & JACOBSON, S. H. 2011. The impact of aviation checkpoint queues on optimizing security screening effectiveness. *Reliability Engineering & System Safety*, 96, 900-911.
- LEE, A. J., NIKOLAEV, A. G. & JACOBSON, S. H. 2008. Protecting air transportation: a survey of operations research applications to aviation security. *Journal of Transportation Security*, 1, 160-184.
- LEONE, K. & LIU, R. 2005. The key design parameters of checked baggage security screening systems in airports. *Journal of Air Transport Management*, 11, 69-78.
- LEONE, K. & LIU, R. 2011. Improving airport security screening checkpoint operations in the US via paced system design. *Journal of Air Transport Management*, 17, 62-67.
- LI, L., LI, M., SUN, B., LIU, J.-H. & ZHANG, F. 2010. Confirm of the optimum detection angles of several substances using energy dispersive X-ray diffraction. *Procedia Engineering*, 7, 147-150.
- LOEFFEN, P. W., MASKALL, G., BONTHRON, S., BLOOMFIELD, M., TOMBLING, C. & MATOUSEK, P. Spatially offset Raman spectroscopy (SORS) for liquid screening. 2011. 81890C-81890C-10.
- LUGGAR, R. D., FARQUHARSON, M. J., HORROCKS, J. A. & LACEY, R. J. 1998. Multivariate analysis of statistically poor EDXRD spectra for the detection of concealed explosives. *X-ray spectroscopy*, 27, 87-94.
- LUGGAR, R. D. & GILBOY, W. B. 1999. Recent developments in industrial applications of elastic scatter X-ray inspection. *Radiation Physics and Chemistry*, 56, 213-227.
- LUGGAR, R. D., HORROCKS, J. A., SPELLER, R. D. & LACEY, R. J. 1996. Determination of the geometric blurring of an energy dispersive X-ray diffraction (EDXRD) system and its use in the simulation of experimentally derived diffraction profiles. *Nuclear Instruments and Methods in Physics Research A*, 383, 610-618.
- LUGGAR, R. D., HORROCKS, J. A., SPELLER, R. D. & LACEY, R. J. 1997. Low Angle X-ray Scatter for Explosives Detection: a Geometry Optimization. *Appl. Radiat. Isot.*, 48, 215-224.

REFERENCES

- MACCABE, K., KRISHNAMURTHY, K., CHAWLA, A., MARKS, D., SAMEI, E. & BRADY, D. 2012. Pencil beam coded aperture x-ray scatter imaging. *Optics Express*, 20, 16310-16320.
- MACCABE, K. P., HOLMGREN, A. D., TORNAL, M. P. & BRADY, D. J. 2013. Snapshot 2D tomography via coded aperture x-ray scatter imaging. *Applied Optics*, 52, 4582-4589.
- MACWILLIAMS, F. J. & SLOANE, N. J. 1976. Pseudo-random sequences and arrays. *Proceedings of the IEEE*, 64, 1715-1729.
- MADDEN, R. W., MAHDAVIEH, J., SMITH, R. C. & SUBRAMANIAN, R. 2008. An explosives detection system for airline security using coherent x-ray scattering technology. *Proceedings of SPIE*, 7079, 707915-1 - 707915-11.
- MALDEN, C. H. & SPELLER, R. D. 2000. A CdZnTe array for the detection of explosives in baggage by energy-dispersive X-ray diffraction signatures at multiple scatter angles. *Nuclear Instruments and Methods in Physics Research A*, 449, 408-415.
- MARTINEAU, A., ROCCHISANI, J. M. & MORETTI, J. L. 2010. Coded aperture optimization using Monte Carlo simulations. *Nuclear Instruments and Methods in Physics Research A*, 616, 75-80.
- MATOUSEK, P., CLARK, I. P., DRAPER, E. R. C., MORRIS, M. D., GOODSHIP, A. E., EVERALL, N., TOWRIE, M., FINNEY, W. F. & PARKER, A. W. 2005. Subsurface probing in diffusely scattering media using spatially offset Raman spectroscopy. *Appl. Spectrosc.*, 59, 393-400.
- MCCRICKERD, J. T. 1971. Coherent processing and depth of focus of annular aperture imagery. *Applied Optics*, 10, 2226-2230.
- MEGHERBI, N., BRECKON, T. P. & FLITTON, G. T. Investigating existing medical CT segmentation techniques within automated baggage and package inspection. 2013. 89010L-89010L-9.
- MERTZ, L. & YOUNG, N. O. Proceeding of the International Conference on Optical Instruments, 1961 London. 305-310.
- MEYER, H. H. 1930. Über den einfluss der temperatur und gelöster elektrolyte auf das monochromatische Debye-Scherrer-diagramm des wassers. *Annalen der Physik*, 397, 701-734.
- MILLER, J. B. 2007. Nuclear quadrupole resonance detection of explosives. In: YINON, J. (ed.) *Counterterrorist Detection Techniques of Explosives*. 1st ed. Oxford: Elsevier.
- MORGAN, J. & WARREN, B. E. 1938. XRAY analysis of the structure of water. *Journal of Chemical Physics*, 6, 666-673.

REFERENCES

- MU, Z., HONG, B., LI, S. & LIU, Y. H. 2009. A novel three-dimensional image reconstruction method for near-field coded aperture single photon emission computerized tomography. *Medical Physics*, 36, 1533-1542.
- MURRAY, N. C., LACEY, R. J. & MASON, P. H. Exploitation of X-ray technology for the detection of contraband-aviation security applications. Security and Detection, 1997. ECOS 97., European Conference on, 28-30 Apr 1997 1997. 13-18.
- NARTEN, A. H., DANFORD, M. D. & LEVY, H. A. 1967. X-ray diffraction study of liquid water in the temperature range 4-200°C. *Discussions of the Faraday Society*, 43, 97-107.
- NOVAKOFF, K. 1992. FAA bulk technology overview for explosive detection. *SPIE*, 1824, 2-12.
- O'FLYNN, D., DESAI, H., REID, C. B., CHRISTODOULOU, C., WILSON, M. D., VEALE, M. C., SELLER, P., HILLS, D., WONG, B. & SPELLER, R. D. 2013a. Identification of simulants for explosives using pixellated X-ray diffraction. *Crime Science*, 2, 1-6.
- O'FLYNN, D., REID, C., CHRISTODOULOU, C., WILSON, M. D., VEALE, M. C., SELLER, P. & SPELLER, R. 2012. Pixellated diffraction signatures for explosives detection. *Proceedings of SPIE*, 8357, 83570X-1 - 83570X-7.
- O'FLYNN, D., REID, C. B., CHRISTODOULOU, C., WILSON, M. D., VEALE, M. C., SELLER, P., HILLS, D., DESAI, H., WONG, B. & SPELLER, R. 2013b. Explosive detection using pixellated X-ray diffraction (PixD). *Journal of Instrumentation*, 8, P03007.
- O'NEIL, K. E. *The bio-sensor: an effective drugs and explosives edtection system* [Online]. Advanced Aviation Technology. Available: <http://www.aatl.net/publications/Bio-sensor.htm> [Accessed 13th January 2012].
- OLAPIRIYAKUL, S. & DAS, S. 2007. Design and analysis of a two-stage security screening and inspection system. *Journal of Air Transport Management*, 13, 67-74.
- OLIVO, A., IGNATYER, K., MUNRO, P. R. T. & SPELLER, R. D. 2011. A coded-aperture based method allowing non-interferometric phase contrast imaging with incoherent X-ray sources. *Nuclear Instruments and Methods in Physics Research A*, 648, S28-S31.
- OLIVO, A., IGNATYEV, K., MUNRO, P. R. & SPELLER, R. D. 2009. Design and realization of a coded-aperture based X-ray phase contrast imaging for homeland security applications. *Nuclear Instruments and Methods in Physics Research A*, 610, 604-614.

REFERENCES

- OLIVO, A. & SPELLER, R. 2007. A coded-aperture technique allowing x-ray phase contrast imaging with conventional sources. *Applied Physics Letters*, 91, 07416-1 - 07416-3.
- OLIVO, A. & SPELLER, R. 2008a. Image formation principles in coded-aperture based x-ray phase contrast imaging. *Physics in Medicine and Biology*, 53, 6461-6474.
- OLIVO, A. & SPELLER, R. D. 2008b. A novel X-ray imaging technique based on coded apertures making phase contrast imaging feasible with conventional sources. *IEEE Nuclear Science Symposium Conference Record*.
- OSTER JR, C. V., STRONG, J. S. & ZORN, C. K. 2013. Analyzing aviation safety: Problems, challenges, opportunities. *Research in Transportation Economics*, 43, 148-164.
- PANI, S., COOK, E., HORROCKS, J., GEORGE, L., HARDWICK, S. & SPELELR, R. 2009. Modelling an energy-dispersive X-ray diffraction system for drug detection. *IEEE Transactions on Nuclear Science*, 56, 1238-1241.
- PARRISH, W. & LOWITZSCH, K. 1959. Geometry, alignment and angular calibration of X-ray diffractometers. *The American Mineralogist*, 44, 765-787.
- RABBANY, S. Y., LANE, W. J., MARGANSKI, W. A., KUSTERBECK, A. W. & LIGLER, F. S. 2000. Trace detection of explosives using a membrane-based displacement immunoassay. *Journal of Immunological Methods*, 246, 69-77.
- ROGERS, K., EVANS, P., PROKOPIOU, D., DICKEN, A., GODBER, S. & ROGERS, J. 2012. Fundamental parameters approach applied to focal construct geometry for X-ray diffraction *Nuclear Instruments and Methods in Physics Research Section A*, 690, 1-6.
- ROGERS, K., EVANS, P., ROGERS, J., CHAN, J. W. & DICKEN, A. 2010. Focal construct geometry - a novel approach to the acquisition of diffraction data. *J. Appl. Cryst.*, 43, 264-268.
- RONDESCHAGEN, D., ARNOLD, G., BOCKISCH, S., FRANCKE, K.-P., LEONHARDT, J. & KUSTER, A. 2008. Trace and bulk detection of explosives by ion mobility spectrometry and neutron analysis. In: SCHUBERT, H. & KUZNETSOV, A. (eds.) *Detection of Liquid Explosives and Flammable Agents in Connection with Terrorism*. The Netherlands: Springer.
- RONTGEN, W. C. 1896. On a new kind of rays. *Nature*, 53, 274-277.
- SCHUBERT, H. & KUZNETSOV, A. 2008. *Detection of Liquid Explosives and Flammable Agents in Connection with Terrorism*, The Netherlands, Springer.
- SCHULTZ, L. J., WALLACE, M. S., GALASSI, M. C., HOOVER, A. S., MOCKO, M., PALMER, D. M., TONGA, S. R., KIPPEN, R. M., HYNES, M. V., TOOLIN, M. J., HARRIS, B., MCELROY, J. E., WAKEFORD, D. & LANZA, R. C. 2009. Hybrid coded aperture and Compton imaging using an active mask. *Nuclear Instruments and Methods in Physics Research A*, 608, 267-274.

REFERENCES

- SHEA, D. A. & MORGAN, D. 2007. Detection of explosives on airline passengers: recommendation of the 9/11 commission and related issues. CRS Report for Congress.
- SILVA, R. & ROGERS, G. L. 1981a. Coded aperture imaging. *Optica Acta: International Journal of Optics*, 28, 1125-1134.
- SILVA, R. & ROGERS, G. L. 1981b. Coding and decoding pictures in nuclear medicine. *Pattern Recognition*, 14, 3-10.
- SILVA, R. & ROGERS, G. L. 1982. Tomographical possibilities in coded aperture imaging optical simulations. *Optica Acta: International Journal of Optics*, 29, 257-264.
- SIMPSON, R. G. 1978. *Annular coded-aperture imaging system for nuclear medicine* Doctor of Philosophy, The University of Arizona.
- SIMPSON, R. G., BARRETT, H. H., SUBACH, J. A. & FISHER, H. D. 1975. Digital processing of annular coded-aperture imagery. *Optical Engineering*, 14, 490-494.
- SINGH, S. & SINGH, M. 2003. Explosives detection systems (ADS) for aviation security: a review. *Signal Processing*, 83, 31-55.
- SKINNER, G. K. 1984. Imaging with coded-aperture masks. *Nuclear Instruments and Methods in Physics Research*, 221, 33-40.
- SPELLER, R. 2001. Radiation-based security. *Radiation Physics and Chemistry*, 61, 293-300.
- STEWART, G. W. 1931. X-Ray diffraction in water: the nature of molecular association. *Phys. Rev.*, 37, 9-16.
- STRECKER, H. 1998. Automatic detection of explosives in airline baggage using elastic X-ray scatter. *medicamundi*, 42, 30-33.
- SUN, B., LI, M., ZHANG, F., ZHONG, Y., KANG, N., LU, W. & LIU, J. 2010. The performance of a fast testing system for illicit materials detection based on energy-dispersive X-ray diffraction technique. *Microchemical Journal*, 95, 293-297.
- TURCSANY, D., MOUTON, A. & BRECKON, T. P. Improving feature-based object recognition for X-ray baggage security screening using primed visual words. Industrial Technology (ICIT), 2013 IEEE International Conference on, 25-28 Feb. 2013 2013. 1140-1145.
- VERTATCHITSCH, E. & HAYKIN, S. 1986. Nonredundant Arrays. *Proceedings of the IEEE*, 74, 217.
- VOGEL, H. 2007. Search by X-rays applied technology. *European Journal of Radiology* 63, 227-236.

REFERENCES

- WALTON, P. W. 1973. An aperture imaging system with instant decoding and tomographic capabilities. *Journal of Nuclear Medicine*, 14, 861-863.
- WARREN, B. E. 1990. *X-ray Diffraction* New York, Addison - Wesley.
- WEISS, H. 1975. Nonredundant point distribution for coded aperture imaging with application to three-dimensional on-line X-ray information retrieving. *IEEE Transactions on computers*, c-4, 391-394.
- WEISS, H., KLOTZ, E., LINDE, R., RABE, G. & TIEMENS, U. 1977. Coded aperture imaging with X-rays (flashing tomosynthesis). *Optica Acta*, 24, 305-325.
- WELLS, K. & BRADLEY, D. A. 2012. A review of X-ray explosives detection techniques for checked baggage. *Applied Radiation Isotopes*, 70, 1729-1746.
- WENK, H. R. & HOUTTE, P. V. 2004. Texture and anisotropy. *Reports on Progress in Physics*, 67, 1367-1428.
- WETTER, O. E. 2013. Imaging in airport security: Past, present, future, and the link to forensic and clinical radiology. *Journal of Forensic Radiology and Imaging*, 1, 152-160.
- WOOLFSON, M. M. 1997. *An introduction to X-ray crystallography*, Cambridge, Cambridge University Press.
- YING, Z., NAIDU, R. & CRAWFORD, C. R. 2006. Dual energy computed tomography for explosive detection. *Journal of X-Ray Science and Technology*, 14, 235-256.
- YING, Z., NAIDU, R., GUILBERT, K., SCHAFFER, D. & CRAWFORD, C. R. 2007. Dual energy volumetric X-ray tomographic sensor for luggage screening. *Sensors Applications Symposium*. San Diego, California, USA.
- YINON, J. 2007. Detection of explosives by mass spectrometry. In: YINON, J. (ed.) *Counterterrorist detection techniques of explosives*. Oxford: Elsevier.
- ZHANG, Y., WENG, D., WANG, Y. & ZHENG, S. 2013. A new method to accelerate depth extraction for aperture-coded camera. *Optik*, 124, 4231-4235.
- ZHONG, Y., LI, M., SUN, B., WANG, J., ZHANG, F., YU, D., ZHANG, Y. & LIU, J. 2012. Non-invasive investigation of liquid materials using energy dispersive X-ray scattering. *Measurement*, 45, 1540-1546.
- ZHONG, Y., SUN, B., YU, D., LI, W., ZHANG, Y., LI, M. & LIU, J. 2010. Identification of liquid materials using energy dispersive X-ray scattering. *Procedia Engineering*, 7, 135-142.

APPENDICES

Appendix A PEAK BROADENING

A.1 Collimation optics

A.1.1 X-ray source - to - collimator distance

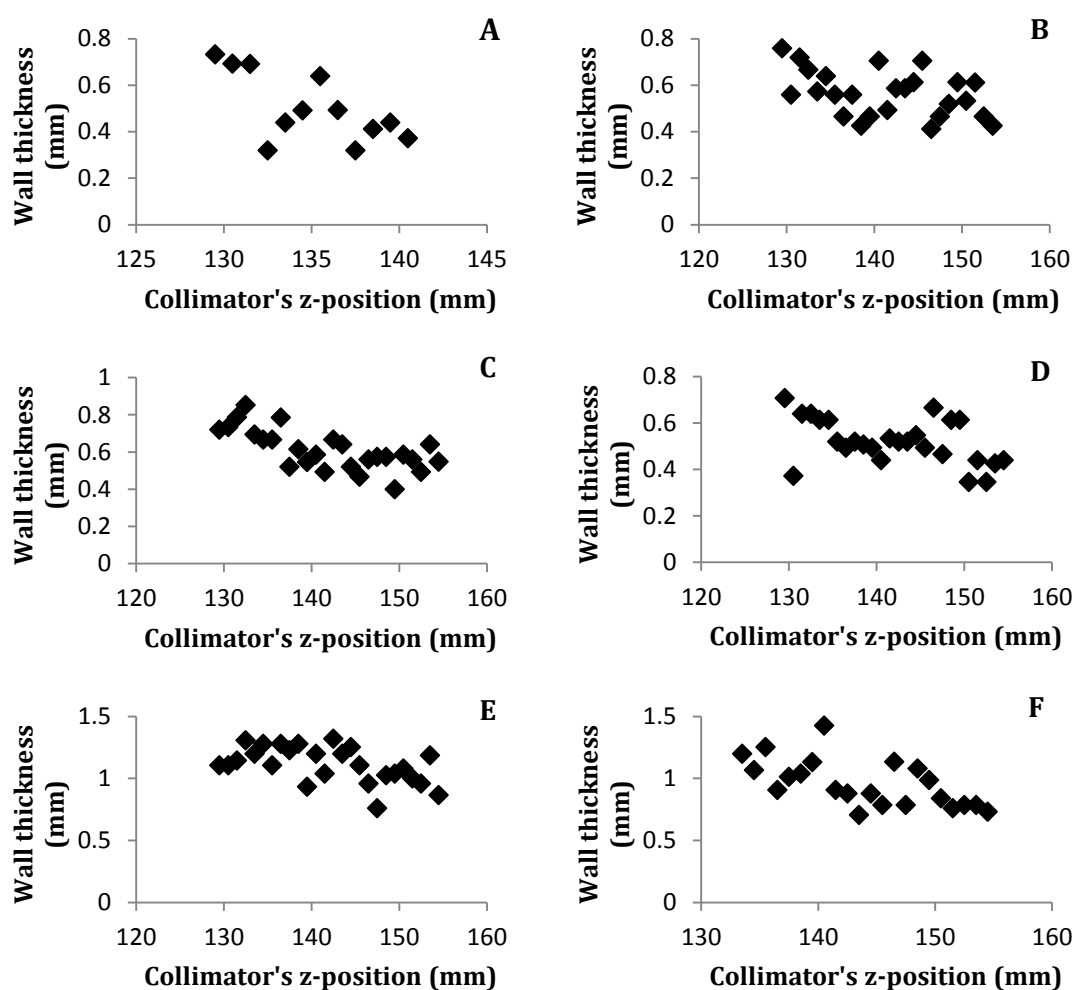


Figure A.1 Relationship between measured widths of Debye rings' wall thickness as the collimator was translated from 129.1 mm - 155.5 mm in steps of 1 mm. Graphs A-F correspond to the six Debye rings from low to high 2θ angles for experiment *DPtr106* (see Table 6.6).

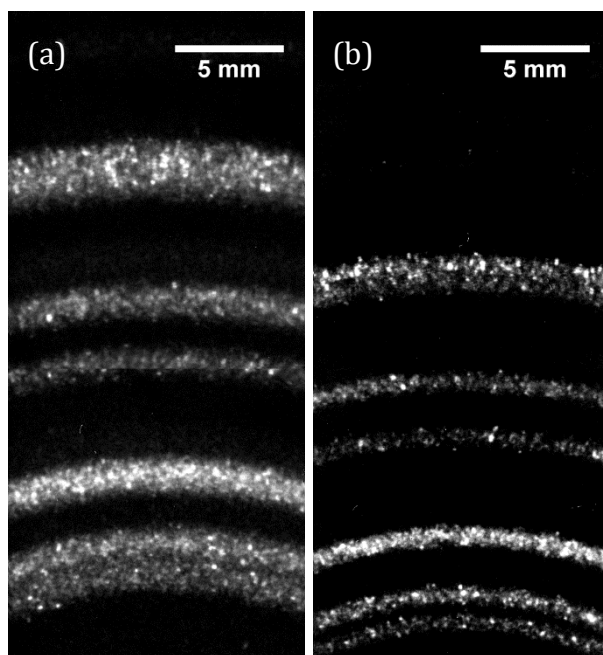


Figure A.2 Diffraction images of Al_2O_3 acquired with 0.38° (a) and 0.14° (b) total pencil beam divergence ($2\phi_{\text{PB}}$) during experiments *DPtr115* and *DPtr143*, respectively (see Table 6.6).

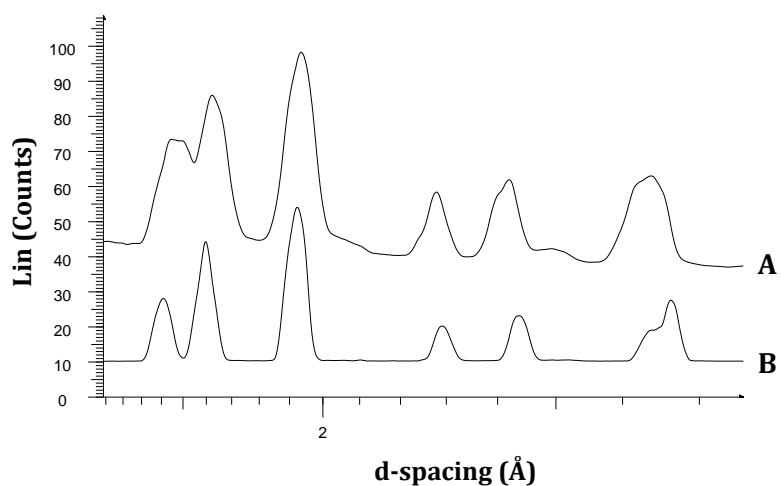


Figure A.3 Scattering profile from Al_2O_3 acquired with 0.38° (A) and 0.14° (B) total pencil beam divergence ($2\phi_{\text{PB}}$) during experiments *DPtr115* (A) and *DPtr143* (B).

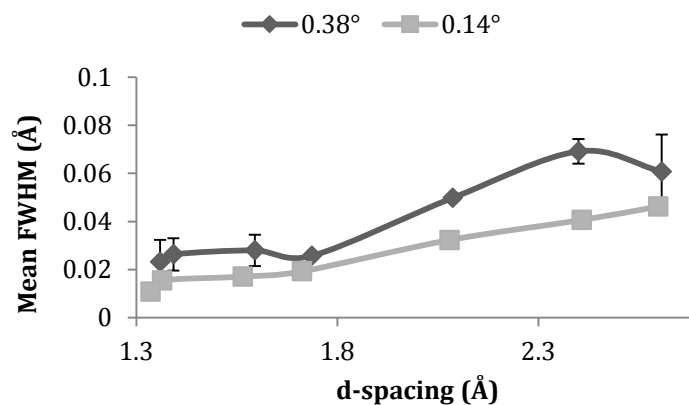


Figure A.4 Mean FWHM values of the scattering maxima of Al_2O_3 obtained with 0.38° and 0.14° total pencil beam divergence ($2\phi_{\text{PB}}$) during experiments *DPtr115* and *DPtr143* respectively.

A.1.2 Collimator's pinhole size and length

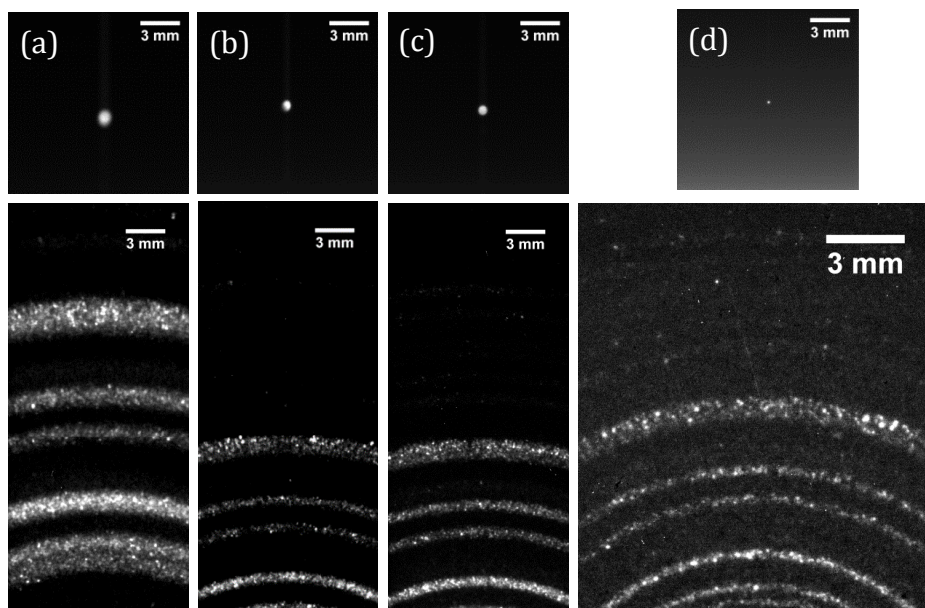


Figure A.5 Images of the primary beam (top) resulting from collimator *PB5* attached to the X-ray source (a), collimator *PB5* positioned 129.1 mm from the X-ray source (b), collimator *PB6* (c) and collimator *PB7* (d). The corresponding scattering distributions from Al_2O_3 sample are also presented (bottom images).

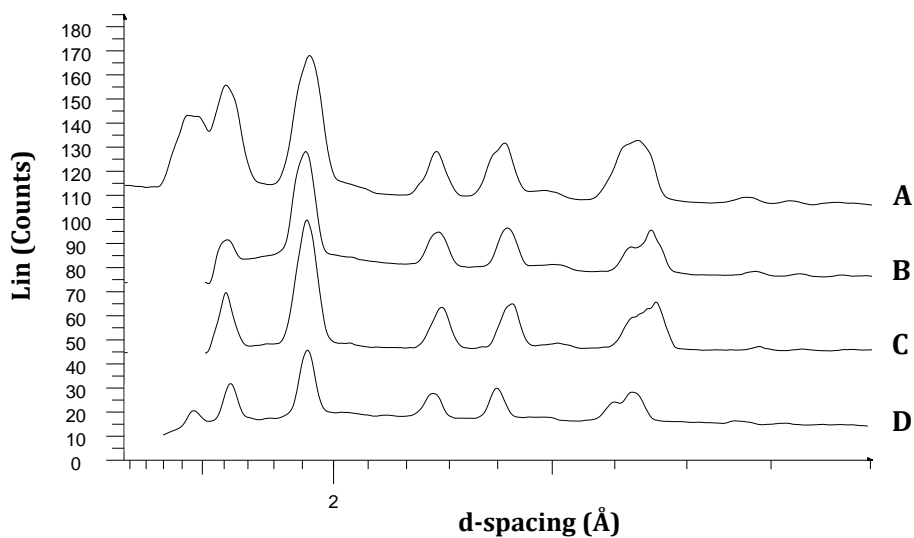


Figure A.6 Scattering profiles of Al_2O_3 when illuminated by a pencil beam of total divergence of 0.38° (A), 0.14° (B), 0.16° (C) and 0.015° (D).

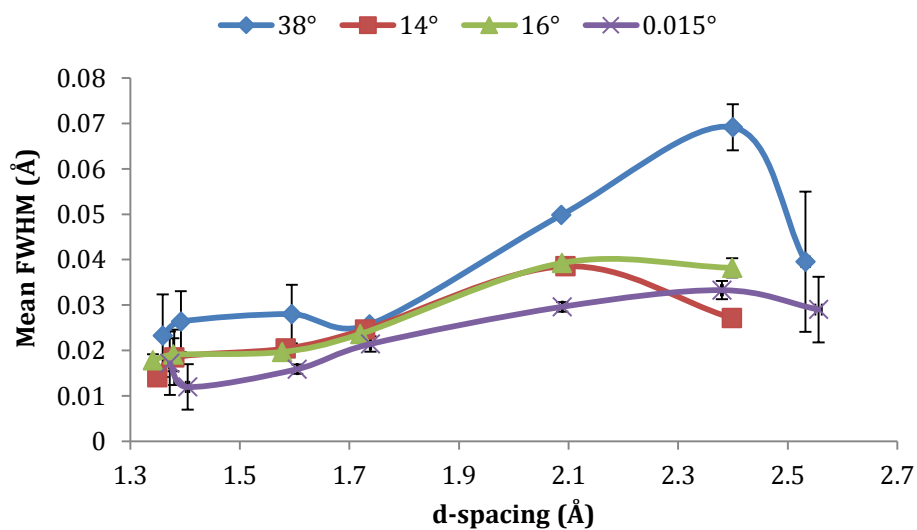


Figure A.7 Mean FWHM values of the scattering maxima of Al_2O_3 obtained with 0.38° , 0.14° , 0.16° and 0.015° total pencil beam divergence.

A.2 Sample - to- detector distance

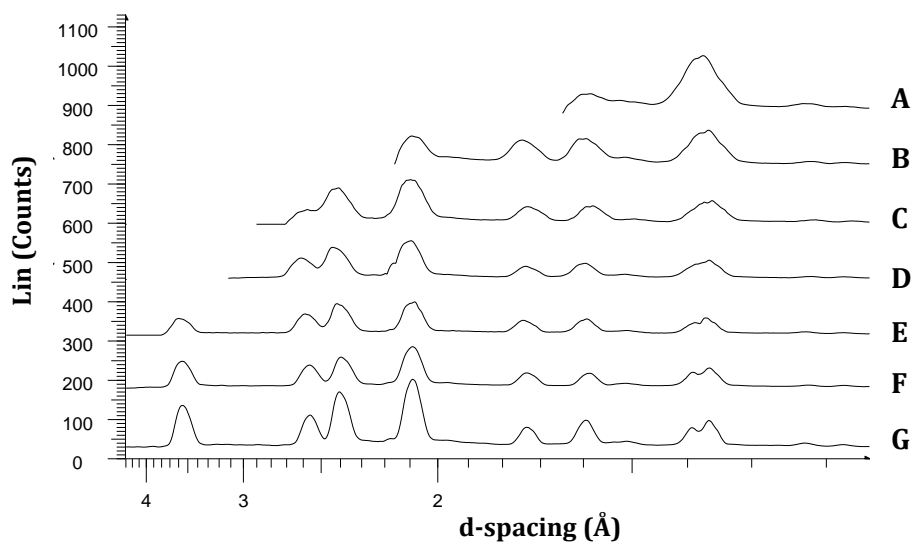


Figure A.8 Scattering profiles of Al_2O_3 when illuminated by a pencil beam at 28 mm (A), 38 mm (B), 48 (C), 58 mm(D), 68 mm (E), 78 mm (F) and 88 mm (G) sample-to-detector distances.

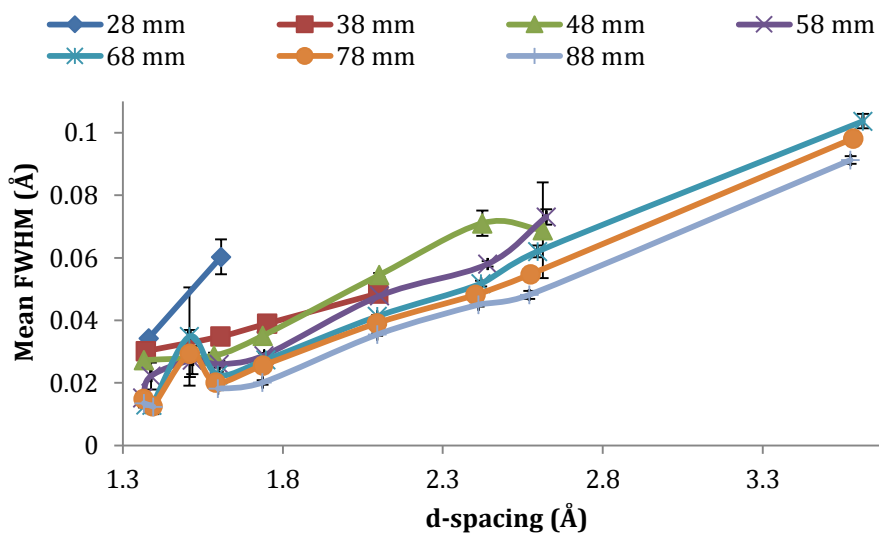


Figure A.9 Mean FWHM values of the scattering maxima of Al_2O_3 with a sample-to-detector distance from 28-88 mm.

A.3 X-ray source - to - sample distance

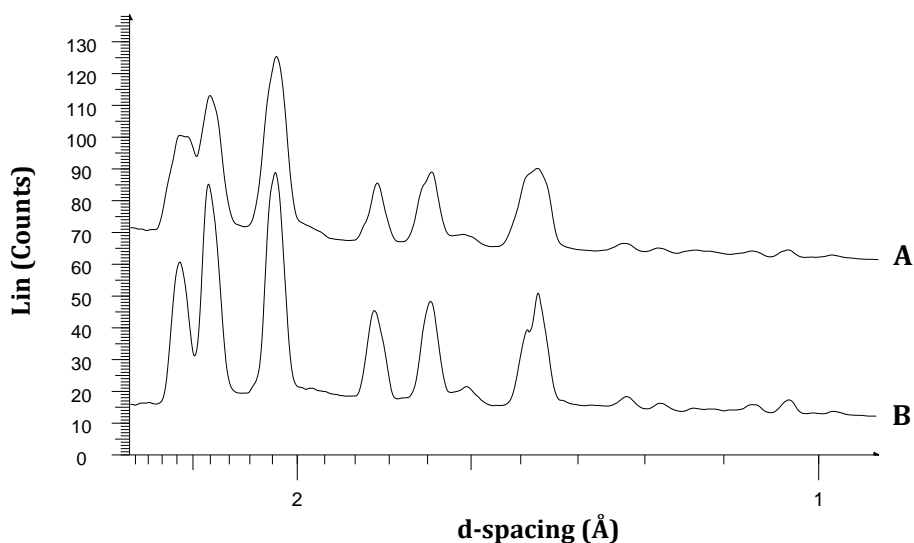


Figure A.10 Comparison of the scattering profiles of an Al_2O_3 sample at a different position along the primary axis; 176 mm (A) and 162 mm (B) with similar sample-to-detector distance of 64 mm and 68 mm respectively.

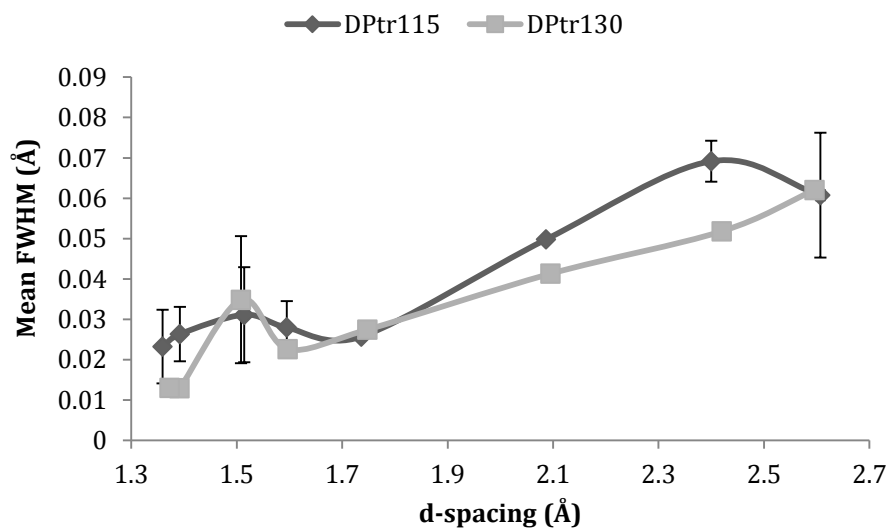


Figure A.11 Mean FWHM values of the scattering maxima of Al_2O_3 when positioned 176 mm (DPTr115) and 162 mm (DPTr130) from the X-ray source; at a 64 mm and 68 mm sample-to-detector distance, respectively.

A.4 Sample thickness

A.4.1 Powder samples (annular beam)

Table A.1 List of FWHM values of FCG data for Al_2O_3 , hydroxyapatite and NaCl with 1.6 mm and 3 mm sample thickness, and corresponding calculated lengths of the condensation foci.

	1.6 mm sample thickness		3 mm sample thickness	
	d-spacing (nm)	FWHM (nm)	d-spacing (nm)	FWHM (nm)
Al_2O_3	$0.349 \pm 1.45 \times 10^{-4}$	$0.007 \pm 1.97 \times 10^{-5}$	$0.347 \pm 2.28 \times 10^{-4}$	$0.010 \pm 2.91 \times 10^{-5}$
	$0.256 \pm 7.64 \times 10^{-5}$	$0.006 \pm 1.85 \times 10^{-5}$	$0.256 \pm 5.99 \times 10^{-4}$	$0.009 \pm 2.25 \times 10^{-4}$
	$0.239 \pm 8.71 \times 10^{-5}$	$0.006 \pm 3.17 \times 10^{-5}$	$0.238 \pm 1.19 \times 10^{-3}$	$0.009 \pm 2.27 \times 10^{-4}$
	$0.210 \pm 2.72 \times 10^{-5}$	$0.005 \pm 6.66 \times 10^{-6}$	$0.210 \pm 1.02 \times 10^{-4}$	$0.008 \pm 2.37 \times 10^{-5}$
	$0.176 \pm 4.57 \times 10^{-5}$	$0.004 \pm 1.52 \times 10^{-5}$	$0.176 \pm 3.58 \times 10^{-4}$	$0.010 \pm 4.92 \times 10^{-4}$
	$0.162 \pm 4.06 \times 10^{-5}$	$0.004 \pm 8.62 \times 10^{-6}$	$0.162 \pm 1.94 \times 10^{-4}$	$0.007 \pm 6.09 \times 10^{-5}$
	$0.140 \pm 1.57 \times 10^{-5}$	$0.004 \pm 5.20 \times 10^{-6}$	$0.141 \pm 4.88 \times 10^{-5}$	$0.007 \pm 2.99 \times 10^{-5}$
Hydroxyapatite	$0.391 \pm 1.89 \times 10^{-3}$	$0.043 \pm 8.57 \times 10^{-4}$	$0.391 \pm 3.93 \times 10^{-3}$	$0.024 \pm 1.57 \times 10^{-3}$
	$0.345 \pm 7.99 \times 10^{-4}$	$0.014 \pm 2.03 \times 10^{-4}$	$0.345 \pm 1.17 \times 10^{-3}$	$0.012 \pm 1.65 \times 10^{-4}$
	$0.313 \pm 6.54 \times 10^{-4}$	$0.012 \pm 2.49 \times 10^{-4}$	$0.313 \pm 6.39 \times 10^{-4}$	$0.009 \pm 1.10 \times 10^{-4}$
	$0.280 \pm 3.12 \times 10^{-5}$	$0.012 \pm 1.32 \times 10^{-5}$	$0.280 \pm 8.43 \times 10^{-5}$	$0.013 \pm 1.50 \times 10^{-5}$
	$0.229 \pm 1.41 \times 10^{-4}$	$0.009 \pm 1.58 \times 10^{-4}$	$0.230 \pm 2.20 \times 10^{-4}$	$0.010 \pm 4.46 \times 10^{-5}$
	$0.198 \pm 2.02 \times 10^{-4}$	$0.009 \pm 1.53 \times 10^{-4}$	$0.187 \pm 1.01 \times 10^{-4}$	$0.014 \pm 4.06 \times 10^{-5}$
	$0.185 \pm 4.34 \times 10^{-4}$	$0.010 \pm 1.53 \times 10^{-4}$		
	$0.150 \pm 3.53 \times 10^{-5}$	$0.005 \pm 1.07 \times 10^{-5}$	$0.152 \pm 1.13 \times 10^{-4}$	$0.007 \pm 4.23 \times 10^{-5}$
$0.130 \pm 3.89 \times 10^{-5}$	$0.006 \pm 5.78 \times 10^{-5}$	$0.130 \pm 1.11 \times 10^{-4}$	$0.004 \pm 3.58 \times 10^{-3}$	
NaCl	$0.330 \pm 5.85 \times 10^{-4}$	$0.004 \pm 8.28 \times 10^{-5}$	$0.314 \pm 9.57 \times 10^{-4}$	$0.009 \pm 1.86 \times 10^{-4}$
	$0.286 \pm 1.67 \times 10^{-4}$	$0.004 \pm 9.91 \times 10^{-5}$	$0.284 \pm 1.31 \times 10^{-4}$	$0.006 \pm 2.10 \times 10^{-5}$
	$0.278 \pm 7.91 \times 10^{-4}$	$0.003 \pm 4.23 \times 10^{-4}$	$0.211 \pm 3.63 \times 10^{-4}$	$0.006 \pm 3.92 \times 10^{-4}$
	$0.202 \pm 4.10 \times 10^{-5}$	$0.003 \pm 1.31 \times 10^{-5}$	$0.200 \pm 1.99 \times 10^{-4}$	$0.006 \pm 1.08 \times 10^{-4}$
	$0.194 \pm 2.24 \times 10^{-5}$	$0.003 \pm 5.09 \times 10^{-6}$	-	-
	$0.141 \pm 2.12 \times 10^{-5}$	$0.002 \pm 6.86 \times 10^{-6}$	$0.137 \pm 3.06 \times 10^{-4}$	$0.002 \pm 1.07 \times 10^{-4}$

A.4.2 Powder samples (pencil beam)

Table A.2 List of FWHM values of conventional XRD data for Al₂O₃, hydroxyapatite and NaCl with 1.6 mm and 3 mm sample thickness.

	1.6 mm sample thickness		3 mm sample thickness	
	d-spacing (nm)	FWHM (nm)	d-spacing (nm)	FWHM (nm)
Al ₂ O ₃	0.347 ± 1.38 x 10 ⁻³	0.014 ± 1.60 x 10 ⁻³	0.350 ± 3.44 x 10 ⁻³	0.014 ± 3.35 x 10 ⁻³
	0.254 ± 1.20 x 10 ⁻³	0.007 ± 2.51 x 10 ⁻³	0.253 ± 6.73 x 10 ⁻³	0.010 ± 3.03 x 10 ⁻²
	0.235 ± 1.34 x 10 ⁻³	0.007 ± 4.64 x 10 ⁻³	0.235 ± 1.10 x 10 ⁻²	0.008 ± 8.06 x 10 ⁻²
	0.206 ± 8.09 x 10 ⁻⁴	0.005 ± 1.03 x 10 ⁻³	0.205 ± 2.08 x 10 ⁻³	0.005 ± 2.62 x 10 ⁻³
	0.195 ± 5.94 x 10 ⁻³	0.006 ± 9.40 x 10 ⁻³	0.192 ± 4.12 x 10 ⁻²	0.007 ± 6.96 x 10 ⁻²
	0.173 ± 1.10 x 10 ⁻³	0.004 ± 1.04 x 10 ⁻³	0.172 ± 4.38 x 10 ⁻³	0.005 ± 3.51 x 10 ⁻³
	0.159 ± 4.60 x 10 ⁻⁴	0.003 ± 9.17 x 10 ⁻⁴	0.158 ± 2.90 x 10 ⁻³	0.004 ± 6.74 x 10 ⁻³
	0.151 ± 3.53 x 10 ⁻³	0.003 ± 6.21 x 10 ⁻³	0.148 ± 1.54 x 10 ⁻²	0.003 ± 2.68 x 10 ⁻²
	0.137 ± 4.89 x 10 ⁻⁴	0.003 ± 1.73 x 10 ⁻³	0.136 ± 1.95 x 10 ⁻³	0.004 ± 4.44 x 10 ⁻³
	0.123 ± 1.60 x 10 ⁻³	0.006 ± 2.68 x 10 ⁻²	0.120 ± 9.95 x 10 ⁻³	0.013 ± 2.66 x 10 ⁰
Hydroxyapatite	0.351 ± 1.02 x 10 ⁻²	0.013 ± 143 x 10 ⁻²	0.352 ± 5.17 x 10 ⁻³	0.014 ± 2.49 x 10 ⁻³
	0.319 ± 3.94 x 10 ⁻²	0.006 ± 4.31 x 10 ⁻²	0.317 ± 2.22 x 10 ⁻²	0.009 ± 4.59 x 10 ⁻²
	0.282 ± 1.74 x 10 ⁻³	0.012 ± 1.95 x 10 ⁻³	0.281 ± 1.31 x 10 ⁻³	0.013 ± 2.07 x 10 ⁻³
	0.226 ± 1.25 x 10 ⁻²	0.003 ± 1.49 x 10 ⁻²	0.226 ± 1.08 x 10 ⁻²	0.009 ± 5.94 x 10 ⁻²
	0.207 ± 6.17 x 10 ⁻³	0.009 ± 2.80 x 10 ⁻¹	0.209 ± 2.24 x 10 ⁻³	0.003 ± 5.35 x 10 ⁻²
	0.195 ± 1.46 x 10 ⁻²	0.007 ± 2.70 x 10 ⁻²	0.195 ± 1.44 x 10 ⁻²	0.009 ± 6.08 x 10 ⁻²
	0.184 ± 1.28 x 10 ⁻²	0.007 ± 8.46 x 10 ⁻³	0.182 ± 8.56 x 10 ⁻³	0.010 ± 2.01 x 10 ⁻²
NaCl	0.497 ± 6.78 x 10 ⁻³	0.021 ± 8.35 x 10 ⁻³	0.474 ± 5.26 x 10 ⁻²	0.027 ± 5.15 x 10 ⁻²
	0.306 ± 2.96 x 10 ⁻³	0.005 ± 3.38 x 10 ⁻³	0.329 ± 1.74 x 10 ⁻¹	0.018 ± 2.16 x 10 ⁻¹
	0.268 ± 5.33 x 10 ⁻⁴	0.006 ± 5.82 x 10 ⁻⁴	0.296 ± 2.99 x 10 ⁻²	0.009 ± 9.69 x 10 ⁻²
	0.220 ± 3.77 x 10 ⁻³	0.006 ± 1.32 x 10 ⁻²	0.221 ± 2.03 x 10 ⁻¹	0.027 ± 2.71 x 10 ⁻¹
	0.204 ± 5.71 x 10 ⁻³	0.002 ± 1.27 x 10 ⁻²	0.204 ± 5.69 x 10 ⁻²	0.002 ± 6.76 x 10 ⁻²
	0.195 ± 4.73 x 10 ⁻³	0.002 ± 8.54 x 10 ⁻³	0.198 ± 3.82 x 10 ⁻²	0.003 ± 1.19 x 10 ⁻¹
	0.164 ± 2.41 x 10 ⁻³	0.002 ± 2.92 x 10 ⁻³	0.162 ± 1.32 x 10 ⁻²	0.001 ± 1.76 x 10 ⁻²
	0.143 ± 1.21 x 10 ⁻³	0.002 ± 1.95 x 10 ⁻³	-	-

Appendix B MULTIPLE SCATTERERS

B.1 Same material characteristics

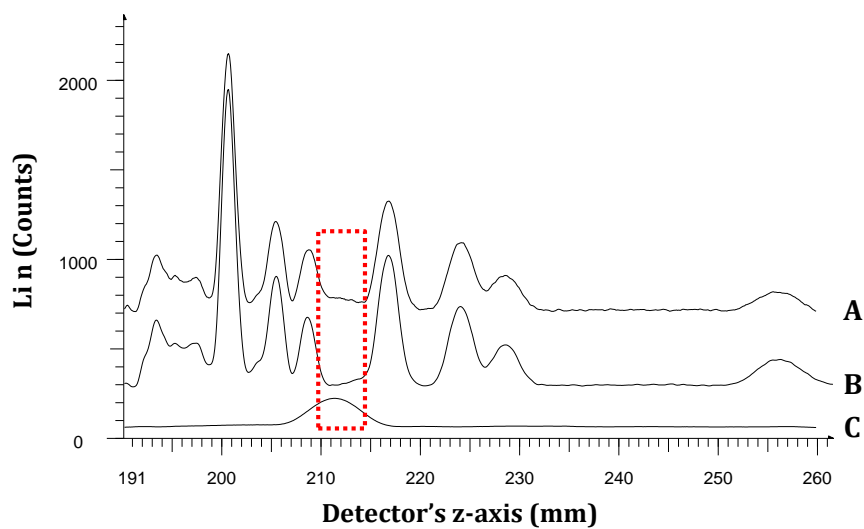


Figure B.1 Diffraction signatures from two Al_2O_3 (*S1* and *S2*) plates separated by 31 mm along the z-axis (A), a single Al_2O_3 (*S2*) plate (B) and a single Al_2O_3 (*S1*) plate (C).

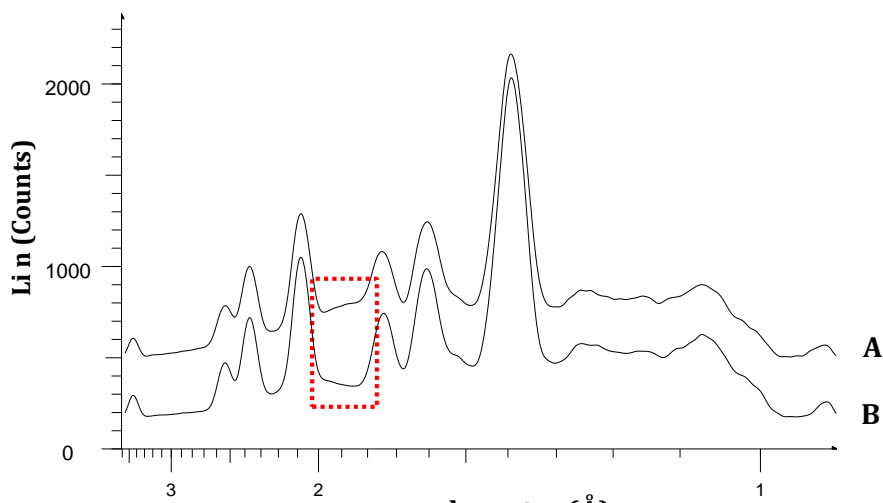


Figure B.2 Diffraction signatures from two Al_2O_3 (*S1* and *S2*) plates separated by 31.3 mm along the z-axis (A) and a single Al_2O_3 (*S2*) plate (B).

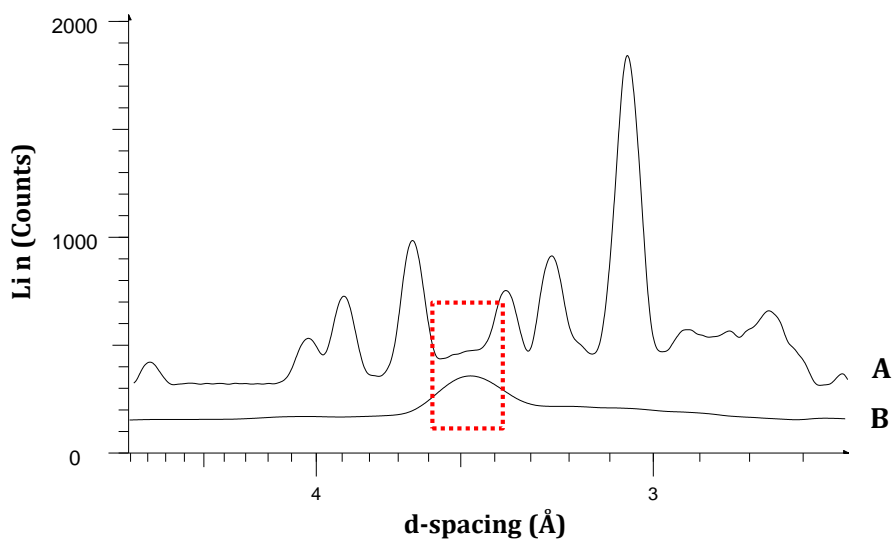


Figure B.3 Diffraction signatures from two Al_2O_3 (*S1* and *S2*) plates separated by 31.3 mm along the *z*-axis (*A*) and a single Al_2O_3 (*S1*) plate (*B*).

B.2 Different material characteristics

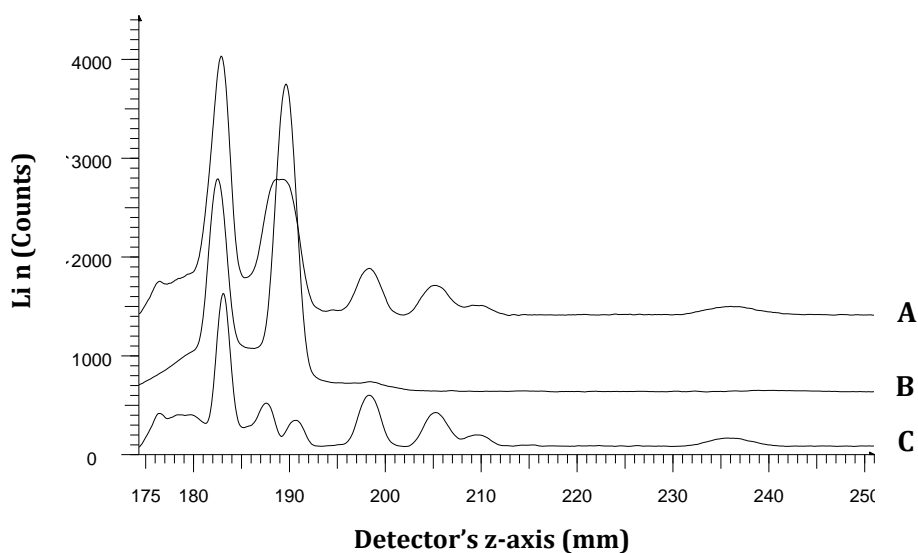


Figure B.4 Diffraction signatures from an Al_2O_3 (*S1*) and Al (*AS*) plates separated by 11.8 mm along the *z*-axis (*A*), a single Al (*AS*) plate (*B*) and a single Al_2O_3 (*S1*) plate (*C*).

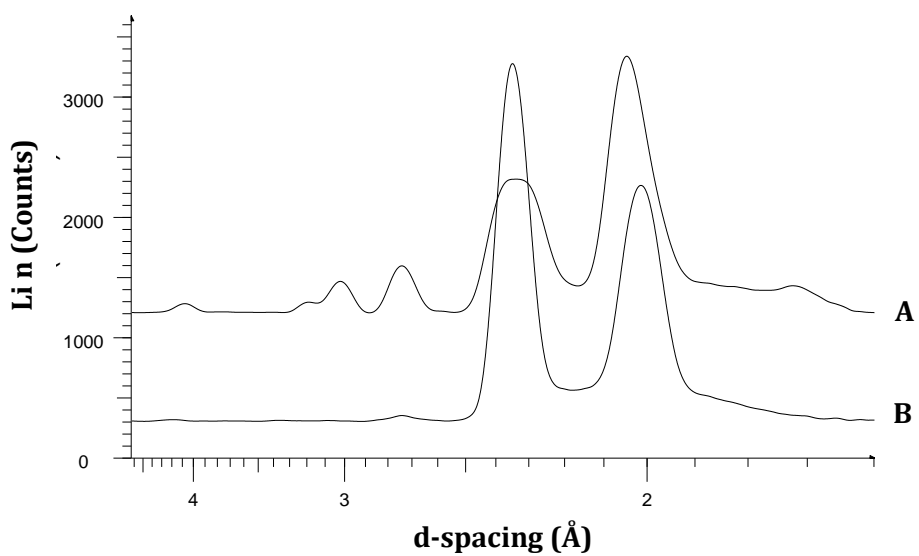


Figure B.5 Diffraction signatures from an Al_2O_3 (S1) and Al (AS) plates separated by 11.8 mm along the z-axis (A) and a single Al (AS) plate (B).

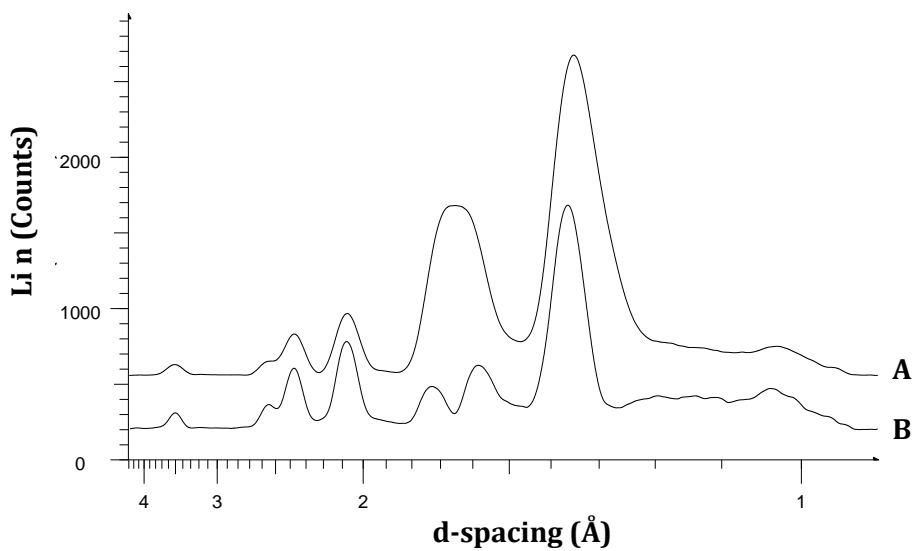


Figure B.6 Diffraction signatures from an Al_2O_3 (S1) and Al (AS) plates separated by 11.8 mm along the z-axis (A) and a single Al_2O_3 (S1) plate (B).

Appendix C CODED APERTURE

C.1 Limited area of FCG data

Table C.1 Information on the limitation of the FCG images obtained from two different primary beam annuli in terms of circular and squared area in which the diffraction data are limited to either around the centre of the image (central) or around the outer circumference of the FCG data (peripheral). The percentage of data availability with respect to the complete diffraction pattern is given.

Image index	Circular areas				Square areas			
	Peripheral		Central*		Peripheral		Central	
	mm ²	%	mm ²	%	mm ²	%	mm ²	%
0	41.03	100	41.03	100	41.03	100	41.03	100
1	40.42	98.50	33.18	80.87	40.50	98.71	37.02	90.21
2	37.46	91.30	11.63	28.34	38.43	93.7	21.90	53.38
3	34.25	83.48	7.27	17.71	36.49	88.92	12.14	29.58
4	31.21	76.07	5.00	12.19	32.85	80.07	9.25	22.55
5	6.78	16.52	0.45	1.09	26.82	65.36	7.03	17.14
6	-	-	-	-	17.65	43.00	5.00	12.19
7	-	-	-	-	3.38	8.24	2.12	5.17
8	-	-	-	-	-	-	0.42	1.03

*Presented in Figure 8.23 (Section 8.1.1.3 (b))

C.2 Increased thickness of the annulus

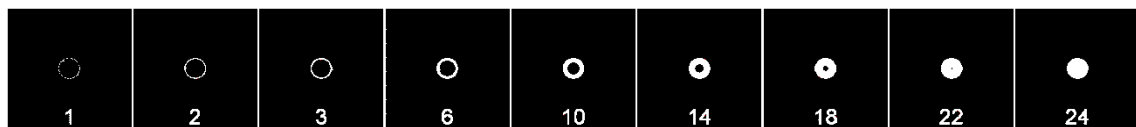


Figure C.1 Representative examples of simulated images of a series of annular apertures when the wall thickness increased to 0.03 mm (1), 0.08 mm (2), 0.13 mm (3), 0.28 mm (6), 0.48 mm (10), 0.68 mm (14), 0.88 mm (18), 1.08 mm (22) and 1.18 mm (24).

C.3 Elliptical aperture

Table C.2 Details on the ellipses employed as a primary beam indicating with x-axis as the major axis and constants (a, b) of each $ax^2 + by^2 = 1$ ellipse.

Index	a	b	Axes ratio (x:y)
ell_x1	0.100	1.032	1.15
ell_x2	0.090	0.467	1.17
ell_x3	0.077	0.256	1.2
ell_x4	0.065	0.160	1.26
ell_x5	0.055	0.111	1.32
ell_x6	0.046	0.079	1.42
ell_x7	0.040	0.063	1.57
ell_x8	0.033	0.048	1.78
ell_x9	0.029	0.040	2.37
ell_x10	0.025	0.033	3.17
ell_x11	0.022	0.028	12.48
-	-	-	-

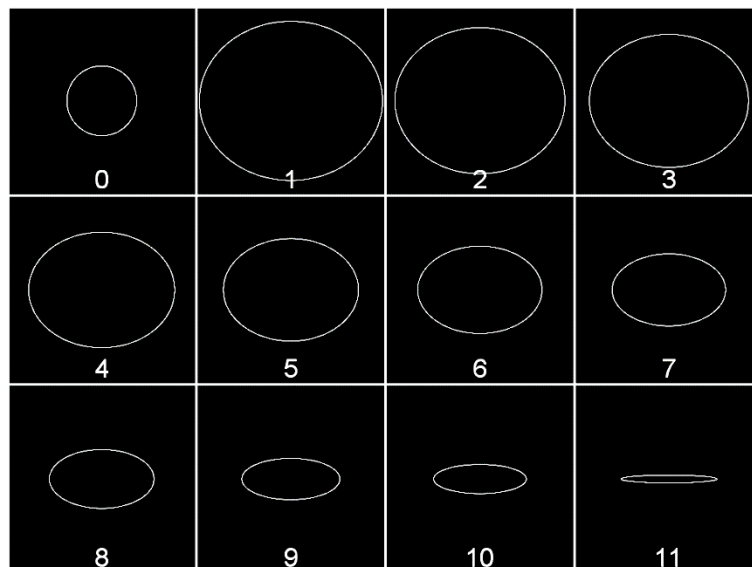


Figure C.2 Simulated images of the elliptical apertures with major axis in the x direction.

Appendix D PUBLICATIONS

Title	Discrimination of liquids by a focal construct X-ray diffraction geometry
Authors	D. Prokopiou, K. Rogers, P. Evans, S. Godber and A. Dicken
Journal	Applied Radiation and Isotopes
Date received	18 th December 2012
Date accepted	12 th March 2013

Title	X-ray diffraction with novel geometry
Authors	D. Prokopiou, K. Rogers, P. Evans, S. Godber, J. Shackel and A. Dicken
Journal	Nuclear Instruments and Methods in Physics Research A
Date received	9 th July 2013
Date accepted	30 th August 2013

Title	Fundamental parameters approach applied to focal construct geometry for X-ray diffraction
Authors	K. Rogers, P. Evans, D. Prokopiou, A. Dicken, S. Godber and J. Rogers
Journal	Nuclear Instruments and Methods in Physics Research A
Date received	13 th April 2012
Date accepted	18 th June 2012

Title	X-ray diffraction tomography employing an annular beam
Authors	P. Evans, K. Rogers, A. Dicken, S. Godber and D. Prokopiou
Journal	Optics Express
Date received	8 th April 2014
Date accepted	29 th April 2014

Title	Validation study of a ray-tracing simulator for focal construct geometry
Authors	A. Dicken, K. Rogers, S. Godber, D. Prokopiou, A. Shevchuk, G. Tranfield and P. Evans
Journal	Applied Radiation and Isotopes
Date received	10 th June 2014
Date accepted	29 th August 2014
